frontiers | Research Topics

Observation characteristics and formation mechanisms of severe weather events

Edited by
Jianhua Sun, Yanping Li, Shenming Fu
and Xiao-Ming Hu

Published in
Frontiers in Earth Science

ISSN 1664-8714
ISBN 978-2-8325-3896-8
DOI 10.3389/978-2-8325-3896-8

About Frontiers

Frontiers is more than just an open access publisher of scholarly articles: it is a pioneering approach to the world of academia, radically improving the way scholarly research is managed. The grand vision of Frontiers is a world where all people have an equal opportunity to seek, share and generate knowledge. Frontiers provides immediate and permanent online open access to all its publications, but this alone is not enough to realize our grand goals.

Frontiers journal series

The Frontiers journal series is a multi-tier and interdisciplinary set of open-access, online journals, promising a paradigm shift from the current review, selection and dissemination processes in academic publishing. All Frontiers journals are driven by researchers for researchers; therefore, they constitute a service to the scholarly community. At the same time, the *Frontiers journal series* operates on a revolutionary invention, the tiered publishing system, initially addressing specific communities of scholars, and gradually climbing up to broader public understanding, thus serving the interests of the lay society, too.

Dedication to quality

Each Frontiers article is a landmark of the highest quality, thanks to genuinely collaborative interactions between authors and review editors, who include some of the world's best academicians. Research must be certified by peers before entering a stream of knowledge that may eventually reach the public - and shape society; therefore, Frontiers only applies the most rigorous and unbiased reviews. Frontiers revolutionizes research publishing by freely delivering the most outstanding research, evaluated with no bias from both the academic and social point of view. By applying the most advanced information technologies, Frontiers is catapulting scholarly publishing into a new generation.

What are Frontiers Research Topics?

Frontiers Research Topics are very popular trademarks of the *Frontiers journals series*: they are collections of at least ten articles, all centered on a particular subject. With their unique mix of varied contributions from Original Research to Review Articles, Frontiers Research Topics unify the most influential researchers, the latest key findings and historical advances in a hot research area.

Find out more on how to host your own Frontiers Research Topic or contribute to one as an author by contacting the Frontiers editorial office: frontiersin.org/about/contact

Observation characteristics and formation mechanisms of severe weather events

Topic editors

Jianhua Sun — Institute of Atmospheric Physics, Chinese Academy of Sciences (CAS), China

Yanping Li — University of Saskatchewan, Canada

Shenming Fu — Institute of Atmospheric Physics, Chinese Academy of Sciences (CAS), China

Xiao-Ming Hu — University of Oklahoma, United States

Citation

Sun, J., Li, Y., Fu, S., Hu, X.-M., eds. (2023). *Observation characteristics and formation mechanisms of severe weather events*. Lausanne: Frontiers Media SA. doi: 10.3389/978-2-8325-3896-8

Table of contents

frontiers | Frontiers in Earth Science

TYPE Editorial
PUBLISHED 26 October 2023
DOI 10.3389/feart.2023.1308347

OPEN ACCESS

EDITED AND REVIEWED BY
Yuqing Wang,
University of Hawaii at Manoa,
United States

*CORRESPONDENCE
Shen-Ming Fu,
fusm@mail.iap.ac.cn

RECEIVED 06 October 2023
ACCEPTED 16 October 2023
PUBLISHED 26 October 2023

CITATION
Fu S-M, Huang T-T, Sun J-H and Wang Z-G (2023), Editorial: Observation characteristics and formation mechanisms of severe weather events. *Front. Earth Sci.* 11:1308347. doi: 10.3389/feart.2023.1308347

Editorial: Observation characteristics and formation mechanisms of severe weather events

Shen-Ming Fu[1]*, Ting-Ting Huang[2], Jian-Hua Sun[2] and Zhen-Guo Wang[3]

[1]International Center for Climate and Environment Sciences, Institute of Atmospheric Physics, Chinese Academy of Sciences, Beijing, China, [2]Laboratory of Cloud–Precipitation Physics and Severe Storms, Institute of Atmospheric Physics, Chinese Academy of Sciences, Beijing, China, [3]Research Institute of State Grid Zhejiang Electric Power Company, Hangzhou, China

KEYWORDS

mesoscale, heavy rainfall, typhoon, strong winds, severe weather, vortex

Editorial on the Research Topic
Observation characteristics and formation mechanisms of severe weather events

Under global warming, disastrous weathers (e.g., rainstorms, thunderstorms, high winds, heat waves, etc.) show a notable increasing trend in their occurrence frequency and social impacts (IPCC, 2023), particularly in China (Song, 2018). In order to further the understanding of disastrous weathers and to enhance the capability of disaster prevention and mitigation, we organized this Research Topic. The primary purposes of this Research Topic are to unravel the observation characteristics of severe convective weather events; to clarify the formation mechanisms of convective systems, special heavy rainfall and thunderstorm high-wind events; to develop forecast methods of severe convective weather events; and to show the climate variability of severe weather events. All these are currently the most concerned scientific issues in the research field of severe weathers (Markowski and Richardson, 2010; Sun et al., 2019; Luo and Coauthors, 2020; Cui et al., 2021; https://public.wmo.int/en/programmes/world-weather-research-programme). There is a total of 12 published papers in this Research Topic, covering almost all the primary research objectives mentioned above. The new findings from these researches would contribute to an in-depth understanding of the severe weather events.

For the observation characteristics, Chen et al. explored key microphysics features of the outer rainband of Typhoon "Mekkhala" by using the dual-polarization radar. They pointed out that the precipitation below the freezing level was mainly composed of moderate to light raindrops, and large raindrops mainly appeared in the mid to upper levels. Huang et al. analyzed the spatial distribution of the rainstorms associated with the Northeast China cold vortices based on 20-year station observations. They determined five typical types of events by using the Self-Organizing Maps method, and found that different types were accompanied by distinctive large-scale circulation backgrounds, thermodynamic and moisture conditions. These findings based on observational data filled the knowledge gaps in existing researches.

FIGURE 1
Urbanization enhances the tornado potential through two pathways: 1) enhanced low-level storm-relative streamwise horizontal vorticity (SRSHV) feeding updrafts due to stronger east-west pressure perturbation gradient as a result of faster, stronger storm outflow, and 2) intensified near-surface SRSHV which is more aligned with the easterly storm-relative inflow because of stronger cold pool front which increases southeasterly winds. Both pathways are associated with a stronger storm at the initial and developing stages resulting from the Kansas City urbanization. Derived from Fan et al.

For the mechanisms, Fan et al. discussed the impacts of Kansas City urbanization on the tornado potential. By using sensitivity simulations, they found that urbanization might enhance tornado potential by strengthening the low-level streamwise vorticity in the storm inflow region, and intensifying near-surface horizontal vorticity near the boundary of the forward-flank cold pool (Figure 1). Li et al. analyzed a trough which induced a catastrophic rainstorm in Kyushu, Japan. They found that, the trough was transformed from a Tibetan Plateau vortex, and the horizontal potential-vorticity flux convergence acted as the primary contributor to the trough's maintenance and eastward displacement. Yin et al. examined an eastward-moving heavy rainfall event in South China in winter and discovered that the Rossby wave train propagating along the subtropical westerly jet played an important role in "pushing" the eastward displacement of the rainfall event. Yang et al. explored the correlation between extreme precipitation over the middle and lower reaches of the Yangtze River and their atmospheric circulations, and found that, the Western Pacific Subtropical High showed the most significant impact, and the South China Sea high ranked the second. Tang et al. analyzed the moisture transport for the famous "7.20" rainstorm event in Henan, China. By separating the effects from tropical cyclones one by one, they found that In-fa dominated the main water vapor transport for the rainfall in the meridional direction, Cempaka mainly affected intermediate moisture transport, and the Tibetan Plateau exerted a modulation effect on the remote moisture transport associated with the two typhoons. Airflow decomposition (Ma et al.) and theoretical derivation methods (Zhou et al.) were applied in the numerical simulation analyses of the snowstorms and deep convections in Xinjiang Province, respectively. Of these, Ma et al. found that the flow-around and flow-over components from the near-surface wind field resulted in symmetric instability and stratified instability, which played a dominant role in moisture convergence and snowfall triggering, respectively. Zhou et al. pointed out that, the three-dimensional divergence showed a better correlation with precipitation, and the local change in pressure was affected mainly by the three-dimensional divergence forcing term. Three-dimensional convergence in the lower layers converted to divergence with height, leading to air mass loss in the upper layers. The air mass redistributed vertically owing to the positive vertical gradient of three-dimensional divergence. This motivated the upward vertical pressure gradient force, which was highly correlated with the vertical velocity. All these new findings contributed to render a more comprehensive understanding of the formation mechanisms of the severe weathers.

For the forecast methods, Huang and Bai evaluated the performances of seven planetary boundary layer schemes in reproducing the low-level urban atmosphere over the Greater Bay Area, South China, and they found that the MRF scheme showed an overall better performances than all the other schemes. This provided a useful reference for the forecasts of severe weathers in this region. Li et al. conducted a series of simulations by using 72 different physical parameterization scheme combinations. Their purpose was to determine the optimal cumulus convection scheme and the land surface process schemes in the upper reaches of the Yangtze River Basin by using the RegCM4 model. They pointed out that, the Kain-Fritsch scheme and the Biosphere-Atmosphere Transfer Scheme could better reproduce the precipitation and temperature characteristics of the targeted region than the remaining schemes. This provided a baseline for the localization of the RegCM4's parameterization schemes in China. Li et al. contrasted and analyzed the differences between the two-moment bulk scheme (BULK) and the spectral bin microphysics scheme (BIN) in forecasting the precipitation, radar reflectivity, and cloud microphysical processes for a heavy snowfall event in Beijing during the 2022 Winter Olympics. They found that, while the 24-h accumulated precipitation in both simulations was lower than the observation, the BIN simulation was closer to the observation, in terms of the trend of precipitation rate and radar reflectivity during the period of heavy precipitation. This provided useful information for forecasting the snowfall in China during the cold season.

For the climate variabilities, Yang et al. analyzed the observed precipitation data from 1979 to 2015, and found that, an overall increase appeared in the frequency, intensity, and duration of precipitation in the middle and lower Yangtze River basin. The

areas with large extreme precipitation indices are mainly concentrated in the Poyang Lake basin. These results would provide effective reference bases for policymakers.

Overall, the severe weathers pose a significant threat to human society (IPCC, 2023), and how to cope with disastrous weathers is a common challenge faced by all meteorological society (https://www.cma.gov.cn/2011xwzx/2011xmtjj/202205/t202205264856882.html). Our Research Topic has provided some useful results for furthering the studies on severe weathers, however, as the spatiotemporal scales of these systems are relatively small, and the physical mechanisms governing their formations are quite complicated, we encourage scholars in relevant fields to conduct more studies in the future, which would contribute to reach a more comprehensive understanding of the severe weathers.

Author contributions

S-MF: Conceptualization, Data curation, Formal Analysis, Funding acquisition, Investigation, Project administration, Supervision, Validation, Writing–original draft, Writing–review and editing. T-TH: Writing–original draft, Writing–review and editing. J-HS: Supervision, Writing–review and editing. Z-GW: Writing–original draft.

Funding

The authors declare that this study received funding from Science and Technology Foundation of State Grid Corporation of China. The funder had the following involvement in the study: study design; and the decision to submit it for publication.

Conflict of interest

Author Z-GW was employed by Research Institute of State Grid Zhejiang Electric Power Company.

The remaining authors declare that the research was conducted in the absence of any commercial or financial relationships that could be construed as a potential conflict of interest.

Publisher's note

References

Cui, X. Y., Chen, M. X., Qin, R., and Han, L. (2021). Research advances in the convective initiation mechanisms. *Meteor. Mon.* 47, 1297–1318. doi:10.7519/j.issn.1000-0526.2021.11.001

IPCC (2023). in *Climate change 2023: synthesis report. Contribution of working groups I, II and III to the sixth assessment report of the intergovernmental panel on climate change [core writing team*. Editors H. Lee and J. Romero (Geneva, Switzerland: IPCC), 35–115. doi:10.59327/IPCC/AR6-9789291691647

Luo, Y. L., Sun, J., Li, Y., Xia, R., Du, Y., Yang, S., et al. (2020). Science and prediction of heavy rainfall over China: research progress since the reform and opening-up of new China. *J. Meteor. Res.* 34, 427–459. doi:10.1007/s13351-020-0006-x

Markowski, P. M., and Richardson, Y. P. (2010). *Mesoscale meteorology in midlatitudes*. Hoboken, NJ: Wiley–Blackwell, 407.

Song, L. C. (2018). *Yearbook of meteorological disasters in China*. China Meteorological Press, 229.

Sun, J.-H., Zhang, Y.-C., Liu, R. X., Fu, S. M., and Tian, F. Y. (2019). A review of research on warm-sector heavy rainfall in China. *Adv. Atmos. Sci.* 36, 1299–1307. doi:10.1007/s00376-019-9021-1

frontiers | Frontiers in Earth Science

TYPE Original Research
PUBLISHED 03 January 2023
DOI 10.3389/feart.2022.1066070

OPEN ACCESS

EDITED BY
Ping Huang,
Institute of Atmospheric Physics (CAS), China

REVIEWED BY
Shenming Fu,
Institute of Atmospheric Physics (CAS), China
Jie Cao,
Nanjing University of Information Science and Technology, China

*CORRESPONDENCE
Xiaopeng Cui,
xpcui@mail.iap.ac.cn

SPECIALTY SECTION
This article was submitted to Atmospheric Science, a section of the journal Frontiers in Earth Science

RECEIVED 10 October 2022
ACCEPTED 18 November 2022
PUBLISHED 03 January 2023

CITATION
Huang L, Cui X, Chen L, Zou Q and Yang Y (2023), Objective circulation classification of rainstorm days associated with Northeast China cold vortexes in the warm seasons of 2000–19.
Front. Earth Sci. 10:1066070.
doi: 10.3389/feart.2022.1066070

Objective circulation classification of rainstorm days associated with Northeast China cold vortexes in the warm seasons of 2000–19

Lijun Huang[1,4], Xiaopeng Cui[1,2,3,4]*, Liqiang Chen[3], Qiangli Zou[1,4] and Yuting Yang[1,4]

[1]Key Laboratory of Cloud-Precipitation Physics and Severe Storms, Institute of Atmospheric Physics, Chinese Academy of Sciences, Beijing, China, [2]Collaborative Innovation Center on Forecast and Evaluation of Meteorological Disasters (CIC-FEMD), Nanjing University of Information Science & Technology, Nanjing, China, [3]Institute of Atmospheric Environment, China Meteorological Administration, Shenyang, China, [4]University of Chinese Academy of Sciences, Beijing, China

This study conducts objective circulation classifications of rainstorm days associated with Northeast China Cold Vortexes (NECVs) in the northeast of China (NEC) during the warm seasons (May–September). To determine the optimal method and number of types, the performances of ten objective circulation classification methods are first evaluated by several evaluation indexes. Self-Organizing Maps method is then used as the optimal method to classify rainstorms into five types. The results show that the different synoptic circulation patterns are accompanied by distinctive large-scale circulation backgrounds, precipitation characteristics, thermodynamic and moisture conditions. In type 1, the strong western Pacific subtropical high extends north to connect with the mid-latitude ridge in the east of the NEC, and a shallow trough lies in the west of the NEC. This configuration brings the most daily and hourly mean precipitation of all types. A low-pressure anomaly with an obvious trough controls the NEC in type 2, which has a higher frequency. In type 3, the low-pressure anomaly shrinks to the south of the NEC, and the NEC is controlled by the cut-off low vortex. Type 4 has the strongest hourly precipitation and features a meridional high-low-high pressure anomaly, and the narrow zonal low-pressure anomaly is in the NEC. Two low-pressure anomalies and a westerly trough can be found in type 5 and are distributed in a southwest-northeast orientation. These synoptic circulation patterns and the corresponding spatial distribution of rainstorm-day precipitation indicate that the objective circulation classification is effective in helping understand the large-scale circulation and precipitation characteristics associated with NECVs.

KEYWORDS

objective circulation classification, rainstorm day, northeast cold vortexes, Northeastern China, self-organizing maps method

1 Introduction

The Northeast China Cold Vortex (NECV) is one of the major high-impact weather systems in the northeast of China (NEC) (Tao, 1980). NECVs are usually persistent and quasi-stationary and often cause severe convective weather, such as rainstorms and floods in the NEC (Zheng et al., 1992; Sun et al., 1994; Zhao and Sun, 2006). Given the significant impact of NECVs, numerous relevant studies have been carried out, including the identification and tracking of NECVs (Sun et al., 1994; Hu et al., 2010; Wang et al., 2012), climatical characteristics of NECVs (Zhang et al., 2008; Hu et al., 2010), mechanisms of occurrence and development of NECVs (Zhong, 2011; Fu and Sun, 2012), and the mesoscale features of NECVs (Chen et al., 2005; Zhong et al., 2013).

The rainstorm is caused by the interaction of multiple-scale atmospheric circulation systems (Tao, 1980). NECVs can provide favorable large-scale circulation conditions for the occurrence and development of rainstorms in the NEC. Thus, it is essential to classify the circulation of the rainstorms associated with NECVs, which can help understand the large-scale circulation background and the formation mechanism of the rainstorm, improving rainstorm forecasting. Huth et al. (2008) characterized circulation classification methods into three basic types: subjective (also called manual), mixed (hybrid), and objective (computer-assisted, automated). With the assistance of computers and objective classification technology, the objective method has been developed based on statistical theory, providing classification for large samples using consistent standards. It compensates for some limitations of the subjective and mixed classification methods, such as subjectivity, non-repeatability, and extremely high time consumption. As a result, objective classification methods have been widely applied in synoptic and climatological studies (Schmutz and Wanner, 1998; Liu et al., 2015; Cahynova and Huth, 2016; Zhang et al., 2018; Zhao et al., 2019; Wang et al., 2021).

Some studies have been conducted to classify NECV systems. Based on the generation locations of NECVs, Sun et al. (1994) grouped NECVs into "south vortex, middle vortex, and north vortex." Xie and Bueh (2015) used a rotating EOF analysis method by ridges (or blocks) to classify the NECVs into four types. Fang et al. (2021) divided NECV activity paths into four types by applying machine learning methods. The aforementioned classification studies focused on NECVs but seldom considered the relationship between NECVs and rainstorms. More attention should be focused on the NECVs that cause rainstorms. It is of great significance to classify rainstorms associated with NECVs by objective classification methods. In addition, previous studies have pointed out that there is no universal classification method available for all regions and climate variables. Classification performance significantly varies due to many factors, such as regions, periods, and variables

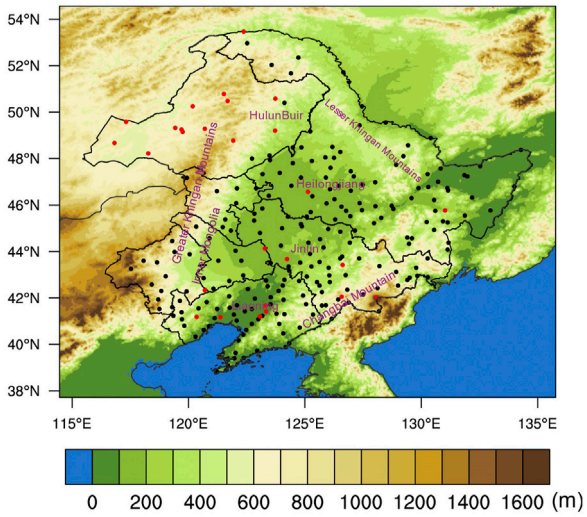

FIGURE 1
Spatial distribution of AWSs in the NEC, superimposed with topographic height (units: m). The black dots denote the AWSs that pass quality control, and the red dots denote the AWSs that fail quality control.

(Beck and Philipp, 2010; Casado and Pastor, 2016). To further study the relationship between synoptic circulation and rainstorms associated with NECVs, it is necessary to assess the ability of different classification methods.

Based on previous research, we focus on the classification of large-scale circulation during the rainstorms associated with NECVs in the warm seasons (May–September) from 2000 to 2019. First, multiple objective classification methods and the number of types are evaluated. The method and the number of types with the best performance are selected and employed in the following research. In addition, the anomaly has been reported as a better indicator for rainstorms compared with observation (Qian et al., 2012). Therefore, the 500 hPa geopotential height anomaly is selected as the objective classification variable in this study. Section 2 briefly introduces the data, objective circulation methods, and evaluation measures. The results of the objective circulation method, the precipitation characteristics, and the water vapor conditions of rainstorms associated with NECVs are presented in Section 3. Conclusion and relevant discussions are given in Section 4.

2 Data and evaluation of objective circulation methods

2.1 Data

The NECV dataset during 2000–2019 is from Huang and Cui (2022).

TABLE 1 Classification methods compared in this study.

Group	Classification name	Abbreviation	Key Reference
PCA	T-mode PCA obliquely rotated	PCT	Huth (1993)
	T-mode PCA orthogonally rotated	PTT	Philipp (2009)
LDR	Lund-method	LND	Lund (1963)
	Kirchhofer-method	KIR	Kirchhofer (1974)
HCL	Hierarchical cluster analysis	HCL	Murtagh (1985)
OPT	k-means with dissimilar seeds	CKM	Enke and Spekat (1997)
	Partitioning around medoids	KMD	Kaufman and Rousseeuw (1990)
	Self-organizing maps	SOM	Michaelides et al. (2007)
RAN	Random	RAN	Philipp et al. (2014)
	Randomcent	RAC	Philipp et al. (2014)

The precipitation data are derived from the hourly precipitation dataset of national surface automatic weather stations (AWSs) in the warm seasons (May–September) from 2000 to 2019 provided by the China Meteorological Administration (CMA). Strict quality controls, including climatological extremes, internal consistency, and temporal consistency, have been performed for the dataset (Ren et al., 2015). To avoid the impact of missing values, the AWS will be excluded if the rate of missing values exceeds 5%. Figure 1 shows the spatial distribution of 220 trusted national AWSs (black dots) in the NEC after the quality control of time continuity. Considering that there are only four trusted national AWSs in the HulunBuir region and all of them are distributed in the lower altitude region in the east of HulunBuir, they cannot represent the characteristics of precipitation of the whole region. Thus, all AWSs in HulunBuir are removed, and 216 AWSs in the NEC are finally selected for the following analysis.

A rainstorm day is defined as a day in which the accumulated precipitation is greater than or equal to 50 mm from 0800 local standard time (LST, LST = UTC + 8 h) to 0800 LST of the next day for an AWS. A rainstorm day associated with NECVs is defined as a rainstorm day occurring during the influence period of NECVs. A total of 306 rainstorm days associated with NECVs are identified during the warm seasons of 2000–2019 for the study of objective circulation classification.

NCEP/NCAR reanalysis data (Kalnay et al., 1996) with a horizontal resolution of $2.5^{\circ} \times 2.5^{\circ}$ from 1991 to 2020 are used for the objective classifications and subsequent synthetic analysis. The variables include geopotential height, wind, relative humidity, and specific humidity.

2.2 The evaluation of objective circulation classification methods

Cost733class (Philipp et al., 2014) is a widely used classification software. There are five groups of objective classification methods in the Cost733class, including classifications based on principal component analysis (PCA), classifications using the leader algorithm (LDR), hierarchical cluster analysis (HCL), optimization algorithms (OPT), and random classifications (RAN). In this study, ten objective circulation classification methods are utilized and evaluated (Table 1).

PCA (or empirical orthogonal functions) aims to select principal components (PCs) by decomposition and then assign each case to a PC according to some rule. Both PCT (Huth, 1993) and PTT (Philipp, 2009) are in T-mode, but PCT uses oblique rotation while PTT uses orthogonal rotation.

Methods based on LDR can also be called "correlation-based" methods. The main idea is to find leader patterns by considering the number of elements that are similar to the potential leader pattern exceeding a certain threshold. In LND (Lund, 1963), at first, set Pearson correlation coefficient ($r > 0.7$) to determine leader patterns, and then assign each case to the type of the most similar leader. KIR (Kirchhofer, 1974) is similar to LND but takes similarity in all parts of the map into account. And the threshold in KIR is usually 0.4.

HCL (Murtagh, 1985) is also a widespread classification method that first splits up all cases into two types according to some criterion. On a second hierarchy level, it splits up one of these types again into two types, and so on.

OPT works non-hierarchically and can be considered a standardized method. The aim of OPT is to minimize within-type variability and achieve optimal partitioning. CKM (Enke and Spekat, 1997) modifies the minimum distance to produce the seeds for k-means clustering. KMD (Kaufman and Rousseeuw, 1990) is similar to k-means, but it employs given data points as centers of the clusters. SOM (Michaelides et al., 2007) arranges types defined by their features (grid point values) in a structure where similar types are adjacent to each other (a map).

RAN (Philipp et al., 2014) randomly selects any arbitrary number as type number for each case and chooses the best result according to the explained cluster variance after 1,000 iterations.

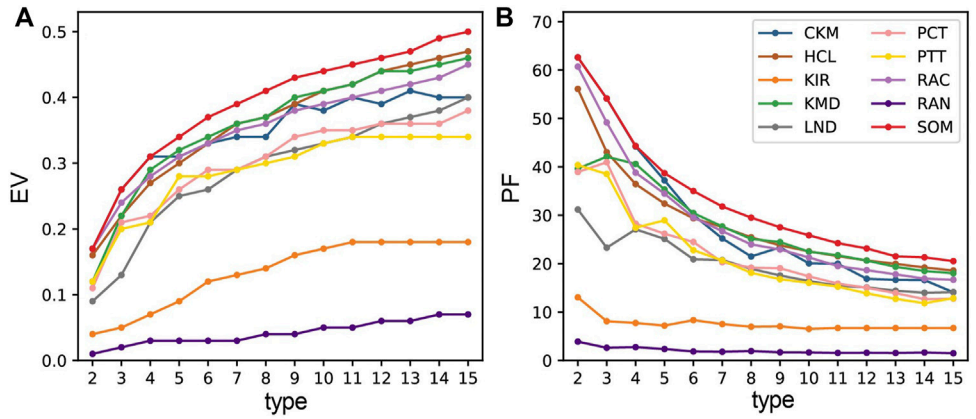

FIGURE 2
Evaluation results of different objective classification methods by line charts. **(A)** EV; **(B)** PF.

RAC (Philipp et al., 2014) is similar to RAN, except for any arbitrary case used as a centroid for each type. All the other cases are then assigned to these centroids by the minimum Euclidean distance.

In this study, the 500 hPa geopotential height anomaly at 08 LST is used to classify the circulation background of rainstorm days associated with NECVs in the warm seasons from 2000 to 2019. The region is set as 90–150°E, 20–70°N. The geopotential height anomaly is calculated by the 500 hPa geopotential height minus the monthly mean of 30 years (1991–2020).

Generally, a better objective classification method should achieve smaller within-type differences and bigger between-type differences. The following evaluation indicators are used in this study to obtain the optimal objective classification method and the corresponding number of types.

The first selected evaluation index is the explained variation (EV), which can be used to quantify the proportion of variance of the dependent variable as well as to represent within-type differences (Buishand and Brandsma, 1997; Beck and Philipp, 2010; Casado et al., 2010). EV can be calculated as follows:

$$EV = 1 - \frac{WSS}{TSS} \tag{1}$$

$$WSS = \sum_{j=1}^{k}\sum_{i=1}^{n}\left(y_{ji} - \bar{y}_j\right)^2 \tag{2}$$

$$TSS = \sum_{i=1}^{n}\left(y_i - y\right)^2 \tag{3}$$

WSS and TSS represent the within-type sum of squares and the total sum of squares, thereby taking into account the number of all elements (n) and types (k), respectively. $\bar{y}_j$ denotes the mean value for elements of each type ($1, \ldots, k$) and y is the mean value for all elements. EV ranges from 0 to 1, with a value closer to 1 indicating better quality of classifications.

The second evaluation index is the pseudo-F statistic (PF) (Calinski and Harabasz, 1974; Broderick and Fealy, 2015), which is the ratio of the between-type sum of squares (BSS) to WSS, and its formula is:

$$PF = \frac{BSS/(k-1)}{WSS/(n-k)} \tag{4}$$

$$BSS = \sum_{j=1}^{k}\left(\bar{y}_j - y\right)^2 \tag{5}$$

The larger PF implies bigger between-type differences and better quality of the classification.

Figure 2 shows the evaluation results of different objective classification methods using EV and PF, respectively. Except for KIR and RAN, other classification methods exhibit better ability for classification. Among all the classification methods, SOM performs best in both EV and PF. However, when the number of types is increasing, EV of all the classification methods shows a tendency to increase. It indicates that the within-type differences decrease, and the proficiency of classification improves at the same time. The result of PF shows opposition compared with EV. Based on the evaluation results of EV and PF, SOM can be decided as the optimal classification method.

For the optimal classification number of types based on SOM, a new evaluation index (EVPF) is created by considering both EV and PF. First, to eliminate the dimensional influence between EV and PF, min-max normalization is performed on these two indices:

$$X' = \frac{X - X_{min}}{X_{max} - X_{min}} \tag{6}$$

In which X' represents the normalized result of EV or PF when X represents EV or PF, X_{min} and X_{max} are the minimum and maximum values of EV or PF, respectively.

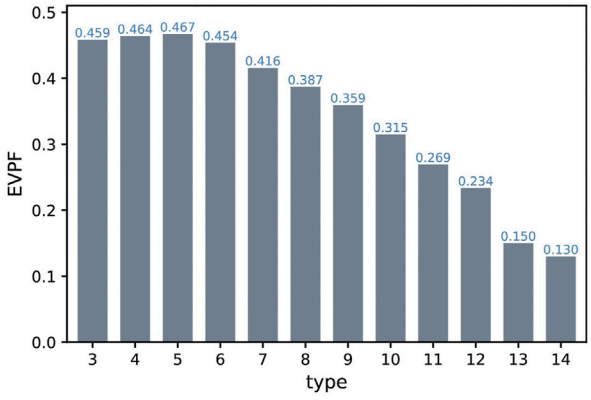

FIGURE 3
Evaluation of SOM method using EVPF.

The new evaluation index can be expressed as:

$$EVPF = \sqrt{EV' \times PF'} \tag{7}$$

EVPF ranges from 0 to 1. A larger EVPF value indicates better classification quality.

With min-max normalization, EVPF equals 0 when the number of types is 2 or 15. Therefore, Figure 3 presents the evaluation results of EVPF for the optimal classification method (SOM), with the number of types between 3 and 14. It can be found that SOM shows a better classification performance when the number of types is between three and six. The highest value of EVPF is 0.467 when the number of types is five. If the number of types is larger than five, the quality of classification grows worse.

Based on the above results, SOM is finally determined as the optimal objective circulation classification method to classify the rainstorm days associated with NECVs in the

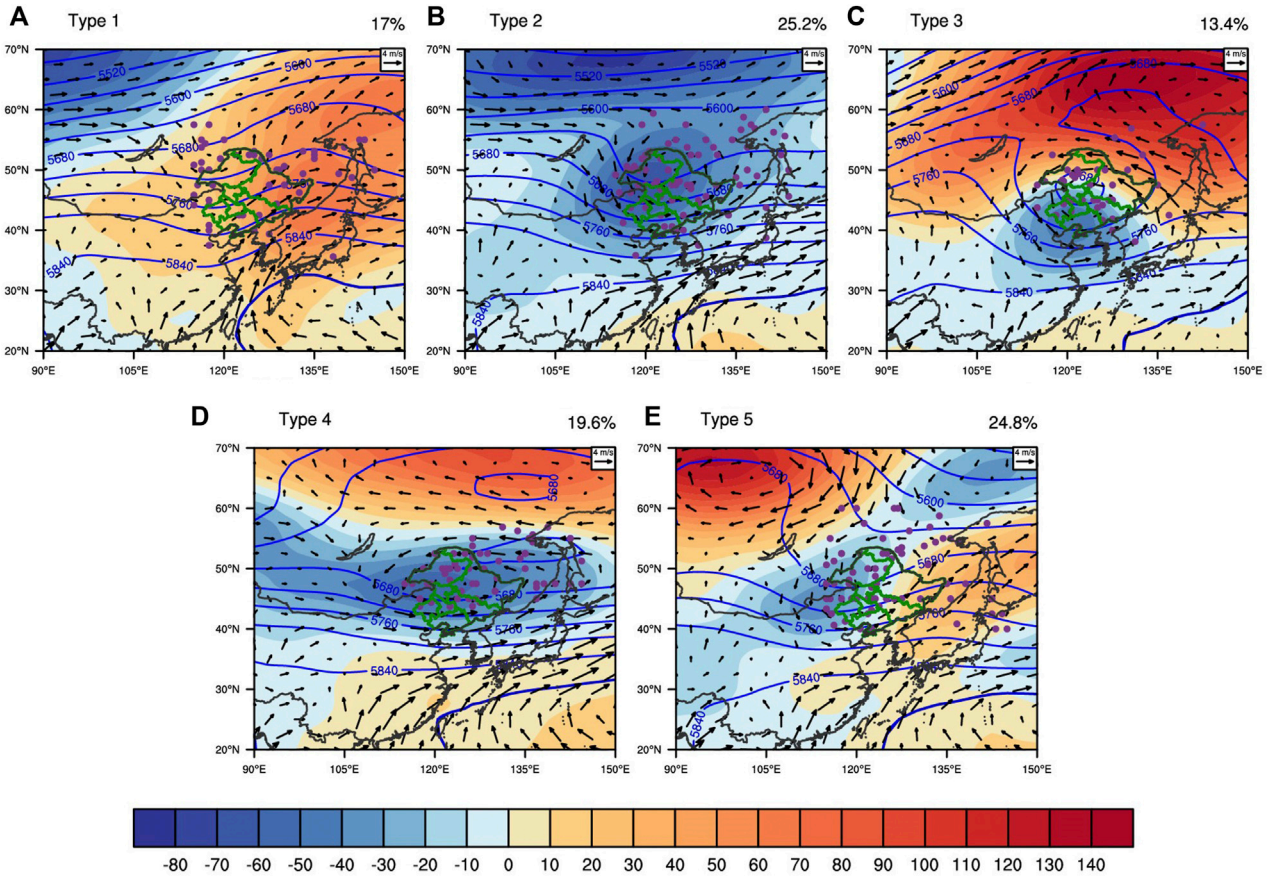

FIGURE 4
Geopotential height (solid blue lines, units: gpm), geopotential height anomaly (shaded, units: gpm) at 500 hPa, and wind at 850 hPa (arrow, units: m/s) under five types of synoptic circulation patterns **(A-E)** obtained by SOM. The percentages for each circulation type are shown on the top right. Composite fields for the rainstrom days associated with NECVs of each type are shown in FIGUREs (similarly to Figures 8, 9). The purple dots represent the daily mean locations of the NECVs, and the green map denotes the NEC.

warm seasons from 2000 to 2019, and the optimal classification number is five.

3 Results

3.1 Circulation patterns of rainstorm days associated with Northeast China cold vortexes

Figure 4 shows the five types of rainstorm days associated with NECVs in the NEC over the warm seasons from 2000 to 2019 based on the 500 hPa geopotential height anomaly at 08 LST by SOM.

Type 1 accounts for about 17% (Figure 4A). In this type, the western Pacific subtropical high (WPSH) extends west to the east coast of Taiwan Island and north to the southwest coast of Japan, which is connected to the mid-latitude ridge in the east of the NEC. In addition, the centers of the high-pressure anomalies are located in the eastern part of the NEC and East Siberia. In the northwest of Lake Baikal, there is a low-pressure anomaly, and a mid-latitude westerly trough is in the west of the NEC. The mean intensity of NECVs is the weakest (5,638 gpm) and the mean size is also the smallest (766 km) of all types.

Type 2 accounts for about 25.2%, which is the majority (Figure 4B). Except for the region where the WPSH is occupied, the other region of this type is controlled by the low-pressure anomaly, and the two centers of the low-pressure anomalies at 500 hPa are located in the NEC and its north. There is an obvious trough in the NEC. Compared with type 1 (Figure 4A), the WPSH retreats southeasterly. NECVs of this type have the strongest mean intensity (5,575 gpm) and their mean size (856 km) is larger than that of type 1.

The proportion of type 3 is the least of all five types, at roughly 13.4% (Figure 4C). In this type, the region north of 45°N is controlled by a strong high-pressure anomaly. The low-pressure anomaly shrinks to the south of the NEC, and the NEC is controlled by the cut-off low vortex. Compared with the above two types, the WPSH retreats further to the southeast. The mean intensity of NECVs (5,635 gpm) is similar to that of type 1, while the mean size (1,014 km) is the largest.

Type 4 accounts for nearly 19.6% of the total (Figure 4D). The high-pressure and low-pressure anomalies are distributed alternately from north to south. The center of the low-pressure anomaly is located in the west of the NEC. The WPSH at 500 hPa is the most westward of these five types, reaching the Taiwan Strait. The mean intensity of NECVs (5,587 gpm) is a little weaker than that of type 2, with the mean size (889 km) larger than both type 1 and 2.

Type 5 accounts for about 24.8% (Figure 4E). The two low-pressure anomalies are distributed southwest to northeast, with their centers located in the west of the NEC and East Siberia, respectively. A northeast-southwest trough line can be found in the westerly trough, and the WPSH at 500 hPa is similar to that of type 2. The mean intensity of NECVs ranks third (5,601 gpm) and the mean size (892 km) is similar to that of type 4.

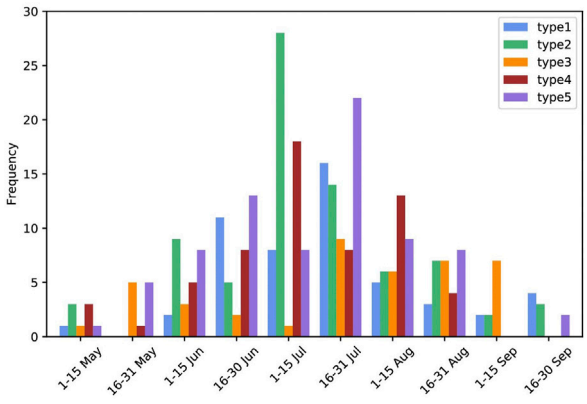

FIGURE 5
Semi-monthly variation of the frequency of rainstorm days associated with NECVs under five types of synoptic circulation patterns.

The wind at 850 hPa of each type corresponding to NECV systems presents cyclonic vortexes except for type 1, where there is a deep low trough. However, the morphology, size, and location of the cyclonic vortexes of each type at 850 hPa are slightly different (Figure 4).

It is observed in Figure 4 that the large-scale circulation backgrounds of rainstorm days associated with NECVs under different types present distinct discrepancies. Different large-scale circulation backgrounds can lead to differences in water vapor transport and convergence, as well as different precipitation characteristics of rainstorms associated with NECVs.

3.2 Precipitation characteristics in different circulation patterns

Rainstorm days associated with NECVs frequently occur from June to August, especially in July (132 times), accounting for about 43% of the total (not shown). Figure 5 further presents the semi-monthly variation of the frequency of rainstorm days associated with NECVs under different synoptic circulation patterns in the warm seasons during 2000–2019. Rainstorm days associated with NECVs in type 1 mainly occur in the second half of July and the second half of June. The frequency of rainstorm days associated with NECVs in type 2 peaks in the first half of July at 28, followed by the second half of July (14 times), while the frequencies in other periods of the warm seasons are all less than 10. Type 3 is mostly in the second half of July to the first half of September, while type 4 predominantly appears from June to August, especially in the first half of July and August. Rainstorm days associated

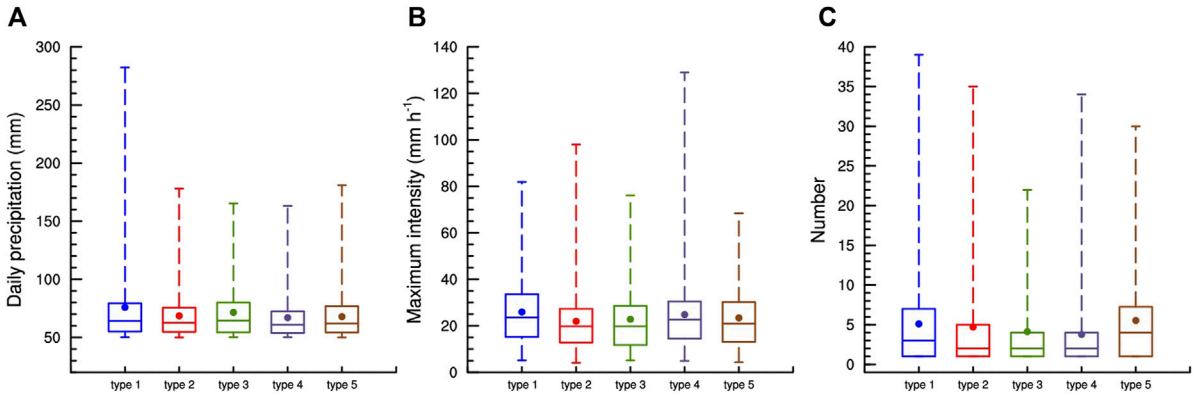

FIGURE 6
Box-and-whisker plots of daily accumulated precipitation **(A)**, units: mm, maximum hourly precipitation **(B)**, units: mm/h, and the number of AWSs reaching rainstorm level **(C)** in a rainstorm day associated with the NECV under five types of synoptic circulation patterns. The highest line denotes the maximum and the lowest line denotes the minimum. The uppermost border of boxes denotes the 75% percentile and the lowermost border denotes the 25% percentile; medians and mean values are denoted by the black solid line and the solid dot in boxes, respectively.

with NECVs in type 5 are more frequent in the second half of July, which ranks second only to type 2 in the first half of July.

In different synoptic circulation patterns, the daily precipitation characteristics of rainstorms associated with the NECVs in the warm seasons differ dramatically (Figure 6). Under the control of NECVs, rainstorms occur in the NEC with strong local characteristics (Bai andJin, 1993), which can also be found in Figure 6C. For type 1 and 5, the mean number of AWSs reaching the rainstorm level is about five in a rainstorm day, which is more than that of other types. The mean daily precipitation of rainstorm days associated with NECVs in type 1 is the largest among all five types, reaching 76 mm. The extreme value exceeds 280 mm/24 h and hits the level of an extremely heavy rainstorm, while the extremes of daily precipitation of other types are all less than 200 mm. Meanwhile, the mean hourly maximum of this type is more than 25 mm/h, which is stronger than the others. However, the hourly extreme of rainfall on rainstorm days associated with NECVs appears in type 4, reaching about 130 mm/h. Note that in type 1, the high-pressure anomaly hinders the upstream NECV from moving to the east (Figure 4A). This configuration is favorable for water vapor transport to the NEC and results in more daily precipitation and large-scale rainstorms (Figures 6A,C). A similar configuration of the high-pressure anomaly block can also be found in type 5 (Figures 4E, 6C). Moreover, type 4 frequently occurs in the first half of July and the first half of August (Figure 5), when the WPSH is active and extends most westward among all types. The NEC of this type is in the narrow zonal low-pressure anomaly with a little stronger NECVs (Figure 4D). It is favorable to the eastward movement of the low-value systems in the upstream area of the NEC, further leading to extreme hourly precipitation (Figure 6D). In addition, the maximum hourly precipitation in type 2 can reach 100 mm/h (Figure 6B). The low-value system is also active in mid and high latitudes, and the mean intensity of NECVs is the strongest. Similar to type 4, the NEC is also mainly controlled by a low-pressure anomaly (Figure 4B), which is also conducive to the occurrence of stronger hourly precipitation (Figure 6B).

The spatial distribution of accumulated precipitation on rainstorm days associated with NECVs in the warm seasons during 2000–2019 demonstrates remarkable non-uniformity and differences under different synoptic circulation patterns (Figure 7). In addition, the spatial distribution of the frequency of rainstorms shows consistencies with accumulated precipitation (not shown). The rainstorms mostly concentrate near Changbai Mountain and the narrow northeast plain regions in the middle of Liaoning Province, which reflects the effect of topography on the rainstorms. Rainstorms of type 1 mainly occur in the central plain of Liaoning province and central Jilin Province (Figure 7A). The extreme precipitation center of type 2 is mostly located near Changbai Mountain, especially in the southern part of Changbai Mountain in Liaoning Province (Figure 7B). The accumulated precipitation of rainstorms in type 3 and 4 is weaker than that of other types, and the precipitation center in type 3 is in the southwest of Changbai Mountain (Figure 7C). Unlike in other types, the precipitation centers in type 4 are scattered around the topography (Figure 7D). The extreme precipitation centers of type 5 are found near Changbai Mountain and the coastal areas in the southeast of Liaoning Province. The sub-extreme center is distributed in the northwest of Heilongjiang Province where Greater and Lesser Khingan Mountains intersect (Figure 7E).

Previous research has revealed that the local topography of the NEC has a great impact on the circulation and rainfall of NECVs (Wang and Xie, 1994; Zhong, 2011). Moreover, our study also shows that the interaction of local topography and different

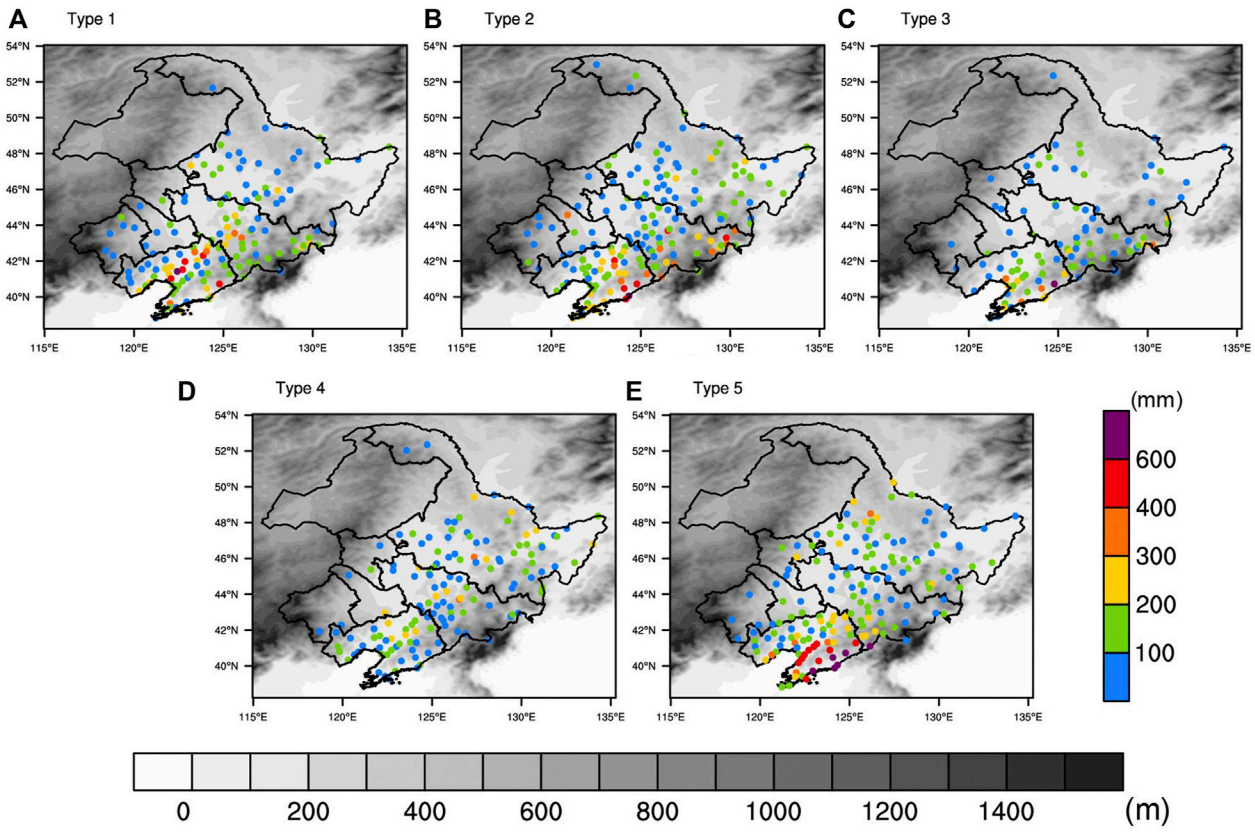

FIGURE 7
Spatial distribution of accumulated precipitation (units: m) of rainstorm days associated with NECVs under five types of synoptic circulation patterns **(A-E)** in the warm seasons from 2000 to 2019, superimposed with topographic height (units: m).

large-scale circulations can lead to different water vapor transport and convergence ascending processes, which can partially explain the unique precipitation characteristics of different circulation types.

3.3 Thermodynamic and moisture conditions during rainstorm days in different circulation patterns

In type 1 (Figure 8A), a low-pressure vortex center at 925 hPa is located in the northwest NEC, and there is a positive equivalent potential temperature (θ_e) anomaly greater than 12 K in the southeast NEC. The NEC is controlled by warm and moist southerly airflows. Under the low-pressure vortex, a northwest-southeast-oriented high-θ_e belt can be found in the north of the NEC, and northerly dry and cold air flows to the west of the NEC. In this type, the upstream low-value system in the NEC is blocked by the WPSH and the high-pressure ridge, resulting in a relatively small size of the NECVs (Figure 4A). The warm and moist air consistently interacts with dry and cold air, which is conducive to the occurrence of more accumulated daily precipitation (Figure 6A). The low-pressure vortex center of type 2 (Figure 8B) is located near the border of Heilongjiang Province and Inner Mongolia. Under the influence of the low-pressure circulation, the high-θ_e region shrinks to the south compared with type 1, but there is still a high-θ_e anomaly center in the southeastern part of the NEC. In this type, the cold air at middle-high latitudes is active, and the mean intensity of the NECVs is the strongest (Figure 4B). The warm and cold air collaborating with the terrain near Changbai Mountain results in rainstorms (Figure 7B). The center of the low-pressure vortex of type 3 (Figure 8C) is to the south of that of type 2, with the warm air and rainstorm scope (Figure 7C) also located farther south. In type 4 (Figure 8D), the location of the low-pressure vortex center is similar to that in type 3 (Figure 8C), but the vortex is more east-west oriented. The central and southern parts of the NEC are controlled by warm and moist air. There is a high-θ_e anomaly center of more than 8 K in the southeast of the NEC. Although the location of the center of the low-pressure vortex and the spatial distribution of the high-θ_e in type 5 (Figure 8E) are similar to type 2 (Figure 8B), the northeast-southwest stretch of the low-

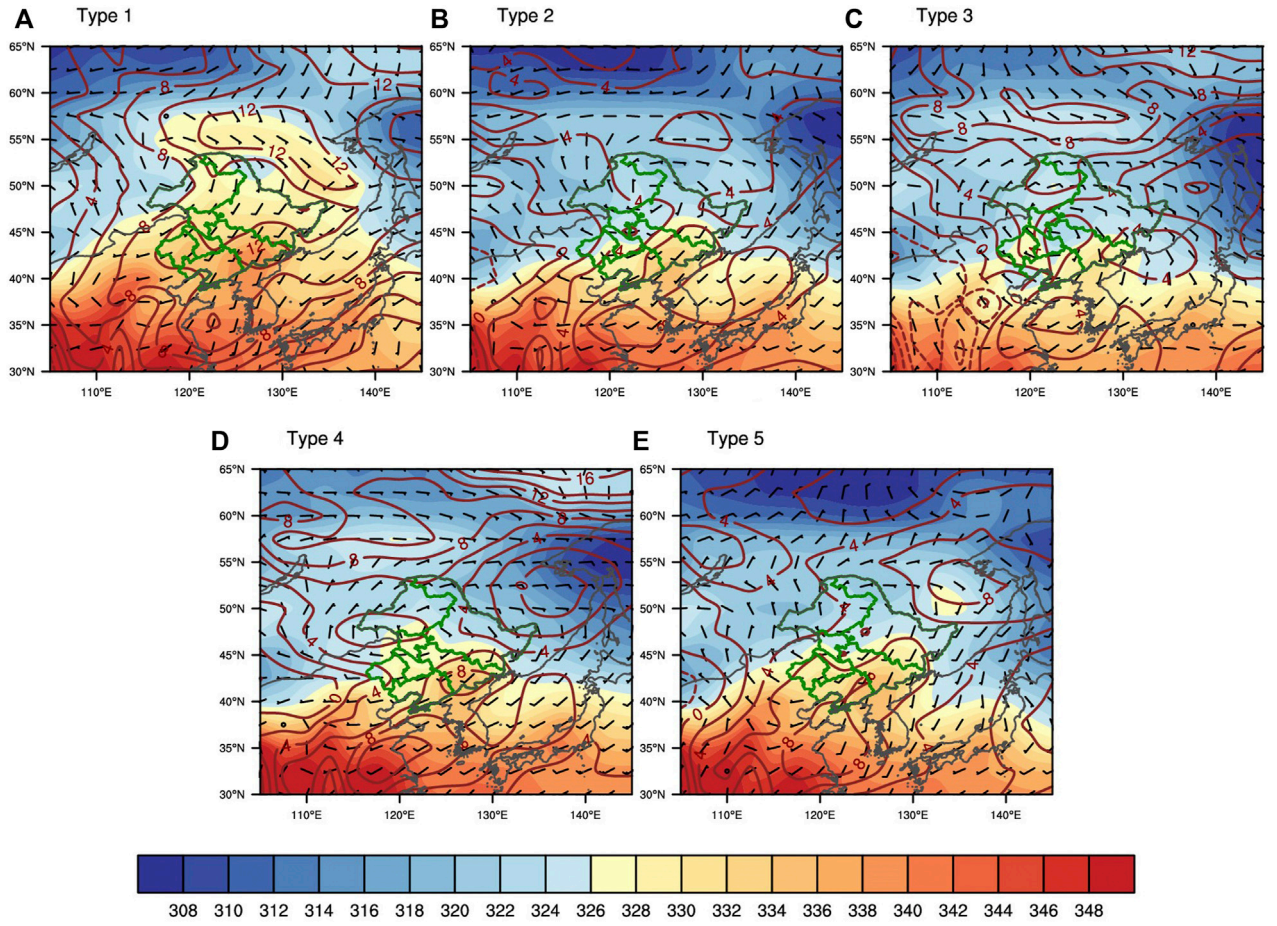

FIGURE 8
Wind (wind barb, units: m/s), equivalent potential temperature anomaly (red solid lines, units: K) at 925 hPa under five types of synoptic circulation patterns **(A-E)**. The green map denotes the NEC.

pressure vortex is more remarkable. The northeastward transport of warm and moist air is more obvious, and the high-θ_e anomaly center in the southeastern NEC is also stronger, which leads to a larger scope of rainstorms (Figure 7E) than that of type 2 (Figure 7B).

Water vapor transport and convergence are indispensable for the occurrence of heavy precipitation. Figure 9 shows water vapor transport and convergence in the whole atmosphere layer under different circulation patterns. In the NEC, southwesterly wind transport and convergence are apparent in type 1 and 5, whereas westerly wind transport and convergence are dominant in type 2 and 4, and the wind convergence of type 3 is stronger than that of other types, resulting in different heavy precipitation characteristics (Figures 6, 7). Differences can also be found in the ratio of rainstorm-day accumulated precipitation under different circulation types. The AWSs of type 1, accounting for more than 50%, are concentrated in the central and southern parts of the NEC (Figure 9A). The AWSs of type 2 are mostly located in the northeast and southwest parts of the NEC (Figure 9B). Only four AWSs in type 3 account for more than 50%, which is the least among all five types (Figure 9C). The AWSs accounting for more than 50% of type 4 are also mainly in the west-southwest to the east-northeast direction (Figure 9D), while those of type 5 (Figure 9E) are widely distributed in the southwest-northeast orientation. The distribution of ASWs with a high proportion of precipitation shows consistency with water vapor convergence areas of different circulation patterns. Furthermore, the precipitable water in the NEC can reach more than 40 mm (not shown). However, for a rainstorm, water vapor of this magnitude is obviously insufficient. Therefore, the transport and convergence of water vapor under the influence of different circulations are of vital importance.

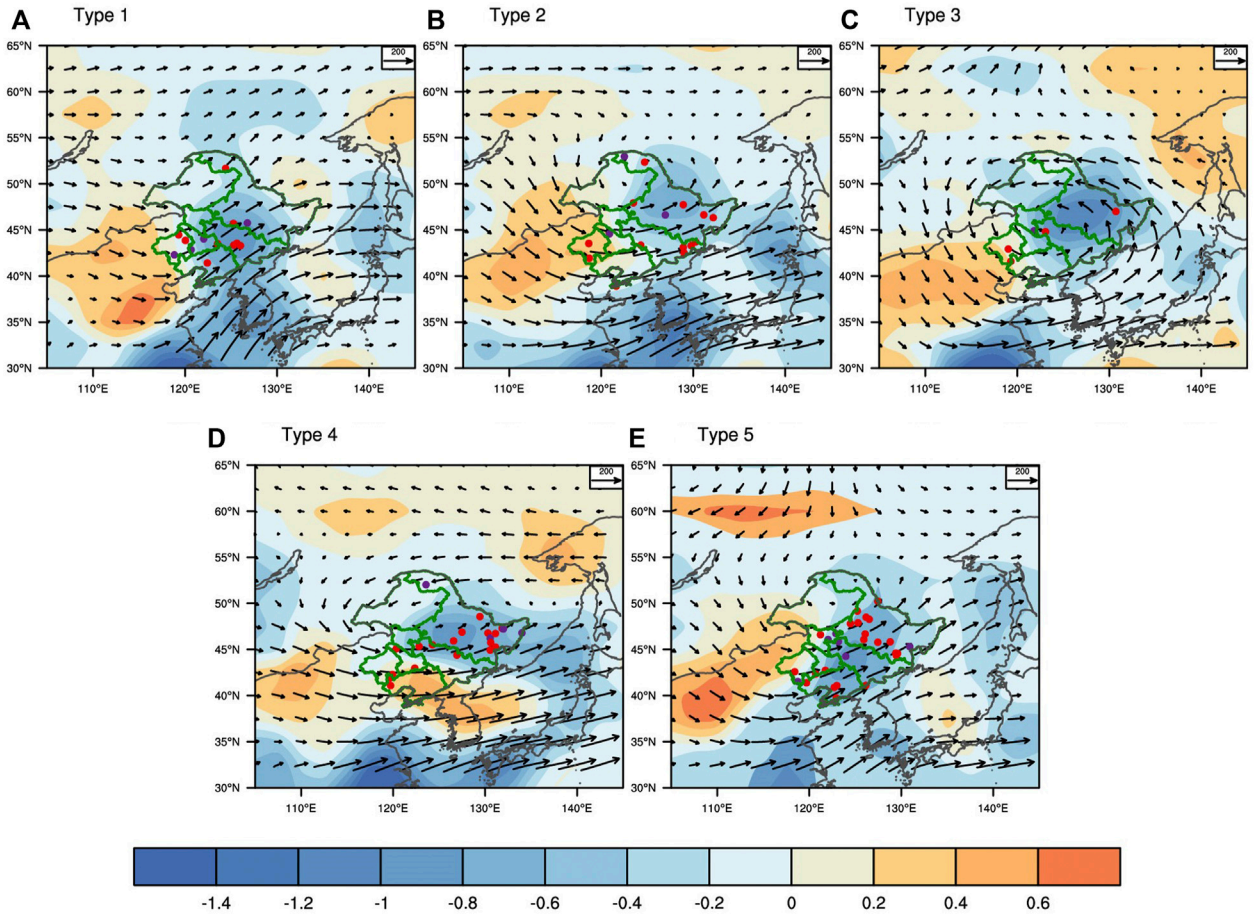

FIGURE 9
Water vapor fluxes of the whole atmosphere layer (vector, units: kg m^{-1} s^{-1}) and its divergence (shaded, units: 10^{-4} kg m^{-1} s^{-1}) under five types of synoptic circulation patterns **(A-E)**. The red dots represent the accumulated precipitation of rainstorm days associated with NECVs in this type accounts for 50%–80% of all accumulated precipitation of rainstorm days associated with NECVs and the purple dots represent equal to or greater than 80%. The green map denotes the NEC.

4 Conclusion and discussion

In this study, to reveal the large-scale synoptic circulation patterns on the rainstorm days associated with NECVs in the warm seasons (May–September), ten objective circulation classification methods are selected to conduct objective circulation classifications on the 500 hPa geopotential height anomaly. The optimal objective classification method and the corresponding type number are determined after evaluation. Large-scale circulation backgrounds, precipitation characteristics, thermodynamic and moisture conditions under different synoptic circulation patterns are further discussed. The main conclusion are summarized as follows:

(1) After evaluating the performance of ten objective circulation classification methods by EV, PF, and EVPF, SOM is decided as the optimal objective classification method, and the optimal number of classification types is five.

(2) The large-scale circulation backgrounds of different classification types at 500 hPa are investigated. In type 1, the strong WPSH extends north and connects with the mid-latitude ridge in the east of the NEC. There is a shallow trough in the west of the NEC. NECVs of this type have the weakest mean intensity and the smallest mean radius. Type 2 has a higher frequency (25.2%). In this type, except for the region occupied by the WPSH, the other region is controlled by the low-pressure anomaly. There is an obvious trough in the NEC. Compared with type 1, the WPSH retreats to the southeast. NECVs of this type have the strongest mean intensity. Type 3 accounts for the least (13.4%). The low-pressure anomaly shrinks to the south of the NEC, and the NEC is controlled by the cut-off low vortex. The mean size of

NECVs of this type is the largest. Type 4 presents a meridional high-low-high pressure anomaly, and the center of the low-pressure anomaly is in the west of the NEC. The WPSH extends the most westward of these five types. The two low-pressure anomalies in type 5 are distributed from southwest to northeast, with their centers located in the west of the NEC and East Siberia, respectively, and the westerly trough is also distributed in a northeast-southwest orientation. In addition, the wind at 850 hPa of each type corresponding to NECV systems shows cyclonic vortexes except for type 1, where there is a deep low trough.

(3) There are distinct differences in the characteristics of daily precipitation under different synoptic circulation patterns. The mean number of AWSs reaching the rainstorm level on a rainstorm day of type 1 and 5 is greater than other types. Type 1 has the largest mean and maximal daily accumulated precipitation, as well as the mean hourly precipitation. However, type 4 has the strongest hourly precipitation.

(4) The spatial distribution of accumulated precipitation on rainstorm days associated with NECVs in the warm seasons of 2000–2019 presents remarkable non-uniformity and differences. The rainstorms are mostly located near Changbai Mountain and the narrow northeast plain region in the middle of Liaoning Province. The precipitation centers of type 1 mainly occur in the central plain of Liaoning province and central Jilin Province. Rainstorms of type 2 are mostly located near the southern part of Changbai Mountain in Liaoning Province. Precipitation centers in type 5 are observed near Changbai Mountain and the coastal areas in the southeast of Liaoning Province, whose scope is larger than that in type 2. The accumulated precipitation of rainstorms in type 3 and 4 are weaker than that of other types.

Based on the objective circulation classification, it is beneficial to better understand the characteristics of rainstorm days under the background of NECVs. In the future, quantifying the water vapor sources and transport paths of rainstorms in the NEC is necessary to in-depth investigate rainstorms associated with NECVs. Moreover, rainstorms are the result of the interaction of multi-scale weather systems. Therefore, high-resolution numerical simulation and other technological means are also needed to further analyze the occurrence mechanism of the rainstorms associated with NECVs.

Data availability statement

The data analyzed in this study is subject to the following licenses/restrictions: The data that support the findings of this study are available from the corresponding author upon reasonable request. Requests to access these datasets should be directed to xpcui@mail.iap.ac.cn.

Author contributions

LH and XC carried out data analysis and wrote the manuscripts. LC was involved in the discussion. QZ and YY participated in the manuscript revision. All authors contributed to the article and approved the submitted version.

Funding

This work was supported by the Institute of Atmospheric Environment of China Meteorological Administration (2020SYIAEZD4).

Acknowledgments

We thank the China Meteorological Administration for providing the hourly precipitation dataset.

Conflict of interest

The authors declare that the research was conducted in the absence of any commercial or financial relationships that could be construed as a potential conflict of interest.

Publisher's note

References

Bai, R., and Jin, Y. (1993). *The research on heavy rain in Heilongjiang province*. Beijing: China Meteorological Press.

Beck, C., and Philipp, A. (2010). Evaluation and comparison of circulation type classifications for the European domain. *Phys. Chem. Earth Parts A/B/C* 35 (9–12), 374–387. doi:10.1016/j.pce.2010.01.001

Broderick, C., and Fealy, R. (2015). An analysis of the synoptic and climatological applicability of circulation type classifications for Ireland. *Int. J. Climatol.* 35 (4), 481–505. doi:10.1002/joc.3996

Buishand, T., and Brandsma, T. (1997). Comparison of circulation classification schemes for predicting temperature and precipitation in The Netherlands. *Int. J. Climatol.* 26, 461–483. doi:10.1002/(SICI)1097-0088(19970630)17:8<875

Cahynová, M., and Huth, R. (2016). Atmospheric circulation influence on climatic trends in europe: An analysis of circulation type classifications from the COST733 catalogue. *Int. J. Climatol.* 36 (7), 2743–2760. doi:10.1002/joc.4003

Caliński, T., and Harabsz, J. (1974). A dendrite method for cluster analysis. *Comm. Stats. - Simul. Comp.* 3 (1), 1–27. doi:10.1080/03610917408548446

Casado, M., and Pastor, M. (2016). Circulation types and winter precipitation in Spain. *Int. J. Climatol.* 36 (7), 2727–2742. doi:10.1002/joc.3860

Casado, M., Pastor, M., and Doblas-Reyes, F. (2010). Links between circulation types and precipitation over Spain. *Phys. Chem. Earth Parts A/B/C* 35 (9), 437–447. doi:10.1016/j.pce.2009.12.007

Chen, L., Chen, S., Zhou, X., and Pan, X. (2005). A numerical study of the MCS in a cold vortex over northeastern China. *Acta Meteorol. Sin.* (02), 173–183. doi:10.11676/qxxb2005.017

Enke, W., and Spekat, A. (1997). Downscaling climate model outputs into local and regional weather elements by classification and regression. *Clim. Res.* 8, 195–207. doi:10.3354/cr008195

Fang, Y., Chen, H., Lin, Y., Zhao, C., Lin, Y., and Zhou, F. (2021). Classification of Northeast China Cold Vortex activity paths in early summer based on k-means clustering and their climate impact. *Adv. Atmos. Sci.* 38 (3), 400–412. doi:10.1007/s00376-020-0118-3

Fu, S., and Sun, J. (2012). Circulation and eddy kinetic energy budget analyses on the evolution of a northeastnortheast China cold vortex (NCCV) in may 2010. *J. Meteorological Soc. Jpn.* 90 (4), 553–573. doi:10.2151/jmsj.2012-408

Hu, K., Lu, R., and Wang, D. (2010). Seasonal climatology of cut-off lows and associated precipitation patterns over Northeast China. *Meteorol. Atmos. Phys.* 106 (1–2), 37–48. doi:10.1007/s00703-009-0049-0

Huang, L., and Cui, X. (2022). *Statistical characteristics of the Northeast China Cold Vortex and its impact on precipitation distribution from 2000 to 2019*. Chinese Journal of Atmospheric Sciences. In press (In Chinese with English abstract). doi:10.3878/j.issn.1006-9895.2203.21227

Huth, R., Beck, C., Philipp, A., Demuzere, M., Ustrnul, Z., Cahynova, M., et al. (2008). Classifications of atmospheric circulation patterns. *Ann. N. Y. Acad. Sci.* 1146 (1), 105–152. doi:10.1196/annals.1446.019

Huth, R. (1993). Ein Beispiel für die Anwendung der Hauptkomponentenanalyse zur Auffindung von Zirkulationstypen über Europa. *metz.* 2, 285–293. doi:10.1127/metz/2/1993/285

Kalnay, E., Kanamitsu, M., Kistler, R., Collins, W., Deaven, D., Gandin, L., et al. (1996). The NCEP/NCAR 40–year reanalysis project. *Bull. Am. Meteorol. Soc.* 77 (3), 437–471. doi:10.1175/1520-0477(1996)077<0437:tnyrp>2.0.co;2

Kaufman, L., and Rousseeuw, P. (1990). "Finding groups in data an introduction to cluster Analysis," in *Wiley series in probability and mathematical statistics: Applied probability and statistics* (New York, NY: John Wiley), 342.

Kirchhofer, W. (1974). *Classification of European 500 mb patterns*, 43. Zurich, Switzerland: Arbeitsbericht der Schweizerischen Meteorologischen Zentralanstalt, 1.

Liu, W., Wang, L., Chen, D., Tu, K., Ruan, C., and Hu, Z. (2015). Large-scale circulation classification and its links to observed precipitation in the eastern and central Tibetan Plateau. *Clim. Dyn.* 46, 3481–3497. doi:10.1007/s00382-015-2782-z

Lund, I. (1963). Map-pattern classification by statistical methods. *J. Appl. Meteor.* 2, 56–65. doi:10.1175/1520-0450(1963)002<0056:mpcbsm>2.0.co;2

Michaelides, S., Liassidou, F., and Schizas, C. (2007). Synoptic classification and establishment of analogues with artificial neural networks. *Pure Appl. Geophys.* 164, 1347–1364. doi:10.1007/s00024-007-0222-7

Murtagh, F. (1985). "Multidimensional clustering algorithms," in *COMPSTAT lectures* (Wurzburg: Physica-Verlag), Vol. 4.

Philipp, A., Beck, C., Huth, R., and Jacobeit, J. (2014). Development and comparison of circulation type classifications using the COST 733 dataset and software. *Int. J. Climatol.* 36 (7), 2673–2691. doi:10.1002/joc.3920

Philipp, A. (2009). Comparison of principal component and cluster analysis for classifying circulation pattern sequences for the European domain. *Theor. Appl. Climatol.* 96, 31–41. doi:10.1007/s00704-008-0037-1

Qian, W., Shan, X., and Zhu, Y. (2012). Capability of regional-scale transient wind anomalies to indicate region heavy rains. *Chin. J. Geophys.* 55 (5), 1513–1522. doi:10.6038/j.issn.0001-5733.2012.05.008

Ren, Z., Zhang, Z., Sun, C., Liu, Y., Li, J., Ju, X., et al. (2015). Development of three-step quality control system of real-time observation data from AWS in China. *Meteorological Monthly.* 41 (10), 1268–1277. doi:10.7519/j.issn.1000-0526.2015.10.010

Schmutz, C., and Wanner, H. (1998). Low frequency variability of athmospheric circulation over Europe between 1785 and 1994. *erd.* 52, 81–94. doi:10.3112/erdkunde.1998.02.01

Sun, L., Zheng, X., and Wang, Q. (1994). The climatological characteristics of Northeast Cold vortex in China. *Q. J. Appl. Meteorology* 5 (3), 297.

Tao, S. (1980). *Heavy rain in China*. Beijing: Science Press.

Wang, C., Xu, H., and Ren, L. (2012). The objective identification method of northeast cold vortex. *J. Meteorology Environ.* 28 (02), 1. doi:10.3969/j.issn.1673-503X.2012.02.001

Wang, C., Zhao, K., Huang, A., Chen, X., and Rao, X. (2021). The crucial role of synoptic pattern in determining the spatial distribution and diurnal cycle of heavy rainfall over the south China coast. *J. Clim.* 34 (7), 2441–2458. doi:10.1175/JCLI-D-20-0274.1

Wang, X., and Xie, J. (1994). The analysis of the effects of topography in northeast China on strong convection weather. *Sci. Geogr. Sin.* 14 (4), 347.

Xie, Z., and Buhe, C. (2015). Different types of cold vortex circulations over northeast China and their weather impacts. *Mon. Wea. Rev.* 143 (3), 845–863. doi:10.1175/MWR-D-14-00192.1

Zhang, C., Zhang, Q., Wang, Y., and Liang, X. (2008). Climatology of warm season cold vortices in east asia: 1979–2005. *Meteorol. Atmos. Phys.* 100 (1–4), 291–301. doi:10.1007/s00703-008-0310-y

Zhang, X., Chen, D., and Yao, T. (2018). Evaluation of circulation-type classifications with respect to temperature and precipitation variations in the central and eastern Tibetan Plateau. *Int. J. Climatol.* 38, 4938–4949. doi:10.1002/joc.5708

Zhao, S., and Sun, J. (2006). Study on cut-off low-pressure systems with floods over northeast asia. *Meteorol. Atmos. Phys.* 96 (1–2), 159–180. doi:10.1007/s00703-006-0226-3

Zhao, Y., Xu, X., Li, J., Zhang, R., Kang, Y., Huang, W., et al. (2019). The large-scale circulation patterns responsible for extreme precipitation over the northnorth China plain in midsummer. *JGR. Atmos.* 124 (23), 12794–12809. doi:10.1029/2019JD030583

Zheng, X., Zhang, T., and Bai, R. (1992). *Rainstorm in northeast China*. Beijing: China Meteorological Press.

Zhong, S. (2011). *Structural features of cold vortex and its formation mechanism of heavy rainfall over northeast China*. Dissertation/doctor's thesis. Beijing: Chinese Academy of Sciences & Chinese Academy of Meteorological Sciences.

Zhong, S., Wang, D., Zhang, R., and Liu, Y. (2013). Study of mesoscale convective system in heavy rainstorm process at a cold vortex development stage. *Plateau Meteorol.* 32 (2), 435–445. (in Chinese with English abstract). doi:10.7522/j.issn.1000-0534.2012.00042

frontiers | Frontiers in Earth Science

TYPE Original Research
PUBLISHED 10 January 2023
DOI 10.3389/feart.2022.1065074

OPEN ACCESS

EDITED BY
Shenming Fu,
Institute of Atmospheric Physics (CAS), China

REVIEWED BY
Xiaolan Li,
CMA, China
Yunji Zhang,
The Pennsylvania State University (PSU), United States

*CORRESPONDENCE
Lanqiang Bai,
bailanqiang@foxmail.com

SPECIALTY SECTION
This article was submitted to Atmospheric Science, a section of the journal Frontiers in Earth Science

RECEIVED 09 October 2022
ACCEPTED 14 November 2022
PUBLISHED 10 January 2023

CITATION
Huang L and Bai L (2023), Evaluation of planetary boundary layer schemes on the urban heat islands in the urban agglomeration over the greater bay area in South China.
Front. Earth Sci. 10:1065074.
doi: 10.3389/feart.2022.1065074

Evaluation of planetary boundary layer schemes on the urban heat islands in the urban agglomeration over the greater bay area in South China

Ling Huang [1] and Lanqiang Bai [2]*

[1]Guangdong Provincial Key Laboratory of Regional Numerical Weather Prediction, Institute of Tropical and Marine Meteorology, CMA, Guangzhou, Guangdong, China, [2]Foshan Tornado Research Center, CMA, Southern Marine Science and Engineering Guangdong Laboratory (Zhuhai), Zhuhai, Guangdong, China

Urbanization of large cities exerts significant changes in surface air temperature, which subsequently lead to inadvertent local weather and climate changes. The exchanges of momentum, moisture and heat within the planetary boundary layer (PBL) impact the urban atmosphere representation. The applicability of PBL schemes in regional modeling varies with different climate regimes and underlying surface. As the first step to gaining a better forecast of urban climates, the performances of multiple PBL schemes (YSU, MRF, ACM2, BL, MYNN, UW and GBM) on reproducing the low-level urban atmosphere are evaluated over the Greater Bay Area, South China, during April–June 2018. With the aid of observations from *in situ* weather stations and radiosondes, the urban environmental characteristics, including surface air temperature and humidity, temperature profile, urban heat island (UHI), and PBL height, are assessed. The results show a cool/moist bias near the surface during nighttime and a warm/dry bias during daytime for all PBL schemes. The daytime bias is significant on weak-UHI days while the nocturnal bias appears to be significant on strong-UHI days. The so-called best scheme depends on the exact meteorological variables, diurnal cycles, and thermodynamic conditions that are of interest. Specifically, the MYNN and MRF schemes perform the best for the daytime and nighttime air temperature, respectively. The MRF scheme also presents the best performance in simulating the observed UHI, with a good agreement with the observed diurnal variation. The numerical exercises in this study may serve as a reference for an efficient operational way that is readily accessible to forecast air temperature in the urban agglomeration over South China.

KEYWORDS

urban heat island, urban agglomeration, PBL parameterization, surface thermal parameters, PBL structures

Key points

- The predictability of urban heat islands over the Great Bay Metropolis is discussed based on ensemble simulations and observations.
- The long-term modeled surface temperature presents a warm bias in the day and a cool bias at night.
- The MRF scheme shows a better performance than other PBL schemes in reproducing the diurnal variation in urban heat island intensity.

Introduction

The rise in the proportion of global human populations in urban regions has resulted in widespread concern regarding the emergence of natural disasters. Under a changing climate, the highly populated metropolises are particularly vulnerable to the increasing extreme severe weather (Hallegatte et al., 2013; Zhang 2020; Sun X. et al., 2021). It will become increasingly likely that weather hazards will affect the interests of humankind due to the "expanding bull's eye effect" (Ashley et al., 2014). Investigating the modeled characteristics of urban environment is thus a first step to forecasting and issuing warnings for extreme weather, especially over urban agglomerations on coasts which are often highly populated.

The local severe weather over the urban surface is closely linked to the thermal perturbations associated with the urban heat island (UHI) (e.g., Huff and Vogel 1978; Li et al., 2011; Zhang et al., 2015; Wu et al., 2019; Doan et al., 2021), which is typically characterized by an evident lower-troposphere temperature contrast between the urban and surrounding rural regions (Oke 1995). The UHI effect tends to destabilize the planetary boundary layer (PBL), triggering low-level updrafts, gravity waves, and horizontal convergence (Niyogi et al., 2011). Based on observations, a recent study documented a possible link between enhanced rainfall and rapid urbanization in the Greater Bay region in South China. It was found that more and stronger extreme rainfall occurs in the strong-UHI scenario (Wu et al., 2019). Thus, an accurate representation of the UHI is important for improving regional severe weather forecasts because a forecast failure may result from the nonnegligible error of a necessary condition (Johns and Doswell 1992).

The exchanges of momentum, moisture and heat within PBL through turbulent processes, which affect the representation of low-level thermodynamic structures, are a substantial source of forecast inaccuracy in numerical models (Jankov et al., 2005; Stensrud 2007; Hacker 2010; Hu et al., 2010; Nielsen-Gammon et al., 2010; Cohen et al., 2015). Several PBL parameterization schemes have been developed in some widely used numerical models, such as the WRF model (Skamarock et al., 2008), to depict the lower-level environment by various possible physical processes. These PBL schemes are roughly categorized into local schemes and nonlocal schemes, depending on the depth over which the variables are allowed to affect a given level. Thus, the extents of the vertical gradient of the perturbation quantities at each vertical level are different between the two groups (e.g., Ching et al., 2014; Dzebre and Adaramola 2020). In the case of local schemes, such as MYNN, BL, and GBM (Table 1), only the variables at the given point can impact the points directly vertically adjacent to it. On the other hand, variables at a given level in nonlocal schemes are determined by multiple vertical levels (e.g., YSU; Table 1). Nonlocal schemes usually produce stronger turbulent mixing than local schemes.

PBL schemes may use different turbulence-closure hypotheses, vertical mixing processes, and PBL height calculations, leading to different levels of accuracy when describing lower-tropospheric turbulence. The diversity of PBL physics among these parameterization schemes will have different impacts on the thermodynamics in the lower troposphere. The impact of the abovementioned PBL schemes on meteorological variables has been emphasized in recent decades over different climate regimes worldwide (Hu et al., 2010; Xie et al., 2012). The results revealed that there is no optimal PBL scheme for all cases; their performances vary depending on the underlying surface, specific weather season, geographical location that affects moisture conditions (e.g., arid/humid regions) and atmospheric radiation, and time of day. For example, while some studies have suggested a cold bias of modeled near-surface temperature (T2) over Europe and the USA during daytime (e.g., Hu et al., 2010; Garcia-Diez et al.,

TABLE 1 Summary of the PBL schemes examined in the study.

PBL scheme name	Abbreviation	Type	Reference
MRF scheme	MRF	nonlocal	Hong and Pan (1996)
Yonsei University scheme	YSU	nonlocal	Hong and Noh (2006)
Mellor-Yamada Nakanishi and Niino Level 2.5 scheme	MYNN	local	Nakanishi and Niino (2004)
BouLac scheme	BL	local	Bougeault and Lacarrere (1989)
ACM2 scheme	ACM2	nonlocal	Pleim (2007)
Grenier-Bretherthon-McCaa scheme	GBM	local	Grenier and Bretherton (2001)
University of Washington moist turbulence scheme	UW	local	Bretherton and Sungsu (2009)

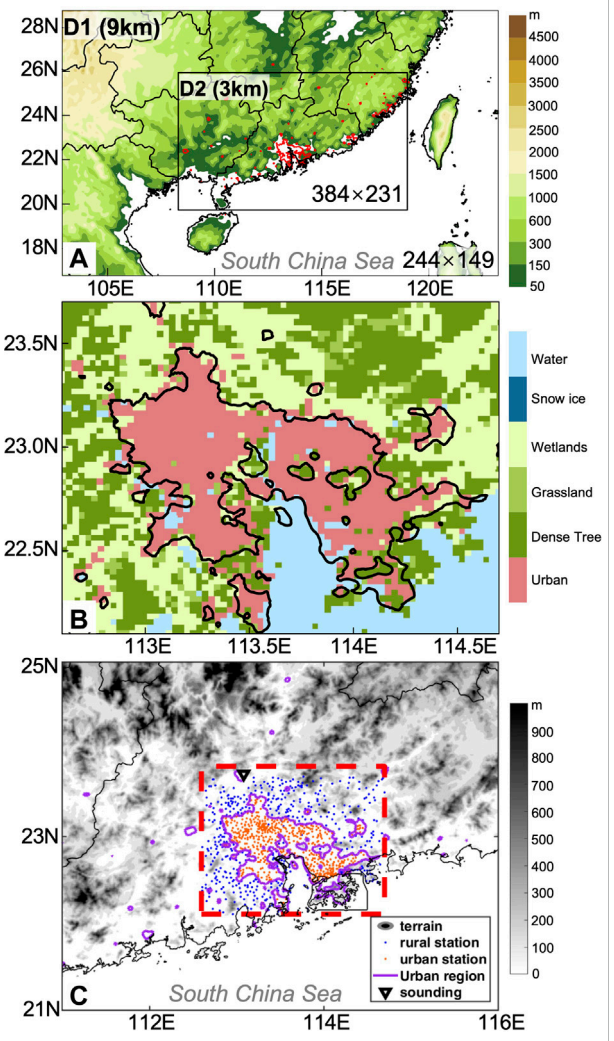

FIGURE 1
(A) The two nested domains of WRF with terrain heights (shadings). The urban areas (red isopleths) are identified by the DMSP nighttime light data in 2013. The grid point in each domain is indicated on the bottom right. **(B)** Enlarged Greater Bay Area. The shadings denote the type of underlying surface. The black contours are the urban areas shown in **(A)**. **(C)** Distribution of observations within the key region. The colored dots are the AWS over the key region (red-dashed box; the region in **(B)**), with orange (blue) dots indicating stations over the urban (rural) region. The black inverted triangle denotes the location of the sounding at Qingyuan. The shadings indicate the terrain heights. The magenta contours are the urban areas in **(A)**.

2011; Banks and Baldasano, 2016; Avolio et al., 2017; Huang et al., 2019), several other studies reported a daytime warm bias over the United Arab Emirates and India (Chaouch et al., 2017; Gunwani and Mohan, 2017). For a single parametrization scheme, it may perform better than other schemes according to the cases and the variables being evaluated (e.g., Borge et al., 2008; Hariprasad et al., 2014; Banks and Baldasano, 2016; Barlage et al., 2016; Li et al., 2016; Chaouch et al., 2017; Gunwani and Mohan, 2017; Ferrero et al., 2018; Wang and Ying, 2020; Martilli et al., 2021; Wang et al., 2021; Huang, 2020). It is thus necessary to investigate the applicability of PBL schemes over a specific climate regime, which would be helpful to determine the optimized parameterizations for regional mesoscale modeling, especially over the highly populated urban agglomerations.

The Guangdong-Hong Kong-Macao Greater Bay Area (GBA) has expanded rapidly during the past 3 decades. By 2021, it covers an area of approximately 56,000 km^2, with a population of over 86 million. Adjacent to the northern part of the South China Sea (SCS, Figure 1), the GBA is located in a relatively flat region surrounded by mountains (Figure 1C). The surrounding rural areas are covered by a variety of vegetation types, such as wetlands, grassland and dense trees (Figure 1B). Over the GBA, where an intense UHI is centered, Wu et al., 2019 demonstrated an increasing occurrence of severe weather during the early summer rainy season (April–June) in South China (Ding 1994). Recent studies have suggested the importance of UHI effects on nocturnal convection initiation over the GBA (Yin et al., 2020), the regulation of extreme rainfall (Li et al., 2021), and the distribution of extreme hourly rainfall (Sun Y. et al., 2021). Although the urban-canopy model in WRF has been developed and evaluated (e.g., Barlage et al., 2016; Huang et al., 2019; Sun X. et al., 2021), the expensive cost of computational resources prevents it from being the routine operational system for daily forecasts. Therefore, investigating the characteristics among the PBL schemes for the early summer rainy season over the GBA is an important step to identifying potential weaknesses, which may lead to substantial model inaccuracy. This is relevant for operational meteorology systems in representing the urban environment, with the primary focus of the present work being on model performance in urban–rural environments.

This study attempts to evaluate the performances of seven commonly used PBL schemes in simulating the thermodynamic conditions over the GBA region during the early summer rainy season, when afternoon thunderstorms frequently occur. Multisource observations were collected to provide a comprehensive validation dataset for model evaluation. Section 2 describes the experimental design and data. Section 3 presents the evaluation of PBL schemes, including near-surface and vertical condition analysis. The final section provides a brief discussion and summary.

Model design, data and methods

Design of numerical experiments

A set of WRF (Skamarock et al., 2008; version 4.0) simulations were conducted over the period from 2 April to 29 June 2018. They were initialized every day at 0800 local solar

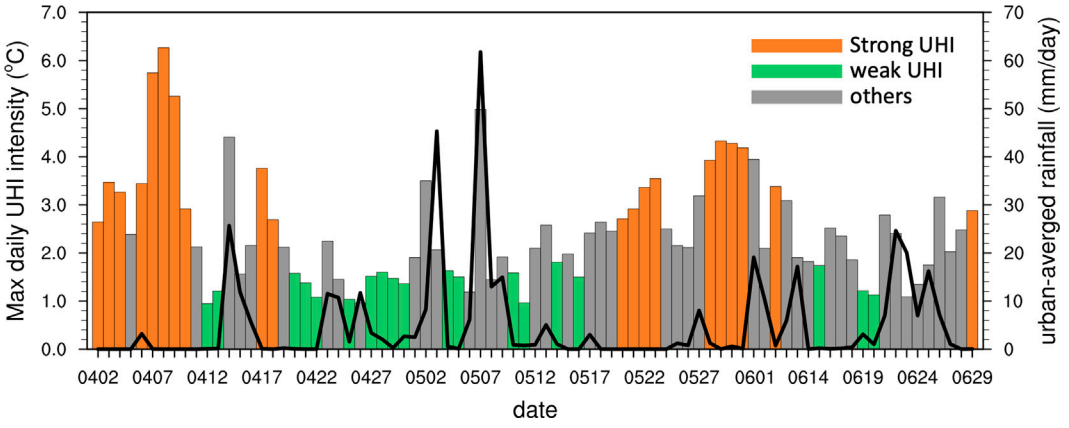

FIGURE 2
The evolution of the observed daily maximum urban heat island intensity (urban minus rural; colored bars on left axis) and the daily average rainfall over the urban region (black line on right axis) from 2nd April to 29th June, excluding the days when tropical cyclones made landfalls (5th to 12th June). The orange (green) bars indicate strong (weak) UHI days without daily rainfall accumulation exceeding 5 mm/day. The gray bars indicate the remaining days.

time [LST; LST = UTC (Universal Time Coordinated) + 8 h] and integrated for 36 h. The first 12 model hours were regarded as the spin-up periods (Huang et al., 2022) and the following 24 model hours were used to obtain continuous numerical outputs from April to June. Initial and lateral boundary conditions are provided by the National Centers for Environmental Prediction (NCEP) Global Data Assimilation System (GDAS) Model analysis data, with a horizontal resolution of 0.25° and a time interval of 6 h (available at 0000, 0600, 1200 and 1800 UTC). The two-way nested domains covered part of South China, with horizontal grid spacings of 9 km and 3 km, respectively (Figure 1A). The innermost domain with fine resolutions is characterized by the complex terrain, GBA, and land/sea contrast. A total of 40 terrain-following hydrostatic-pressure vertical levels are used with finer grid spacing in the boundary layer. Seven PBL parameterization schemes, which are available in WRF, are examined in this study (Table 1), including four local schemes (i.e., MYNN, BL, UW and GBM) and three nonlocal schemes (i.e., YSU, ACM2 and MRF). For more details on the dataset and model setup, please refer to Huang et al. (2022).

Observations

The observations from the automated weather stations (AWS) of the China Meteorological Administration (CMA) were used to evaluate these simulations. The near-surface air temperature (T2) was hourly available from 1088 AWS over the region of interest (red dashed line in Figure 1C) which covers the GBA and its nearby rural areas (Figures 1B,C). The urban and rural stations are distinguished by the DMSP nighttime light data in 2013 (magenta solid line contours in Figure 1C; Wu et al., 2019). The high light values fit well with the urban outline in the numerical model (Figures 1B,C). Data from 597 urban stations and 491 rural stations were processed with strict quality-control procedures, including the climatological limit value test, internal consistency test and space/time continuity test. Observations collected by an L-band radiosonde located in the rural region were also used to examine the model behaviors on vertical levels. The sounding data were collected at a time interval of 1 s with a high vertical resolution of several meters near the surface (Liu and Chen 2014), providing observations at 1100 and 2300 UTC, including temperature, pressure, humidity, heights, and horizontal winds.

Definition of strong and weak UHI days

To thoroughly investigate the model performance in reproducing UHIs, the early summer rainy season in 2018 (excluding the days on which a tropical cyclone made landfall, i.e., 5th to 12th June) was categorized into strong, moderate and weak UHI days, according to the daily maximum of the hourly UHI:

$$UHI = T_{urban} - T_{rural} \quad (1)$$

where T_{urban} is the hourly domain-averaged T2 within the urban region and T_{rural} is the hourly domain-averaged T2 within the rural region (Figure 1C). Thus, UHIs represent the hourly temperature difference between the urban area and its surrounding area (Oke 1995). The days

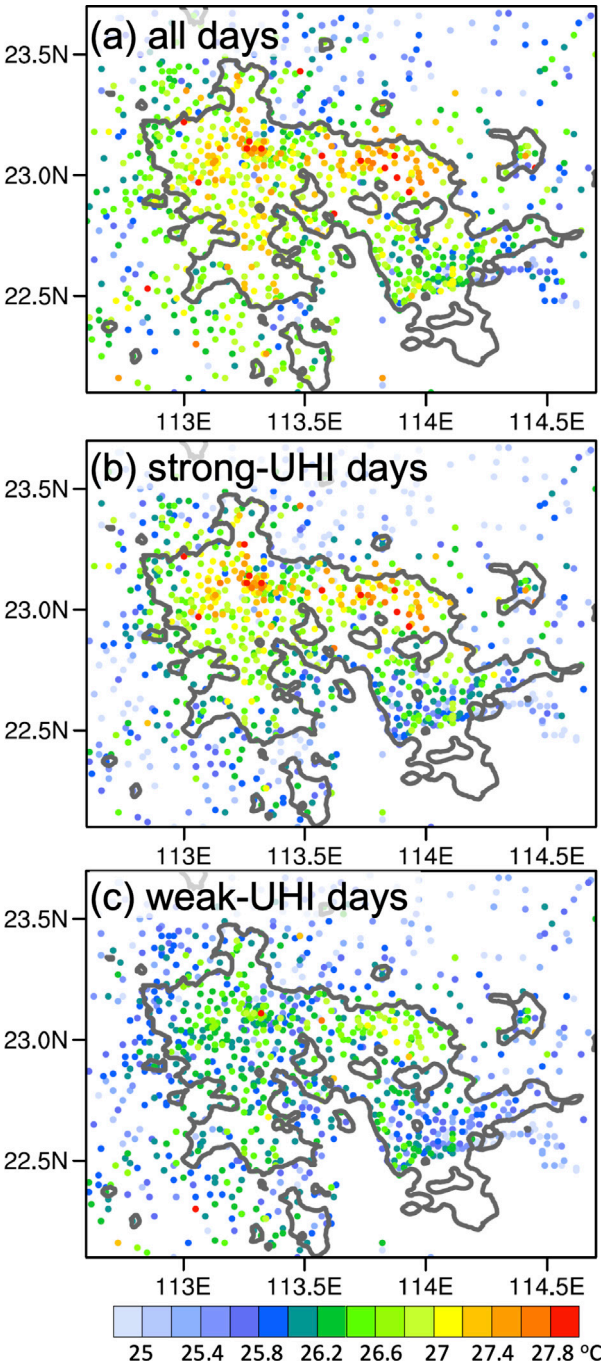

FIGURE 3
The observed daily average surface temperature (mm day^{-1}) for **(A)** all days from April to June 2018, **(B)** strong-UHI days, and **(C)** weak-UHI days. The gray isopleths denote the urban areas defined the DMSP nighttime light data in 2013.

are sorted by the daily maximum of hourly UHI from large to small, with the top/last 33% of days defined as strong-/weak-UHI days, while the rest are defined as moderate-UHI days (Kassomenos and Katsoulis, 2006). The range of UHI for weak-, moderate-, and strong-UHI days are (−∞, 1.81°C], (1.81°C, 2.86°C], and (2.86°C, +∞). To eliminate the cooling impact of rainfall on the GBA, the days with domain-averaged daily rainfall exceeding 5 mm are excluded. A total of 20 strong-UHI days and 19 weak-UHI days were examined in the current study (Figure 2).

Results

The simulated results are compared with lower-troposphere observations to evaluate the model performances in reproducing the thermodynamic conditions in urban areas by different PBL schemes. The near-surface and vertical structures of the thermodynamic parameters are examined, and the possible mechanisms are discussed to evaluate the superiority and deficiency of the abovementioned schemes.

Observational analysis

There are several distinguishing features in the observed T2 between the strong- and weak-UHI days. The strong-UHI days exhibit the highest T2, especially over the northern part of the urban area, where the daily average temperature reaches a maximum of 28°C (Figure 3). During the weak-UHI condition in this region, the average temperature is approximately 1°C lower (Figures 3B,C; Table 2). The T2 difference between the strong- and weak-UHI days is primarily contributed by the temperature in daytime (Table 2; Figures 4A,B). This phenomenon also leads to a larger amplitude in diurnal variation on strong-UHI days over the urban region (3.67°C vs. 1.92°C; Table 2). On the other hand, the strong-UHI days present a higher warming rate from 0600 to 0800 LST, with the unobstructed rural surface warming more rapidly as it receives direct solar radiation shortly after sunrise (Figure 4C), which is related to the thermal properties and the shading of some walls and portions of the canyon floor (Oke et al., 2017). Cooling rates for both the urban and rural regions on the strong-UHI days maximize at 1800 LST because of an evident decrease in solar radiation. The urban cooling is weaker relative to the rural region, leading to a gradual re-intensification of the UHI after sunset (Figures 4C,E). In contrast, the temperature variations in the urban and rural regions on weak-UHI days are comparable (Figure 4D). Overall, the diurnal amplitude of the UHI intensity on strong-UHI days is 0.73°C greater than that on weak-UHI days (Table 2; Figures 4E,F). Therefore, the strong-UHI days featured higher near-surface temperatures in the daytime and higher UHI intensities at nighttime, with larger diurnal amplitudes (Figure 4) relative to those of the weak-UHI days. Such features are closely related to the higher surface pressure and weaker prevailing southwesterlies (Figure 5) so that weaker vertical upward motion and horizontal advection that favor the urban heat can be preserved.

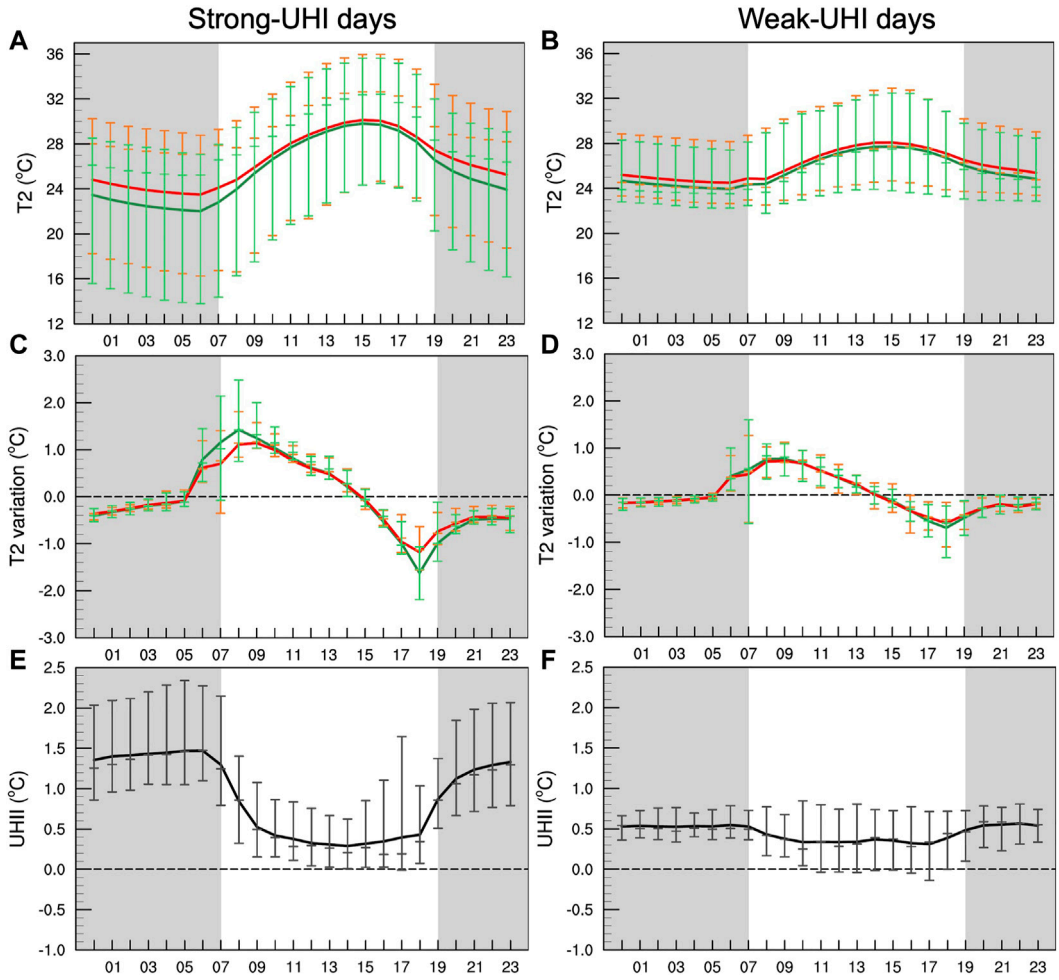

FIGURE 4
(A) The diurnal variations in the observed domain-averaged surface air temperature over the urban (red) and rural (green) regions averaged on the strong-UHI days. The error bars show the outliers (i.e., 10th and 90th percentiles are whiskers). **(C)** is similar to **(A)** but for the warming/cooling rates. **(E)** The diurnal variations in UHI intensity, with error bars representing the outliers (i.e., 10th and 90th percentiles are whiskers). **(B)**, **(D)**, and **(F)** are similar to **(A)**, **(C)**, and **(E)** but on the weak-UHI days. The gray zones denote the nocturnal time window from 1900 LST to 0700 LST.

Overall performances for near-surface temperature

Figure 6 presents the spatial distributions of the daily averaged T2 during the early summer rainy season for multiple PBL schemes. Compared to the observations (Figure 3A), the seven sets of seasonal simulations generally reproduced the prominent urban warm zone over the western part of 113.5°E well, while the simulated T2 in the northeastern portion of the urban area is underestimated (Figures 6A–C, Figures 6E,F), except for the MRF (Figure 6G) and BL (Figure 6D) groups. Because T2 results from the model diagnosis based on the surface and lowest model layer values, errors in the vertical transition between the surface and upper levels in different PBL schemes will lead to different T2 biases (Hu et al., 2010). The nonlocal closure MRF scheme shows the most severe overestimation of T2, followed by the local BL scheme, which is more comparable with the observation relative to other schemes (c.f., Figure 6 and Figure 3A). The higher T2 determined by the BL scheme is also indicated in a study that focused on the Phoenix and Tucson metropolitan areas (Palou and Mahalov 2019), yet the comparison of the MRF and other well-developed schemes has not been thoroughly investigated. The explicit entrainment at the top of the PBL represented in the YSU scheme tends to simulate the deeper vertical extent of mixing more accurately within the PBL, which alleviates the well-known problems in the MRF PBL (Hong and Noh 2006). Consequently, some systematic biases of the large-scale features, such as an afternoon cold bias at 850 hPa and warm bias near the surface in the MRF PBL, are resolved by the

TABLE 2 Statistics of observed (OBS) and modeled surface air temperature (T2) over urban and rural regions on strong and weak-UHI days. The "Nocturnal" values are calculated by the hourly T2 mean from 2000 LST to 0700 LST, while the "daytime" values are obtained from the T2 mean from 0800 LST to 1900 LST. The model means are the arithmetic means of the outputs from the seven PBL schemes.

		Strong-UHI days		Weak-UHI days	
		OBS	Model mean (RMSE)	OBS	Model mean (RMSE)
Urban temp (°C)	nocturnal	24.56	22.88 (1.99)	25.07	24.38 (1.05)
	daytime	28.23	28.52 (1.51)	26.99	28.19 (1.76)
	diurnal amplitude (day minus night)	3.67	5.64 (2.71)	1.92	3.81 (2.32)
Rural temp (°C)	nocturnal	23.24	22.39 (1.35)	24.56	23.79 (1.06)
	daytime	27.81	27.44 (1.40)	26.65	27.37 (1.40)
	diurnal amplitude (day minus night)	4.57	5.05 (1.53)	2.09	3.58 (1.85)
UHII (°C) Urban-rural	nocturnal	1.32	0.49 (1.07)	0.51	0.59 (0.24)
	daytime	0.42	1.08 (0.86)	0.34	0.82 (0.66)

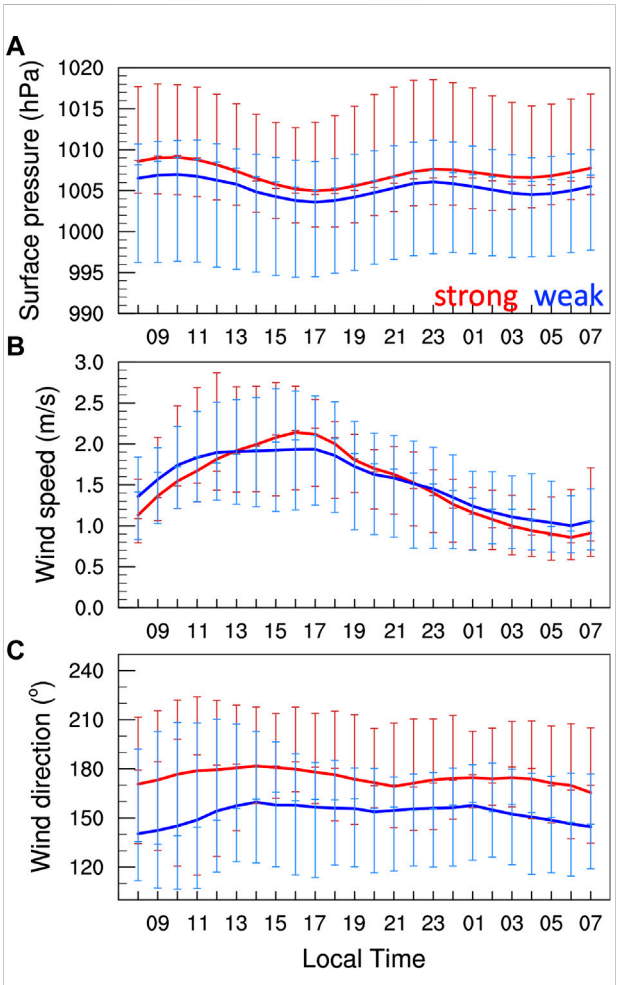

FIGURE 5
Diurnal variation of the domain-averaged **(A)** surface pressure (units: hPa), **(B)** wind speed (units: m/s), and **(C)** wind direction (units: degree) for strong-UHI days (red) and weak-UHI days (blue). The error bars denote the 25th, 50th and 75th percentile of the data at each local time.

YSU (Hong and Noh 2006). Moreover, the local BL scheme shows a higher near-surface temperature due to the weaker mixing that constrains the high-θ_e air within the near-surface layer. Other local schemes, such as MYNN and UW, exhibit cooler T2 than that of the BL, but the T2 is higher than that of the nonlocal schemes (i.e., YSU and ACM2). These model biases of near-surface temperature among the simulations suggest a significant difference in the model outcome, even those with a similar extent of vertical mixing, such as the YSU and the MRF, or BL and the MYNN.

To further diagnose the model errors on subdaily time scale, the diurnal cycle of the urban-averaged T2 is analyzed (Figure 7). In the GBA region, the model tends to overestimate the daytime T2 and underestimate the nocturnal T2 on both strong- and weak-UHI days (Figures 7C–F), except that the MRF produces a warmer nighttime T2 than the observations on weak UHI days (Figure 7E). The model can capture the observed difference in daytime T2 between weak- (26.99°C; Table 2) and strong-UHI (28.23°C; Table 2) days, which might be related to the model's capability to differentially reproduce cloud cover, soil moisture, radiation, etc., between these two scenarios (e.g., Hu et al., 2010). Notably, the simulated nocturnal T2 on the weak-UHI days is relatively higher than that on the strong-UHI days, with a smaller RMSE, which is speculated to be associated with more cloud cover on weak-UHI days that preserved the heat loss during nighttime (Kassomenos and Katsoulis, 2006; Figures 7C–F). Collectively, the models reproduce the larger diurnal amplitude for the strong-UHI days (5.64°C; Table 2) and smaller diurnal amplitude for the weak-UHI days (3.81°C; Table 2) over the urban region, as the observation indicated. These results suggest that to some extent, the models can distinguish among days with strong UHIs and days with weak UHIs.

The performances of each PBL parameterization scheme and the associated error sources on T2 are further discussed. Generally, T2 is more sensitive to PBL schemes on weak-UHII days (Figures 7E,F) when the daytime T2 is relatively low, and

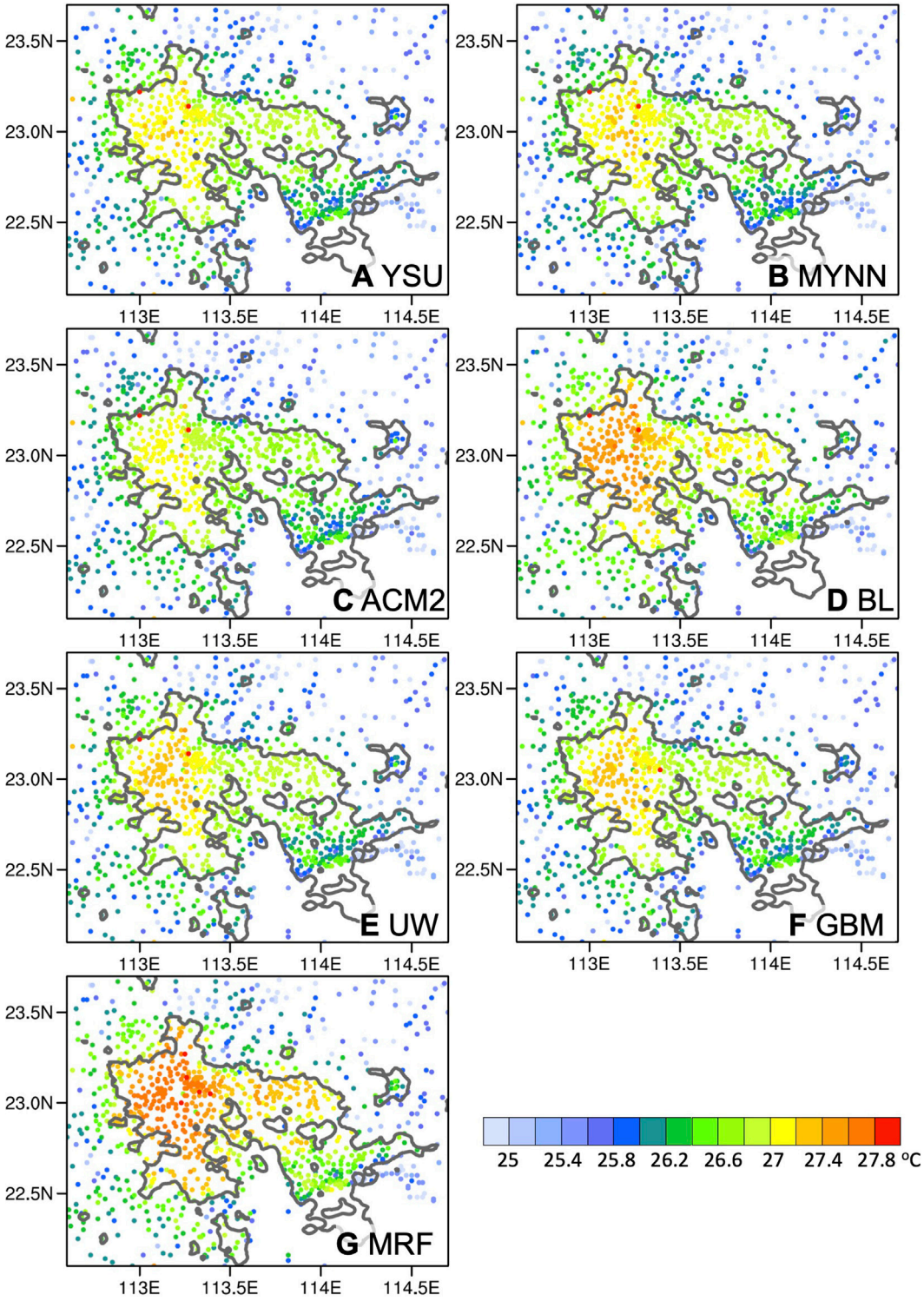

FIGURE 6
Simulated daily average of surface air temperature (mm day^{-1}) averaged from 2nd April to 30 June 2018 for **(A)** YSU, **(B)** MYNN, **(C)** ACM2, **(D)** BL, **(E)** UW, **(F)** GBM, and **(G)** MRF. The gray isopleths denote the urban areas defined by the DMSP nighttime light data in 2013.

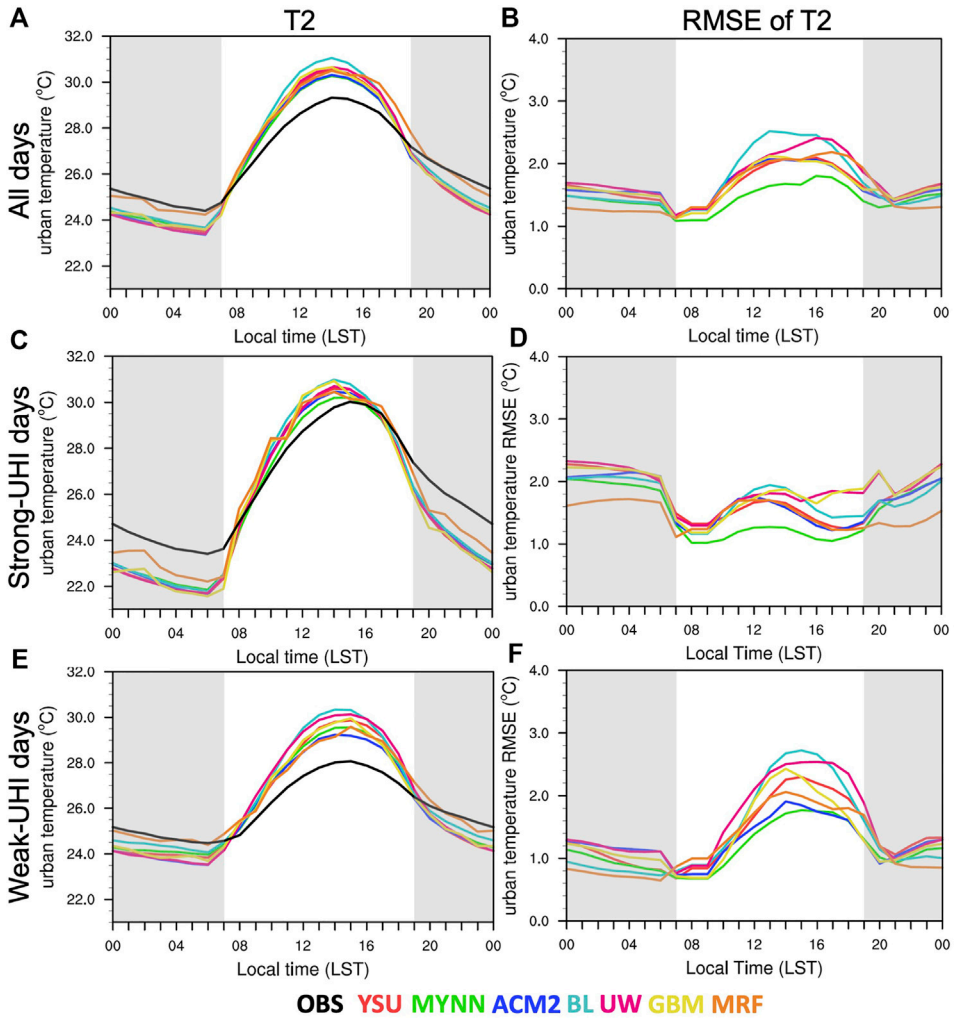

FIGURE 7
(A) Comparisons of the observed and simulated diurnal variations in the domain-averaged near-surface temperature for the entire early summer rainy season (excluding the days when TCs made landfall) and **(B)** the corresponding root mean square error of the model. **(C,D)** and **(E,F)** are similar to **(A,B)** but for the strong- and weak-UHI days. The gray zones denote the nocturnal time window from 1900 LST to 0700 LST.

thus, stable conditions are more frequent (Garcia-Diez et al., 2011). In such a scenario, BL and UW show the greatest error during the daytime (Figure 7F), with an overestimation of 2.7°C at 1400 LST (Figure 7E). Therefore, with diurnal amplitudes comparable to other schemes on the strong-UHI days, the BL seasonal daily averaged T2 (Figure 6D) is mostly contributed by the daytime overestimation on the weak-UHI days (Figures 7A,B,E,F). In contrast, the severe overestimation of the seasonal daily average T2 of the MRF (Figure 6G) is mostly contributed by the overestimation of daytime T2 and comparable nocturnal T2 on both weak- and strong-UHI days. Notably, the nocturnal T2 of the MRF is closest to the observation in all scenarios among all PBL schemes (Figure 7). The MYNN scheme shows the least daytime bias on both weak- and strong-UHI days, followed by ACM2, suggesting a reasonable performance by MYNN in reproducing daytime T2 among all PBL schemes for the urban region.

The performances of the model in reproducing the urban–rural thermal contrast, a. k.a., the urban heat island, are discussed in Figure 8. Most of the PBL parameterization schemes present similar diurnal cycles on strong- and weak-UHI days with comparable diurnal amplitudes but are antiphase relative to the observations (Figure 8). Specifically, the maximum/minimum of the observed UHI intensity occurs at midnight/afternoon, while that of the simulation occurs at afternoon/midnight. The simulated errors of the UHI intensity are probably due to the stronger simulated radiated urban heating in daytime and the stronger simulated urban cooling at night relative to the rural region. The model deficiency in

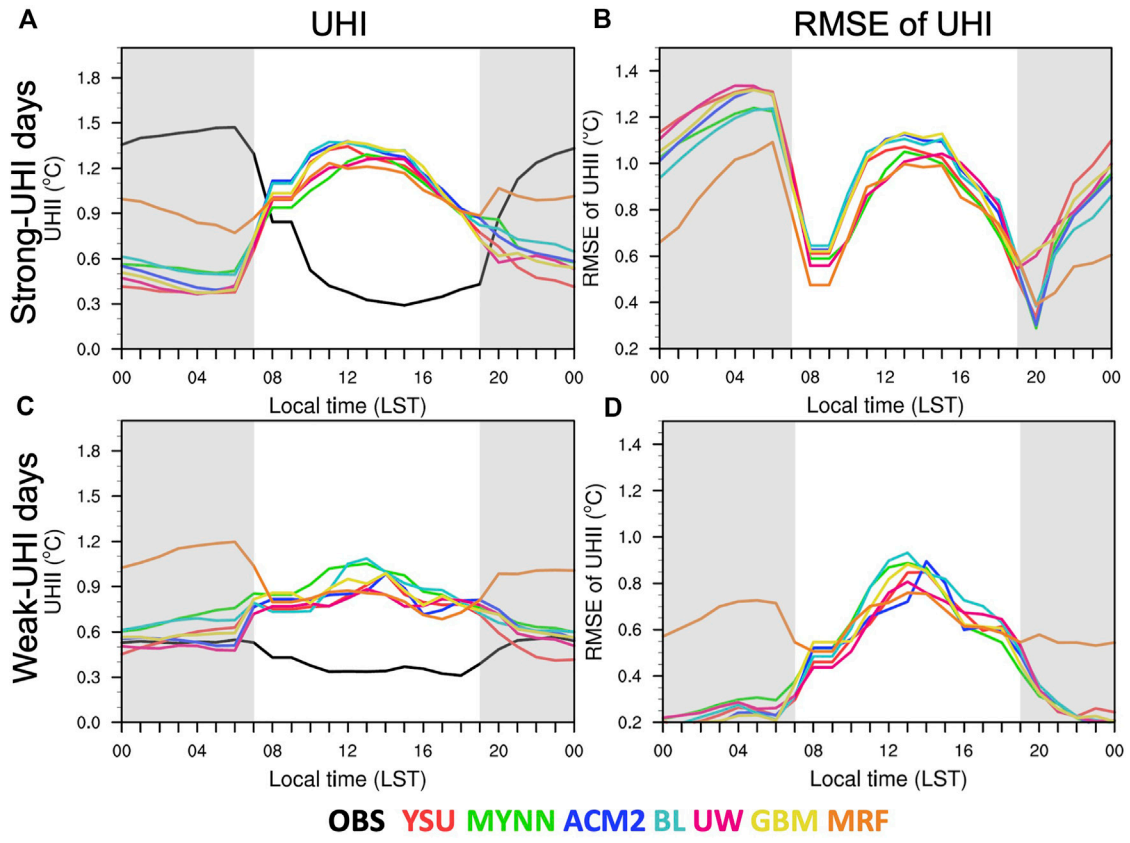

FIGURE 8
(A) Comparisons of the observed and simulated diurnal variations in the domain-averaged UHI on strong-UHI days and **(B)** the corresponding root mean square error of the model. **(C,D)** and are similar to **(A,B)** but on weak-UHI days. The gray zones denote the nocturnal time window from 1900 LST to 0700 LST.

representing the relative difference in the diurnal variation in near-surface variables is speculated to be due to 1) the errors in the mechanism of radiated heating on natural and artificial underlying surfaces and 2) the failure to accurately represent the urban cooling rate due to the lack of an urban-canopy model, since the utilization of the urban-canopy model modulates the nighttime cooling of urban areas, thus helping to reproduce the diurnal maximum of the UHI intensity during nighttime (Palou and Mahalov 2019). Among all the evaluated PBL schemes, only the MRF can reproduce a distinguishable, significant UHI effect at midnight that occurs in phase with the observation, especially on the weak-UHI days, with overestimation relative to the observation (Figures 8C,D).

Model performances for surface heat flux

One possible cause of the T2 differences among the evaluated PBL schemes is the difference in the surface energy. The surface energy balance on strong- and weak-UHI days are examined, as shown in Figure 9, for comparison with Figure 7. The surface energy balance equation is given as follows (Miao et al., 2012):

$$Q^* = Q_h + Q_e + Q_s \quad (2)$$

where Q^*, Q_h, Q_e, and Q_s represent the net all-wave radiation, sensible heat, latent heat, and storage heat, respectively.

The above heat fluxes affect the heat, moisture and momentum exchanges through thermal and dynamic actions in the boundary layer. As the urban region of the GBA primarily consists of concrete, the net radiation flux variations are mainly contributed by the sensible heat flux. Therefore, the diurnal variations in the seasonal sensible heat flux on strong- and weak-UHI days are examined to further investigate their relationship to the urban temperatures (Figure 9). Generally, the daytime sensible heat flux on the strong-UHI days is larger than that on the weak-UHI days (Figure 9), corresponding to the cooler daytime T2 on weak-UHI days (Figures 7C,E), suggesting that the T2 variations are

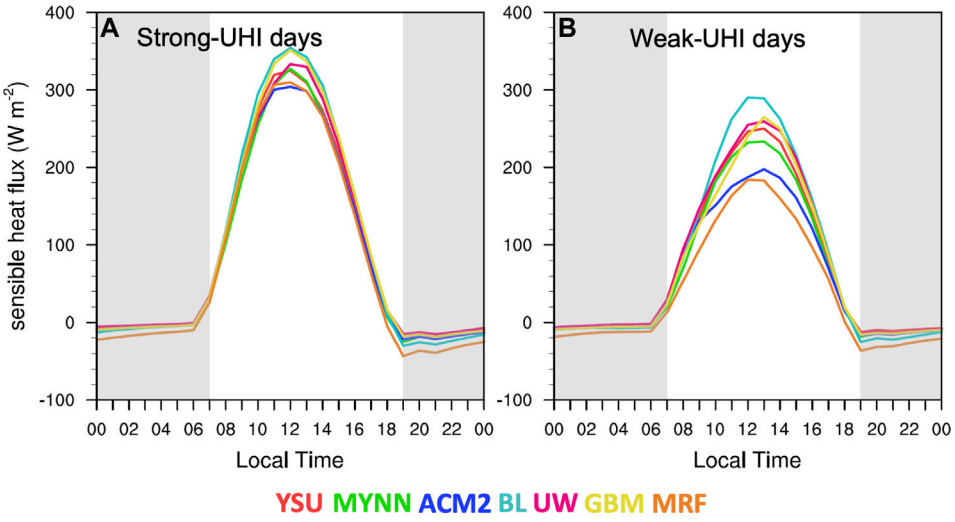

FIGURE 9
(A) Comparisons of the PBL schemes on the composite domain-averaged sensible heat flux over the urban region on strong-UHI days, **(B)** is similar to **(A)** but on weak-UHI days. The gray zones denote the nocturnal time window from 1900 LST to 0700 LST.

attributed to the sensible heat flux. The maximum sensible heat flux over the urban region among the seven PBL schemes appears at noon (~1300 LST; Figure 9), an hour before T2 reaches its diurnal peak. The relatively higher daytimeT2 of BL, YSU and UW are closely associated with the higher sensible heat flux, especially on the weak-UHI days (Figure 7E, 9B). At nighttime, the different performance of nocturnal T2 is more related to the model's preservation mechanism of the urban/rural heat. Collectively, the comparisons of the sensible heat fluxes suggest that the differences in performance among different parameterization schemes on daytime temperature likely arise directly within differences in the energy budget, while the difference in the nocturnal temperature can be partially explained by external feedback mechanisms, such as changes in cloud cover (Hu et al., 2010).

Model performances for vertical structure

Composite profiles of the simulations are produced for the early summer rainy season in 2018 based on the sounding station over the rural region north of the GBA (Figure 1C). Figure 10 shows the observed and simulated mean profiles of temperature at 0700 and 1900 LST on weak- and strong-UHI days. Simulations predict lower temperatures than observations in the lower troposphere in the morning, implying some source of error common to all model runs, such as incorrect urban land surface characteristics (Figures 10B,D). Owing to the overestimation during daytime and underestimation during nighttime, the underestimation of vertical profiles of temperature is even worse in the early morning than in early evening (Figure 10), when solar heating is absent. The vertical profiles of temperature for each PBL scheme are comparable on strong-UHI days, which is consistent with the results of T2 (Figures 10A–D). It is worth to note that the all PBL schemes fail to reproduce the near-surface temperature inversion only on strong-UHI days. On these days, low-level meteorological conditions are relatively stable featured by higher surface pressure (Figure 5A). Such a failure could be attributed to the model's deficiency to represent of the extent of radiative cooling in the clear sky that mostly occur during the higher surface pressure condition. On weak-UHI days, the temperature profiles are distinguishable, especially after intense solar heating at 1900 LST (Figures 10C,D). The nonlocal schemes (i.e., YSU and AMC2) with stronger vertical mixing do not always lead to a warmer PBL, as suggested in Hu et al. (2010). Instead, the ACM2 shows the coolest PBL at 1900 LST and the warmest PBL at 0700 LST. This result is closely related to the different responses of PBL schemes to heat transport to entrain warmer air into the PBL under unstable conditions due to solar heating and stable nocturnal conditions. The local scheme of UW shows a warmer PBL at 1900 LST. Nevertheless, the simulated temperatures are lower than the observations.

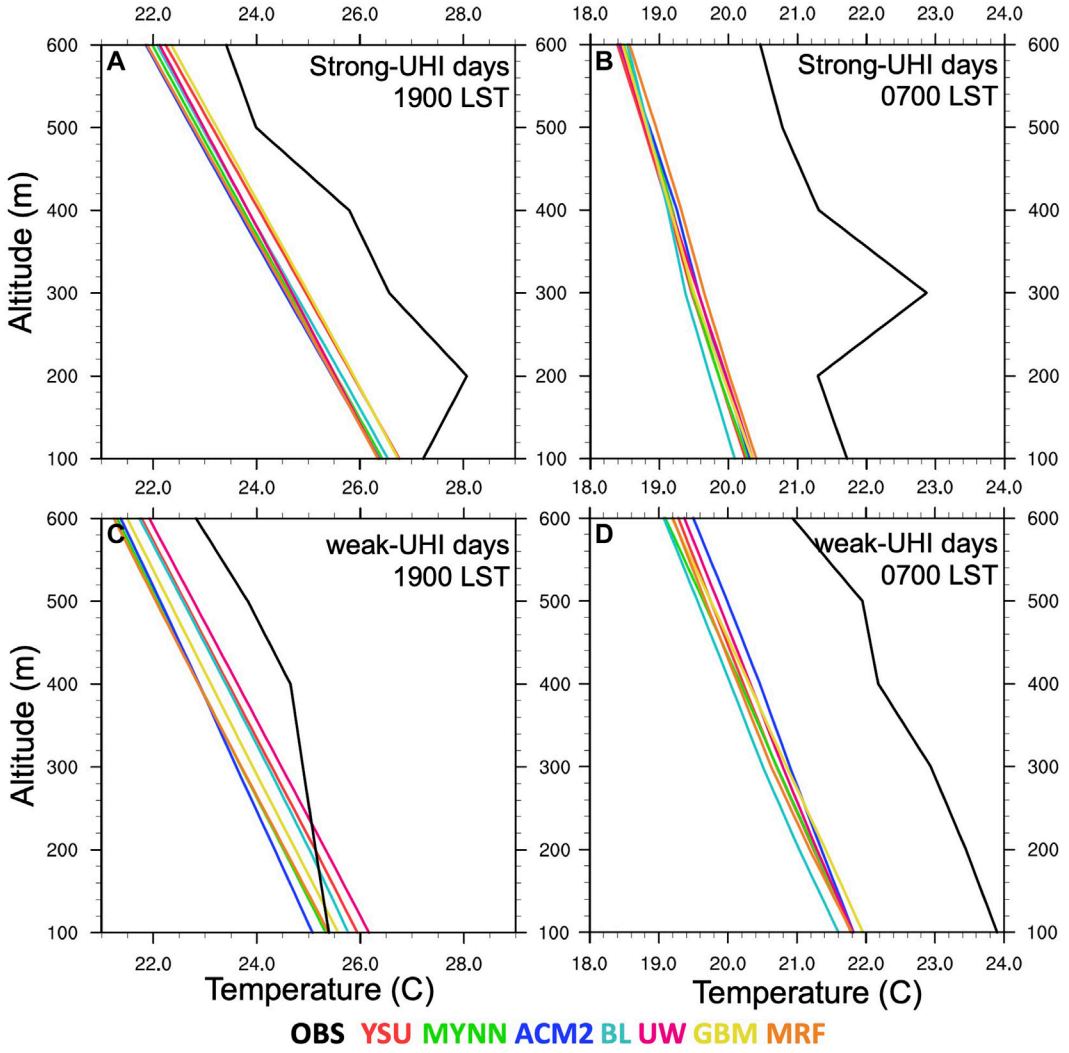

FIGURE 10
(A) Comparisons of the lower-level vertical profiles for the observed and simulated surface air temperatures at the Qingyuan station (Figure 1C) on strong-UHI days at 1900 LST. **(B)** is similar to **(A)** but at 0700 LST. **(C,D)** are similar to **(A,B)** but on weak-UHI days.

Model performances for PBL height

The other error source of the thermodynamic forecast within the boundary layer is the entrainment process near the top of PBL. The air entrained near the PBL top has a higher potential temperature but less moisture than that in lower PBL, leading to a tendency of stabilization. Consequently, the vertical structure of the temperature would be regulated by errors in entrainment, which is closely related to the PBL height (PBLH; Hu et al., 2010). Local and nonlocal schemes compute PBLH differently. The PBLHs of the local schemes are primarily based on total kinetic energy (TKE) predictions, while those of the nonlocal schemes are computed by empirical formulas considering wind speed, vertical gradients of vertical potential temperature, and the critical Richardson number (Stensrud, 2007). Given the different approaches to obtain PBLH in local and nonlocal schemes, this study used a consistent method to determine PBLH for the different PBL parameterization schemes and radiosondes (Coniglio, 2012). Specifically, the PBLH is defined as the first level above which the virtual temperature was 0.6 K greater than the peak virtual potential temperature in the lowest three levels. The same method is also used by the developers of Rapid Update Cycle (Benjamin et al., 2004).

The observed and simulated PBLHs obtained by the abovementioned definition are compared (Figure 11). The higher daytime PBLHs on the strong-UHI days than on the

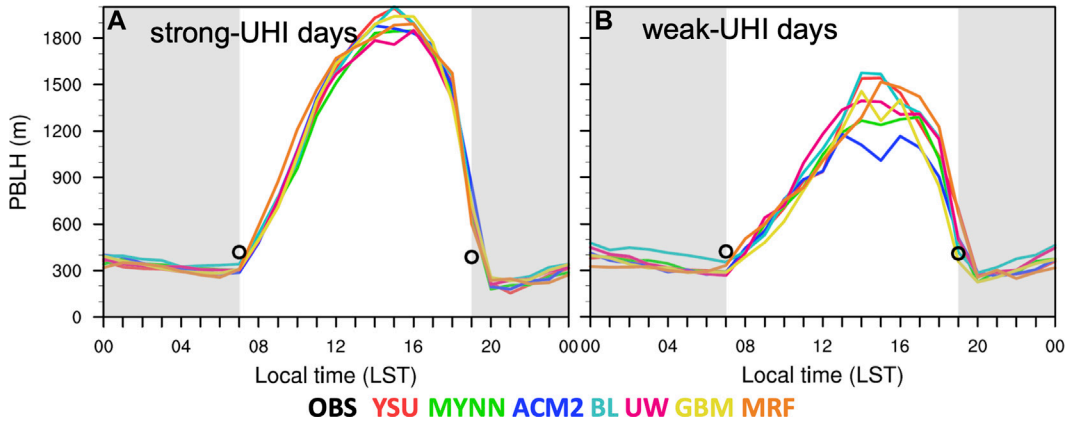

FIGURE 11
Comparisons of the observed (black circle) and simulated (colored lines) PBL heights at Qingyuan station (Figure 1C) on **(A)** strong-UHI days and **(B)** weak-UHI days.

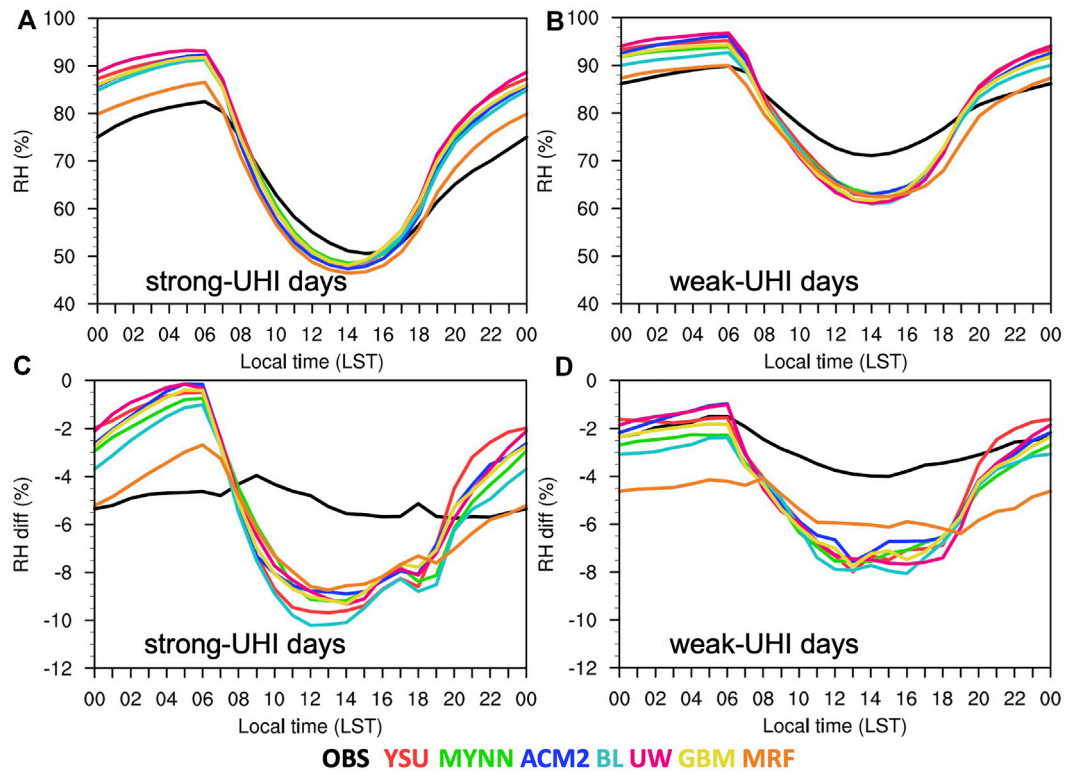

FIGURE 12
(A) Comparisons of the PBL schemes on the composite domain-averaged near-surface relative humidity over the urban region on strong-UHI days and **(C)** the corresponding relative humidity difference between urban and rural areas (urban minus rural). **(B,D)** are similar to **(A,C)** but on weak-UHI days.

weak-UHI days may be 1) due to the higher sensible heat flux (Figure 9, 11), which is demonstrated by Dang et al. (2016), who found a strong positive correlation between surface sensible heat fluxes and PBLH, and 2) higher surface temperature that is found to be positively correlated with PBLH (Xi et al., 2022; Figure 5A). The models underestimate

the early morning PBLH and overestimate the early evening PBLH on both strong/weak UHI days, with those on strong UHI days showing larger biases (Figure 11). The underestimation/overestimation of the PBLH may be partly due to the inappropriate vertical heat flux representation, which might be associated with different calculations of the sensible heat flux. Specifically, the local BL scheme shows the highest daytime sensible heat flux among the schemes, corresponding to the highest daytime PBLH and the highest daytime T2. The lower PBLHs and near-surface temperatures of ACM2 and MYNN in the afternoon correspond to their lowest sensible heat flux among all schemes (Figure 7E, 9, 11B). Such results imply that the sensible heat flux plays a key role in the performance of the model at the local scale.

Model performance for moisture conditions

Moisture condition is another important perspective that characterizes the difference between the urban and rural environments. Figure 12 shows the diurnal variations in the relative humidity (RH) over the urban region and the urban–rural contrast (urban minus rural). Similar to T2, the observed diurnal amplitude of RH over the urban region is larger on strong-UHI days than on weak-UHI days, which is also well captured by the model (Figures 7C,E, 12A,B), suggesting that the model is also able to distinguish among the observed moisture condition differences on strong-/weak-UHI days. Different from the UHI, the observed RH difference between urban and rural areas shows less diurnal variation under both scenarios. However, the model still presents a large diurnal amplitude (Figures 12C,D), implying that the model has difficulties in reproducing the urban–rural contrast of moisture conditions, which may be due to the simplicity of the model in representing the urban and rural underlying surface that leads to the bias in latent heating and sensible heating processes. The abovementioned features are shown in most of the PBL schemes except for the MRF, which presents better nocturnal RH over the urban region and better urban–rural contrast, especially on weak-UHI days.

Discussion of the dependence of model performance on moisture conditions

A comparison of recent studies that evaluated multiple PBL schemes has been conducted to discuss the applicability of these schemes to different climate zones. A survey of 12 published papers that focus on the impacts of PBL schemes on surface air temperature in North America, Europe and Asia were conducted. The overestimation or underestimation of surface air temperature is mostly dependent on the seasonal weather and regional climate in the region of interest. Specifically, the models usually show a cool bias on all days during warm seasons over North America and Europe (e.g., Kleczek et al., 2014; Banks and Baldasano, 2016; Avolio et al., 2017) but a warm bias during cold seasons (Shin and Hong 2011; Gunwani and Mohan, 2017). For Asia, which is influenced by monsoonal flows, the model shows that the diurnal variation in bias is dependent on the geographical situation. A cold bias during nighttime and a warm bias during daytime are noticed over humid coastal regions (Xie et al., 2012; Hariprasad et al., 2014), which is also suggested by the current study. On the other hand, there is a cold bias during the daytime and a warm bias during the nighttime for inland arid regions (Xu et al., 2019; Wang et al., 2021). The performance of the PBL schemes is less variational. Nine out of twelve published papers suggested that the nonlocal schemes (i.e., YSU and ACM2) were the closest schemes to the observations in most climate zones. BL was the best scheme for the regions over the junction of humid and arid regions (Xu et al., 2019). For the current study, the performance of the PBL schemes in simulating the near-surface temperature mostly resembles that of Xie et al. (2012), with BL overestimated the most and a reasonable performance by the ACM2. These results indicate that the selection of the PBL scheme for any study can be based on the diurnal cycle of the meteorological parameter or climatic zone where the area under consideration resides. Further understanding the adaptability of PBL schemes is a necessary step before improving them in the future.

Summary

Urbanization of large cities exerts significant changes in surface air temperature that can lead to inadvertent local weather and regional climate changes. As the first step to improve the forecasting for the urban environment, this study evaluates the performances of multiple PBL schemes in reproducing the lower-troposphere thermodynamic environments over the Greater Bay Area in South China. Seven PBL schemes, including three nonlocal (YSU, ACM2 and MRF) and four local (MYNN, GBM, UW and BL) schemes, are evaluated. Biases of meteorological variables vary with PBL schemes when different metrics are assessed while there are also several common characteristics, such as higher daytime and lower nighttime surface air temperature in urban regions compared to the observations. The results in this study can be used as a basis for PBL scheme selection for simulations in similar regions or under similar climate conditions.

To evaluate the performances of PBL schemes in different thermodynamic scenarios, the period from April to June in 2018 is first categorized into strong UHI days and weak UHI days. The performance of near-surface temperature and vertical temperature profiles, UHI intensity, PBL

structure, and humidity are then evaluated from seasonal and diurnal perspectives. Our conclusions are described as follows.

1) The seasonal simulations show a systematic bias in reproducing the low-level thermodynamic features and PBL structure over the urban and surrounding rural regions. Cool and moist biases during nighttime and warm and dry biases in the day are identified. Except for the MRF, other PBL schemes exhibit antiphase structures for the diurnal variation in the UHI intensity relative to those in the observation. Such antiphase structure could be modified by utilizing the land-surface model that accompanied by the urban canopy model, which describes the canopy trapping by the cities so the residual heat can be preserved (Oke et al., 2017). The nocturnal surface temperature over the city is therefore higher than the simulation without urban canopy model. The modeled PBL heights show an underestimation in the early morning and overestimation in the early evening. This underestimation/overestimation is closely associated with the sensible heat flux diagnosed by different PBL schemes. The higher the sensible heat flux is, the higher the near-surface temperature and PBL height are.
2) The model errors associated with PBL schemes are dependent on the diurnal cycles and thermodynamic conditions, as well as the geographical location that affects the moisture condition and the energy budget. Specifically, the MYNN performs best for the daytime near-surface temperature, while the MRF shows the lowest RMSE of T2 during nighttime, especially on the strong-UHI days. MRF also shows the best performance in simulating the observed urban heat island, with a similar pattern of diurnal variation, while the rest of the schemes are antiphase with respect to the observation. The nonlocal schemes with strong vertical mixing do not always lead to a warmer PBL, as suggested in previous studies, as indicated by the local UW showing higher vertical temperatures from a seasonal perspective. These issues must be considered in model configuration selection, parametrization scheme improvement, and bias correction for modeling studies.

Although there may not be a one-size-fits-all approach to the selection of a "best" PBL scheme, the current study aims to improve our understanding of the relative representation of multiple PBL schemes in severe weather modeling over the urban agglomeration in the Greater Bay Area. Further research is ongoing to expand and generalize the results by a wide array of cases.

Data availability statement

Publicly available datasets were analyzed in this study. This data can be found here: https://rda.ucar.edu/datasets/ds083.3/, http://data.cma.cn/data/online.html?t51.

Author contributions

LH: drafts the work, formal analysis, visualization LB: supervision, review and editing.

Funding

This study was supported by the National Natural Science Foundation of China (41805035, 41905043 and 42030610) and Guangdong Basic and Applied Basic Research Foundation (2021A1515011647 and 2022A1515011288).

Conflict of interest

The authors declare that the research was conducted in the absence of any commercial or financial relationships that could be construed as a potential conflict of interest.

Publisher's note

All claims expressed in this article are solely those of the authors and do not necessarily represent those of their affiliated organizations, or those of the publisher, the editors and the reviewers. Any product that may be evaluated in this article, or claim that may be made by its manufacturer, is not guaranteed or endorsed by the publisher.

References

Ashley, W., Strader, S., Rosencrants, T., and Krmenec, A. (2014). Spatiotemporal changes in tornado hazard exposure: The case of the expanding bull's-eye effect in chicago, Illinois. *Weather, Clim. Soc.* 6, 175–193. doi:10.1175/wcas-d-13-00047.1

Avolio, E., Federico, S., Miglietta, M., Lo Feudo, T., Calidonna, C., and Sempreviva, A. (2017). Sensitivity analysis of WRF model PBL schemes in simulating boundary layer variables in southern Italy: An experimental campaign. *Atmos. Res.* 192, 58–71. doi:10.1016/j.atmosres.2017.04.003

Banks, R., and Baldasano, J. M. (2016). Impact of WRF model PBL schemes on air quality simulations over Catalonia, Spain. *Sci. Total Environ.* 572, 98–113. doi:10.1016/j.scitotenv.2016.07.167

Barlage, M., Miao, S., and Chen, F. (2016). Impact of physics parameterizations on high-resolution weather prediction over two Chinese megacities. *J. Geophys. Res. Atmos.* 121, 4487–4498. doi:10.1002/2015jd024450

Benjamin, S., Devenyi, D., Weygandt, S., Brundage, K. J., Brown, J. M., Grell, G. A., et al. (2004). An hourly assimilation– forecast cycle: The RUC. *Mon.*

Weather Rev. 132, 495–518. doi:10.1175/1520-0493(2004)132<0495:ahactr>2.0.co;2

Borge, R., Alexandrov, V., Vas, J., Lumbreras, J., and Rodriguez, E. (2008). A comprehensive sensitivity analysis of the WRF model for air quality applications over the Iberian Peninsula. *Atmos. Environ.* 42, 8560–8574. doi:10.1016/j.atmosenv.2008.08.032

Bougeault, P., and Lacarrere, P. (1989). Parameterization of orography-induced turbulence in a mesobeta-scale model. *Mon. Weather Rev.* 117, 1872–1890. doi:10.1175/1520-0493(1989)117<1872:pooiti>2.0.co;2

Bretherton, C., and Sungsu, P. (2009). A new moist turbulence parameterization in the community atmosphere model. *J. Clim.* 22, 3422–3448. doi:10.1175/2008jcli2556.1

Chaouch, N., Temimi, M., Weston, M., and Ghedira, H. (2017). Sensitivity of the meteorological model WRF-ARW to planetary boundary layer schemes during fog conditions in a coastal arid region. *Atmos. Res.* 187, 106–127. doi:10.1016/j.atmosres.2016.12.009

Ching, J., Rotunno, R., LeMone, M., Martilli, A., Kosovic, B., Jimenez, P. A., et al. (2014). Convectively induced secondary circulations in fine-grid mesoscale numerical weather prediction models. *Mon. Weather Rev.* 142, 3284–3302. doi:10.1175/mwr-d-13-00318.1

Cohen, A., Cavallo, S., Coniglio, C., and Brooks, H. (2015). A review of planetary boundary layer parameterization schemes and their sensitivity in simulating southeastern U.S. cold season severe weather environments. *Weather Forecast.* 30, 591–612. doi:10.1175/waf-d-14-00105.1

Coniglio, M. (2012). Verification of RUC 0–1-h forecasts and SPC mesoscale analyses using VORTEX2 soundings. *Weather Forecast.* 27, 667–683. doi:10.1175/waf-d-11-00096.1

Dang, R., Li, H., Liu, Z., and Yang, Y. (2016). Statistical analysis of relationship between daytime lidar-derived planetary boundary layer height and relevant atmospheric variables in the semiarid region in Northwest China. *Adv. Meteorology* 2016, 1–13. doi:10.1155/2016/5375918

Ding, Y. (1994). *Monsoons over China*. Netherlands: Kluwer Acad, 419.

Doan, Q., Dipankar, A., Simón-Moral, A., Sanchez, C., Prasanna, V., Roth, M., et al. (2021). Urban-induced modifications to the diurnal cycle of rainfall over a tropical city. *Q. J. R. Meteorol. Soc.* 147, 1189–1201. doi:10.1002/qj.3966

Dzebre, D., and Adaramola, M. (2020). A preliminary sensitivity study of Planetary Boundary Layer parameterisation schemes in the weather research and forecasting model to surface winds in coastal Ghana. *Renew. Energy* 146, 66–86. doi:10.1016/j.renene.2019.06.133

Ferrero, E., Alessandrini, S., and Vandenberghe, F. (2018). Assessment of planetary-boundary-layer schemes in the weather research and forecasting model within and above an urban canopy layer. *Bound. Layer. Meteorol.* 168, 289–319. doi:10.1007/s10546-018-0349-3

Garcia-Diez, M., Fernandex, J., Fita, L., and Yague, C. (2011). Seasonal dependence of WRF model biases and sensitivity to PBL schemes over Europe. *Q. J. R. Meteorological Soc.* 00, 2–21. doi:10.1002/qj.1976

Grenier, H., and Bretherton, C. (2001). A moist PBL parameterization for large-scale models and its application to subtropical cloud-topped marine boundary layers. *Mon. Weather Rev.* 129, 357–377. doi:10.1175/1520-0493(2001)129<0357:amppfl>2.0.co;2

Gunwani, P., and Mohan, M. (2017). Sensitivity of WRF model estimates to various PBL parameterizations in different climatic zones over India. *Atmos. Res.* 194, 43–65. doi:10.1016/j.atmosres.2017.04.026

Hacker, J. (2010). Spatial and temporal scales of boundary layer wind predictability in response to small-amplitude land surface uncertainty. *J. Atmos. Sci.* 67, 217–233. doi:10.1175/2009jas3162.1

Hallegatte, S., Green, C., Nicholls, R., and Corfee-Morlot, J. (2013). Future flood losses in major coastal cities. *Nat. Clim. Chang.* 3, 802–806. doi:10.1038/nclimate1979

Hariprasad, K., Srinivas, C., Singh, A., Vijaya Bhaskara Rao, S., Baskaran, R., and Venkatraman, B. (2014). Numerical simulation and intercomparison of boundary layer structure with different PBL schemes in WRF using experimental observations at a tropical site. *Atmos. Res.* 145, 27–44. doi:10.1016/j.atmosres.2014.03.023

Hong, S., Noh, Y., and Dudhia, J. (2006). A new vertical diffusion package with an explicit treatment of entrainment processes. *Mon. Weather Rev.* 134, 2318–2341. doi:10.1175/mwr3199.1

Hong, S., and Pan, H. (1996). Nonlocal boundary layer vertical diffusion in a medium-range forecast model. *Mon. Weather Rev.* 124, 2322–2339. doi:10.1175/1520-0493(1996)124<2322:nblvdi>2.0.co;2

Hu, X., Nielsen-Gammon, J., and Zhang, F. (2010). Evaluation of three planetary boundary layer schemes in the WRF Model. *J. Appl. Meteorology Climatol.* 49, 1831–1844. doi:10.1175/2010jamc2432.1

Huang, L., Luo, Y., and Bai, L. (2022). An evaluation of convection-permitting ensemble simulations of coastal nocturnal rainfall over SouthSouth China during the early-summer rainy season. *JGR. Atmos.* 127, e2021JD035656. doi:10.1029/2021jd035656

Huang, L. (2020). Sensitivity analysis of ensemble simulations on a torrential rainfall case over SouthSouth China using multiple PBL and SL parameterizations. *J. Trop. Meteorology* 26, 208–222. doi:10.16555/j.1006-8775.2020.019

Huang, M., Gao, Z., Miao, S., and Chen, F. (2019). Sensitivity of urban boundary layer simulation to urban canopy models and PBL schemes in Beijing. *Meteorol. Atmos. Phys.* 131, 1235–1248. doi:10.1007/s00703-018-0634-1

Huff, F., and Vogel, J. (1978). Urban, topographic, and diurnal effects on rainfall in the St. Louis region. *J. Appl. Meteor.* 17, 565–577. doi:10.1175/1520-0450(1978)017<0565:utadeo>2.0.co;2

Jankov, I., Gallus, W., Segal, M., Shaw, B., and Koch, S. E. (2005). The impact of different WRF Model physical parameterizations and their interactions on warm season MCS rainfall. *Weather Forecast.* 20, 1048–1060. doi:10.1175/waf888.1

Johns, R., and Doswell, C., III (1992). Severe local storms forecasting. *Weather Forecast.* 7, 588–612. doi:10.1175/1520-0434(1992)007<0588:slsf>2.0.co;2

Kassomenos, P., and Katsoulis, B. (2006). Mesoscale and macroscale aspects of the morning urban heat island around Athens, Greece. *Meteorol. Atmos. Phys.* 94, 209–218. doi:10.1007/s00703-006-0191-x

Kleczek, M., Steeneveld, G., and Holtslag, A. (2014). Evaluation of the weather research and forecasting mesoscale model for GABLS3: impact of boundary-layer schemes, boundary conditions and spin-up. *Bound. Layer. Meteorol.* 152, 213–243. doi:10.1007/s10546-014-9925-3

Li, M., Luo, Y., Zhang, D., Chen, M., Wu, C., Yin, J., et al. (2021). Analysis of a record-breaking rainfall event associated with a monsoon coastal megacity of South China using multisource data. *IEEE Trans. Geosci. Remote Sens.* 59, 6404–6414. doi:10.1109/tgrs.2020.3029831

Li, T., Wang, H., Zhao, T., Xue, M., Wang, Y., Che, H., et al. (2016). The impacts of different PBL schemes on the simulation of PM2.5 during severe haze episodes in the jing-jin-ji region and its surroundings in China. *Adv. Meteorology* 2016, 1–15. doi:10.1155/2016/6295878

Li, W., Chen, S., Chen, G., Sha, W., Luo, C., Feng, Y., et al. (2011). Urbanization signatures in strong versus weak precipitation over the Pearl River Delta metropolitan regions of China. *Environ. Res. Lett.* 6, 049503. doi:10.1088/1748-9326/6/4/049503

Liu, M., and Chen, M. (2014). Evaluation of BJ-RUC system for the forecast quality of planetary boundary layer in Beijing Area (in Chinese). *J. Appl. Meteorological Sci.* 25, 212–221.

Martilli, A., Sanchez, B., Rasilla, D., Pappaccogli, G., Allende, F., Martin, F., et al. (2021). Simulating the meteorology during persistent Wintertime Thermal Inversions over urban areas. The case of Madrid. *Atmos. Res.* 263, 105789. doi:10.1016/j.atmosres.2021.105789

Miao, S., Dou, J., Chen, F., Li, J., and Li, A. (2012). Analysis of observations on the urban surface energy balance in Beijing. *Sci. China Earth Sci.* 55, 1881–1890. doi:10.1007/s11430-012-4411-6

Nakanishi, M., and Niino, H. (2004). An improved mellor–yamada level-3 model with condensation physics: Its design and verification. *Bound. Layer. Meteorol.* 112, 1–31. doi:10.1023/b:boun.0000020164.04146.98

Nielsen-Gammon, J., Hu, X., Zhang, F., and Pleim, J. (2010). Evaluation of planetary boundary layer scheme sensitivities for the purpose of parameter estimation. *Mon. Weather Rev.* 138, 3400–3417. doi:10.1175/2010mwr3292.1

Niyogi, D., Pyle, P., Lei, M., Arya, S. P., Kishtawal, C. M., Shepherd, M., et al. (2011). Urban modification of thunderstorms—an observational storm climatology and model case study for the indianapolis urban region. *J. Appl. Meteorology Climatol.* 50, 1129–1144. doi:10.1175/2010jamc1836.1

Oke, T., Mills, G., Christen, A., and Voogt, J. (2017). *Urban climates*. Cambridge, United Kingdom: Cambridge University Press, 546pp.

Oke, T. (1995). *The heat island of the urban boundary layer: Characteristics, causes, and effects in: Wind climate in cities*. New York, NY Norwell, MA London, UK: Kluwer Academic, 81–102.

Palou, F., and Mahalov, A. (2019). Summer- and wintertime variations of the surface and near-surface urban heat island in a semiarid environment. *Weather Forecast.* 34, 1849–1865. doi:10.1175/waf-d-19-0054.1

Pleim, J. (2007). A combined local and nonlocal closure model for the atmospheric boundary layer. Part I: Model description and testing. *J. Appl. Meteorology Climatol.* 46, 1383–1395. doi:10.1175/jam2539.1

Shin, H., and Hong, S. (2011). Intercomparison of planetary boundary-layer parameterizations in the WRF model for a single day from CASES-99. *Bound. Layer. Meteorol.* 139, 261–281. doi:10.1007/s10546-010-9583-z

Skamarock, W., Klemp, J., and Dudhia, J., (2008). A description of the Advanced Research WRF version 3. *NCAR Tech.*, 113. Note TN-4751STR.

Stensrud, D. (2007). *Parameterization schemes: Keys to understanding numerical weather prediction models*. Cambridge, United Kingdom: Cambridge University Press, 459.

Sun, X., Luo, Y., Gao, X., Wu, M., Li, M., Huang, L., et al. (2021a). On the localized extreme rainfall over the Great Bay area in SouthSouth China with complex topography and strong UHI effects. *Mon. Weather Rev.* 149, 2777–2801. doi:10.1175/mwr-d-21-0004.1

Sun, Y., Zhang, N., Miao, S., and Kong, F. (2021b). Urban morphological parameters of the main cities in China and their application in the WRF model. *J. Adv. Model. Earth Syst.* 13, e2020MS002382. doi:10.1029/2020ms002382

Wang, C., and Ying, M. (2020). The uncertainty of tropical cyclone intensity and structure based on different parameterization schemes of planetary boundary layer. *J. Trop. Meteorology* 26, 377–389. doi:10.46267/j.1006-8775.2020.033

Wang, Y., Sayit, H., Mamtimin, A., Zhu, J., Zhou, C., Huo, W., et al. (2021). Evaluation of five planetary boundary layer schemes in WRF over China's largest semi-fixed desert. *Atmos. Res.* 256, 105567. doi:10.1016/j.atmosres.2021.105567

Wu, M., Luo, Y., Chen, F., and Wong, W. (2019). Observed link of extreme hourly precipitation changes to urbanization over coastal South China. *J. Appl. Meteorology Climatol.* 58, 1799–1819. doi:10.1175/jamc-d-18-0284.1

Xi, X., Zhang, Y., Gao, Z., Yang, Y., Zhou, S., Duan, Z., et al. (2022). Diurnal climatology of correlations between the planetary boundary layer height and surface meteorological factors over the contiguous United States. *Int. J. Climatol.* 42, 5092–5110. doi:10.1002/joc.7521

Xie, B., Fung, J., Chan, A., and Lau, A. (2012). Evaluation of nonlocal and local planetary boundary layer schemes in the WRF model. *J. Geophys. Res.* 117, D12103. doi:10.1029/2011jd017080

Xu, L., Hui, H., Du, Q., and Xu, X. (2019). The assessment of the planetaryboundary layer schemes in WRF over the central Tibetan Plateau. *Atmos. Res.* 230, 104644. doi:10.1016/j.atmosres.2019.104644

Yin, J., Zhang, D., Luo, Y., and Ma, R. (2020). On the extreme rainfall event of 7 May 2017 over the coastal city of Guangzhou. Part I: Impacts of urbanization and orography. *Mon. Weather Rev.* 148, 955–979. doi:10.1175/mwr-d-19-0212.1

Zhang, D. (2020). Rapid urbanization and more extreme rainfall events. *Sci. Bull.* 65, 516–518. doi:10.1016/j.scib.2020.02.002

Zhang, N., Wang, X., Chen, Y., Dai, W., and Wang, X. (2015). Numerical simulations on influence of urban land cover expansion and anthropogenic heat release on urban meteorological environment in Pearl River Delta. *Theor. Appl. Climatol.* 126, 469–479. doi:10.1007/s00704-015-1601-0

frontiers | Frontiers in Earth Science

TYPE Original Research
PUBLISHED 20 January 2023
DOI 10.3389/feart.2022.1092368

OPEN ACCESS

EDITED BY
Jianhua Sun,
Institute of Atmospheric Physics (CAS), China

REVIEWED BY
Zhenhua Li,
University of Saskatchewan, Canada
Danqiong Dai,
Institute of Atmospheric Physics (CAS), China

*CORRESPONDENCE
Ya Huang,
hygccw@hhu.edu.cn

SPECIALTY SECTION
This article was submitted to Atmospheric Science, a section of the journal Frontiers in Earth Science

RECEIVED 08 November 2022
ACCEPTED 21 November 2022
PUBLISHED 20 January 2023

CITATION
Li B, Huang Y, Du L and Wang D (2023), Sensitivity experiments of RegCM4 using different cumulus and land surface schemes over the upper reaches of the Yangtze river. *Front. Earth Sci.* 10:1092368. doi: 10.3389/feart.2022.1092368

Sensitivity experiments of RegCM4 using different cumulus and land surface schemes over the upper reaches of the Yangtze river

Bingxue Li[1], Ya Huang[2]*, Lijuan Du[3] and Dequan Wang[4]

[1]Department of the Aviation Manufacturing, Shanghai Civil Aviation College, Shanghai, China, [2]College of Oceanography, Hohai University, Nanjing, China, [3]State Key Laboratory of Simulation and Regulation of Water Cycle in River Basin, China Institute of Water Resources and Hydropower Research, Beijing, China, [4]School of Civil and Hydraulic Engineering, Ningxia University, Yinchuan, China

For the optimal performance of climate simulation, it is critical to localize physical parameterization schemes of climate models, especially in regions with unique geographic characteristics. To study the performance of different physical parameterization schemes for climate simulation in the upper reaches of the Yangtze River Basin (UYRB), we conducted short-term simulations with a resolution of 50 km from 1990 to 1993 using RegCM4 driven by ERA-Interim. Simulations with 72 different scheme combinations were conducted and analyzed to identify the optimal cumulus convection schemes (CSs) and the land surface process schemes in the RegCM4 model. Using the multi-standard scoring method, we evaluated the model performance of precipitation and temperature over the UYRB with different physical parameterization schemes. The results show that precipitation is more sensitive to the CSs than the LSPs. Among the selected CSs, the Kain-Fritsch scheme can better reproduce precipitation characteristics of the UYRB, with a wet bias of only 0.2 mm/day for the multi-year average precipitation. Compared to the community land model (CLM 3.5 and CLM4.5), the Biosphere-Atmosphere Transfer Scheme (BATS) performs better in reproducing temperature characteristics of the UYRB, with an average cold bias of only 0.2°C for all BATS schemes. The soil moisture, evapotranspiration and precipitation are lower and sensible heat flux is higher in CLM simulations, which can account for CLMs simulating warmer temperatures than BATS. The results provide a baseline for the localization of the RegCM4's parameterization schemes in the UYRB and other regions of China.

KEYWORDS

RegCM4, physical parameterization scheme, precipitation, temperature, Yangtze River Basin

Introduction

During the last decades, regional climate models (RCMs) have been increasingly used to produce climate information at scales finer than those of global climate models (GCMs) over regions around the world (Giorgi and Gutowski, 2015). The advantages and disadvantages of RCMs have been discussed in many papers (Centella-Artola et al., 2015; Giorgi and Gutowski, 2015; Martínez-Castro et al., 2018). The performance of regional climate models (RCMs) varies with the study region and season, making it difficult to find a physical parameterization scheme that is universally applicable. Furthermore, because the parameterization of regional climate models is often developed for specific climate conditions and resolutions, identical schemes perform very differently in different simulation regions (Giorgi and Marinucci, 1996). Therefore, it is critical to identify the appropriate parameterization schemes for a given study area to optimize model performance. In East Asia (Singh et al., 2006; Kang and Hong, 2008; Bao, 2013; Huang et al., 2013; Kang et al., 2014), Southeast Asia (Juneng et al., 2016; Ngo-Duc et al., 2017), South Africa (Kalognomou et al., 2013; Llopart et al., 2017), and South America (Reboita et al., 2014), numerous sensitivity tests have been conducted on physical parameters to identify the optimal schemes, and some research has improved the simulation performance of the RegCM by introducing or modifying the parameters of the current physical parameterization schemes (Chow et al., 2006; Gianotti and Eltahir, 2014; Zou et al., 2014).

Many studies have shown that the cumulus convection parameterization scheme has a great impact than other schemes on the simulation performance of the RegCM (Liu and Ding, 2001; Dash et al., 2006; Cao et al., 2007; Zou and Zhou, 2011). Different cumulus convection parameterization schemes have varying effects on the performance of the Chinese monsoon area (Jinsong et al., 2002; Liu et al., 2005; Li and Wang, 2008). Gao et al. (2016) and Gao et al. (2017) compared the simulation performance of several cumulus convection schemes (CSs) in major river basins in China and found that the Emanuel scheme performs better. Although the cumulus convection scheme significantly impacts precipitation, the effect of LSPs on precipitation is also important. In East Asia, Kang et al. (2014) and Li et al. (2016) compared simulations with BATS (Dickinson et al., 1993) and CLM3 (Oleson et al., 2004; Steiner et al., 2009) using the Emanuel convection scheme in RegCM and discovered that BATS' simulations tend to produce more summer precipitation than those of CLM.

Of the RCMs that are applied to East Asia (e.g., RIMES (Fu and Yuan, 2001), IPRCRegCM (Wang et al., 2003), PRECIS (Xu et al., 2006), MM5 (Qian and Leung, 2007), and WRF (Yu et al., 2015)), the RegCM system is among the most commonly used. There have been many case studies in China on the RegCM physical parameterization scheme. However, previous studies typically focused on East Asia or China as a whole and paid less attention to sub-regions. The upper reaches of the Yangtze River Basin (UYRB) have strong spatiotemporal heterogeneity in temperature and precipitation in the transition zone between the subtropical and temperate zones. Under the influence of the East Asian and South Asian monsoon systems, extreme weather and climate events frequently occur in the basin. Due to the influences of two monsoon systems at various time scales and the region's highly heterogeneous topographical and geographical features, climate simulation in UYRB is still a considerable challenge, especially for precipitation. Previous studies have not yet clarified the most suitable physical parameterization scheme for the UYRB. Therefore, if climate simulation is to improve in the region, it is critical to evaluate the simulation performance of various RegCM physical parameterization schemes.

The main purpose of the study is to evaluate the simulation performance of precipitation and temperature over the UYRB using the selected CSs and land surface process schemes (LSPs) and to analyze the causes of the differences in performance of the various schemes. Sections 3, Sections 4 present comprehensive evaluation results and discussion of precipitation and temperature for all schemes. The results provide a scientific basis for selecting physical parameterization schemes for regional climate simulation using RegCM4 in the UYRB.

Experiments and methodology

Model description

RegCM4 is an RCM developed by the Abdus Salam International Center for Theoretical Physics (Giorgi and Anyah, 2012; Giorgi et al., 2012) and has been widely used in multi-decadal climate change simulations in East Asia (Gao et al., 2008; Zhang et al., 2015; Gao and Giorgi, 2017). RegCM4 provides five CSs and three LSPs for users to choose and can run different CSs over land and ocean, referred to as "mixed convection." More detailed information about the RegCM4 can be found in Giorgi et al. (2012).

Experimental design and data

The parameterization set of RegCM4 includes planetary boundary layer scheme, sea surface flux scheme, cumulus scheme, radiation scheme, and land surface scheme. The study used the planetary boundary layer scheme and sea surface flux scheme developed by Holtslag et al. (1990) and Zeng et al. (1998), respectively. The computational domain of RegCM4 is shown in Figure 1. ERA-Interim reanalysis data provided the experiments' initial and lateral boundary conditions (Uppala et al., 2008). The meteorological observation data used for evaluation in the UYRB were

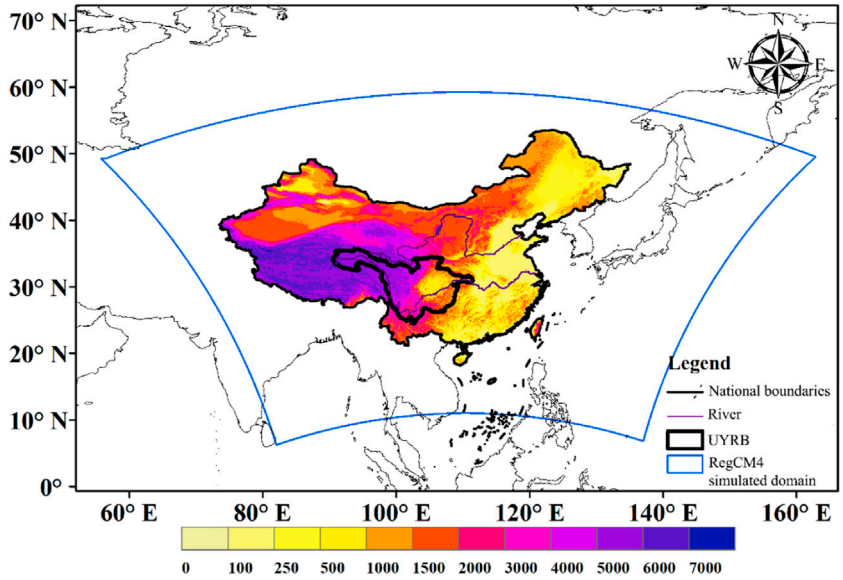

FIGURE 1
Computation domain and topography (unit: m) of RegCM4.

TABLE 1 RegCM4 model configuration used in this study.

Contents	Description
Domain	50 km horizontal resolution Central Lat. and Lon.: 35 °N, 115 °E 200 (Lon) × 130 (Lat)
Vertical layers (top)	18 vertical sigma levels (1 hPa)
PBL scheme	Holtslag
Short-/longwave radiation scheme	NCAR CCM3
Boundary data	ERA-Interim reanalysis data
Simulation period	October 1989–December 1993
Analysis period	January 1990–December 1993

extracted based on CN05 with a resolution of 0.5° developed by Wu and Gao (2013). The inverse distance weighted method was used to interpolate CN05 data into the computational grid center of the RegCM4 model. Details of the model parameter configuration are presented in Table 1.

In this study, RegCM4 with 72 sets of physical parameterization schemes was used to simulate the coordinated regional climate downscaling experiment East Asia phase II domain, and only the UYRB was selected for analysis. As shown in Table 2, among the 72 sets of physical parameterization schemes, the LSP schemes used by Nos. 1–24, Nos. 25–48, and Nos. 49–72 were BATS, CLM3.5, and CLM4.5, respectively. Further details of both BATS and CLM schemes are presented in Llopart, Steiner and Dickinson (Dickinson et al., 1993; Steiner et al., 2005; Steiner et al., 2009; Llopart et al., 2017). The mixed CSs were used overland (LCS) and ocean (OCS), and the convection scheme was selected from Kuo, Grell, Emanuel, Tiedtke, and Kain-Fritsch (Anthes, 1977; Emanuel, 1991; Grell, 1993; Kain, 2004).

Methods

This study uses a multi-standard scoring method to evaluate the performances of different physical parameterization schemes in RegCM4. The criteria include mean annual precipitation (or temperature), standard deviation, annual climate cycle, normalized root mean square error (NRMSE), spatial distribution, empirical orthogonal function (EOF), and probability density function (PDF). Table 3 shows the criteria used in the evaluation and the corresponding weights. The rank score (RS) from 0 to 9, which is used to assess each assessment criterion, is written as follows:

TABLE 2 Physical parameterization schemes used in the study.

No.	LCS	OCS	LSP	No.	LCS	OCS	LSP	No.	LCS	OCS	LSP
1	K	K	BATS	25	K	K	CLM3.5	49	K	K	CLM4.5
2	G-AS	G-AS	BATS	26	G-AS	G-AS	CLM3.5	50	G-AS	G-AS	CLM4.5
3	G-AS	E	BATS	27	G-AS	E	CLM3.5	51	G-AS	E	CLM4.5
4	G-AS	T	BATS	28	G-AS	T	CLM3.5	52	G-AS	T	CLM4.5
5	G-AS	KF	BATS	29	G-AS	KF	CLM3.5	53	G-AS	KF	CLM4.5
6	G-FC	G-FC	BATS	30	G-FC	G-FC	CLM3.5	54	G-FC	G-FC	CLM4.5
7	G-FC	E	BATS	31	G-FC	E	CLM3.5	55	G-FC	E	CLM4.5
8	G-FC	T	BATS	32	G-FC	T	CLM3.5	56	G-FC	T	CLM4.5
9	G-FC	KF	BATS	33	G-FC	KF	CLM3.5	57	G-FC	KF	CLM4.5
10	E	G-AS	BATS	34	E	G-AS	CLM3.5	58	E	G-AS	CLM4.5
11	E	G-FC	BATS	35	E	G-FC	CLM3.5	59	E	G-FC	CLM4.5
12	E	E	BATS	36	E	E	CLM3.5	60	E	E	CLM4.5
13	E	T	BATS	37	E	T	CLM3.5	61	E	T	CLM4.5
14	E	KF	BATS	38	E	KF	CLM3.5	62	E	KF	CLM4.5
15	T	G-AS	BATS	39	T	G-AS	CLM3.5	63	T	G-AS	CLM4.5
16	T	G-FC	BATS	40	T	G-FC	CLM3.5	64	T	G-FC	CLM4.5
17	T	E	BATS	41	T	E	CLM3.5	65	T	E	CLM4.5
18	T	T	BATS	42	T	T	CLM3.5	66	T	T	CLM4.5
19	T	KF	BATS	43	T	KF	CLM3.5	67	T	KF	CLM4.5
20	KF	G-AS	BATS	44	KF	G-AS	CLM3.5	68	KF	G-AS	CLM4.5
21	KF	G-FC	BATS	45	KF	G-FC	CLM3.5	69	KF	G-FC	CLM4.5
22	KF	E	BATS	46	KF	E	CLM3.5	70	KF	E	CLM4.5
23	KF	T	BATS	47	KF	T	CLM3.5	71	KF	T	CLM4.5
24	KF	KF	BATS	48	KF	KF	CLM3.5	72	KF	KF	CLM4.5

*Convection schemes are abbreviated as follows: KUO (K), Grell (G), Emanuel (E), Tiedtke (T), Kain-Fritsch (KF), Arakawa-Schubert Cumulus Closure Scheme (AS), and Fritsch-Chappell Cumulus Closure Scheme (FC).

TABLE 3 Statistics of climate variables and their weights.

Statistics of climate variables	Criteria	Weights
Mean value	RE (%)	1.0
Standard deviation	RE (%)	1.0
Temporal change	NRMSE	1.0
Monthly distribution	Correlation coefficient (R^2)	1.0
Spatial distribution	Correlation coefficient (R^2)	1.0
Spatiotemporal variability	EOF1 (first vector)	0.5
	EOF2 (second vector)	0.5
Probability density functions	BS	0.5
	Sscore	0.5

$$RS_i = \frac{x_i - x_{\min}}{x_{\max} - x_{\min}} \times 9 \quad (1)$$

where x_i is the relative error (*RE*) or other relevant statistics between the observation and the *i*th RegCM result. When x_i represents *RE*, the larger the x_i, the higher the RS of the *i*th RegCM result in the assessment criterion. The performance score of each sensitivity test is obtained by the weighted summation of RS for all assessment criteria. *RE* is used to evaluate the annual mean and standard deviation of the climate variables simulated by RegCM4. NRMSE (Hanna and Heinold, 1985) is used to evaluate RegCM4's ability to simulate climate variables.

$$NRMSE = \frac{\sqrt{\frac{1}{n}\sum_{i=1}^{n}(X_{Gi} - X_{oi})^2}}{\sqrt{\frac{1}{n-1}\sum_{i=1}^{n}(X_{oi} - \bar{X}_o)^2}} \quad (2)$$

Where X_{Gi} and X_{Oi} are the values of the simulated and observed climate variables in RegCM4, respectively, during the simulation period *i*, *n* is the length of the RegCM4 simulation period, and $\bar{X}_o$ is the average value of the observed data during the observation period.

The annual cycle and spatial distribution of climate variables simulated by RegCM4 are evaluated using correlation coefficients. Since the empirical orthogonal function (EOF) can qualitatively and quantitatively analyze the relevant characteristics of the spatial field of climate variables (Mu et al., 2004), we used this method to compare the temporal and spatial changes in the climate variables

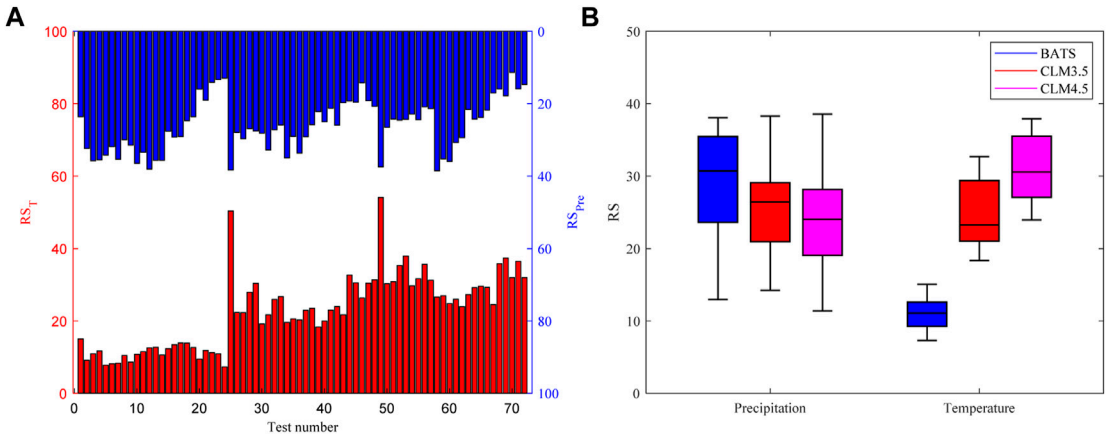

FIGURE 2
Histogram and box plot of the precipitation and temperature ranking score for the 72 sets of physical parameterization schemes. **(A)** Blue histogram represents precipitation scores, and red histogram represents temperature scores; **(B)** Blue, red and purple boxes represent BATS, CLM3.5 and CLM4.5 scenarios, respectively.

TABLE 4 Evaluation results for air temperature in China and the UYRB in nine groups.

	No.	Mean value (°C)	Standard deviation	NRMSE	Correlation coefficient during the year	Spatial correlation coefficient	EOF		PDF		Score
							EOF_1	EOF_2	BS	Sscore	
T	OBS	10.6	7.0				98.6	0.8			
	12	10.5	8.1	0.20	0.992	0.991	99.0	0.4	0.07	82.76	12.58
	19	10.3	8.4	0.24	0.992	0.992	98.9	0.5	0.06	85.15	12.65
	24	10.9	7.9	0.17	0.992	0.992	98.8	0.6	0.04	86.62	7.31
	36	12.9	7.5	0.37	0.986	0.990	98.6	0.6	0.18	72.65	20.31
	43	12.9	7.8	0.38	0.989	0.989	98.4	0.7	0.18	70.78	21.71
	48	14.0	7.3	0.51	0.987	0.982	98.2	0.6	0.21	72.00	31.33
	60	12.3	8.2	0.32	0.989	0.987	97.8	0.9	0.19	68.73	24.79
	67	12.7	8.4	0.36	0.995	0.986	98.0	0.8	0.20	69.43	24.54
	72	13.8	7.6	0.46	0.993	0.983	97.7	1.0	0.29	61.08	31.99
Pre	OBS	3.0	1.8				54.8	20.0			
	12	4.9	2.4	1.32	0.864	0.125	54.6	15.8	2.82	20.05	38.06
	19	4.5	2.2	1.03	0.882	0.372	49.2	19.8	1.56	40.79	23.62
	24	3.3	1.6	0.55	0.847	0.253	40.8	21.9	0.20	79.31	12.96
	36	4.7	2.3	1.12	0.924	0.111	57.3	14.6	2.96	35.13	33.66
	43	4.1	2.1	0.86	0.863	0.444	46.6	25.1	0.90	53.36	19.73
	48	2.3	1.3	0.68	0.823	0.127	44.2	19.6	0.56	64.99	20.73
	60	4.7	2.7	1.25	0.907	0.165	57.1	15.3	2.22	30.80	35.96
	67	4.1	2.2	0.80	0.914	0.441	50.1	23.0	0.93	52.60	17.04
	72	2.5	1.4	0.54	0.893	0.176	47.7	17.4	0.49	74.23	14.68

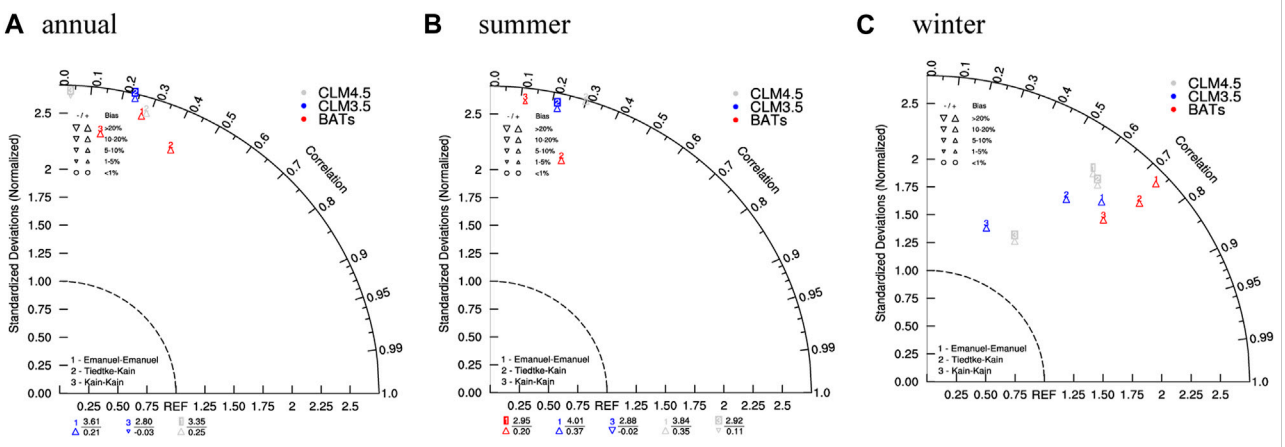

FIGURE 3
Taylor diagrams of annual, summer and winter precipitation in the UYRB. (Values at the bottom are statistics that exceed the threshold of Taylor diagrams.)

simulated by RegCM4 and in observation on a monthly scale (Harvey and Wigley, 2003). The majority of the variance in EOF can be represented by the first two eigen vectors, so this study only analyses these first two.

Two indicators, the BS and the significance score (Sscore), are used to evaluate the probability density distribution of climate variables on a monthly scale for the RegCM4 simulation results. The BS is the mean square error of the probability prediction (Brier, 1950; Fraedrich and Leslie, 1987), and Sscore is the smallest cumulative probability of the observed and simulated distribution in each equal sequence of values.

$$BS = \frac{1}{n}\sum_{i=1}^{n}(P_{mi} - P_{oi})^2 \tag{3}$$

$$\text{Sscore} = \sum_{i=1}^{n}\text{Minimum}\,(P_{mi}, P_{oi}) \tag{4}$$

In the formula, P_{mi} and P_{oi} are the probabilities that the climate variables simulated and observed by RegCM4 appear in the ith data segment, respectively, and n is the sequence length divided equally according to the original sequence values of the climate variables. The smaller the BS or the larger the Sscore, the better the simulation ability of the RegCM for the probability density distribution in the region.

Results

Comprehensive evaluation of the physical parameterization scheme

Figure 2 and Table 4 show the evaluation results of the simulated temperature and precipitation from 72 sets of parameterization schemes in the UYRB. As shown in Figure 2, the BATS group (Nos.1–24) has the best performance for temperature, followed by the CLM3.5 group (Nos.25–48), while the CLM4.5 group (Nos.49–72) has the worst performance for temperature. For precipitation, the BATS group performs the worst, followed by the CLM3.5 and CLM4.5 groups. In general, temperature is more sensitive to the change of the LSPs, while precipitation is more sensitive to the CSs.

According to the RS score, the Kain-Fritsch groups perform best among the 72 schemes. All tests using Kain-Fritsch scheme (e.g., Nos.20–24, Nos.44–48 and Nos.68–72) have better total RS value for precipitation and temperature than other schemes (Table 2; Figure 2A). Therefore, the following nine schemes (three groups) are selected to further analyze the performance differences between different CSs and LSPs in the YRB (Table 4): 1) the LCS and OCS are Emanuel (Nos.12, 36, and 60); 2) The Kain-Fritsch is used for LCS, and Tiedtke-Kain is used for OCS (Nos.19, 43, and 67); 3) Both LCS and OCS are Kain-Fritsch (Nos.24, 48, and 72). For each group of three simulations according to CSs, the LSPs for the first, second, and third members are BATS, CLM3.5, and CLM4.5, respectively.

Performance evaluation for climatological of precipitation and temperature

Figures 3A–C shows the Taylor diagrams of the simulated annual, summer, and winter precipitation in the UYRB. As shown in Figure 4 and Supplementary Figure S1, the selected nine schemes can capture the spatial pattern of precipitation in the UYRB, and the simulation performance in winter is better than that in summer, but there are large wet biases as a

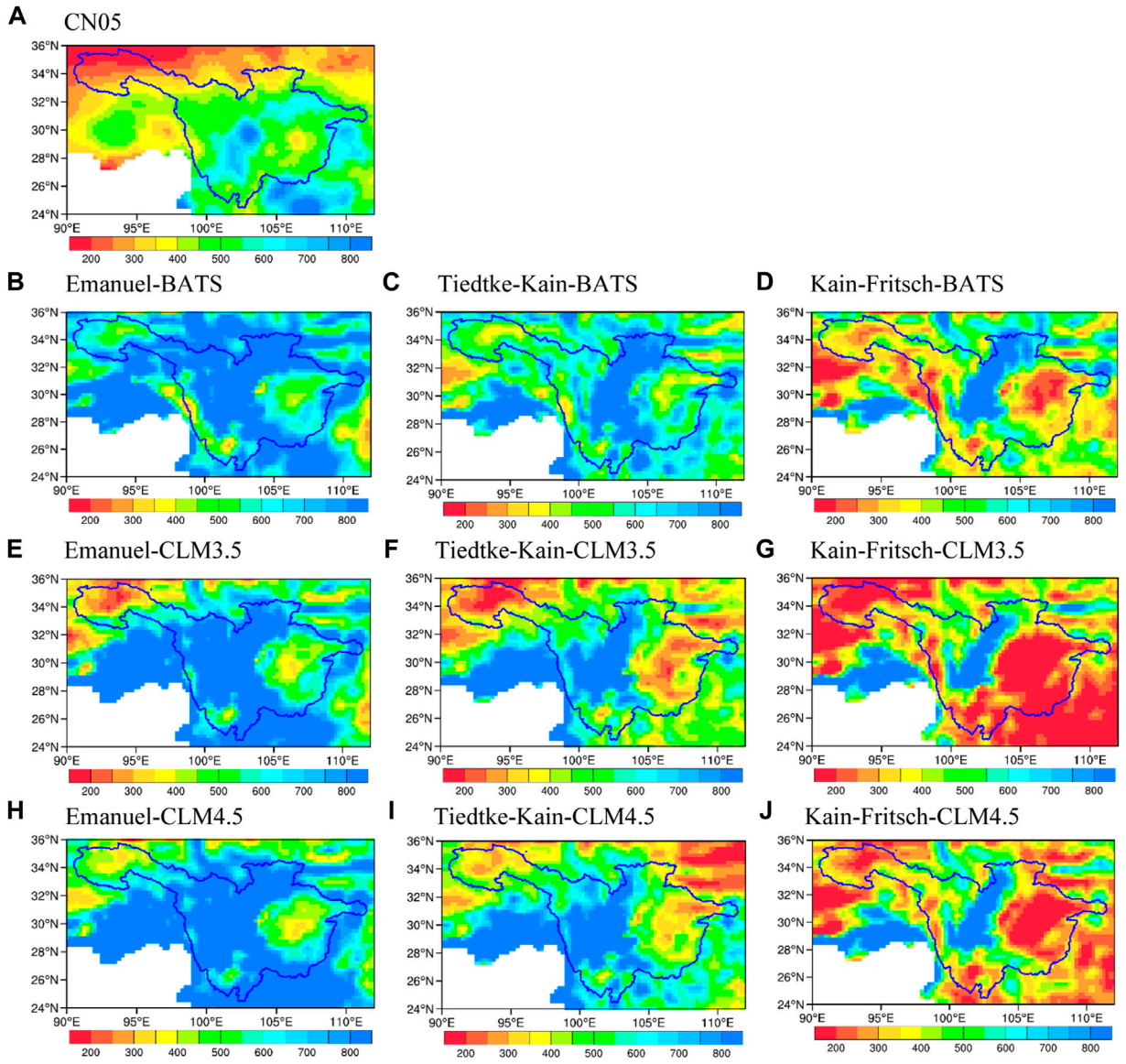

FIGURE 4
Spatial distribution of observed and simulated multi-year average summer total precipitation (unit: mm) for the current climate (1991–1993) over the UYRB. [**(A)** CN05, **(B)** simulation of the combination scheme of Emanuel and BATS, **(C)** simulation of the combination scheme of Tiedtke-Kain and BATS, **(D)** simulation of the combination scheme of Kain-Fritsch and BATS, **(E–G)** same as **(B–D)** but for CLM3.5, and **(H–J)** same as **(B–D)** but for CLM4.5].

whole. The spatial correlation coefficient between the observed and simulated summer precipitation over the UYRB by the Emanuel, Kain-Fritsch, and Tiedtke-Kain schemes is about 0.2, but it can reach more than 0.6 in winter. As for the precipitation pattern, the precipitation simulated by the selected nine schemes shows a wet bias in the southwestern mountainous area of the Sichuan Basin, while the precipitation is low in the eastern part of the Sichuan Basin (Figure 4). In addition, when the spatial patterns of precipitation in summer and winter are compared, the wet biases of precipitation in winter are smaller than in summer. The precipitation patterns simulated by different CSs (e.g., Emanuel, Kain-Fritsch, and Tiedtke-Kain) in BATS, CLM3.5, and CLM4.5 experiments are significantly different. The Emanuel, Kain-Fritsch, and Tiedtke-Kain schemes overestimate the annual precipitation by 2.7 mm/day, 1.6 mm/day, and 0.2 mm/day, respectively. The wet biases of precipitation simulated by Emanuel are significantly higher than those of other CSs related to Emanuel's parameterization setting (Fraedrich and Leslie,

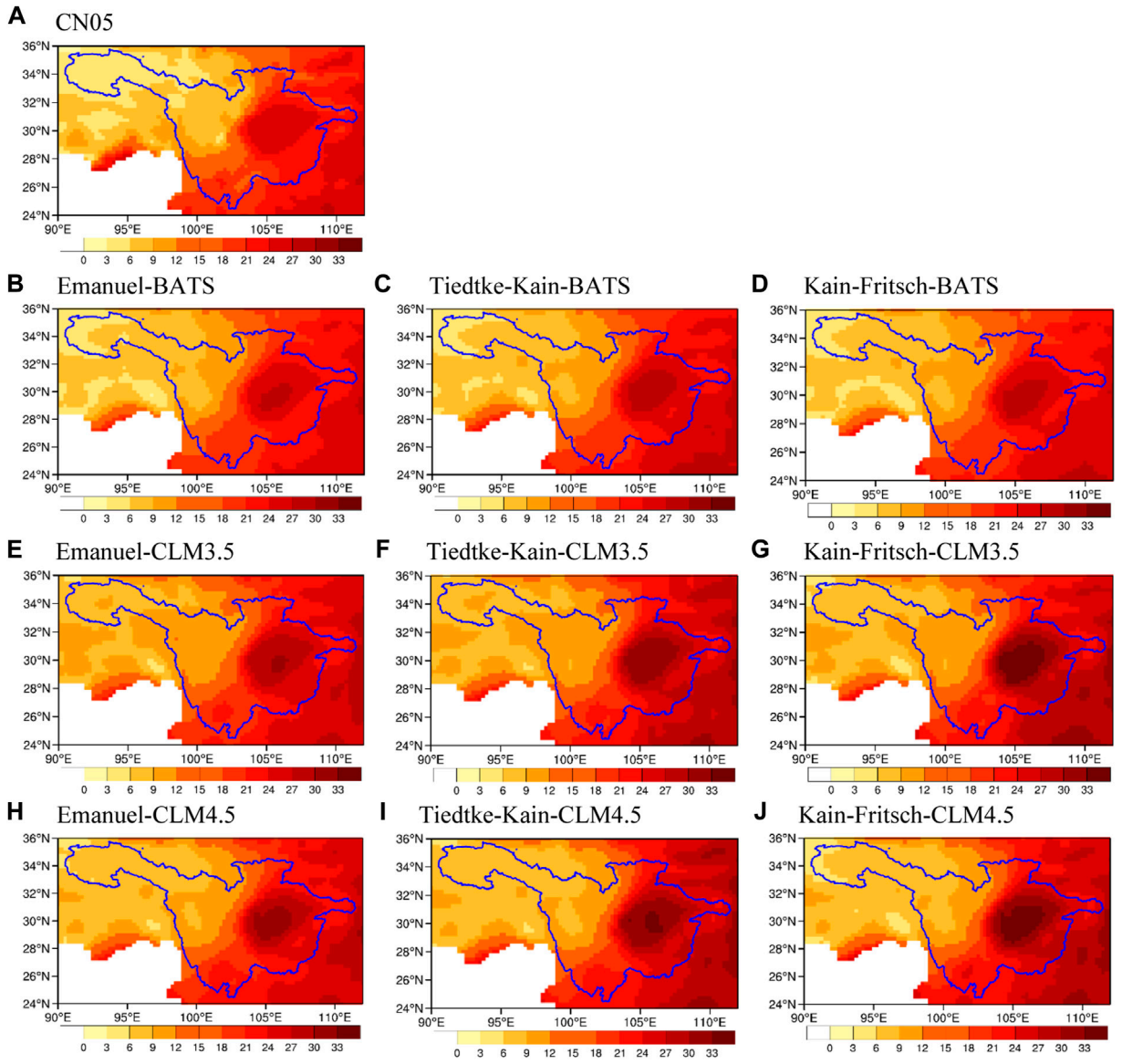

FIGURE 5
Spatial distribution of observed and simulated multi-year summer average temperature (unit: °C) for the current climate (1991–1993) over the UYRB. [**(A)** CN05, **(B)** simulation of the combination scheme of Emanuel and BATS, **(C)** simulation of the combination scheme of Tiedtke-Kain and BATS, **(D)** simulation of the combination scheme of Kain-Fritsch and BATS, **(E–G)** same as **(B–D)** but for CLM3.5, and **(H–J)** same as **(B–D)** but for CLM4.5].

1987; Im et al., 2008). Moreover, except in the east of the Sichuan Basin, the precipitation in the UYRB simulated by the selected scheme generally has a large wet bias, which is related to the incomplete characterization of mesoscale weather activities by the RegCM4. The precipitation biases between the simulations and observations may be due to the imperfection of the convective parameterization scheme (Wang and Seaman, 1997) and the resolution of the downscaling experiment (Shi et al., 2018), resulting in strong wet biases. The same phenomenon has also been found in other regions (Oh and Suh, 2018). In addition, previous studies have shown that the precipitation simulation by RegCM exhibits a significant systematic bias (Oh and Suh, 2018), especially in mountainous areas (Gao et al., 2017; Huang et al., 2020).

As shown in Figures 5 and Supplementary Figure S2, the spatial pattern of multi-year average summer and winter temperature simulated by the selected schemes is very close

TABLE 5 Differences in hydrometeorological elements in the UYRB between the CLMs (CLM3.5 and CLM4.5) and BATS schemes.

Month	Precipitation (mm/day)		Evaporation (mm/day)		SM (%)		SH (W/m^2)	
	CLM3.5	CLM4.5	CLM3.5	CLM4.5	CLM3.5	CLM4.5	CLM3.5	CLM4.5
1	−0.3	−0.5	−0.5	−0.5	−43.9	−20.0	4.8	2.5
2	−0.7	−0.9	−0.7	−0.7	−42.7	−24.4	10.1	2.8
3	−1.0	−0.9	−1.0	−0.9	−37.0	−23.3	18.7	9.3
4	−0.7	−1.0	−1.2	−1.1	−36.8	−25.9	22.0	15.9
5	−1.0	−1.2	−1.3	−1.1	−34.6	−25.2	16.5	11.9
6	−1.2	−0.4	−1.5	−1.1	−23.2	−8.9	10.6	2.6
7	−2.2	−0.5	−1.4	−0.9	−19.6	−2.2	11.0	1.2
8	−1.5	−1.6	−1.2	−1.0	−16.7	−2.2	7.7	1.8
9	−1.0	−1.2	−1.1	−1.1	−16.5	−2.8	9.1	7.5
10	−0.8	−0.8	−1.0	−0.9	−17.1	−1.0	8.8	5.1
11	−0.4	−0.7	−0.8	−0.9	−30.2	−10.5	5.0	1.5
12	−0.2	−0.4	−0.6	−0.7	−41.4	−6.1	3.0	1.1
Mean	−0.9	−0.8	−1.0	−0.9	−30.0	−13.5	10.6	5.3

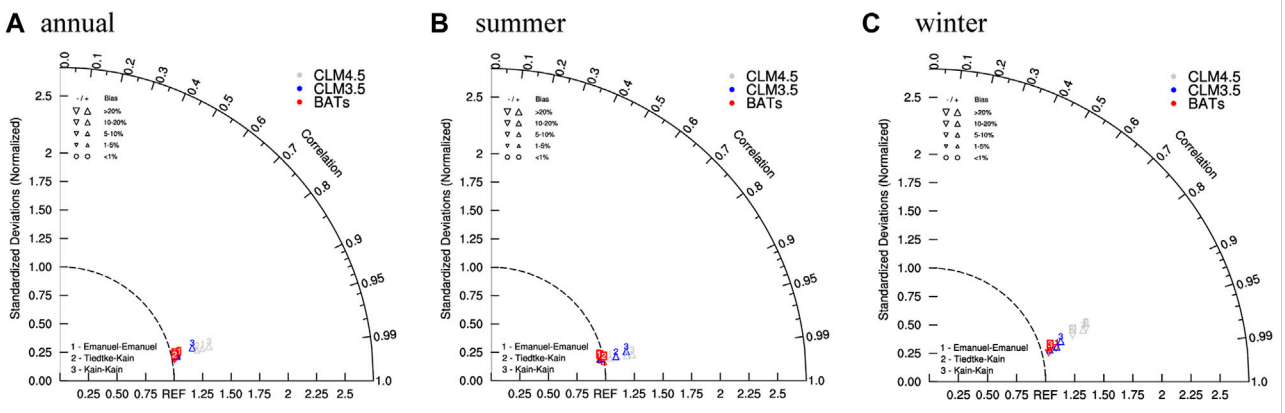

FIGURE 6
Taylor diagrams of annual, summer, and winter air temperatures in the UYRB.

to the observation, and the temperature gradient from northwest to southeast in the UYRB can be well captured. The spatial correlation coefficients of both simulated summer and winter temperatures are above 0.95, but there is a small bias (Figure 6). As for the spatial pattern of temperature, there is no apparent difference between the Emanuel, Kain-Fritsch, and Tiedtke-Kain schemes. In summer, there is a large warm bias in the Sichuan Basin, while in winter, there is a large cold bias in the northwest Qinghai-Tibet Plateau. In general, the annual mean biases of temperature simulated by the Emanuel, Tiedtke-Kain, and Kain-Fritsch schemes (average of the three LSPs) are 1.01°C, 1.16°C, and 2.07°C, respectively.

Performance evaluation for annual cycle and probability density

As shown in Figures 7A–C, compared with the Tiedtke-Kain and Kain-Fritsch schemes, the Emanuel scheme has a larger overestimation of annual precipitation, especially in summer. In the Kain-Fritsch scheme, the annual precipitation cycle obtained using three different LSPs (BATS, CLM3.5, and CLM4.5) is consistent with the observation. For air temperature, the Emanuel, Tiedtke-Kain, and Kain-Fritsch schemes can simulate the annual cycle well (Figure 7D-F). Overall, the Emanuel scheme simulation results for the annual

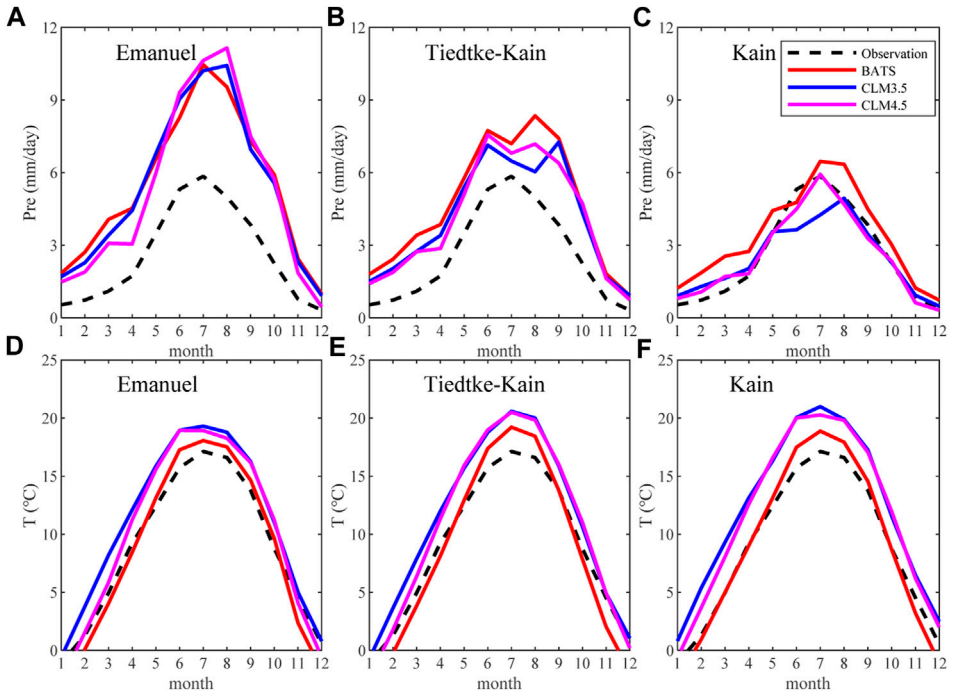

FIGURE 7
Observed and simulated annual cycles of precipitation (mm/day) and temperature (°C) for the UYRB. [**(A)** precipitation simulated by Emanuel, **(B)** precipitation simulated by Tiedtke-Kain, **(C)** precipitation simulated by Kain-Fritsch, and **(D–F)** same as **(A–C)** but for temperature].

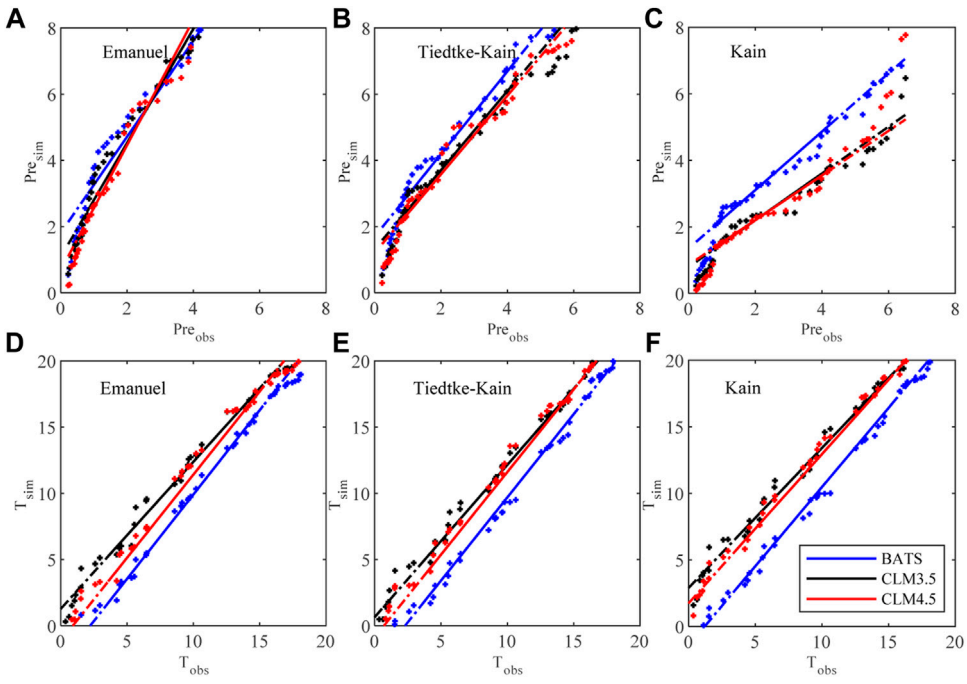

FIGURE 8
The Q-Q plot of precipitation **(A–C)** and temperature **(D–F)** in the UYRB between the simulation and observation. [**(A)** precipitation simulated by Emanuel, **(B)** precipitation simulated by Tiedtke-Kain, **(C)** precipitation simulated by Kain-Fritsch, and **(D–F)** same as **(A–C)** but for the temperature].

air temperature cycle are slightly better than those of Tiedtke-Kain and Kain-Fritsch.

In general, in the precipitation simulation of the UYRB, the parameterization combination of CLMs and Kain-Fritsch in RegCM4 performs better than other scheme combinations. As shown in Figures 8A–C, different intensities of precipitation simulated by Emanual and Tiedtke-Kain are generally higher than those observed. Among the selected CSs, the Kain-Fritsch scheme simulates precipitation intensity more closely to the observation. However, different LSPs may lead to slight differences between simulated and observed precipitation intensities. For example, precipitation intensities simulated by BATS (blue line) are higher than the observation, while those simulated by CLM3.5 (black line) and CLM4.5 (red line) are lower.

For air temperature, the air temperature Q-Q plots obtained by Emanual, Tiedtke-Kain, and Kain-Fritsch schemes show little difference, and the probability density distributions of air temperature simulated by the three groups of CSs are close to the observed distribution (Figure 8D-F). Among the three LSPs, the quantile distribution simulated by BATS is closer to the observed values, followed by CLM4.5.

Discussion

From the above analysis, the different CSs and LSPs have different simulation performances on precipitation and temperature, and the scheme with a better simulation effect on temperature may have a worse simulation effect on precipitation, and *vice versa*. Therefore, in practical applications, appropriate schemes need to be selected according to the research objectives. In this study, the Kain-Fritsch scheme, combined with three LSPs, is selected to further analyze the impact of different LSPs on the simulation performance of temperature and precipitation. The statistical differences of climatic factors in different months between CLMs (CLM3.5 and CLM4.5) and BATS are presented in Table 5. As seen in the table, the total precipitation and evaporation simulated by CLMs is less than that of BATS, and the surface soil moisture (SM) simulated by CLMs is significantly drier than that of BATS. The difference between CLMs and BATS in domain-averaged precipitation and evaporation over the UYRB is −0.8–0.9 mm/day and −0.9–1.0 mm/day, respectively. For soil moisture, CLM3.5 is 30% drier than BATS and reaches 13.5% in CLM4.5, consistent with previous studies (Diro et al., 2012). Compared with CLM, BATS can produce higher soil moisture, resulting in higher latent heat and moist static energy (Im et al., 2014), which in turn enhances convective activity and results in larger convective precipitation (Alfieri et al., 2006; Myoung and Nielsen-Gammon, 2010; Hauck et al., 2011). The annual average sensible heat flux of CLM3.5 and CLM4.5 is 10.6W/m^2 and 5.3W/m^2 higher than that of BATS respectively, indicating that soil moisture influences the surface energy budget by regulating the relative distribution of latent and sensible heat fluxes. In addition, there is a strong connection between the convective precipitation scheme and large-scale precipitation scheme in RegCM4, and the bias of convective precipitation also affects large-scale precipitation (Gianotti et al., 2011).

The warm-dry difference between the BATS scheme and CLMs (CLM3.5 and CLM4.5) further affects the water vapor transport and atmospheric circulation in the region, impacting the simulated precipitation. As shown in Figure 9 and Supplementary Figure S3, the temperature difference between the CLMs scheme and the BATS scheme gradually decreases with the increase of altitude, as the land surface schemes mainly affect surface fluxes. For example, the winter temperatures at 850 hPa in the eastern part of the study area simulated by the CLMs scheme are more than 5°C higher than those of BATS. With altitudes up to 500 hPa, the warm bias in the CLMs is reduced to -1-1°C.

Similarly, the wind field between CLMs and BATs also shows great differences. As shown in Figure 9 and Supplementary Figure S3, the summer wind field simulated by CLMs is weaker than that of BATS. The wind field difference at 850 hPa in the UYRB is mainly an easterly wind, which may hinder the transport of low-level water vapor from the Bay of Bengal to the basin. In winter, the wind field difference between CLMs and BATS is larger than that in summer, and the differential wind field at 850 hPa is southerly, indicating that the intensity of dry cold air from the north simulated using CLMs is weakened. In addition, the summer specific humidity in the UYRB simulated by CLMs is generally smaller than that of BATS, especially at 850 hPa. The dry bias makes CLMs simulate less summer precipitable water than BATS, which tends to reduce the production of summer precipitation. Therefore, the differences in the atmospheric circulation field and water vapor flux jointly affect the precipitation in the UYRB simulated by CLMs and BATS.

Conclusion

In this study, the ERA-Interim reanalysis data were used as the initial and lateral boundary conditions for the RegCM4 to conduct 4-year simulations of 72 parameterization schemes. Additionally, the multi-standard scoring method was used to evaluate the performance of the selected schemes for the UYRB. Finally, the influence of different CSs and LSPs on the precipitation and temperature simulation performance over the UYRB was analyzed. The main findings are as follows:

The RegCM4 simulated temperature performed better than the simulated precipitation. RegCM4 captured the main spatial distribution characteristics of temperature and

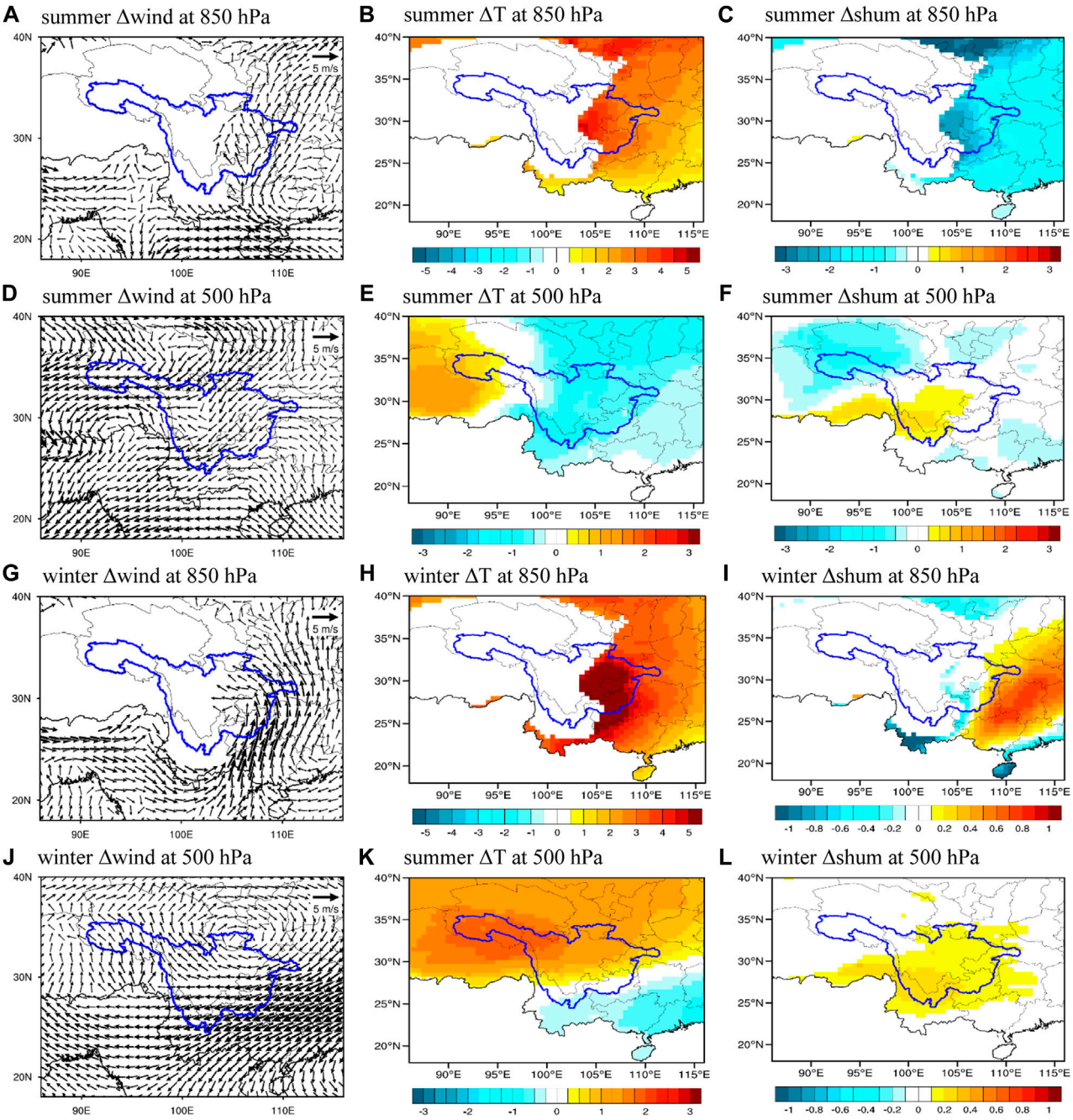

FIGURE 9
Difference in the wind field (m/s), temperature (°C), and specific humidity (g/kg) between CLM3.5 and BATS (defined as CLM3.5-BATS). [**(A)** difference in summer winds at 850 hPa, **(D)** difference in summer winds at 500 hPa, **(G)** difference in winter winds at 850 hPa, **(J)** difference in winter winds at 850 hPa; **(B,E,H,K)** same as **(A,D,G,J)** but for temperature; and **(C,F,I,L)** same as **(A,D,G,J)** but for specific humidity].

precipitation, annual cycle processes, and probability density. In simulating temperature, RegCM4 was particularly successful at capturing the main spatial pattern of observation and showed a high performance. The simulated total precipitation overestimated the observations in the study area and deviated from the observed spatial distribution in summer.

Precipitation was highly sensitive to the cumulus convective parameterization scheme. The commonly used Emanuel scheme overestimated the annual average

precipitation by approximately 2.7 mm/day. Among the tested CSs, the Kain-Fritsch scheme had the best comprehensive simulation performance for precipitation in the UYRB, only overestimating the simulated annual average precipitation by 0.2 mm/day. Among the LSPs examined, the BATS group (Nos. 1–24) had the best comprehensive simulation performance for temperature in the UYRB, with an average cold bias of only 0.2°C, while the CLMs group (Nos. 25–72) had a warm bias of approximately 2.5°C.

Under the best performing CS Kain-Fritsch, the soil moisture in the UYRB simulated by CLMs was 13.5%–30% drier than that of BATS. Compared with BATS, the warmer temperature and weaker evapotranspiration in CLMs resulted in weaker horizontal and vertical water vapor transport capacity in the UYRB and less atmospheric precipitable water, leading to less precipitation in simulations using CLMs. In addition, the drier atmosphere simulated by CLMs increased the net radiation flux to the surface and changed the surface energy budget, resulting in a difference in air temperature between CLMs and BATS.

It is important to note that all the selected schemes possess common deficiencies in their precipitation simulations for the UYRB, characterized by a wet bias in mountainous areas. Substantial effort is needed in the future, including more extensive analysis of simulations, implementation, and testing of new physical processes in models, and more numerical experiments, to better understand and further improve the RegCM.

Data availability statement

The data analyzed in this study is subject to the following licenses/restrictions: The authors greatly appreciate the data availability and service provided by the RegCM4 science team. Requests to access these datasets should be directed to http://clima-dods.ictp.it/Data/RegCM_Data/.

Author contributions

BL designed the study, completed the original draft. YH provided some software for the study. LD provided financial support for the research. DW revised the original draft. All authors commented on the manuscript and agreed to the published version of the manuscript.

Funding

8This study was jointly funded by the Open Research Fund of State Key Laboratory of Simulation and Regulation of Water Cycle in River Basin, China Institute of Water Resources and Hydropower Research (IWHR-SKL-KF202204), the Jiangsu Funding Program for Excellent Postdoctoral Talent (2022ZB147), the Natural Science Foundation of China (51909275), and TianHe Qingsuo Project special fund project in the field of climate, meteorology and ocean. In addition, high-performance computing resources were provided by the national supercomputer center in Tianjin, China.

Acknowledgments

The authors greatly appreciate the data availability and service provided by the RegCM4 science team.

Conflict of interest

The authors declare that the research was conducted in the absence of any commercial or financial relationships that could be construed as a potential conflict of interest.

Publisher's note

Supplementary material

The Supplementary Material for this article can be found online at: https://www.frontiersin.org/articles/10.3389/feart.2022.1092368/full#supplementary-material

References

Alfieri, L., Claps, P., D Odorico, P., Laio, F., and Over, T.-M. (2006). An analysis of the soil moisture feedback on convective and stratiform precipitation. *J. Hydrometeorol.* 2, 280–291. doi:10.1175/2007jhm863.1

Anthes, R.-A. (1977). A cumulus parameterization scheme utilizing a one-dimensional cloud model. *Mon. Weather Rev.* 3, 270–286. doi:10.1175/1520-0493(1977)105<0270:acpsua>2.0.co;2

Bao, Y. (2013). Simulations of summer monsoon climate over East Asia with a regional climate model (RegCM) using Tiedtke convective parameterization scheme (CPS). *Atmos. Res.* 134, 35–44. doi:10.1016/j.atmosres.2013.06.009

Brier, G.-W. (1950). Verification of forecasts expressed in terms of probability. *Mon. Weather Rev.* 1, 1–3. doi:10.1175/1520-0493(1950)078<0001:vofeit>2.0.co;2

Cao, J., Zhang, X.-N., You, Y.-L., and Yang, R.-W. (2007). Applicability of cumulus convective parameter schemes in RegCM3 to the rainfall over the Longitudinal Range-Gorge Region. *Chin. Sci. Bull.* 2, 115–121. doi:10.1007/s11434-007-7015-3

Centella-Artola, A., Taylor, M.-A., Bezanilla-Morlot, A., Martinez-Castro, D., Campbell, J.-D., Stephenson, T.-S., et al. (2015). Assessing the effect of domain size over the Caribbean region using the PRECIS regional climate model. *Clim. Dyn.* 7, 1901–1918. doi:10.1007/s00382-014-2272-8

Chow, K.-C., Chan, J.-C.-L., Pal, J.-S., and Giorgi, F. (2006). Convection suppression criteria applied to the MIT cumulus parameterization scheme for simulating the Asian summer monsoon. *Geophys. Res. Lett.* 24, 247099–L25199. doi:10.1029/2006gl028026

Dash, S.-K., Shekhar, M.-S., and Singh, G.-P. (2006). Simulation of Indian summer monsoon circulation and rainfall using RegCM3. *Theor. Appl. Climatol.* 1, 161–172. doi:10.1007/s00704-006-0204-1

Dickinson, R.-E., Henderson-Sellers, A., and Kennedy, J. (1993). *Biosphere atmosphere transfer scheme (BATS) version 1e as coupled to the NCAR community climate modelNCAR Technical Note NCAR/TN-387+STR*. Boulder, Colorado: National Center for Atmospheric Research.

Diro, G.-T., Rauscher, S.-A., Giorgi, F., and Tompkins, A.-M. (2012). Sensitivity of seasonal climate and diurnal precipitation over Central America to land and sea surface schemes in RegCM4. *Clim. Res.* 52, 31–48. doi:10.3354/cr01049

Emanuel, K.-A. (1991). A scheme for representing cumulus convection in large-scale models. *J. Atmos. Sci.* 21, 2313–2329. doi:10.1175/1520-0469(1991)048<2313:asfrcc>2.0.co;2

Fraedrich, K., and Leslie, L.-M. (1987). Evaluation of techniques for the operational, single station, short-term forecasting of rainfall at a midlatitude station (Melbourne). *Mon. Wea. Rev.* 115, 1645–1654. doi:10.1175/1520-0493(1987)115<1645:eotfto>2.0.co;2

Fu, C.-B., and Yuan, H.-L. (2001). An virtual numerical experiment to understand the impacts of recovering natural vegetation on the summer climate and environmental conditions in East Asia. *Chin. Sci. Bull.* 14, 1199–1203. doi:10.1007/bf02900602

Gao, X.-J., and Giorgi, F. (2017). Use of the RegCM system over East Asia: Review and perspectives. *Engineering* 5, 766–772. doi:10.1016/j.eng.2017.05.019

Gao, X.-J., Shi, Y., Han, Z.-Y., Wang, M.-L., Wu, J., Zhang, D.-F., et al. (2017). Performance of RegCM4 over major river basins in China. *Adv. Atmos. Sci.* 4, 441–455. doi:10.1007/s00376-016-6179-7

Gao, X.-J., Shi, Y., Song, R., Giorgi, F., Wang, Y., and Zhang, D.-F. (2008). Reduction of future monsoon precipitation over China: Comparison between a high resolution RCM simulation and the driving GCM. *Meteorol. Atmos. Phys.* 1-4, 73–86. doi:10.1007/s00703-008-0296-5

Gao, X.-J., Ying, S., and Giorgi, F. (2016). Comparison of convective parameterizations in RegCM4 experiments over China with CLM as the land surface model. *Atmos. Ocean. Sci. Lett.* 4, 246–254. doi:10.1080/16742834.2016.1172938

Gianotti, R.-L., and Eltahir, E.-A.-B. (2014). Regional climate modeling over the maritime continent. Part II: New parameterization for autoconversion of convective rainfall. *J. Clim.* 4, 1504–1523. doi:10.1175/jcli-d-13-00171.1

Gianotti, R.-L., Zhang, D., and Eltahir, E.-A.-B. (2011). Assessment of the regional climate model version 3 over the maritime continent using different cumulus parameterization and land surface schemes. *J. Clim.* 2, 638–656. doi:10.1175/jcli-d-11-00025.1

Giorgi, F., and Anyah, R.-O. (2012). INTRODUCTION the road towards RegCM4 F. Giorgi1, *, R. O. Anyah2. *Clim. Res.* 52, 3–6. doi:10.3354/cr01089

Giorgi, F., Coppola, E., Solmon, F., Mariotti, L., Sylla, M.-B., Bi, X., et al. (2012). RegCM4: Model description and preliminary tests over multiple CORDEX domains. *Clim. Res.* 52, 7–29. doi:10.3354/cr01018

Giorgi, F., and Gutowski, W.-J., Jr (2015). Regional dynamical downscaling and the CORDEX initiative. *Annu. Rev. Environ. Resour.* 40, 467–490. doi:10.1146/annurev-environ-102014-021217

Giorgi, F., and Marinucci, M.-R. (1996). A investigation of the sensitivity of simulated precipitation to model resolution and its implications for climate studies. *Mon. Weather Rev.* 1, 148–166. doi:10.1175/1520-0493(1996)124<0148:aiotso>2.0.co;2

Grell, G.-A. (1993). Prognostic evaluation of assumptions used by cumulus parameterizations. *Mon. Weather Rev.* 3, 764–787. doi:10.1175/1520-0493(1993)121<0764:peoaub>2.0.co;2

Hanna, S.-R., and Heinold, D.-W. (1985). *Development and application of a simple method for evaluating air quality models*. American Petroleum Institute.

Harvey, L., and Wigley, T. (2003). Characterizing and comparing control-run variability of eight coupled AOGCMs and of observations. Part 1: Temperature. *Clim. Dyn.* 7, 619–646. doi:10.1007/s00382-003-0357-x

Hauck, C., Barthlott, C., Krauss, L., and Kalthoff, N. (2011). Soil moisture variability and its influence on convective precipitation over complex terrain. *Q. J. R. Meteorol. Soc.* S1, 42–56. doi:10.1002/qj.766

Holtslag, A.-A.-M., De Bruijn, E.-I.-F., and Pan, H. (1990). A high resolution air mass transformation model for short-range weather forecasting. *Mon. Wea. Rev.* 8, 1561–1575. doi:10.1175/1520-0493(1990)118<1561:ahramt>2.0.co;2

Huang, W.-R., Chan, J.-C.-L., and Au-Yeung, A.-Y.-M. (2013). Regional climate simulations of summer diurnal rainfall variations over East Asia and Southeast China. *Clim. Dyn.* 7-8, 1625–1642. doi:10.1007/s00382-012-1457-2

Huang, Y., Xiao, W., Hou, G., Yi, L., Li, Y., and Zhou, Y. (2020). Changes in seasonal and diurnal precipitation types during summer over the upper reaches of the Yangtze River Basin in the middle twenty-first century (2020–2050) as projected by RegCM4 forced by two CMIP5 global climate models. *Theor. Appl. Climatol.* 3, 1055–1070. doi:10.1007/s00704-020-03364-4

Im, E.-S., Gutowski, W.-J., Jr, and Giorgi, F. (2008). Consistent changes in twenty-first century daily precipitation from regional climate simulations for Korea using two convection parameterizations. *Geophys. Res. Lett.* 14, L14706. doi:10.1029/2008gl034126

Im, E., Marcella, M.-P., and Eltahir, E.-A.-B. (2014). Impact of potential large-scale irrigation on the west african monsoon and its dependence on location of irrigated area. *J. Clim.* 3, 994–1009. doi:10.1175/JCLI-D-13-00290.1

Jinsong, P., Guoqing, Z., and Kun, G. (2002). Comparisons of three convection parameterization schemes in regional climate simulations. *Chin. J. Atmos. Sci.* 2, 220–228. (In Chinese).

Juneng, L., Tangang, F., Chung, J.-X., Ngai, S.-T., Tay, T.-W., Narisma, G., et al. (2016). Sensitivity of Southeast Asia rainfall simulations to cumulus and air-sea flux parameterizations in RegCM4. *Clim. Res.* 1, 59–77. doi:10.3354/cr01386

Kain, J.-S. (2004). The kain–fritsch convective parameterization: An update. *J. Appl. Meteor.* 1, 170–181. doi:10.1175/1520-0450(2004)043<0170:tkcpau>2.0.co;2

Kalognomou, E.-A., Lennard, C., Shongwe, M., Pinto, I., Favre, A., Kent, M., et al. (2013). A diagnostic evaluation of precipitation in CORDEX models over southern Africa. *J. Clim.* 23, 9477–9506. doi:10.1175/jcli-d-12-00703.1

Kang, H.-S., and Hong, S.-Y. (2008). Sensitivity of the simulated East Asian summer monsoon climatology to four convective parameterization schemes. *J. Geophys. Res.* 113, D15119. doi:10.1029/2007jd009692

Kang, S., Im, E.-S., and Ahn, J.-B. (2014). The impact of two land-surface schemes on the characteristics of summer precipitation over East Asia from the RegCM4 simulations. *Int. J. Climatol.* 15, 3986–3997. doi:10.1002/joc.3998

Li, J.-Y., and Wang, H.-J. (2008). Influences of modeling the summer heavy rain process in southern China using cumulus convective parameterization schemes. *Clim. Environ. Res.* 2, 149–160. (In Chinese).

Li, Y.-B., Tam, C.-Y., Huang, W.-R., Cheung, K.-K.-W., and Gao, Z.-Q. (2016). Evaluating the impacts of cumulus, land surface and ocean surface schemes on summertime rainfall simulations over East-to-southeast Asia and the Western north Pacific by RegCM4. *Clim. Dyn.* 7-8, 2487–2505. doi:10.1007/s00382-015-2714-y

Liu, X.-D., Jiang, Z.-H., and Luo, S.-R. (2005). A simulation of summer precipitation over eastern China with RegCM3. *J. Nanjing Inst. Meteorology* 3, 351–359. (In Chinese).

Liu, Y.-M., and Ding, Y.-H. (2001). Modified mass flux cumulus parameterization scheme and its simulation experiment partI: Mass flux scheme and its simulation of the flooding in 1991. *Acta Meteorol. Sin.*, 10–22.

Llopart, M., Da Rocha, R.-P., Reboita, M., and Cuadra, S. (2017). Sensitivity of simulated South America climate to the land surface schemes in RegCM4. *Clim. Dyn.* 11-12, 3975–3987. doi:10.1007/s00382-017-3557-5

Martínez-Castro, D., Vichot-Llano, A., Bezanilla-Morlot, A., Centella-Artola, A., Campbell, J., Giorgi, F., et al. (2018). The performance of RegCM4 over the Central America and Caribbean region using different cumulus parameterizations. *Clim. Dyn.* 11, 4103–4126. doi:10.1007/s00382-017-3863-y

Mu, Q., Jackson, C.-S., and Stoffa, P.-L. (2004). A multivariate empirical-orthogonal-function-based measure of climate model performance. *J. Geophys. Res.* D15, D15101. doi:10.1029/2004jd004584

Myoung, B., and Nielsen-Gammon, J.-W. (2010). The convective instability pathway to warm season drought in Texas. Part I: The role of convective

inhibition and its modulation by soil moisture. *J. Clim.* 17, 4461–4473. doi:10.1175/2010jcli2946.1

Ngo-Duc, T., Tangang, F.-T., Santisirisomboon, J., Cruz, F., Trinh-Tuan, L., Nguyen-Xuan, T., et al. (2017). Performance evaluation of RegCM4 in simulating extreme rainfall and temperature indices over the CORDEX-Southeast Asia region. *Int. J. Climatol.* 3, 1634–1647. doi:10.1002/joc.4803

Oh, S.-G., and Suh, M.-S. (2018). Changes in seasonal and diurnal precipitation types during summer over South Korea in the late twenty-first century (2081–2100) projected by the RegCM4.0 based on four RCP scenarios. *Clim. Dyn.* 51, 3041–3060. doi:10.1007/s00382-017-4063-5

Oleson, K., Dai, Y., Bonan, G., Mike, B., Dickinson, R., Dirmeyer, P., et al. (2004). *Technical description of the community land model (CLM)*. Boulder, Colorado: National center for atmospheric research, 10–5065.

Qian, Y., and Leung, L.-R. (2007). A long-term regional simulation and observations of the hydroclimate in China. *J. Geophys. Res.* 112, D14104. doi:10.1029/2006jd008134

Reboita, M., Fernandez, J., Pereira Llopart, M., Porfirio, D.-R.-R., Albertani Pampuch, L., and Cruz, F. (2014). Assessment of RegCM4.3 over the CORDEX South America domain: Sensitivity analysis for physical parameterization schemes. *Clim. Res.* 3, 215–234. doi:10.3354/cr01239

Shi, Y., Wang, G.-L., and Gao, X.-J. (2018). Role of resolution in regional climate change projections over China. *Clim. Dyn.* 5-6, 2375–2396. doi:10.1007/s00382-017-4018-x

Singh, G.-P., Oh, J.-H., Kim, J.-Y., and Kim, O.-Y. (2006). Sensitivity of summer monsoon precipitation over East Asia to convective parameterization schemes in RegCM3. *SOLA - Sci. Online Lett. Atmos.* 9, 29–32. doi:10.2151/sola.2006-008

Steiner, A.-L., Pal, J.-S., Giorgi, F., Dickinson, R.-E., and Chameides, W.-L. (2005). The coupling of the Common Land Model (CLM0) to a regional climate model (RegCM). *Theor. Appl. Climatol.* 3, 225–243. doi:10.1007/s00704-005-0132-5

Steiner, A.-L., Pal, J.-S., Rauscher, S.-A., Bell, J.-L., Diffenbaugh, N.-S., Boone, A., et al. (2009). Land surface coupling in regional climate simulations of the West African monsoon. *Clim. Dyn.* 6, 869–892. doi:10.1007/s00382-009-0543-6

Uppala, S.-M., Dee, D., Berrisford, P., and Simmons, A. (2008). *Towards a climate data assimilation system: Status update of ERA-Interim*. Reading, United Kingdom: ECMWF NewsletterECMWF. 115. doi:10.21957/byinox4wot

Wang, W., and Seaman, N.-L. (1997). A comparison study of convective parameterization schemes in a mesoscale model. *Mon. Weather Rev.* 2, 252–278. doi:10.1175/1520-0493(1997)125<0252:acsocp>2.0.co;2

Wang, Y.-Q., Sen, O.-L., and Wang, B. (2003). A highly resolved regional climate model (IPRC-RegCM) and its simulation of the 1998 severe precipitation event over China. Part I: Model description and verification of simulation. *J. Clim.* 11, 1721–1738. doi:10.1175/1520-0442(2003)016<1721:ahrrcm>2.0.co;2

Wu, J., and Gao, X.-J. (2013). A gridded daily observation dataset over China region and comparison with the other datasets. *Chin. J. Geophys.* 04, 1102–1111. (In Chinese).

Xu, Y.-L., Zhang, Y., Lin, E., Lin, W.-T., Dong, W.-J., Jones, R., et al. (2006). Analyses on the climate change responses over China under SRES B2 scenario using PRECIS. *Chin. Sci. Bull.* 18, 2260–2267. doi:10.1007/s11434-006-2099-8

Yu, E.-T., Sun, J.-Q., Chen, H.-P., and Xiang, W.-L. (2015). Evaluation of a high-resolution historical simulation over China: Climatology and extremes. *Clim. Dyn.* 7, 2013–2031. doi:10.1007/s00382-014-2452-6

Zeng, X.-B., Zhao, M., and Dickinson, R.-E. (1998). Intercomparison of bulk aerodynamic algorithms for the computation of sea surface fluxes using TOGA COARE and TAO data. *J. Clim.* 10, 2628–2644. doi:10.1175/1520-0442(1998)011<2628:iobaaf>2.0.co;2

Zhang, S.-B., Lü, S.-H., Bao, Y., and Ma, D. (2015). Sensitivity of precipitation over China to different cumulus parameterization schemes in RegCM4. *J. Meteorol. Res.* 1, 119–131. doi:10.1007/s13351-014-4042-2

Zou, L.-W., Qian, Y., Zhou, T.-J., and Yang, B. (2014). Parameter tuning and calibration of RegCM3 with MIT–emanuel cumulus parameterization scheme over CORDEX East Asia domain. *J. Clim.* 20, 7687–7701. doi:10.1175/jcli-d-14-00229.1

Zou, L.-W., and Zhou, T.-J. (2011). Sensitivity of a regional ocean-atmosphere coupled model to convection parameterization over Western North Pacific. *J. Geophys. Res.* 116, D18106. doi:10.1029/2011jd015844

frontiers | Frontiers in Earth Science

TYPE Original Research
PUBLISHED 08 February 2023
DOI 10.3389/feart.2023.1107674

OPEN ACCESS

EDITED BY
Jianhua Sun,
Institute of Atmospheric Physics (CAS), China

REVIEWED BY
Cholaw Bueh,
Institute of Atmospheric Physics (CAS), China
Yali Zhu,
Institute of Atmospheric Physics (CAS), China

*CORRESPONDENCE
Junpeng Yuan,
jpyuan@ynu.edu.cn

SPECIALTY SECTION
This article was submitted to Atmospheric Science, a section of the journal Frontiers in Earth Science

RECEIVED 25 November 2022
ACCEPTED 27 January 2023
PUBLISHED 08 February 2023

CITATION
Yin J, Yuan J, Peng J, Cao X, Duan W, Nan Y, Mao M and Feng T (2023), Role of the subtropical westerly jet wave train in the eastward-moving heavy rainfall event over southern China in winter: A case study.
Front. Earth Sci. 11:1107674.
doi: 10.3389/feart.2023.1107674

Role of the subtropical westerly jet wave train in the eastward-moving heavy rainfall event over southern China in winter: A case study

Juyue Yin[1,2], Junpeng Yuan[1]*, Juan Peng[1], Xiaohang Cao[1], Wei Duan[3], Yating Nan[1], Mengni Mao[1] and Tao Feng[1]

[1]Key Laboratory of Atmospheric Environment and Processes in the Boundary Layer Over the Low-Latitude Plateau Region, Department of Atmospheric Sciences, Yunnan University, Kunming, China, [2]Yuxi Meteorological Bureau, Yuxi, China, [3]Yunnan Institute of Meteorology Sciences, Kunming, China

Under the wintertime background of westerly flows, heavy rainfall often occurs first over southwestern China and then spreads eastward downstream to southeastern China, causing serious impact on a large scope of southern China. By using the synoptic diagnosis and dynamic analysis methods, we examined a typical eastward-moving heavy rainfall event that occurred over southwestern China on January 8–9, 2015 and then gradually spread eastward to southeastern China on January 10–13. The results show the important role of the Rossby wave train propagating along the subtropical westerly jet in "pushing" the eastward movement of heavy rainfall over southern China. The remote Rossby wave train influenced the variation of heavy rainfall by modifying the local circulation. The Rossby wave train can change the morphology of the East Asian subtropical jet via wave—jet interactions and modify the related secondary upward circulation in the entrance area of the jet, providing favorable dynamic conditions for the occurrence of heavy rainfall. The Rossby wave train can also influence the low-level south branch trough by modifying the associated baroclinic energy conversion process under a background of deep layer subsidence, which favors the transport of plentiful water vapor to the region of heavy rainfall over southern China. The eastward-propagating Rossby wave train pushed the upper level East Asian subtropical jet and the lower level south branch trough as a whole while simultaneously moving east, which caused the region of heavy rainfall to move from southwestern to southeastern China. These results will help to provide a scientific basis for forecasting winter rainfall over southern China.

KEYWORDS

eastward moving heavy rainfall event, southern China, Rossby wave train, south branch trough, East Asian subtropical jet

1 Introduction

The winter climate of China is relatively dry and cold and heavy rainfall mainly occurs south of 35°N (Gao et al., 2020). Heavy rainfall in winter often brings severe icing conditions and may cause serious disasters and great losses to both human society and the economy (Huang et al., 2019; Tan et al., 2022). In the dry, cold conditions of winter, the occurrence of heavy rainfall over southern China is closely related to the triggering effect of warm, moist air flows originating from the tropical regions (Zong et al., 2014; Li et al., 2020). A semi-permanent trough forms in the southern branch of the westerly winds at lower levels (Yeh, 1950). This trough appears south of the Qinghai–Tibetan Plateau and is known as the South Branch Trough (SBT) or the India–Burma Trough (Figure 1). Numerous studies revealed that the SBT shows

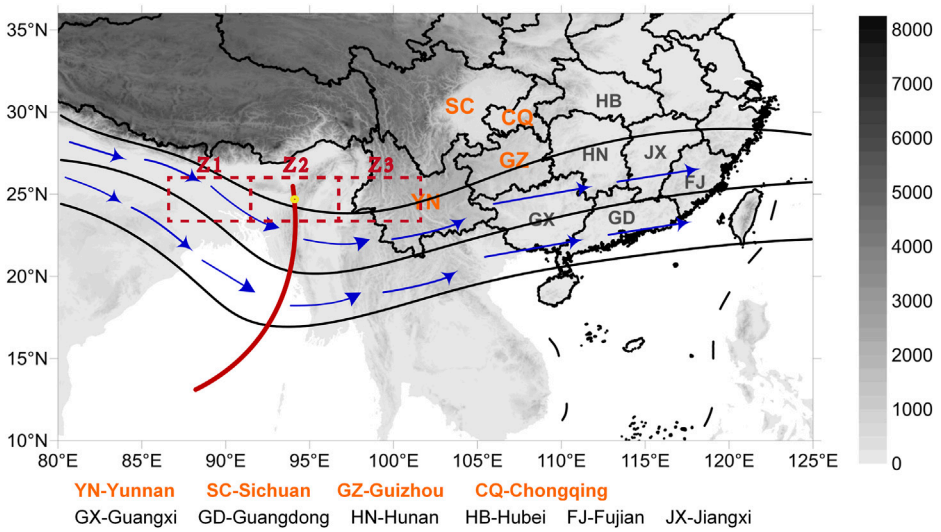

FIGURE 1
Schematic diagram of the topography and southern branch of the westerly winds around the Qinghai–Tibetan Plateau and southern China. The locations of provinces in southwestern (southeastern) China are marked with red (black) acronyms. The digital elevation model of the topography is shown in gray. The black contours and blue vectors show the geopotential height field and the wind field at 700 hPa, respectively. The red solid line shows the trough line of the SBT. The red boxes shown as dashed lines of Z2, Z1, and Z3 represent the trough line region and the regions behind and in front of the SBT in the objective SBT identification method, respectively.

energetic synoptic variation (e.g., Suo et al., 2008; Duan et al., 2012; Zong et al., 2012; Li and Sun, 2015; Li and Zhou, 2016; Li et al., 2017; Chen and Li, 2022). The SBT often intensifies and migrates from the Bay of Bengal to the South China Sea along the south westerly flow, which is termed an SBT process appearing every 5–6 days (Qin et al., 1991; Guo et al., 2010; Li et al., 2017). The SBT has an essential role in the occurrence of winter rainfall over southern China (Zong et al., 2012; Li and Sun, 2015; Lin, 2016; Liu et al., 2018). The southwesterly flow in front of the SBT can transport large amounts of warm, moist water vapor from the Bay of Bengal to southern China, which favors the occurrence of heavy rainfall in this region (Wang et al., 2011; Li and Zhou, 2016). When the deepening SBT meets the westward-expanding western Pacific subtropical high, widespread heavy rainfall can occur in southwestern China and also further downstream in southeastern China (Duan et al., 2012; Zong et al., 2014; Yuan et al., 2019).

In the upper level, the subtropical westerly jet is located near 30°N, the center of which is located over East Asia and south of Japan, where it is referred to as the East Asian subtropical westerly jet (EASJ; Huang et al., 2014). The EASJ is an important circulation system which is closely related to the variation of the East Asian winter monsoon (Ha et al., 2012; Luo and Zhang, 2015; Liu et al., 2022), and it strongly influences the weather and climate variations over East Asia (Yang et al., 2002; Liao and Zhang, 2013; Ding and Li, 2017; Liu et al., 2022). In winter, Southern China is located under the equator-ward region of the entrance of the EASJ and therefore the secondary upward circulation of the EASJ favors the occurrence of heavy rainfall over southern China (Huang et al., 2017). Thus, both of the variation in the intensity and meridional shift of the EASJ are important to the occurrence of rainfall over southern China (Zhang et al., 2019; Liu et al., 2022). The EASJ was also an important bridge that linked the remote upstream disturbance to the winter precipitation over East Asian (Watanabe, 2004; Hu et al., 2018; Zhang and Chen, 2021). Previous studies have shown that a Rossby wave train originating from the North Atlantic or Mediterranean region may propagate eastward along the subtropical westerly jet into East Asia and have an important role in generating circulation patterns conducive to persistent heavy rainfall events over southern China (Zong et al., 2012; Li and Sun, 2015; Ding and Li, 2017; Li et al., 2017; Huang et al., 2019; Li et al., 2020; Chen and Li, 2022; Tan et al., 2022). The variation in the lower level of the SBT may be closely related to the upstream Rossby wave train (Li and Zhou, 2016; Li et al., 2017). The Rossby wave train propagates eastward along the subtropical westerly jet and strengthen the SBT, which favors the transport of plentiful moisture from the Bay of Bengal and the South China Sea to southern China (Ding and Li, 2017; Li et al., 2017). The Rossby wave train also can modulate the vertical motion and convergence (divergence) in high (low) layers along the eastward-propagating path of the Rossby wave train (Hu et al., 2018; Huang et al., 2019; Tan et al., 2022), favoring dynamic conditions of uplift over southern China (Li and Sun, 2015; Li and Li, 2019). Numerous studies have emphasized that the propagation of the Rossby wave train along the subtropical westerly jet is an important precursory signal influencing the occurrence of heavy rainfall over southern China in winter (Zong et al., 2014; Huang et al., 2019; Li et al., 2020).

Previous studies have mainly focused on the conditions favoring the large region of persistent heavy rainfall over the whole of southern China in winter. Numerous case studies have shown that persistent heavy rainfall events over southern China feature an eastward movement from the perspective of daily variations in the weather (Li and Sun, 2015; Li and Li, 2019; Yuan et al., 2019). Under the winter background of westerly flows over southern China, precipitation tends to occur first over southwestern China and then spreads eastward downstream to southeastern China. For example, a 6-day strong intense and extensive rainfall event occurred over southern China from January 8 to 13, 2015 (Figure 2), causing record-breaking heavy rainfall in most parts of southern China (Li and Li, 2019). Detailed analyses showed that the rainfall process was eastward-moving and that heavy rainfall occurred over southwestern China on January

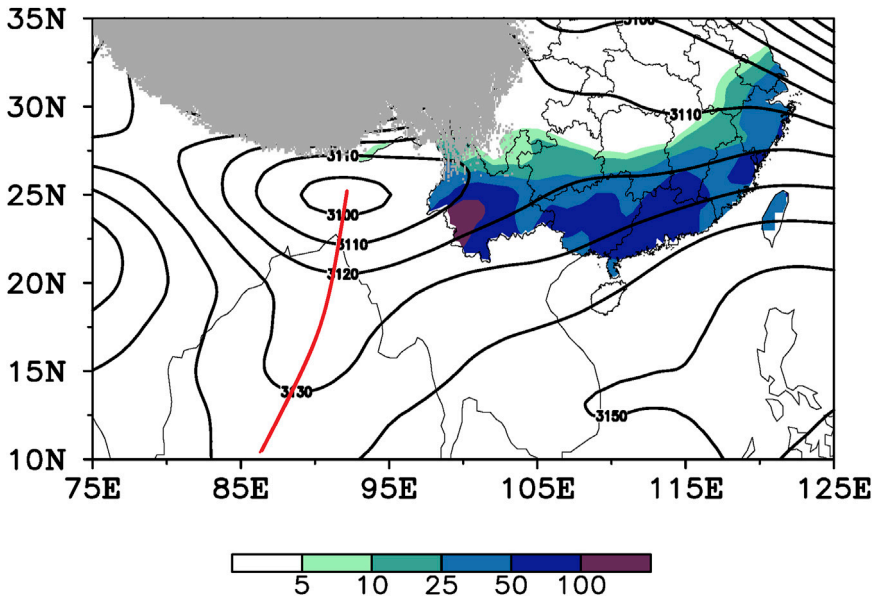

FIGURE 2
Average geopotential height field at 700 hPa (black contours, units: gpm) and the total accumulated precipitation (shading; units: mm) from January 8 to 13, 2015. The red line shows the trough line of the SBT. The gray shading represents the shape of the Qinghai-Tibetan Plateau.

8–9 and then gradually moved eastward to southeastern China on January 10–13 (Figure 3).

Recently, Chen and Li (2022) reported that about 50% of rainfall events over southwestern China move eastward to southeastern China over the next one to 3 days. It is therefore important to investigate the detailed changes in weather processes and the mechanisms related to eastward-moving rainfall events over southern China in winter. Chen and Li (2022) showed that strong cold air intruding into East Asia is an important factor in blocking heavy rainfall migrating eastward from southwestern to southeastern China. With the strong cold air intruding southward, the related cold Siberian high at the lower level can block the SBT–a low-pressure system–expanding eastward, thus the water vapor transported by the southwesterly wind flow in front of the SBT cannot be converged over southeastern China. Numerous studies also highlighted that the strong cold air activity is unfavorable for the occurrence of heavy rainfall over southeastern China (Wen et al., 2009; Bueh et al., 2011; Li et al., 2020). While, the reason for pushing the eastward movement of rainfall remains unclear. A clear and abnormally active Rossby wave train pattern appears along the subtropical westerly jet in both many individual events (e.g., Li and Sun, 2015; Li and Li, 2019) and the composited results of eastward-moving rainfall events (Chen and Li, 2022). Is the eastward-propagating Rossby wave train along the subtropical westerly jet a crucial factor in "pushing" the heavy rainfall eastward? How does the Rossby wave train along the subtropical westerly jet affect the local circulations favorable for the eastward movement of rainfall over southern China? These questions need further investigation.

A large area of heavy rainfall persisted over southern China for 6 days from January 8 to 13, 2015 (Figure 2). Li and Li (2019) have shown that the continuous eastward propagation of Rossby waves along the subtropical westerly jet helped to maintain this stable and persistent heavy rainfall event. Detailed analysis has shown that the rainfall process clearly moved eastward. Heavy rainfall occurred over southwestern China on January 8–9 and then gradually spread eastward to southeastern China on January 10–13 (Figure 3). We therefore selected this event as a case study of a typical eastward-moving rainfall event to investigate its detailed movement and the influence of the Rossby wave train along the subtropical westerly jet.

The remainder of this paper is organized as follows. The datasets and methods are introduced in Section 2. The detailed characteristics of the eastward-moving heavy rainfall events are described in Section 3. Sections 4, 5 describe the atmospheric circulations and the factors that may affect the variations in heavy rainfall. Our summary is presented in Section 6.

2 Data and methods

2.1 Data

We used the Reanalysis data from the National Center for Environmental Prediction - National Center for Atmospheric Research, with a horizontal resolution of (2.5°× 2.5°) and a vertical resolution of 17 levels (Kalnay et al., 1996). The daily precipitation data used were obtained from the observation data of 834 stations nationwide provided by the China Meteorological Administration. For terrain distribution chart, we used the Shuttle Radar Topography Mission (SRTM) 90 m Digital Elevation Database v4.1 from the Consortium for Spatial Information (CGIAR-CSI). More information is available at the following website (http://srtm.csi.cgiar.org).

2.2 Methods

2.2.1 Wave activity fluxes

To investigate the propagation of the Rossby wave train along the subtropical westerly jet, we calculated the wave activity fluxes using Eq. 1, developed by Takaya and Nakamura (2001):

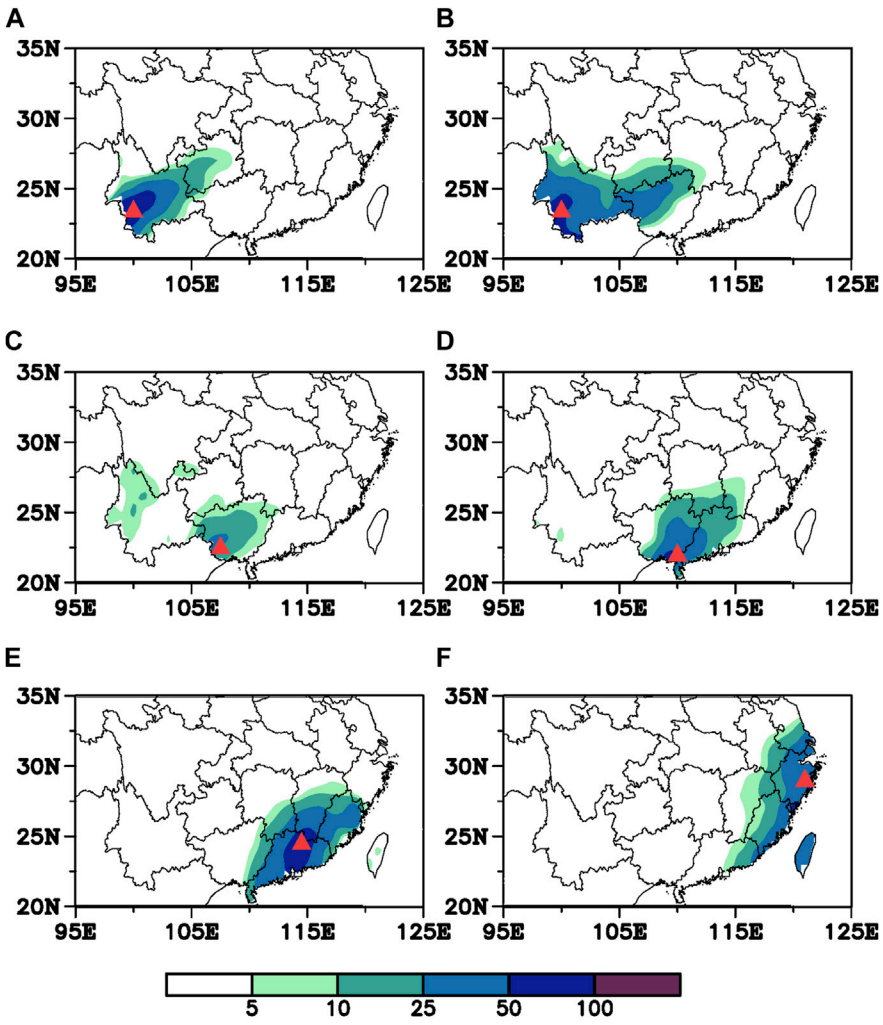

FIGURE 3
Distribution of the daily precipitation on January **(A)** 8, **(B)** 9, **(C)** 10, **(D)** 11, **(E)** 12 and **(F)** 13 in 2015 (units: mm). The red triangle indicates the large-value center of precipitation.

$$W = \frac{P \cdot \cos\varphi}{2|\mathbf{U}|} \cdot \begin{pmatrix} \frac{U}{a^2\cos^2\varphi}\left[\left(\frac{\partial\psi'}{\partial\lambda}\right)^2 - \psi'\frac{\partial^2\psi'}{\partial\lambda^2}\right] + \frac{V}{a^2\cos\varphi}\left[\frac{\partial\psi'}{\partial\lambda}\frac{\partial\psi'}{\partial\varphi} - \psi'\frac{\partial^2\psi'}{\partial\lambda\partial\varphi}\right] \\ \frac{U}{a^2\cos\varphi}\left[\frac{\partial\psi'}{\partial\lambda}\frac{\partial\psi'}{\partial\varphi} - \psi'\frac{\partial^2\psi'}{\partial\lambda\partial\varphi}\right] + \frac{V}{a^2}\left[\left(\frac{\partial\psi'}{\partial\varphi}\right)^2 - \psi'\frac{\partial^2\psi'}{\partial\varphi^2}\right] \\ \frac{f_0^2}{N^2}\left\{\frac{U}{a\cos\varphi}\left[\frac{\partial\psi'}{\partial\lambda}\frac{\partial\psi'}{\partial z} - \psi'\frac{\partial^2\psi'}{\partial\lambda\partial z}\right] + \frac{V}{a}\left[\frac{\partial\psi'}{\partial\varphi}\frac{\partial\psi'}{\partial z} - \psi'\frac{\partial^2\psi'}{\partial\varphi\partial z}\right]\right\} \end{pmatrix} \tag{1}$$

where ψ denotes the stream function, f is the Coriolis parameter, and λ, φ, Φ, a and Ω represent the longitude, latitude, geopotential, the radius of the Earth and the Earth's rate of rotation, respectively. U and V represent the steady zonal and meridional basic flow respectively, $|\mathbf{U}| = (U, V)$, $z = -H\ln P$, where $P = \frac{\text{pressure}}{1000\text{hPa}}$ and H = 8,000 m is a constant scale height. $\psi' = \frac{\Phi'}{f}$ is the quasi-geostrophic perturbation stream function and N is the buoyancy frequency. The basic flow calculated as the January mean during the period of 1985–2015, the perturbation denotes the daily disturbances calculated by removing the monthly climatology.

2.2.2 Evaluation of energy conversion

The evaluation of the conversion of energy between the perturbations of the wave train and the mean flows are based on the wave energy Eq. 2, the same as those used by Duan and Wu (2005):

$$\begin{cases} S_A = -\bar{u}_y u'v' \\ S_B = -\dfrac{Rf\bar{u}_p}{P\sigma}v'T' \end{cases} \tag{2}$$

where u and v denote the zonal and meridional wind velocities, respectively. P and T are atmospheric pressure, and temperature, respectively. R is the dry air gas constant, f is the Coriolis parameter and σ is the static stability parameter. The subscripts y and p represent the meridional and vertical derivatives, respectively. Overbars and primes denote the zonal mean and perturbation of the related variables. The positive values of S_A and S_B indicate the conversion of the kinetic energy and available potential energy from the mean flow into the wave train, respectively.

2.2.3 Identification of the SBT

We used the westerly trough identification method proposed by García et al. (2001) and Knippertz (2004) to identify the SBT on the daily weather chart. The SBT is climatologically manifested as cyclonic trough and low-pressure system, which frequently appeared over the southern Qinghai–Tibetan Plateau and the northern Bay of Bengal (Figure 1). According to the suggestions of Lin (2015), the area (15°–30°N, 80°–100°E) was chosen as the domain to identify SBT signals.

Z2 area (see Figure 1) was taken to represent the SBT trough line area, and adjacent areas Z1 and Z3 were taken to represent the areas behind and in front of the SBT, respectively. The daily geopotential height at 700 hPa was used to calculate the difference of average geopotential height (DH) between the trough line region of Z2 and the adjacent areasZ1 and Z3, as shown in Eq. 3. A positive value of DH indicated that a trough appeared in the study area. The region with a DH value greater than 35 gpm, which is approximately 1 standard deviation higher than the climatological value over the domain region, was considered an SBT area. The average DH value of the whole area of the SBT was calculated as the intensity of SBT. The location of the maximum DH value at each latitude was linked to the SBT trough line.

$$DH = \frac{1}{2}\left(H_{z1} + H_{z3}\right) - H_{z2} \tag{3}$$

About 90% of SBT may move eastward to downstream areas under the background of westerly flows in winter (Duan et al., 2012). We therefore also tracked the trajectory of the moving SBT. On the basis of the identification of the SBT signal in the domain region, we gradually moved the three identification boxes in Figure 1 eastward within 10° of longitude at 2.5 intervals over the next few days. We repeated these processes until the SBT signal could not be identified and thus the eastward shift of the SBT could be shown.

The two-dimensional horizontal frontogenesis function was calculated to investigate the frontogenesis related to rainfall process (Ninomiya, 1984), which was also used in Yuan et al. (2019) and shown good performance in diagnosing frontogenesis over southern China. Empirical orthogonal function (EOF) analysis was used to investigate the modes of SBT variation. We performed a significance test using the Student's *t*-test, which represent the probability that the anomalies were statistically different from the climatological state at the 90% or 95% confidence level. The anomalies mentioned in Sections 3–5 were calculated by removing the monthly climatology from 1985 to 2015.

3 Overview of the eastward-moving heavy rainfall event

A 6-day heavy rainfall event occurred over southern China from January 8 to 13, 2015. A large area of heavy rainfall was present in the zonal region 20°–30°N. The climatological daily mean maximum precipitation in winter was about 2 mm in south China (Ding and Li, 2017), while the total accumulated precipitation during the rainfall process exceeded 25 mm in most parts of southern China, including Yunnan, Guizhou, Guangxi, Guangdong, and Fujian provinces (Figure 2), although the spatial distribution of rainfall was uneven, with two large-value centers over southwestern and southeastern China. One center was located in Yunnan Province, southwestern China, where the maximum rainfall was more than 100 mm. The other center was located in Guangdong and Guangxi provinces, southern China, with the maximum rainfall more than 50 mm.

Further detailed analyses showed that the heavy rainfall process exhibited a clearly eastward-moving feature. On January 8, heavy rainfall mainly occurred in Yunnan and Guizhou provinces in southwestern China. Six meteorological stations in southwest Yunnan Province recorded maximum rainfall more than 80 mm (Figure 3A). On January 9, the center of heavy rainfall remained in southwest Yunnan Province, but extended eastward to Guangxi Province (Figure 3B). On January 8–9, heavy rainfall mainly occurred in southwestern China, with 20 counties and cities breaking the records of extreme January precipitation in the time period 1951–2015. The flood disasters and snowstorms caused by this heavy rainfall event affected 1.4 million people and led to about 11.5 billion RMB of economic losses.

The rainfall weakened on January 10, especially in Yunnan Province (Figure 3C). On January 11, the area of heavy rainfall moved eastward to Guangxi and Guangdong provinces and the precipitation over southwestern China gradually weakened and disappeared (Figure 3D). The rainfall continued to move east of 110°E and restrengthened on January 12 (Figure 3E). The main areas of heavy rainfall were located in Guangdong and Fujian provinces, where 18 meteorological stations recorded rainstorms with maximum daily rainfall of about 70 mm (Figure 3E). On January 13, the area of rainfall moved eastward to the coastal areas of southeastern China (Figure 3F).

The eastward-moving heavy rainfall event included multiple complex processes. The whole rainfall process occurred in two stages. In the first stage on January 8–9, 2015, the heavy rainfall was stable over southwestern China. In the second stage on January 10–13, 2015, the area of heavy rainfall gradually moved eastward to southeastern China, while the heavy rainfall weakened and disappeared in southwestern China.

4 Favorable atmospheric environments for the heavy rainfall event

4.1 Background atmospheric circulation in January

In January, the westerly winds in the lower troposphere are divided into northern and southern branches as a result of the blocking effect of the Qinghai–Tibetan Plateau. In the southern branch of the westerlies, the SBT extends from the south of the Qinghai–Tibetan Plateau to the northern Bay of Bengal. The SBT shows a strong cyclonic curve in the wind field and lower pressure signals at 700 hPa, but is relatively weak at 500 hPa (Figures 4A, B), indicating that in the climatology the SBT mainly exists in the mid-to lower troposphere as a result of the blocking effect of the Qinghai–Tibetan Plateau. The western Pacific subtropical high presents as a zonal band expanding from the western Pacific Ocean to the South China Sea around 15°N (Figures 4A, B). As a result of the strong pressure gradient in the regions between the SBT and the western Pacific subtropical high, southwesterly flows emerge in the front of the SBT, which may be favorable for transporting warm, moist air from the northern Bay of Bengal and the South China Sea to southern China (Figure 4C).

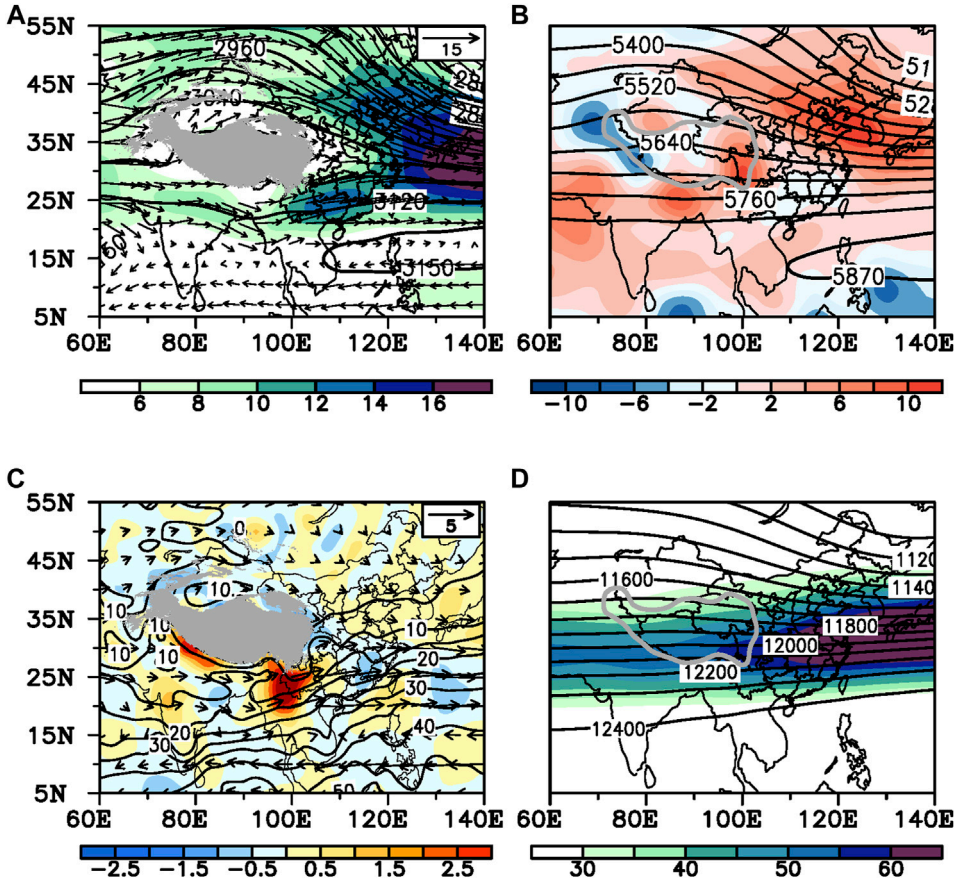

FIGURE 4
Climatology in January for the time period 1985–2015. **(A)** Geopotential height field (contours; units: gpm), wind field (vectors; units: m s^{-1}) and horizonal wind speed (shading; units: m s^{-1}) at 700 hPa. **(B)** Geopotential height field (contours; units: gpm) and omega field (shading, units: 10^{-2} Pa·s^{-1}) at 500 hPa. **(C)** Water vapor flux (vectors; units: kg m^{-1}·s^{-1}), divergence of the water vapor flux (shading; units: 10^{-6} kg·m^{-2}·s^{-1}) at 700 hPa and the precipitable water (contours; units: mm). **(D)** Geopotential height field (contours; units: gpm) and zonal wind speed at 200 hPa. Wind speeds greater than 30 m·s^{-1} are shaded with intervals of 5 m·s^{-1}. The gray-shaded areas **(A,C)** and isolines **(B,D)** show the shape of the Qinghai–Tibetan Plateau.

The water vapor transported by the southwesterly flow in front of the SBT contributes greatly to the rainfall over southern China in winter. In the climatology, the water vapor field shows that the southwesterly water vapor flux diverges over southwestern China and converges over southeastern China, thus the precipitable water value is slightly higher over southeastern China than over southwestern China (Figure 4C). But it should be noted that the climate of southern China is relatively dry in January, the average precipitable water value over the whole of southern China is about 20 mm. In addition, the subtropical westerly jet, which is located between 20° and 35°N in the upper troposphere, extends in a straight line from the Qinghai–Tibetan Plateau to East Asia. Southern China lies below the equator-ward side of the EASJ (Figure 4D).

4.2 Favorable local conditions for the occurrence of heavy rainfall

4.2.1 First stage: Occurrence of heavy rainfall over southwestern China on January 8–9, 2015

On January 8–9, a strong, stable SBT was located around 90°E, with the trough line extending from the south of the Qinghai–Tibetan Plateau to the northern Bay of Bengal at 700 hPa (Figures 5A, B). The average intensity of the SBT was 68 gpm, which was roughly 2.7 times that of the climatic state in winter. An anticyclonic system appeared over the South China Sea, indicating that the western Pacific subtropical high expanded to the west of 110°E. Because of the strong zonal pressure gradient between the SBT and the western Pacific subtropical high, a vigorous low-level southwesterly jet appeared in front of the SBT. Abundant warm, moist air was therefore transported from the Bay of Bengal and the western Pacific Ocean to southwestern China (Figures 6A, B, 7A, B). Strong water vapor converged over the northern Indochina Peninsula and southern China (Figures 6A, B). The average precipitable water was about 25 mm in southwestern China, which was higher than the climatology by about 1.5 standard deviations. The southerly flow in front of the SBT therefore transported plentiful water vapor from the Bay of Bengal and the western Pacific Ocean to southwestern China at this stage, providing favorable moisture conditions for the occurrence of heavy rainfall over southwestern China. A wide ridge was presented in the region (70°–110°E, 40°–50°N) in the northwesterly branch at 700 hPa (Figures 5A, B), whereas strong northerly winds and cold air advection mainly appeared north of 30° N (Figures 7A, B). The heavy rainfall mainly occurred in the warm advection region.

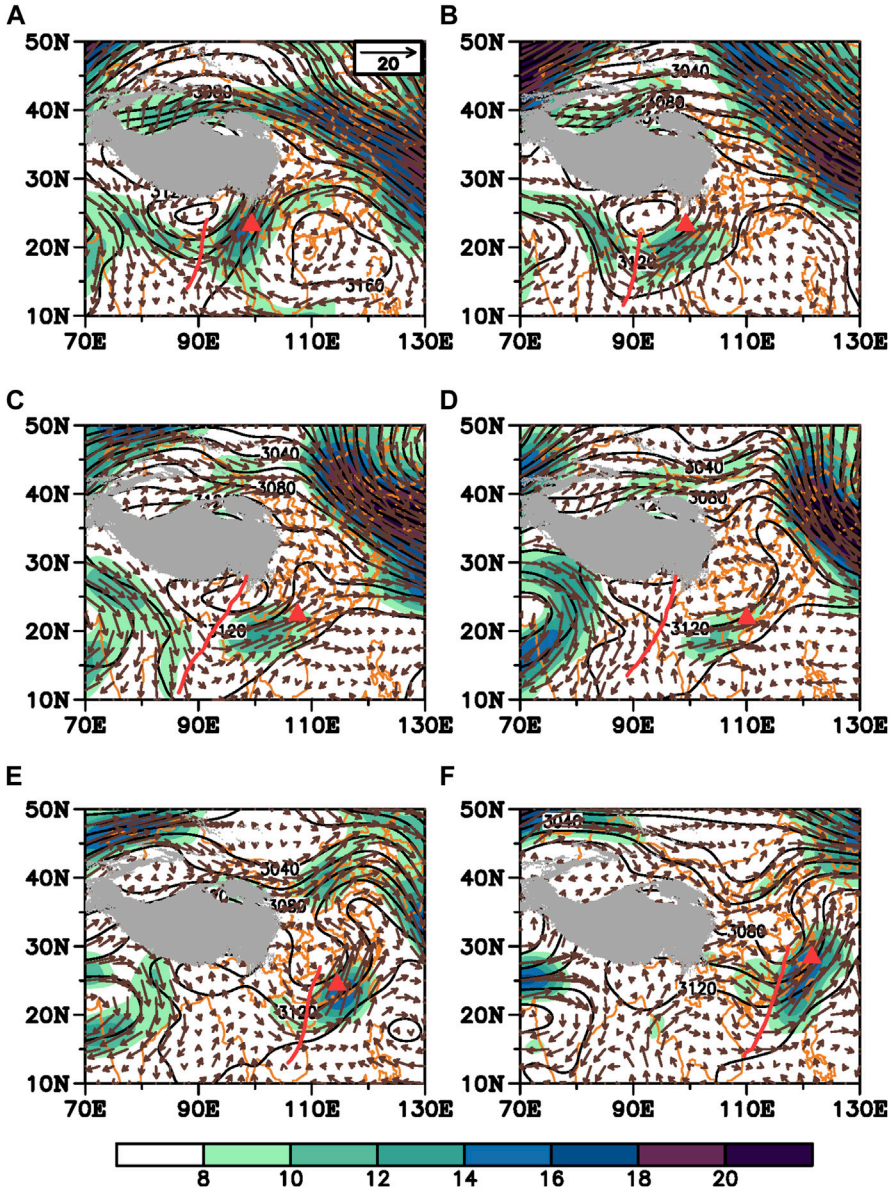

FIGURE 5
Geopotential height (black contours; units: gpm) and wind field (vectors; units: m s^{-1}) at 700 hPa on January **(A)** 8, **(B)** 9, **(C)** 10, **(D)** 11, **(E)** 12 and **(F)** 13 in 2015. Wind speeds greater than 8 m·s^{-1} are shaded in color. The red line shows the trough line of the SBT. The red triangle indicates the large-value center of precipitation. The gray shading shows the shape of the Qinghai-Tibetan Plateau.

In the upper level, the EASJ differed significantly from the climatology. There was a cyclonic curve in the upper level subtropical westerly jet over the eastern Qinghai–Tibetan Plateau (Figures 8A, B). This indicated that the upper level jet was weakened in the cyclonic curve region and the straight jet seemed to "break" over the eastern Qinghai–Tibetan Plateau. The South Asian and East Asian jets were therefore separated. The trough line of the upper level cyclonic curve region can be treated as a boundary between the South Asian jet and the East Asian jet. The center of the EASJ was mainly located east of 120°E over the western Pacific Ocean. Hence, the region of southwestern China was underneath the equator-ward side of the entrance of the upper level EASJ, which exhibited strong anomalous divergence at 200 hPa. The upper level divergence was closely related to the secondary circulation of the EASJ, which can induce strong upward motion and thus favors the occurrence of heavy rainfall over southwestern China.

4.2.2 Second stage: Rainfall moving eastward to southeastern China on January 10–13, 2015

On January 10, the SBT began moving downstream in an eastward direction. Especially in the northern part of the SBT, the location of the SBT trough line at 20°–30°N shifted eastward from 90°E to east of 95°E on January 10 (Figure 5C). The intensity of the SBT weakened to 58 gpm. The subtropical high also began to weaken and retreat eastward (Figure 5C). As a result of this weakening of the SBT and the subtropical high, the low-level southwesterly jet and the related transport of water vapor and advection of warm air were also weakened (Figures 6C, 7C). At the same time, the rainfall that

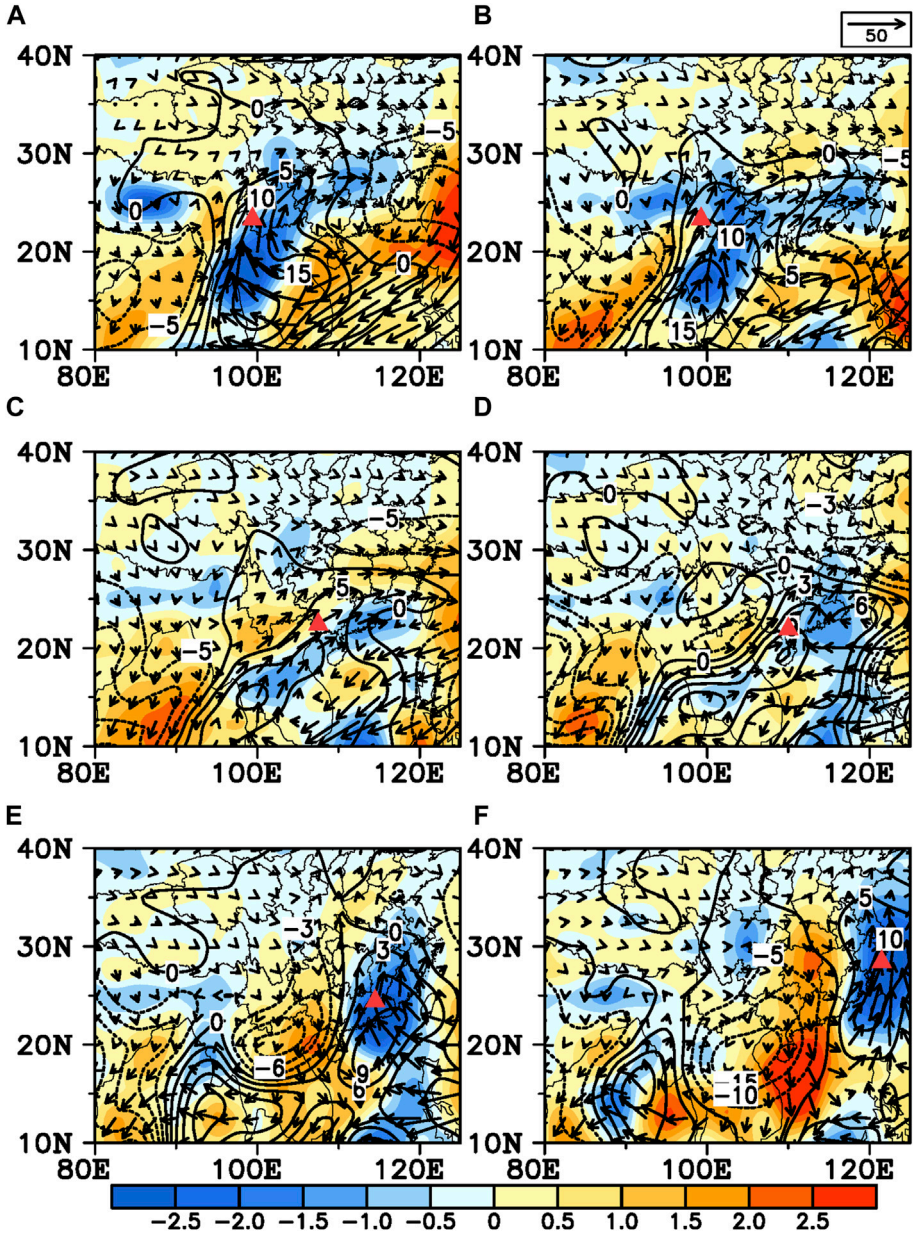

FIGURE 6
Column-integrated water vapor flux (vectors; units: kg $m^{-1}·s^{-1}$), the divergence of the column-integrated (surface–300 hPa) water vapor flux (shading; units: 10^{-5} kg·$m^{-2}·s^{-1}$) and the precipitable water anomalies (contours; units: mm) on January **(A)** 8, **(B)** 9, **(C)** 10, **(D)** 11, **(E)** 12 and **(F)** 13 in 2015. The red triangle indicates the large-value center of precipitation.

occurred over southwestern China began to weaken, especially in Yunnan Province (Figure 3C).

The SBT continued moving eastward on January 11 (Figure 5D) and its intensity weakened to 37 gpm. The circulations in the northern branch of the westerlies also clearly varied. Compared with January 8–9, the ridge in the northern branch of the westerlies disappeared and was replaced by a trough located over the northeast of the Qinghai–Tibetan Plateau on January 11. The SBT in the southern branch of the westerlies and the trough in the northern branch of the westerlies were therefore superimposed in the east of the Qinghai–Tibetan Plateau near 100°–110°E (Figure 5D). The advection of cold air was seen on the eastern edge of the Qinghai–Tibetan Plateau, behind the trough of the northern branch of the westerlies (Figure 7D). The advection of cold air may have invaded southward and interacted with the SBT. In addition, as a result of the eastward movement of the SBT, the tropical water vapor transported by the southwesterly flow appeared in front of the SBT and mainly concentrated in the eastern region of southeastern China (Figure 6D). As a result, the rainfall also moved eastward. Heavy rainfall mainly occurred in Guangdong and Guangxi provinces, while the precipitation over southwestern China gradually weakened and disappeared (Figure 3D).

The SBT continued to move eastward on January 12 to nearly 110°E (Figure 5E). The cold advection originating from mid-latitude

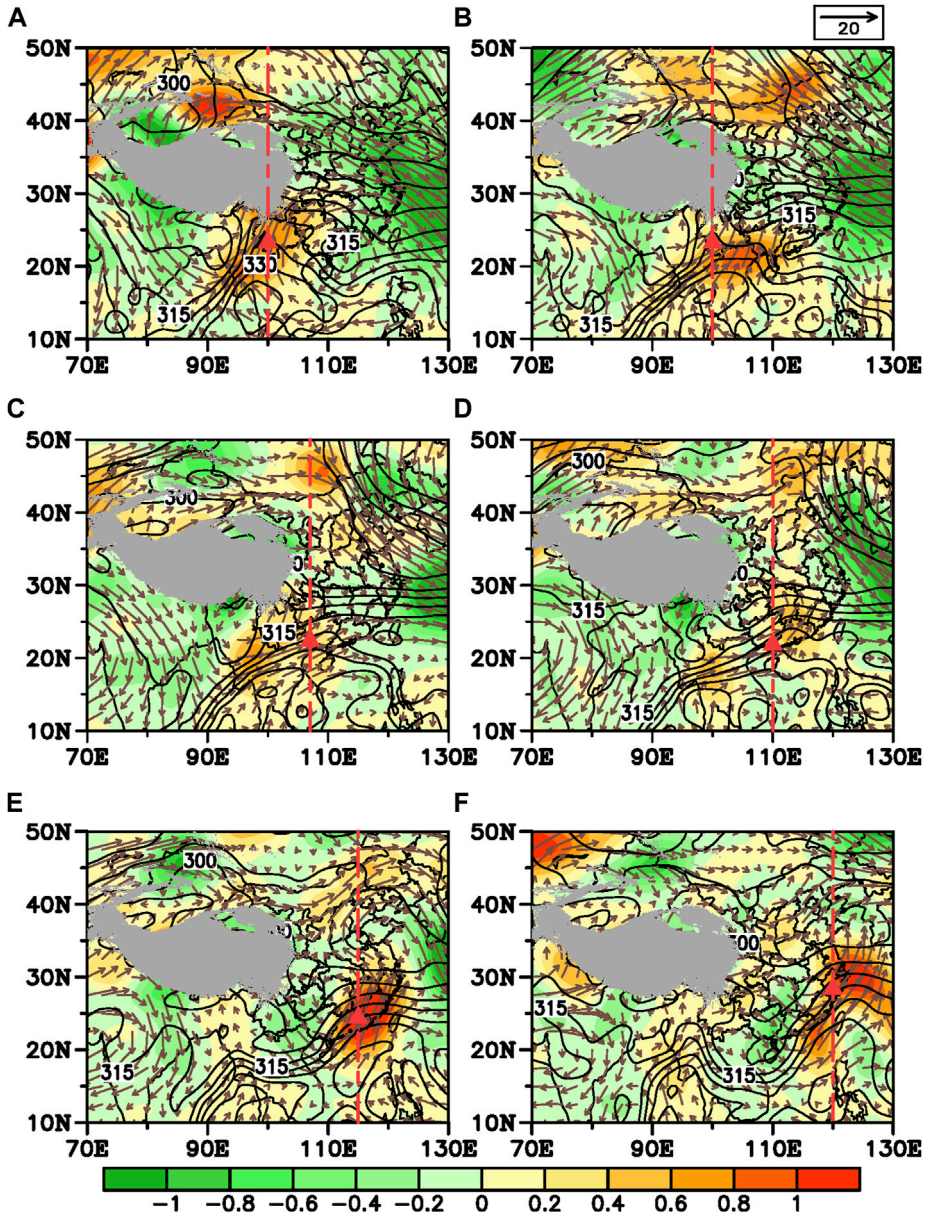

FIGURE 7
Equivalent potential temperature (black contours; units: K), the wind field (vectors; units: m s^{-1}) and the temperature advection (shading; units: 10^{-4} K·s^{-1}) at 700 hPa on January **(A)** 8, **(B)** 9, **(C)** 10, **(D)** 11, **(E)** 12 and **(F)** 13 in 2015. The red triangle indicates the large-value center of the precipitation. The red dotted line shows the crossing line used for depicting the vertical cross-section profiles in Figures 11, 12. The gray shading shows the shape of the Qinghai-Tibetan Plateau.

invaded southward along the northeastern edge of the Qinghai–Tibetan Plateau to about 20°N and interacted with the SBT, resulting in restrengthening of the SBT (Figure 7E). The intensity of the SBT was reinforced to 58 gpm. The circulation around the SBT showed an almost closed cyclonic system (Figures 5E, 7E). A strong, low-level southerly jet, which appeared in front of the SBT and to the west of the western Pacific subtropical high, transported a plume of warm, moist air from the tropical western Pacific Ocean to southeastern China (Figures 5E, 6E). A warm ridge expanded from the subtropics to mid-latitudes over eastern China (Figure 7E). Correspondingly, rainfall was reinforced in the warm, moist region in front of the SBT and the main areas of heavy rainfall were located in Guangdong and Fujian provinces (Figure 3E). On January 13, the SBT moved eastward to nearly 115° E and gradually merged with the trough of the northern branch of the westerlies (Figure 3F). The regions of heavy rainfall also moved eastward to the coastal areas of southeastern China (Figure 4F).

With the eastward movement of the lower level SBT, the upper level EASJ also exhibited eastward movement during the time period January 10–13 (Figures 8C–F). It seems that the variations in the upper level EASJ were covariant with the lower level SBT activities. The cyclonic curve in the upper level subtropical jet overlapped above the low-level SBT, with slight vertical titling to the west. As a result, the region of strong

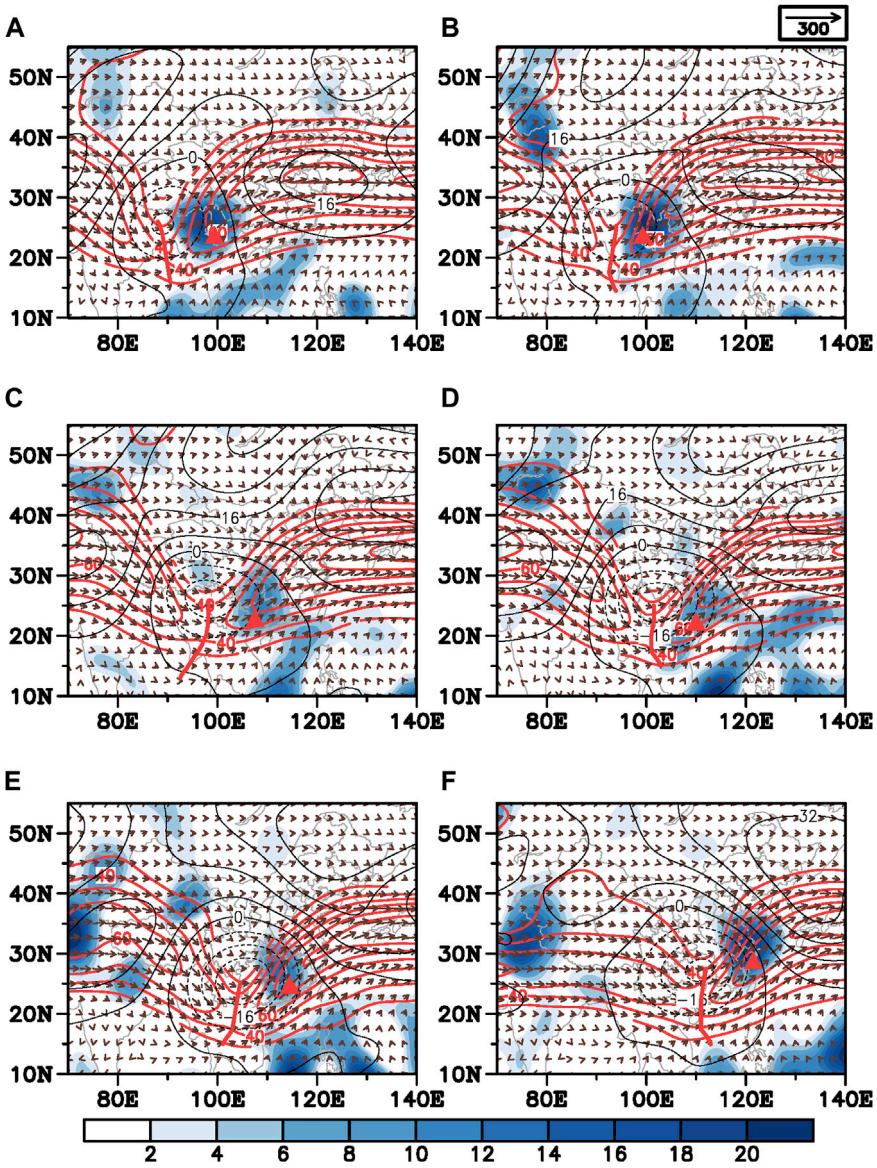

FIGURE 8
Wind field (vectors; units: m s^{-1}), geopotential height anomalies field (black contours; units: 10 gpm) and the divergence of the horizontal winds (shading; units: 10^{-6} s^{-1}) at 200 hPa on January **(A)** 8, **(B)** 9, **(C)** 10, **(D)** 11, **(E)** 12 and **(F)** 13 in 2015. The red triangle indicates the large-value center of precipitation. Red contours represent zonal wind speeds greater than 30 m·s^{-1} and the thick red line shows the trough line of the cyclonic curve appearing in the upper westerly jet.

divergence in the upper levels, which was located on the equator-ward side of the EASJ entrance, overlapped with the lower level region of convergence of moist air, which appeared in the front of the SBT. These vertical configurations contributed to moisture and dynamic conditions favorable for the occurrence of heavy rainfall. Accompanying the synchronous eastward movement of the low-level SBT and the upper level EASJ, the regions of heavy rainfall moved gradually from southwestern to southeastern China (Figure 3).

These variations in the local circulation further confirmed that the heavy rainfall event from January 8 to 13 consisted of two stages. The first stage was from January 8 to 9. The low-level SBT remained stable over the northern Bay of Bengal and the western Pacific subtropical high expanded to the Indochina Peninsula. Southwestern China was located underneath the equator-ward side of the entrance of the upper level EASJ. In this stage, the heavy rainfall mainly occurred over southwestern China. In the second stage (January 10–13), the low-level SBT, the western Pacific subtropical high and the upper level EASJ moved eastward concurrently and the region of heavy rainfall also moved eastward to southeastern China.

4.3 Rossby wave trains along the subtropical westerly jet

In addition to the favorable local conditions, numerous studies have emphasized that the Rossby wave train along the subtropical

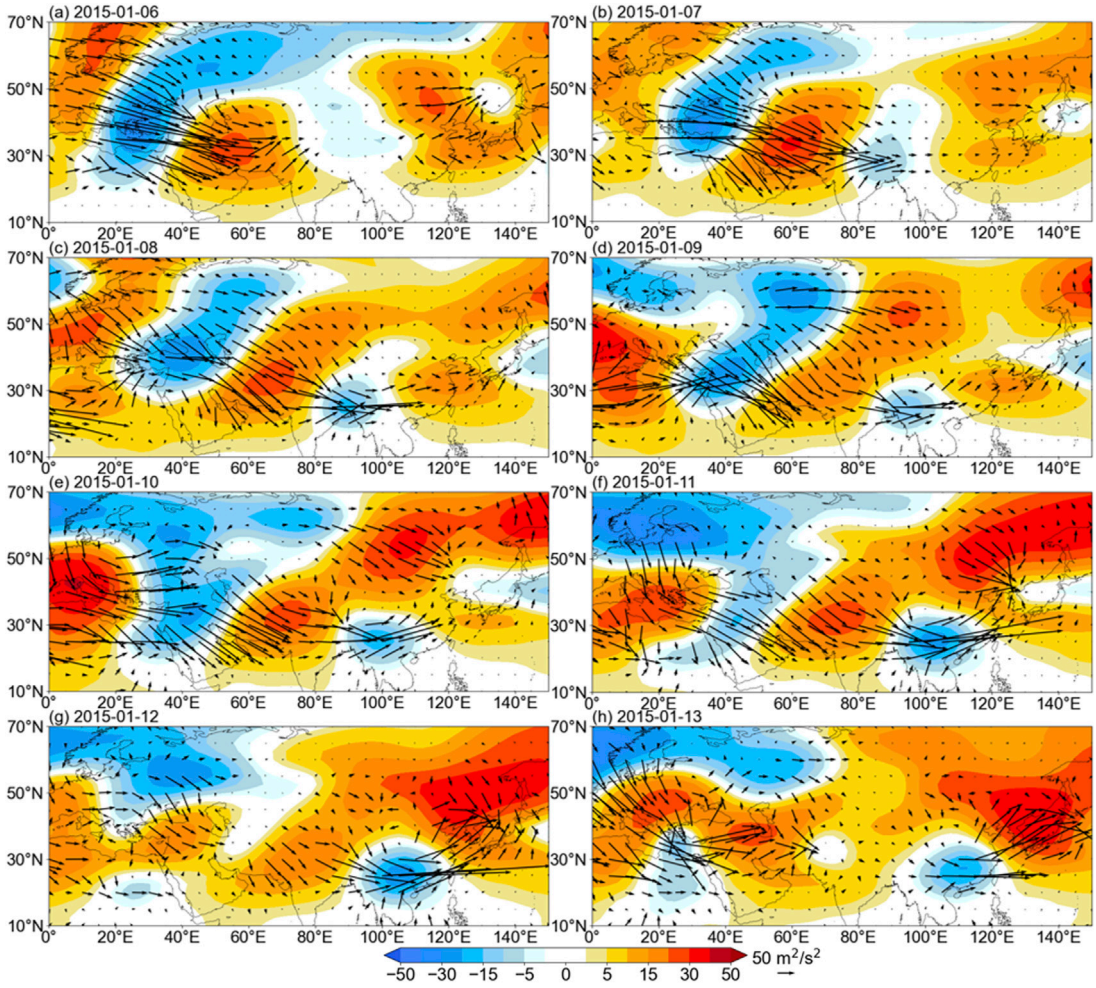

FIGURE 9
Wave activity flux (vectors; units: $m^2 \cdot s^{-2}$) and geopotential height anomalies field (shading; units: 10 gpm) at 250 hPa on January **(A)** 6, **(B)** 7, **(C)** 8, **(D)** 9, **(E)** 10, **(F)** 11, **(G)** 12 and **(H)** 13 in 2015.

westerly jet is an important factor in the occurrence of heavy rainfall over southern China in winter (Zong et al., 2014; Huang et al., 2019; Li et al., 2020; Tan et al., 2022). During this rainfall event, the Rossby wave trains clearly propagated downstream in an eastward direction along the subtropical westerly jet (Figure 9). On January 6, the Rossby wave energy originating from western Europe propagated southeastward to the Middle and Eastern Mediterranean and forced disturbance in the subtropical westerly jet (Figure 9A). The waveguide effect of the subtropical westerly jet led to the wave energy dissipating downstream in an eastward direction along the jet (Figure 9B). On January 8–9, the wave energy converged over the Bay of Bengal and southwestern China (Figures 9C, D). The convergence of the wave energy on January 10–13 was gradually moved eastward from southwestern to southeastern China (Figures 9D–H).

The time–latitude profiles along the axis of the subtropical westerly jet at 25°N shown that there were two distinct Rossby wave packets propagating eastward along the subtropical westerly jet (Figure 10). On January 5–6, the disturbance invaded to the subtropical westerly jet and evoked the Rossby wave trains propagating eastward (Figures 9A, 10). About 4 to 5 days later, the wave energy propagated eastward to, and converged over, southwestern China, where it was associated with the maintenance and occurrence of a stable region of heavy rainfall over southwestern China on January 8–9. The wave train propagated eastward to the west of 100°E and terminated after January 9 as a result of the decay of the wave energy. The rainfall over southwestern China also began to weaken on January 10. On January 8–9, strong wave active fluxes converged near 20°–40°E and evoked a new Rossby wave packet propagating eastward downstream (Figures 9C, D, 10). With the continuous eastward propagation of wave energy, the region of convergence of wave energy over southern China also gradually moved downstream to the east, concurrent with the region of heavy rainfall moving from southwestern to southeastern China.

The eastward propagation of the Rossby wave trains along the subtropical westerly jet were closely related to the maintenance and movement of rainfall over southern China. The occurrence and development of heavy rainfall over southern China were jointly influenced by the local circulation anomalies and the remote propagation of the Rossby wave train along the upper level subtropical westerly jet.

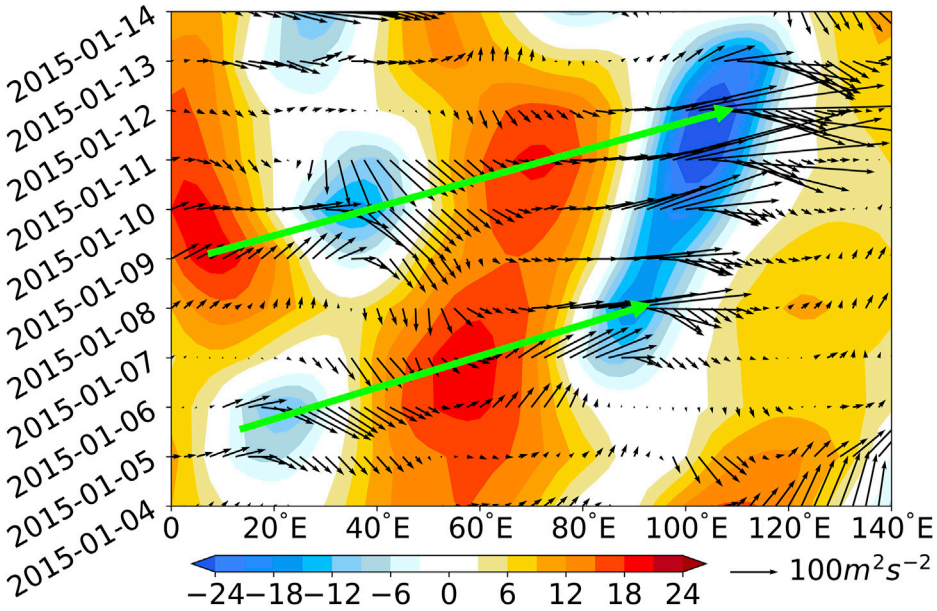

FIGURE 10
Time–longitude profile of the geopotential height anomalies (shading; units: 10 gpm) and the wave activity flux (vectors; units: $m^2 \cdot s^{-2}$) at 250 hPa along the axis of the jet stream at 25°N on January 4–14, 2015. The green arrow shows the propagation of the wave train.

5 Mechanisms for the variation in heavy rainfall over southern China

5.1 Mechanisms for the occurrence of heavy rainfall over southwestern and southeastern China

5.1.1 First stage: Occurrence of heavy rainfall over southwestern China on January 8–9, 2015

In the first stage, the SBT was stable around 90°E in the northern Bay of Bengal (Figures 5A, B). The western Pacific subtropical high was located over the South China Sea and its western edge expanded to about 105°E (Figure 5A). As a result of the strong pressure gradient between the SBT and the western Pacific subtropical high, a strong low-level southerly jet appeared in front of the SBT (Figures 5A, B) and transported abundant water vapor and warm air from the Bay of Bengal and the western Pacific Ocean to southwestern China (Figures 6A, B, 7A, B). The equivalent potential temperature field was therefore seen as a ridge expanding from the Indochina Peninsula to southwestern China (Figures 7A, B). Strong warm, wet air advection dominated over southwestern China, especially in Yunnan Province.

The topography of southwestern China is very complex (Yuan et al., 2019), which is higher in the northwest and lower in the southeast, and strong orographic gradient appears in the northwest–southeast direction (Figure 1). The southwesterly flow impinged almost perpendicularly on the windward slopes of the mountains in southwestern China. Forced by the topography, the warm, wet air carried by the southerly flow converged and led to frontogenesis at lower levels, thus strong upward motion appeared on the windward slopes of the mountains over southwestern China (Figures 11A, B, 12B). The upward motion transported water vapor from low levels to the mid-troposphere and positive humidity anomalies and saturated moist layers with a relative humidity greater than 90% appeared from the base to the middle of the troposphere over southwestern China, especially on the windward slopes in southwestern China (Figures 11A, B). This is clearly different from the winter climatological condition in that the water vapor is mainly concentrated in the lower troposphere below 700 hPa over southwestern China (Yuan et al., 2018).

The anomalous increase in moisture in the mid-troposphere led to thickening of the saturated moist layer, which favored the occurrence of heavy rainfall over southwestern China. The orographic effect is therefore an important factor in the first stage, forcing low-level frontogenesis and upward motion and therefore favoring the heavy rainfall that occurred on the southwest windward slopes of the mountains in southwestern China.

Southwestern China was located below the equator-ward side of the entrance of the upper level EASJ (Figures 8A, B). Strong divergence at the upper level caused by the secondary circulation of the EASJ may also have contributed to precipitation over southwestern China. To investigate the configurations of the upper and lower level circulations related to the heavy rainfall process, Figure 12 shows vertical cross-sections along the center of heavy rainfall. On January 8–9, strong, low-level frontogenesis and upward motion appeared on the windward slopes as a result of the orographic forcing effect (Figures 13A, B). As shown in Figure 8A, due to the "deceleration" of the jet stream caused by the wave-current interaction, the upper level of the subtropical jet "broke" on the eastern side of the Qinghai-Tibet Plateau and forms a cyclonic curve, or trough, strong secondary upward motion and related frontogenesis appeared in the mid-to upper levels below the equator-ward side of the entrance of the EASJ (Figure 12B). Deep upward motion therefore occurred throughout the whole troposphere on the windward slopes in southwestern China as a result of the surface orographic forcing effect and the secondary circulation of the upper level EASJ, favoring the occurrence of

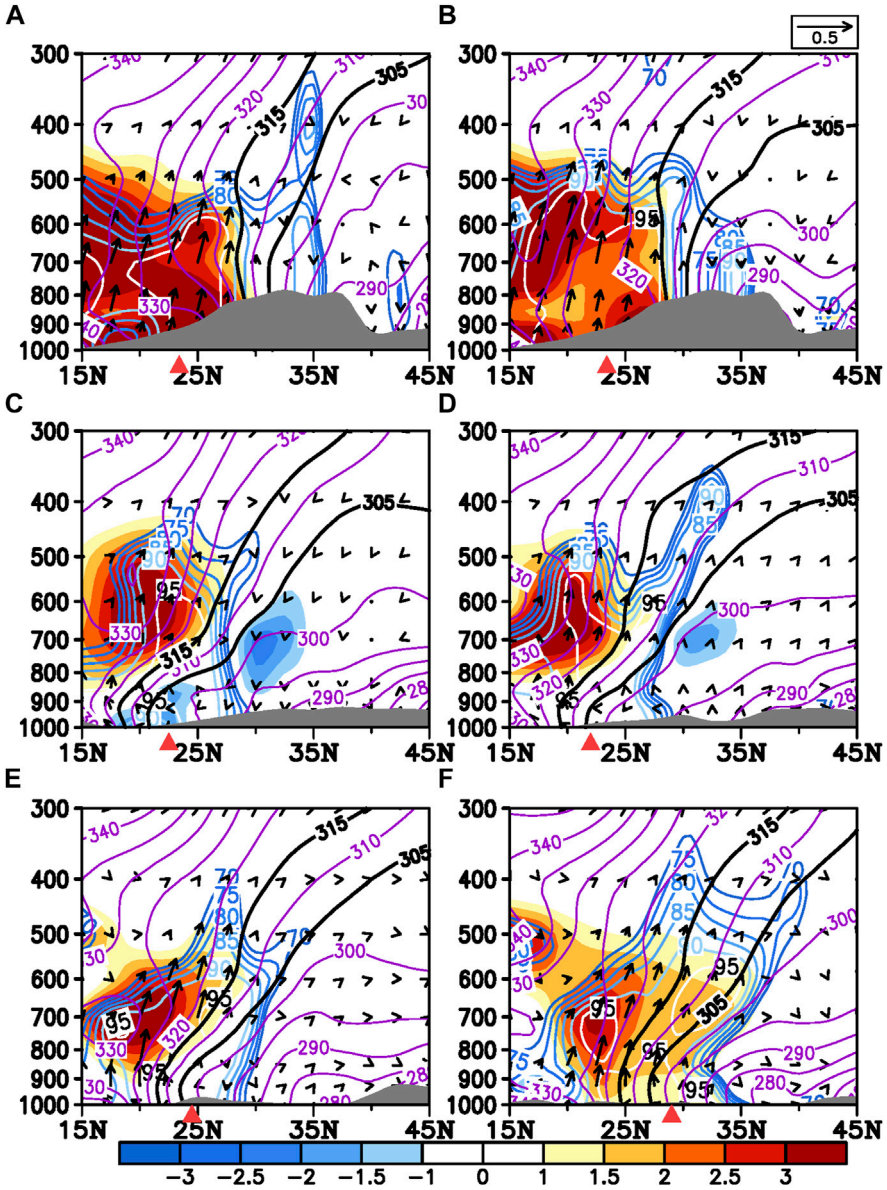

FIGURE 11
Vertical cross-sections along the red dotted lines in Figure 7 for the water vapor flux (vectors; units: kg $m^{-1}{\cdot}s^{-1}$), the specific humidity anomalies (shading; units: kg kg^{-1}), the relative humidity (colored contours; units: %), the equivalent potential temperature (purple contour; units: K) along **(A)** 100°E on January 8, **(B)** 100°E on January 9, **(C)** 107°E on January 10, **(D)** 110°E on January 11, **(E)** 115°E on January 12 and **(F)** 120°E on January 13 in 2015. The latitude with the maximum center of daily precipitation is represented by the red triangle. The thick black lines represent the isolines of the equivalent potential temperature at 305 and 315 K. The gray shading shows the shape of the topography.

heavy rainfall. The deep jet-front system, including low-level orographic forcing frontogenesis and the secondary circulation of the upper level EASJ, therefore greatly contributed to the occurrence of heavy rainfall over southwestern China during the first stage of the rainfall event on January 8–9.

5.1.2 Second stage: Occurrence of heavy rainfall over southeastern China on January 10–13, 2015

The subtropical high weakened from January 10 to 13 and its western edge retreated from the Indochina Peninsula to the western Pacific Ocean. The SBT also began to move eastward (Figures 5C–F). On January 10–11, a southwesterly airflow appeared in the front of the SBT and to the west of the subtropical high, transporting water vapor from the Bay of Bengal and the South China Sea to southern China (Figures 6C, D). However, the strength of the transport of water vapor seemed to be weaker than in the first stage on January 8–9 and the region of convergence was further to the east (Figures 6, 11C, D). Correspondingly, the rainfall over southwestern China weakened and the center of rainfall moved from Yunnan Province to the eastern regions of Guangxi and Guangdong provinces (Figures 3C, D).

On January 12–13, the SBT moved eastward to the southeast of the Qinghai–Tibetan Plateau (Figures 5E, F), leading warm, wet air from the South China Sea and the western Pacific Ocean to southeastern China (Figures 6E, F, 7E, F). There was also a deep trough on the

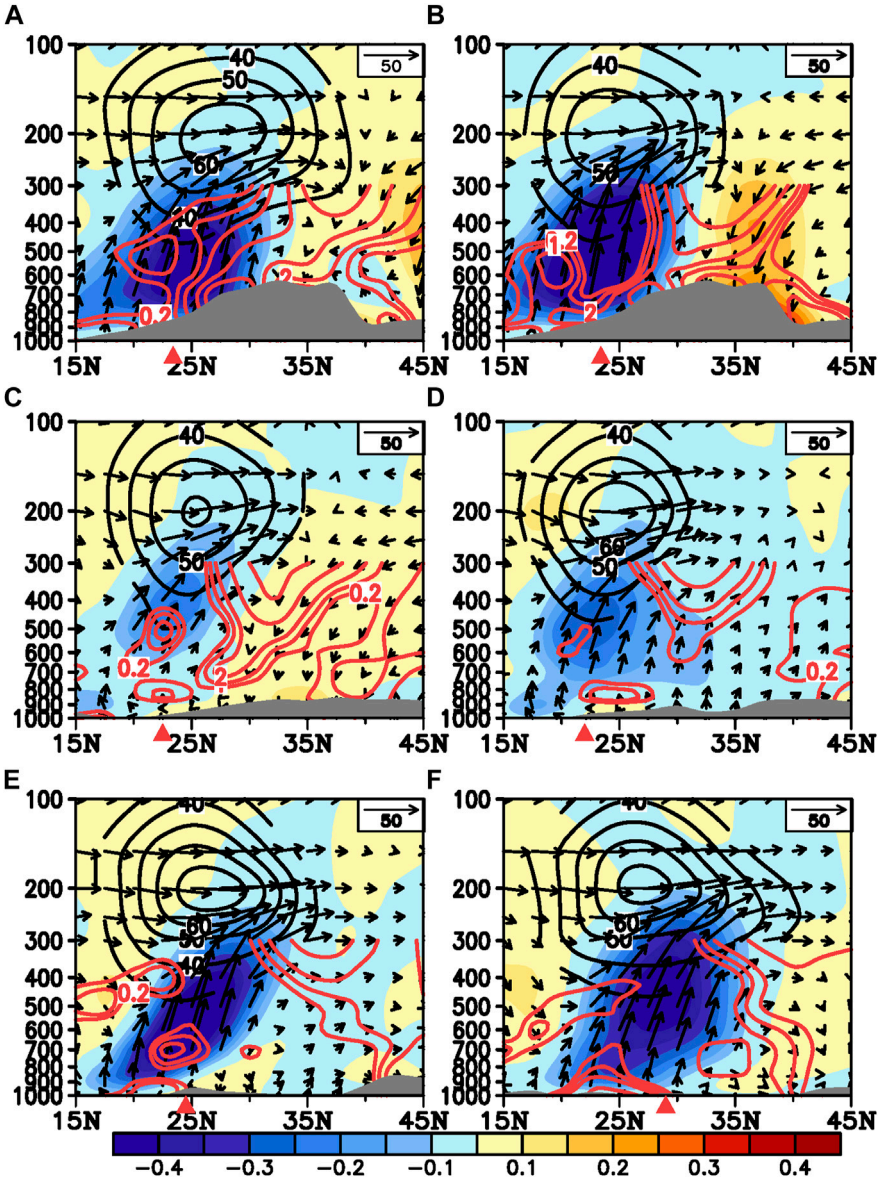

FIGURE 12
Vertical cross-sections along the red dotted lines in Figure 7 for the frontogenesis (positive value as red contours; units: 10 K·m^{-1}·s^{-1}), omega field (shading; units: Pa s^{-1}) and wind field (horizontal wind, units: m s^{-1}; vertical omega, units: 10^{-2} Pa·s^{-1}) along **(A)** 100°E on January 8, **(B)** 100°E on January 9, **(C)** 107°E on January 10, **(D)** 110°E on January 11, **(E)** 115°E on January 12 and **(F)** 120°E on January 13 in 2015. The black contour indicates the upper level jet with a zonal wind speed greater than 30 m·s^{-1}. The latitude with the maximum center of daily precipitation is represented by the red triangle. The gray shading shows the shape of the topography.

northern branch of the westerlies, which was located on the northeast of the Qinghai–Tibetan Plateau (Figures 5E, F). The troughs on the northern and southern branches of the westerlies gradually overlapped near 110°–120°E on January 12–13 (Figures 5E, F). This led to strong advection of the cold air intruding into southeastern China along the southeastern edge of the Qinghai–Tibetan Plateau, which interacted with the warm, wet flow in the front of the SBT, causing it to restrengthen. The average intensity of the SBT on January 12–13 was 73 gpm, which was about 2.9 times that of the climatological value.

The robust warm advection in the front of the SBT intensified the temperature gradient and densified the temperature isolines that appeared in the region (110°–120°E, 25°–30°N) over southeastern China. The cold flow intruding into the back of the SBT also caused an increase in the temperature gradient in the region (100°–115°E, 15°–20°N) (Figures 7E, F). This suggests that warm and cold fronts were both formed in the deep SBT, which therefore featured a cyclonic system over southern China (Figures 5E, F, 7E, F). The heavy rainfall mainly occurred in the region of the warm front over southeastern China, which may be a result of the favorable warm, moist conditions in the front of the SBT.

The vertical profiles showed that the moist airflow in the lower level was transported upward along the warm front and thickened the moist layer from the surface to 500 hPa (Figures 11E, F). The low-level baroclinic frontogenesis forced strong upward motion and transported plentiful water vapor upward to the mid-troposphere,

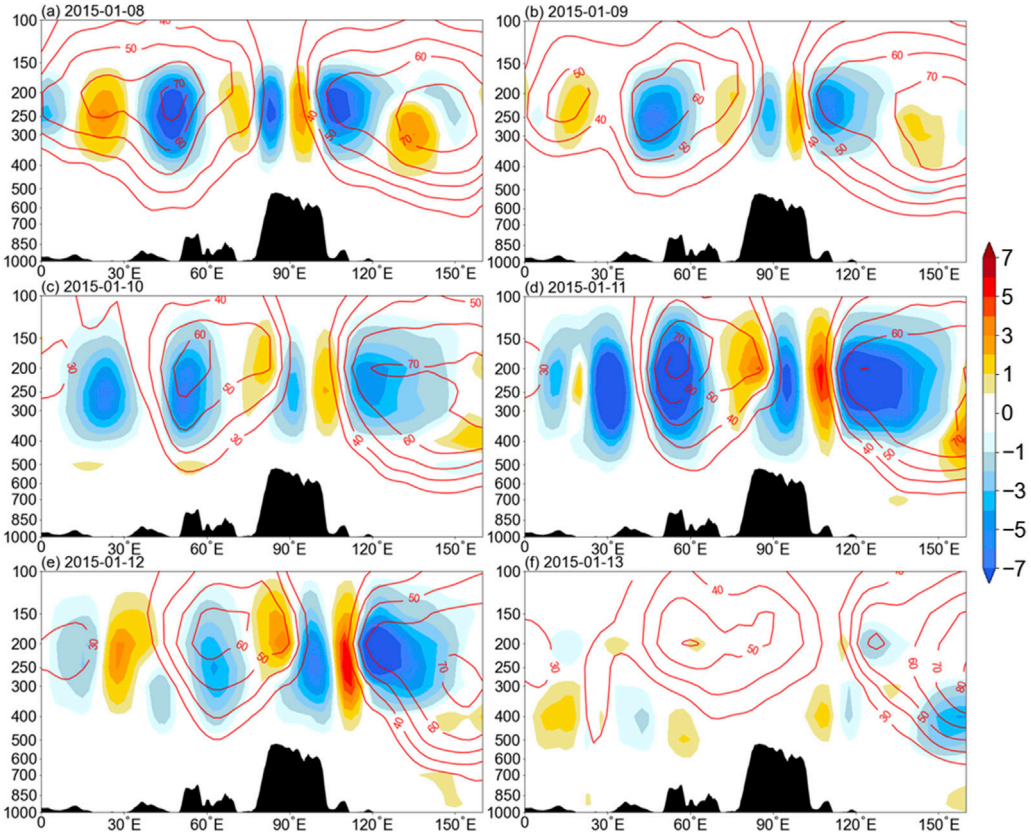

FIGURE 13
The term S_A for the transformation of the zonal mean and wave disturbance kinetic energy (shading; units: 10^{-3} $m^2 \cdot s^{-3}$) along the subtropical westerly jet stream axis of 30°N on January **(A)** 8, **(B)** 9, **(C)** 10, **(D)** 11, **(E)** 12 and **(F)** 13 in 2015. The red contour indicates zonal wind speeds greater than 30 $m \cdot s^{-1}$. The black shading shows the shape of the topography.

which reinforced the favorable thermal and dynamic conditions for heavy rainfall over southeastern China. Horizontal temperature advection and baroclinic frontogenesis in the second stage therefore greatly contributed to the reinforcement of heavy rainfall over southeastern China.

Interestingly, the "broken" region of the subtropical westerly jet at the upper level also presented an eastward movement during the time period January 10–13. The trough line of the cyclonic curve and the "broken" region moved eastward from 100 to 115°E from January 10 to 13 (Figures 8C–F). The trough line of the cyclonic curve region can be treated as the dividing boundary between the upper level South Asian jet and the East Asian jet. This indicates that the entrance region of the EASJ gradually moved eastward in the second stage. Accordingly, the regions of heavy rainfall were always located below the equator-ward side of the entrance of the EASJ, which exhibited strong divergence in the upper level. Apparent secondary vertical upward motion appeared in the mid-to upper level over the EASJ entrance region (Figures 12C–F). This suggests that the upper level EASJ also had an essential role in the occurrence of heavy rainfall over southeastern China in the second stage. Strong upward motion dominated the whole of the troposphere in the region of heavy rainfall over southeastern China, especially on January 12–13 (Figures 12E, F), indicating that both the lower level upward motion forced by the baroclinic frontogenesis and mid-to upper level uplifting related to the secondary circulation of the EASJ were favorable dynamic factors for the reinforcement of heavy rainfall over southeastern China.

5.2 Roles of the Rossby wave train associated with the occurrence of heavy rainfall

5.2.1 Interactions with the upper level EASJ

The Rossby wave can spread downstream to the east along the subtropical westerly jet. There may be strong interactions between the eastward-propagating Rossby wave train and the westerly jet flow. The wave energy kinetic conversion terms were calculated for the heavy rainfall event of January 8–13 (Figure 13). Associated with the Rossby wave train propagating eastward along the subtropical westerly jet, the conversion term of kinetic energy showed a positive–negative wave train-like pattern and mainly occurred in the upper troposphere above 400 hPa.

On January 8–9, the Rossby wave train triggered by the disturbance near the Mediterranean on January 5–6 propagated eastward and arrived at the eastern Qinghai–Tibetan Plateau (Figures 9, 10). There was positive kinetic energy conversion over the eastern side of the Qinghai–Tibetan Plateau at 90°–110°E above 400 hPa (Figures 13A, B). This indicated that the kinetic energy of the westerly mean flow was converted to the kinetic energy of the wave

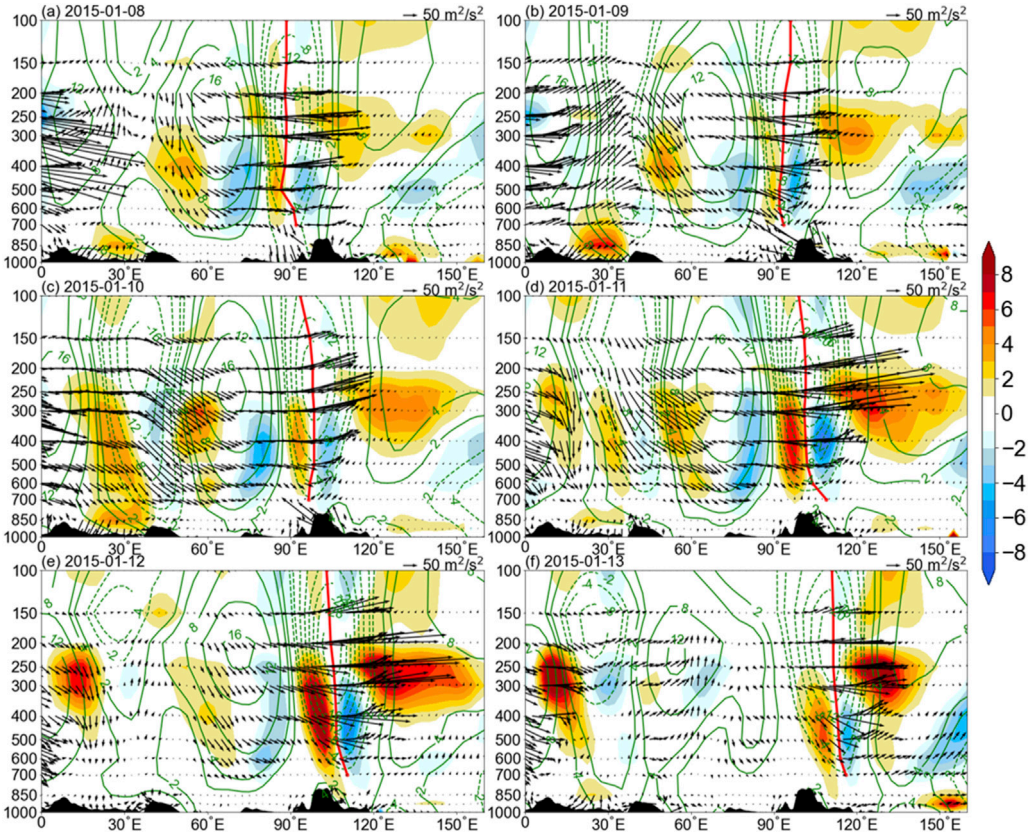

FIGURE 14
The term S_B for the potential energy conversion (shading; units: 10^{-3} m^2·s^{-3}), the wave activity flux (vectors; units: m^2·s^{-2}) and the geopotential height anomalies (contours; units: 10 gpm) along the subtropical westerly jet stream axis at 25° N on January **(A)** 8, **(B)** 9, **(C)** 10, **(D)** 11, **(E)** 12 and **(F)** 13 in 2015. The red line shows the vertical trough line with the maximum DH value in each layer. The black shading shows the shape of the topography.

train. The westerly mean flow therefore weakened and the disturbance of the wave strengthened over the eastern side of the Qinghai–Tibetan Plateau. The subtropical westerly jet was relatively weak and featured as a "break" in the zonal wind speed and a characteristic of the cyclonic curve of the horizontal flow in the upper level (Figures 8A, B). The weakness of the subtropical westerly jet at 90°–110°E caused the jet to "break" and this area became the entrance area of the EASJ. Southwestern China was located underneath the equatorial side of the entrance of the EASJ (Figures 8A, B). The secondary upward circulation of the EASJ favored the powerful dynamic conditions required for the occurrence of heavy rainfall over southwestern China. As a result of the decay of the wave energy, the eastward propagation of the Rossby wave packets just arrived at the eastern side of the Qinghai–Tibetan Plateau and gradually terminated after January 9 (Figure 10). The precipitation process also began to weaken on January 10 (Figure 3C). However, with a new Rossby wave packet propagating eastward downstream on January 8–9, the eastward propagation of the Rossby wave train along the jet stream was re-excited on January 11–12 and spread further eastward downstream to southeastern China (Figure 9D). On January 11–12, associated with the eastward propagation of the Rossby wave train, there was strong positive kinetic energy conversion over the eastward downstream area of 100°–120°E, implying the kinetic energy loss and weakening of the zonal mean flow over there, and the entrance region of the upper level EASJ move further eastward to and above southeastern China. This may have partly contributed to the eastward shift in the heavy rainfall over southern China on January 11–12. On January 13, with the decaying of the wave energy, the eastward propagation of the Rossby wave packets and the conversion of the kinetic energy of the jet wave also gradually weakened (Figure 13F).

The eastward-propagating Rossby wave train can change the morphology of the EASJ *via* wave–jet interactions and lead to variations in the location of the entrance area of the EASJ. The related secondary upward circulation in the entrance area of the EASJ provided favorable dynamic conditions for the occurrence of heavy rainfall over southwestern and southeastern China.

5.2.2 Impact on the lower level SBT

The Rossby wave train that propagated along the subtropical westerly jet showed a barotropic structure from 700 to 100 hPa, with a slight westward tilt in the vertical direction over East Asia (Figure 14). Associated with the Rossby wave train propagating eastward along the subtropical westerly jet, the conversion term of baroclinic energy also showed a positive–negative wave train-like pattern and mainly occurred in the mid-to lower troposphere below 300 hPa. On January 8–9, accompanying the wave packets eastward propagation and convergence of the Rossby wave train over the northern Bay of Bengal and the western side of the Qinghai–Tibetan Plateau (Figure 10), negative geopotential height

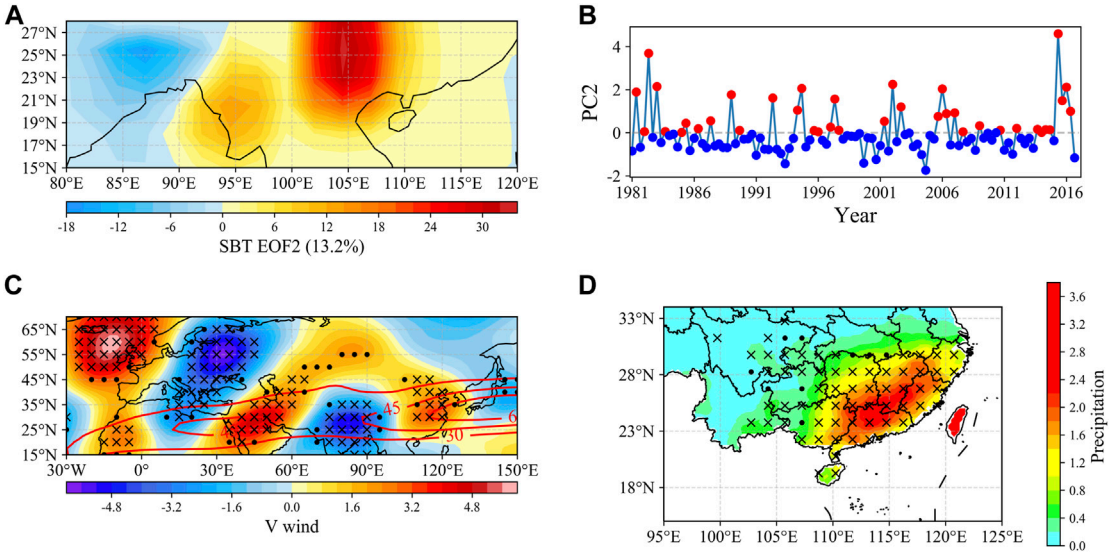

FIGURE 15
EOF2 mode of the SBT appearance frequency during the time period 1981–2016. **(A)** Spatial distribution. **(B)** Time series. **(C)** The 200 hPa meridional wind anomalies (shading; units: m s^{-1}) and zonal winds (red contours; units: m s^{-1}) and **(D)** the precipitation anomalies (shading; units: mm day–1). The values in parts **(C,D)** are both composited using the PC2 time series >1.0 standard deviation. The black cross (solid circle) represents the meridional winds in part **(C)** and the precipitation anomalies in part **(D)** that are significant at the 95% (90%) confidence level.

anomalies appeared in almost the whole troposphere. This was related to the cyclonic curve trough that appeared in the upper level jet and the strong SBT located at mid-to lower levels over the northern Bay of Bengal. A deep trough was present in the whole of the troposphere over the northern Bay of Bengal (Figures 14A, B). Positive conversion of baroclinic energy appeared behind the vertical deep trough line over the northern Bay of Bengal near 90°E. This indicated that the available potential energy was converted from the basic westerly mean flow to the wave disturbance, which favored the maintenance and strengthening of the SBT in the mid-to lower troposphere. The strengthened SBT provided favorable water vapor conditions for the occurrence of heavy rainfall over southwestern China. On January 10–13, accompanying the second time of the advent of the Rossby wave packets that propagated further eastward downstream along the subtropical westerly jet (Figures 10C–F), the deep trough, which included both the cyclonic trough in the upper level jet and the SBT at mid-to lower levels, gradually moved further eastward from the western to the eastern side of the Qinghai–Tibetan Plateau. (Figures 14C–F). Associated with the deep trough moving eastward, positive and negative conversion of baroclinic energy always accompanied behind and in front of the deep trough line, respectively. While, the positive values behind the trough line were greater than the negative values in front of the trough line. Thus, the net positive baroclinic energy conversion over the deep trough region was favorable for strengthening the lower level SBT, thus keeping the deep trough as a whole move to eastward. This indicated that the eastward movement of the mid-to lower level SBT may be closely related to the eastward propagation of the Rossby wave train. The eastward-propagating Rossby wave train can push the mid-to lower level SBT eastward by modifying the associated baroclinic energy conversion process under the background of the subsidence behind the deep vertical trough over the Qinghai–Tibetan Plateau region. Hence the Rossby wave train along the upper level jet may be an important factor pushing the SBT eastward, which favored the transport of plentiful water vapor further east in the downstream region *via* the southerly flow in front of the SBT, causing the occurrence of heavy rainfall over southeastern China.

6 Summary

Under the background of westerly winds in winter, persistent heavy rainfall over southern China often presents an eastward-moving feature. Heavy rainfall may first occur over southwestern China and then move eastward to southeastern China during the next few days. We analyzed a 6-day heavy rainfall process that occurred over southwestern China on January 8–9, 2015 and then gradually spread eastward to southeastern China on January 10–13, from the perspective of the daily variations in the weather.

Our results showed the important role of the Rossby wave train propagating along the subtropical westerly jet in “pushing” the eastward movement of heavy rainfall over southern China. The remote Rossby wave train influenced the variation of heavy rainfall by modifying the local circulation. The Rossby wave train can change the morphology of the East Asian subtropical jet *via* wave–jet interactions and modify the related secondary upward circulation in the entrance area of the jet, providing favorable dynamic conditions for the occurrence of heavy rainfall. The Rossby wave train can also influence the low-level SBT by modifying the associated baroclinic energy conversion process, which favors the transport of plentiful water vapor to the region of heavy rainfall over southern China. The eastward-propagating Rossby wave train pushed the upper level East Asian subtropical jet and the lower level SBT as a whole while simultaneously moving east, which caused the region of heavy rainfall to move from southwestern to southeastern China.

The result indicated that the covariations of the upper level jet and lower level SBT linked with the Rossby wave train were important for the eastward movement of the rainfall event. We also obtained the related co-variation mode from the climatological perspective. Previous studies have shown that the activity of the lower level SBT is closely related to the location of the rainfall over southern China in winter (Duan et al., 2012; Li and Li, 2019). Heavy rainfall often occurs over southwestern China when a stationary SBT was located in the northern Bay of Bengal, whereas the expansion of heavy rainfall to southeastern China was associated with eastward movement of the SBT. By identifying the signal of the moving SBT as introduced in Section 2, we carried out EOF analysis of the SBT appearance frequency during the winter in 1981–2016. The EOF2 mode was shown to be an eastward-moving mode of the SBT, with the SBT frequently appearing in the eastern Bay of Bengal and moving further eastward in the downstream regions (Figure 15A). The composite analysis, obtained by using the months in PC2 that were greater than one standard deviation, indicated that the eastward-moving SBT mode is closely related to the pattern of the Rossby wave train along the subtropical westerly jet, and the related rainfall mode shown as a zonal expansion from southwestern to southeastern China that was located under the equatorial-ward of the entrance of the EASJ (Figures 15C, D). These configurations were very similar to the results for the case study on January 8–13, 2015.

Therefore, the results from our case study might successfully revealed the common features in the eastward-moving heavy rainfall events that occurred over southern China in winter. These results will help to provide a scientific basis for forecasting winter rainfall over southern China. However, further more case studies are needed to confirm these features from the climatological perspective.

In addition, the results also shown that this persistent heavy rainfall event occurred in two different stages. In the first stage—that was, from January 8 to 9, 2015—the related heavy rainfall occurred mainly on the windward slopes of the mountains in southwestern China. In the second stage—that was, from January 10 to 13, 2015—the regions of heavy rainfall moved eastward to southeastern China. The favorable configurations of the large-scale circulation were similar during the two rainfall stages. At the lower to mid-level, strong southerly flows, which appeared in front of the SBT and to the west of the subtropical high, transported abundant water vapor to the regions of rainfall. At the upper level, the EASJ had an important role in the occurrence of heavy rainfall over both southwestern and southeastern China. While, the detailed local physical processes and mechanisms favorable to the occurrence of heavy rainfall in southwestern and southeastern China showed some differences. The heavy rainfall over southwestern China was closely related to orographic forcing and mainly occurred on the windward slopes of mountains. The rainfall over southeastern China was mainly attributed to the baroclinic frontogenesis caused by strong warm, wet advection. Numerous previous studies also revealed that the local conditions favored for heavy rainfall occurrence over southwestern China and southeastern China were different, including the underlying surface conditions, the impact of weather systems and cold air activity (Yuan et al., 2018; Li and Li, 2019; Yuan et al., 2019; Chen and Li, 2022; Li et al., 2022), etc. These findings suggested that the characteristics of rainfall and its mechanisms may have regional differences in southern China. These questions also require further deep discussion in the future.

Data availability statement

The original contributions presented in the study are included in the article/supplementary material, further inquiries can be directed to the corresponding author.

Author contributions

Conceptualization, JYu, JYi; formal analysis, JYi, JYu; methodology, JYi, JYu; resources, JYu, WD; writing—original draft, JYi, JYu; writing—review and editing, JYu, TF, JYi; visualization, JYi, JP, XC, MM; translation, JYu, YN, JYi.

Funding

This work was supported by the National Natural Science Foundation of China (Grant No. 41875109 and Grant No. 41930972) and the Natural Science Foundation of Yunnan Province (Grant No. 2018FB074).

Acknowledgments

The authors thank all the scientists and crew members who were involved in the program.

Conflict of interest

The authors declare that the research was conducted in the absence of any commercial or financial relationships that could be construed as a potential conflict of interest.

Publisher's note

References

Bueh, C., Shi, N., and Xie, Z. (2011). Large-scale circulation anomalies associated with persistent low temperature over southern China in January 2008. *Atmos. Sci. Lett.* 12, 273–280. doi:10.1002/asl.333

Chen, W. L., and Li, X. Z. (2022). Synergistic effects of winter heavy precipitation and high and low latitude wave trains in South China. *J. Atmos. Sci.* 46 (01), 55–69. (In Chinese). doi:10.3878/j.issn.1006-9895.2102.20246

Ding, F., and Li, C. (2017). Subtropical westerly jet waveguide and winter persistent heavy rainfall in south China. *J. Geophys. Res. Atmos.* 122, 7385–7400. doi:10.1002/2017jd026530

Duan, A. M., and Wu, G. X. (2005). Wave-current interaction and atmospheric energy cycling under non-adiabatic conditions. *Sci. China Earth Sci.* 04, 352–360.

Duan, X., Tao, Y., and Xu, M. L. (2012). Influence of the south branch trough of the westerly flow on the weather in Yunnan. *Plateau Meteorol.* 31, 1059–1065. (In Chinese).

Gao, T., Zhang, Q., and Luo, M. (2020). Intensifying effects of El Niño events on winter precipitation extremes in southeastern China. *Clim. Dyn.* 54, 631–648. doi:10.1007/s00382-019-05022-6

García, H. R., Gallego, P. D., Hernández, M. E., Presa, L. G., and Rodriguez, P. R. (2001). Influence of the North Atlantic oscillation on the canary islands precipitation. *J. Clim.* 14 (19), 3889–3903. doi:10.1175/1520-0442(2001)014<3889:iotnao>2.0.co;2

Guo, R. F., Gao, A. S., and Yang, S. Y. (2010). Comparison analysis of two heavy rain processes on the plateau at low latitude caused by the southern branch trough in winter Trans. *J. Atmos. Sci.* 33 (1), 82–88. (In Chinese).

Ha, K. J., Heo, K. Y., Lee, S. S., Yun, K. S., and Jhun, J. G. (2012). Variability in the East asian monsoon: A review. *Meteorol. Appl.* 19, 200–215. doi:10.1002/met.1320

Hu, K. M., Gang, H., Wu, R. G., and Wang, L. (2018). Structure and dynamics of a wave train along the wintertime Asian jet and its impact on East Asian climate. *Clim. Dyn.* 51, 4123–4137. doi:10.1007/s00382-017-3674-1

Huang, D. Q., Zhu, J., Zhang, Y. C., and Huang, A. N. (2014). The different configurations of the East Asian polar front jet and subtropical jet and the associated rainfall anomalies over eastern China in summer. *J. Clim.* 27, 8205–8220. doi:10.1175/jcli-d-14-00067.1

Huang, D., Dai, A., Zhu, J., Zhang, Y., and Kuang, X. (2017). Recent winter precipitation changes over Eastern China in different warming periods and the associated East Asian jets and oceanic conditions. *J. Clim.* 30 (12), 4443–4462. doi:10.1175/jcli-d-16-0517.1

Huang, W. Y., Yang, Z. F., He, X. S., Lin, D. Y., Wang, B., JonathonWrightChen, S. R. Y., et al. (2019). A possible mechanism for the occurrence of wintertime extreme precipitation events over South China. *Clim. Dyn.* 52, 2367–2384. doi:10.1007/s00382-018-4262-8

Kalnay, E., Kanamitsu, M., Kistler, R., Collins, W., Deaven, D., Gandin, L., et al. (1996). The NCEP/NCAR 40-year Reanalysis project. *Am. Meteorological Soc.* 3, 437–471. doi:10.1175/1520-0477(1996)077<0437:tnyrp>2.0.co;2

Knippertz, P. (2004). A simple identification scheme for upper–level troughs and its application to winter precipitation variability in northwest africa. *J. Clim.* 17 (6), 1411–1418. doi:10.1175/1520-0442(2004)017<1411:asisfu>2.0.co;2

Li, Y., and Li, C. (2019). An analysis on a heavy rain weather process during 8-13 January, 2015 in Southern China. *Period. Ocean Univ. China* 49, 11–19. (In Chinese). doi:10.16441/j.cnki.hdxb.20180157

Li, C., and Sun, J. (2015). Role of the subtropical westerly jet waveguide in a southern China heavy rainstorm in December 2013. *Adv. Atmos. Sci.* 32, 601–612. doi:10.1007/s00376-014-4099-y

Li, X. Z., and Zhou, W. (2016). Modulation of the interannual variation of the India–Burma Trough on the winter moisture supply over Southwest China. *Clim. Dyn.* 46, 147–158. doi:10.1007/s00382-015-2575-4

Li, X. Z., Chen, D., and Zhou, W. (2017). Response of winter moisture circulation to the India–Burma trough and its modulation by the South asian waveguide. *J. Clim.* 30 (4), 1197–1210. doi:10.1175/jcli-d-16-0111.1

Li, X. Z., Wen, Z. P., and Huang, W. R. (2020). Modulation of south Asian jet wave train on the extreme winter precipitation over southeast China: Comparison between 2015/16 and 2018/19. *J. Clim.* 33, 4065–4081. doi:10.1175/jcli-d-19-0678.1

Li, C., Li, Y., Fu, S. M., Jiang, X. W., Wang, X. F., Li, S. S., et al. (2022). A new perspective on the orographic effect of the windward slope on the multi-scale eastward-Moving southwest vortex systems. *Atmos. Res.* 279, 106365. doi:10.1016/j.atmosres.2022.106365

Liao, Z., and Zhang, Y. (2013). Concurrent variation between the East Asian subtropical jet and polar front jet during persistent snowstorm period in 2008 winter over southern China. *J. Geophys. Res. Atmos.* 118 (12), 6360–6373. doi:10.1002/jgrd.50558

Lin, Z. Q. (2015). Objective identification method of south branch trough and its climatic characteristics. *Plateau Meteorol.* 34, 684–689. (In Chinese). doi:10.7522/j.issn.100020534.2014.00016

Lin, Z. Q. (2016). Influence of the south trough on the half-year daily precipitation in winter over the southwest plateau region. *Plateau Meteorol.* 35, 1456–1463. (In Chinese).

Liu, K., Zha, J. L., Yang, R. W., and Chen, J. L. (2018). A new dynamical index for India-Burma trough. *Adv. Meteorol.* 2018, 1–10. doi:10.1155/2018/5215093

Liu, A., Huang, Y., and Huang, D. (2022). Inter-model spread of the simulated winter surface air temperature over the Eurasian continent and the physical linkage to the jet streams from the CMIP6 models. *J. Geophys. Res. Atmos.* 127, e2022JD037172. doi:10.1029/2022JD037172

Luo, X., and Zhang, Y. (2015). The linkage between upper-level jet streams over East Asia and East Asian winter monsoon variability. *J. Clim.* 28 (22), 9013–9028. doi:10.1175/jcli-d-15-0160.1

Ninomiya, K. (1984). Characteristics of Baiu front as a predominant subtropical front in the summer Northern Hemisphere. *J. Meteorol. Soc. Jpn.* 62, 880–894. doi:10.2151/jmsj1965.62.6_880

Qin, J., Pan, L. N., and Shi, L. (1991). Influences of the southern trough and strong cold air on the winter weather over Yunnan province. *Meteorological* 17, 39–43. (In Chinese). doi:10.7519/j.issn.1000-0526.1991.3.009

Suo, M. Q., Ding, Y. H., and Wang, J. Y. (2008). Relationship between Rossby wave propagation in southern branch of westerlies and the formation of the southern branch trough in wintertime. *J. Appl. Meteorol.* 19 (6), 731–740. (In Chinese). doi:10.11898/1001-7313.20080613

Takaya, K., and Nakamura, H. (2001). A formulation of a phase-independent wave-activity flux for stationary and migratory quasi-geostrophic eddies on a zonally varying basic flow. *J. Atmos. Sci.* 58, 608–627. doi:10.1175/1520-0469(2001)058<0608:afoapi>2.0.co;2

Tan, G. R., Wang, X. Z., Wang, Y. G., and Yu, M. (2022). Possible causes of the excessive precipitation over South China in 2021/22 winter. *Atmos. Res.* 280, 106432. doi:10.1016/j.atmosres.2022.106432

Wang, T. M., Yang, S., Wen, Z. P., Wu, R. G., and Zhao, P. (2011). Variations of the winter India–Burma Trough and their links to climate anomalies over southern and eastern Asia. *J. Geophys. Res. Atmos.* 116 (D23). doi:10.1029/2011jd016373

Watanabe, M. (2004). Asian jet waveguide and a downstream extension of the North Atlantic oscillation. *J. Clim.* 17, 4674–4691. doi:10.1175/JCLI-3228.1

Wen, M., Song, Y., Kumar, A., and Zhang, P. (2009). An analysis of the large-scale climate anomalies associated with the snowstorms affecting China in january 2008. *Mon. Weather Rev.* 137 (3), 1111–1131. doi:10.1175/2008mwr2638.1

Yang, S., Lau, K. M., and Kim, K. M. (2002). Variations of the East Asian jet stream and Asian—Pacific—American winter climate anomalies. *J. Clim.* 15 (3), 306–325. doi:10.1175/1520-0442(2002)015<0306:VOTEAJ>2.0.CO;2

Yeh, T. C. (1950). The circulation of the high troposphere over China in the winter of 1945-46. *Tellus* 2, 173–183. doi:10.1111/j.2153-3490.1950.tb00329.x

Yuan, J. P., Zhao, D., Yang, R. W., and Yang, H. F. (2018). Predecessor rain events over China's low-latitude highlands associated with Bay of Bengal tropical cyclones. *Clim. Dyn.* 50, 825–843. doi:10.1007/s00382-017-3643-8

Yuan, J. P., Lü, J., Feng, D., Mao, M. N., Feng, T., Yin, J. Y., et al. (2019). Heavy rainfall events in southern China associated with tropical cyclones in the Bay of bengal: A case study. *Atmosphere* 10, 574. doi:10.3390/atmos10100574

Zhang, D., and Chen, L. (2021). Possible mechanisms for persistent anomalous rainfall over the middle and lower reaches of Yangtze River in winter 2018/2019. *Int. J. Climatol.* 41, 6324–6335. doi:10.1002/joc.7197

Zhang, Y., Yan, P., Liao, Z., Huang, D., and Zhang, Y. (2019). The winter concurrent meridional shift of the East Asian jet streams and the associated thermal conditions. *J. Clim.* 32 (7), 2075–2088. doi:10.1175/JCLI-D-18-0085.1

Zong, H. F., Bueh, C., Wei, J., and Chen, L. T. (2012). Intensity of the trough over the Bay of bengal and its impact on the southern China precipitation in winter. *Atmos. Ocean. Sci. Lett.* 5, 246–251. doi:10.1080/16742834.2012.11446998

Zong, H. F., Bueh, C., and Ji, L. (2014). Wintertime extreme precipitation event over southern China and its typical circulation features. *Chin. Sci. Bull.* 59 (10), 1036–1044. doi:10.1007/s11434-014-0124-x

frontiers | Frontiers in Earth Science

TYPE Original Research
PUBLISHED 15 February 2023
DOI 10.3389/feart.2023.1127299

OPEN ACCESS

EDITED BY
Chenghai Wang,
Lanzhou University, China

REVIEWED BY
Anning Huang,
Nanjing University, China
Ziqian Wang,
Sun Yat-Sen University, China

*CORRESPONDENCE
Lun Li,
lilun@cma.gov.cn

SPECIALTY SECTION
This article was submitted to Atmospheric Science, a section of the journal Frontiers in Earth Science

RECEIVED 19 December 2022
ACCEPTED 26 January 2023
PUBLISHED 15 February 2023

CITATION
Li L, Huang H and Zhu C (2023), Causation of the heavy rainfall in Kyushu in early July 2020: A perspective of the depression that originated over the Tibetan Plateau. *Front. Earth Sci.* 11:1127299. doi: 10.3389/feart.2023.1127299

Causation of the heavy rainfall in Kyushu in early July 2020: A perspective of the depression that originated over the Tibetan Plateau

Lun Li[1,2]*, Honghui Huang[1] and Congwen Zhu[1]

[1]State Key Laboratory of Severe Weather, Chinese Academy of Meteorological Sciences, Beijing, China, [2]Collaborative Innovation Center on Forecast and Evaluation of Meteorological Disasters (CIC-FEMD), Nanjing University of Information Science and Technology, Nanjing, China

Heavy rain fell in Kyushu, Japan, in early July 2020, which caused huge life and economic losses. The present work reports that a Tibetan Plateau vortex (TPV) generated over the Tibetan Plateau transformed into a trough at the eastern edge of the Tibetan Plateau, and the trough continued to move eastward and was responsible for the heavy rainfall in Kyushu. Accordingly, the maintenance and eastward movement of the trough and the influencing mechanism of the trough on the rainfall in Kyushu are explored based on the final analysis data (FNL) from NCEP and the JRA-55 reanalysis from JMA. Diagnoses of the potential vorticity (PV) tendency equation indicate that the horizontal PV flux convergence east of the trough is the primary contributor to the eastward movement and maintenance of the trough. Furthermore, the trough is proved to have important effects on the moisture condition and the ascending motion around Kyushu. That is, the trough increases the moisture in Kyushu by intensifying the eastward moisture transportation to Kyushu; the positive vorticity and warm center, as well as the wind perturbation related to the trough, are in favor of stronger ascending motion in Kyushu. The findings in this work provide extended knowledge on the causation of rainfall in Japan, which is beneficial for further precipitation prediction.

KEYWORDS

Tibetan Plateau vortex, trough, eastward movement, moisture, ascending motion

1 Introduction

Heavy rainfall hit south Japan in early July 2020, with the precipitation in Kyushu breaking the historic record. The heavy rainfall caused severe floods and resulted in huge life and economic losses. Previous studies have revealed some crucial factors contributing to the heavy rainfall in Japan (shown as follows). Baiu fronts always appear in the Baiu season, and the mesoscale disturbances are frequently observed on Baiu fronts, which are responsible for the heavy rainfall in Japan (Mohri, 1956; Matsumoto et al., 1971; Nguyen-Le et al., 2017). The moisture transported by southerlies is important in triggering rainfall in Japan (Ogura et al., 1985; Kato, 2005; Sekizawa et al., 2019; Shimpo et al., 2019), which can be enhanced by the warm sea surface (Tsuguti and Kato, 2014; Sekizawa et al., 2019). Some rainfall events are related to depressions/tropical cyclone/extratropical cyclone activities (Krishnan and Sugi, 2001; Nguyen-Le et al., 2017), and typhoons in West Pacific always cause heavy rainfall in Japan (Misumi, 1996; Wang et al., 2009; Yoshida and Itoh, 2012; Kanada et al., 2017). In addition, upper-tropospheric troughs and jets are also important rainfall contributors (Shimpo et al., 2019; Tsuji et al., 2020; Yokoyama et al., 2020). In this work, a trough that transformed from a Tibetan Plateau vortex (TPV) at 500 hPa was found to be responsible for the heavy rainfall in

Kyushu on 3–4 July 2020. Because both the TPV and trough are low-pressure systems, they are collectively called depression here.

TPVs are generated over the Tibetan Plateau at 500 hPa mainly during May to August, which are local major rainfall producers. Most of them die out *in situ*, but some can emigrate from the Tibetan Plateau under certain conditions and impose significant effects on the rainfall in east China. Formally, a TPV is defined as a low-pressure system which forms over the Tibetan Plateau with closed contour lines or cyclonic winds at three observation stations at 500 hPa (Lhasa Workgroup for Tibetan Plateau Meteorology Research, 1981). TPVs are shallow when located on the Tibetan Plateau, with the horizontal and vertical scales being 400–800 km and 2–3 km, respectively (Ye and Gao, 1979; Lhasa Workgroup for Tibetan Plateau Meteorology Research, 1981; Luo, 1992; Luo et al., 1994; Feng et al., 2014). After the TPVs emigrate from the Tibetan Plateau, the structures become deeper than those before moving off (Li et al., 2020a). Lots of heavy rainfalls in Southwest and East China are linked to the TPVs emigrating from the Tibetan Plateau (Yang et al., 2001; Zhang et al., 2001; Yu, 2008). Particularly, some eastward-moving TPVs can persist for several days and reach the West Pacific, which affects the rainfall in Japan (Yu and Gao, 2006).

Although our previous work revealed that the mid-upper level trough near Japan is responsible for the heavy rainfall there, the origination and evolution of the trough are not clear yet. In addition, previous studies pointed out that the TPVs emigrating from the Tibetan Plateau can affect the rainfall in Japan, but the ones not emigrating from the Tibetan Plateau are always not concerned. In the present work, a trough at the eastern edge of the Tibetan Plateau was found to be transformed from a TPV, which greatly affected the rainfall in Kyushu on 3–4 July 2020. Accordingly, the maintenance and eastward movement of the trough and its influencing mechanism on the rainfall are investigated. This work attempts to provide extended information about the causation of heavy rainfall in Kyushu, which is helpful for future precipitation prediction.

Data and methods utilized in this work are provided in Section 2. In Section 3, the rainfall which occurred in early July 2020 in Kyushu is introduced, and the maintenance and eastward movement mechanism of the trough transformed from the TPV are explored. In Section 4, the effects of the trough on the rainfall in Kyushu are investigated. Conclusions and discussions are given in Section 5.

2 Data and methods

2.1 Data

The final operational global analysis (FNL) data are used to investigate the large-scale circulations and the evolution of depression originating over the Tibetan Plateau, which is derived from the Global Forecasting System of the National Centers for Environment Prediction (NCEP) (http://rda.ucar.edu/datasets/ds083.2, ds083.2|DOI: 10.5065/D6M043C6). The FNL data are at a 6 h interval and cover globally with a 1°×1° horizontal resolution. The reliability of the FNL data in researching the circulations related to the depressions over the Tibetan Plateau has been verified in our previous work (Li et al., 2014a; Li et al., 2020b). Because the FNL data start from July 1999, the climatic means are taken as the averages between 2000 and 2019. Accordingly, anomalies of the variables (e.g., geopotential height, zonal and meridional winds, moisture flux, etc.) are calculated as differences between the original data and the climatic means. The 6-hourly JRA-55 precipitation data provided by Japan Meteorological Agency (https://jra.kishou.go.jp/JRA-55/) are used in this work, which performs well in displaying extreme rainfall events in East Asia (Kim et al., 2019).

2.2 Trough-centered composites

Because the trough transformed from the TPV is a moving system, composites of the variables at different times in geographic coordinates will be greatly smoothed. To exhibit the features of the trough, the trough-centered composites are conducted. That is, at a specific time, the center of the trough (maximum of the positive vertical vorticity at 500 hPa in the trough area) is taken as the origin of the coordinates, and then, the variables at different times are composed. Thus, the composed center of the trough is the origin of the coordinates, and the coordinates on the x-axis (y-axis) are the relative coordinates from the composed center of the trough in the zonal (meridional) direction.

2.3 Potential vorticity (PV) tendency equation and quasi-geostrophic ω equation

PV budgets analyses can well-interpret the evolution of TPVs (Li et al., 2011; Zheng et al., 2013; Li et al., 2014b), which is conducted in this work to investigate the maintenance and eastward movement mechanism of the trough influencing the rainfall in Kyushu. PV tendency equation without frictional effects is shown in Eq. 1 (Li et al., 2017). Because the trough is accompanied by rainfall during its eastward movement, Q in Eq. 1 is calculated as the condensational latent heating. The formula of the condensational latent heating rate and the meanings of variables and each term can be found in the study by Li et al. (2017).

$$\frac{\partial P_E}{\partial t} = -\frac{\partial u P_E}{\partial x} - \frac{\partial v P_E}{\partial y} - \frac{\partial \omega P_E}{\partial p} + g\frac{\partial v}{\partial p}\frac{\partial Q}{\partial x} - g\frac{\partial u}{\partial p}\frac{\partial Q}{\partial y} - g(f+\zeta p)\frac{\partial Q}{\partial p}. \tag{1}$$

Additionally, given that the ascending motion is a key factor in triggering the rainfall, the adiabatic quasi-geostrophic ω equation (Tam and Li, 2006; Kosaka et al., 2011) is calculated to explore the effect of the trough that originated from the Tibetan Plateau on the vertical motion around Kyushu. Variables in the adiabatic quasi-geostrophic ω equation are decomposed into zonal means (denoted by over bars) and their perturbations (denoted by primes), and the processed equation is shown in Equation 2. All operators and variables are of conventional usage in meteorology. In general on the right hand side of Eq. 2, terms 1–6 represent the vertical differentials of vorticity advection, and terms 7–11 denote temperature advection. The specific meanings of the crucial terms in this rainfall event are introduced in detail in Section 4.

$$\left(\sigma\nabla^2 + f_0{}^2\frac{\partial^2}{\partial p}\right)\omega' = f_0\frac{\partial}{\partial p}\left(\overline{u_g}\frac{\partial \zeta_g{}'}{\partial x} + u_g{}'\frac{\partial \zeta_g{}'}{\partial x} + \overline{v_g}\frac{\partial \zeta_g{}'}{\partial y} + v_g{}'\frac{\partial \zeta_g{}'}{\partial y} + v_g{}'\frac{\partial \overline{\zeta_g}}{\partial y} + v_g{}'\frac{\partial f}{\partial y}\right)$$
$$\nabla^2\left[\frac{R}{P}\left(\overline{u_g}\frac{\partial T'}{\partial x} + u_g{}'\frac{\partial T'}{\partial x} + \overline{v_g}\frac{\partial T'}{\partial y} + v_g{}'\frac{\partial \overline{T}}{\partial y} + v_g{}'\frac{\partial T'}{\partial y}\right)\right]. \tag{2}$$

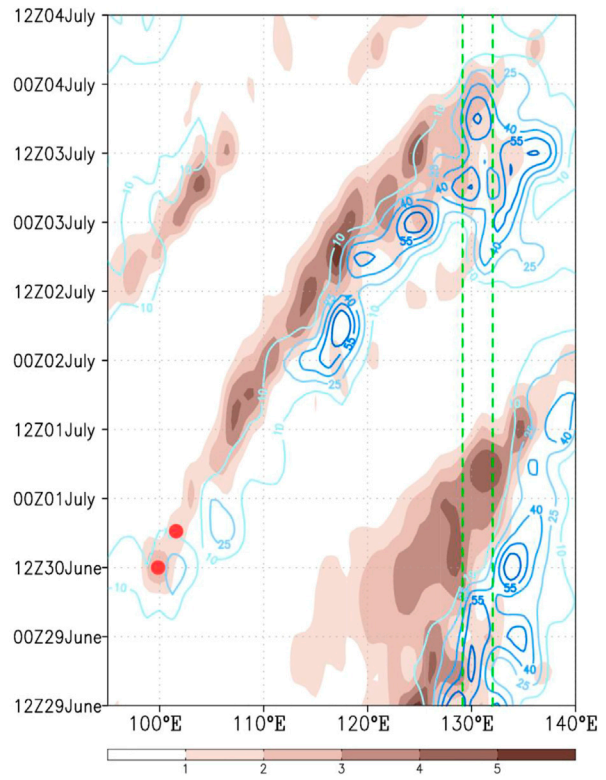

FIGURE 1
Time-longitude sections of 6-hourly precipitation averaged between 31°N and 34°N (contours; unit: mm day^{-1}) and 500 hPa vertical vorticity averaged between 28°N and 38°N (shadings; unit: 10^{-5} s^{-1}). The green dotted lines indicate the zonal range of Kyushu, and the red dots represent the zonal positions of the TPV.

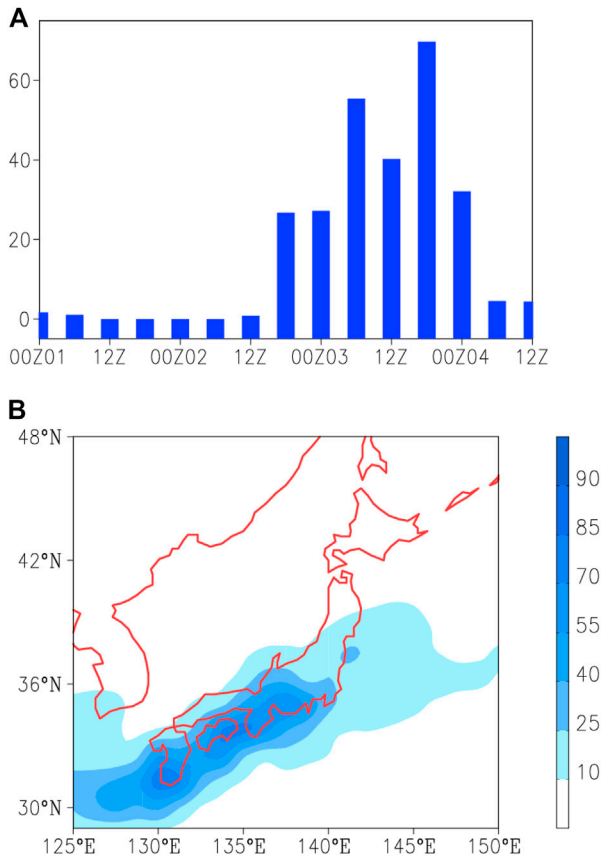

FIGURE 2
(A) Temporal variation of the 6-hourly precipitation averaged in Kyushu (129–132°E, 31–34°N) (unit: mm day^{-1}), and **(B)** spatial distribution of the average 6-hourly precipitation from 00 UTC 03 July to 00 UTC 04 July (unit: mm day^{-1}).

3 Introduction of the rainfall event in Kyushu in early July 2020

3.1 Rainfall

The 6-hourly precipitation averaged between 31°N and 34°N, covering the meridional range of Kyushu, is displayed by the contours in Figure 1. The rainfall centers are observed to propagate eastward between late June and early July, from 100°E to 135°E. The precipitation was weak when falling on and near the Tibetan Plateau and became stronger in central and east China. The rainfall in Kyushu persisted from 12 UTC 02 July to 00 UTC 04 July; however, only the rainfall episode between 00 UTC 03 July and 00 UTC 04 July is related to the rainband stretching from the Tibetan Plateau. Because this work aims to reveal the effect of the eastward-moving depression that originated over the Tibetan Plateau, the rainfall episode from 00 UTC 03 July to 00 UTC 04 July is of primary concern. To further demonstrate the relationship between the rainfall in Kyushu and the depression originating over the Tibetan Plateau, the vertical vorticity at 500 hPa averaged between 28°N and 38°N, which covers the meridional range of the Tibetan Plateau, is represented by shadings in Figure 1. A TPV was generated at 12 UTC 30 June at around 100°E over the Tibetan Plateau, which moved eastward and arrived at 102°E at 18 UTC 30 June. The TPV weakened when reaching the eastern edge of the Tibetan Plateau and then transformed into a trough. The trough emigrated from the Tibetan Plateau and continued to move eastward. The eastward movement of TPV and the related trough corresponds to the eastward extension of the positive vorticity and the eastward-propagating rainfall centers shown in Figure 1, indicating that the depression emigrating from the Tibetan Plateau has a close relationship with the rainfall in Kyushu. Additionally, the rainfall at each time is generally located east of the positive vorticity, which implies that the rainfall usually happens east of the depression.

Temporal variation and spatial distribution of the precipitation in Kyushu are shown in Figure 2. Figure 1 reveals that the rainfall episode related to the depression over the Tibetan Plateau was from 00 UTC 03 July to 00 UTC 04 July. As shown in Figure 2A, the precipitation became stronger after 00 UTC 03 July, with the peaks appearing at 06 UTC 03 July and 18 UTC 03 July; after 00 UTC 04 July, the precipitation weakened sharply. The average 6-hourly precipitation from 00 UTC 03 July to 00 UTC 04 July was distributed from southwest to northeast and covered wide areas of Japan, with the maximum being in south Kyushu.

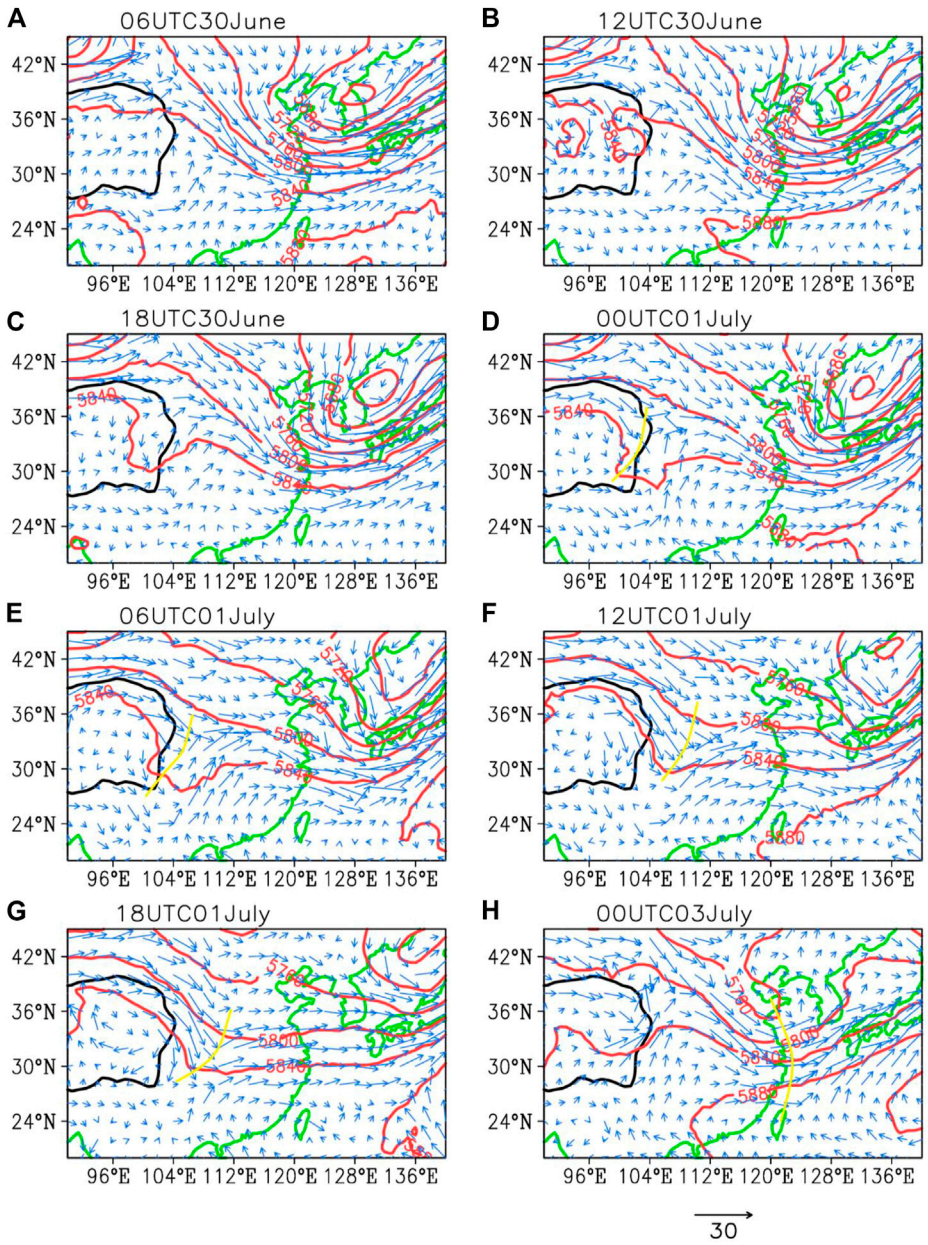

FIGURE 3
Geopotential height (red contours; unit: gpm) and wind (vectors; unit: m s^{-1}) at 500 hPa. **(A)** 06UTC30June, **(B)** 12UTC30June, **(C)** 18UTC30June, **(D)** 00UTC01July, **(E)** 06UTC01July, **(F)** 12UTC01July, **(G)** 18UTC01July, and **(H)** 00UTC03July. The yellow curves in **(D–G)** represent the trough. The thick black lines are the topographic contours of 3,000 m, indicating the border of the Tibetan Plateau.

3.2 Evolution of the depression that originated over the Tibetan Plateau

Geopotential height and wind at 500 hPa are shown in Figure 3. At 06 UTC on 30 June, there were strong westerlies north of the Tibetan Plateau, and no obvious depression was observed at this time. At 12 UTC on 30 June, the westerlies north of the plateau branched into two flows, with one turning into northerlies and the other remaining westerlies. Cyclonic shear is formed by the northerlies and southerlies over the eastern Tibetan Plateau, and accordingly, a TPV was generated at 100°E, 33°N. Similar to the previously revealed genesis mechanism of TPVs (Li et al., 2011, 2014a; Ma et al., 2022; Wu et al., 2022), both the cyclonic wind convergence and the condensational latent heating favor the genesis of the TPV, and the vertically uneven heating plays as a dominant role in the genesis process of this TPV, based on the calculations on PV tendency equation (figure not shown). The surface sensible heating can produce favorable early conditions for the later condensational latent heat release, which also has an important but indirect effect on the genesis of TPVs (Dell'Osso and Chen,

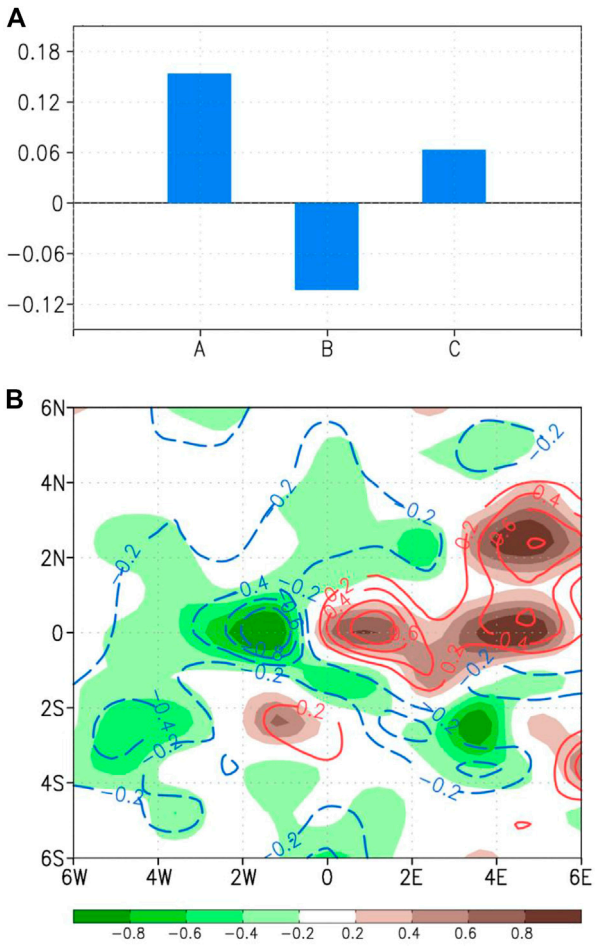

FIGURE 4
(A) PV tendencies (bars; unit: PVU (6 h)$^{-1}$, 1PVU=10^{-6} m^2 s^{-1} K kg^{-1}) induced by horizontal PV flux divergence (A), vertical PV flux divergence (B) and condensational latent heat (C), averaged in the region east of the trough (0°–4° in zonal direction, −2°–2° in meridional direction) after the trough emigrates from the Tibetan Plateau (00 UTC 01 July–00 UTC 04 July). **(B)** Net PV tendency induced by the three terms (shadings; unit: PVU (6 h)$^{-1}$) and the PV tendency induced by horizontal PV flux divergence (contours; unit: PVU (6 h)$^{-1}$). Coordinates on the *x*-axis (*y*-axis) in **(B)** are the relative coordinates from the composed center of the trough in the zonal (meridional) direction.

1986; Wang, 1987; Li et al., 2014a; Zhang et al., 2019). At the following time (18 UTC 30 June), the TPV moved eastward and was located at 102°E, 33°N. At 00 UTC 01 July, the westerlies north of the TPV strengthened, which was unfavorable for the maintenance of the TPV's close cyclonic circulation. Thus, the TPV transformed into a trough at 00 UTC on 01 July, which continues to move eastward. The trough transformed from the TPV was relatively weak when it was near the eastern edge of the Tibetan Plateau (at 00 UTC 01 July and 06 UTC 01 July) and became stronger after 12 UTC 01 July (Figure 1), which is similar to the evolution of a TPV emigrating from the Tibetan Plateau (Li et al., 2014b). At 00 UTC 03 July (Figure 3G), the trough was located at the eastern boundary of China, which started affecting the rainfall in Japan. It is of note that the activities of the trough and the related circulations are not provided here, but are introduced in detail in Section 4.

Although the evolution mechanisms of the TPVs are analyzed in our previous work, and the convergence east of the TPVs is considered the primary factor dominating the evolution of TPVs after they emigrate from the Tibetan Plateau (Li et al., 2019), the maintenance and eastward movement mechanism of the trough originated over the Tibetan Plateau is not clear yet. Therefore, the evolution mechanism of the trough is investigated by diagnosing the PV tendency equation. The 500 hPa PV tendencies east of the trough induced by the horizontal PV flux divergence, the vertical PV flux divergence, and the condensational latent heat, after the trough emigrates from the Tibetan Plateau, are presented in Figure 4A. The horizontal PV convergence and condensational latent heat have positive effects on the increase in PV east of the trough, and the former is obviously larger than the latter. Meanwhile, because of the strong ascending motion around the trough, negative PV tendency induced by the vertical PV divergence is found east of the trough, which is unfavorable for the maintenance and eastward movement of the trough. Thus, the horizontal PV flux convergence contributes the most to the positive PV tendency among these three terms, indicating that the maintenance and eastward movement of the trough is mainly supported by the horizontal PV flux convergence to its east. Actually, the horizontal PV flux convergence contributes to the enhancement of the trough at 12 UTC on 01 July. To further confirm the role of the horizontal PV flux divergence, its spatial distribution and that of the net PV tendency induced by the three terms are shown in Figure 4B. Positive net PV tendency is observed east and northeast of the trough, which corresponds to the general eastward moving direction with a slight northeastward shift. Moreover, the distribution of the horizontal PV flux divergence coincides well with that of the net PV tendency, implying the dominant role of the former. Therefore, horizontal PV flux convergence east of the trough, which is induced by both the PV advection and the wind convergence there, plays a very important role in the maintenance and eastward movement of the trough.

4 Effects of the trough on the rainfall in Kyushu

To highlight the activities of the trough that originated over the Tibetan Plateau when it approached Japan, the anomalies of geopotential height and wind at 500 hPa from 06 UTC 03 July to 00 UTC 04 July are shown in Figure 5. We found that the high north of the trough was stronger than the climatic mean state, whose anomaly easterlies were beneficial for the maintenance of the cyclonic system in the south from 06 UTC 03 July to 00 UTC 04 July. Kyushu was located southeast of the trough before 18 UTC 03 July and south of the trough at 00 UTC 04 July. Accordingly, Kyushu was affected by the southwesterlies associated with the trough in the former period and by the northwesterlies in the latter. Locations of the trough from 06 UTC 03 July to 00 UTC 04 July are 122°E, 35°N, 125°E, 36°N, 128°E, 36°N, and 130°E, 37°N, respectively.

Given that the moisture condition and vertical motion are crucial to trigger rainfall, the effects of the trough on these two factors are investigated in the following text. The moisture condition is analyzed first.

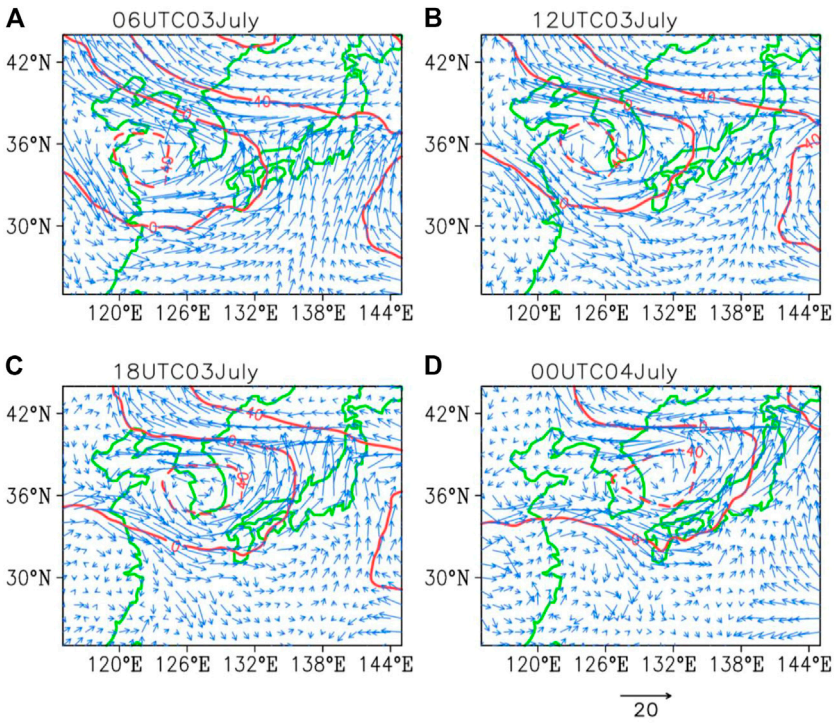

FIGURE 5
Same as Figure 3, but for anomaly geopotential height (red contours; unit: gpm) and wind (vectors; unit: m s^{-1}) at 500 hPa from 06 UTC 03 July to 00 UTC 04 July. **(A)** 06UTC03July, **(B)** 12UTC03July, **(C)** 18UTC03July, and **(D)** 00UTC04July.

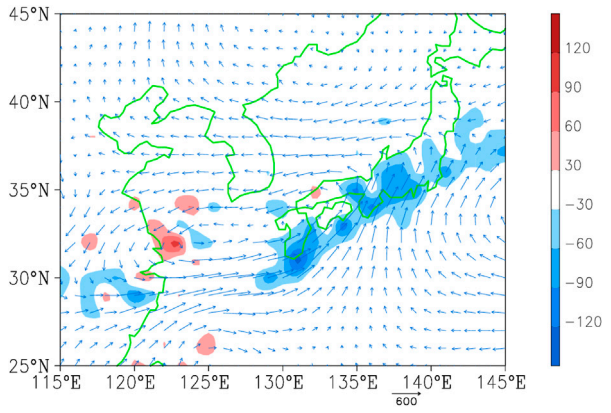

FIGURE 6
Vertical integrated anomaly moisture flux (vectors; unit: kg m^{-1} s^{-1}) and moisture flux divergence (shadings; unit: 10^{-5} kg m^{-2} s^{-1}), averaged between 00 UTC 03 July and 00 UTC 04 July.

The anomalies of vertically integrated (from surface to 100 hPa) moisture flux and its divergence in the rainfall episode from 00 UTC 03 July to 00 UTC 04 July are presented in Figure 6. The moisture converged in Kyushu, which is greatly attributed to the moisture transported by the westerlies west of Kyushu. According to the circulations at 500 hPa shown in Figure 5, strong westerly anomalies were observed south of the trough, which greatly contributed to the eastward transportation of the moisture. To further confirm the role of anomaly westerlies associated with the trough in transporting the moisture, time series of the anomaly vertically integrated zonal moisture flux and speed of westerlies at the western boundary of Kyushu (approximately 129°E) averaged between 30°N and 35°N are shown in Figure 7. It is found that the moisture transported through the western boundary of Kyushu increased sharply at 06 UTC 03 July, corresponding to the robust increase in westerly speed at this time. Actually, the westerlies associated with the trough in Kyushu were apparently stronger at 06 UTC 03 July than those at 00 UTC 03 July because the trough was located farther from Kyushu at the latter time. The eastward transported moisture increased during the following times, reached the peak at 18 UTC 03 July, and then decreased at 00 UTC 04 July. Variation of the moisture transported by the westerlies generally coincides with that of the westerly speed and the precipitation in Kyushu, indicating that the trough that originated over the Tibetan Plateau contributed to the favorable moisture condition for the rainfall in Kyushu.

Second, the effect of the trough on the vertical motion in the region around Kyushu is explored. The anomaly vertical velocity at 500 hPa averaged in 127°E–135°E, 30°N–35°N, which includes Kyushu, is shown in Figure 8A to demonstrate the variation of the vertical motion there under the influence of the eastward-moving trough. The ascending motion strengthened during the eastward movement of the trough, was the strongest at 18 UTC 03 July, and

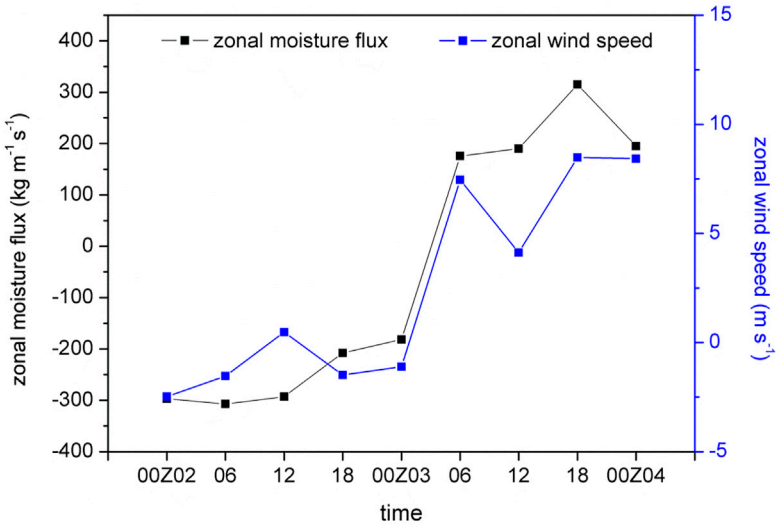

FIGURE 7
Average vertically integrated zonal moisture flux (black line; unit: kg m^{-1} s^{-1}) and 500-hPa zonal wind speed (blue line; unit: m s^{-1}) anomalies at 129°E (approximately the most west longitude of Kyushu) between 30°N and 35°N.

then weakened sharply at 00 UTC 04 July. Actually, the ascending motion associated with the trough appeared on its east and southeast sides, and the descending motion on its west side (Figure 8B). Because Kyushu was located south of the trough at 00 UTC 04 July and southeast at the previous times, the ascending motion in Kyushu at 00 UTC 04 July was much weaker than that at the previous times. According to the aforementioned analyses, the ascending motion in the region around Kyushu is closely related to the eastward movement of the trough. Furthermore, the variation of the vertical motion coincides well with the precipitation variation from 00 UTC 03 July to 00 UTC 04 July, which further verifies the significant impact of the trough on the rainfall in Kyushu by changing the vertical motion there.

The quasi-geostrophic ω equation is calculated to diagnose the vertical motion at 500 hPa in Kyushu, and the results are shown in Figure 9. In Figure 9, terms 1, 7, 8, and 10 are the four primary contributors to the ascending motion in the region around Kyushu, among which term 1 is the leading factor. To help understand the meanings of these four primary terms, the horizontal structure of the trough at 500 hPa is provided in Figure 10. Term 1 represents the vertical differential of vorticity perturbation advection by the mean zonal flow. The trough is a cyclonic circulation with positive vorticity (Figure 10), and accordingly, there is positive zonal gradient of vorticity perturbation in the region east of the trough. Meanwhile, mean westerlies control East Asia, which transports the positive vorticity perturbation associated with the trough eastward. Thus, positive advection of vorticity perturbation by mean westerlies is produced in the region around Kyushu. Additionally, the maximum vorticity perturbation advection by mean zonal flow appears at approximately 400 hPa (figure not shown), which is in favor of the ascending motion at 500 hPa in Kyushu ($\omega' \propto -\frac{\partial}{\partial p}\overline{u}_g\frac{\partial \zeta_g'}{\partial x} < 0$). Term 7 indicates temperature perturbation advection by mean zonal flow, which is the secondary contributor to the ascending motion in Kyushu. The horizontal thermodynamic structure of the trough shows that the warm center is located on its southwest side (Figure 10). Because Kyushu was located southeast and south of the trough from 00 UTC 03 July to 00 UTC 04 July (Figure 5), warm advection by mean westerlies was produced in Kyushu, which favored the ascending motion there ($\omega' \propto \bar{u}_g\frac{\partial T'}{\partial x} < 0$). Term 8 represents the temperature perturbation advection by zonal wind perturbation. As mentioned above, a warm center is located on the southwest side of the trough, and simultaneously, the westerlies prevail there (Figure 10). Thus, the warm advection by westerly perturbation ($\omega' \propto u_g'\frac{\partial T'}{\partial x} < 0$) is also an important contributor to the ascending motion. Term 10 means the mean temperature advection by meridional wind perturbation. The trough is a cyclonic system with southerly perturbation on its east side (Figure 10), and zonal mean temperature decreases from south to north. Thus, southerly perturbation induces warm advection in Kyushu, contributing to the ascending motion there ($\omega' \propto v_g'\frac{\partial \overline{T}}{\partial y} < 0$). Horizontal gradients of vorticity and temperature perturbations, as well as the wind perturbation discussed earlier, are all linked to the circulation of the trough that originated over the Tibetan Plateau, implying the important effect of the trough on the vertical motion in Kyushu, and thereby, the rainfall there.

In a word, the trough that originated over the Tibetan Plateau enhanced the rainfall in Kyushu on 3–4 July 2020 by intensifying the moisture transportation to Kyushu and the ascending motion there.

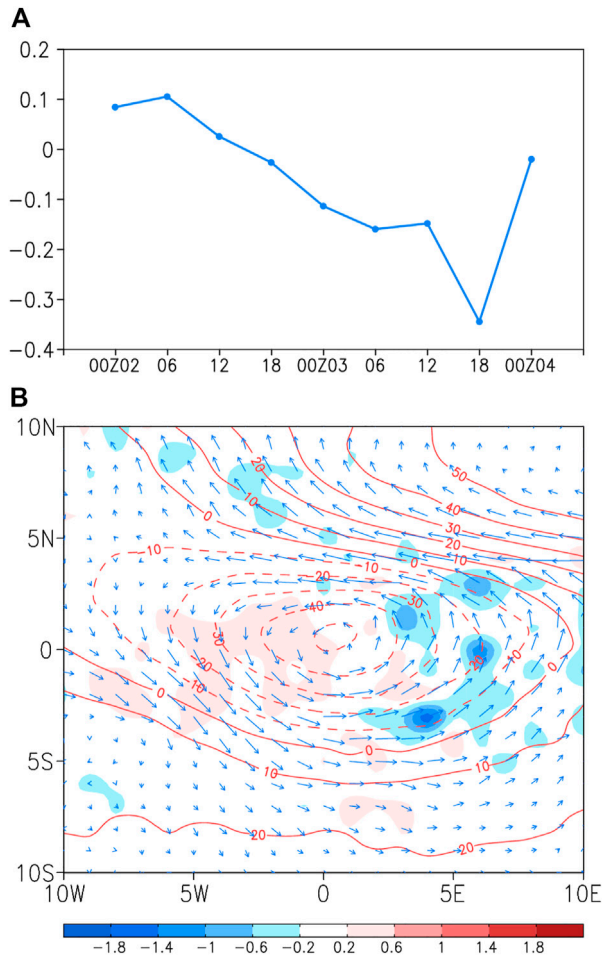

FIGURE 8
(A) Time series of anomaly vertical velocity at 500 hPa averaged in 127–132°E, 30–35°N (unit: Pa s^{-1}). **(B)** Trough-centered composites of anomaly geopotential height (contours; unit: gpm), vertical velocity (shadings; unit: s^{-1}), and wind (vectors; unit: m s^{-1}) at 500 hPa from 00 UTC 03 July to 00 UTC 04 July. Coordinates on the x-axis (y-axis) in **(B)** are the relative coordinates from the composed center of the trough in the zonal (meridional) direction.

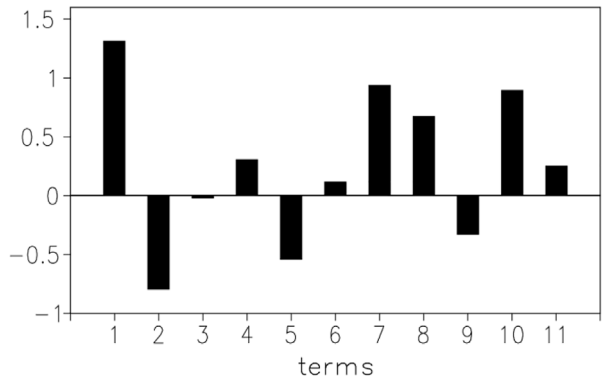

FIGURE 9
Terms 1–11 in Eq. 2 averaged in 127–132°E, 30–35°N from 00 UTC 03 July to 00 UTC 04 July (unit: 10^{-18} m s^{-1} kg^{-1}).

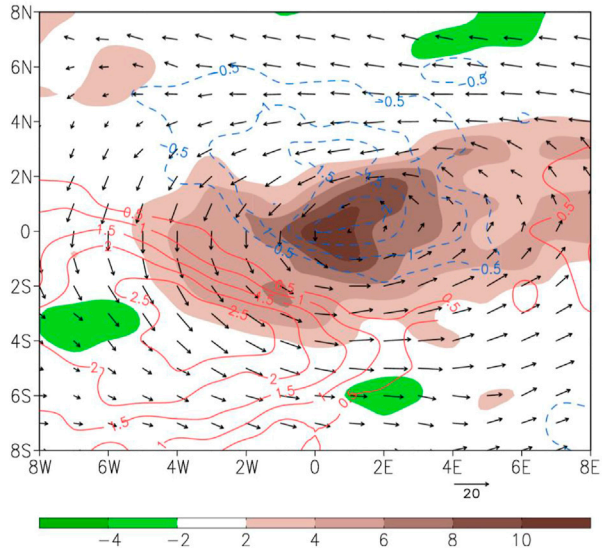

FIGURE 10
Trough-centered composites of vorticity perturbation (shadings; unit: 10^{-5} s^{-1}), temperature perturbation (contours; unit: K), and wind perturbation (vectors; unit: m s^{-1}) at 500 hPa. Coordinates on the x-axis (y-axis) are the relative coordinates from the composed center of the trough in the zonal (meridional) direction.

5 Conclusion

Heavy rainfall affected Kyushu in early July 2020, causing huge damage and life and economic losses. The rainfall episode on 3–4 July 2020 is found to be greatly related to the Tibetan Plateau vortex (TPV) over the Tibetan Plateau, which transformed into a trough near the eastern edge of the Tibetan Plateau. This work analyzes the maintenance and eastward movement mechanism of the trough transformed from the TPV and further investigates the effects of the trough on the rainfall in Kyushu. The results are beneficial for understanding the causation of the rainfall in Kyushu and helpful for future precipitation prediction in this region. The results are summarized as follows:

A TPV is generated over the eastern Tibetan Plateau and transformed into a trough at the eastern edge of the Tibetan Plateau. The trough transformed from the TPV continues to move eastward and affects the rainfall in Kyushu when it approaches Japan in the zonal direction. The eastward movement and maintenance mechanism of the trough emigrating from the Tibetan Plateau are subsequently investigated. It is found that the horizontal PV flux convergence and condensational latent heat east of the trough are beneficial for its eastward movement and maintenance, and the contribution of the former is apparently larger than that of the latter.

The trough that originated over the Tibetan Plateau enhances the rainfall by increasing the moisture transportation and intensifying the ascending motion in Kyushu. First, there are anomaly westerlies south of the trough, which enhances the zonal moisture transportation to Kyushu. Generally, variation of the zonal moisture flux at the western boundary of Kyushu coincides well with that of the zonal wind speed, indicating the important role of the trough in producing favorable moisture condition for the rainfall in Kyushu. Second, the ascending

motion in Kyushu becomes stronger when the trough is zonally approaching Kyushu, indicating that the vertical motion in Kyushu is closely related to the eastward-moving trough. The influencing mechanism of the trough on the vertical motion in Kyushu is further explored by diagnosing the quasi-geostrophic ω equation. It is found that the vertical differential of vorticity perturbation advection by the mean zonal flow, temperature perturbation advection by mean zonal flow, temperature perturbation advection by zonal wind perturbation, and mean temperature advection by meridional wind perturbation are the four primary contributors to the ascending motion in Kyushu, among which the first one is the leading factor. The four aforementioned terms are related to the positive vorticity, warm center, and wind perturbation associated with the trough, which implies that the trough is responsible for the ascending motion in Kyushu to a great extent.

It should be noted that there were several rainfall episodes in Kyushu in early July 2020, and we only selected the one during 3–4 July 2020 that was affected by the trough that originated over the Tibetan Plateau. Additionally, the rainfall in Kyushu is the result of the coaction of multi-scale circulations. Although the trough emigrating from the Tibetan Plateau plays an important role in the rainfall in Kyushu, it is just part of the causations. This work aims to reveal the effect of the trough that originated over the Tibetan Plateau; thus, the roles of the other weather systems are not discussed here. Moreover, understanding the quantitative contribution of the trough to the record-breaking rainfall is important to understand the effect of the trough, which is not involved in the present work but is worthy of further investigation by conducting numerical experiments in future works.

Data availability statement

The original contributions presented in the study are included in the article/Supplementary Material; further inquiries can be directed to the corresponding author.

Author contributions

LL and CZ designed the manuscript, and LL and HH wrote the draft.

Funding

This work was supported by the Second Tibetan Plateau Scientific Expedition and Research (STEP) program (Grant No. 2019QZKK0105), Heavy Rain and Drought–Flood Disasters in Plateau and Basin Key Laboratory of Sichuan Province (Grant No. SZKT202202), and Basic Scientific Research and Operation Foundation of CAMS (Grant No. 2021Z007).

Acknowledgments

FNL data can be obtained at http://rda.ucar.edu/datasets/ds083.2. 6-hourly precipitation data are provided by the Japan Meteorological Agency at https://jra.kishou.go.jp/JRA-55/.

Conflict of interest

The authors declare that the research was conducted in the absence of any commercial or financial relationships that could be construed as a potential conflict of interest.

Publisher's note

References

Dell'Osso, L., and Chen, S. J. (1986). Numerical experiments on the Genesis of vortices over the qinghai-xizang plateau. *Tellus* 38 (A), 235–250.

Feng, X. Y., Liu, H. C., Rusmussen, R., and Fan, G. Z. (2014). A 10-yr climatology of Tibetan plateau vortices with NCEP climate forecast system reanalysis. *J. Appl. Meteor. Climatol.* 53, 34. doi:10.1175/JAMC-D-13-014.1

Kanada, S., Tsuboki, K., Aiki, H., Tsujino, S., and Takayabu, I. (2017). Future enhancement of heavy rainfall events associated with a typhoon in the midlatitude regions. *SOLA* 13, 246–251. doi:10.2151/sola.2017-045

Kato, T. (2005). Statistical study of band-shaped rainfall systems, the Koshikijima and Nagasaki lines, observed around Kyushu island, Japan. *J. Meteor. Soc. Jpn.* 83, 943–957. doi:10.2151/jmsj.83.943

Kim, I., Oh, J., Woo, S., and Kripalani, R. H. (2019). Evaluation of precipitation extremes over the asian domain: Observation and modelling studies. *Clim. Dyn.* 52, 1317–1342. doi:10.1007/s00382-018-4193-4

Kosaka, Y., Xie, S., and Nakamura, H. (2011). Dynamics of interannual variability in summer precipitation over East Asia. *J. Clim.* 24, 5435–5453. doi:10.1175/2011JCLI4099.1

Krishnan, R., and Sugi, M. (2001). Baiu rainfall variability and associated monsoon teleconnections. *J. Meteor. Soc. Jpn.* 79, 851–860. doi:10.2151/jmsj.79.851

Lhasa group for Tibetan Plateau meteorology research (1981). *Research of 500 hPa vortices and shear lines over the Tibetan plateau in summer*. Beijing: Science Press. (in Chinese).

Li, L., Zhang, R. H., and Wen, M. (2011). Diagnostic analysis of the evolution mechanism for a vortex over the Tibetan Plateau in June 2008. *Adv. Atmos. Sci.* 28, 797–808. doi:10.1007/s00376-010-0027-y

Li, L., Zhang, R. H., and Wen, M. (2014a). Diurnal variation in the occurrence frequency of the Tibetan Plateau vortices. *Meteorology Atmos. Phys.* 125, 135–144. doi:10.1007/s00703-014-0325-5

Li, L., Zhang, R. H., Wen, M., and Duan, J. (2019). Development and eastward movement mechanisms of the Tibetan Plateau vortices moving off the Tibetan Plateau. *Clim. Dyn.* 52, 4849–4859. doi:10.1007/s00382-018-4420-z

Li, L., Zhang, R. H., and Wen, M. (2017). Genesis of southwest vortices and its relation to Tibetan Plateau vortices. *Q. J. R. Meteor. Soc.* 143, 2556–2566. doi:10.1002/qj.3106

Li, L., Zhang, R. H., Wen, M., and Liu, L. (2014b). Effect of the atmospheric heat source on the development and eastward movement of the Tibetan plateau vortices. *Tellus A* 66, 24451. doi:10.3402/tellusa.v66.24451

Li, L., Zhang, R. H., and Wen, M. (2020a). Structure characteristics of the vortices moving off the Tibetan Plateau. *Meteorol. Atmos. Phys.* 132, 19–34. doi:10.1007/s00703-019-00670-z

Li, L., Zhang, R. H., and Wu, P. L. (2020b). Evaluation of NCEP-FNL and ERA-interim data sets in detecting Tibetan plateau vortices in may–august of 2000–2015. *Earth Space Sci.* 7, e2019EA000907. doi:10.1029/2019EA000907

Luo, S. W., He, M. L., and Liu, X. D. (1994). Study on the vortex of the qinghai-xizang (tibet) plateau in summer. *Sci. China Ser B* 37, 601–612. (in Chinese). doi:10.1007/BF00717371

Luo, S. W. (1992). *Study on some kinds of weather systems over and around the qinghai-xizang plateau*. Beijing: China Meteorological Press. (in Chinese).

Ma, T. T., Wu, G. X., Liu, Y. M., and Mao, J. Y. (2022). Abnormal warm sea-surface temperature in the Indian Ocean, active potential vorticity over the Tibetan Plateau, and

severe flooding along the Yangtze River in summer 2020. *Q. J. R. Meteorological Soc.* 148, 1001–1019. doi:10.1002/qj.4243

Matsumoto, S., Ninomiya, K., and Yoshizumi, S. (1971). Characteristic features of “Baiu” front associated with heavy rainfall. *J. Meteor. Soc. Jpn.* 49, 267–281. doi:10.2151/jmsj1965.49.4_267

Misumi, R. (1996). A study of the heavy rainfall over the ohsumi peninsula (Japan) caused by typhoon 9307. *J. Meteor. Soc. Jpn.* 74, 101–113. doi:10.2151/jmsj1965.74.1_101

Mohri, K. (1956). An aerological study of heavy rainfall over west and central Japan during early summer 1953. *J. Meteor. Soc. Jpn.* 34, 244–253. doi:10.2151/jmsj1923.34.5_244

Nguyen-Le, D., Yamada, T. J., and Tran-Anh, D. (2017). Classification and forecast of heavy rainfall in northern Kyushu during Baiu season using weather pattern recognition. *Atmos. Sci. Lett.* 18, 324–329. doi:10.1002/asl.759

Ogura, Y., Asai, T., and Dohi, K. (1985). A case study of a heavy precipitation event along the Baiu front in northern Kyushu, 23 july 1982: Nagasaki heavy rainfall. *J. Meteor. Soc. Jpn.* 63, 883–900. doi:10.2151/jmsj1965.63.5_883

Sekizawa, S., Miyasaka, T., Nakamura, H., Shimpo, A., Takemura, K., and Maeda, S. (2019). Anomalous moisture transport and oceanic evaporation during a torrential rainfall event over western Japan in early july 2018. *SOLA* 15A, 25–30. doi:10.2151/sola.15A-005

Shimpo, A., Takemura, K., Wakamatsu, S., Togawa, H., Mochizuki, Y., Takekawa, M., et al. (2019). Primary factors behind the heavy Rain event of july 2018 and the subsequent heat wave in Japan. *SOLA* 15A, 13–18. doi:10.2151/sola.15A-003

Tam, C. Y., and Li, T. (2006). The origin and dispersion characteristics of the observed tropical summertime synoptic-scale waves over the western pacific*. *Mon. Wea. Rev.* 134, 1630–1646. doi:10.1175/MWR3147.1

Tsuguti, H., and Kato, T. (2014). Contributing factors of the heavy rainfall event at amami-oshima island, Japan, on 20 october 2010. *J. Meteor. Soc. Jpn.* 92, 163–183. doi:10.2151/jmsj.2014-202

Tsuji, H., Yokoyama, C., and Takayabu, Y. N. (2020). Contrasting features of the july 2018 heavy rainfall event and the 2017 northern Kyushu rainfall event in Japan. *J. Meteor. Soc. Jpn.* 98, 859–876. doi:10.2151/jmsj.2020-045

Wang, B. (1987). The development mechanism for Tibetan Plateau warm vortices. *J. Atmos. Sci.* 44, 2978–2994. doi:10.1175/1520-0469(1987)044<2978:tdmftp>2.0.co;2

Wang, Y. Q., Wang, Y. Q., and Fudeyasu, H. (2009). The role of typhoon songda (2004) in producing distantly located heavy rainfall in Japan. *Mon. Weather Rev.* 137, 3699–3716. doi:10.1175/2009MWR2933.1

Wu, G. X., Tang, Y. Q., He, B., Liu, Y. M., Mao, J. Y., Ma, T. T., et al. (2022). Potential vorticity perspective of the Genesis of a Tibetan Plateau vortex in June 2016. *Clim. Dyn.* 58, 3351–3367. doi:10.1007/s00382-021-06102-2

Yang, K. M., Bi, B. G., Li, Y. A., and Dong, L. Q. (2001). On flood-causing torrential rainfall in the upstream distrct of Changjiang River in 1998. *Meteorol. Mon.* 27, 9–14. (in Chinese).

Ye, D. Z., and Gao, Y. X. (1979). *The Tibetan Plateau Meteorology*. Beijing: Science Press. (in Chinese).

Yokoyama, C., Tsuji, H., and Takayabu, Y. N. (2020). The effects of an upper-tropospheric trough on the heavy rainfall event in july 2018 over Japan. *J. Meteor. Soc. Jpn.* 98, 235–255. doi:10.2151/jmsj.2020-013

Yoshida, K., and Itoh, H. (2012). Indirect effects of tropical cyclones on heavy rainfall events in Kyushu, Japan, during the Baiu season. *J. Meteor. Soc. Jpn.* 90, 377–401. doi:10.2151/jmsj.2012-303

Yu, S. H., and Gao, W. L. (2006). Observational analysis on the movement of vortices before/after moving out the Tibetan Plateau. *Acta Meteor. Sin.* 64, 392–399. (in Chinese). doi:10.3321/j.issn:0577-6619.2006.03.014

Yu, S. H. (2008). New research advances of the Tibetan Plateau vortex in summer. *Torrential Rain Disasters* 27, 367–372. (in Chinese).

Zhang, F. M., Wang, C. H., and Pu, Z. X. (2019). Genesis of Tibetan Plateau vortex: Roles of surface diabatic and atmospheric condensational latent heating. *J. Appl. Meteorology Climatol.* 58, 2633–2651. doi:10.1175/jamc-d-19-0103.1

Zhang, S. L., Tao, S. Y., Zhang, Q. Y., and Zhang, X. L. (2001). Meteorological and hydrological characteristics of severe flooding in China during the summer of 1998. *Q. J. Appl. Meteorol.* 12, 442–457. (in Chinese).

frontiers | Frontiers in Earth Science

TYPE Original Research
PUBLISHED 23 February 2023
DOI 10.3389/feart.2023.1106990

OPEN ACCESS

EDITED BY
Jianhua Sun,
Institute of Atmospheric Physics (CAS), China

REVIEWED BY
Shuai Yang,
Institute of Atmospheric Physics (CAS), China
Yuanchun Zhang,
IAP (CAS), China

*CORRESPONDENCE
Xiangde Xu,
xuxd@cma.gov.cn

SPECIALTY SECTION
This article was submitted to Atmospheric Science, a section of the journal Frontiers in Earth Science

RECEIVED 24 November 2022
ACCEPTED 13 February 2023
PUBLISHED 23 February 2023

CITATION
Tang J, Xu X, Zhang S, Xu H and Cai W (2023), Response of remote water vapor transport to large topographic effects and the multi-scale system during the "7.20" rainstorm event in Henan Province, China.
Front. Earth Sci. 11:1106990.
doi: 10.3389/feart.2023.1106990

Response of remote water vapor transport to large topographic effects and the multi-scale system during the "7.20" rainstorm event in Henan Province, China

Jiahui Tang[1,2], Xiangde Xu[2]*, Shengjun Zhang[2], Hongxiong Xu[2] and Wenyue Cai[2]

[1]Collaborative Innovation Center on Forecast and Evaluation of Meteorological Disasters/Key Laboratory of Meteorological Disasters of Ministry of Education, Nanjing University of Information Science and Technology, Nanjing, China, [2]State Key Laboratory of Severe Weather, Chinese Academy of Meteorological Sciences, Beijing, China

A high-resolution numerical simulation was carried out for the extremely heavy rainfall in Henan Province caused by the remote water vapor transport of the binary typhoons In-fa and Cempaka on 20 July 2021. The control simulation successfully captured the evolution process and spatial distribution of the rainfall. The key water vapor supply area of the event was a triangle moisture transport influence domain formed by the local low vortex and the multi-vapor vortex system at low-latitude. By separating the effects of multiple tropical cyclones one by one, we found that In-fa dominated the main water vapor transport in the meridional direction, and directly affected the local water vapor supply in this rainfall process. Cempaka affected intermediate moisture transfer and impacted the location of precipitations, by regulating the distribution of water vapor input and output in the meridional and zonal directions. Removing Cempaka, In-fa, and binary typhoons can reduce the rainstorm area by about 7%, 65%, and 86%, respectively. These differences underscore the importance of binary typhoons in transforming a normal heavy rain event into a high-impact, record-breaking rain event. In addition, the Qinghai-Tibet Plateau exerts a modulation effect on the remote moisture transport of typhoons by multi-scale interactions. Eliminating the influence of plateau topography weakens the maximum precipitation by about 30% and the distribution of heavy rain by about 62%. After comprehensive diagnosis, a conceptual model of typhoon remote water vapor transport based on moisture multi-vortex structure under multi-scale interactions is proposed. The extremity and uncertainty of this rainstorm event can be attributed to the maintenance and development of binary typhoons, the northward extension of the subtropical high, and the anomalous convergence mechanism of water vapor due to the large terrain blocking effect on the plateau.

KEYWORDS

remote rainfall, binary typhoons, multi-vortex, water vapor transport, monsoon

1 Introduction

Generally, summer water vapor transport in China is closely related to the activities of the Asian monsoon. Large-scale monsoon circulation is one of the key factors of water vapor transport carrying warm and humid air from tropical regions to high latitudes (Wu et al., 2009). The interaction in synergy with tropical cyclones (TCs), the summer monsoon and the large plateau topography is further influences the water circulation in East Asia and its surrounding areas (Zhao et al., 2019; Zhao et al., 2020). Xu et al. (2019) suggested a key area of water vapor transport affecting China and its downstream East Asian region with precipitation anomalies that is a large triangular water vapor transport domain formed by the shift of moisture from the Bay of Bengal through the eastern Qinghai-Tibet Plateau to the Yangtze River basin of China and Japanese Archipelago. Under the influence of large plateau topography, the Indian southwest monsoon drives water vapor transport along the southern edge of the Qinghai-Tibet Plateau and across the Indo-China Peninsula, which then converges with the moisture of the western Pacific in the South China Sea or the East China Sea (Xu and Du, 2015; Chen and Wu, 2016). The above mechanism forms the basic water vapor transport pattern of TC-related precipitation over China in summer.

In addition, TC act as water vapor sources, resulting in TC-related heavy rainfall due to multi-scale interactions (Galarneau et al., 2010; Lin and Wu, 2021). The high-value area of the pressure gradient between TCs and the subtropical high is conducive to the formation of a low-level jet, which pulls water vapor along the channel between the north side of the TCs and the subtropical high, and deep in front of the TCs resulting in the East Asian monsoon, thereby forming local precipitation (Yu and Cheng, 2014; Chen and Wu, 2016). Such long-distance moisture transport can generate a long-lived, quasi-stationary mesoscale convective system outside the TC's circulation, and associated precipitation event is called predecessor rain event (PRE) (Cote, 2007; Galarneau et al., 2010; Schumacher, 2011).

PREs are of extraordinary significance to precipitation in northern China, as one-third to one-half of the rainfall events in northern China are typhoon-induced indirect precipitation caused by the interaction of mid- and low-latitude systems with TCs (Chou, 1997; Sun and Zhao, 2000). Historically, many typical northern catastrophic heavy rains displayed the characteristics of PRE, such as the rainstorm events known as "75.8 Henan," "7.21 Beijing," and "7.20 Zhengzhou".

From 17 to 22 July 2021, an extremely heavy rainfall event occurred in Zhengzhou, China, and produced an hourly rainfall rate of 201.9 mm, which broke the station record for mainland China. As a typical and extreme PRE, the diagnosis and simulation of multi-scale characteristics showed that the rainstorm was caused by the interaction of atmospheric systems in the middle and lower latitudes, and combined with the influence of topography (Ran et al., 2021; Liang et al., 2022). The terrestrial and oceanic moisture over southern China-western North Pacific was both crucial for the extreme precipitation event over Henan (Nie and Sun, 2022). The main moisture transport was driven by airflows on the peripheries of binary tropical typhoon (BT) In-fa and Cempaka (Deng et al., 2022; Sun et al., 2023). The event produced well-organized mesoscale convective systems whose unique dynamic structure contributes significantly to record-high hourly rainfall (Yin et al., 2021).

Although some studies have been carried out on the mesoscale conditions, topographic effects, and the triggering and development process of the convective system, some studies have shown that the predictability of this event is essentially limited, and the rainfall prediction accuracy is insufficient (Zhang et al., 2022). The interactions between multiple TCs and atmospheric circulation are very complex. For BT, differences in the distance, intensity, influence radius, and peripheral airflow all have an impact on the interaction (Bosart et al., 2012; Xu et al., 2022a; Xu et al., 2022b). It is still challenging to forecast and understand the water vapor transport of this extreme precipitation events under the influence of BT.

Previous studies have shown that moisture transport in front of TCs can substantially increase rainfall in mid-latitudes and exacerbate the impact of the resulting disaster events. However, the specific mechanism of moisture transport caused by the interaction between TCs and mid-latitude systems remains unclear. High-resolution numerical models can be used to study the uncertainty of the effect of BT on extreme precipitation events and further express the overall effect of large-scale water vapor budget of PREs. These initiatives help to quantify water vapor transport and the ultimate impact on precipitation.

Our study focuses on the Zhengzhou rainstorm event on 20 July 2021. We investigate the effect of abnormal water vapor transport caused by the related circulation of the multi-system on this extreme precipitation event. Specifically, this paper aims to quantify the remote effects of the BTs moisture on extreme precipitation, discuss the water vapor transport effect between multiple vortex systems at low latitudes, and further explore the contribution and correlation mechanism of the large topography of the Qinghai-Tibet Plateau to the development and maintenance of heavy rainfall events in the north of China.

2 Model configuration and experimental design

In this paper, WRF Advanced Research Weather (WRF-ARW) model, version 4 (Skamarock et al., 2019) was used to simulate the extreme rainstorm in Henan Province on 20 July 2021. The initial field and lateral boundary conditions was from the ECMWF Reanalysis v5 (ERA5, 0.25° × 0.25°) data set (Hersbach et al., 2020). Other data used in this paper included ground station observation data and high spatiotemporal resolution (10 km grid spacing and 1 h temporal resolution) gauge-satellite merged (Shen et al., 2014) precipitation analysis data set provided by the China Meteorological Administration (CMA). The rainfall product of CMA was estimated based on >30,000 hourly rainfall gauge station data from China and the Climatic Prediction Center Morphing Technique (CMORPH) precipitation products. Compared with the station data, the grid point precipitation was more advantageous for reflecting precipitation characteristics in areas with sparse stations and mountains.

All the simulations were initialized at 0000 UTC on 19 July 2021 with 76 h integration time. We also carried out the simulation with earlier initial times (not shown), but the results were not as good as with the above settings. The horizontal grids include three nested domains with a minimum size of 3 km (Figure 1). The

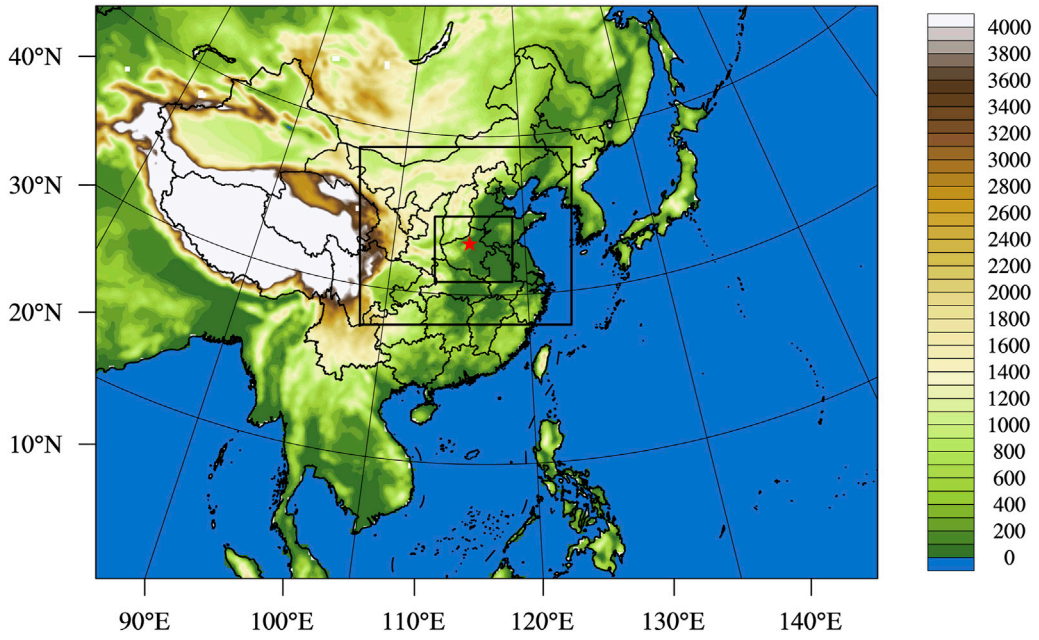

FIGURE 1
Configuration of the Weather Research and Forecasting (WRF) model domains (D01-D03); shading represents the terrain height (unit: m). The location of Zhengzhou city is marked as a red pentagram.

TABLE 1 Model configuration and parameters.

Model options	Parameters
Horizontal resolution	27 km, 9 km, 3 km
Cumulus convective parameterization scheme	Kain-Fritsch Kain, (2004)
Microphysics scheme	WSM6 Hong and Lim, (2006)
Radiation scheme	CAM Collins et al. (2004)
Land-surface model	Pleim-Xiu Xiu and Pleim, (2001)
Surface layer scheme	Pleim-Xiu Pleim, (2006)
Planetary boundary layer	ACM2 Pleim, (2007a); Pleim, (2017b)

TABLE 2 List of experiments.

Experiment	Name	Remarks
1	CTRL	Original numerical simulation
2	NO_IF_Lev1	Typhoon In-fa is removed within a radius of 300 km from the storm center (slight level)
3	NO_IF_Lev2	Typhoon In-fa is removed within a radius of 600 km from the storm center (middle level)
4	NO_IF_Lev3	Typhoon In-fa is removed within a radius of 900 km from the storm center (severe level)
5	NO_CK	Typhoon Cempaka is removed within a radius of 300 km from the storm center
6	NO_IF&CK	Both typhoon In-fa and typhoon Cempaka are removed as set in 4 and 5
7	NO_TP	The terrain of plateau is weakened to 500 m

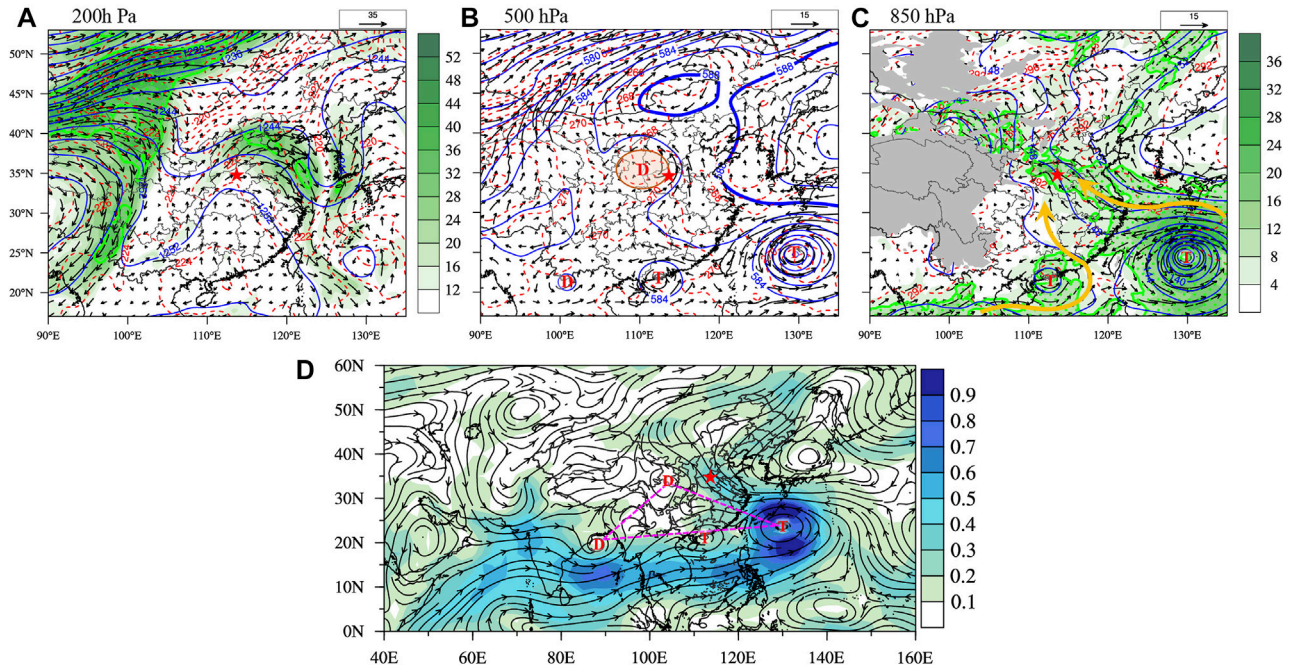

FIGURE 2
(A–C) 200, 500, and 850 hPa large-scale circulation fields at 0600 UTC July 20. The blue solid line represents the potential height (unit: gpm), the blue bold line indicates the isoline of 588 hPa, the red dashed line denotes the isotherm (K), the arrow means the vector wind (unit: m/s), color shading represents wind speed (unit: m/s), the gray shadows represent the terrain, the two yellow arrow means the west and east moisture branch, and the circled area of green dots is upper- and low-level jet areas. **(D)** Vertically integrated water vapor flux field (unit: 10^3 kg $m^{-1}s^{-1}$). The letters "D" and "T" represent the low-pressure center and typhoon, respectively, and the red pentagram represents the location of Zhengzhou.

38 vertical levels expand from the surface to 10 hPa, with 8 levels below 1 km. The parameterization scheme settings of the schema are shown in Table 1.

We consider that the extreme precipitation event was influenced by remote binary typhoons with the interaction of multi-scale systems, the multiple vortex systems at low latitudes exerting a significant water vapor transport effect (Xu et al., 2022b). To investigate the mechanism of the influence of the BT on this extreme precipitation, the following sensitivity experiments were designed in Table 2.

Experiment 1 was a control experiment, representing the original simulation results of the precipitations. Three additional sensitivity experiments (Experiments 2–4) were conducted to quantitatively determine the water vapor transport effect of typhoon In-fa, by removing In-fa slightly, moderately, and severely in the initial fields. Experiment 5 was designed to remove Typhoon Cempaka, while Experiment 6 removed the binary typhoons. The sensitive experiments 2–6 are conducted by modifying the TC-related dynamic and thermodynamic fields in the initial condition using the TC bogussing scheme (Low-Nam and Davis, 2001). In order to remove TC circulation in background field, the TC-related correlation vorticity, divergence and geostrophic vorticity are removed within different influencing radius of TC center. The slightly, moderately and severely elimination of typhoon In-fa corresponded to the radius of 300, 600 and 900 km respectively. Due to the small scale of the typhoon Cempaka, the revised radius is limited to 300 km.

Generally, China in topography descends from the west to the east, and forms a three-step "staircase" according to altitude. To further discuss the influence of the large plateau topography on the moisture transport during this extreme rainstorm, the altitude above the second step of China terrain was reduced to 500 m in Experiment 7.

3 Results and discussion

3.1 Background analysis of extreme precipitation event

The configuration of the large-scale environmental field of the "7.20"extreme rainstorm in Henan had significant features. The 200 hPa situation field indicated that the geopotential height field in the upper layer was a distribution pattern of two troughs and one ridge. Among them, the western trough was of large meridional span, extending from the Loess Plateau to the Yunnan-Guizhou Plateau, and the eastern trough was positioned at the Yellow Sea. Henan was in between the two troughs, affected by the ridge of high pressure. Thus, Henan presented an anticyclonic circulation in which the wind direction changed from southwest to northwest, and it was located in the south of the upper jet stream area with remarkable divergences in the upper layer (Figure 2A).

Figure 2B shows the typical BT system composed of In-fa and Cempaka in 500 hPa. The Huang-Huai region was affected by cyclonic circulations twice before and after, the first of which occurred on 19 July from 0000 to 1500 UTC in southeastern Henan Province (Figure omitted), and the second was a new mesoscale vortex that developed at 2200 UTC 19 July, which was

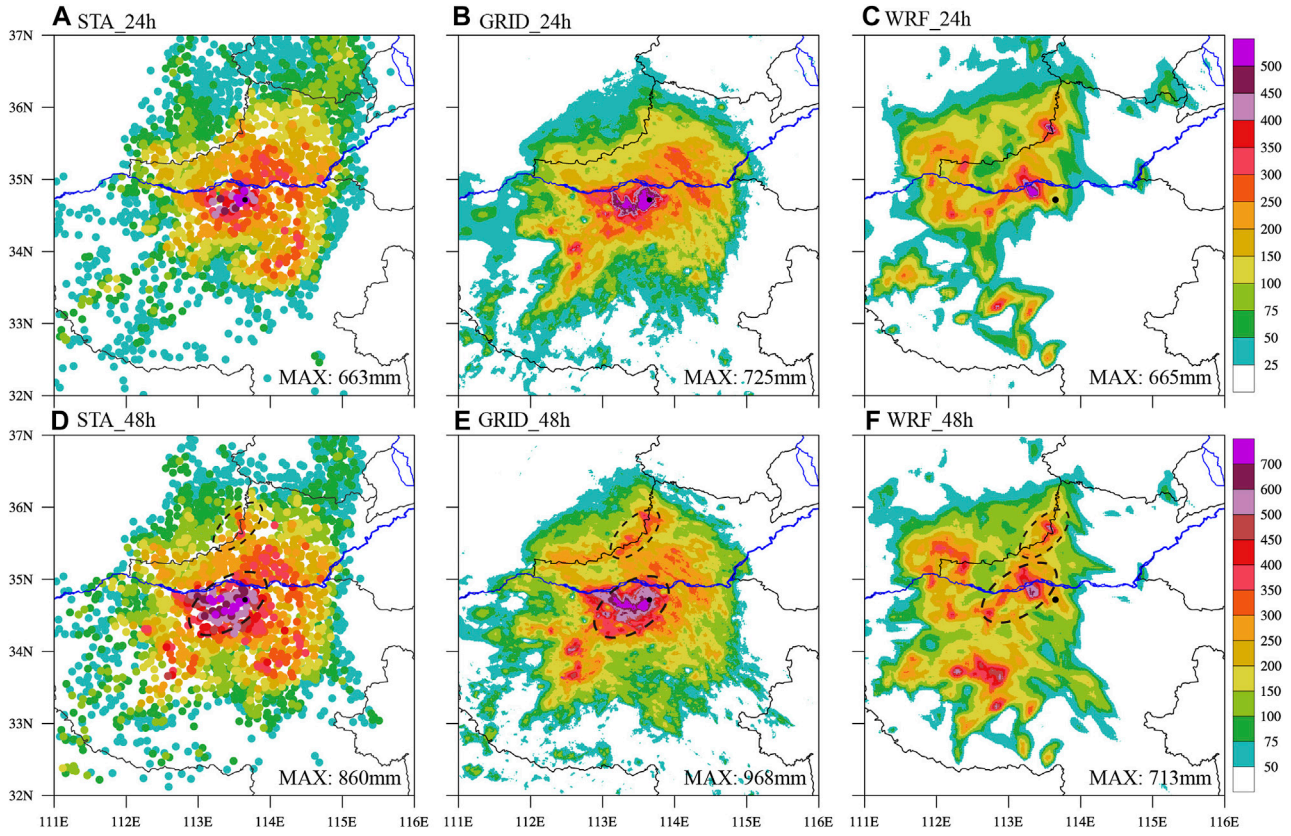

FIGURE 3
Observed and simulated 24 h cumulated precipitation distributions from 0000 UTC July 20 to 0000 UTC 21 July 2021 **(A–C)** and 48 h **(D–F)** cumulated precipitation distributions from 0000 UTC July 19 to 0000 UTC 21 July 2021 (unit: mm) **(A, D)** Observation precipitation of stations **(B, E)** Grid point precipitation from the China Meteorological Administration observations **(C, F)** Simulated precipitation distribution of control test. The black dashed circle represents the main rain belt. The black dot represents the location of Zhengzhou.

the main system influencing this heavy rainfall in Henan (Yin et al., 2021; Xu et al., 2022a). The Huang-Huai cyclone occurred at the intersection of Shaanxi, Shanxi, and Henan, with Henan in the east. The strong northerly position of the subtropical high was conducive to the transport of southeastern water flow along the edge of the subtropical high to the key rainstorm area; the 588 hPa line was nearly connected with the high pressure near Inner Mongolia at 45°N, developing a "high pressure dam". This blocked the southeastern airflow from continuing northward and made it gather and sustain in the central plain.

At 850 hPa (Figure 2C), Henan was under the control of a strong low-level jet. The southeastern airflow between subtropical high and In-fa transported a large amount of moisture, which formed the east branch of the typhoon. At the same time, Typhoon Cempaka also acted as a transit station to transfer some of water vapor, which formed the west branch. Blocked by Taihang Mountain, the airflow of the east and west branches accumulated and converged on a windward slope terrain (west of Zhengzhou), which promoted the development of the precipitation system.

The vertically integrated water vapor flux (Figure 2D) shows that a low vortex circulation zone formed, composed of several water vapor vortices in low latitude. This is referred to as a multi-vortex system in this paper. This moisture transport feature combined with the subtropical high to facilitate transport of water vapor from low latitude to high latitude by the typhoon. The South Asian low pressure, typhoons, and local low vortex formed a triangle (dashed lines in Figure 2D), which constituted the key water vapor supply area for this extreme event.

In summary, the large-scale circulation characteristics of this storm were remarkable, with upper-level dispersion and lower-level convergence providing dynamic conditions conducive to the generation of heavy rainfall. The subtropical high, typhoons, and local low vortices were the main influencing systems, triggering strong convective processes with the topographic effects under the interaction of multi-scale systems. In addition, the multi-vortex transport system of moisture based on the BT provided a steady source of water vapor. The resultant dynamic, thermal, and water vapor conditions drove the development of the extreme rainstorm event in Henan.

3.2 Verification of the control run

The heaviest precipitation during this event occurred on July 20. The observed precipitation displayed distribution characteristics along the terrain, with strong mesoscale rain clusters (Figures 3A,

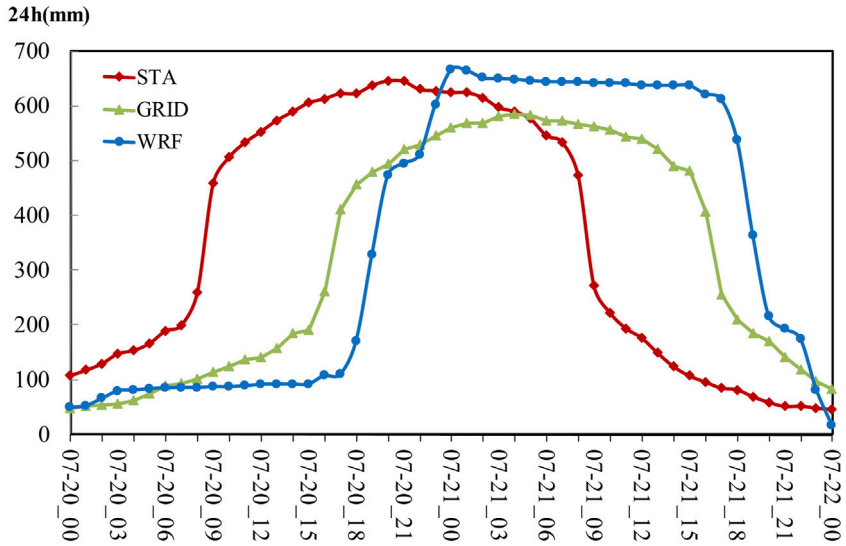

FIGURE 4
24 h precipitation time series (unit: mm) observed at the Zhengzhou station (The black dot in Figures 3A, B) and simulated locations of maximum precipitation. The red line is the station observation, the grid line is grid point precipitation and the blue line is the simulated precipitation of control test.

B, D, E). The large-range precipitation area was located in the northwest of Henan, and the main center was located in Zhengzhou. The long duration, wide range of heavy rainfall, and high intensity over a short time were the remarkable characteristics of this event.

A control simulation provided a reasonable replication of the observed event, with a simulated 24 h accumulated maximum rainfall amount of 665 mm (Figure 3C), consistent with the observed station maximum of 663 mm (Figure 3A). The location of the centers and distribution pattern of rainfall compared well with observations, although the rain clusters were slightly smaller in the simulation relative to the observations. Further comparing the 48 h accumulated precipitation, the simulated results showed two small-scale intense centers consistent with the observations (dashed circles in Figures 3D–F), which were located in the urban area of Zhengzhou and on the windward slope in the north. The simulated rainfall levels matched with the observations in the 24 h time series of precipitation in the center (Figure 4), while the overall timing of cumulated precipitation lagged behind the observations. In addition to the complexity of the weather process itself, the initial field error and systematic error, as well as the coordination of the parameterization scheme and the spin-up process may lead to the lag of the precipitation forecast.

In summary, the simulation results accurately captured the evolution process and spatial distribution of the event, and the reproduction of the double rainfall center in the urban area and mountainous areas. The simulation was well suited for use as a control run for quantifying the precipitation change and response caused by tropical moisture transport ahead of the typhoon.

3.3 Sensitivity experimental diagnosis of typhoon

Three quantitative sensitivity numerical experiments were designed for typhoon In-fa. Experiment Lev1-Lev3 represented the gradual attenuation of In-fa, to study the water vapor transport and the interaction mechanism of typhoon In-fa on the typhoon remote rainstorm.

Figures 5A–D shows that with the gradual elimination of In-fa, the precipitation in each experimental area changed compared to the CTRL experiment (Figure 5A). With the slight attenuation of In-fa in Lev1 test (Figure 5B), the change of overall precipitation was not obvious, with even a slightly enhanced trend in extreme precipitation in local areas (Figure 5F). When the typhoon weakened further in Lev2 test (Figure 5C), the rainfall area still occurred, but its organizational structure changed. The heavy precipitation center near Zhengzhou weakened significantly, and the precipitation cluster in the northern mountains began to dissipate (Figure 5G), with maximum precipitation decreased by 58 mm compared with the CTRL experiment (Figure 5I). After complete elimination of In-fa in Lev3 test (Figure 5D), the heavy precipitation center dissipated completely, and the previous heavy precipitation center turned into sparse and scattered light rain areas (Figure 5H), with maximum precipitation reduced by about 135 mm (Figure 5I).

The precipitation levels and distribution of heavy precipitation in several groups of experiments were analyzed to obtain the histogram in Figure 5I. Precipitation gradually weakened as the intensity of In-fa gradually decreased. When In-fa was completely removed, the maximum precipitation decreased from 665.2 mm to 530.5 mm, a reduction of about 20%. The number of grids with daily precipitation greater than 250 mm indicate the overall regional distribution of extreme rainfall. Completely removing typhoon In-fa caused the grid number with heavy rainfall to decrease from 429 to 151, which means that the overall distribution of extreme precipitation area decreased by about 65%.

Typhoon In-fa directly affected the rainfall of the rainstorm in Henan Province. This can be temporarily attributed to the close relationship between the intensity of In-fa and the moisture channel

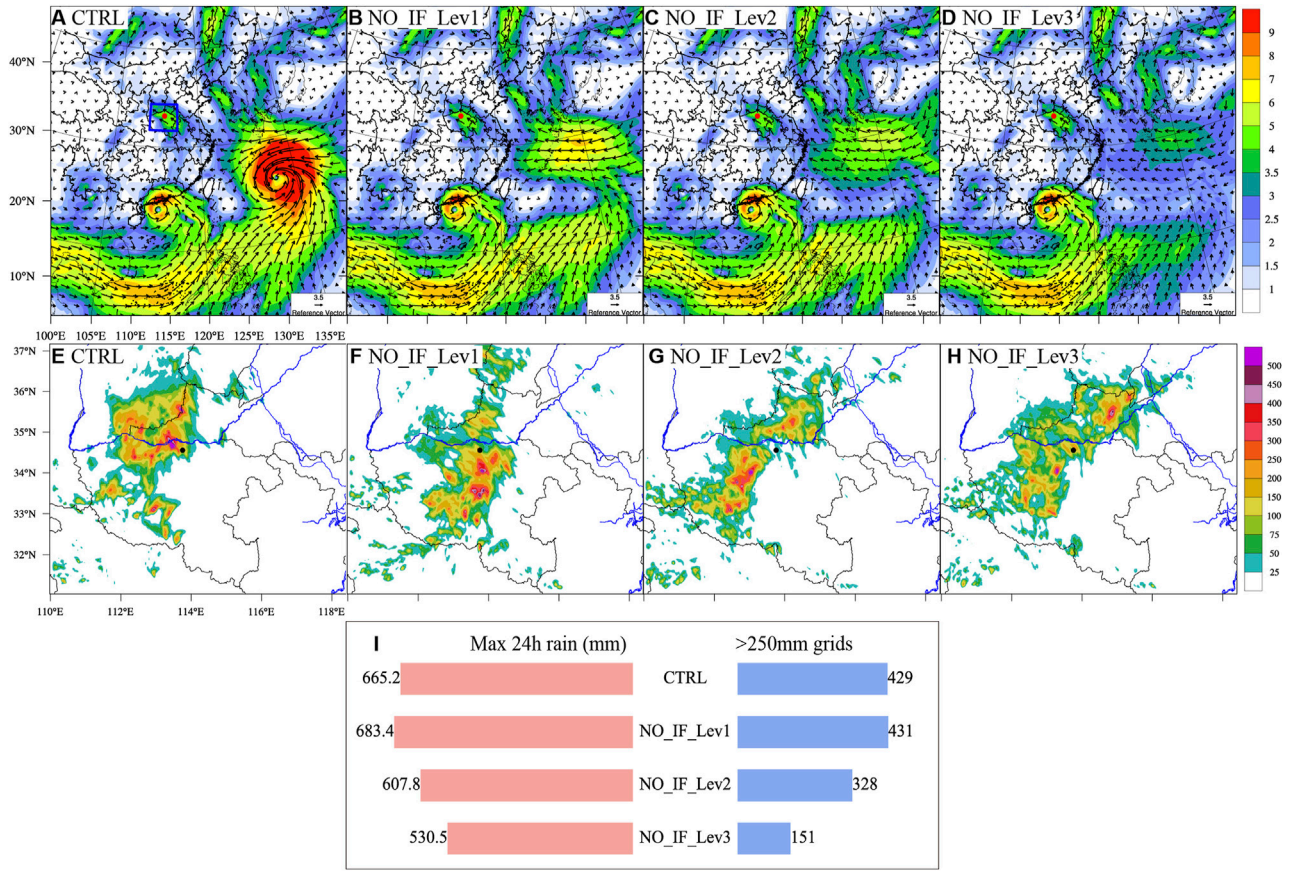

FIGURE 5
Comparison of experiments CTRL, NO_IF_Lev1, NO_IF_Lev2, and NO_IF_Lev3. **(A–D)** Vertically integrated water vapor flux (unit: 10^2 kg $m^{-1}s^{-1}$) of the initial field at 0000 UTC July 19. **(E–H)** 24 h precipitation (unit: mm) from 0000 UTC July 20 to 0000 UTC 21 July 2021. **(I)** Histograms of the maximum 24 h precipitation (unit: mm) from 0000 UTC July 20 to 0000 UTC 21 July 2021 and the number of precipitation grid points >250 mm for the above experiment.

formed by In-fa and the subtropical high. This will be verified later in the paper.

Based on previous analyses of weather background and existing studies, we know that extreme rainstorm processes in Henan involve water vapor transport effect among the low-latitude multi-vortex systems, as well as abnormal configuration of the subtropical high and multi-scale circulation (Xu and Du, 2015; Ran et al., 2021). In this study, we removed the single and binary typhoons in the multi-vortex system respectively to investigate the effect of the interaction of typhoons and mid-low latitude circulation on water vapor transport of extreme rainstorm events in northern China.

In Figures 6B, F, typhoon Cempaka was removed compared with the control tests (Figures 6A, E). The corresponding precipitation center moved obviously eastward, but high daily precipitation was still maintained, with a maximum value of 599.2 mm. After the removal of In-fa, the overall rainfall in the entire region significantly weakened, the heavy precipitation center mostly dissipated, and the maximum value was reduced to about 530.5 mm (Figures 6C, G). After the binary typhoons were removed simultaneously, precipitation in the entire region largely disappeared, as well as the pattern of the extreme rainstorm, and maximum precipitation stayed at around 387.2 mm (Figures 6D, H).

As seen in the histogram (Figure 6I), the gradual elimination of single and double typhoons gradually weakened precipitation. Specifically, maximum precipitation was reduced by about 10%, 20%, and 42%, respectively, and the corresponding distribution area of extreme rainfall was reduced by about 7, 65, and 86%, respectively, after Cempaka, In-fa, and the binary typhoons were removed.

Therefore, in the multi-vortex type TC remote moisture transport associated with Henan's "7.20" rainstorm, the western small typhoon Cempaka mainly affected the location of precipitation areas, and the eastern typhoon In-fa located in the western Pacific dominated the distribution pattern and intensity of extreme rainstorms. The combined action of the binary typhoons maintained the basic precipitation pattern of this extreme event. Supposing they disappeared simultaneously, the extreme rainfall would be greatly weakened, and the rainstorm area would dissipate as well.

3.4 Response of large plateau terrain to extreme precipitation

As the "Water Tower of Asia," the Qinghai-Tibet Plateau is of great significance to water vapor transport under multi-scale

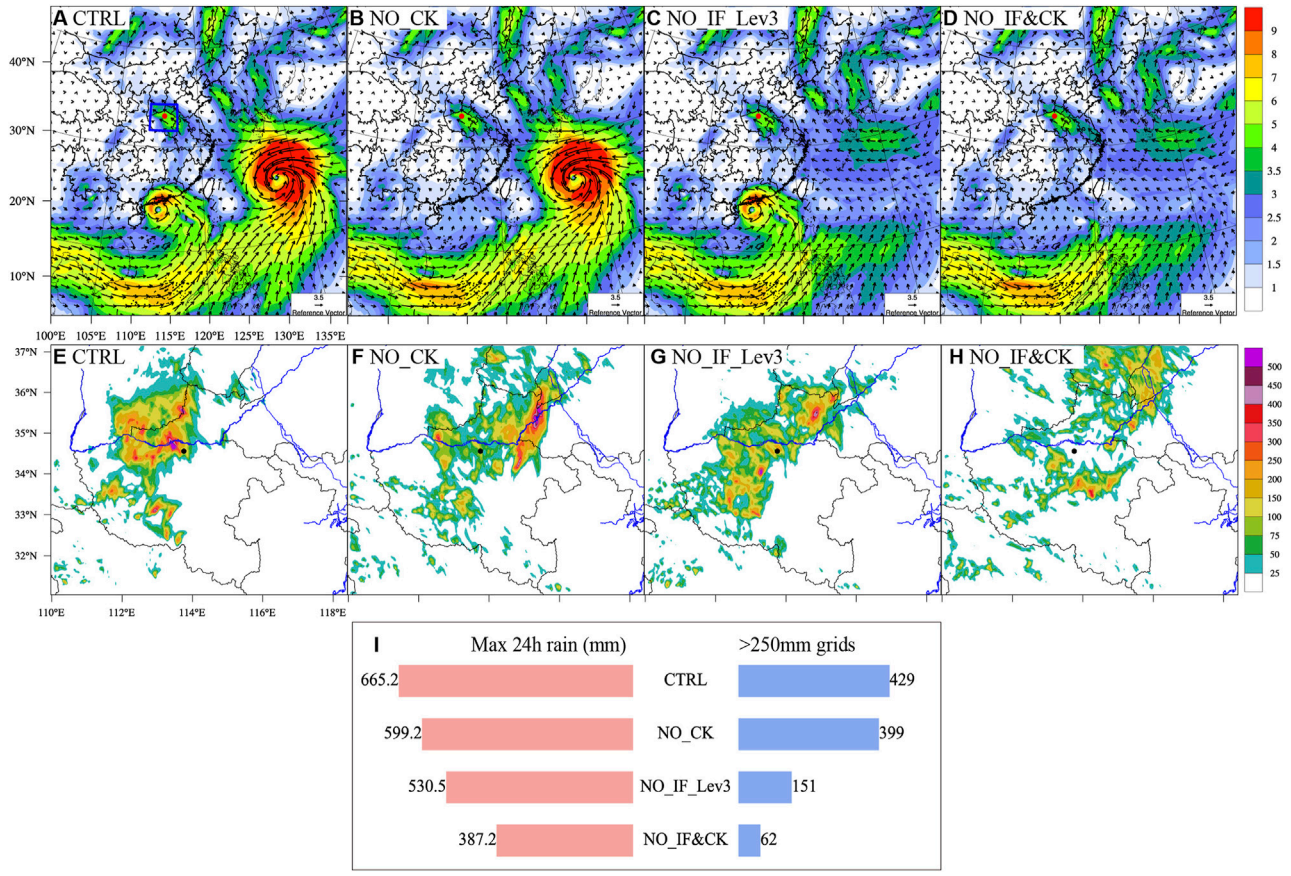

FIGURE 6
Comparison of experiment CTRL, NO_CK, NO_IF_Lev3, and NO_IF&CK. **(A–D)** Vertically integrated water vapor flux (unit: 10^2 kg $m^{-1}s^{-1}$) of the initial field at 0000 UTC July 19. **(E–H)** 24 h precipitation (unit: mm) from 0000 UTC July 20 to 0000 UTC 21 July 2021. **(I)** Histograms of the maximum 24 h precipitation (unit: mm) from 0000 UTC July 20 to 0000 UTC 21 July 2021 and the number of precipitation grid points >250 mm for the above experiment.

interaction (Xu et al., 2019). The terrain effect is also a critical factor influencing sudden and prolonged local extreme precipitation. To further explore the contribution of the large plateau terrain on water vapor transport during this event, the altitude above the second step of China terrain was reduced to 500 m. By comparing with the control run (Figures 7A, C), we found that eliminating the influence of large terrain led to a cluster pattern of precipitation. Due to the lack of terrain obstacles, the rain area shifted to the northwest, which was mountainous in the control run (Figures 7C, D). There were large differences in the distribution of heavy precipitation. The maximum precipitation was reduced by about 30% from 665 mm to 467 mm, and the number of grid points for heavy rainstorm dropped by about 62%–165% (Figure 7E).

Such changes in displacement and intensity of precipitation can be attributed to the elimination of plateau changing the moisture transport path on a large scale (Li et al., 2016), and can affect the local moisture convergence on a meso- and micro-scale (Shi et al., 2008; Hua et al., 2020). It has been suggested that during the summer monsoon phase, the Tibetan Plateau and its extended topography affected water transport channels, forcing the moisture from tropical oceans to flow along the eastern and northern part of the Qinghai-Tibet Plateau through low air vortex (Xu et al., 2004; Zhao et al., 2019). The results in this subsection also confirmed the role of the Tibetan Plateau in guiding water vapor from typhoons at low latitudes, which indirectly affected the development of local rainstorm.

3.5 Diagnosis of regional water vapor budgets in different tests

The water vapor budget of the specified key rainstorm area (Figure 5A box) during the "7.20"rainstorm in Henan was diagnosed and analyzed, to further refine the water vapor contribution of each typhoon in the multi-vortex. The time series of water vapor flux in each experiment is given in Figure 8. The positive income for moisture was shown in the all tests, which rose sharply at night on the 20th days.

According to Figure 8A, the weakening of moisture transport caused by In-fa mainly occurred during the period of 1500 to 2100 UTC on July 20, corresponding to the peak of water vapor transport in the control test. With the gradual elimination of In-fa, the moisture peak of sensitivity tests gradually flattened and the

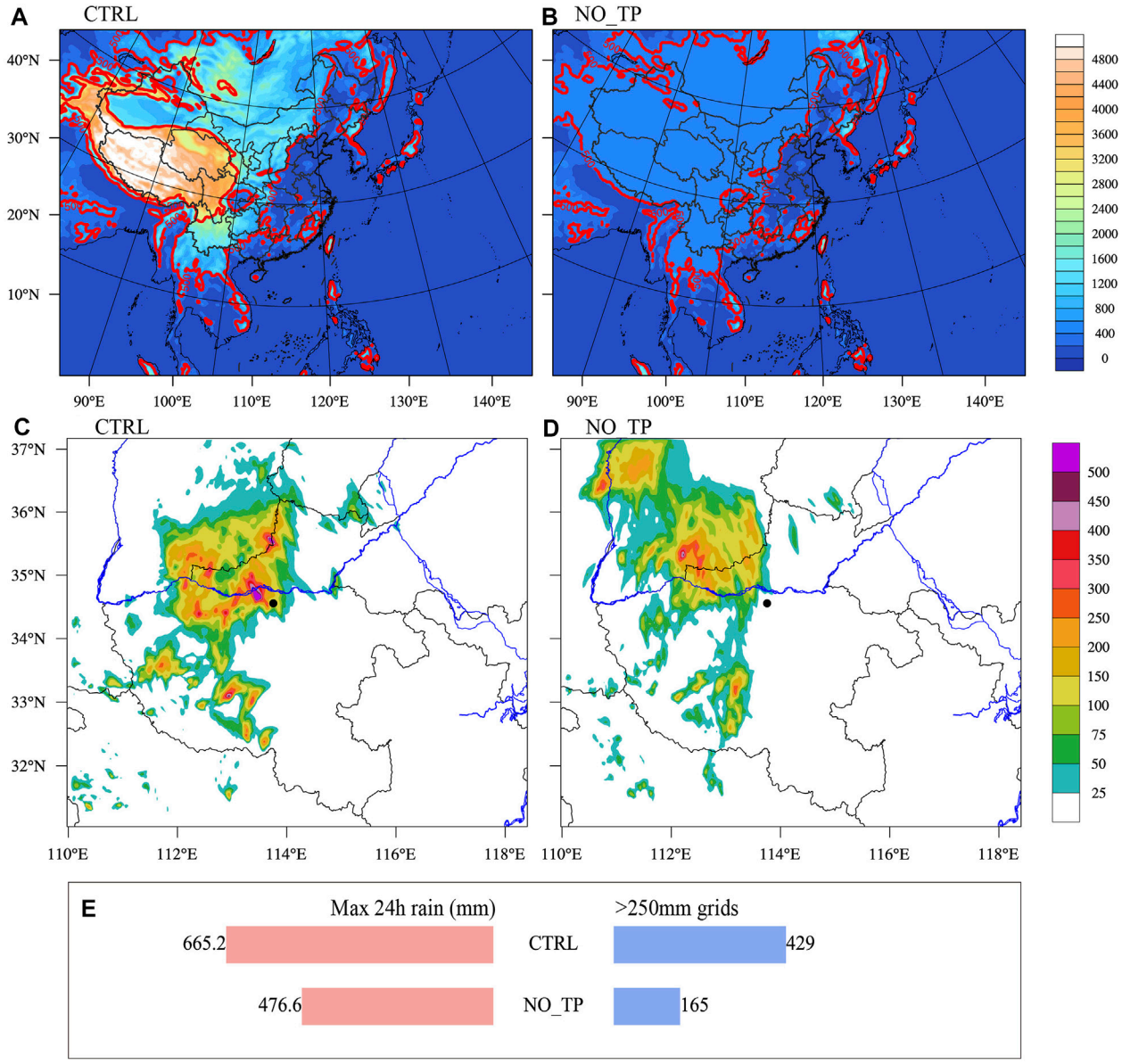

FIGURE 7
Comparison of experiment CTRL and NO_TP. **(A–B)** Terrain height (unit: m) of the initial field at 1900 UTC. **(C–D)** 24 h precipitation (unit: mm) from 0000 UTC July 20 to 0000 UTC 21 July 2021. **(E)** Histograms of the maximum 24 h precipitation (mm) from 0000 UTC July 20 to 0000 UTC 21 July 2021 and the number of precipitation grid points >250 mm for the above experiment.

magnitude decreased, reflecting that the transport of In-fa to the key rainstorm area gradually decreased.

Figure 8B shows the water vapor transport budget of the removal tests for different objects. When Cempaka alone was removed, the curve of the transport was similar to that in the control test. The difference in magnitude was not particularly obvious, and only the position was shifted, suggesting that the timing of moisture transport was changed. This further supports the shift of the rain area mentioned above (Figure 6F). After In-fa was removed, the transport curve became gentle and the volume of moisture transported was reduced. After the binary typhoons were removed simultaneously, the magnitude in the peak range of water vapor transport weakened further, to about 75% of the control. In the experiment where the large plateau terrain was eliminated, the transport was also remarkably reduced in the late stages of the event.

Table 3 provides the average regional water vapor budget on the four boundaries. The eastern and southern boundaries were net input (>0), while the western and northern boundaries were net output (<0), consistent with the prevailing southeasterly winds in large-scale circulation of the key area. When In-fa was removed at different intensities in Lev1-Lev3 experiments, the net input slowly weakened compared with the control test. Upon the removal of Lev3, the input of the south and east boundaries and the output of the west and north boundaries were all weakened. In the Lev1 and Lev2 tests, the input at the

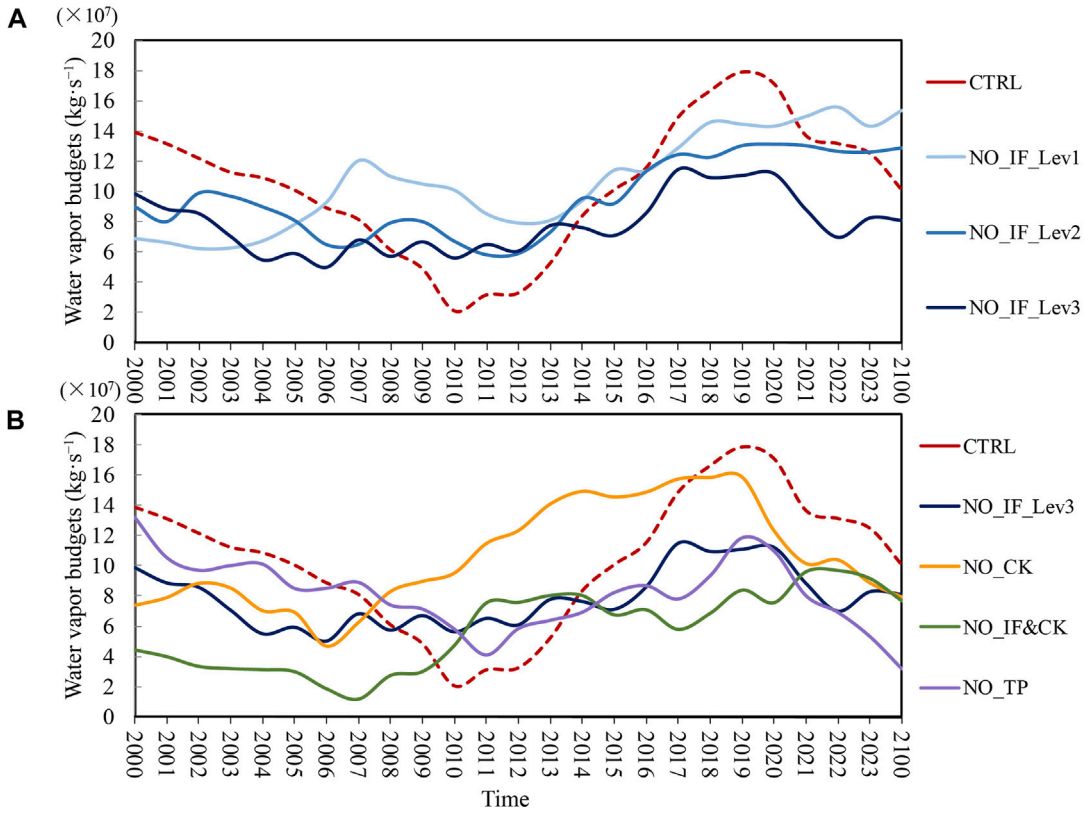

FIGURE 8
Time series of the vertically integrated water vapor flux (from the surface to 50 hPa, unit: 10^7 kg s^{-1}, positive inward and negative outward) and budget (the sum of four boundaries of box in Figure 5E). **(A)** Comparison groups of NO_IF in Lev1-Lev3. **(B)** Comparison groups of CTRL, NO_IF_Lev3, NO_CK, NO_IF&CK, and NO_TP.

TABLE 3 The average regional water vapor budgets on July 20 (unit: 10^7 kg s^{-1}, positive inward and negative outward).

Experiment	East	West	South	North	Net
CTRL	10.16	−4.75	15.60	−10.65	**10.37**
NO_IF_Lev1	11.26	−5.13	12.79	−8.46	**10.46**
NO_IF_Lev2	11.87	−6.06	12.72	−8.92	**9.61**
NO_IF_Lev3	9.15	−3.48	11.73	−9.58	**7.82**
NO_CK	11.83	−4.60	13.68	−10.27	**10.64**
NO_IF&CK	10.32	−6.69	9.62	−7.54	**5.72**
NO_TP	12.00	−2.86	16.59	−17.40	**8.33**

The bold values represents the sum of the first four terms (East+West+South+North).

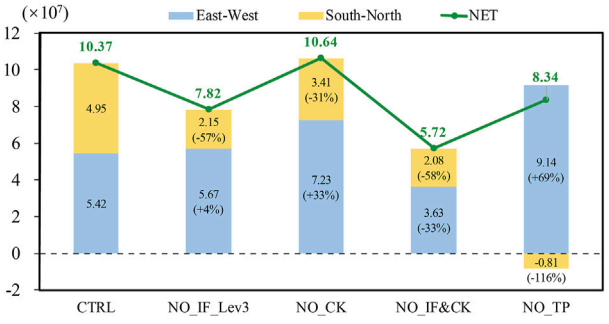

FIGURE 9
Average regional water vapor budgets on July 20 (unit:10^7 kg s^{-1}) in the meridional and zonal directions of comparison groups.

southern boundary and the output at the northern boundary decreased, while the input at the eastern boundary and the output at the western boundary increased marginally. When the overall net budget changes little, the entry of moisture shifted from the south boundary to the east boundary, indicating the eastward displacement of the water vapor branches. A similar feature of the water vapor budget also appeared after removal of Cempaka alone.

Simultaneously removing the binary typhoons resulted in the largest weakening of the water vapor input (9.62×10^7 kg s^{-1}) at the southern boundary, and the lowest water vapor net input. After the blocking effect of the plateau terrain disappeared, the water vapor continuously output from the northern boundary.

The water vapor budgets of the sensitivity tests in the meridional direction (S-N) and zonal direction (E-W) were diagnosed

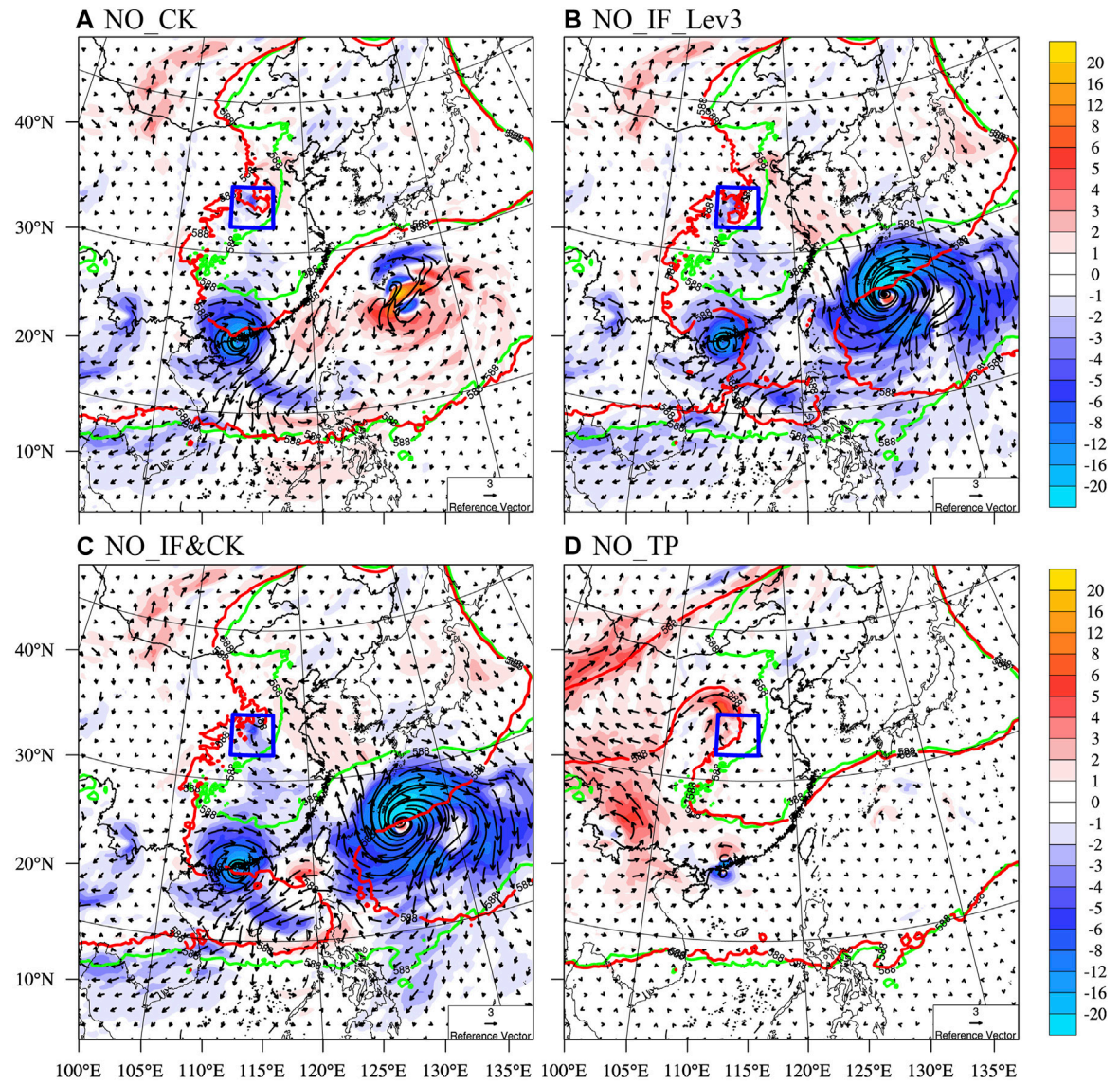

FIGURE 10
Deviation distribution field of the vertically integrated water vapor flux (unit: kg $m^{-1}s^{-1}$) of each sensitivity test compared with the CTRL test at 1800 UTC on July 20. **(A)** NO_CK **(B)** NO_IF_Lev3 **(C)** NO_IF&CK **(D)** NO_TP. The shading represents deviation of water vapor flux (sensitivity test minus ctrl test, unit: kg $m^{-1}s^{-1}$) and the arrow represents the vector flux (unit: kg $m^{-1}s^{-1}$). The green solid line represents the isoline of 588 dagpm geopotential height in the CTRL test, and the solid red line represents the isoline of 588 dagpm in the sensitivity tests. The blue box represents the key area associated with rainstorm.

respectively (Figure 9). The E-W input differences were not obvious after typhoon In-fa was removed, while the S-N input was significantly reduced by 57% compared to the control test. The single removal of Cempaka increased E-W input by 33% and decreased S-N input by 31%, which jointly resulted in little difference between the total budgets compared with the control test. The simultaneous elimination of the binary typhoons substantially reduced both the meridional and zonal inputs, reducing the S-N input by 58% and the E-W input by about 33%.

As can be seen from the above results, In-fa mainly affected the water vapor budget in the meridional direction, widely influencing the overall moisture transport in the key rainstorm area, while Cempaka modulated the distribution of water vapor budget in the meridional and especially in the zonal direction. Removing the binary typhoons generally cut off the supply of moisture branches, and the water vapor in both the meridional and zonal directions was significantly weakened.

After the effect of the plateau terrain was eliminated (Figure 9), the E-W input increased by 69%, while the net S-N output of moisture reduced by 116% compared with the control test. This resulted in a net input of overall water vapor in NO_TP test. The change of meridional water vapor from input to output indicated that the blocking and convergence effect of the terrain disappeared, and the water vapor largely flowed out from the northern boundary. The increase of zonal water vapor, on the other hand, may be related to the displacement of the Huang-huai cyclone.

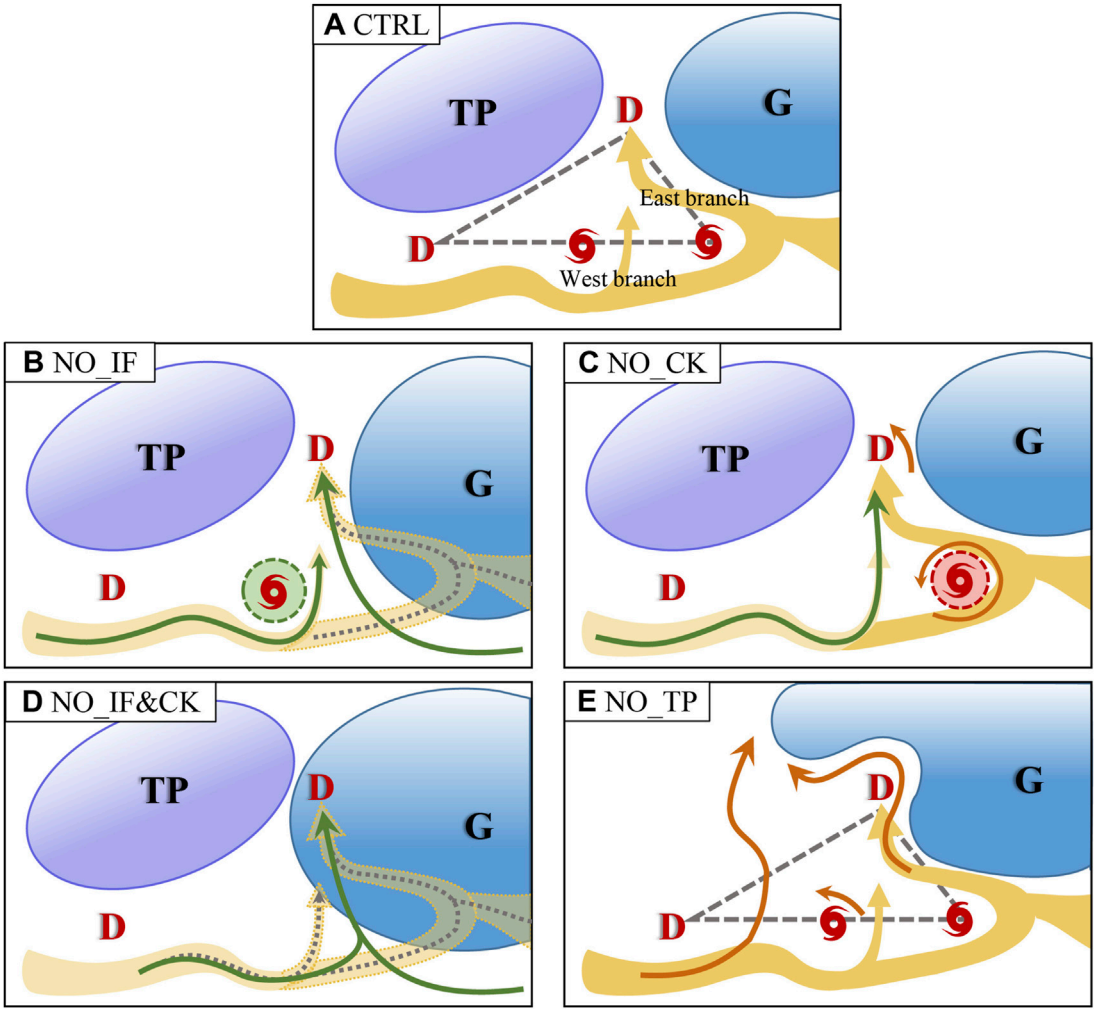

FIGURE 11
Conceptual model of water vapor transport during the extreme rainstorm in Henan under multi-system configuration **(A)** CTRL **(B)** NO_CK **(C)** NO_IF_Lev3 **(D)** NO_IF&CK **(E)** NO_TP. "G" represents the subtropical high and "TP" represents the large plateau terrain. "D" and typhoon marks correspond to low-pressure water"vapor vortexes and typhoons, respectively. The thick yellow arrows represent the main water vapor transport branches, and yellow color depth represents changes in strength. Thin green and orange arrows represent weakened and increased water vapor flow directions. Grey dotted lines represent the disappearance of the water vapor branches. The colored areas surrounded by green and red dashed lines represent the weakening and strengthening of the cyclone, respectively.

To further investigate the specific mechanism of water vapor transport in the late stage of the rainfall event, we conducted sensitivity tests on moisture deviation distribution (Figure 10). Compared to the CTRL, removing Cempaka (NO_CK) resulted in the intensity of typhoon In-fa increasing marginally, and positive and negative moisture transport anomalies were seen in the northeast and interior of the key area associated with rainstorm, respectively. Both positive and negative were of comparable intensity (Figure 10A). The effects of removing In-fa (NO_IF_Lev3) included a weakening of the intensity of minor Typhoon Cempaka, decrease in water vapor from the Indian Ocean, and a gradual southward expansion of the subtropical high. The negative anomalies on the south side of the precipitation key area led to the weakening of the main water vapor branch, and the east side of the key area had positive anomalies but basically did not involve the area (Figure 10B). After the simultaneous removal of the binary typhoons (NO_IF&CK), the deviation distribution field of water vapor flux was similar to NO_CK, but with more remarkable southward and westward expansion of the subtropical high. The rainstorm key area was almost covered by the subtropical high causing the local low-pressure vortex to weaken further. The positive abnormal transport in the east side of the key region basically disappeared, and more extreme negative anomalies were seen in the interior and south of the key area (Figure 10C). Without the obstruction of terrain, the water vapor passed directly through the key area to the north, resulting in moisture-positive anomalies in the northwest of the key area. The cyclonic anomalous circulation in the northwest region of the box indicated that the Huang-Huai cyclone of the NO_TP test shifted to the northwest area which was mountainous in the original CTRL test (Figure 10D).

The well-organized mesoscale convective system is the primary producer of extremely heavy rainfall. The variation of the mesoscale

system can be seen in the blue boxes of Figure 10, especially the NO_IF&CK. The divergence of the geostrophic wind was strengthened during NO_IF&CK, and the rainstorm key area was almost covered by the subtropical high. The intensity of the corresponding mesoscale vortex weakened in the area around Zhengzhou (Figure 10C). The max reflectivity of the convective system of NO_IF&CK (Supplementary Figure 1D) also showed that the heavy rain well-organized convective cell was dissipated and the wind speed at the lower level of 850 hPa was significantly reduced.

Compare to the CTRL test, the strong center of reflectivity dispersed and split into two parts in NO_IF_Lev3 (Supplementary Figure 1C). In NO_CK and NO_TP, the convective system moved to the northeast and northwest respectively (Supplementary Figures 1B, E), which coincided with the change of the rain belt.

3.6 Conceptual model of water vapor transport under multi-system configuration during the extreme rainstorm in Henan

Based on the above analysis, the water vapor transport mechanism of the remote extreme typhoon rainstorm under the multi-system interaction is summarized into the following conceptual diagram (Figure 11). The South Asian low pressure, multiple typhoons, and local low vortex formed a triangle region, which constituted the key water vapor supply area for this extreme event. There were two main sources of water vapor in this extreme rainstorm, namely, the west branch and east branch. The abnormal vortex belt of water vapor formed by the zonal distribution of low-latitude multiple vortices resulted in transport eastward from the Indian Ocean. The west typhoon Cempaka in BT acted as a transit station, transporting part of the moisture from low-latitudes to the northern mid-latitudes (west branch) and part to the typhoon In-fa. The water vapor from the Indian and Pacific Oceans converged on the east side of In-fa, and were then continuously transported for a long distance along the northeast channel between the northern side of TC and subtropical high (east branch), causing extreme precipitation under the effect of terrain convergence (Figure 11A).

As the effect of typhoon In-fa was eliminated, Cempaka weakened and the subtropical high extended southward, connecting with the low-latitude subtropical high. At this point, both water vapor branches decreased. The weakening of the west branch was accompanied by the weakening of minor typhoon Cempaka, while the east branch was influenced by the interaction between typhoon In-fa and the subtropical high. The removal of In-fa greatly reduced the pressure gradient in the channel between it and the subtropical high, which further cut the moisture transport within this channel. As a result, the concentrated heavy precipitation became scattered and sparse (Figure 11B).

With the elimination of Cempaka alone, the water vapor transport in the west branch decreased, and some water vapor transferred to the east branch, resulting in a slight increase in the intensity of typhoon In-fa. The increasing and decreasing trends were of comparable intensity. The entry of moisture in the rainstorm area shifted from the south boundary to the east boundary, indicating the eastward displacement of the water vapor branches, manifested in the precipitation distribution as a marked shift of the final precipitation area to the east (Figure 11C).

The elimination of binary typhoons resulted in a pattern similar to the elimination of In-fa alone, but the westward extension of the subtropical high was more significant, and the weakening of moisture transport *via* the west branch and east branch was greatly increased. Without the multi-vortex synergistic transport mechanism, the water vapor from both the Indian Ocean and the West Pacific was reduced, which converged at the base of the subtropical high in the south, then directly entered the North China Plain, with its intensity weakened much (Figure 11D).

The Qinghai-Tibet Plateau played an important role in modulating the water vapor transport in the middle and lower reaches. After the large plateau terrain was eliminated, the northern end of the subtropical high extended further westward, and the Huang-Huai cyclone shifted to the northwest. Moreover, the main water vapor branches of the key precipitation area passed directly through the Taihang Mountains, a barrier that blocked and gathered water vapor. Then the water vapor flowed out of the key area along the north side of the Huang-Huai cyclone, leading to the dispersion of water vapor, thus failing to develop an extremely intense local rainstorm (Figure 11E).

4 Conclusion and discussion

We explored the mechanism of the extreme rainstorm event in Henan with the interaction between the water vapor transport anomalies and the mid-low latitude circulation system. The corresponding BT remote water vapor transport characteristics and the abnormal structure of remote moisture paths were affected by the large plateau terrain. The main conclusions are as follows:

During this extreme rainstorm event on 20 July 2021, the triangular influence domain of water vapor transport composed of the multi-vortex systems at low latitudes and the local low vortex represented the key water vapor supply area. Under the above configuration, the moisture multi-vortex belt transported water vapor from low latitudes to middle latitudes, and the BT produced double moisture transport channels in the east and west.

By separating the individual TC in BT, it is found that the water vapor transport mechanism of each individual was diverse. After eliminating Cempaka, the precipitation area shifted eastward. It was closely related to the modulating effect of Cempaka on the distribution of water vapor input and output in the meridional and zonal directions. After eliminating In-fa, the subtropical high expanded to the south, and Cempaka gradually weakened, which resulted in the reduction of water vapor transport at the southern boundary. The presence of In-fa enhanced the transport effect of BT on water vapor of low-latitude.

When simultaneously removing BT, the water vapor from both the Indian Ocean and the West Pacific all decreased, and the transport of the double moisture channels was reduced remarkably. Due to the lack of multi-vortex synergistic transport mechanism, the local maximum precipitation dropped by about 46%, and the fall area of extremely rainstorms shrank by 86%, which means that the rainstorm pattern disappeared completely.

As the "Asian Water Tower," the Qinghai-Tibet Plateau exerts a modulating effect for the remote typhoon water vapor transport under multi-scale interaction, and its large terrain blocking effect results in an abnormal convergence mechanism for water vapor.

After the influence of the large terrain of the plateau was eliminated, the Huang-Huai cyclone moved to the northeast, and most water vapor passed through the northern mountains and flowed out of the rainfall key area, resulting in water vapor divergence. The precipitation area shifted to the northwest, and its central intensity decreased by about 30%.

Our studies demonstrate the "7.20"extreme precipitation event in Henan had the characteristics of multi-vortex typhoon remote water vapor transport. The BT dominated the remote moisture transport from the South China Sea and the Northwest Pacific Ocean, in which typhoon In-fa played a major role. This impact of BT on large-scale circulation has been demonstrated in moisture sources and moisture proportions of different trajectories experiments (Nie and Sun, 2022; Sun et al., 2023). Compared with the general overview of the BT effect above, our conclusions highlight the specific mechanism of the Western Pacific typhoon in BT. The Western Pacific typhoon not only directly dominated the moisture transport in the Northwest Pacific but also transported water vapor to the South China Sea, which conducted the strength of typhoons and moisture distribution in this region. It is worth noting that our study further demonstrated this conclusion through a quantitative water vapor budget and emphasized the complex effects of plateau terrain and of the subtropical high on the uncertainty of the PRE process.

Finally, the proposed conceptual model provided a multi-system perspective to assess unexpected weather disasters in real-time forecasting caused by remote rainfall effect of TCs, especially the unpredictable effects of double typhoons with multi-vortex water vapor flux structure. In the future, larger sample sizes are required to further investigate the dynamical processes and the source of errors governing the predictability and variability of these contributing factors.

Data availability statement

The raw data supporting the conclusion of this article will be made available by the authors, without undue reservation.

Author contributions

XX conceptualized this study. JT was responsible for methodology, model and data analyses, writing-original drafts, writing-review, editing, and visualization. SZ, HX, and WC contributed to methodology, writing-review, and editing. All authors contributed to the article and approved the submitted version.

Funding

This study was supported by the Second Tibetan Plateau Scientific Expedition and Research (STEP, 2019QZKK0105) program, the S&T Development Fund of CAMS (2022KJ021) and the Major Program of the National Natura Science Foundation of China (91337000).

Conflict of interest

The authors declare that the research was conducted in the absence of any commercial or financial relationships that could be construed as a potential conflict of interest.

Publisher's note

All claims expressed in this article are solely those of the authors and do not necessarily represent those of their affiliated organizations, or those of the publisher, the editors and the reviewers. Any product that may be evaluated in this article, or claim that may be made by its manufacturer, is not guaranteed or endorsed by the publisher.

Supplementary material

The Supplementary Material for this article can be found online at: https://www.frontiersin.org/articles/10.3389/feart.2023.1106990/full#supplementary-material

References

Bosart, L. F., Cordeira, J. M., Galarneau, T. J., Moore, B. J., and Archambault, H. M. (2012). An analysis of multiple predecessor rain events ahead of tropical cyclones ike and lowell: 10–15 september 2008. *Mon. Wea. Rev.* 140 (4), 1081–1107. doi:10.1175/MWR-D-11-00163.1

Chen, T., and Wu, C. (2016). The remote effect of Typhoon Megi (2010) on the heavy rainfall over northeastern Taiwan. *Mon. Wea. Rev.* 144 (9), 3109–3131. doi:10.1175/MWR-D-15-0269.1

Chou, Y. (1997). Weather patterns and interannual variations of typhoon torrential rain during midsummer in North China (in Chinese). *Meteor. Mon.* 07, 3–9. doi:10.7519/j.issn.1000-0526.1997.7.001

Collins, W. D., Rasch, P. J., Boville, B. A., Hack, J. J., McCaa, J. R., Williamson, D. L., et al. (2004). Description of the NCAR community atmosphere model (CAM 3.0). *NCAR Tech. Note NCAR/TN-464+ Str.* 226, 1326–1334.

Cote, M. R. (2007). Predecessor rain events in advance of tropical cyclones. M.S. thesis. New York: Dept. of Atmospheric and Environmental Sciences. University at Albany, State University, 200.

Deng, L., Feng, J., Zhao, Y., Bao, X., Huang, W., Hu, H., et al. (2022). The remote effect of binary Typhoon Infa and Cempaka on the "21.7" heavy rainfall in Henan Province, China. *J. Geophys. Res.* 127, e2021JD036260. doi:10.1029/2021JD036260

Galarneau, T. J., Bosart, L. F., and Schumacher, R. S. (2010). Predecessor rain events ahead of tropical cyclones. *Mon. Wea. Rev.* 138 (8), 3272–3297. doi:10.1175/2010MWR3243.1

Hersbach, H., Bell, B., Berrisford, P., Hirahara, S., Horányi, A., Muñoz-Sabater, J., et al. (2020). The ERA5 global reanalysis. *Q. J. Roy. Meteor. Soc.* 146 (730), 1999–2049. doi:10.1002/qj.3803

Hong, S. Y., and Lim, J. O. J. (2006). The WRF single-moment 6-class microphysics scheme (WSM6). *J. Korean Meteor. Soc.* 42 (2), 129–151.

Hua, S., Xu, X., and Chen, B. (2020). Influence of multiscale orography on the initiation and maintenance of a precipitating convective system in north China: A case study. *J. Geophys. Res.* 125 (13), e2019JD031731. doi:10.1029/2019JD031731

Kain, J. S. (2004). The kain–fritsch convective parameterization: An update. *J. Appl. Meteor.* 43 (1), 170–181. doi:10.1175/1520-0450(2004)043<0170:TKCPAU>2.0.CO;2

Li, C., Zuo, Q., Xu, X., and Gao, S. (2016). Water vapor transport around the Tibetan Plateau and its effect on summer rainfall over the Yangtze River valley. *J. Meteorol. Res.* 30 (4), 472–482. doi:10.1007/s13351-016-5123-1

Liang, X., Xia, R., Bao, X., Zhang, X., Wang, X., Su, A., et al. (2022). Preliminary investigation on the extreme rainfall event during July 2021 in Henan Province and its multi-scale processes. *Chin. Sci. Bull.* 67 (10), 997–1011. doi:10.1360/TB-2021-0827

Lin, Y., and Wu, C. (2021). Remote rainfall of Typhoon Khanun (2017): Monsoon mode and topographic mode. *Mon. Wea. Rev.* 149 (3), 733–752. doi:10.1175/MWR-D-20-0037.1

Low-Nam, S., and Davis, C. (2001). "Development of a tropical cyclone bogussing scheme for the MM5 system," in *11th PSU–ncar mesoscale model users' workshop* (Boulder, CO: PSU–NCAR), 130–134.

Nie, Y., and Sun, J. (2022). Moisture sources and transport for extreme precipitation over Henan in July 2021. *Geophys. Res. Lett.* 49 (4), e2021GL097446. doi:10.1029/2021GL097446

Pleim, J. E. (2007a). A combined local and nonlocal closure model for the atmospheric boundary layer. Part I: Model description and testing. *J. Appl. Meteor. Clim.* 46 (9), 1383–1395. doi:10.1175/JAM2539.1

Pleim, J. E. (2007b). A combined local and nonlocal closure model for the atmospheric boundary layer. Part II: Application and evaluation in a mesoscale meteorological model. *J. Appl. Meteor. Clim.* 46 (9), 1396–1409. doi:10.1175/JAM2534.1

Pleim, J. E. (2006). A simple, efficient solution of flux–profile relationships in the atmospheric surface layer. *J. Appl. Meteor. Clim.* 45 (2), 341–347. doi:10.1175/JAM2339.1

Ran, L., Li, S., Zhou, Y., Yang, S., Ma, S., Zhou, K., et al. (2021). Observational analysis of the dynamic, thermal, and water vapor characteristics of the "7.20" extreme rainstorm event in Henan province (in Chinese). *Chin. J. Atmos. Sci.* 45 (6), 1366–1383. doi:10.3878/j.issn.1006-9895.2109.21160

Schumacher, R. S. (2011). Ensemble-based analysis of factors leading to the development of a multiday warm-season heavy rain event. *Mon. Wea. Rev.* 139 (9), 3016–3035. doi:10.1175/MWR-D-10-05022.1

Shen, Y., Zhao, P., Pan, Y., and Yu, J. (2014). A high spatiotemporal gauge-satellite merged precipitation analysis over China. *J. Geophys. Res.* 119 (6), 3063–3075. doi:10.1002/2013JD020686

Shi, X., Wang, Y., and Xu, X. (2008). Effect of mesoscale topography over the Tibetan plateau on summer precipitation in China: A regional model study. *J. Geophys. Res.* 35 (19), L19707. doi:10.1029/2008GL034740

Skamarock, W. C., Klemp, J. B., Dudhia, J., Gill, D. O., Liu, Z., Berner, J., et al. (2019). *A description of the advanced research WRF model version 4.* Boulder, CO, USA: National Center for Atmospheric Research, 145.

Sun, J., Fu, S., Wang, H., Zhang, Y., Chen, Y., Su, A., et al. (2023). Primary characteristics of the extreme heavy rainfall event over Henan in July 2021. *Atmos. Sci. Lett.* 24 (1), e1131. doi:10.1002/asl.1131

Sun, J., and Zhao, S. (2000). Diagnoses and simulations of typhoon (Tim) landing and producing heavy rainfall in China (in Chinese). *Chin. J. Atmos. Sci.* 24 (2), 15. doi:10.3878/j.issn.1006-9895.2000.02.11

Wu, C. C., Cheung, K. K., and Lo, Y. Y. (2009). Numerical study of the rainfall event due to the interaction of Typhoon Babs (1998) and the northeasterly monsoon. *Mon. Wea. Rev.* 137 (7), 2049–2064. doi:10.1175/2009MWR2757.1

Xiu, A., and Pleim, J. E. (2001). Development of a land surface model. Part I: Application in a mesoscale meteorological model. *J. Appl. Meteor. Clim.* 40 (2), 192–209. doi:10.1175/1520-0450(2001)040<0192:DOALSM>2.0.CO;2

Xu, H., and Du, B. (2015). The impact of typhoon Danas (2013) on the torrential rainfall associated with typhoon Fitow (2013) in East China. *Adv. Meteorol.* 2015, 1–11. doi:10.1155/2015/383712

Xu, H., Duan, Y. H., Li, Y., and Wang, H. (2022b). Indirect effects of binary typhoons on an extreme rainfall event in henan province, China from 19 to 21 july 2021: 2. Numerical study. *J. Geophys. Res.* 127, 36083. doi:10.1029/2021JD036083

Xu, H., Duan, Y. H., and Xu, X. D. (2022a). Indirect effects of binary typhoons on an extreme rainfall event in henan province, China from 19 to 21 july 2021: 1. Ensemble-Based analysis. *J. Geophys. Res. e2021JD036265* 127, 36265. doi:10.1029/2021JD036265

Xu, X., Chen, L., Wang, X., Miao, Q., and Tao, S. (2004). Moisture transport source/sink structure of the Meiyu rain belt along the Yangtze River valley (in Chinese). *Chin. Sci. Bull.* 49, 181–188. doi:10.1360/03wd0047

Xu, X., Dong, L., Zhao, Y., and Wang, Y. (2019). Effect of the asian water tower over the Qinghai-Tibet Plateau and the characteristics of atmospheric water circulation. *Chin. Sci. Bull.* 64 (27), 2830–2841. doi:10.1360/TB-2019-0203

Yin, J., Gu, H., Liang, X., Miao, Y., Sun, J., Xie, Y., et al. (2021). A possible dynamic mechanism for rapid production of the extreme hourly rainfall in Zhengzhou City on 20 July 2021. *J. Meteorol. Res.* 36 (1), 6–25. doi:10.1007/s13351-022-1166-7

Yu, C., and Cheng, L. (2014). Dual-Doppler-derived profiles of the southwesterly flow associated with southwest and ordinary typhoons off the southwestern coast of Taiwan. *J. Atmos. Sci.* 71 (9), 3202–3222. doi:10.1175/JAS-D-13-0379.1

Zhang, Y., Yu, H., Zhang, M., Yang, Y., and Meng, Z. (2022). Uncertainties and error growth in forecasting the record-breaking rainfall in Zhengzhou, Henan on 19–20 July 2021. *Sci. China Earth Sci.* 65 (10), 1903–1920. doi:10.1007/s11430-022-9991-4

Zhao, Y., Chen, D., Li, J., Chen, D., Chang, Y., Li, J., et al. (2020). Enhancement of the summer extreme precipitation over North China by interactions between moisture convergence and topographic settings. *Clim. Dyn.* 54 (5–6), 2713–2730. doi:10.1007/s00382-020-05139-z

Zhao, Y., Xu, X., Zhao, T., and Yang, X. (2019). Effects of the Tibetan Plateau and its second staircase terrain on rainstorms over North China: From the perspective of water vapour transport. *Int. J. Climatol.* 39 (7), 3121–3133. doi:10.1002/joc.6000

frontiers | Frontiers in Earth Science

TYPE Original Research
PUBLISHED 15 March 2023
DOI 10.3389/feart.2023.1162220

OPEN ACCESS

EDITED BY
Shenming Fu,
Institute of Atmospheric Physics (CAS), China

REVIEWED BY
Danqiong Dai,
Institute of Atmospheric Physics (CAS), China
Shuanglei Wu,
The University of Queensland, Australia

*CORRESPONDENCE
Ya Huang,
hygccw@163.com

SPECIALTY SECTION
This article was submitted to Atmospheric Science, a section of the journal Frontiers in Earth Science

RECEIVED 09 February 2023
ACCEPTED 03 March 2023
PUBLISHED 15 March 2023

CITATION
Yang J, Huang Y, Li G and Li Y (2023), Changes of extreme precipitation in the middle and lower reaches of the Yangtze River and their correlation with atmospheric circulation.
Front. Earth Sci. 11:1162220.
doi: 10.3389/feart.2023.1162220

Changes of extreme precipitation in the middle and lower reaches of the Yangtze River and their correlation with atmospheric circulation

Jing Yang[1], Ya Huang[1,2]*, Guiping Li[1] and Yanping Li[1,3]

[1]College of Oceanography, Hohai University, Nanjing, China, [2]Guangxi Key Laboratory of Disaster Prevention and Engineering Safety, Guangxi University, Nanning, China, [3]Global Institute for Water Security, University of Saskatchewan, Saskatoon, SK, Canada

Under the backdrop of climate change, the rising frequency and intensity of extreme precipitation events in the middle and lower Yangtze River (MLYR) region are causing serious consequences and economic losses. To assess regional risk and understand the impact of atmospheric circulation on extreme precipitation, it's crucial to analyze the spatial and temporal fluctuations of these events, focusing on the time-frequency phase relationship. Using the observed precipitation data from 1979 to 2015, nine extreme precipitation indices were calculated and a trend analysis and wavelet coherence analysis were performed to evaluate their variation. The results show that: 1) an overall increase in the frequency, intensity, and duration of precipitation in the MLYR, with significant rises in the wet daily precipitation and highest precipitation amount in 1-day period; 2) a higher likelihood of extreme precipitation events in the southeast of the MLYR, and an uneven spatial distribution; 3) the Western Pacific Subtropical High (WPSH), the South China Sea high (SCSH), and the East Asian westerly jet (EAJ) all play a role in precipitation changes in the MLYR, with the WPSH having the most significant impact, followed by the SCSH, and the EAJ being weaker. The results deepen our understanding of the various characteristics and causes of extreme precipitation in the MLYR.

KEYWORDS

extreme precipitation, spatial-temporal variation characteristics, atmospheric circulation, Yangtze River, climate change

1 Introduction

The occurrence of extreme precipitation events has become more frequent with global climate change, leading to significant human, economic, and societal losses (Liang, 2022). The study of extreme precipitation events has gained worldwide attention with a recent rise in frequency and intensity reported in various regions, including the United States (Gizaw et al., 2021), Japan (Hatsuzuka et al., 2021), Australia (Liu et al., 2020), India (Saha and Sateesh, 2022) and others. Several studies have shown that while extreme precipitation in China follows the global trend, it also exhibits regional and local differences (Li Y et al., 2021). For instance, the indices of precipitation intensity and frequency in Guangdong-Hong Kong-Macao Greater Bay and the middle and lower reaches of the Yangtze River (MLYR) have been increasing due to urbanization (Zhou et al., 2022). Meanwhile, the contribution rate of extreme precipitation in northwest China has risen due to afforestation (Zhang et al.,

2007). Extreme precipitation can lead to disastrous floods and mudslides that impact agriculture, industry, transportation and cause huge economic losses (Chou et al., 2018). Hence, research into the spatial and temporal variations of extreme precipitation and its driving forces is crucial for effective water resource management, rational disaster prevention, and mitigation policy enactment.

Influenced by monsoon activities (Jin and Zhao, 2012), the MLYR exhibits unique climatic characteristics and is subject to complex precipitation mechanisms, resulting in frequent flood disasters (Gill et al., 2020). Research indicates that precipitation in the MLYR is closely linked to the Western Pacific Subtropical High (WPSH) and the South China Sea high (SCSH). The South China Sea serves as one of the sources of water vapor for MLYR, transporting it to eastern China through the summer monsoon (Que et al., 2016; Chu et al., 2021). Additionally, the location of WPSH highly affects precipitation in the MLYR by controlling the position of the precipitation belt and transporting water vapor along the edge of the subtropical high (Tian et al., 2000). The East Asian westerly jet (EAJ) is another key system that affects precipitation in the MLYR, with divergent updrafts occurring on either side of the upper-level jet inlet and outlet area (Wang and Zuo, 2016; Wang et al., 2018), which are conducive to the formation and maintenance of precipitation in the MLYR. In conclusion, the SCSH and WPSH can affect regional precipitation by transporting water vapor, while the EAJ affects it through favorable dynamic conditions. Although various researchers have studied the impact of atmospheric circulation from different perspectives, the phase relationship and periodic characteristics between precipitation and atmospheric circulation remain underexplored. Additionally, most studies focused on the time-frequency phase relationship have neglected the effect of the SCSH and the EAJ at high latitudes on extreme precipitation in the MLYR.

This study aims to thoroughly examine the spatial-temporal distribution and time-frequency phase relationship of extreme precipitation in the MLYR and its relationship with large-scale atmospheric circulation factors, including the WPSH, SCSH, and EAJ. The study will analyze the spatial-temporal variations of extreme precipitation indices using observation data from stations and conduct a Mann-Kendall test (MK test) to determine the trend of extreme precipitation in the MLYR. Finally, wavelet coherence analysis will be applied to examine the time-frequency phase correlation between extreme precipitation indices and atmospheric circulation indices such as the WPSH intensity index, the WPSH area index, the South China Sea Subtropical High Intensity index (SCSHI), and the East Asian Westerly Jet Intensity index (EASJI). This research will deepen our understanding of the various characteristics and causes of extreme precipitation in the MLYR.

2 Data and methods

2.1 Study area

The MLYR, which is located in the Yangtze River basin east of Yichang, Hubei province (as shown in Figure 1), has a typical subtropical monsoon climate (Ye et al., 2017). The MLYR experiences convergence of the summer monsoon and cold air from high latitudes, leading to the formation of Meiyu in June and July each year and resulting in a rainy summer season (Niu et al., 2021; Wang et al., 2021). The MLYR is known for its frequent drought and flood disasters, which are primarily caused by the uneven distribution of precipitation (Qi et al., 2021). Thus, it is of great significance to further study the spatial-temporal variation characteristics and the driving forces of extreme precipitation, which is possible to worsen the uneven temporal and spatial distribution of precipitation in the MLYR.

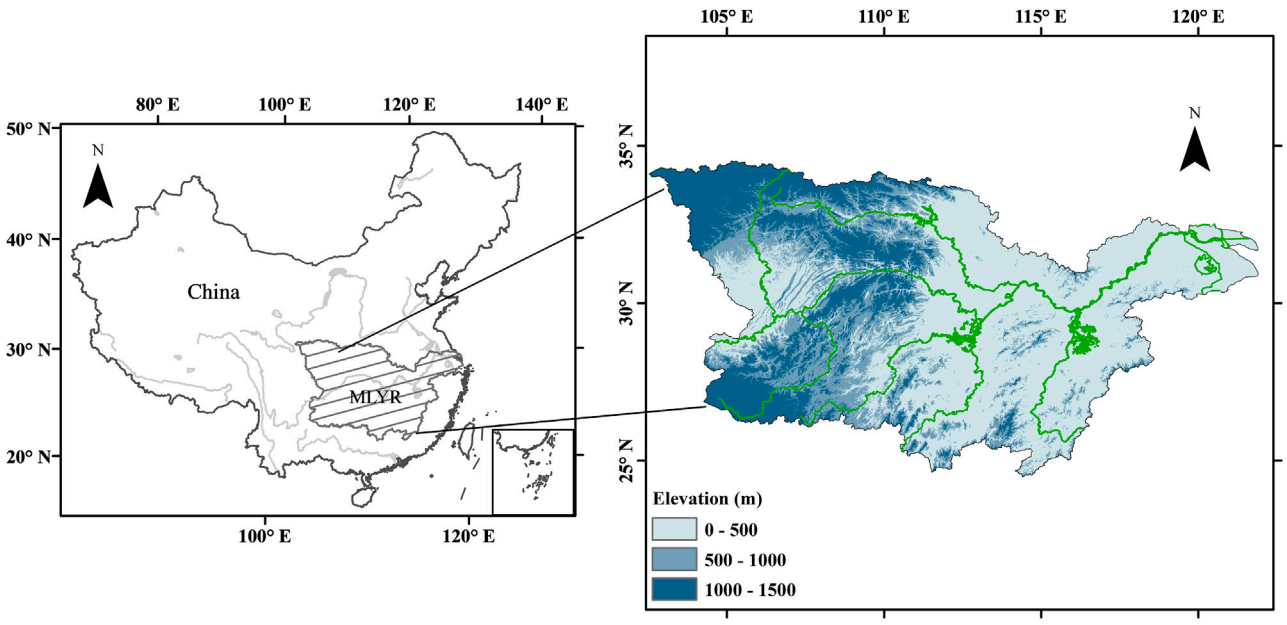

FIGURE 1
The MLYR domain and topography (m).

TABLE 1 Definition of the precipitation indices used in this study.

Index type	Name (Abbreviation)	Definition	Units
Duration Indices	Consecutive dry days (CDD)	Maximum length of dry spell (RR <1 mm)	day
	Consecutive wet days (CWD)	Maximum length of wet spell (RR ≥1 mm)	day
Frequency Indices	Extremely heavy precipitation days (R25 mm)	Number of days per year with RR ≥25 mm	day
Intensity Indices	Precipitation on very wet days (R95)	Total daily precipitation exceeding 95% of the quantile (1979–2015)	mm
	Precipitation on extremely wet days (R99)	Total daily precipitation exceeding 99% of the quantile (1979–2015)	mm
	Highest precipitation amount in 1-day period (RX1day)	Annual maximum precipitation on 1-day intervals	mm
	Highest precipitation amount in 5 consecutive days (RX5day)	Highest precipitation amount in 5 consecutive days	mm
	Simple daily intensity index (SDII)	Annual total precipitation divided by number of wet days (≥1 mm)	mm
	Annual total wet-day precipitation (PRCPTOT)	Annual total precipitation from days ≥1 mm	mm

2.2 Data sources

In this study, the daily precipitation indices were derived from the CN05 dataset, which spans from 1979 to 2015 and was provided by the National Climate Center of China with a horizontal resolution of 0.25°×0.25° (Shang et al., 2020). The dataset is generated by applying the thin-disk spline function method (ANUSPLIN) and the angular distance weight method (ADW) and has been widely used for climate assessments in China (Hu and Wang, 2021; Li et al., 2022).

The WPSH area index, WPSH intensity index, and SCSHI were obtained from the China Meteorological Administration's website to analyze their correlations with extreme precipitation indices. To quantify the meandering of the westerly jet, the standardized value of the sum of the latitudinal winds at 200 hPa in the region of 27.5°–60°N, 70°–120°E, where the East Asian Westerly Jet (EAJ) is typically located (Chen et al., 2020), was defined as the East Asian Westerly Jet Intensity index (EASJI).

2.3 Precipitation indices

This study analyzes the duration, intensity, and frequency of extreme precipitation events in the MLYR based on various indices defined by the Expert Team on Climate Change Detection and Indices (ETCCDI) (Thomas and David, 1999). These indices include Consecutive dry days (CDD), Consecutive wet days (CWD), Extremely heavy precipitation days (R25 mm), Simple daily intensity index (SDII), Highest precipitation amount in 1-day period (RX1day), Highest precipitation amount in 5 consecutive days (RX5day), Precipitation on very wet days (R95), Precipitation on extremely wet days (R99) and wet daily precipitation (PRCPTOT). The definition of these precipitation indices are shown in Table 1.

2.4 Wavelet analysis

Wavelet coherence refers to the similarity of two synchronized time series in the time-frequency domain, in the region of common variation (not necessarily with high energy). The wavelet coherence spectrum can reveal not only the common high-energy region and phase relationship of the two-time series, but also measure the proximity of local correlation between them in the time-frequency domain (Juthasirorat et al., 2021; Zhao and Luo, 2021).

For time series of two simultaneous records x_n, y_n, the wavelet coherence coefficient is defined as:

$$R_{\mathrm{n}}^2(s) = \frac{\left|S\left(s^{-1}W_n^{XY}(s)\right)\right|^2}{S\left[s^{-1}\left|W_n^X(s)\right|^2\right] \times S\left[s^{-1}\left|W_n^Y(s)\right|^2\right]} \tag{1}$$

where s is the circular standard deviation; W_n^X, W_n^Y, W_n^{XY} are wavelet transform and cross wavelet transform of time series x_n, y_n, respectively; S is a smooth operator, which is defined as follows:

$$S(W) = S_{scale}\{S_{time}[W_n(s)]\} \tag{2}$$

where S_{scale} denotes a smooth along the wavelet scale axis; the expression of S_{time} is as follows:

$$S_{scale}(W)|_s = \left[W_n(s) \times c_1 \frac{-t^2}{2s^2}\right]\Big|_s \tag{3}$$

$$S_{time}(W)|_s = \left[W_n(s) \times c_2 \prod(0.6s)\right]\Big|_n \tag{4}$$

where c_1, c_2 is a dimensionless constant, determined by the value of the specific time series and $\prod$ is a rectangular function. In Formula 4, the coefficient is 0.6, which is the Morlet wavelet scale decorrelation length determined empirically.

2.5 Mann–Kendall test

The MK test is used to test the significance of the change trend of extreme precipitation indices in the time series (Bhatti et al., 2020). One advantage of this method is that it is suitable for sequences that do not follow a normal distribution. Let a stationary sequence be $x_1, x_2, x_3, x_4, \ldots, x_n$, the statistic S is defined as (Ostadi et al., 2021):

$$S = \sum_{i=1}^{n-1} \sum_{j=i+1}^{n} Sgn\left(x_i - x_j\right) \tag{5}$$

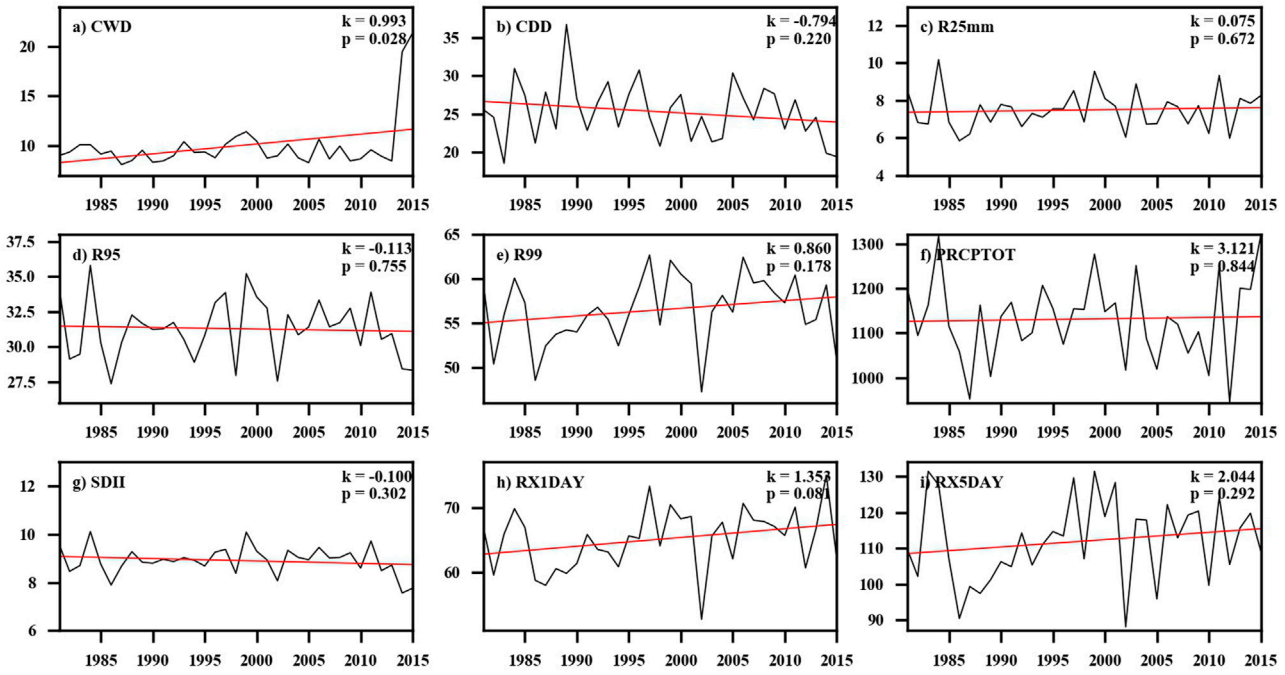

FIGURE 2
Time series of precipitation indices over the MLYR from 1979 to 2015. The red line indicates a linear trend. **(A)** CWD; **(B)** CDD; **(C)** R25mm; **(D)** R95; **(E)** R99; **(F)** PRCPTOT; **(G)** SDII; **(H)** RX1DAY; **(I)** RX5DAY.

$$\mathrm{Sgn}\left(x_i - x_j\right) = \begin{cases} 1 & x_i > x_j \\ 0 & x_i = x_j \\ -1 & x_i < x_j \end{cases} \tag{6}$$

where x_i and x_j are the data at moment i and j, respectively; n is the data length of the time series.

The variance of the statistic S is:

$$Variance\,(S) = \frac{m(m-1)(2m+5)}{18} \tag{7}$$

The expression for the standardized test statistic Z is as follows:

$$Z = \begin{cases} \dfrac{S-1}{\sqrt{Variance\,(S)}} & S > 0 \\ 0 \quad S = 0 & \\ \dfrac{S+1}{\sqrt{Variance\,(S)}} & S < 0 \end{cases} \tag{8}$$

When $Z>0$ and $|Z|\leq 1.96$ mean that the series is a significant upward trend, when $Z<0$ and $|Z|\leq 1.96$, the series is a significant downward trend.

3 Results

3.1 Temporal variation characteristics of extreme precipitation indices

During 1979–2015, the frequency, intensity, and duration of precipitation in the MLYR presented an overall rising trend. Among the duration indices, CWD fluctuated between 9 and 20 days with a significant rising trend of 0. 99 days/10 years (Figure 2A), while CDD, ranging from 16 days to 35 days, showed a decreasing trend of −0.79 days/10 years (Figure 2B), indicating that the persistence of precipitation had intensified significantly and the continuous drought had weakened since 1979. Meanwhile, R25 mm showed a slightly increasing trend of 0.07 days/10 years (Figure 2C), suggesting that extreme precipitation had become more frequent. For indices of percentile intensity, R95 and R99 showed a downward trend and an upward trend, respectively, with slopes of −0.11 mm/10 years and 0.86 mm/10 years (Figures 2D,E). In intensity indices, PRCPTOT, RX1day, and RX5 day all presented an increasing trend, with climate tendency rates of 3.12 mm/10 years, 1.35 mm/10 years, and 2.04 mm/10 years, respectively, among which RX1day passed the 90% significance test (Figures 2F–I). In general, a consistently increasing trend of precipitation indices was observed in the MLYR from 1979 to 2015, expect for CDD, indicating that the annual mean precipitation, continuous heavy precipitation, and extreme precipitation in the MLYR tend to ascent from 1979.

3.2 Spatial distribution of precipitation indices

Continuous heavy precipitation tended to occur in the southeast of MLYR, while the longest durations of drought events occurred in the northwest of MLYR. The spatial distributions of different precipitation indices in the MLYR from 1979 to 2015 are shown in Figure 3. Among duration indices, the minimum value of CWD was 7 days, while the maximum value was 17 days. The high values mainly concentrated in the southeast of the MLYR, while the low

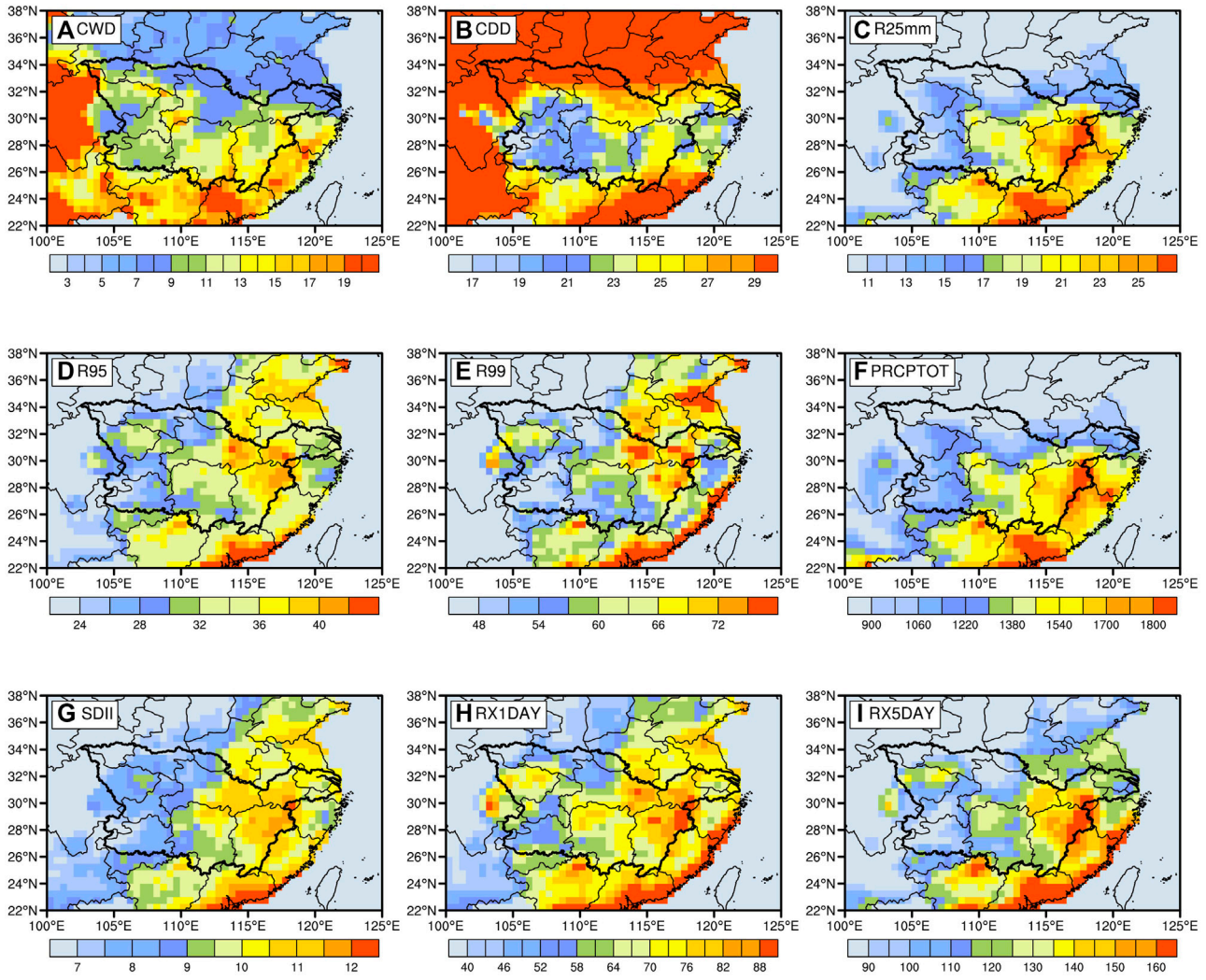

FIGURE 3
Spatial distributions of annual mean precipitation indices over the MLYR from 1979 to 2015. The area surrounded by the thick black line is the MLYR. **(A)** CWD; **(B)** CDD; **(C)** R25mm; **(D)** R95; **(E)** R99; **(F)** PRCPTOT; **(G)** SDII; **(H)** RX1DAY; **(I)** RX5DAY.

values were distributed in the Han River basin, located northwest of MLYR, and the lower reaches of the Yangtze River (LRYR), located in the northeast of MLYR (Figure 3A). The spatial distribution of CWD presented a downward trend from the southeast to the northwest of the MLYR. Meanwhile, CDD varied from seventeen to 29 days and presented an opposite spatial distribution of CWD, with the high values mainly distributed in the Han River basin and the low-value areas concentrated in the Dongting Lake basin in the southwest of MLYR (Figure 3B). The duration is a critical factor in the occurrence of catastrophic rainstorms and drought events, so more attention should be paid to flood prevention in the southeast of MLYR and the supply of water resources in the northwest of MLYR.

The frequency and intensity of precipitation in the MLYR present similar spatial distribution characteristics, which decrease from the southeast coast to the northwest inland. Among indices regarding the frequency of extreme precipitation, the high values of R25 mm are centered around the Poyang Lake basin in the southeast of MLYR, while the low value is concentrated in the Han River basin and LRYR, with only single-digit magnitudes in some regions (Figure 3C). For indices of precipitation intensity, the high-value areas of R95 and R99 are concentrated in the Poyang Lake basin, while the low-value regions are located in the Han River basin and the Dongting Lake basin (Figures 3D,E). The spatial distribution characteristics of PRCPTOT are more similar to that of R25 mm, with high values concentrated in the southeast of MLYR (Figure 3F). Meanwhile, SDII, RX1day, and RX5day have similar spatial distributions with a descending trend from the southeast to the northwest of the MLYR (Figures 3G–I). The areas with large extreme precipitation indices are mainly concentrated in the Poyang Lake basin, while the areas with low values were mainly concentrated in the Han River Basin.

The overall trends of the extreme precipitation indices in the MLYR from 1979 to 2015 are upward except for CDD, which is conducive to aggravating the uneven distribution of precipitation. Figure 4 illustrates the spatial distribution of the variation tendency of extreme precipitation indices in the MLYR. Among duration

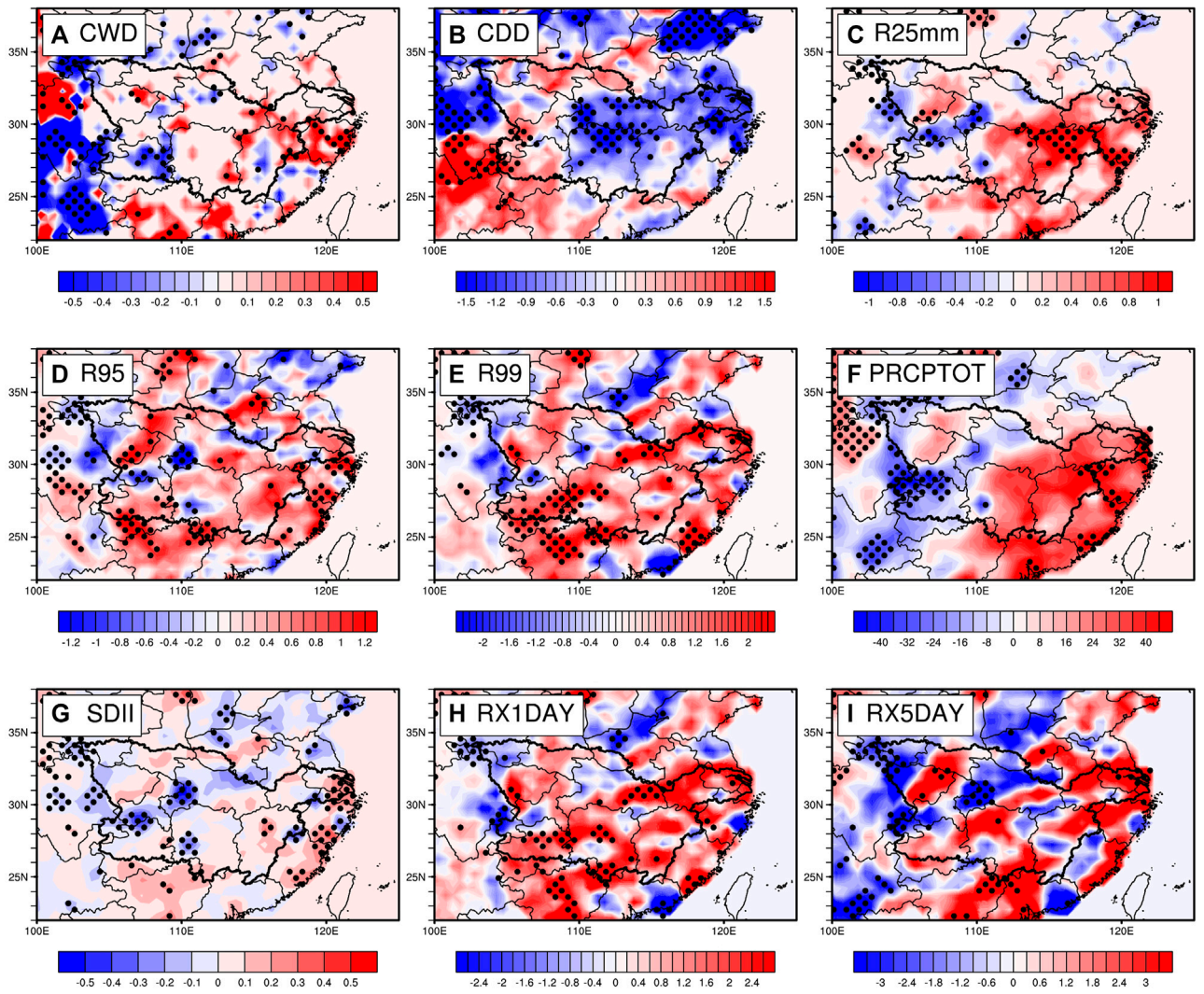

FIGURE 4
Spatial distributions of the variation tendency of annual mean precipitation indices over the MLYR from 1979 to 2015. The area surrounded by the thick black line is the MLYR. The dotted areas are indicated to pass the 95% confidence test. **(A)** CWD; **(B)** CDD; **(C)** R25mm; **(D)** R95; **(E)** R99; **(F)** PRCPTOT; **(G)** SDII; **(H)** RX1DAY; **(I)** RX5DAY.

indices, the variation trend of CWD decreased from the southeast to the northwest of the MLYR and the growth trend of CWD was centered over the Poyang Lake Basin, while the downward trend was mainly distributed in the Han River Basin and the lower reaches of the Dongting Lake Basin (Figure 4A). CDD diminished in most regions, but no region passed the significance test (Figure 4B). For the extreme precipitation frequency index, R25 mm showed a consistent upward trend in most regions of the MLYR, and the dramatic growth trend was mainly centered over the Poyang Lake Basin and the Taihu Lake Basin, indicating that the extreme heavy precipitation days in these regions tend to increase continuously from 1979 to 2015. The Han River Basin and some parts of the Dongting Lake Basin showed an insignificant moderating trend with a rate of −0.6%/10a (Figure 4C). Among extreme precipitation intensity indices, R95 and R99 have a similar spatial distribution which shows a continuous upward trend in most areas (Figures 4D,E). Meanwhile, PRCPTOT tended to increase in the eastern coast of MLYR (Figure 4F), which was also the region with the highest annual average precipitation (Figure 3F). With the exception of Yichang province, SDII presented a slight upward trend in most regions (Figure 4G), and the spatial distribution of the trends of RX1day and RX5day was relatively complex, showing a declining trend in the lower reaches of Dongting Lake and the Han River, and an insignificant upward trend in most regions of Poyang Lake, Taihu, and lower reaches of the Yangtze River (Figures 4H,I).

3.3 Response of extreme precipitation indices to atmospheric circulation factors

The precipitation indices regarding extreme precipitation are positively correlated with WPSH and SCSH, while there is a difference in the correlation with EAJ (Table 2). R25 mm is significantly affected by the area ($r = 0.6$, $p < 0.05$) and the

TABLE 2 The correlation coefficient of atmospheric circulation indices with annual mean precipitation indices in the MLYR from 1979 to 2015.

Index	CDD	CWD	R25 mm	R95	R99	PRCPTOT	SDII	RX1DAY	RX5DAY
WPSH area	0.08	0.35**	0.60**	0.41***	0.37**	0.49***	0.41**	0.38**	0.34**
WPSH intensity	0.05	0.36**	0.57***	0.38**	0.33*	0.47***	0.36**	0.35**	0.33**
SCSHI	0.09	0.35**	0.69***	0.46***	0.35**	0.59***	0.45***	0.38**	0.44***
EASJI	−0.12	0.15	0.32**	0.13	−0.07	0.30*	0.25	−0.09	0.07

*, **, *** indicates a confidence level of 90%, 95%, and 99% respectively.

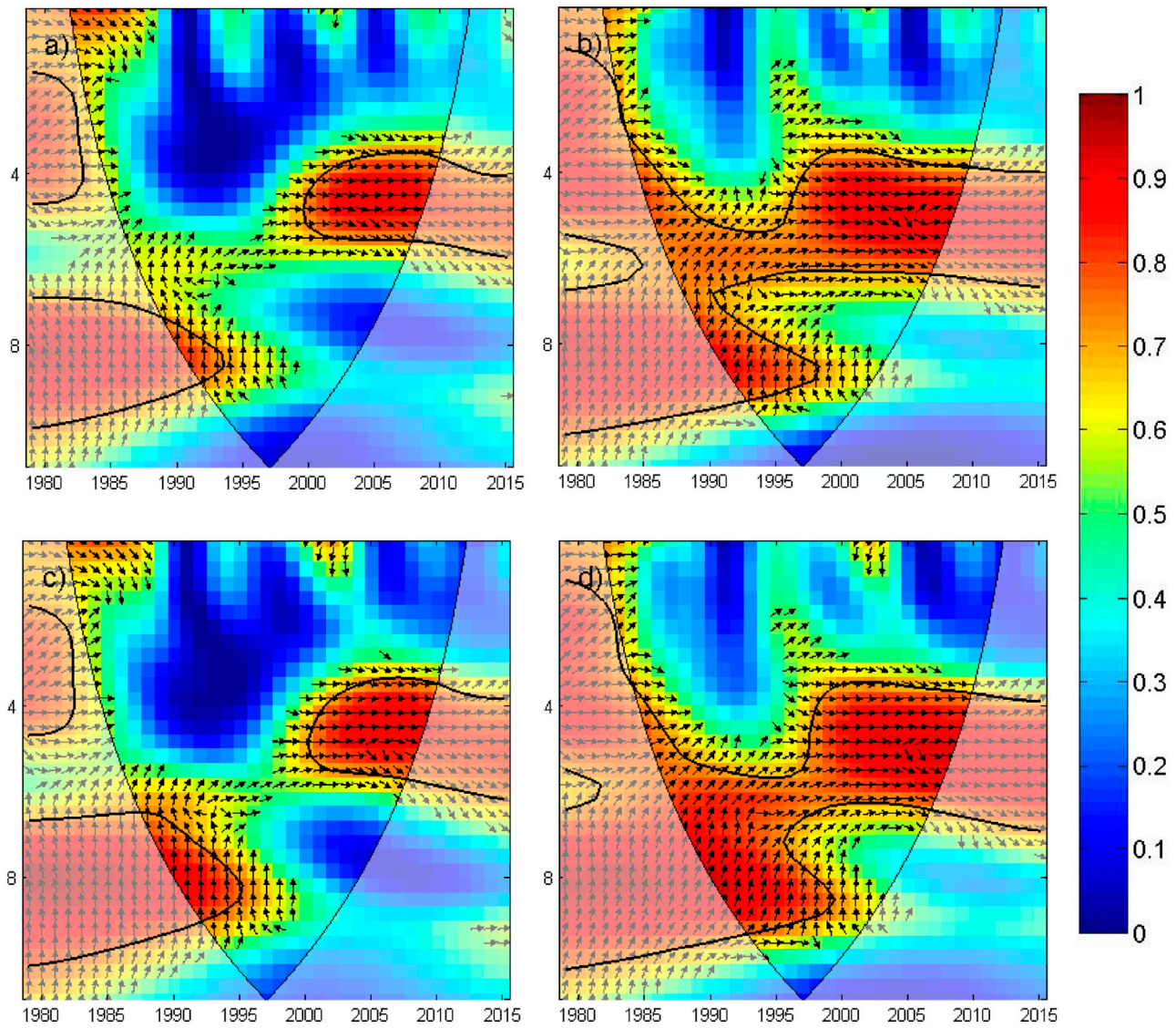

FIGURE 5
Wavelet coherent spectra of annual mean precipitation indices and WPSH over the MLYR from 1979 to 2015: **(A)** PRCPTOT and WPSH area, **(B)** R25 mm and WPSH area, **(C)** PRCPTOT and WPSH intensity, **(D)** R25 mm and WPSH intensity.

intensity (r = 0.57, $p < 0.01$) of the WPSH, indicating that the extreme precipitation in the MLYR is significantly affected by the activity of the WPSH. Meanwhile, a high level of correlation exists between PRCPTOT and WPSH area (r = 0.49, $p < 0.01$), WPSH intensity (r = 0.47, $p < 0.01$), indicating that there is a significant positive correlation between total precipitation and the activity of the WPSH. In terms of SCSHI, which lacks research in previous studies, it is significantly correlated with R25 mm (r = 0.69, $p < 0.01$) and PRCPTOT (r = 0.59, $p < 0.01$). Moreover, there is a significant positive correlation between the EASJI and R25 mm, as well as

EASJI and PRCPTOT, while a negative correlation exists between the EASJI and CDD, R99, RX1day. However, none of the negative correlations pass the significance test and the correlation coefficients are quite small.

Based on the wavelet coherence analysis, the relationship between large-scale climatic factors and extreme precipitation indices in the time-frequency domain is studied. All climate indices are calculated from annual averages. The area surrounded by the tapered thin arc represents the effective spectral value, while the rest areas represent the invalid spectral value. Regions surrounded by a thick line indicate that they pass the test of the red noise standard spectrum at the 0.05 significance level. The arrows indicate the phase relationship between the two signal sequences, with the arrows to the right (left) indicating that the extreme precipitation indices and the atmospheric circulation factors are in the same (anti) phase. The downward (upward) arrow indicates that the phase difference between the extreme precipitation indices and the atmospheric circulation factor is 90°, meaning that the precipitation is 1/4 cycle ahead (later) than the circulation in the time series. Warm colors indicate a strong correlation, while cold colors indicate a weak correlation. Two signal sequences with significant correlation and large correlation coefficient in Table 2 are selected for wavelet coherence analysis to study the phase relationship between extreme precipitation and atmospheric circulation.

The precipitation in the MLYR is prone to trigger and intensify when the area of WPSH expands. Figure 5 illustrates the wavelet power spectrum of WPSH and precipitation indices. During 1987–1993, PRCPTOT and the WPSH area index have a significant resonance period of 8–10 years, and the phase difference is 90°, indicating that the variation of the area of WPSH precedes that of PRCPTOT. From 1998 to 2008, there exists a significant positive correlation resonance period with a time scale of 4–6 years, and the correlation coefficient is as high as 0.9. The arrow pointing to the right indicates that the area of the WPSH changed simultaneously with PRCPTOT (Figure 5A). Meanwhile, there is a significant resonance period between R25 mm and the area of the WPSH on a time scale of 4–10a from 1985 to 2009, and the correlation coefficient reaches 0.9, indicating a continuous influence of WPSH activity on the frequency of extreme precipitation (Figure 5B).

The intensification of WPSH leads to an increase in total precipitation and the frequency of extreme precipitation. From 1987 to 1996, there was a significant resonance period of 6–10 years between PRCPTOT and the WPSH intensity index, with the variation of PRCPTOT being delayed by 1/4 cycle from WPSH. From 2000 to 2008, the two signals have a resonance period of 3–6 years and a correlation coefficient greater than 0.8. There is a significant in-phase variation between PRCPTOT and WPSH intensity, with most arrows pointing to the right (Figure 5C). During 1985–1998, R25 mm and WPSH intensity have a significant resonance period of 4–11 years, with the arrows mostly pointing to the upper right, indicating that the intensity of WPSH is ahead of the changes in R25 mm. From 2000 to 2010, the phase difference is 90°, indicating that the change of WPSH is 1/4 cycle ahead of the change of R25 mm (Figure 5D). There is also a significant positive correlation between WPSH intensity and other extreme precipitation indices. The results from time-frequency phase analysis show that changes in large-scale circulation during the expansion or contraction and intensification or weakening of WPSH have a positive or negative effect on monsoon rainfall.

The intensification of the SCSH has a favorable impact on summer precipitation in the MLYR. During the period of 4–6 years, there is a significant resonance period between PRCPTOT and SCSHI from 2000 to 2008, and the two signals vary simultaneously (Figure 6A). In the 7–9 years period, the two signals show a significant positive correlation resonance period from 1986 to 1995, with a 90° phase difference, indicating that the variation of PRCPTOT lags behind that of SCSHI by 1/4 period in the time series (Figure 6A). The same pattern is observed between R25 mm and SCSHI, the two signals have a resonance period of 4–8 years and a correlation coefficient greater than 0.9. Most arrows point to the upper right, indicating that the frequency of extreme precipitation is positively correlated with the SCSH, and the variation of SCSH precedes that of R25 mm (Figure 6B).

The relationship between the EAJ and precipitation indices as shown by the time-frequency phase analysis indicates a significant positive correlation between the two sequences. The correlation coefficient between PRCPTOT and EASJI reaches 0.9 and most of the arrows point to the right or upper right, indicating that the total precipitation in the MLYR and EAJI are in phase (Figure 7A). The same relationship exists between R25 mm and EASJI, with the arrows mostly pointing to the upper right, indicating that the variation of EAJ is ahead of the changes in R25 mm. There is a significant resonance period between R25 mm and EASJI on a time scale of 1–5a from 1985 to 1994, and the correlation coefficient reaches 0.9, indicating a continuous positive influence of EAJ on the frequency of extreme precipitation (Figure 7B).

4 Discussion

The MLYR, located in one of the world's most well-known monsoon regions, is a central area of subtropical East Asia. Heavy flooding in the MLYR is often influenced by the precipitation change of summer season, which has been appreciated extensively (Huang et al., 2013). In this study, it is concluded from Figure 2 that summer precipitation displays a strong increasing trend, which agrees with previous research (Cui et al., 2012; Tian et al., 2017). Such phenomena were reported for several provinces in the MLYR such as Jiangxi, Hunan, and Hubei province (Hu and Wang, 2021; Li X et al., 2021; Yang et al., 2021). Some regions in the MLYR have a low-lying topography and belong to a highly flood-prone area. The trends of precipitation amount in summer might be enhancing the possibility of flood risk in these provinces in the MLYR (Huang et al., 2013).

Although worldwide changes in extreme climate events have been detected in the past few decades, various studies have attempted to assess climate change-related extreme events at a regional level. For China as a whole, the regional trend for mean precipitation amount on PRCPTOT, RX1day, and RX5day is 0.3, 1.37, and 1.90 mm/decade, respectively (You et al., 2011; Zhou et al., 2016). Similarly, the majority of the extreme precipitation indices for MLYR show positive changes. However, compared with the regional trend of China, the indices such as RX5day (2.04 mm/decade) and

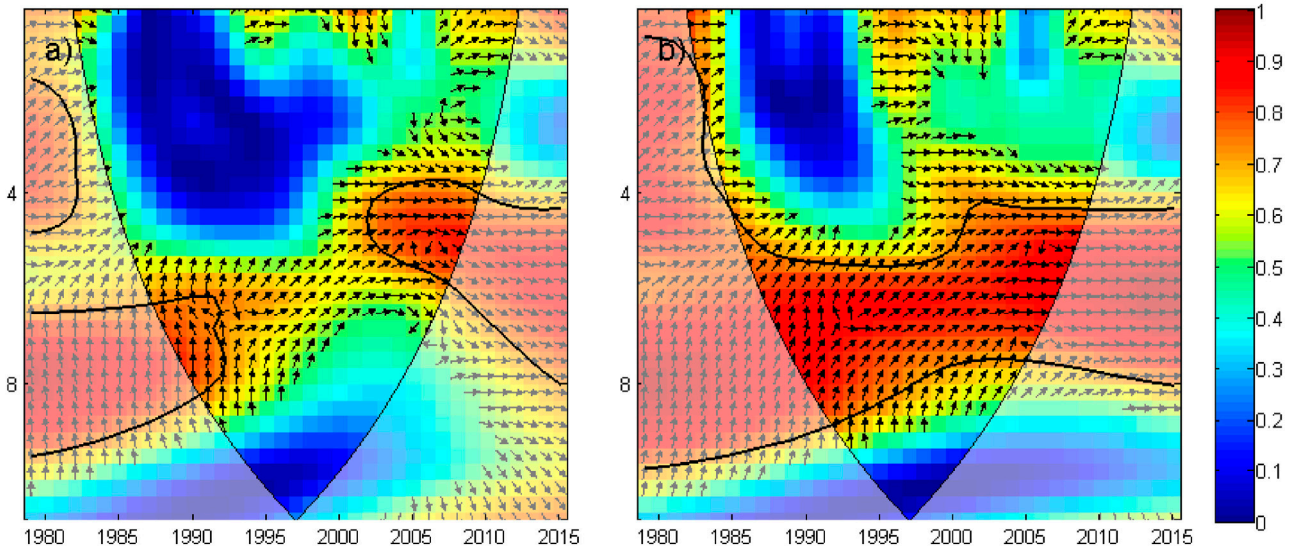

FIGURE 6
Wavelet coherent spectra of annual mean precipitation indices and SCSH over the MLYR from 1979 to 2015: **(A)** PRCPTOT and SCSHI, **(B)** R25 mm and SCSHI.

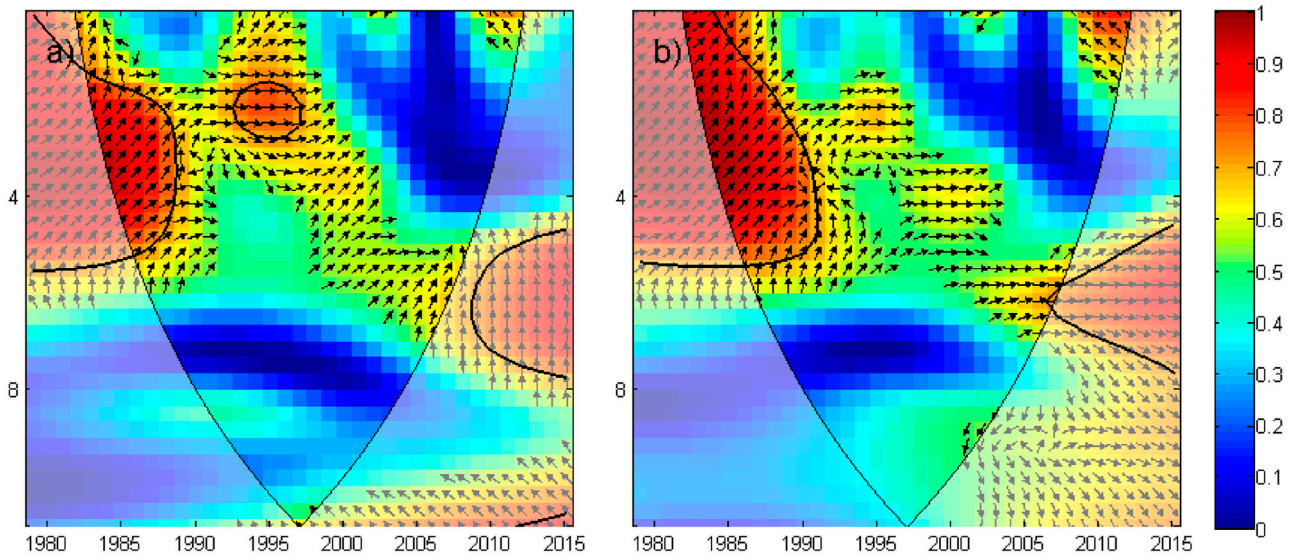

FIGURE 7
Wavelet coherent spectra of annual mean precipitation indices and EASJI over the MLYR from 1979 to 2015: **(A)** PRCPTOT and EASJI, **(B)** R25 mm and EASJI.

PRCPTOT (3.1 mm/decade) in the MLYR have larger variations (Figure 2). Meanwhile, R99 and RX1day in the MLYR display a positive trend, indicating that increases in total precipitation are projected to be mainly due to the increasing trends of intensity of extreme heavy precipitation. Although most of the trends are non-significant, it also suggests that there is a weak increasing tendency for precipitation in MLYR. Changes in extreme heavy precipitation are likely to have a greater immediate impact on human society than any likely small changes in mean rainfall amount, which have the potential to result in higher variability of flood risk in some regions (Cui et al., 2019; Hu and Wang, 2021).

Correlations between large-scale atmospheric indices and precipitation indices over the MLYR have been calculated. The precipitation in the MLYR is controlled mainly by the summer monsoon (Wang et al., 2021), which transports a huge amount of atmospheric moisture from the Pacific Ocean and the South China Sea to the MLYR along the periphery of the WPSH (Hui and Fang, 2016). Meanwhile, the sea surface temperature anomalies in the

Pacific Ocean and the South China Sea could affect atmospheric circulation through air-sea interaction, thus precipitation changes in the MLYR lag behind the variation of large-scale atmospheric factors (Figures 5, 6). The sea surface temperature, which affects climate change and atmospheric cycle, is referred as atmospheric signals and has received a lot of attention as a precursor to precipitation (Helali et al., 2020; Xu et al., 2020). Moreover, the activity of EAJ represents the movement of extratropical cyclone or cold air masses and can cause large-scale precipitation through dynamic effects (Wang and Zuo, 2016; Wang et al., 2018).

Atmospheric circulation and the formation of precipitation are complex processes that are coordinated by various factors at various scales, including other constituents of the climate system (such as land, ocean, cryosphere, and biosphere) (Shao et al., 2016; Wu et al., 2021). This study mainly focused on the relationship between atmospheric circulation and extreme precipitation. However, the mechanism by which atmospheric circulation affects precipitation is not elaborated and the correlation coefficients do not necessarily imply causation. Meanwhile, the human activities (such as greenhouse gas emissions, urban heat islands, reclamation, artificial afforestation, and deforestation) also play a vital role in extreme precipitation variations (Cheng et al., 2013; Feng et al., 2014; Ashish et al., 2017). Especially with the current impetus on economic development, the impact of human factors on extreme precipitation must be considered. Further research should combine human activities with natural factors, to design a precipitation change model and provide a detailed understanding of the physical mechanisms that drive these relationships (Luo et al., 2013). Furthermore, it will be necessary to build models to predict future development trends in future research, since this research is limited to a specific time period (1979–2015), and it is important to consider the potential impact of long-term climate variability and change.

5 Conclusion

The MLYR region is particularly prone to flood disasters and is highly sensitive to global warming. In this study, nine annual mean precipitation indices were selected based on precipitation observation data to examine the spatial and temporal variation characteristics of extreme precipitation events in the MLYR from 1979 to 2015. The correlations between various atmospheric circulation factors and extreme precipitation were also investigated using wavelet coherence analysis. The main results of this study are summarized as follows.

(1) Except for CDD and SDII, all the precipitation indices in the MLYR show an upward trend from 1979 to 2015. Among them, CWD and RX1day have a significant upward trend, and PRCPTOT increased at the fastest rate. Despite most of the variations showing no significant change, the intensity, frequency, and duration of extreme precipitation events in the MLYR have increased over time, which is more likely to result in extreme precipitation events in the MLYR over time.
(2) The extreme precipitation indices in the MLYR show a downward trend from the southeast to the northwest, indicating that extreme precipitation is more likely to occur in the southeast part of the MLYR. Most of the increasing trends in extreme precipitation indices are located in the Poyang Lake Basin, the LRYR, and the lower reaches of Dongting Lake, indicating that the frequency of extreme precipitation events in these regions probably increases significantly in the days to come, exacerbating the uneven distribution of precipitation.
(3) Four atmospheric circulation indices (i.e., the WPSH intensity index, WPSH area index, SCSHI, and EASJI) significantly influence the frequency of extreme precipitation and total precipitation in the MLYR. The WPSH has the most significant impact, followed by the SCSH, while the EAJ has the weakest effect. The results support the conclusion that these large-scale climatic factors play a crucial role in the variation of extreme precipitation in the MLYR from a time-frequency phase relationship perspective.

Data availability statement

The original contributions presented in the study are included in the article/Supplementary Material, further inquiries can be directed to the corresponding author.

Author contributions

JY designed the study, completed the original draft. YH provided some software for the study and revised the original draft. YL provided financial support for the research. GL revised the original draft. All authors commented on the manuscript and agreed to the published version of the manuscript.

Funding

This research was funded by the Open Research Fund of State Key Laboratory of Simulation and Regulation of Water Cycle in River Basin, China Institute of Water Resources and Hydropower Research (IWHR-SKL-KF202204), the Jiangsu Funding Program for Excellent Postdoctoral Talent (2022ZB147), the Key Scientific and Technological Project of the Ministry of Water Resources. P.R.C (SKS-2022001) and the Systematic Project of Guangxi Key Laboratory of Disaster Prevention and Engineering Safety (2022ZDK026).

Acknowledgments

The authors greatly appreciate the data availability and service provided by China Meteorological Administration and ERA-Interim science team. The authors also appreciate the support of Jun Wang (Researcher, Institute of Atmospheric Physics, Chinese Academy of Sciences) for providing observational data sets used in this study.

Conflict of interest

The authors declare that the research was conducted in the absence of any commercial or financial relationships that could be construed as a potential conflict of interest.

Publisher's note

References

Ashish, S., Harindra, J. S. F., Alan, F. H., Jessica, J. H., Michael, B., and Fei, C. (2017). Urban meteorological modeling using WRF: A sensitivity study. *Int. J. Climatol.* 37 (4), 1885–1900. doi:10.1002/joc.4819

Bhatti, A. S., Wang, G., Ullah, W., Ullah, S., Fiifi Tawia Hagan, D., Kwesi Nooni, I., et al. (2020). Trend in extreme precipitation indices based on long term *in situ* precipitation records over Pakistan. *Water-Sui* 12 (3), 797. doi:10.3390/w12030797

Chen, H., Liu, P., and Zhou, C. (2020). Correction to: Zonally asymmetric mode of anomalous activity in summer Asian subtropical westerly jet and its possible sources. *Theor. Appl. Climatol.* 140 (1-2), 805. doi:10.1007/s00704-020-03110-w

Cheng, F., Hsu, Y., Lin, P., and Lin, T. (2013). Investigation of the effects of different land use and land cover patterns on mesoscale meteorological simulations in the taiwan area. *J. Appl. Meteorol. Clim.* 52 (3), 570–587. doi:10.1175/JAMC-D-12-0109.1

Chou, J., Xian, T., Dong, W., and Xu, Y. (2018). Regional temporal and spatial trends in drought and flood disasters in China and assessment of economic losses in recent years. *Sustainability* 11 (1), 55. doi:10.3390/su11010055

Chu, Q., Wang, Q., Feng, G., Jia, Z., and Liu, G. (2021). Roles of water vapor sources and transport in the intraseasonal and interannual variation in the peak monsoon rainfall over East China. *Clim. Dynam* 57 (7-8), 2153–2170. doi:10.1007/S00382-021-05799-5

Cui, L., Wang, L., Qu, S., Ramesh, P. S., Lai, Z., and Yao, R. (2019). Spatiotemporal extremes of temperature and precipitation during 1960–2015 in the Yangtze River Basin (China) and impacts on vegetation dynamics. *Theor. Appl. Climatol.* 136 (1), 675–692. doi:10.1007/s00704-018-2519-0

Cui, Y., Jiang, Z., Chen, W., and Zhang, R. (2012). Projections of the 21st century changjiang-huaihe River Basin extreme precipitation events. *Adv. Clim. Chang. Res.* 3 (2), 76–83. doi:10.3724/SP.J.1248.2012.00076

Feng, C., Xuchao, Y., and Weiping, Z. (2014). WRF simulations of urban heat island under hot-weather synoptic conditions: The case study of Hangzhou City, China. *Atmos. Res.* 138, 364–377. doi:10.1016/j.atmosres.2013.12.005

Gill, M. M., Nick, J. D., Adam, A. S., and Philip, E. B. (2020). Predicting June mean rainfall in the middle/lower Yangtze River Basin. *Adv. Atmos. Sci.* 37 (01), 29–41. (in Chinese). doi:10.1007/s00376-019-9051-8

Gizaw, M. S., Gan, T. Y., Yang, Y., and Gan, K. E. (2021). Changes to the 1979–2013 summer convective available potential energy (CAPE) and extreme precipitation over north America. *Phys. Chem. Earth* 123, 103047. doi:10.1016/j.pce.2021.103047

Hatsuzuka, D., Sato, T., and Higuchi, Y. (2021). Sharp rises in large-scale, long-duration precipitation extremes with higher temperatures over Japan. *Npj Clim. Atmos. Sci.* 4 (1), 29. doi:10.1038/S41612-021-00184-9

Helali, J., Salimi, S., Lotfi, M., Hosseini, S. A., Bayat, A., Ahmadi, M., et al. (2020). Investigation of the effect of large-scale atmospheric signals at different time lags on the autumn precipitation of Iran's watersheds. *Arab. J. Geosci.* 13 (18), 932. doi:10.1007/s12517-020-05840-7

Hu, R., and Wang, L. (2021). Variation of high and low level circulation of Meiyu in Jiangsu province in recent 30 years. *Atmosphere* 12 (10), 1258. doi:10.3390/atmos12101258

Huang, J., Sun, S., and Zhang, J. (2013). Detection of trends in precipitation during 1960-2008 in Jiangxi province, southeast China. *Theor. Appl. Climatol.* 114 (1-2), 237–251. doi:10.1007/s00704-013-0831-2

Hui, P., and Fang, J. (2016). Comparison of the multi-scale features in two persistent heavy rainfall events in the middle and lower reaches of Yangtze River. *J. Meteorol. Res-Prc* 30 (4), 528–546. doi:10.1007/s13351-016-6028-8

Jin, L., and Zhao, P. (2012). Observational and modeling studies of impacts of the South China Sea monsoon on the monsoon rainfall in the middle-lower reaches of the Yangtze River during summer. *Acta Meteorol. Sin.* 26 (2), 176–188. doi:10.1007/s13351-012-0204-2

Juthasirorat, N., Anusasananan, P., Suwanarat, S., and Thangprasert, N. (2021). Using wavelet analysis to study floods in Bangkok. *J. Phys. Conf. Ser.* 1719 (1), 012037. doi:10.1088/1742-6596/1719/1/012037

Li, X., Wei, Z., Wang, H., Ma, L., and Guo, S. (2022). Variations in the precipitation extremes over the Guangdong-Hong Kong-Macao greater Bay area in China. *Theor. Appl. Climatol.* 147 (1-2), 381–394. doi:10.1007/s00704-021-03829-0

Li, X., Zhang, K., Gu, P., Feng, H., Yin, Y., Chen, W., et al. (2021). Changes in precipitation extremes in the Yangtze River Basin during 1960–2019 and the association with global warming, ENSO, and local effects. *Sci. Total Environ.* 760, 144244. doi:10.1016/j.scitotenv.2020.144244

Li, Y., Bai, J., You, Z., Hou, J., and Li, W. (2021). Future changes in the intensity and frequency of precipitation extremes over China in a warmer world: Insight from a large ensemble. *Plos One* 16 (5), e0252133. doi:10.1371/JOURNAL.PONE.0252133

Liang, X. Z. (2022). Extreme rainfall slows the global economy. *Nature* 601 (7892), 193–194. doi:10.1038/D41586-021-03783-X

Liu, D. L., Teng, J., Ji, F., Anwar, M. R., Feng, P., Wang, B., et al. (2020). Characterizing spatiotemporal rainfall changes in 1960–2019 for continental Australia. *Int. J. Climatol.* 41 (S1), E2420–E2444. doi:10.1002/JOC.6855

Luo, Y., Wang, H., Zhang, R., Qian, W., and Luo, Z. (2013). Comparison of rainfall characteristics and convective properties of monsoon precipitation systems over south China and the Yangtze and huai River Basin. *J. Clim.* 26 (1), 110–132. doi:10.1175/jcli-d-12-00100.1

Niu, R., Zhai, P., and Tan, G. (2021). Anomalous features of extreme Meiyu in 2020 over the yangtze-huai River Basin and attribution to large-scale circulations. *J. Meteorol. Res-Prc* 35 (5), 799–814. doi:10.1007/S13351-021-1018-X

Ostadi, E., Jahanbakhsh, S., Rostamzadeh, H., Rezaibanafsheh, M., and Khorshiddust, A. M. (2021). Spatio-temporal trend analysis of solid precipitation in Northwest Iran. *Arab. J. Geosci.* 14 (17), 1709. doi:10.1007/s12517-021-07812-x

Qi, H., Zhi, X., Zhi, T., Bai, Y., Lin, C., and Chen, W. (2021). Using stratified Bayesian model averaging in probabilistic forecasts of precipitation over the middle and lower Yangtze River region. *Meteorol. Atmos. Phys.* 133, 961–972. doi:10.1007/S00703-021-00799-W

Que, Z., Wu, F., Bi, C., Long, Y., and Li, C. (2016). Impacts of monthly anomalies of intraseasonal oscillation over south China sea and south Asia on the activity of summer monsoon and rainfall in Eastern China. *J. Trop. Meteorol.* 22 (2), 145–158. doi:10.16555/j.1006-8775.2016.02.005

Saha, U., and Sateesh, M. (2022). Rainfall extremes on the rise: Observations during 1951–2020 and bias-corrected CMIP6 projections for near- and late 21st century over Indian landmass. *J. Hydrol.* 608, 127682. doi:10.1016/J.JHYDROL.2022.127682

Shang, S., Zhu, G., Li, R., Xu, J., Gu, J., Chen, H., et al. (2020). Decadal change in summer precipitation over the east of Northwest China and its associations with atmospheric circulations and sea surface temperatures. *Int. J. Climatol.* 40 (8), 3731–3747. doi:10.1002/joc.6424

Shao, J., Wang, J., Lv, S., and Bing, J. (2016). Spatial and temporal variability of seasonal precipitation in Poyang Lake basin and possible links with climate indices. *Hydrol. Res.* 47 (S1), 51–68. doi:10.2166/nh.2016.249

Thomas, R. K., and David, R. E. (1999). Climate extremes: Selected review and future research directions. *Clim. Change* 42 (1), 309–325. doi:10.1023/A:1005436904097

Tian, J., Liu, J., Wang, J., Li, C., Nie, H., and Yu, F. (2017). Trend analysis of temperature and precipitation extremes in major grain producing area of China. *Int. J. Climatol.* 37 (2), 672–687. doi:10.1002/joc.4732

Tian, J., Xu, J., and Wei, E. (2000). The wavelet analysis of satellite sea surface temperature in the South China Sea and the Pacific Ocean. *Chin. Sci. Bull.* 45 (23), 2187–2192. doi:10.1007/BF02886327

Wang, S., and Zuo, H. (2016). Effect of the EastEast Asian westerly jet's intensity on summer rainfall in the Yangtze River valley and its mechanism. *J. Clim.* 29 (7), 2395–2406. doi:10.1175/JCLI-D-15-0259.1

Wang, S., Zuo, H., Zhao, S., Zhang, J., and Lu, S. (2018). How East Asian westerly jet's meridional position affects the summer rainfall in Yangtze-Huaihe River Valley? *Clim. Dynam* 51 (11-12), 4109–4121. doi:10.1007/s00382-017-3591-3

Wang, T., Wei, K., and Ma, J. (2021). Atmospheric rivers and mei-yu rainfall in China: A case study of summer 2020. *Adv. Atmos. Sci.* 38 (12), 2137–2152. doi:10.1007/S00376-021-1096-9

Wu, S., Hu, Z., Wang, Z., Cao, S., Yang, Y., Qu, X., et al. (2021). Spatiotemporal variations in extreme precipitation on the middle and lower reaches of the Yangtze River Basin (1970–2018). *Quatern Int.* 592 (10), 80–96. doi:10.1016/j.quaint.2021.04.010

Xu, K., Tam, C., Liu, B., Chen, S., Yang, X., He, Z., et al. (2020). Attenuation of central pacific el niño amplitude by north pacific sea surface temperature anomalies. *J. Clim.* 33 (15), 6673–6688. doi:10.1175/JCLI-D-19-0767.1

Yang, X., Wu, J., Liu, J., and Ye, X. (2021). Changes of extreme precipitation and possible influence of ENSO events in a humid basin in China. *Atmosphere* 12 (11), 1522. doi:10.3390/ATMOS12111522

Ye, X., Xu, C., Li, Y., Li, X., and Zhang, Q. (2017). Change of annual extreme water levels and correlation with river discharges in the middle-lower Yangtze River: Characteristics and possible affecting factors. *Chin. Geogr. Sci.* 27 (02), 325–336. (in Chinese). doi:10.1007/s11769-017-0866-x

You, Q., Kang, S., Aguilar, E., Pepin, N., Flügel, W., Yan, Y., et al. (2011). Changes in daily climate extremes in China and their connection to the large scale atmospheric circulation during 1961–2003. *Clim. Dynam* 36 (11-12), 2399–2417. doi:10.1007/s00382-009-0735-0

Zhou, B., Xu, Y., Wu, J., Dong, S., and Shi, Y. (2016). Changes in temperature and precipitation extreme indices over China: Analysis of a high-resolution grid dataset. *Int. J. Climatol.* 36 (3), 1051–1066. doi:10.1002/joc.4400

Zhang, Z., Zhang, Q., and Jiang, T. (2007). Changing features of extreme precipitation in the Yangtze River basin during 1961–2002. *J. Geogr. Sci.* 17 (1), 33–42. doi:10.1007/s11442-007-0033-x

Zhao, Y., and Luo, Y. (2021). Wavelet analysis on temperature and precipitation changes in dabie mountain of west anhui. *J. Phys. Conf. Ser.* 1732 (1), 012105. doi:10.1088/1742-6596/1732/1/012105

Zhou, Y., Luo, Z., Li, S., Liu, Z., Shen, Y., and Zhuo, W. (2022). Temporal and spatial variations of extreme precipitation in the Guangdong-Hong Kong-Macao Greater Bay area from 1961 to 2018. *J. Water Clim. Change* 13 (1), 304–314. doi:10.2166/WCC.2021.078

frontiers | Frontiers in Earth Science

TYPE Original Research
PUBLISHED 07 April 2023
DOI 10.3389/feart.2023.1128672

OPEN ACCESS

EDITED BY
Youcun Qi,
Institute of Geographic Sciences and Natural Resources Research, Chinese Academy of Sciences (CAS), Beijing, China

REVIEWED BY
Zhai Guoqing,
Zhejiang University, China
Hui Yu,
China Meteorological Administration, China

*CORRESPONDENCE
Fan Ping,
pingf@mail.iap.ac.cn

SPECIALTY SECTION
This article was submitted to Atmospheric Science, a section of the journal Frontiers in Earth Science

RECEIVED 21 December 2022
ACCEPTED 29 March 2023
PUBLISHED 07 April 2023

CITATION
Li Y, Li J, Ping F, Li L and Li J (2023), Comparative study of bin and bulk microphysical schemes in simulating a heavy snowfall event that occurred in Beijing during the 2022 Winter Olympic Games.
Front. Earth Sci. 11:1128672.
doi: 10.3389/feart.2023.1128672

Comparative study of bin and bulk microphysical schemes in simulating a heavy snowfall event that occurred in Beijing during the 2022 Winter Olympic Games

Yupeng Li[1,2,3], Jingyuan Li[1,2], Fan Ping[1,2,4]*, Lin Li[5] and Ji Li[6]

[1]Laboratory of Cloud-Precipitation Physics and Severe Storms (LACS), Institute of Atmospheric Physics, Chinese Academy of Sciences, Beijing, China, [2]University of Chinese Academy of Sciences, Beijing, China, [3]Key Laboratory of Changbai Mountain Meteorology and Climate Change, Institute of Meteorological Sciences of Jilin Province, Changchun, China, [4]School of Remote Sensing and Geomatics Engineering, Nanjing University of Information Science and Technology, Nanjing, China, [5]Beijing Meteorological Observation Center, Beijing, China, [6]Meteorological Observatory of Jilin Province, Changchun, China

A heavy snowfall event that struck Beijing during February 12-13, 2022, affected some of the training sessions and events of the Winter Olympic Games. This heavy snowfall event was simulated using the Advanced Research Weather Research and Forecasting Model with both the two-moment bulk scheme (BULK) and the spectral bin microphysics scheme (BIN), and the differences in surface precipitation, radar reflectivity, and cloud microphysics processes were compared and analyzed. It was found that surface precipitation was dominated by solid precipitation particles. The 24-h accumulated precipitation of the BULK simulation was larger than that of the BIN simulation, but both were smaller than that observed. The BIN simulation was closer to the observations in terms of the trends of variation in precipitation rate and radar reflectivity during the period of heavy precipitation. The maximum and minimum vertical velocities of the BIN simulation were notably higher than those of the BULK simulation, and the water vapor content of the BIN scheme at the heights of the −10 to −20°C levels and above the −38°C level was substantially higher than that of the BULK scheme. The contents of cloud water and snow simulated by the BIN scheme were much higher than those simulated by the BULK scheme. The nucleation of ice crystals in the middle and high layers of the BULK scheme was obvious, whereas such a process was not evident in the BIN scheme. The net production rate of ice crystals and snow simulated by the BULK scheme was stronger near the surface than that simulated by the BIN scheme, and a second peak in the conversion rate existed at heights very close to the surface below 1 km, which might account for the greater intensity of precipitation in the BULK scheme. The latent heat simulated by the BULK scheme was larger (smaller) than that simulated by the BIN scheme below (above) the height of 2 km.

KEYWORDS

heavy snowfall, numerical simulation, microphysical scheme, bin, bulk

1 Introduction

Heavy snowfall is one of the major catastrophic weather events that occur in high-latitude regions in winter. Such events are often accompanied by high winds, cold waves, low visibility, and freezing weather that can affect transportation, water conservancy, electricity supply, agricultural production, and people's lives. Spatially extensive and long-duration blizzard events cause the most serious impact, but local heavy or extremely heavy blizzards are typical high-impact events that can often endanger life and property (Changnon and Changnon, 2006; Wang et al., 2010; Jiao et al., 2021; Wang et al., 2022). Heavy snowfall in winter occurs frequently in northern China and on the Qinghai–Tibet Plateau. For example, heavy snowfall occurred in November 2021 in Liaoning Province (Northeast China), which paralyzed transportation, closed schools, damaged crops, affected 152,000 people, and caused direct economic losses of 4.496 billion yuan. Wintertime precipitation can also affect southern China such as the freezing rain and snowfall that occurred in 2008, which caused severe damage to many southern provinces (Sun et al., 2010; Li et al., 2021).

Heavy snowfall is mainly caused by cold cloud processes, and the ice-phase cloud microphysics process plays a very important role in the formation of heavy snowfall. Therefore, it is important to study the microphysics process of ice-phase cloud and the parameterization scheme of cloud microphysics for improved prediction of heavy snowfall events (Lin and Bueh, 2006). Currently, there are very large uncertainties regarding both the characteristics of ice-phase particles within clouds and the ice-phase cloud microphysical processes. Consequently, obtaining a reasonable description of ice-phase cloud microphysical processes is one of the important challenges that must be addressed to improve cloud microphysical parameterization and numerical weather prediction models (Khain and Pinsky, 2018; Morrison et al., 2020).

The description of cloud microphysical processes in numerical weather models is achieved using microphysical parameterization schemes. Depending on the description of the hydrometeors, cloud microphysical parameterization schemes can be divided broadly into two categories: bulk schemes (hereafter, BULK) and bin schemes (hereafter, BIN). In a BULK scheme, the particle size distribution (PSD) of the hydrometeors is assumed as an empirical function that does not change during the simulation. A BULK scheme consumes fewer computational resources and is therefore used widely in practical operations and theoretical studies. However, a BULK scheme is suitable only for describing the overall PSD of the hydrometeors in clouds, and is not suitable for describing the evolution of the PSD caused by the change in particle size within a specific range (Xu and Duan, 1999). In contrast, a BIN scheme divides cloud particles into tens or hundreds of bins according to the microphysical characteristics of the hydrometeors, e.g., phase state, particle size, shape, and density, and it describes the prediction equations of each bin of particles and the interconversion process between them (Li et al., 2009a; Yin et al., 2017).

Earlier comparative analyses of BIN and BULK simulations focused on using idealized models to study strong convective weather. Lynn et al. (2005) found that the radar echoes simulated by the BIN scheme can more reasonably characterize the initiation and progression of strong convection in comparison with those simulated by the BULK scheme. Khain et al. (2009) also determined that the BIN scheme can simulate the dynamics and cloud microphysical structure of a squall line more realistically. Li et al. (2009a) revealed that the BULK scheme simulated a multicell storm with rapid and strong evolution leading to convection on a summertime squall line, whereas the BIN scheme produced a unicell storm with little temporal variation in the regeneration of its leading cell. Igel and van den Heever. (2017) studied the difference in condensation and evaporation rates in non-precipitating shallow cumulus clouds using simulations of BIN and BLK schemes in the same model framework, and found that the condensation rate is significantly affected by the width of drop size distribution (DSD).

With recent improvements in computer performance, it is now possible to compare the BIN scheme and the BULK scheme in relation to real cases. Fan et al. (2012) conducted a comparison of the two-moment BULK and BIN schemes for a case of strong convection in China. Their results showed that the BULK scheme simulated much higher cloud droplet numbers, and that the cloud condensation nuclei had contrasting effects on convection and precipitation between the two schemes. Yin et al. (2017) used the BIN and BULK schemes for a comparative analysis of a squall line in eastern China. Their results showed that the BULK scheme produced a well-organized but shorter radar structure, whereas the BIN scheme simulated scattered but stronger radar echoes that were more consistent with the observations. Moreover, the BULK scheme produced better performance in simulating strong rainfall areas and precipitation amounts. Chen et al. (2021) analyzed the differences between the BIN and BULK schemes with regard to the simulation of the initiation of a mesoscale convective system in the area of Beijing (China). They found that the BIN scheme simulated a lower rainwater mass center, stronger latent heat release, and more intense precipitation. Zhang et al. (2022) used the BULK and BIN schemes to analyze Typhoon In-Fa which struck mainland China in 2021. They reported considerable differences between the two microphysics schemes in the simulation of the precipitation, path, and intensity of the typhoon. Moreover, the performance of each scheme was greatly affected during the different periods of typhoon landfall.

Earlier comparative studies on summertime strong convection, simulated using the BIN and BULK schemes and idealized experiments or real case scenarios, have revealed new understanding. However, similar research on weak convection such as wintertime heavy snowfall remains lacking. Furthermore, it has been identified that cold cloud-related microphysical properties such as ice nuclei and the PSD of snow in China differ markedly from those in other regions (Yin et al., 2011; Wang et al., 2015). Therefore, it is of great scientific importance to conduct a comparative study of the BULK and BIN schemes in relation to wintertime snowfall in China, to investigate their performance in simulating winter precipitation, and to clarify the main cloud microphysical processes and their differences. The findings will improve cloud microphysical parameterization, local optimization of sensitive parameters, and the capability of numerical models in forecasting winter precipitation.

In this study, a heavy snowfall event that occurred during the Winter Olympic Games in Beijing, on February 12-13, 2022, was simulated using the Weather Research and Forecasting (WRF)

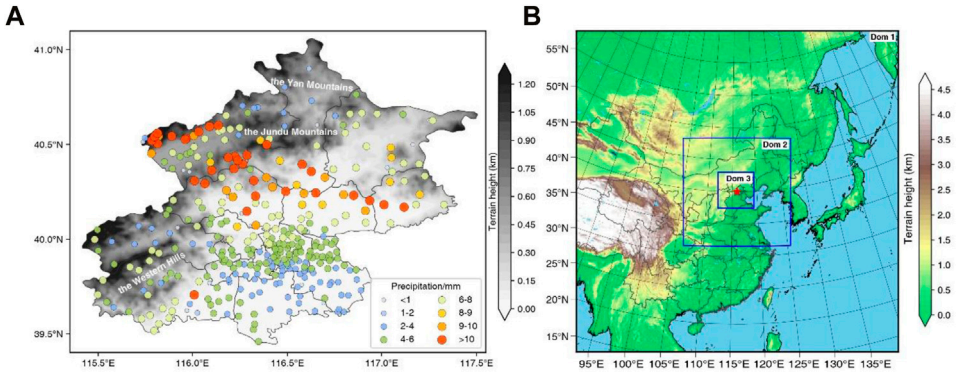

FIGURE 1
(A) Observed 24-h accumulated precipitation (colored scatter points, unit: mm) and terrain height (shading, unit: km) in the Beijing area from 1800 UTC on February 12 to 1800 UTC on February 13, 2022. **(B)** Domain configuration of the simulation and terrain height (shading; unit: km). Red asterisk indicates the location of the center of the domain.

regional numerical model with the BULK and BIN cloud microphysics schemes. Based on the simulations, the precipitation, radar reflectivity, and dynamic characteristics simulated by the BIN and BULK schemes were further compared, and the cloud microphysical characteristics of the two simulations such as the spatiotemporal evolution characteristics of the hydrometeors, main microphysical process, and release of latent heat were analyzed. The findings of these analyses will help reveal the differences in cloud microphysical processes between the BULK and BIN schemes and provide a basis for the improvement of both schemes. Moreover, the results will also help improve understanding of the mechanism of snowfall development in northern China, and provide reference for improved forecasting of wintertime precipitation.

The remainder of this paper is organized as follows. Section 2 introduces the data and methodology. Section 3 provides an overview of the heavy snowfall event and the setup of the numerical experiments. Section 4 analyzes the simulation results. Our discussion and conclusions are presented in Section 5.

2 Data and methods

2.1 Data

The model initial and boundary conditions were obtained from the 6-hourly National Centers for Environmental Prediction Final Analysis (NCEP-FNL) 0.25° × 0.25° dataset. The NCEP-FNL was also used for the analysis of the synoptic-scale circulation situation.

Surface rain gauge observations were observed by Automated Weather Stations (AWS), which were provided by the National Meteorological Information Center of the China Meteorological Administration. The locations of the AWSs are marked in Figure 1A, and the precipitation accumulated at 1-h intervals at the location of each AWS is used. We also used the operational S-band radar observation at Beijing station. The location of the radar is marked in Figure 1A. The radar operates in the volume coverage pattern 21 (VCP-21) scanning mode, consisting of nine elevation angles: 0.5°, 1.5°, 2.4°, 3.4°, 4.3°, 6.0°, 9.9°, 14.6°, and 19.5°. The temporal resolution of radar reflectivity data is 6 min. We interpolated the station and radar observations onto a 0.01° × 0.01° latitude-longitude grid in the Beijing area to facilitate comparison and analysis of the observations with the simulations.

TABLE 1 Setup of model parameters.

Parameter	Domain 1	Domain 2	Domain 3
Horizontal grid spacing (km)	9 × 9	3 × 3	1 × 1
Simulation time	1200 UTC Feb 12 to 0000 UTC Feb 14, 2022		
Horizontal grid	601 × 601		
Vertical model levels	51		
Cumulus scheme	Kain–Fritsch	—	
Shortwave radiation scheme	Dudhia		
Longwave radiation scheme	Rapid Radiative Transfer Model		
Land surface scheme	Noah		
Surface layer scheme	Monin–Obukhov		
Planetary boundary scheme	Yonsei University		

2.2 Model description and setup of numerical experiment

The numerical simulations were performed using the WRF Version 4.2 model. The WRF model is a fully compressible non-hydrostatic, primitive equation model with multiple-nesting capabilities that can enhance the resolution over areas of interest (Skamarock et al., 2019). Figure 1B shows the configuration of the three nested domains used in this research, and Table 1 lists the configurations of the simulation. Domain 1 had the coarsest mesh with 601 × 601 grid points in the north–south and east–west directions, respectively, and horizontal grid spacing of 9 km.

TABLE 2 Differences between BIN and BULK schemes.

Description	BULK	BIN
Mixing ratio	Qc、Qr、Qi、Qs、Qg	Qc、Qr、Qi、Qs、Qg、Qh
Number concentration	Nc、Nr	Nc、Nr、Ni、Ns、Ng、Nh
DSD	The DSD is prescribed in the form of exponential distribution or gamma distribution	Solving a system of kinetic equations for DSD
Sedimentation	The bulk terminal velocity for the same type of particles	Differential terminal velocity depending on particle size, shape, and air density
Condensation/evaporation	No equation for diffusion growth or evaporation; the strategy of saturation adjustment is used	The diffusion growth/evaporation equations are used
Collisions	Simplified equations are used	Stochastic collision equations are used
Melting/freezing	The shape of DSD changes during these non-linear processes	The shape of DSD remains fixed during the highly non-linear processes

Domain 2 was nested within domain 1 with 601 × 601 grid points at 3-km grid spacing. Domain 3 was nested within domain 2 with 601 × 601 grid points at 1-km grid spacing. The three domains were run together with a one-way nest. All domains were centered over Beijing to represent the regional-scale circulation and to resolve the complex flows within this region. The number of vertical layers was 51 and the model top was set at 50 hPa. The model data from the 1 × 1 km domain output at 1-h intervals were used for the analysis.

The NCEP-FNL analyses were interpolated to the WRF model grid to provide the initial conditions for 1200 UTC on February 12, 2022, as well as the 6-hourly lateral boundary conditions for the outermost domain. The boundary conditions for the 3 × 3 km grid and the 1 × 1 km grid were obtained from the outer domain. The simulations over all domains started at 1200 UTC on February 12, 2022, and they were integrated for 36 h.

The model physics schemes used included the following: 1) the Kain–Fritsch cumulus scheme (Kain, 2004) in the outermost domain (disabled in the two inner domains); 2) the Yonsei University planetary boundary layer scheme (Hong et al., 2006); 3) the revised MM5 Monin–Obukhov similarity scheme for the surface layer (Jiménez et al., 2012); 4) the unified Noah land surface scheme (Chen and Dudhia, 2001a; 2001b); 5) the Rapid Radiative Transfer Model (Mlawer et al., 1997) for longwave radiative flux calculations; and 6) the Dudhia shortwave scheme (Dudhia, 1989).

With other model configurations remaining fixed, two microphysical schemes, namely the two-moment WDM6 bulk parameterization scheme (Lim and Hong, 2010) and the HUJI (Hebrew University of Jerusalem, Israel) spectral bin full version microphysics scheme (Khain et al., 2004) were selected to represent the BULK and BIN schemes, respectively. The BULK scheme includes five categories of cloud particles (i.e., cloud water, rainwater, ice crystals, snow, and graupel); the BIN scheme includes the same five categories of cloud particles but with the addition of hail. Moreover, the ice crystal particles in the BIN scheme are expanded into three detailed subcategories: column, dendrite, and plate. Each category of cloud particles is divided into 33 bins according to their mass. And the ratio between 2 adjacent bins is set to a constant value of 2 (Khain et al., 2004), In contrast, the PSD in BULK scheme is typically assumed to follow a gamma or exponential distribution. Table 2 gives a further description of the differences between the two schemes.

2.3 Calculation of latent heating and cooling rates

The heating process in the cloud microphysics includes condensation, freezing and deposition. Evaporation, melting and sublimation are considered cooling processes. Based on the methods used by (Hjelmfelt et al., 1989), the latent heating and cooling rates were defined as follows:

$$R_h = \left(\frac{L_v}{C_p}\right)P_{\text{cond}} + \left(\frac{L_f}{C_p}\right)P_{frz} + \left(\frac{L_s}{C_p}\right)P_{dep}$$

$$R_c = \left(\frac{L_v}{C_p}\right)P_{\text{evp}} + \left(\frac{L_f}{C_p}\right)P_{\text{mlt}} + \left(\frac{L_s}{C_p}\right)P_{sub}$$

Where L_v, L_f and L_s are the latent heats of evaporation, melting, and sublimation, respectively. C_p is the specific heat at a constant pressure. P_{cond}, P_{frz}, P_{dep}, P_{evp}, P_{mlt}, and P_{sub} are the rates of mass change due to condensation, freezing, deposition, evaporation, melting, and sublimation.

3 Event overview and synoptic conditions

The first snowfall after the Chinese New Year of the Tiger struck Beijing on February 12-13, 2022. Some of the training sessions and events related to the Winter Olympic Games were affected by unfavorable weather conditions such as low visibility and high wind speed associated with this snowfall event. Figure 1. A shows the distribution of the 24-h accumulated precipitation in Beijing from 1800 UTC on February 12 to 1800 UTC on February 13, 2022. It can be seen that the accumulated precipitation in Beijing was generally more than 4 mm; however, it was more than 8 mm in central–northern areas and more than 10 mm at several stations. The band of heaviest snowfall was aligned broadly in a northwest–southeast pattern, and the center of heaviest snowfall was mainly located over the southern slopes of the Jundu Mountains, indicating that topography had an important influence on this snowfall event.

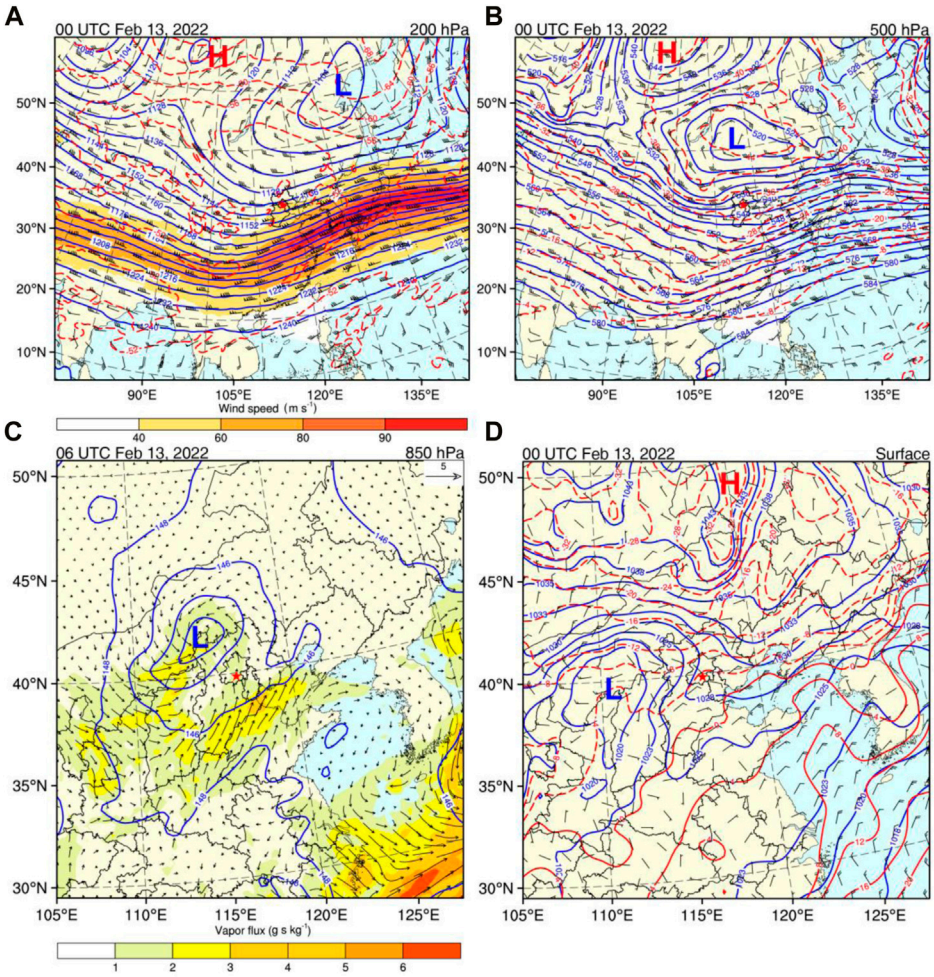

FIGURE 2
Synoptic-scale atmospheric circulation fields on February 13, 2022. **(A)** Upper-level jet (shading; unit: m s^{-1}), geopotential height (blue contours; unit: dagpm), temperature (red contours; unit: °C), and wind field (barb symbols) at 200 hPa for 0000 UTC. **(B)** Geopotential height (blue contours; unit: dagpm), temperature (red contours; unit: °C), and wind field (barbs) at 500 hPa for 0000 UTC. **(C)** Geopotential height (blue contours; unit: dagpm) and water vapor flux (shading and vector arrows; unit: g s kg^{-1}) at 850 hPa for 0600 UTC. **(D)** Sea level pressure (blue contours; unit: hPa), temperature (red contours; unit: °C), and wind field (barb symbols) at the surface for 0000 UTC. Red asterisk indicates the location of the Beijing station (No.: 54,511). Half and full wind barb symbols denote 2 and 4 m s^{-1}, respectively.

Figure 2 shows the synoptic-scale circulation situation of different pressure levels on February 13, 2022. As can be seen from Figures 1B, 2A, before the occurrence of the snowfall, an upper-level cold vortex was maintained over Northeast Asia at 500 hPa, with its center located over the northwest of Heilongjiang Province, China. The cold air within the southward flow on the western side of the cold vortex was transported from high-latitude regions toward the west of the Beijing area, and the Beijing area was located in the region of positive vorticity advection ahead of the trough. At the same time, there was a strong upper-level jet at 200 hPa. The center of this jet was located to the south of the upper-level cold vortex, and the maximum wind speed was >90 m s^{-1}. The Beijing area was located in the area of the ascent on the left side of the jet stream entrance region, which was conducive to the occurrence of the snowfall event. A low vortex existed at 850 hPa to the northwest of Beijing (Figure 2C), and there was strong water vapor transport toward Beijing from the south. The Beijing area was located in front of the inverted trough at the surface, which was conducive to the occurrence of upward movement (Figure 2D). The 0°C isotherm was located near Tianjin Bay, and the temperature decreased steadily from the southeast toward the northwest and from the coast toward inland areas, indicating that the precipitation of this event was dominated by ice-phase precipitation particles.

Figure 3 shows sounding profiles from Beijing (Station No.: 54,511) obtained on February 12 and 13, 2022. Before the snowfall occurred (Figure 3A), there was cold advection in the lower layer, the dewpoint depression was approximately 10°C, and the air was dry. There was an inversion layer at 950 hPa, indicating the existence of potential instability, and there was an obvious wet layer at 800 hPa above the inversion layer, providing environmental conditions favorable for the occurrence of enhanced convection. Additionally, the temperature was <0°C throughout the entire profile, indicating that the precipitation was mainly in the form

10.3389/feart.2023.1128672

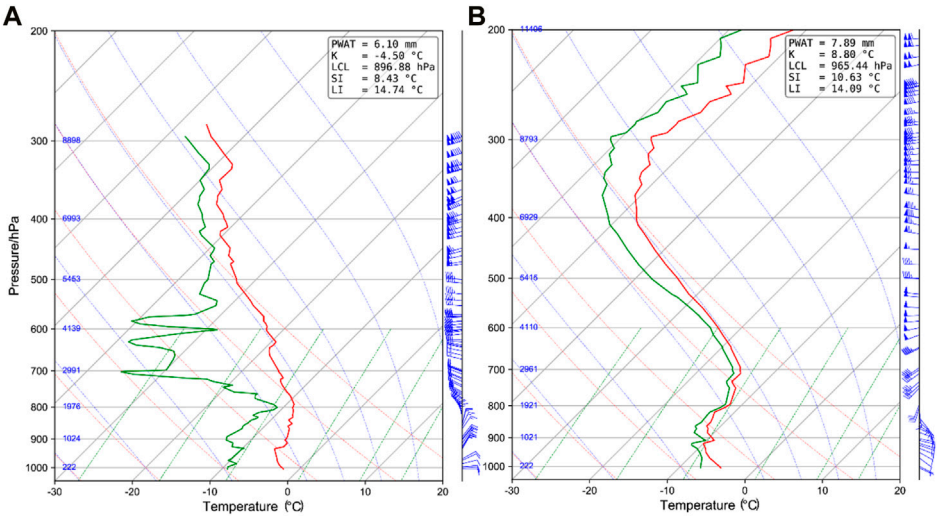

FIGURE 3
Observed sounding over Beijing (Station No.: 54,511): **(A)** 1200 UTC on February 12, 2022 and **(B)** 0000 UTC on February 13, 2022. Full wind barb symbol denotes 4 m s^{-1}.

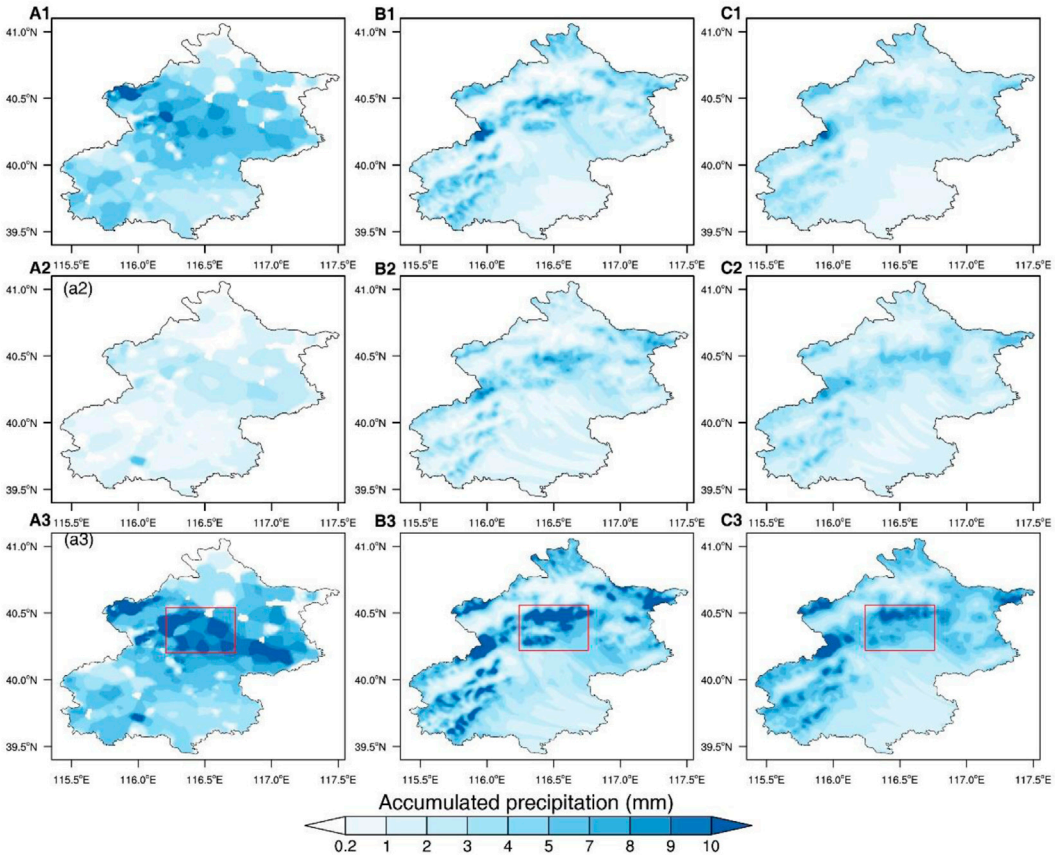

FIGURE 4
Accumulated 12-h and 24-h precipitation (unit: mm) of the **(A1)–(A3)** observations, **(B1)–(B3)** BULK scheme, and **(C1)–(C3)** BIN scheme in the Beijing area. Panels marked **(A)** are for 1800 UTC on February 12 to 0600 UTC on February 13, 2022, panels marked **(B)** are for 0600 UTC to 1800 UTC on February 13, 2022, and panels marked **(C)** are for 1800 UTC on February 12 to 1800 UTC on February 13, 2022. Red rectangle indicates the region selected for later analysis.

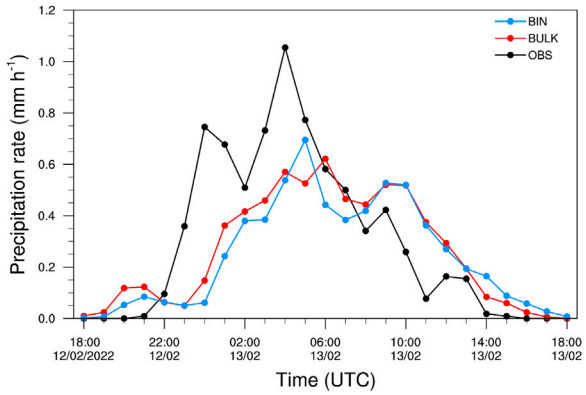

FIGURE 5
Time series of area-averaged precipitation rate in the simulations and observations from 1800 UTC on February 12 to 1800 UTC on February 13, 2022, at 1-h intervals.

of solid precipitation particles. By 0000 UTC on February 13 (Figure 3B), the level below 600 hPa had reached saturation, indicating that snowfall had occurred at this time. The temperature inversion or neutral layer was more obvious and the thickness had increased. The wind direction in the lower level also changed from northeasterly to southeasterly, and the wind direction rotated clockwise from low to high between 900 and 800 hPa in the lower level, indicating warm advection in the lower level that was favorable for further development and maintenance of snowfall.

4 Results

4.1 Precipitation and radar reflectivity

To compare the simulation results of precipitation for both the BULK and the BIN schemes, Figure 4 shows the accumulated surface precipitation of different periods observed by AWSs and simulated by the model using the two different microphysics schemes. The 12-h accumulated precipitation from 1800 UTC on February 12 to 0600 UTC on February 13, 2022 is shown in Figures 4A1–C1. The observations show that the precipitation mainly occurred at the junction between the Jundu Mountains and the southern Beijing Plain, and that the zone of heaviest snowfall was aligned broadly in an east–west direction. The simulation results of the BULK and BIN schemes were generally consistent with the observations but the amount of precipitation was smaller. The 12-h accumulated precipitation during 0600–1800 UTC on February 13, 2022, is shown in Figures 4A2–C2. The precipitation in this period had weakened, and the precipitation was evidently smaller than that accumulated in the previous 12-h period. Moreover, the maximum precipitation observed was <4 mm, whereas the precipitation simulated by the BIN and BULK schemes in this period was greater with centers of heavier precipitation distributed in an east–west band. The 24-h accumulated precipitation from 1800 UTC on February 12 to 1800 UTC on February 13, 2022, is shown in Figures 4A3–C3. The heaviest observed precipitation was mainly located at the junction of the northern mountainous area and the plain area, broadly aligned in the northwest–southeast direction, whereas the heaviest simulated precipitation of the BIN and BULK schemes was aligned in the east–west direction. The precipitation simulated by the BULK scheme was larger than that simulated by the BIN scheme, but the precipitation of both was smaller than that observed.

The distribution of the 24-h accumulated precipitation shows that the area of heaviest precipitation was located over central–northern Beijing, i.e., the southern slopes of the Jundu Mountains. Therefore, we selected this area for further analysis (i.e., the red rectangles in Figure 4).

The evolution of the two simulations and the observed hourly regional average precipitation for the selected area of heaviest precipitation is shown in Figure 5. From 2100 UTC on February 12 to 1600 UTC on February 13, the observed precipitation first strengthened and then weakened. The peak precipitation appeared at 0400 UTC on February 13, with a value of approximately 1.15 mm h^{-1}. Although the simulation results of the two schemes broadly reproduce the temporal evolution characteristics of the observed precipitation, some differences are evident between the precipitation simulated by the two schemes. The peak precipitation of the BIN scheme occurred at 0500 UTC on February 13, whereas the peak precipitation of the BULK scheme occurred at 0600 UTC on February 13. Both schemes underestimated the peak value of precipitation with a 1 to 2-h lag. During the period of heavy precipitation (i.e., during 0200–0700 UTC on February 13), the temporal evolution of precipitation simulated by the BIN scheme was closer to that of the observations, showing a more symmetrical increase and weakening of the precipitation rate, whereas the precipitation rate in the BULK scheme changed slowly and showed a fluctuating characteristic.

Figure 6 shows the composite radar reflectivity of the BULK and BIN schemes at 0400 UTC on February 13, 2022, together with the observed composite radar reflectivity at 0300 UTC on February 13, 2022. The observed radar echoes were mainly located over the south–central part of Beijing, and the echo band with values of >25 dBZ (maximum: >30 dBZ) was mainly aligned in the northwest–southeast direction over the central–northwest part of Beijing. However, the echo band of the BULK scheme was notably further eastward compared with that of the observations. Moreover, the zone of strong echoes was located over the eastern boundary of Beijing, and the echo intensity was weaker than that of the observations; the maximum echo intensity was <25 dBZ. The zone of strong echoes of the BIN scheme was located near the Jundu Mountains, and the maximum intensity of the echoes was also <25 dBZ. The zone of strong echoes was broadly aligned in the northwest–southeast direction but located slightly further north than that observed. Overall, the location of the radar echoes simulated by the BIN scheme was closer to that of the observations.

Figure 7 shows vertical cross sections of the simulated and observed radar reflectivity. As can be seen from Figure 7C, the observed radar echoes had a maximum value of >27 dBZ and the echo top height was approximately 7 km. Liu et al. (2022) found a maximum radar echo top height of approximately 7-8 km in a snowfall event over Beijing, which is consistent with our results (see Figure 4 therein). However, the echo top height is much lower for winter precipitation systems in comparison with that of strong convective systems in summer (Chen et al., 2021; Li et al., 2022).

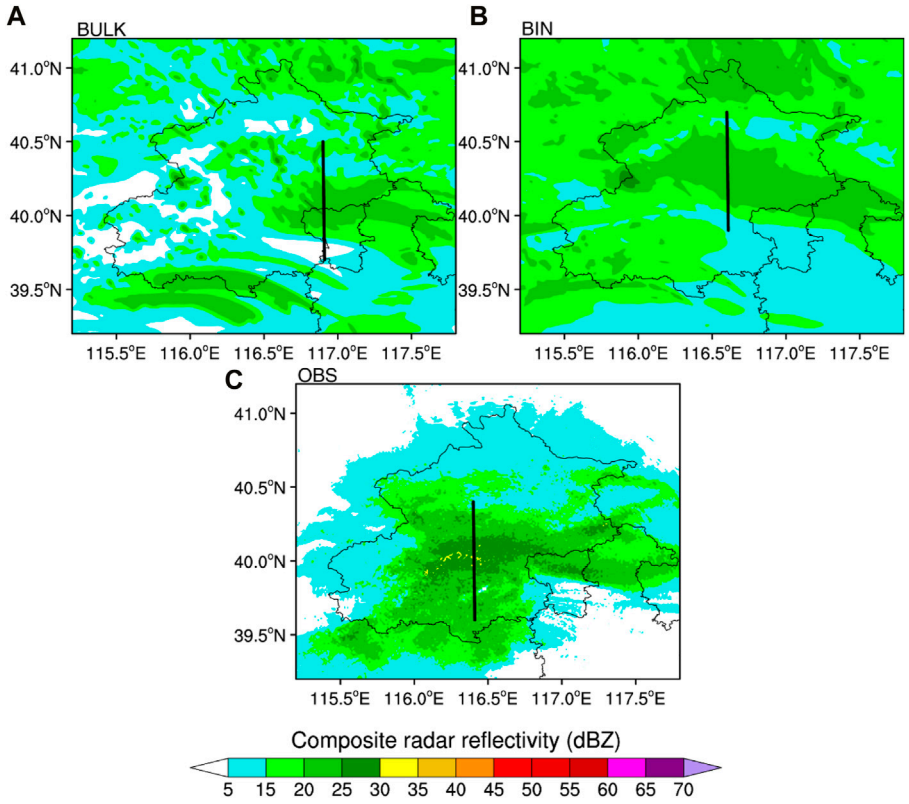

FIGURE 6
Composite radar reflectivity of **(A)** the BULK scheme and **(B)** the BIN scheme at 0400 UTC on February 13, 2022, and **(C)** observed composite radar reflectivity at 0300 UTC on February 13, 2022. Black lines denote the locations of the cross sections shown in Figure 7.

The peak value of the radar echoes simulated by the BULK scheme was >24 dBZ, but the area of the strong echoes was much smaller than that observed. Moreover, the height of the radar echo top was <3 km, i.e., approximately half that observed. The maximum echo simulated by the BIN scheme was >21 dBZ, which was smaller in comparison with the observations, but the area of echoes with values of >21 dBZ was closer to that observed. Moreover, the strong echo heights of both the BIN scheme and the observations ranged from the ground to approximately 2 km. The top of the echoes simulated by the BIN scheme reached the height of up to 6 km, which was also closer to that of the observations.

Figure 8 shows time–height contours of the simulated and observed radar echoes averaged over the region (see red rectangles in Figures 4A3–C3). As can be seen from Figure 8C, the observed radar echoes were most obvious during 0000–1500 UTC on February 13, 2022. The echoes showed a double-peaked feature, with the strongest echoes occurring at approximately 0400 UTC on February 13, and the top height of the echoes extended to approximately 7 km. During 0000–0600 UTC on February 13, 2022, the radar echoes simulated by the BULK scheme, shown in Figure 8A, the BULK scheme failed to reproduce the double-peaked feature at the beginning of precipitation, and the echo top height was lower, i.e., <4 km. In contrast, the BIN scheme reproduced the double-peaked structure of the observed radar echoes during the same period (Figure 8B), with a higher echo top height than the BULK scheme that was closer to that of the observations. While the observed radar echoes were <8 dBZ and the top of the echoes was <4 km during 0600–1000 UTC on February 13, 2022, the radar echoes simulated by both the BIN scheme and the BULK scheme were stronger (>14 dBZ) than those observed.

In summary, it is evident that the radar echoes simulated by the BIN scheme were closer to those of the observations in terms of horizontal distribution, echo top height, and area of strong echoes. Consistent with our results, radar echoes simulated by the BIN scheme were also found to be more realistic in previous studies (Lynn et al., 2005; Li et al., 2009a; Yin et al., 2017). However, the subject of the earlier research was summertime strong convection rather than wintertime precipitation.

4.2 Vertical velocity, water vapor, and hydrometeors

Cloud microphysical processes can provide feedback to the kinematic and moisture fields, which means that it is important to investigate feedback effects on environmental fields when comparing the BIN and BULK schemes. Here, we focus on the effects of the BIN and BULK schemes on environmental conditions such as vertical velocity and water vapor. Figure 9A shows the vertical profiles of the maximum upward and downward velocities during the period of precipitation. It can be seen that the peaks of the

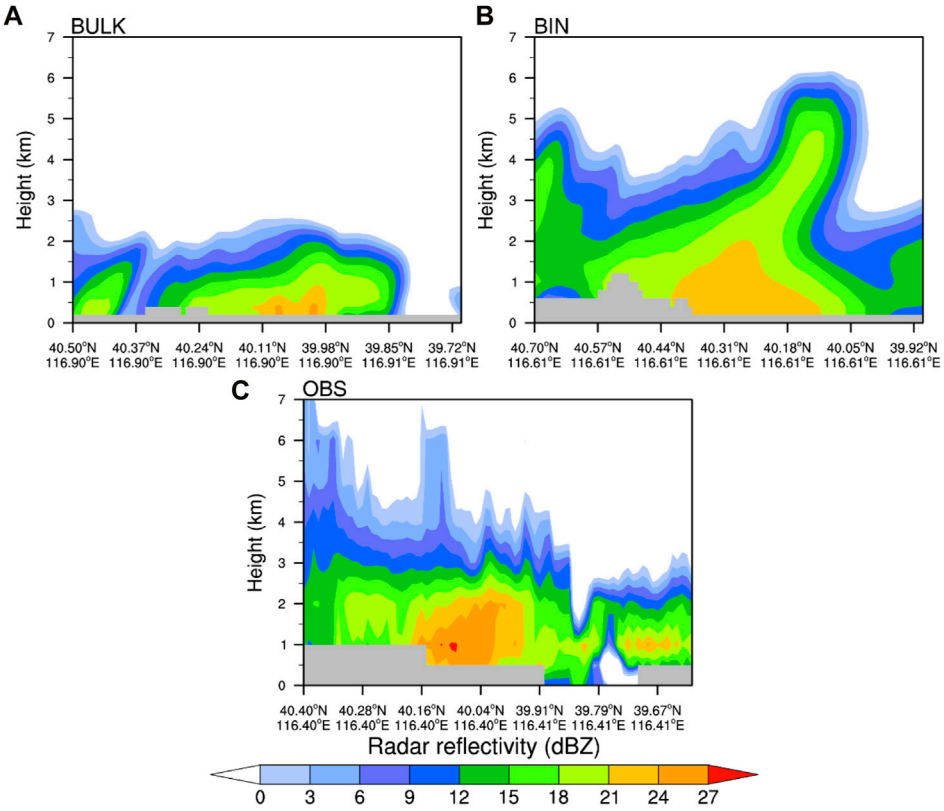

FIGURE 7
As in Figure 6 but for vertical cross sections of radar reflectivity along the black lines shown in Figure 6. The gray zones in the figure indicate the terrain.

maximum updraft and downdraft for both the BIN simulation and the BULK simulation occurred near the surface, i.e., the maximum downward (upward) velocity peaked at a height of approximately 0.5 km (0.8 km). Additionally, the maximum upward and downward velocities of the BIN simulation were markedly stronger than those of the BULK simulation, and the differences were greater at levels with temperatures greater than −38°C (i.e., below 5.8 km). It is clear from the previous analysis that the top height of the radar echoes simulated by the BIN scheme was higher than that of the BULK scheme, indicating that the stronger upward motion in the BIN scheme caused more vigorous convection and a higher top of the radar echo (see Figure 7). Many previous studies on summertime strong convection found stronger updrafts in BULK scheme simulations than in BIN scheme simulations (Li et al., 2009a; 2009b; Khain and Lynn, 2009; Fan et al., 2012; Yin et al., 2017), which is different from our results. This suggests that cloud microphysical processes are substantially different between summertime precipitation and wintertime precipitation. Figure 9B shows the average vertical profile of the water vapor mixing ratio. The water vapor content was maximum in the near-ground layer, decreased with increasing height, and was markedly greater at the heights of the −10 to −20°C levels and above the −38°C level for the BIN scheme than for the BULK scheme, probably because the BULK scheme consumed more water vapor than the BIN scheme in the region selected, which means that the conversion rate of water vapor to cloud particles was higher.

Here, we investigate the differences in the temporal and vertical distributions of the cloud particles during the snowfall event simulated by the BULK and BIN schemes. Figure 10 shows the temporal evolution of different cloud particles. The temporal evolution of cloud water, shown in Figure 10A, indicates that the cloud water simulated by the BULK scheme was mainly concentrated at heights from the ground to 1.3 km, and that the cloud water content was higher at 2000 UTC on February 12, shortly after the onset of the snowfall, and that it then decreased continuously until 0800 UTC on February 13, 2022. The BIN scheme simulated a region with high values of cloud water content up to the height of 3 km, and it indicated notably higher cloud water content in comparison with that of the BULK scheme throughout the period of precipitation, i.e., the maximum value was more than twice that of the BULK scheme. It can be seen from Figure 10B that the rainwater content simulated by the BULK scheme was 0, whereas the BIN scheme simulated a small amount of rainwater near the end of the period of precipitation. Figure 10C shows the evolution of ice crystals. The maximum height to which the ice crystals extended was broadly the same for both the BULK scheme and the BIN scheme, i.e., up to approximately 7 km. The region of high values for both simulations was mainly located between the −20 and −38°C levels, with a multicenter structure, but the peak for the BULK scheme was substantially higher than that for the BIN scheme. Another difference is that the ice crystal content of the BULK simulation was markedly greater than that of the BIN

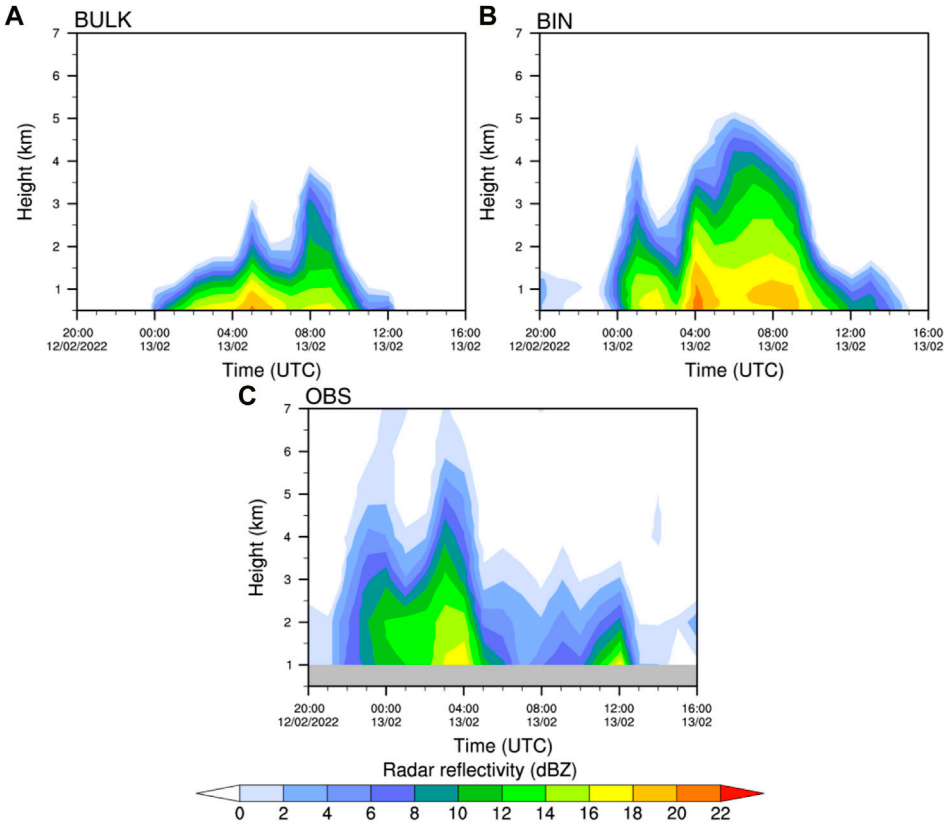

FIGURE 8
Time-height cross sections of regional average radar reflectivity for **(A)** the BULK scheme, **(B)** the BIN scheme, and **(C)** the observations from 2000 UTC on February 12 to 1600 UTC on February 13, 2022 (unit: dBZ). Regions used to calculate the regional average are shown in the red rectangles in Figures 4A3–C3.

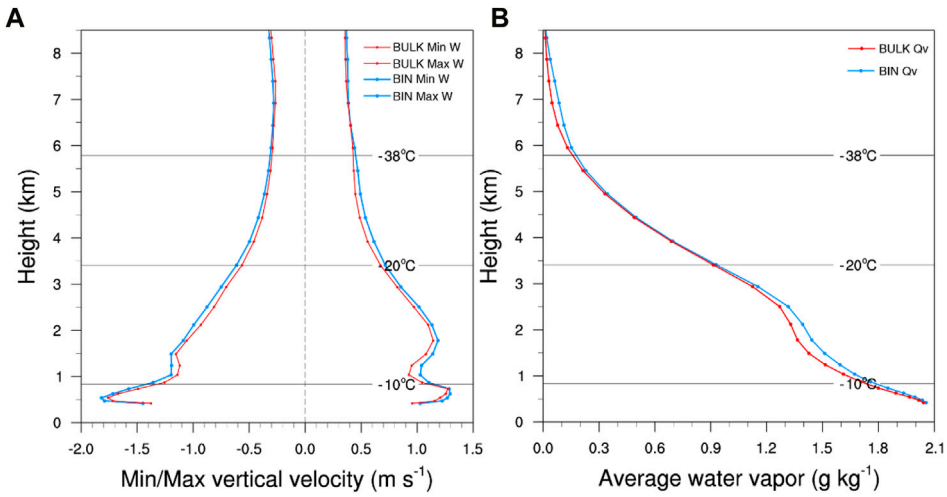

FIGURE 9
Vertical profiles of **(A)** maximum and minimum vertical velocity (unit: m s^{-1}) and **(B)** average water vapor mixing ratio (g kg^{-1}) simulated by the BULK and BIN schemes from 2000 UTC on February 12 to 1600 UTC on February 13, 2022. Regions used to calculate the vertical profiles are shown in Figures 4A3–C3.

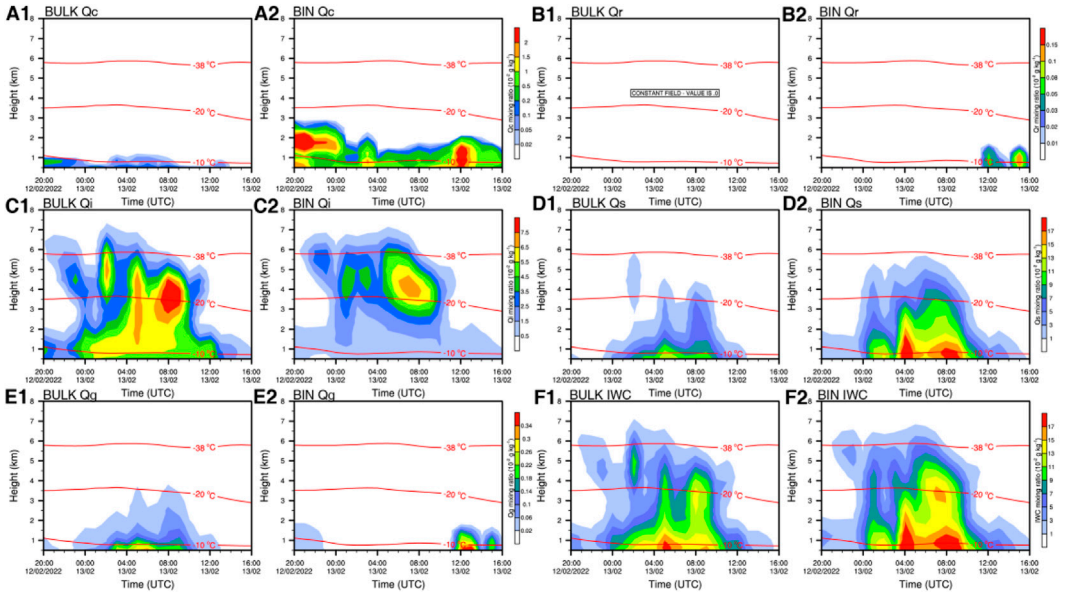

FIGURE 10
Time–height contours of cloud hydrometeors (shading; unit: g kg^{-1}) of the BULK and BIN simulations for 2000 UTC on February 12 to 1600 UTC on February 13, 2022: **(A1,A2)** cloud water (Qc), **(B1,B2)** rainwater (Qr), **(C1,C2)** cloud ice (Qi), **(D1,D2)** snow (Qs), **(E1,E2)** graupel (Qg), and **(F1,F2)** ice water content (IWC). The three horizontal red lines from low to high indicate the −10, −20, and −38°C isotherms, respectively.

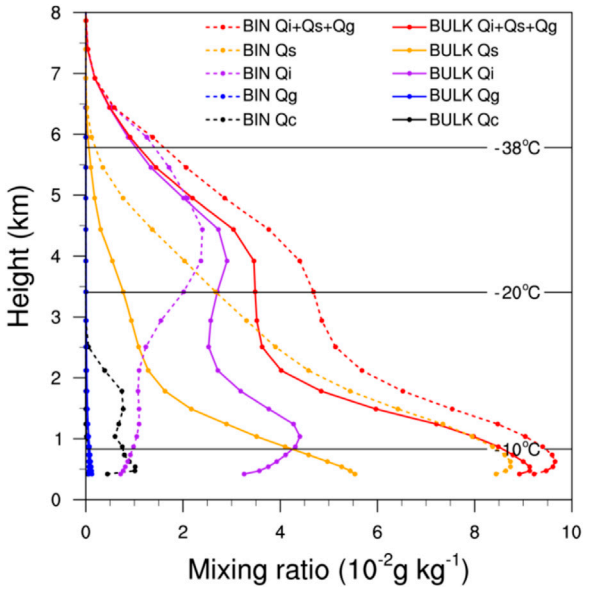

FIGURE 11
Average vertical profiles of the mixing ratio (unit: 10^{-2} g kg^{-1}) for cloud hydrometeors from 2000 UTC on February 12 to 1600 UTC on February 13, 2022, for the BULK and BIN simulations.

scheme at heights between the −20°C level and the ground throughout precipitation, i.e., with a difference of up to 2-3 times. Figure 10D shows the time–height contours of snow for the two simulations. Most snow simulated by the BULK scheme was below 4 km, while that simulated by the BIN scheme could reach up to 5 km in most periods. In contrast to the distribution of ice crystals, the snow simulated by the BULK scheme was much smaller than that simulated by the BIN scheme at heights between the −20°C level and the ground, i.e., the maximum difference was approximately 1 time greater. Figure 10E shows the evolution of graupel. The graupel simulated by the BULK scheme mainly appeared during 0000–1200 UTC on February 13, and it extended vertically up to 3.5 km. The graupel simulated by the BIN scheme mainly appeared near the end of the period of precipitation, i.e., during 1,100–1600 UTC on February 13, and it was mainly distributed at heights of <2 km; however, the content was greater than that of the BULK scheme. Figure 10F shows the time–height contours of the ice water content (IWC). The IWC simulated by the BULK and BIN schemes was mainly distributed below the height of the −38°C level, and the area with values of >0.09 g kg^{-1} mainly appeared near the ground during 0000–1200 UTC on February 13, 2022. The IWC simulated by the BIN scheme was greater than that simulated by the BULK scheme.

Figure 11 shows the average profiles for each cloud hydrometeor simulated by the BULK and BIN schemes for the selected regions throughout precipitation. The main particles in the clouds were ice crystals and snow, and in the near-ground layer (height: <2.5 km), the cloud water content simulated by the BIN scheme was substantially greater than that by the BULK scheme. At heights of 4.5 to 1 km, the ice crystal content simulated by the BULK scheme showed an overall trend of increase with decreasing height, with a peak occurring at approximately 1 km height. Below 1 km, the ice crystal content decreased with decreasing altitude. Conversely, the ice crystal content simulated by the BIN scheme showed a trend of decrease with decreasing height, with a peak occurring at 4.5 km and the lowest ice crystal content occurred at the ground. The snow

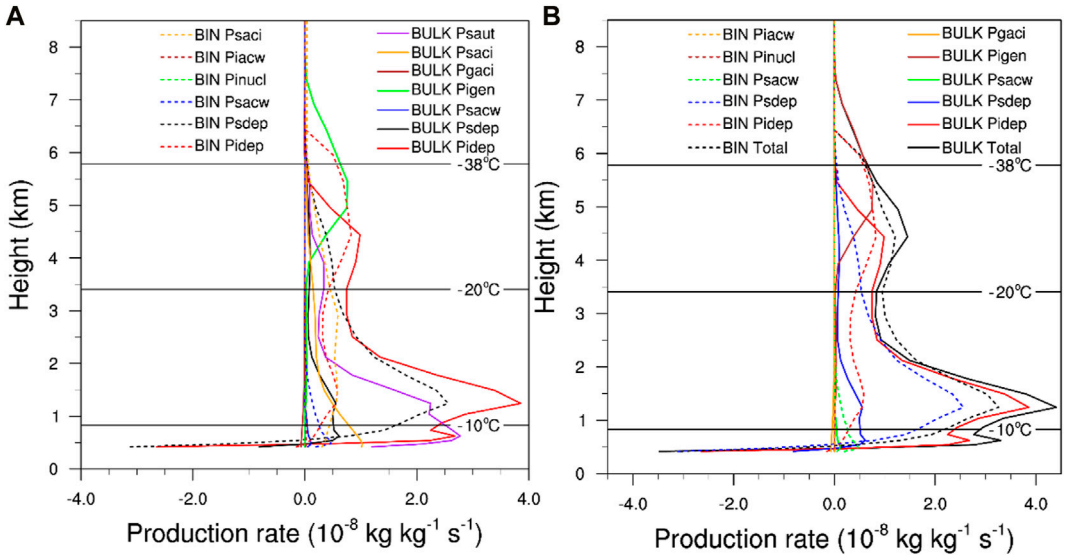

FIGURE 12
Average vertical profiles of production rates of microphysical processes (unit: 10^{-8} kg kg^{-1} s^{-1}) from 2000 UTC on February 12 to 1600 UTC on February 13, 2022 for the BULK and BIN simulations: **(A)** ice-crystal- and snow-related source and sink terms, and **(B)** budget profiles of microphysical conversion for ice crystals and snow combined.

content of the BULK scheme simulation increased with decreasing height and the peak occurred at the ground, whereas that of the BIN scheme simulation also increased with decreasing height, but with the peak at the height of approximately 0.6 km. Moreover, the snow content of the BIN scheme simulation was substantially larger than that of the BULK scheme. The BULK and BIN simulations both showed increase in IWC with decreasing height, with the peak of the BULK scheme occurring at approximately 0.6 km and the peak of the BIN scheme occurring at a slightly higher height than that of the BULK scheme. The IWC of the BIN scheme was greater than that of the BULK scheme at all altitudes. Generally, the vertical profiles of cloud water, snow, and ice crystals simulated by the BULK and BIN schemes exhibited marked differences.

4.3 Microphysical conversion processes and latent heating

Surface precipitation is formed by cloud particles falling to the ground. According to the above analysis, the precipitation particles in this snowfall event were mainly ice-phase particles. Therefore, it is important to determine how the ice-phase particles were generated, how they evolved within the cloud, what specific transformation processes occurred, and which were the main processes involved. Because transformations of cloud particles involve latent heating or cooling processes, the results discussed above indicate that differences exist in the representation of these latent heating or cooling processes between the BULK and BIN schemes. Consequently, this section analyzes the processes related to ice crystal and snow conversion, and the overall cloud microphysical processes of heating or cooling.

Figure 12A shows the average vertical profiles of the conversion rates of ice-crystal- and snow-related cloud microphysical transformation terms simulated by the BULK and BIN schemes.

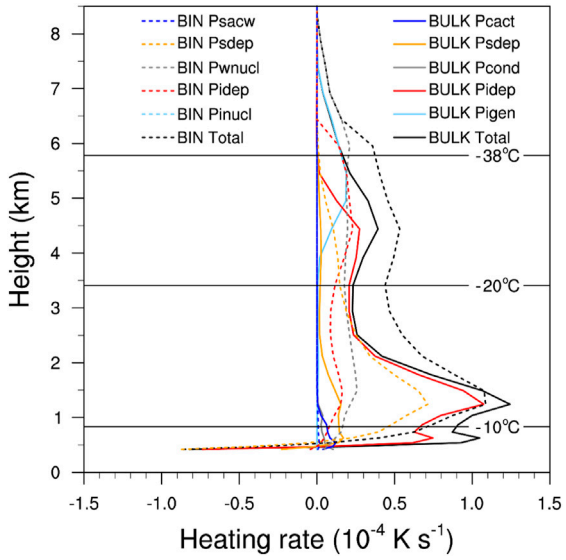

FIGURE 13
Average profiles of latent heating and cooling rates (unit: 10^{-4} K s^{-1}) for various microphysical processes from 2000 UTC on February 12 to 1600 UTC on February 13, 2022, for the BULK and BIN simulations.

The specific meanings of each transformation term are listed in Tables A1, A2. The figure shows that ice first formed at heights of 4–7.5 km through ice nucleation (P_{igen}), and that the ice crystals grew mainly through deposition (P_{idep}), i.e., the main process of ice crystal growth, and that this process mainly occurred below 5 km, with a peak at approximately 1.3 km. The ice crystals grew continuously through collision and collection. When the ice crystals reached a larger size, they

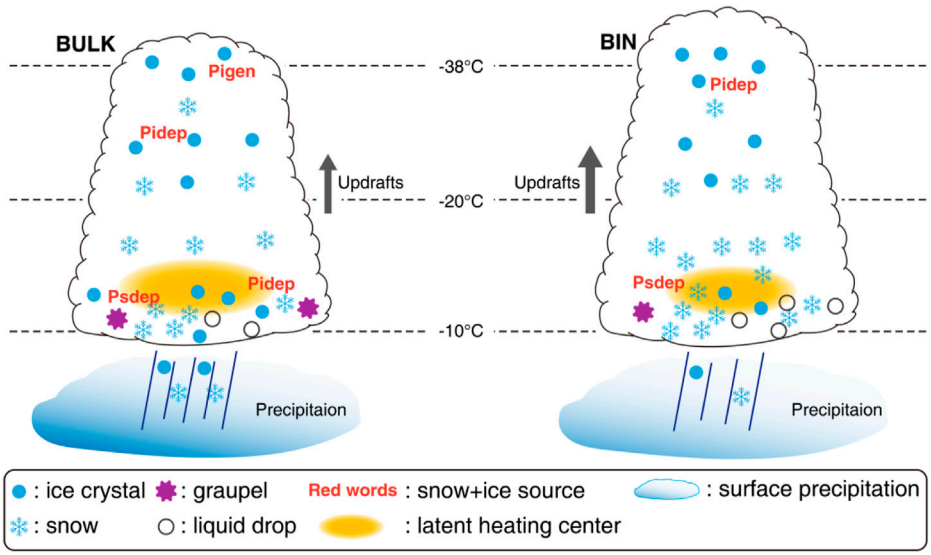

FIGURE 14
Schematic depicting the differences in the simulations between the BULK and BIN schemes.

were converted into snow through autoconversion (P_{saut}). Therefore, the profile shape of P_{saut} is similar to that of P_{idep}, but the height is much lower and the peak is below 1 km. The snow crystals then grew through the processes of deposition (P_{sdep}) and accretion of ice crystals by snow (P_{saci}), both of which occurred at heights below 5 km, i.e., below the P_{saut} profile, because both processes occurred only after the snow crystals were produced. In contrast, snow and ice crystals in the BIN simulation were mainly generated from four microphysical processes, i.e., deposition growth of ice crystals and snow (P_{idep} and P_{sdep}) and accretion of ice crystals and cloud water by snow (P_{saci}, P_{sacw}). At the height of the −38°C level, the ice-phase particles in the BIN scheme were mainly produced by ice crystal deposition, whereas in the BULK scheme, they were mainly produced by ice nucleation. Between the −20 and −10°C levels, the ice-phase particles in the BIN scheme were mainly produced by the deposition of snow, whereas they were mainly generated by the deposition of ice crystals in the BULK scheme.

Figure 12B shows the budgets of the conversion terms of the microphysical process for ice crystals and snow combined for the BULK and BIN simulations. From the source and sink terms of the snow and ice crystals, it can be seen that the overall net production rate of ice crystals and snow simulated by the BULK scheme was larger than that of the BIN scheme at levels below 2 km and above 4 km. In comparison with the BIN scheme, other than the peak in the net conversion rate at approximately 1.3 km, there was also a second peak at a height very close to the surface below 1 km. As can be seen from Figure 11, the simulation of the BULK scheme produced a smaller average snow content than that of the BIN scheme throughout the entire precipitation process, indicating that the BULK scheme simulates more surface precipitation and that the precipitation intensity is greater. One possible reason is that the peak value of each source term of snow in the BULK scheme was closer to the ground than that in the BIN scheme, which allowed snow to fall to the ground faster.

The heating process in cloud microphysics includes condensation, freezing, and deposition; conversely, evaporation, melting, and sublimation are considered cooling processes. Based on the methods used by Hjelmfelt et al. (1989), the average profiles of the latent heating for the BULK and BIN schemes are illustrated in Figure 13. It can be seen that the main latent heating terms in the BULK scheme are ice nucleation (P_{igen}), deposition of ice crystals and snow (P_{idep} and P_{sdep}, respectively), and condensation growth of water vapor (P_{cond}), while those in the BIN scheme are similar. Below the height of 2 km, the latent heat released by cloud microphysical processes in the BULK scheme is larger than that released in the BIN scheme, whereas the converse is true at heights above 2 km.

5 Discussion and conclusion

To investigate the simulation capability of the BIN and BULK microphysical schemes for winter precipitation events and their differences, we used the WRF regional numerical model with the BULK and BIN schemes to simulate a snowfall event that occurred in Beijing during the Winter Olympic Games on February 12-13, 2022. The simulations using the two schemes broadly reproduced the spatiotemporal evolution characteristics of the precipitation event. Based on the refined simulation results, the outputs of the BULK and BIN schemes were further investigated to analyze the differences in precipitation, radar reflectivity, and cloud microphysical processes of the heavy snowfall event dominated by cold cloud processes in winter. The differences between the BULK and BIN simulations are summarized into the conceptual models in Figure 14, and the detailed conclusions are as follows.

(1) The heavy snowfall event in the Beijing area during February 12-13, 2022, mainly occurred against the background of an upper-level cold vortex, formed under the combined favorable conditions of an upper-level jet at 200 hPa and a low-level vortex at 850 hPa. From the soundings and surface temperature field, it was established that

the overall air temperature over the Beijing area was <0°C; thus, the surface precipitation was dominated by solid precipitation particles.

(2) The 24-h accumulated precipitation simulated by the BULK scheme was greater than that simulated by the BIN scheme, but both were smaller in comparison with the observations. For regional average hourly precipitation, although the BULK and BIN schemes both broadly reproduced the precipitation evolution, they underestimated the precipitation with a 1-2-h lag in the early and middle period of the precipitation event (i.e., from 2200 UTC on February 12 to 0700 UTC on February 13, 2022), and in the period of heavy precipitation (i.e., from 0200 to 0700 UTC on February 13, 2022). The precipitation simulated by the BIN scheme showed a pattern of more symmetrical growth and weakening, which was closer to that of the observations than that produced by the BULK scheme. However, the BIN and BULK simulations both overestimated the precipitation in the weakening period (i.e., from 0800 to 1800 UTC on February 13, 2022). Additionally, comparison of the radar reflectivity horizontal distributions, vertical cross sections, and time–height contours revealed that the radar reflectivity simulated by the BIN scheme was generally closer than that simulated by the BIN scheme to that of the observations.

(3) Comparative analysis of the maximum/minimum vertical velocities and water vapor between the BULK and BIN schemes revealed that the maximum upward and downward velocities simulated by the BIN scheme were substantially stronger than those of the BULK scheme, and that the difference between them was greater when the temperature was greater than −38°C (i.e., below 5.8 km), indicating stronger upward motion and more vigorous convection in the BIN scheme. The water vapor content of the BIN scheme was markedly higher than that of the BULK scheme at heights from the −10 to −20°C levels and above the −38°C level, possibly because the BULK scheme converts more water vapor into cloud particles through various cloud microphysical processes in comparison with that converted by the BIN scheme.

(4) The vertical distribution of cloud particles simulated by the BULK and BIN schemes differed substantially, with the BIN scheme simulating much more cloud water and snow than the BULK scheme, and the BULK scheme simulating more snow than the BIN scheme at most altitudes below 5 km. Although the vertical profile of IWC for the two schemes showed similar evolution trends, the IWC simulated by the BIN scheme was larger.

(5) By analyzing the conversion rate and the latent heating of the cloud microphysical processes in the BULK and BIN schemes, it was found that nucleation of ice crystals in the middle and upper layers of the BULK scheme was notable but not as obvious as that in the BIN scheme. The net production rate of ice crystals and snow combined, as simulated by the BULK scheme, was stronger nearer the surface than that simulated by the BIN scheme. Moreover, a second peak in the conversion rate existed at heights very close to the surface below 1 km, which might account for the greater intensity of precipitation in the BULK scheme. Below the height of 2 km, the BULK scheme simulated greater latent heating than that simulated by the BIN scheme, whereas the converse was true at heights above 2 km.

The descriptions of cloud microphysical processes by the BULK and BIN schemes, and by some other multimoment schemes, include certain assumptions and therefore have specific advantages and shortcomings. Consequently, it is very important to undertake detailed comparison and analysis of different cloud microphysical schemes in different applications to improve the understanding and applicability of such schemes (Li et al., 2009a). Previous comparison of the BULK and BIN schemes has mainly focused on strong convection in summer; however, this study focused on their applicability to a snowfall event that occurred in winter. It is expected that the findings of this study will provide a better understanding of the differences between the BULK and BIN schemes with regard to the simulation of microphysical processes during weak convection in winter, and serve as reference for improvement of the BULK and/or BIN schemes. However, this study was based on the results obtained from a single case, which means that our findings are preliminary and case-dependent, and that further simulation studies of other cases will be needed to validate our results. Furthermore, detailed analyses and sensitivity experiments should also be performed to investigate the mechanisms responsible for the distinctive differences between the results produced by the BULK and BIN schemes. Finally, obtaining more detailed observations, especially those that can reveal information within clouds, e.g., aircraft observations and satellite-based cloud radar (Morrison et al., 2020), which can be used in combined with high-resolution numerical simulations, will form an essential part of the continued improvement of cloud microphysical parameterization schemes.

Data availability statement

The raw data supporting the conclusion of this article will be made available by the authors, without undue reservation.

Author contributions

YL designed the study and wrote the initial manuscript; JyL and FP discussed and contributed to the idea; LL improved the manuscript; JiL performed data analysis.

Funding

This research was funded by the National Key R&D Program of China (Grant number 2018YFC1506801), the Key Scientific and Technology Research and Development Program of Jilin Province (Grant number 20180201035SF), the Innovative Development Project of China Meteorological Administration (Grant number CXFZ2022J007), the National Natural Science Foundation of China (Grant number 41875077 and 42105013). Simulations were carried out on the Earth System Numerical Simulation Facility (EarthLab), which was supported by the National Key Scientific and Technological Infrastructure project.

Conflict of interest

The authors declare that the research was conducted in the absence of any commercial or financial relationships that could be construed as a potential conflict of interest.

Publisher's note

References

Changnon, S. A., and Changnon, D. (2006). A spatial and temporal analysis of damaging snowstorms in the United States. *Nat. Hazards* 37, 373–389. doi:10.1007/s11069-005-6581-4

Chen, F., and Dudhia, J. (2001a). Coupling an advanced land surface–hydrology model with the Penn State–NCAR MM5 modeling system. Part I: Model implementation and sensitivity. *Mon. Weather Rev.* 129, 569–585. doi:10.1175/1520-0493(2001)129<0569:caalsh>2.0.co;2

Chen, F., and Dudhia, J. (2001b). Coupling an advanced land surface–hydrology model with the Penn State–NCAR MM5 modeling system. Part II: Preliminary model validation. *Mon. Weather Rev.* 129, 587–604. doi:10.1175/1520-0493(2001)129<0587:caalsh>2.0.co;2

Chen, Y., Ping, F., Zhou, S., Shen, X., and Sun, Y. (2021). Influence of microphysical processes on the initiation of the mesoscale convective system of a rainstorm over Beijing. *Atmos. Res.* 254, 105518. doi:10.1016/j.atmosres.2021.105518

Dudhia, J. (1989). Numerical study of convection observed during the winter monsoon experiment using a mesoscale two-dimensional model. *J. Atmos. Sci.* 46, 3077–3107. doi:10.1175/1520-0469(1989)046<3077:Nsocod>2.0.Co;2

Fan, J., Leung, L. R., Li, Z., Morrison, H., Chen, H., Zhou, Y., et al. (2012). Aerosol impacts on clouds and precipitation in eastern China: Results from bin and bulk microphysics: Aerosol impacts on clouds. *J. Geophys. Res.* 117, 1–21. doi:10.1029/2011JD016537

Hjelmfelt, M. R., Roberts, R. D., Orville, H. D., Chen, J. P., and Kopp, F. J. (1989). Observational and numerical study of a microburst line-producing storm. *J. Atmos. Sci.* 46, 2731–2744. doi:10.1175/1520-0469(1989)046<2731:OANSOA>2.0.CO;2

Hong, S. Y., Noh, Y., and Dudhia, J. (2006). A new vertical diffusion package with an explicit treatment of entrainment processes. *Mon. Weather Rev.* 134, 2318–2341. doi:10.1175/mwr3199.1

Igel, A. L., and van den Heever, S. C. (2017). The role of the gamma function shape parameter in determining differences between condensation rates in bin and bulk microphysics schemes. *Atmos. Chem. Phys.* 17, 4599–4609. doi:10.5194/acp-17-4599-2017

Jiao, B., Ran, L., Shen, X., and Qi, Y. (2021). Trigger mechanism of a snow burst event in Northeast China. *Atmos. Ocean. Sci. Lett.* 14, 100017. doi:10.1016/j.aosl.2020.100017

Jiménez, P. A., Dudhia, J., González-Rouco, J. F., Navarro, J., Montávez, J. P., and García-Bustamante, E. (2012). A revised scheme for the WRF surface layer formulation. *Mon. Weather Rev.* 140, 898–918. doi:10.1175/MWR-D-11-00056.1

Kain, J. S. (2004). The Kain-Fritsch convective parameterization: An update. *J. Appl. Meteorology* 43, 170–181. doi:10.1175/1520-0450(2004)043<0170:Tkcpau>2.0.Co;2

Khain, A., and Lynn, B. (2009). Simulation of a supercell storm in clean and dirty atmosphere using weather research and forecast model with spectral bin microphysics. *J. Geophys. Res. Atmos.* 114, D19209. doi:10.1029/2009JD011827

Khain, A. P., Leung, L. R., Lynn, B., and Ghan, S. (2009). Effects of aerosols on the dynamics and microphysics of squall lines simulated by spectral bin and bulk parameterization schemes. *J. Geophys. Res. Atmos.* 114, D22203. doi:10.1029/2009JD011902

Khain, A., Pokrovsky, A., Pinsky, M., Seifert, A., and Phillips, V. (2004). Simulation of effects of atmospheric aerosols on deep turbulent convective clouds using a spectral microphysics mixed-phase cumulus cloud model. Part I: Model description and possible applications. *J. Atmos. Sci.* 61, 2963–2982. doi:10.1175/JAS-3350.1

Khain, A. P., and Pinsky, M. (2018). *Physical processes in clouds and cloud modeling*. 1st ed. Cambridge University Press. doi:10.1017/9781139049481

Li, N., Jiao, B., Ran, L., Shen, X., and Qi, Y. (2021). On the mechanism of a terrain-influenced snow burst event during midwinter in Northeast China. *Adv. Atmos. Sci.* 38, 800–816. doi:10.1007/s00376-020-0104-9

Li, X., Tao, W.-K., Khain, A. P., Simpson, J., and Johnson, D. E. (2009a). Sensitivity of a cloud-resolving model to bulk and explicit bin microphysical schemes. Part I: Comparisons. *J. Atmos. Sci.* 66, 3–21. doi:10.1175/2008JAS2646.1

Li, X., Tao, W.-K., Khain, A. P., Simpson, J., and Johnson, D. E. (2009b). Sensitivity of a cloud-resolving model to bulk and explicit bin microphysical schemes. Part II: Cloud microphysics and storm dynamics interactions. *J. Atmos. Sci.* 66, 22–40. doi:10.1175/2008JAS2647.1

Li, Y., Li, J., Ping, F., and Gao, Z. (2022). Influence of the terminal velocity of graupel on the simulation of a convective system over Beijing. *Atmos. Res.* 274, 106181. doi:10.1016/j.atmosres.2022.106181

Lim, K.-S. S., and Hong, S.-Y. (2010). Development of an effective double-moment cloud microphysics scheme with prognostic cloud condensation nuclei (CCN) for weather and climate models. *Mon. Weather Rev.* 138, 1587–1612. doi:10.1175/2009MWR2968.1

Lin, W., and Bueh, C. (2006). The cloud processes of a simulated moderate snowfall event in North China. *Adv. Atmos. Sci.* 23, 235–242. doi:10.1007/s00376-006-0235-7

Liu, X., He, H., Chen, Y., Gao, Q., Wang, Y., and Yang, Y. (2022). Numerical simulation studies of atmospheric hydrometeor transportation characteristics and snowfall microphysical mechanism during a snowfall system in beijing. *Chin. J. Atmos. Sci. (in Chinese)* 46, 507–519. doi:10.3878/j.issn.1006-9895.2110.20212

Lynn, B. H., Khain, A. P., Dudhia, J., Rosenfeld, D., Pokrovsky, A., and Seifert, A. (2005). Spectral (bin) microphysics coupled with a mesoscale model (MM5). Part II: Simulation of a CaPE rain event with a squall line. *Monthly Weather Review* 133, 59–71. doi:10.1175/MWR-2841.1

Mlawer, E. J., Taubman, S. J., Brown, P. D., Iacono, M. J., and Clough, S. A. (1997). Radiative transfer for inhomogeneous atmospheres: RRTM, a validated correlated-k model for the longwave. *Journal of Geophysical Research Atmospheres* 102, 16663–16682. doi:10.1029/97JD00237

Morrison, H., van Lier-Walqui, M., Fridlind, A. M., Grabowski, W. W., Harrington, J. Y., Hoose, C., et al. (2020). Confronting the challenge of modeling cloud and precipitation microphysics. *J Adv Model Earth Syst* 12, e2019MS001689. doi:10.1029/2019MS001689

Skamarock, W. C., Klemp, J. B., Dudhia, J., Gill, D. O., Liu, Z., Berner, J., et al. (2019). *A description of the advanced research WRF model version 4*. Boulder, CO, USA: National Center for Atmospheric Research, 145. doi:10.5065/1dfh-6p97

Sun, J., Wang, H., Yuan, W., and Chen, H. (2010). Spatial-temporal features of intense snowfall events in China and their possible change. *Journal of Geophysical Research Atmospheres* 115, D16110. doi:10.1029/2009JD013541

Wang, C., Liu, H., and Lee, S.-K. (2010). The record-breaking cold temperatures during the winter of 2009/2010 in the Northern Hemisphere. *Atmospheric Science Letters* 11, 161–168. doi:10.1002/asl.278

Wang, D., Yin, J., and Zhai, G. (2015). *In-situ* measurements of cloud-precipitation microphysics in the East Asian monsoon region since 1960. *J Meteorol Res* 29, 155–179. doi:10.1007/s13351-015-3235-7

Wang, S., Ping, F., Meng, X., and Li, Y. (2022). Numerical simulation of a large-scale snowstorm process in northern China using different cloud microphysical parameterization schemes. *Chinese Journal of Atmospheric Sciences (in Chinese)* 46, 599–620. doi:10.3878/j.issn.1006-9895.2107.21064

Xu, H., and Duan, Y. (1999). Some questions in studying the evolution of size distribution spectaum of hydrometeor particles. *Acta Meteorologica Sinica (in Chinese)* 57, 451–460.

Yin, J., Wang, D., and Zhai, G. (2011). Long-term *in situ* measurements of the cloud-precipitation microphysical properties over East Asia. *Atmospheric Research* 102, 206–217. doi:10.1016/j.atmosres.2011.07.002

Yin, L., Ping, F., and Mao, J. (2017). A comparative study between bulk and bin microphysical schemes of a simulated squall line in East China: Comparative research between bulk and bin microphysical scheme. *Atmos. Sci. Lett* 18, 195–206. doi:10.1002/asl.742

Zhang, Y., Wu, Z., Zhang, L., and Zheng, H. (2022). A comparison of spectral bin microphysics versus bulk parameterization in forecasting typhoon in-fa (2021) before, during, and after its landfall. *Remote Sensing* 14, 2169. doi:10.3390/rs14092169

Appendix A

TABLE A1 Description of the main microphysical processes in WDM6 scheme.

Name	Description
P_{saut}	Autoconversion of cloud ice to form snow
P_{saci}	Accretion of cloud ice by snow
P_{iacw}	Accretion of cloud water by cloud ice
P_{sacw}	Accretion of cloud water by snow
P_{gaci}	Accretion of cloud ice by graupel
P_{igen}	Generation of ice from vapor
P_{idep}	Deposition/sublimation of ice
P_{cond}	Condensation/evaporation of cloud water
P_{cact}	Activation of CCN
P_{sdep}	Deposition/sublimation of snow

TABLE A2 Description of the main microphysical processes in HUJI bin scheme.

Name	Description
P_{saci}	Accretion of cloud ice by snow
P_{iacw}	Accretion of water by cloud ice
P_{sacw}	Accretion of water by snow
P_{gaci}	Accretion of cloud ice by graupel
P_{inucl}	Nucleation of ice crystal
P_{idep}	Deposition/sublimation of ice crystal
P_{wnucl}	Nucleation of droplets
P_{sdep}	Deposition/sublimation of snow

frontiers | Frontiers in Earth Science

TYPE Original Research
PUBLISHED 18 April 2023
DOI 10.3389/feart.2023.1148506

OPEN ACCESS

EDITED BY
Jianhua SUN,
Chinese Academy of Sciences (CAS), China

REVIEWED BY
Liping Luo,
Nanjing University of Aeronautics and Astronautics, China
Lingkun Ran,
Chinese Academy of Sciences (CAS), China

*CORRESPONDENCE
Jiwen Fan,
jiwen.fan@pnnl.gov
Jingyu Wang,
jingyu.wang@nie.edu.sg

RECEIVED 20 January 2023
ACCEPTED 10 April 2023
PUBLISHED 18 April 2023

CITATION
Fan J, Wang J and Lin Y (2023), Urbanization may enhance tornado potential: A single case report. *Front. Earth Sci.* 11:1148506. doi: 10.3389/feart.2023.1148506

Urbanization may enhance tornado potential: A single case report

Jiwen Fan[1]*, Jingyu Wang[1,2]* and Yun Lin[1,3]

[1]Pacific Northwest National Laboratory, Atmospheric Sciences and Global Change Division, Richland, WA, United States, [2]National Institute of Education, Nanyang Technological University, Singapore, Singapore, [3]Joint Institute for Regional Earth System Science and Engineering, University of California, Los Angeles, Los Angeles, CA, United States

Tornadoes pose a risk of catastrophic economic loss and casualty in the United States. Modification of land use by urbanization alters the meteorological conditions that may impact tornado formation and intensification processes. Here we explored the simulated impact of Kansas City urbanization on the tornado potential of a supercell storm. In this studied case, we found that urbanization might enhance tornado potential by a) strengthening the low-level streamwise vorticity in the storm inflow region, thus forming stronger rotating updrafts; and b) intensifying near-surface horizontal vorticity near the boundary of the forward-flank cold pool which increases the ingestion, tilting, and stretching of streamwise horizontal vorticity into vertical vorticity. The former results from the stronger east-to-west pressure perturbation gradient due to the faster, stronger outflow boundary, and the latter is mainly a result of stronger cold fronts and a better alignment of storm-relative inflow with the horizontal vorticity vector. We emphasize that our conclusions only represent one possibility of how urbanization would affect tornado potential, and a more systematic examination is needed to achieve a more general conclusion.

KEYWORDS

urbanization, supercell, tornado potential, WRF simulation, tornadogenesis

1 Introduction

Tornadoes are one of the most devastating severe weather hazards in the United States, capable of producing significant property damage and casualties (Changnon, 2009). Through decades of scientific exploration of tornadoes and tornado-producing thunderstorms, researchers have made remarkable progress in understanding the characteristics of tornadoes, as well as the physical processes related to tornado formation and intensification (e.g., Lemon and Doswell, 1979; Brooks et al., 1993; Markowski, 2002; Markowski et al., 2002; Wurman et al., 2012; Flournoy et al., 2020). However, few studies have examined how changes in urbanization would be expected to impact supercell and associated tornado activities (Reames and Stensrud, 2018).

Urbanization is an extreme case of land use change (Shepherd, 2005) that modifies surface heat, moisture, and momentum exchanges, which in turn alter low-level atmospheric conditions. It is projected that the global urban land coverage will increase by about 6 times, on average, by end of the 21st century compared with 2010, based on intensive fossil-fueled development (Gao and O'Neill, 2020). This rapid urbanization has motivated sustained research on urban meteorology and climate over the past 50 years (Ching et al., 2018). Many

previous studies have revealed that urbanization has a notable impact on local weather and climate at all scales (Qian et al., 2022). For example, the urban heat island (UHI), along with altered sensible and latent heat flux, soil moisture, etc., could enhance low-level temperature, turbulence, and convergent mesoscale circulations, which promotes storm initiation and subsequent intensification, increased heavy precipitation, large hail, and stronger convective-scale winds (Bornstein and Lin, 2000; Shepherd, 2005; Hubbart et al., 2014; Haberlie et al., 2015; Liu and Niyogi, 2019; Fan et al., 2020; Javanroodi and Nik, 2020; Singh et al., 2020; Lin et al., 2021).

The majority of past studies on urbanization effects investigated precipitation formed from relatively weak convective storms. A few recent modeling studies have explored urbanization impacts on supercell storms interacting with urban areas (Reames and Stensrud, 2018; Lin et al., 2021). Reames and Stensrud (2018) showed that urban areas have a significant impact on low-level rotation and mesocyclone (a meso-gamma scale region of rotation, typically around 3–10 km in diameter) track, but they did not further explore the impact on tornado activity. A long-term analysis of tornado reports showed a correlation between tornado occurrences and land surface heterogeneity—particularly at the boundaries of urban and forested land cover (Kellner and Niyogi, 2014). Higher probabilities of tornado occurrence in urban counties than in rural counties have been reported (Aguirre et al., 1993; Ashley, 2007), although reporting biases due to population density could play a role (Anderson et al., 2007). Early studies have examined long-term climatological near-tornado environments and indicated that low-level moisture content is indispensable for tornadogenesis (e.g., Miller, 1972). Based on this finding, urbanization could be an adverse factor for tornadogenesis because it generally results in a drier planetary boundary layer (PBL). Therefore, process-level studies of the urbanization effect on tornado activities are highly needed.

Tornadogenesis and intensity are associated with storm-scale characteristics and processes (e.g., Brooks et al., 1993; Parker, 2014; Davies-Jones, 2015; Flournoy et al., 2020). There are several key processes for tornado formation in supercells. First, the flux of low-level streamwise horizontal vorticity to a convective updraft and the subsequent vertical tilting and stretching forms the mesocyclone and intensifies the mid-low-level updraft (Barnes, 1978; Doswell and Burgess, 1993; Glickman, 2000; Dahl, 2017). Second, to form a tornadic vortex, the near-surface horizontal vorticity, which can be embedded in the large-scale environment and possibly enhanced by low-level baroclinity (Dahl et al., 2014; Markowski and Richardson, 2014; Parker and Dahl, 2015) or surface friction (Schenkman et al., 2014; Roberts et al., 2016), is vertically tilted, stretched, and advected upward by the low-level updraft. The development of near-surface vertical vorticity commonly involves rear-flank downdrafts through the generation of baroclinic vorticity associated with the outflow temperature gradient and augmentation of vortex lines near the ground (Davies-Jones and Brooks, 1993; Markowski, 2002). Thus, many crucial processes governing tornadogenesis are impacted by the low-level wind and thermodynamic fields that may be affected by the underlying surface.

Tornado potential has been examined using various parameters in model simulations at convection-permitting scales, for example, storm updraft helicity (UH; the vertical integral of the product of vertical velocity and vertical vorticity) between 2 and 5 km altitudes (Clark et al., 2013) and vertical relative vorticity, as well as the characteristics of the storm environment including wind shear at low levels (Markowski and Richardson, 2014; Sobash et al., 2016) and the significant tornado parameter (STP; Thompson et al., 2012). The STP is a composite index of mixed-layer (ML) lifted condensation level (LCL; the level at which a parcel becomes saturated), convective available potential energy (CAPE; the vertically integrated energy that buoyancy would provide for rising air mass), convective inhibition (CIN; the amount of energy that prevents air parcels from rising), effective storm-relative helicity (ESRH; a measure of the potential for cyclonic updraft rotation relative to a right-moving supercell within the effective inflow layer), and effective bulk wind difference (EBWD; the magnitude of the vector wind difference from the effective inflow base upward to 50% of the equilibrium level height for the most unstable parcel in the lowest 300 mb). STP is calculated as below:

$$STP = \frac{MLCAPE}{1500\ J\ kg^{-1}} \times \frac{ESRH}{150\ m^2\ s^{-2}} \times \frac{EBWD}{20\ m\ s^{-1}} \times \frac{2000 - MLLCL}{1000\ m} \times \frac{200 + MLCIN}{150\ J\ kg^{-1}} \tag{1}$$

By interpreting these variables, the Storm Prediction Center (SPC) issues tornado warnings when the occurrences of tornadoes become imminent (Shafer et al., 2010; Tippett et al., 2012; Clark et al., 2018).

Here we explore a possible urbanization effect on the tornado potential of a supercell storm using simulations of an event occurring in Kansas City that was observed during the Plains Elevated Convection at Night (PECAN; Geerts et al., 2017) field campaign on the evening of 1–2 July 2015. This paper continues the work of Lin et al. (2021) (hereafter, "LIN21"), who investigated urbanization effects on storm formation, evolution, and hail occurrences for the same case using numerical simulations. Here, we find that in the studied case the urban area associated with Kansas City might enhance simulated tornado potential through the local enhancement of environmental parameters favorable for supercell tornadoes in the near-storm inflow.

2 Methods

2.1 Case description

A supercell storm occurred over Kansas City on 1–2 July 2015 (Figure 1C). A series of weak tornadoes with the enhanced Fujita (EF) scale rating of 0 or 1 were reported (Figure 1A). Two of them were reported between 23:33 and 01:07 UTC in Lee's Summit and west-southwest of the Pleasant Hill Weather Forecast Office, respectively. These tornadoes caused some building damage. The storm developed along a pre-existing east-west-oriented quasi-stationary front located approximately 100 km north of a warm front (Figure 1B), which was produced by the preceding storm on the previous day. Southerly and southwesterly flow at the low levels advected warm, moist air northward into the region, resulting in an unstable environment with surface-based CAPE (SBCAPE) of more

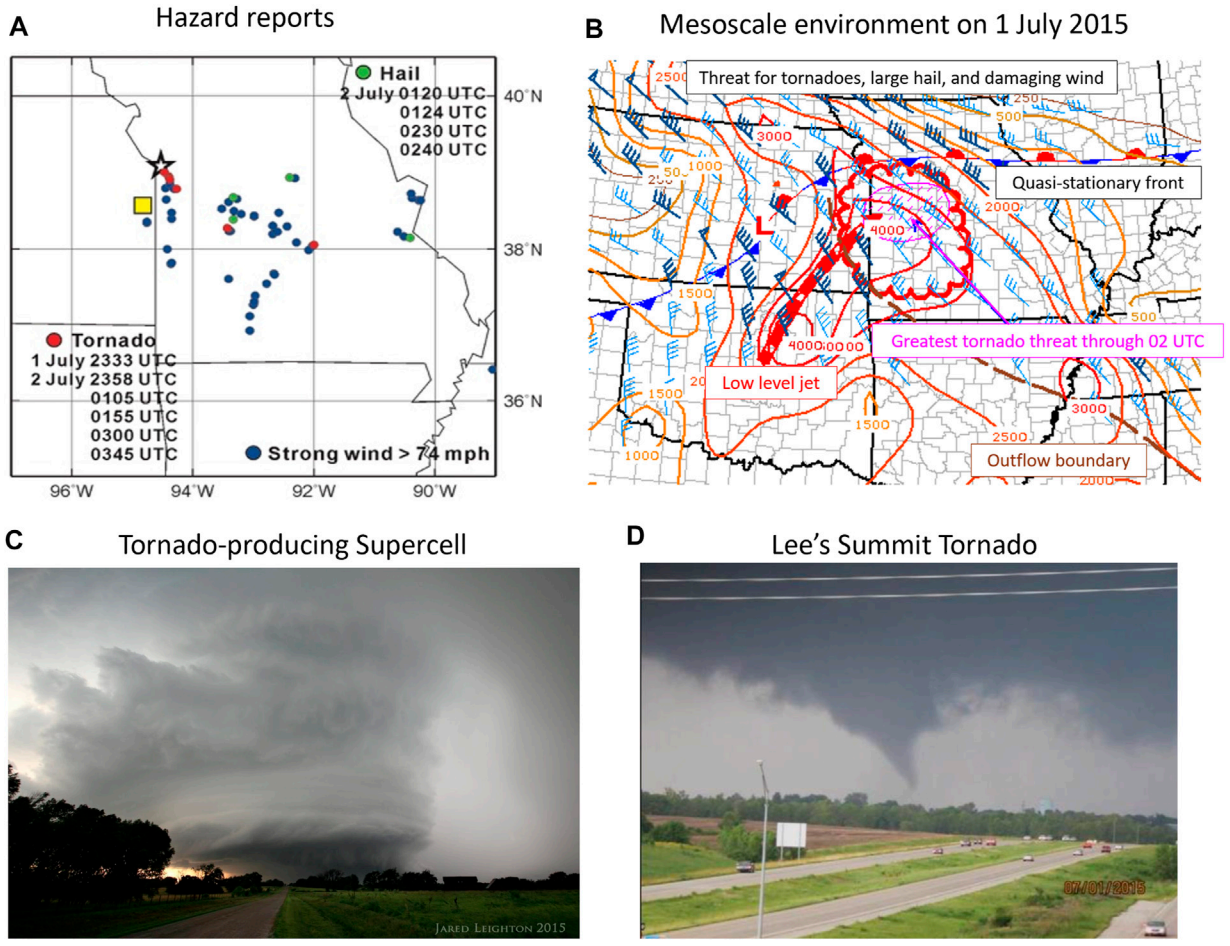

FIGURE 1
(A) The mesoscale environment on 1 July 2015, adapted from the mesoscale discussion #1274 issued by NOAA Storm Prediction Center (https://www.spc.noaa.gov/products/md/2015/md1274.html). LLJ denotes low-level jet. **(B)** The reports of large hail, tornado, and strong winds from the NOAA Storm Prediction Center (SPC). Photos of **(C)** the tornado-producing supercell (photo by Jared Leighton, http://slightrisk.net/chase_2015/july_1), **(D)** the tornado in Lee's Summit (photo by Christopher Gitro).

than 3800 J kg^{-1} (LIN21). After the storm initiated in the area northwest of the Kansas City metro area, it traveled southeastward toward the city, intensified, and eventually developed tornadoes. The first confirmed tornado report was EF0 in Raytown (39.01°N, 94.47°W) at 23:33 UTC, followed by the EF1 in Lee's Summit (38.91°N, 94.38°W) at about 23:51 UTC (Figure 1D).

Before the outbreak of the first tornado, National Weather Service (NWS) issued a tornado watch as shown in Figure 1B (pink area), where the greatest tornado threat has been highlighted over eastern Missouri and eastern Kansas. The supercell, developed along the quasi-stationary front persist from southeast of Kansas eastward through north-central Missouri, grew upscale, and propagated southwestward between the quasi-stationary front and the pre-existing boundary (Figures 1B,C).

During the outbreak of the most intense tornado, the tornado-producing supercell demonstrates the typical hook echo structure as seen in many observational archives of tornadic supercells (Markowski, 2002; Markowski et al., 2002; Wurman and Kosiba, 2013). However, the location of the hook echo is around 44 km to the southeast of the first reported tornado touch-down over Kansas City, indicating the tornado case in this study is not much related to the hook echo. As revealed by previous studies (Maddox, 1980; Markowski et al., 1998; Rasmussen et al., 2000; Wurman et al., 2007), a considerable number of tornadoes occurred near low-level boundaries (e.g., synoptic-scale fronts, or outflow boundaries produced by antecedent systems), which are not associated with a forward flank downdraft (FFD) or rear flank downdraft (RFD). The increased tornado potential has been commonly recorded when supercells move along or across those boundaries due to the enhanced low-level wind shear (Schultz et al., 2014), and many significant tornadoes (i.e., EF5) with the devastating outbreak have been formed in such condition (Markowski et al., 1998; Knupp et al., 2014). The studied tornadic supercell case follows this concept.

2.2 Model simulations

This work leverages simulations described by LIN21. We refer the reader to that study for model details. To briefly summarize the

experiment design, the simulations were run at 1-km grid spacing using the Chemistry version of the Weather Research and Forecasting (WRF) model coupled with the spectral-bin microphysics (SBM) scheme (Gao et al., 2016). Urban physics is represented by the multi-layer urban canopy model Building Environment Parameterization coupled with Building Energy Model (BEP+BEM; Martilli et al., 2002; Salamanca and Martilli, 2010). Two simulations are used in this study to examine the urban land effect on tornado potential. One is a baseline simulation with realistic land surface conditions and anthropogenic emissions. In the second simulation, the urban land surface is replaced by the surrounding cropland. These simulations are referred to as "ULandAero" and "No_ULand", respectively, in LIN21. For simplicity, we have renamed them the "City" and "No-City" simulations, respectively. The baseline simulation ("City") was verified with observations of precipitation, radar reflectivity, and hail as detailed in LIN21.

The evolutions of the observed and simulated storms are compared in Supplementary Figures S2 and S6 of LIN21. Note, LIN21 showed that anthropogenic aerosols did not significantly affect the storm initiation and subsequent development; thus, their effect on the tornado potential is not considered here. Although we do not expect tornadoes to be directly resolved in simulations with a 1-km grid spacing, we do expect that crucial variables and processes impacting the structure and behavior of the parent supercell that may affect tornado potential are adequately represented. Tornado watches are often issued based on the analysis of model simulations conducted with kilometer-scale grid spacings (e.g., Gallo et al., 2016; 2018).

2.3 Diagnostic variables for tornado potential

As discussed earlier, STP and UH are commonly used for indicating the tornado potential of a storm and its ambient environment. Tornadic environments are typically associated with STP values greater than 1 in the model-derived proximity soundings of Thompson et al. (2007). Gallo et al. (2016); Gallo et al. (2018) forecasted tornadoes from convection-permitting simulations using a combination of environmental parameters such as 2–5-km UH $\geq$ 75 m^2 s^{-2}, STP >1, the ratio of SBCAPE to most unstable CAPE (MUCAPE) greater than 0.75, and SBLCL heights below 1.5 km. We employ these variables to quantify the tornado potential in the simulations.

Following the key processes for tornadogenesis associated with supercells discussed in the introduction, we examined streamwise horizontal vorticity and the flux into convective updrafts in two layers: between z = 0.1–1.0 km ("low-levels"), and z = 0.1–0.2 km (the "near-surface" layer). In literature (Flournoy et al., 2020), 'low-level' typically refers to 0–1 km above the ground level (AGL), and 'near-surface' roughly corresponds to tens of meters above AGL. Here 0.1 km AGL is taken as the bottom level of both layers since there is only one model level below 0.1 km. We calculated the storm-relative streamwise horizontal vorticity (SRSHV) in the near-storm environment, which is the dot product between the horizontal vorticity (i.e., the curl of vertical wind shear) and horizontal velocity vectors:

$$SRSHV = \left(-\vec{k}\times\frac{\partial\vec{V}}{\partial z}\right)\cdot(\vec{V}-\vec{c}) \approx \left[-\vec{k}\times\left(\overrightarrow{V_{top}}-\overrightarrow{V_{bot}}\right)\right]/(Z_{top}-Z_{bot})\cdot(\overrightarrow{V_{mid}}-\vec{c}) \quad (2)$$

where V represents the ground-relative wind vector, Z is the height AGL, c is the storm motion vector, and k is the unit vector in the vertical. Subscripts top, mid, and bot represent the upper, middle, and lower height bounds of a prescribed vertical layer over which SRSHV is being evaluated (e.g., 1 km, 0.5 km, and 0.1 km AGL, respectively).

SRSHV describes the critical processes for tornadogenesis, which involves the low-level streamwise horizontal vorticity feeding into the convective updraft. It is different from STP - a composite index for tornado potential.

3 Results

3.1 Enhanced tornado potential

The simulated convective storm initiates northwest of Kansas City near the quasi-stationary front at around 21:20 UTC (all times are UTC hereafter). A much larger storm (regarding both spatial coverage and maximum reflectivity, Figure 2A2, D2 vs Figure 2A3, D3) forms in the City run compared to the No-City run (also see Figure 5 of LIN21). As described in LIN21, in the City simulation, the convective cell develops and moves southeastward, and at ~ 21:40 UTC, it meets with the strong convergence-divergence couplets characteristic of updrafts and their corresponding downdrafts (i.e., secondary circulation) forming at the northern boundary of the city due to stronger moisture and temperature gradients (Figure 8 of LIN21). The convergence-divergence couplets result from the higher low-level temperature and larger urban–rural moisture and temperature gradients at the urban-rural boundaries. These gradients can induce a secondary circulation (Chen and Avissar, 1994; Kang, 2009), as air flows from the cooler to the warmer parts, creating a low-level convergence zone near the interface, and they result from the northward advection of warm and dry air from the city by the southerly-southeasterly low-level winds. The meeting of the convective cell with the convergence-divergence couplets enhances the convection and precipitation, in contrast with the No-City simulation, which lacks the UHI and associated mesoscale convergence pattern (Figure 8 of LIN21). Flow convergence at the northern boundary of Kansas City may also favor updraft development on the flank of the storm nearest to the city, influencing the northerly component of storm motion. Through the examination of the storm evolution depicted by radar reflectivity as shown in Figure 2, the storm traverses the northern and eastern extents of the city for about 2 hours after 21:40 UTC, whereas the storm in the No-City simulation has a more eastward component of motion and a path deviating from the location of Kansas City (also see Figure 6 of LIN21). Note that in all figures the city boundary is marked using gray solid lines for the City simulation and gray dash lines for the No-City simulation.

The low-level UH (calculated from 0.1 to 3 km AGL) and STP begin to show some minor differences between the simulations by 21:40, with higher values in the City case that become discernible by

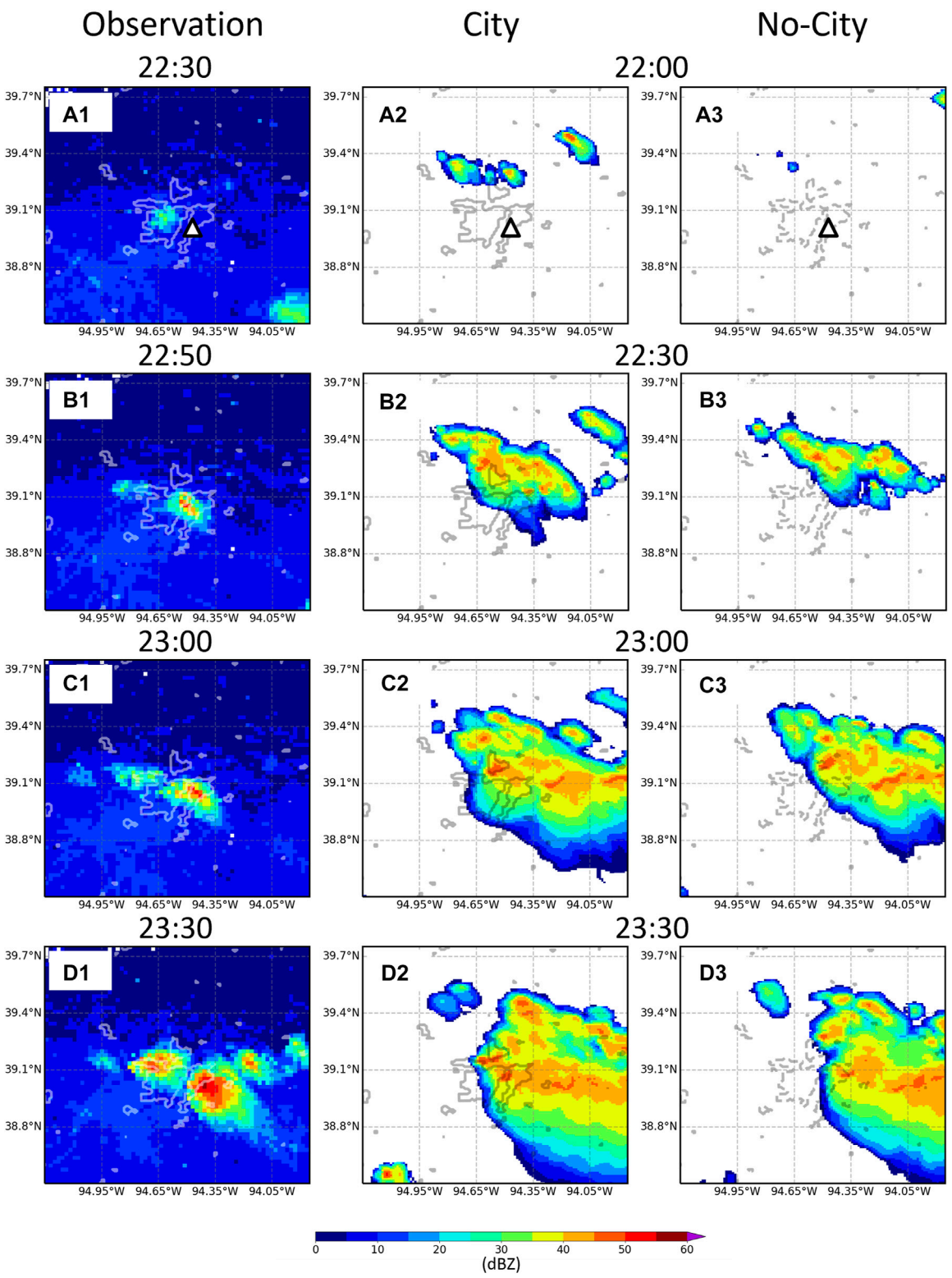

FIGURE 2
Evolution of radar reflectivity for **(A1–A3)** observation, **(B1–B3)** City simulation, and **(C1–C3)** No-City simulation. The time steps are not exactly matched between observation and simulations because the simulated storm initiated about 50 min earlier and grew slower relative to the observed one. The white triangle in **(D1–D3)** indicates the location of the first tornado report at 23:33 UTC.

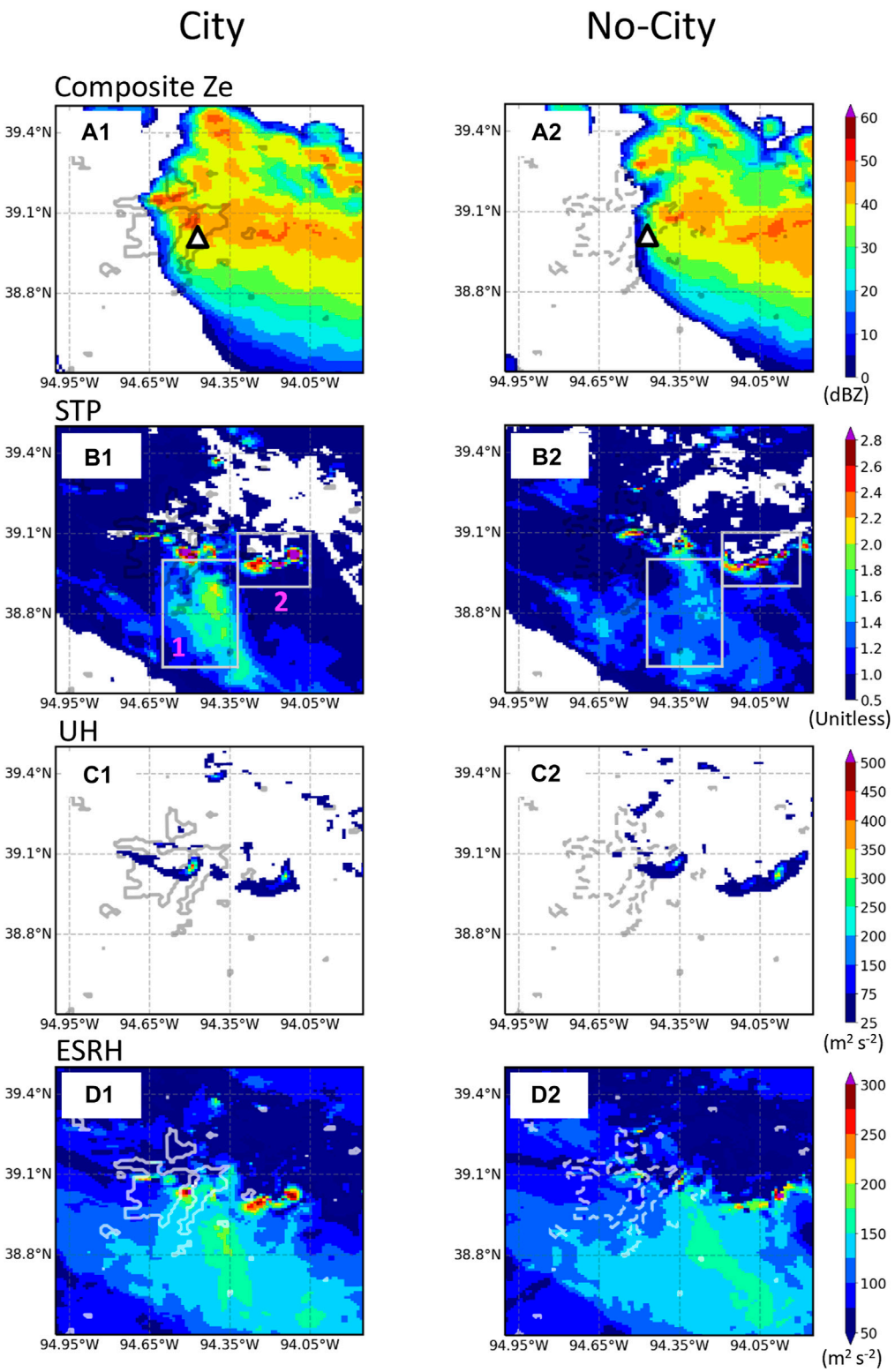

FIGURE 3
Comparisons in **(A1,A2)** composite radar reflectivity, **(B1,B2)** significant tornado parameter (STP), **(C1,C2)** 100m-3 km updraft helicity, and **(D1,D2)** effective storm-relative helicity (ESRH) between the City (left column) and No City (right column) simulations at 23:30 UTC. The white triangle in **(A1,A2)** indicates the location of the first tornado report at 23:33 UTC. The white boxes in **(B1,B2)** denote regions 1 and 2.

23:00 (Supplementary Figure S1). At 23:30, close to the time of the first observed tornado, the spatial coverage of the embedded strong radar echoes (>40 dBZ) within the storm in the City simulation is much larger and has expanded more to the southwest than in the No-City case (Figure 3A1, A2). STP is ~2.0 in the storm inflow region to the south-southeast of the updraft core, approximately 1.0 larger than in the No-City simulation (Figure 3B1, B2). Further, UH in the convective core (>45 dBZ) is greater in the City simulation (>250 m^{-2} s^{-2}) than in the No-City simulation (~150 m^{-2} s^{-2}; Figure 3C1, C2). The greater STP and UH values in the City case suggest that tornado potential is enhanced by the parent storm's response to the Kansas City urbanization. Although SBLCL heights in the urban area in the City case are about 300 m larger than those in the No-City case (Supplementary Figures S2,S3), they are all below 1.5 km and SBCAPE/MUCAPE ~1.0 for both cases, meeting the criteria for elevated tornado potential used by Gallo et al. (2016); Gallo et al. (2018) (see section 2.3).

There are two regions with larger STP in the low-level inflow to the storm that correspond to two critical processes for tornadogenesis (regions 1 and 2, denoted with white boxes in Figure 3B1). Region 1 includes the ambient inflow area, where barotropic low-level streamwise horizontal vorticity associated with vertical shear of the horizontal wind is advected into the convective updraft. The first observed Raytown tornado (EF0) occurred north of this region (the white triangle in Figure 3A1). In the City case, STP in region 1 increases northward and peaks near the city (>2.0; Figure 3B1). However, the STP values in the corresponding region in No-City are smaller (<1.6; Figure 3B2), with the highest values shifted toward the east.

STP is composed of measures of ESRH, LCL, CAPE, and CIN. Their temporal evolutions are shown in Supplementary Figures S2,S3. At 23:30, just before the development of the first tornado, the larger STP within region 1 in the City simulation is primarily attributed to larger values of ESRH because SBLCLs in this region are higher, and both SBCAPE and SBCIN are slightly smaller than in the No-city simulation (acting to reduce STP). Therefore, a slightly less favorable thermodynamic environment for tornadogenesis exists in the City case (Supplementary Figures S2E1–E3 vs. Supplementary Figures S3E1–E3). Similar thermodynamic differences also existed before the storm was initiated (21:00; Supplementary Figures S2A1–A3 vs. Supplementary Figure S3A1–A3), suggesting that they are a result of warmer and drier conditions produced by urbanization (Supplementary Figure S4). Larger ESRH in the inflow region of the City storm appears to be a result of the storm response to the urbanization as it is forming and intensifying as the obvious differences between the City and No-City simulations are shown from 23:00 (Supplementary Figure S2D4 vs. Supplementary Figure S3D4), which will be further scrutinized in the section below. The eastward shift of STP in the No-City case compared to the City case is consistent with the southeastward shift in ESRH.

Region 2 in Figure 3B1 corresponds to the cold pool front where the precipitation interacts with the ambient low-level air, where significant near-surface horizontal vorticity can form as a result of the horizontal temperature gradient associated with the cold pool. The STP in this region is higher (>2.0) and has a larger spatial coverage in the City simulation than in the No-City simulation; again, due to greater ESRH (Supplementary Figures S2, S3). As in region 1, SBLCL in region 2 of the City case is greater, and SBCAPE and SBCIN are smaller compared to the No-City case. However, these differences are much smaller compared with region 1 because this region is embedded in the convective core of the storm, where the strong vertical motions dominate the signature of vertical wind shear.

3.2 Mechanisms for enhanced tornado potential

The formation of the low-level rotation by the tilting and stretching of low-level streamwise horizontal vorticity within the updraft is typically considered a prerequisite for tornadogenesis. The SRSHV at 23:30 is shown in Figure 4A1, A2. The contrast in SRSHV between the two simulations matches well with their contrast in STP, with much higher values in the City simulation in region 1 (by ~60 × 10^{-3} m s^{-2}, or ~40%) and region 2 (Figure 4A3). By matching SRSHV in Figure 4A1 with the maximum low-level updraft in the City case (Figure 4B1), we can see that the SRSHV flow is feeding into updrafts at the location of the first reported tornado as clearly shown in Figure 4C1, facilitating the formation and intensification of the low-level rotating updraft. However, in the No-City case, SRSHV is much weaker and does not flow into the updrafts (Figure 4B2,C2); therefore, the supply of low-level horizontal vorticity into the convective updraft is weaker and perhaps less favorable for tornadogenesis processes than in the City case.

To understand the physical processes resulting in larger SRSHV in the ambient inflow region south-southeast of the updraft of the City case, we divide this region into three portions, the 'center' area with the largest difference in SRSHV, and its adjacent areas on the west and east (areas C, W, and E, respectively, in Figure 4A3). SRSHV has two components, the horizontal storm-relative wind vector in the middle of the layer (500 m, Figure 5B1–B3) and the horizontal vorticity vector calculated between the top (Figure 5C1–C3) and bottom (Figure 5A1–A3) of the 0.1–1 km layer. The 500-m storm-relative winds in area C are stronger and oriented more southeasterly in the City simulation than in the No-City simulation (Figure 5B1–B3 and purple vectors in Figure 4C1, C2). Though horizontal vorticity vectors in area C are oriented similarly across both cases, the magnitude is greater in the City case (about 35% mean increase over area C at 23:30). This is more clearly shown in the time series (Figure 6A) and is also reflected in the vertical wind shear between 0.1–1 km (Figure 6B). Thus, greater SRSHV in the City case is a result of slightly enhanced storm-relative inflow that is much better aligned with the orientation of stronger horizontal vorticity.

Now the question is how the vertical wind shear (and associated horizontal vorticity) and storm-relative inflow are greater in the City case than in the No-City case. We examine the pressure perturbation fields and wind fields at the bottom (100 m AGL), middle (500 m), and top (1 km) layers (Figure 5). At 100 m AGL, area C is dominated by southeasterly winds in both simulations (Figure 5A1–A3). The mean wind in this area veers southerly at the middle layer (500 m) (Figures 5B1–B3), and finally southwesterly at the top layer (Figure 5C1–C3). Over area C, the City case contains stronger easterly winds at 100 m (Figure 5A3) and weaker westerly winds at 1000 m than the No-City case (Figure 5C3). The magnitude of the

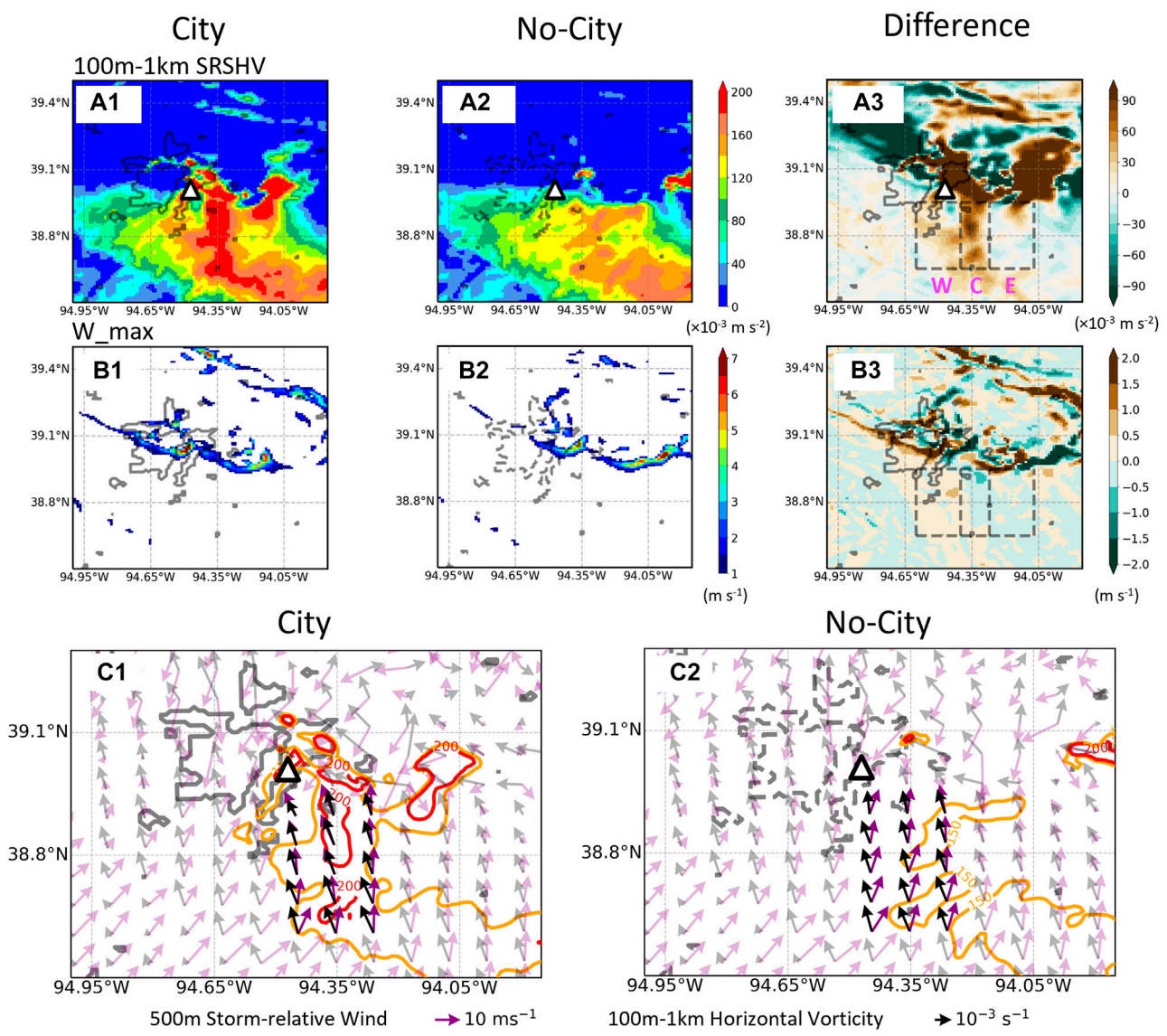

FIGURE 4
Storm-relative streamwise horizontal vorticity (SRSHV) within 100m-1 km for **(A1)** City, **(A2)** No-City, and **(A3)** the difference between City and No-City at 23:30 UTC. **(B1–B3)** same as **(A1–A3)** except for the maximum vertical velocity below 1 km above ground level (AGL). The composite diagnostic maps are shown for **(C1)** City and **(C2)** No-City simulations, where the 500 m storm relative wind (purple barbs) and 100m-1 km horizontal vorticity (black barbs) are overlaid on the SRSHV (contour). Note that barbs within the inflow region of area C are highlighted.

zonal wind difference between City and No-City is larger at the bottom layer than that at the top of the layer (Figure 5A3 vs Figure 5C3). This leads to the larger bulk wind shear (Figure 6B) and subsequently higher horizontal vorticity (black barbs, Figure 4C1,C2).

Stronger easterly winds at the bottom of the layer and weaker westerly winds at the top layer in area C in the City case are associated with the stronger westward-oriented perturbation pressure gradient (PPG) acting across area W and E than in the No-City case (Figure 5A3). Although a similar qualitative pattern of pressure perturbation differences is also found in the middle layer (Figure 5B3) and the top layer (Figure 5C3), the PPG is stronger at the bottom layer compared with the elevated layers (Figure 6D), explaining the larger increase in the magnitude of winds. Time evolution plots show that the stronger easterly wind at the bottom layer (Figure 6C; easterly is negative and westerly is positive), greater wind shear (Figure 6B), and larger SRSHV (Figure 6A) become prominent after 23:10. The largest differences in wind shear and SRSHV between the two simulations occur between 23:30–00:00 when a series of tornados were reported.

How is the pressure perturbation higher in area E and lower in area W in the City simulation compared to the No-City simulation (differences of 14.4 pa and −14.7 pa, respectively)? An outflow boundary (represented by the 30.5°C isotherm in Figure 7) propagates southwestward as the supercell evolves in both simulations. It is noteworthy that the cold pool in the City simulation has higher intensity and larger coverage than the No-City simulation throughout the lifecycle of the storm from 22:00

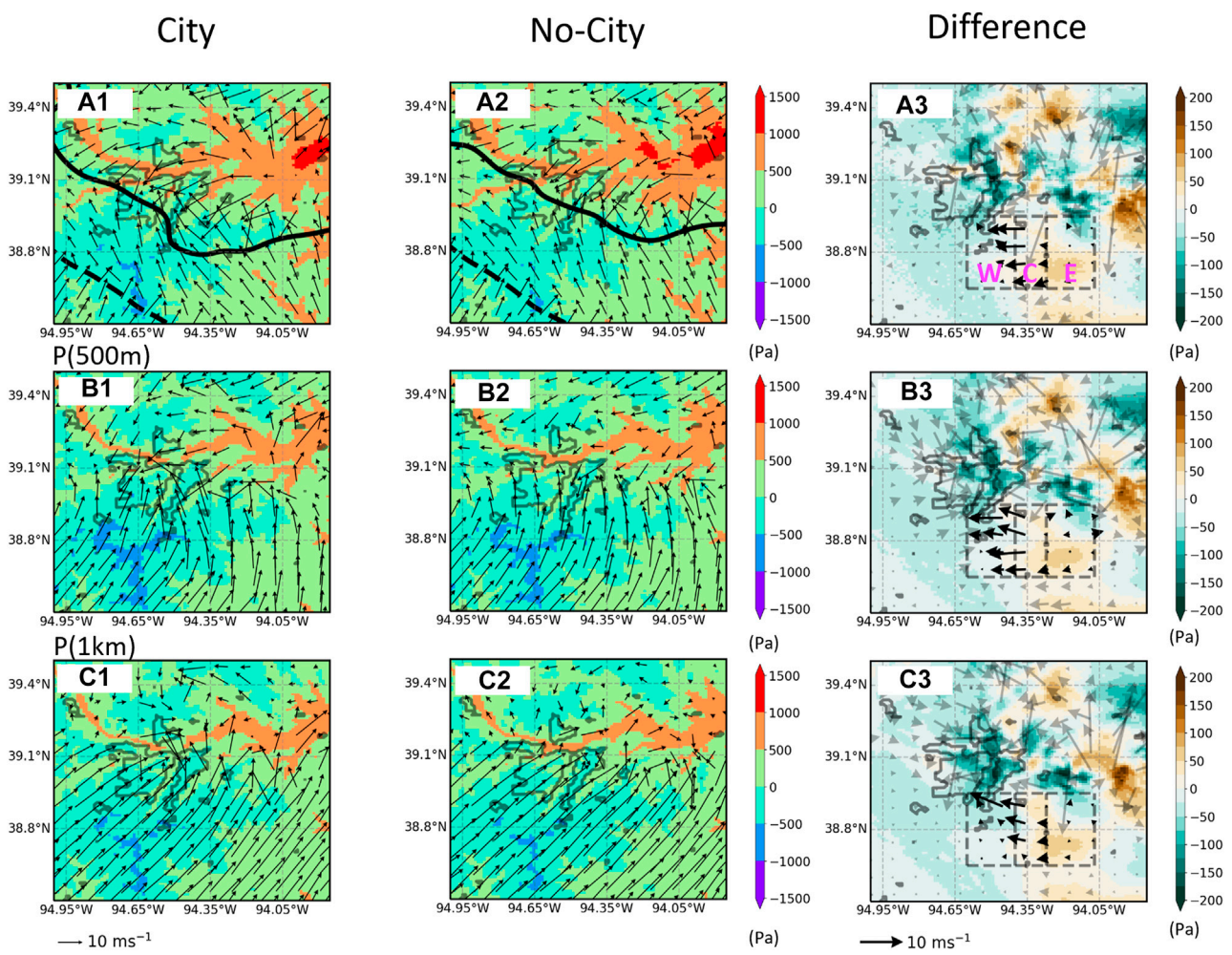

FIGURE 5
Pressure perturbation (contour; calculated by subtracting the mean pressure of the in-flow area (95.25°- 93.85°W, 38.5°- 39.75°N) and wind field (barbs) at 100 m AGL for **(A1)** City, **(A2)** No-City, and **(A3)** the difference between City and No-City at 23:30 UTC. **(B1–B3)** and **(C1–C3)** are the same as **(A1–A3)**, except for 500m and 1 km AGL. The black lines on **(A1,A2)** indicate the 33°C (dashed) and 30.5°C (solid) isotherms. The difference in winds is plotted for the storm-relative winds. The boxes on **(A3,C3)** are the same as those in Figure 4A3.

(Supplementary Figure S5). As the outflow boundary (bold black line in Figure 5A1, A2) travels southward, a positive pressure perturbation develops ahead of it in the ambient inflow in area E. Although the causes of this positive perturbation pressure are unknown and beyond the scope of this paper, its presence is consistent with past schematic models and idealized simulations containing dynamically-induced high pressure leading to an outflow gust front (e.g., Wakimoto, 1982; Markowski and Richardson, 2010). This pressure perturbation is stronger in the City simulation than in the No-City simulation because of its colder outflow and faster motion toward the south (Figure 7A vs Figure 7B). At 23:30 UTC in the City case, the outflow boundary has already passed area E and is moving through area W, but in No-City it has not yet arrived at area E; hence the pressure perturbation is increased in area E in the City simulation as shown in Figure 5A3,C3. Lower pressure in area W in the City simulation may be associated with enhanced inflow drawn by a stronger core storm updraft. The increased pressure perturbation in area E and decrease in area W leads to the larger zonal PPG, resulting in the enhanced easterly wind at the bottom layer (100 m) and subsequently the strong vertical wind shear and streamwise vorticity within 100 m—1 km in area C. Meanwhile, the storm-relative inflow at the middle layer (purple barbs, Figure 4C1, C2) is also better aligned with the vorticity vector (i.e., much smaller angles between the purple and black bards compared with the No-City case), which also contributes to the enhanced SRSHV in City simulation. Note the storm-relative inflow speed is not changed significantly from the City to No-City case (purple bards between Figure 4C1, C2). The better alignment probably results from the stronger PPG at 500 m as well (Figure 5B1–B3). This result may be consistent with past studies showing increases in low-level shear and storm-relative helicity in proximity to supercell thunderstorms, in part due to low-level inflow acceleration by the storm updraft (e.g., Nowotarski and Markowski, 2016; Wade et al., 2018). In addition to PPG, the altered wind pattern and the subsequent production of horizontal vorticity in City simulation could also be influenced by the friction from the planetary boundary layer procession due to the

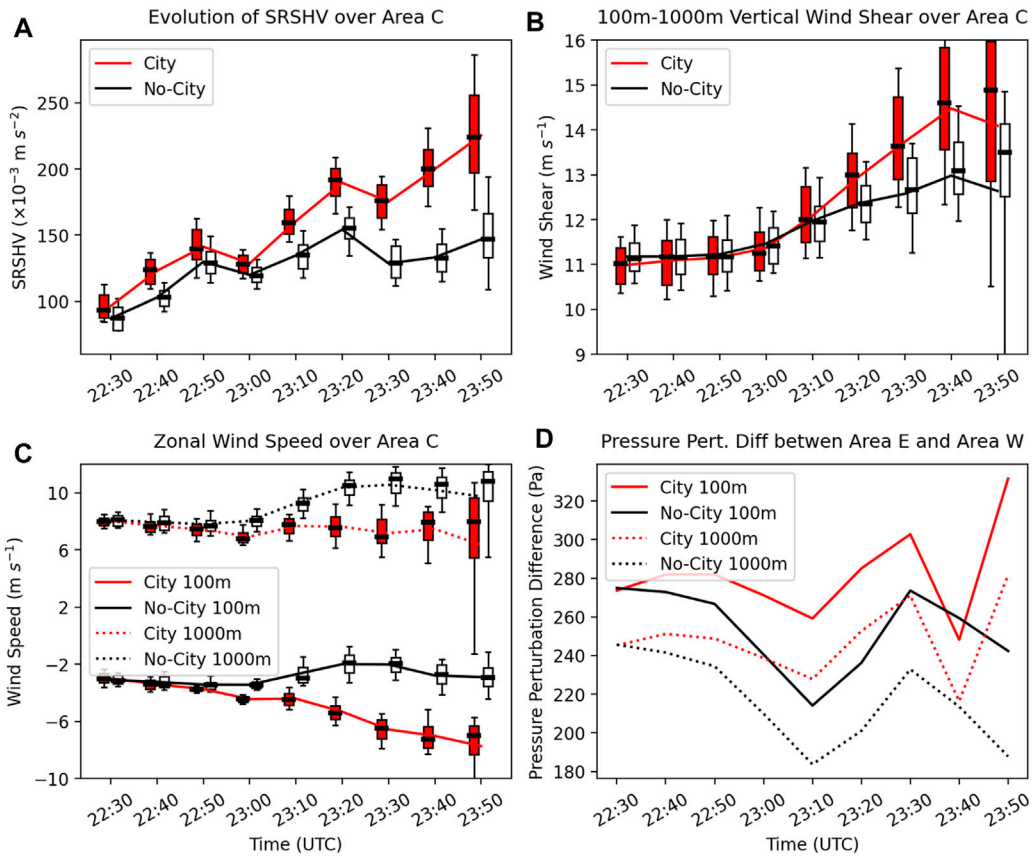

FIGURE 6
Comparison between City and No-City in the temporal evolutions of **(A)** SRSHV, **(B)** vertical wind shear within the 100m-1 km layer in area C, **(C)** the zonal wind speed at 100m and 1 km in area C (easterly is negative and westerly is positive), and **(D)** the difference in pressure perturbation between area E and area W at 100 m and 1 km. The lines represent the domain average values, while the box plots show the 5th percentile value (lower whisker), 25th percentile value (bottom of the box), median value (center of the box), 75th percentile value (top of the box), and 95th percentile value (upper whisker) of all the grid elements within the selected area.

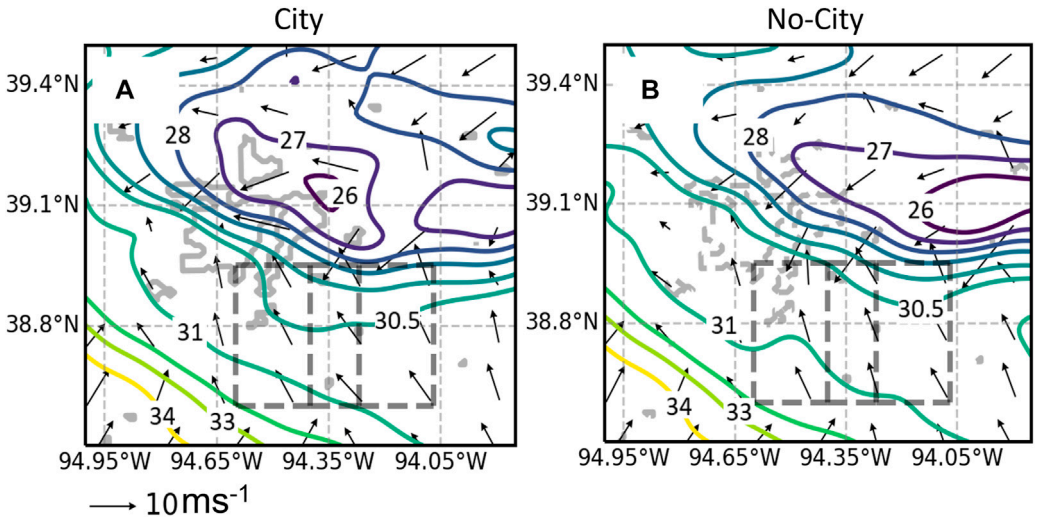

FIGURE 7
Temperature (contoured line) and wind vectors (arrow) 23:30 UTC at 100 m AGL for **(A)** City and **(B)** No-City simulations.

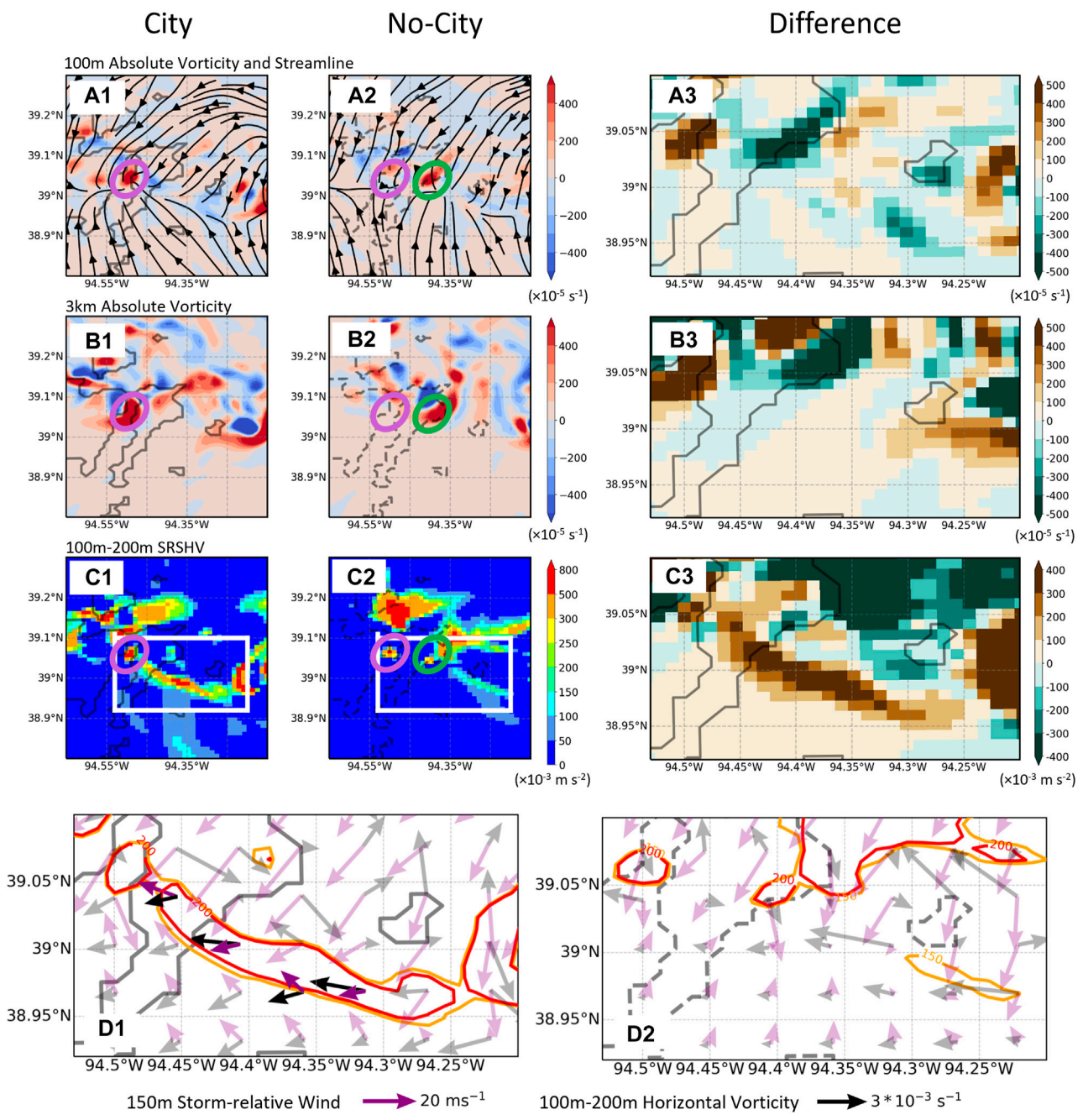

FIGURE 8
The 100 m absolute vorticity (contour) and streamline for **(A1)** City simulation, **(A2)** No-City simulation, and **(A3)** their difference (City—No-City) at 23:30 UTC. **(B1–B3)** are same as **(A1–A3)**, except for 3 km absolute vorticity. **(C1–C3)** 100m–200 m storm-relative streamwise horizontal vorticity (SRSHV). The purple and green circles on **(A1,A2)**, **(B1,B2)**, and **(C1,C2)** indicate the locations of near-surface mesocyclone for City and No-City simulations, respectively. The white boxes on **(C1,C2)** highlights the zoom-in domain used in **(A3,C3)** and **(D1,D2)**. The composite diagnostic maps are shown for **(D1)** City and **(D2)** No-City simulations, where the 150 m storm-relative wind (purple barbs) and 100 m–200 m horizontal vorticity (black barbs) are overlaid on the SRSHV (contour). Note that barbs within the inflow region along the thermal boundary are highlighted in **D1**.

surface roughness change. However, since the BEP + BEM urban canopy model used in this study considers the building energy effects, changing surface roughness is not a straightforward task and it will also impact energy. Therefore, we are not able to separately look at the contribution from the changes in surface roughness in this study.

In summary, the enhanced low-level SRSHV over the storm inflow region in the City case is a result of the combined effects of 1) greater horizontal vorticity induced by the enhanced pressure perturbation gradient, and 2) a storm-relative wind vector that is better aligned with the vorticity vector. Both factors are closely related to the faster southwestward propagation of a stronger

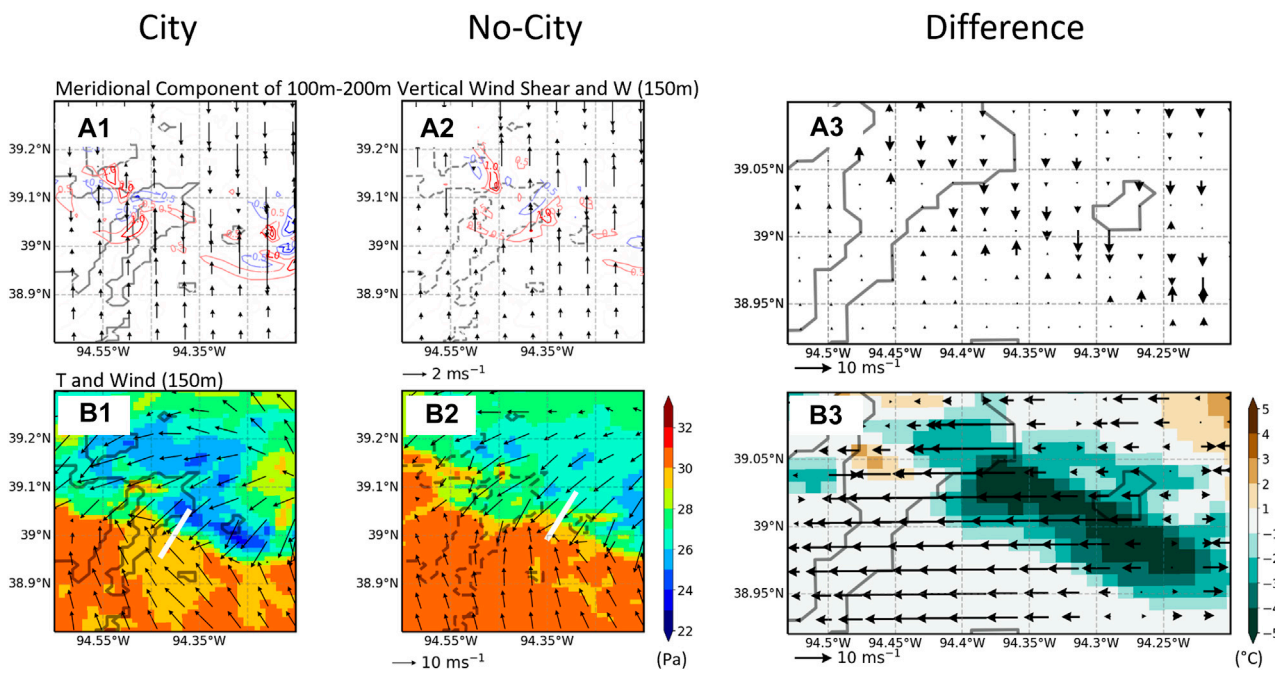

FIGURE 9
Vertical velocity at 150 m (contour lines) overlaid on the meridional component of 100m–200 m vertical wind shear (barbs) for **(A1)** City, **(A2)** No-City, and **(A3)** the difference between City and No-City at 23:30 UTC. **(B1–B2)** 150 m temperature (contour) and wind (barbs) fields. **(B3)** Shows the difference in the storm-relative zonal wind. The temperature gradients in the two simulations are calculated along the white lines in **(B1)** and **(B2)** respectively.

outflow boundary in City simulation which causes a stronger PPG gradient. The stronger outflow boundary in the City case is a result of stronger storm caused by the urban land effect, which produces stronger turbulence and secondary circulation due to the downwind advection of urban heat and large temperature and moisture gradients at the urban-rural boundaries (LIN21). The faster southwestward propagation of the storm in the City case is because the secondary circulation at the northern urban-rural boundaries diverts the pre-existing storm toward the city (more details are presented in LIN21).

3.3 Near-surface rotation and its intensification

The advection, tilting, and stretching of near-surface horizontal vorticity by the low-level updraft is critical for tornadogenesis. As discussed earlier, there is an area of enhanced STP and UH values located east of the urban area in the City case compared to the No-City case (region 2; Figure 3B1, B2 and Figure 3C1, C2). This region of higher STP is collocated with the southeast edge of the low-level mesocyclone (Figure 8A1). By zooming into the eastern part of the urban area, we can see that a mesocyclone forms in the City case (purple circle in Figure 8A1, the enclosed vertical vorticity exceeds 400×10^{-5} s^{-1}). A similar mesocyclone is also found in the No-City simulation but its location is shifted to the east (green circle in Figure 8A2), corresponding to the eastward shift of the storm path compared with the City case, as detailed in LIN21. When comparing with the middle-level mesocyclone (Figure 8B), we can see the near-surface maximum vorticity well aligns with its counterpart at mid-level in the City case (the purple cycle in Figure 8B1 vs Figure 8A1). However, for the No-City case, the mid-level vorticity center is shifted eastward away from the near-surface mesocyclone (the green cycle in Figure 8B2 vs Figure 8A2). This is consistent with several studies that indicate that the potential for tornadogenesis is reduced with an increasing vertical tilt of the mesocyclone and updraft (e.g., Dowell and Bluestein, 2002; Marquis et al., 2012).

The near-surface SRSHV (100–200 m AGL) in region 2 upstream of the main updraft and mesocyclone is stronger in the City case than in the No-City case (Figure 8C1–C3). Again, we decompose SRSHV into the horizontal vorticity component (vertical wind shear; Figure 9A1–A3) and the storm-relative horizontal wind component (horizontal wind, Figure 9B1–B3). Given the fact that the band of enhanced SRSHV is approximately aligned with the easterly wind, only the meridional component of the wind shear is examined in Figure 9A1–A3, and similarly, their difference in storm-relative zonal wind component is examined in Figure 9B1–B3. The difference in storm-relative easterly winds between the City and No-City simulations is more substantial than the difference in the wind shear (Figure 9B3 vs Figure 9A3). Therefore, different from region 1, where the larger SRSHV is driven by differences in the magnitude and orientation of both the horizontal wind and vorticity vectors, in region 2, the enhanced near-surface SRSHV in the City case is mainly caused by the increase in the easterly storm-relative inflow wind speed as well as a more widespread alignment of orientation with the horizontal vorticity vector (Figure 8D1 vs D2).

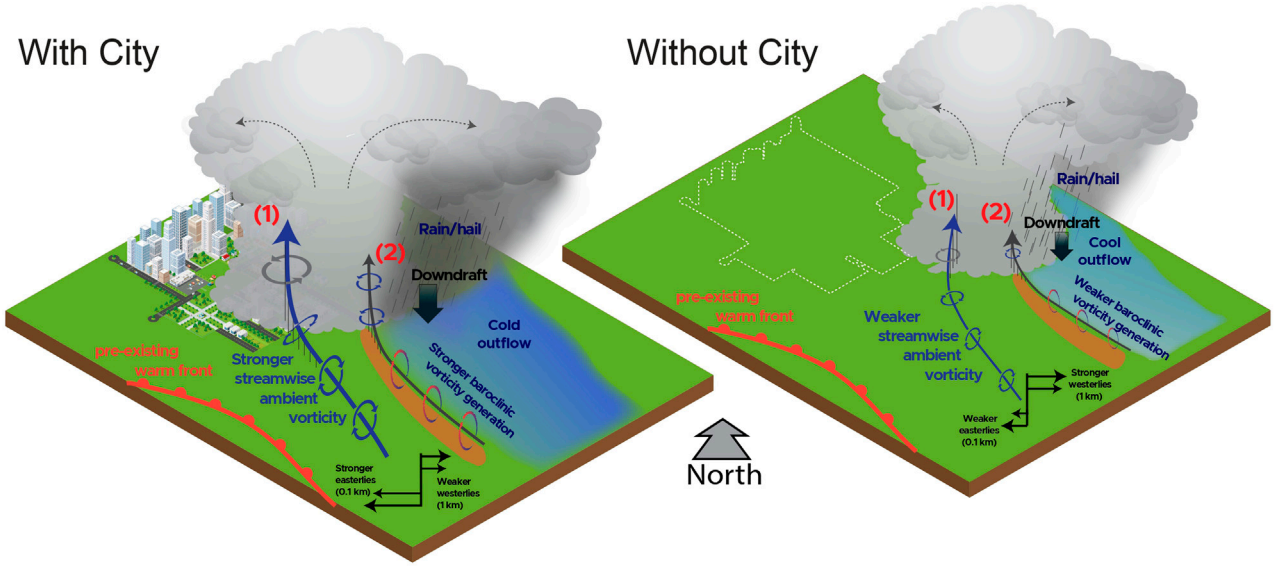

FIGURE 10
Urbanization enhances the tornado potential through two pathways: (1) enhanced low-level SRSHV feeding updrafts due to stronger east-west pressure perturbation gradient as a result of faster, stronger storm outflow, and (2) intensified near-surface SRSHV which is more aligned with the easterly storm-relative inflow because of stronger cold pool front which increases southeasterly winds. Both pathways are associated with a stronger storm at the initial and developing stages resulting from the Kansas City urbanization.

Through the joint examination of the concurrent temperature field (Figure 8C; Figure 9B), the increased southeasterly winds are oriented along the boundary of the temperature contrast in the City simulation whose temperature gradient (as indicated by the white line) reaches 0.7°C/km. The temperature contrast in the No-City simulation is only ~0.1°C/km. It is expected that the stronger temperature gradient in the City case results in the increased baroclinic generation of horizontal vorticity in this region compared to the No-City case. However, increased inflow winds in the City case may temper the portion of SRSHV generated by baroclinic processes because of reduced parcel residence time within the temperature gradient zone. Regardless, the stronger horizontal pressure perturbation gradients ahead of the cold pool in the City case (Figure 5A3) increase SRSHV due to accelerated southeasterly winds. The stronger thermal gradient (i.e., stronger cold pool) in the City case should be due to the stronger precipitation and convective downdrafts.

4 Discussion

We investigate a possible role played by urbanization in enhancing tornado potential by using a pair of high-resolution simulations of a tornadic supercell, one including urbanized land use representing Kansas City and another that replaces Kansas City with cropland similar to its surroundings. We find that urbanization might enhance tornado potential by influencing two key mesoscale and storm-scale processes (summarized in Figure 10). In these simulations, urbanization yielded a larger supercell storm with stronger updrafts and precipitation than in the case without the urban region. This stronger and larger storm occurred because of the secondary circulation at the downwind urban-rural boundaries at its initial and developing stages, as discussed in LIN21. The stronger storm leads to colder outflow that moves faster toward the south. A larger west-to-east pressure perturbation gradient is generated ahead of the cold pool in the ambient inflow of the City case, resulting in stronger easterly winds. As a result, greater low-level (below 1 km) streamwise vorticity is produced ahead of the storm, enhancing the low-level rotating updraft. Without the city, the storm is weaker and its motion is shifted eastward from the path taken in the City case; thus, the outflow from the storm in the No-City case is weaker and moves southward at a slower speed. These differences lead to a weaker horizontal pressure gradient ahead of the cold pool; thus, smaller wind shear and SRSHV changes in the inflow. Further, differences in overall storm motion result in a different storm-relative helicity in the ambient inflow of the City storm.

Also, the low-level rotation (i.e., SRSHV) was enhanced near the boundary of the forward-flank cold pool region, because the outflow in the City case is colder than in the No-City case (i.e., colder cold pool). It was unclear if this enhancement was due in part to increase baroclinic generation of horizontal vorticity. Regardless, in this area the easterly storm-relative inflow wind speed was increased and horizontal vorticity vectors were better aligned with the easterly storm-relative inflow than in the No-City case, increasing the SRSHV that is ingested into, tilted, and stretched by the primary updraft to generate substantial vertical vorticity. Without the city landscape, cold pools are much weaker, resulting in weaker low-level temperature gradients, weaker southeasterly inflow winds, and smaller SRSHV which is not well aligned with the storm-relative inflow.

In summary, in the studied case, the enhancement in tornado potential for the storm with the Kansas City urbanization considered is aided by both the enhanced SRSHV in the low-level inflow region and the storm's forward flank cold pool region near the surface. Both of

these enhancements result from the enhanced storm and altered storm path by the Kansas City urbanization because of the downwind advection of urban heat and large temperature and moisture gradients at the urban-rural boundaries. The mechanisms leading to the enhanced tornado potential by urban land use in this study involve mesoscale and storm-scale processes that are general intrinsic properties of supercell storms. Therefore, we believe this study should be instructive in exploring urbanization impact on tornadoes in other supercell storms. However, we emphasize that these conclusions may differ by urban structure, different initial or boundary meteorological conditions, or the time and location that a storm encounters the urban zone. Due to the large computational cost associated with our simulations with detailed physics, we were not able to do ensemble simulations. Thus, the result presented in this study only represents one possibility of how urbanization would affect tornado potential, and a more systematic examination is needed to achieve a more general conclusion.

Data availability statement

The raw data supporting the conclusion of this article are available at https://portal.nersc.gov/archive/home/w/wang406/www/Publication/Fan2023FES/WRF_Tornado.tar.gz.

Author contributions

JF conceived the idea and guided the work, JW performed the formal analysis and wrote the first draft of the manuscript. YL performed the model simulations used in this study. All authors contributed to manuscript revision and approved the submitted version.

Funding

This study is supported by the U.S. Department of Energy Office of Science Early Career Research Program (Grant no. 70017). JW is supported by the Ministry of Education, Singapore, under its Academic Research Fund Tier 1 (RG74/22).

Acknowledgments

PNNL is operated for the U.S. Department of Energy (DOE) by Battelle Memorial Institute under contract DE-AC05-76RL01830. This research used resources of the PNNL Institutional Computing (PIC), and National Energy Research Scientific Computing Center (NERSC). NERSC is a U.S. DOE Office of Science User Facility operated under Contract DE-AC02-05CH11231. We thank James Marquis from PNNL for the discussion and revision of the manuscript.

Conflict of interest

The authors declare that the research was conducted in the absence of any commercial or financial relationships that could be construed as a potential conflict of interest.

Publisher's note

All claims expressed in this article are solely those of the authors and do not necessarily represent those of their affiliated organizations, or those of the publisher, the editors and the reviewers. Any product that may be evaluated in this article, or claim that may be made by its manufacturer, is not guaranteed or endorsed by the publisher.

Supplementary material

The Supplementary Material for this article can be found online at: https://www.frontiersin.org/articles/10.3389/feart.2023.1148506/full#supplementary-material

References

Aguirre, B. E., Saenz, R., Edmiston, J., Yang, N., Agramonte, E., and Stuart, D. L. (1993). The human ecology of tornadoes. *Demography* 30, 623–633. doi:10.2307/2061810

Allen, J. T., Tippett, M. K., and Sobel, A. H. (2015). An empirical model relating U.S. monthly hail occurrence to large-scale meteorological environment. *J. Adv. Model. Earth Syst.* 7, 226–243. doi:10.1002/2014MS000397

Anderson, C. J., Wikle, C. K., Zhou, Q., and Royle, J. A. (2007). Population influences on tornado reports in the United States. *Wea. Forecasting* 22, 571–579. doi:10.1175/waf997.1

Ashley, W. S. (2007). Spatial and temporal analysis of tornado fatalities in the United States: 1880–2005. *Wea. Forecasting* 22, 1214–1228. doi:10.1175/2007WAF2007004.1

Barnes, S. L. (1978). Oklahoma thunderstorms on 29–30 April 1970. Part I: Morphology of a tornadic storm. *Mon. Wea. Rev.* 106, 673–684. doi:10.1175/1520-0493(1978)106<0673:OTOAPI>2.0.CO;2

Bornstein, R., and Lin, Q. (2000). Urban heat islands and summertime convective thunderstorms in Atlanta: Three case studies. *Atmos. Environ.* 34 (3), 507–516. doi:10.1016/S1352-2310(99)00374-X

Brooks, H. E., Doswell, C. A., III, and Davies-Jones, R. P. (1993). "Environmental helicity and the maintenance and evolution of low-level mesocyclones," in *The tornado: Its structure, dynamics, prediction, and hazards, geophys. Monogr., No. 79.* (Washington, D.C: Amer. Geophys. Union), 97–104.

Brown, M. C., and Nowotarski, C. J. (2020). Southeastern U.S. tornado outbreak likelihood using daily climate indices. *J. Clim.* 33 (8), 3229–3252. doi:10.1175/jcli-d-19-0684.1

Changnon, S. A. (2009). Tornado losses in the United States. *Nat. Hazards Rev.* 10 (4), 145–150. doi:10.1061/(asce)1527-6988(2009)10:4(145)

Chen, F., and Avissar, R. (1994). Impact of land-surface moisture variability on local shallow convective cumulus and precipitation in large-scale models. *J. Appl. Meteor.* 33, 1382–1401. doi:10.1175/1520-0450(1994)033,1382:IOLSMV.2.0.CO;2

Ching, J., Mills, G., Bechtel, B., See, L., Feddema, J., Wang, X., et al. (2018). Wudapt: An urban weather, climate, and environmental modeling infrastructure for the anthropocene. *Bull. Am. Meteorol. Soc.* 99, 1907–1924. doi:10.1175/BAMS-D-16-0236.1

Clark, A. J., Gao, J., Marsh, P. T., Smith, T., Kain, J. S., Correia, J., Jr, et al. (2013). Tornado pathlength forecasts from 2010 to 2011 using ensemble updraft helicity. *Wea. Forecast.* 28 (2), 387–407. doi:10.1175/WAF-D-12-00038.1

Clark, A. J., Jirak, I. L., Dembek, S. R., Creager, G. J., Kong, F., Thomas, K. W., et al. (2018). The community leveraged unified ensemble (Clue) in the 2016 Noaa/hazardous weather testbed spring forecasting experiment. *Bull. Amer. Meteor. Soc.* 99, 1433–1448. doi:10.1175/Bams-D-16-0309.1

Dahl, J. M., Parker, M. D., and Wicker, L. J. (2014). Imported and storm-generated near-ground vertical vorticity in a simulated supercell. *J. Atmos. Sci.* 71, 3027–3051. doi:10.1175/JAS-D-13-0123.1

Dahl, J. M. (2017). Tilting of horizontal shear vorticity and the development of updraft rotation in supercell thunderstorms. *J. Atmos. Sci.* 74, 2997–3020. doi:10.1175/JAS-D-17-0091.1

Davies-Jones, R., and Brooks, H. E. (1993). "Mesocyclogenesis from a theoretical perspective," in *The tornado: Its structure, dynamics, prediction, and hazards, meteor. Monogr., No. 79* (Boston, MA: Amer. Meteor. Soc.), 105–114.

Davies-Jones, R. P. (2015). A review of supercell and tornado dynamics. *Atmos. Res.* 158–159, 274–291. doi:10.1016/j.atmosres.2014.04.007

Doswell, C. A., III, and Burgess, D. W. (1993). "Tornadoes and tornadic storms: A review of conceptual models," in *The tornado: Its structure, dynamics, hazards, and prediction, geophys. Monogr., vol. 79* (Washington, D.C: Amer. Geophys. Union), 161–172.

Dowell, D. C., and Bluestein, H. B. (2002). The 8 June 1995 McLean, Texas, storm.Part II:Cyclic tornado formation, maintenance, and dissipation. *Mon. Wea Rev.* 130 (11), 2649–2670. doi:10.1175/1520-0493(2002)130<2649:TJMTSP>2.0.CO;2

Fan, J., Zhang, Y., Li, Z., Hu, J., and Rosenfeld, D. (2020). Urbanization-induced land and aerosol impacts on sea-breeze circulation and convective precipitation. *Atmos. Chem. Phys.* 20, 14163–14182. doi:10.5194/acp-20-14163-2020

Flournoy, M. D., Coniglio, M. C., Rasmussen, E. N., Furtado, J. C., and Coffer, B. E. (2020). Modes of storm-scale variability and tornado potential in VORTEX2 near- and far-field tornadic environments. *Mon. Wea. Rev.* 148, 4185–4207. doi:10.1175/MWR-D-20-0147.1

Gallo, B. T., Clark, A. J., and Dembek, S. R. (2016). Forecasting tornadoes using convection-permitting ensembles. *Wea. Forecast.* 31, 273–295. doi:10.1175/waf-d-15-0134.1

Gallo, B. T., Clark, A. J., Smith, B. T., Thompson, R. L., Jirak, I., and Dembek, S. R. (2018). Blended probabilistic tornado forecasts: Combining climatological frequencies with NSSL–WRF ensemble forecasts. *Wea. Forecast.* 33 (2), 443–460. doi:10.1175/waf-d-17-0132.1

Gao, J., and O'Neill, B. C. (2020). Mapping global urban land for the 21st century with data-driven simulations and Shared Socioeconomic Pathways. *Nat. Commun.* 11 (1), 2302. doi:10.1038/s41467-020-15788-7

Gao, M., Carmichael, G. R., Wang, Y., Saide, P. E., Yu, M., Xin, J., et al. (2016). Modeling study of the 2010 regional haze event in the North China Plain. *Atmos. Chem. Phys.* 16, 1673–1691. doi:10.5194/acp-16-1673-2016

Geerts, B., Parsons, D., Ziegler, C. L., Weckwerth, T. M., Biggerstaff, M. I., Clark, R. D., et al. (2017). The (2015), plains elevated convection at night field project. *Bull. Amer. Meteor. Soc.* 98, 767–786. doi:10.1175/BAMS-D-15-00257.1

Glickman, T. (2000). *Glossary of meteorology*. 2nd ed. Boston, MA: Amer. Meteor. Soc., 855. Available at: http://glossary.ametsoc.org/.

Grams, J. S., Thompson, R. L., Snively, D. V., Prentice, J. A., Hodges, G. M., and Reames, L. J. (2012). A climatology and comparison of parameters for significant tornado events in the United States. *Wea. Forecast.* 27, 106–123. doi:10.1175/WAF-D-11-00008.1

Haberlie, A. M., Ashley, W. S., and Pingel, T. J. (2015). The effect of urbanisation on the climatology of thunderstorm initiation. *Quart. J. Roy. Meteor. Soc.* 141, 663–675. doi:10.1002/qj.2499

Hubbart, J. A., Kellner, E., Hooper, L., Lupo, A., Market, P., Guinan, P., et al. (2014). Localized climate and surface energy flux alterations across an urban gradient in the central U.S. *Energies* 7, 1770–1791. doi:10.3390/en7031770

Javanroodi, K., and Nik, V. M. (2020). Interactions between extreme climate and urban morphology: Investigating the evolution of extreme wind speeds from mesoscale to microscale. *Urban Clim.* 31, 100544. doi:10.1016/j.uclim.2019.100544

Kang, S.-L. (2009). Temporal oscillations in the convective boundary layer forced by mesoscale surface heat-flux variations. *Bound.-Layer Meteor.* 132, 59–81. doi:10.1007/s10546-009-9391-5

Kellner, O., and Niyogi, D. (2014). Land surface heterogeneity signature in tornado climatology? An illustrative analysis over Indiana, 1950–2012. *Earth Interact.* 18 (10), 1–32. doi:10.1175/2013EI000548.1

Knupp, K. R., Murphy, T. A., Coleman, T. A., Wade, R. A., Mullins, S. A., Schultz, C. J., et al. (2014). Meteorological overview of the devastating 27 April 2011 tornado outbreak. *Bull. Am. Meteorol. Soc.* 95, 1041–1062. doi:10.1175/bams-d-11-00229.1

Lemon, L. R., and Doswell, C. A. (1979). Severe thunderstorm evolution and mesocyclone structure as related to tornadogenesis. *Mon. Weather Rev.* 107 (9), 1184–1197. doi:10.1175/1520-0493(1979)107<1184:Steams>2.0.Co;2

Lin, Y., Fan, J., Jeong, J.-H., Zhang, Y., Homeyer, C. R., and Wang, J. (2021). Urbanization-induced land and aerosol impacts on storm propagation and hail characteristics. *J. Atmos. Sci.* 78, 925–947. doi:10.1175/jas-d-20-0106.1

Liu, J., and Niyogi, D. (2019). Meta-analysis of urbanization impact on rainfall modification. *Sci. Rep.* 9, 7301. doi:10.1038/s41598-019-42494-2

Maddox, R. A. (1980). Meoscale convective complexes. *Bull. Am. Meteorol. Soc.* 61, 1374–1387. doi:10.1175/1520-0477(1980)061<1374:mcc>2.0.co;2

Markowski, P. M., and Richardson, Y. (2010). *Mesoscale meteorology in midlatitudes*. Chichester, UK: Wiley-Blackwell, 424. doi:10.1002/9780470682104

Markowski, P. M., and Richardson, Y. P. (2014). The influence of environmental low-level shear and cold pools on tornadogenesis: Insights from idealized simulations. *J. Atmos. Sci.* 71, 243–275. doi:10.1175/JAS-D-13-0159.1

Markowski, P. M., Rasmussen, E. N., and Straka, J. M. (1998). The occurrence of tornadoes in supercells interacting with boundaries during VORTEX-95. *Weather Forecast* 13, 852–859. doi:10.1175/1520-0434(1998)013<0852:TOOTIS>2.0.CO;2

Markowski, P. M., Straka, J. M., and Rasmussen, E. N. (2002). Direct surface thermodynamic observations within the rear-flank downdrafts of nontornadic and tornadic supercells. *Mon. Weather Rev.* 130, 1692–1721. doi:10.1175/1520-0493(2002)130<1692:dstowt>2.0.co;2

Markowski, P. M. (2002). Hook echoes and rear-flank downdrafts: A review. *Mon. Weather Rev.* 130, 852–876. doi:10.1175/1520-0493(2002)130<0852:hearfd>2.0.co;2

Marquis, J., Richardson, Y., Markowski, P., Dowell D, D., and Wurman, J. (2012). Tornado maintenance investigated with high-resolution dual-Doppler and EnKF analysis. *Mon. Weather Rev.* 140, 3–27. doi:10.1175/MWR-D-11-00025.1

Martilli, A., Clappier, A., and Rotach, M. W. (2002). An urban surface exchange parameterisation for mesoscale models. Bound.-Layer Meteor. 104, 261–304. doi:10.1023/A:1016099921195

Miller, R. C. (1972). "Notes on analysis and severe-storm forecasting procedures of the air force global weather central," in *Air weather Service tech. Rep. 200 (rev.)* (Springfield, VA: Scott Air Force Base), 190.

Nowotarski, C., and Jones, E. (2018). Multivariate self-organizing map approach to classifying supercell tornado environments using near-storm, low-level wind and thermodynamic profiles. *Wea. Forecast.* 33, 661–670. doi:10.1175/WAF-D-17-0189.1

Nowotarski, C. J., and Markowski, P. M. (2016). Modifications to the near-storm environment induced by simulated supercell thunderstorms. *Mon. Weather Rev.* 144 (1), 273–293. doi:10.1175/MWR-D-15-0247.1

Parker, M. D., and Dahl, J. M. (2015). Production of near-surface vertical vorticity by idealized downdrafts. *Mon. Wea. Rev.* 143, 2795–2816. doi:10.1175/MWR-D-14-00310.1

Parker, M. D. (2014). Composite VORTEX2 supercell environments from near-storm soundings. *Mon. Wea. Rev.* 142 (2), 508–529. doi:10.1175/MWR-D-13-00167.1

Qian, Y., Chakraborty, T. C., Li, J., Li, D., He, C., Sarangi, C., et al. (2022). Urbanization impact on regional climate and extreme weather: Current understanding, uncertainties, and future research directions. *Adv. Atmos. Sci.* 39, 819–860. doi:10.1007/s00376-021-1371-9

Rasmussen, E. N., Richardson, S., Straka, J. M., Markowski, P. M., and Blanchard, D. O. (2000). The association of significant tornadoes with a baroclinic boundary on 2 June 1995. *Mon. Wea. Rev.* 128, 174–191.

Roberts, B., Xue, M., Schenkman, A. D., and Dawson, D. T. (2016). The role of surface drag in tornadogenesis within an idealized supercell simulation. *J. Atmos. Sci.* 73, 3371–3395. doi:10.1175/JAS-D-15-0332.1

Rotunno, R. (1981). On the evolution of thunderstorm rotation. *Mon. Wea. Rev.* 109, 577–586. doi:10.1175/1520-0493(1981)109<0577:OTEOTR>2.0.CO;2

Salamanca, F., and Martilli, A. (2010). A new building energy model coupled with an urban canopy parameterization for urban climate simulations—Part II. Validation with one dimension off-line simulations. *Theor. Appl. Climatol.* 99, 345–356. doi:10.1007/s00704-009-0143-8

Schenkman, A. D., Xue, M., and Hu, M. (2014). Tornadogenesis in a high-resolution simulation of the 8 May 2003 Oklahoma City supercell. *J. Atmos. Sci.* 71, 130–154. doi:10.1175/JAS-D-13-073.1

Schultz, D. M., Richardson, Y. P., Markowski, P. M., and Doswell, C. A., III (2014). Tornadoes in the central United States and the "clash of air masses". *Bull. Am. Meteorol. Soc.* 95, 1704–1712. doi:10.1175/BAMS-D-13-00252.1

Shafer, C. M., Mercer, A. E., Leslie, L. M., Richman, M. B., and Doswell, C. A., III (2010). Evaluation of WRF model simulations of tornadic and nontornadic outbreaks occurring in the spring and fall. *Mon. Weather Rev.* 138, 4098–4119. doi:10.1175/2010MWR3269.1

Shepherd, J. M. (2005). A review of current investigations of urban-induced rainfall and recommendations for the future. *Earth Interact.* 9, 1–27. doi:10.1175/EI156.1

Singh, J., Karmakar, S., PaiMazumder, D., Ghosh, S., and Niyogi, D. (2020). Urbanization alters rainfall extremes over the contiguous United States. *Environ. Res. Lett.* 15 (7), 074033. doi:10.1088/1748-9326/ab8980

Sobash, R. A., Romine, G. S., Schwartz, C. S., Gagne, D. J., and Weisman, M. L. (2016). Explicit forecasts of low-level rotation from convection-allowing models

for next-day tornado prediction. *Wea. Forecast.* 31 (5), 1591–1614. doi:10.1175/waf-d-16-0073.1

Thompson, R. L., Mead, C. M., and Edwards, R. (2007). Effective storm-relative helicity and bulk shear in supercell thunderstorm environments. *Wea. Forecast.* 22, 102–115. doi:10.1175/WAF969.1

Thompson, R. L., Smith, B. T., Grams, J. S., Dean, A. R., and Broyles, C. (2012). Convective modes for significant severe thunderstorms in the contiguous United States. Part II: Supercell and QLCS tornado environments. *Wea. Forecast.* 27, 1136–1154. doi:10.1175/WAF-D-11-00116.1

Tippett, M. K., Sobel, A. H., and Camargo, S. J. (2012). Association of U.S. tornado occurrence with monthly environmental parameters. *Geophys. Res. Lett.* 39, L02801. doi:10.1029/2011GL050368

Tippett, M. K. (2018). Robustness of relations between the MJO and U.S. tornado occurrence. *Mon. Wea. Rev.* 146, 3873–3884. doi:10.1175/MWR-D-18-0207.1

Wade, A. R., Coniglio, M. C., and Ziegler, C. L. (2018). Comparison of near- and far-field supercell inflow environments using radiosonde observations. *Mon. Weather Rev.* 146 (8), 2403–2415. doi:10.1175/MWR-D-17-0276.1

Wakimoto, R. M. (1982). The life cycle of thunderstorm gust fronts as viewed with Doppler radar and Rawinsonde data. *Mon. Wea. Rev.* 110 (8), 1060–1082. doi:10.1175/1520-0493(1982)110<1060:tlcotg>2.0.co;2

Wurman, J., and Kosiba, K. (2013). Finescale radar observations of tornado and mesocyclone structures. *Weather Forecast* 28, 1157–1174. doi:10.1175/WAF-D-12-00127.1

Wurman, J., Alexander, C., Robinson, P., and Richardson, Y. (2007). Low-Level winds in tornadoes and potential catastrophic tornado impacts in urban areas. *Bull. Am. Meteorol. Soc.* 88, 31–46. doi:10.1175/BAMS-88-1-31

Wurman, J., Dowell, D., Richardson, Y., Markowski, P., Rasmussen, E., Burgess, D., et al. (2012). The second verification of the origins of rotation in tornadoes experiment: VORTEX2. *Bull. Am. Meteorological Soc.* 93, 1147–1170. doi:10.1175/BAMS-D-11-00010.1

frontiers | Frontiers in Earth Science

TYPE Original Research
PUBLISHED 25 April 2023
DOI 10.3389/feart.2023.1143767

OPEN ACCESS

EDITED BY
Yanping Li,
University of Saskatchewan, Canada

REVIEWED BY
Mingxuan Chen,
China Meteorological Administration, China
Zheng Sheng,
National University of Defense Technology, China

*CORRESPONDENCE
Lingkun Ran,
rlk@mail.iap.ac.cn

RECEIVED 13 January 2023
ACCEPTED 11 April 2023
PUBLISHED 25 April 2023

CITATION
Zhou K, Ran L, Zhang W, Tian L, Chen L and Liu H (2023), The effect analysis of three-dimensional divergence and its vertical gradient on convection initiation. *Front. Earth Sci.* 11:1143767. doi: 10.3389/feart.2023.1143767

The effect analysis of three-dimensional divergence and its vertical gradient on convection initiation

Kuo Zhou[1], Lingkun Ran[1]*, Wancheng Zhang[2], Liqing Tian[3], Lei Chen[4] and Haiwen Liu[5]

[1]Laboratory of Cloud Precipitation Physics and Severe Storms, Institute of Atmospheric Physics, Chinese Academy of Sciences, Beijing, China, [2]Yunnan Institute of Meteorological Science, Kunming, China, [3]Hebei Insititute of Meteorological Science, Shijiazhuang, China, [4]Guizhou Meteorological Service Center, Guiyang, China, [5]Department of Aviation Meteorology, Civil Aviation University of China, Tianjin, China

A severe convection process occurred in southern Xinjiang during June 15–17, 2021. Here, the convection initiation mechanism is revealed by analyzing the impacts of three-dimensional divergence ($\nabla \cdot \boldsymbol{V}$) on the changes in pressure and the vertical pressure gradient force (VPGF). The pressure tendency equation and vertical pressure gradient force equation are derived based on three-dimensional divergence. It is shown that three-dimensional divergence has a better correlation with precipitation. The local change in pressure is affected mainly by the three-dimensional divergence forcing term. The air mass accumulates in the lower layers because of the three-dimensional convergence in the windward slope, strengthening the positive pressure change tendency. Three-dimensional convergence in the lower layers converts to divergence with height, leading to air mass loss in the upper layers. The air mass redistributes vertically owing to the positive vertical gradient of three-dimensional divergence, which motivates the upward VPGF. The local change in VPGF is highly correlated with the vertical velocity. The vertical velocity increases as the upward VPGF strengthens, resulting in convection initiation in southern Xinjiang.

KEYWORDS

three-dimensional divergence, pressure, vertical pressure gradient force, vertical velocity, convection initiation

1 Introduction

Located in the middle of Eurasia, Xinjiang is not directly affected by the monsoon system. It features a typical continental arid and semiarid climate (Wang et al., 2013). However, extreme rainfall events have occurred frequently in recent years (Wang et al., 2017). The annual precipitation can reach 700 mm in favorable terrain conditions in Xinjiang. Unstable stratification, water vapor, and dynamic lifting are three conditions required for the formation of convective weather, among which the first two conditions are generally easy to meet. Therefore, the key to the formation of convective weather is the dynamic lifting condition (Doswell, 2001; Weckwerth et al., 2008; Alexander, 2018).

Deep convective systems are accompanied by intense convergent airflow in lower layers and divergent airflow in higher layers. The contributions from divergence include water vapor transport (Ziegler et al., 1997; Masunaga, 2013), pumping effects (Kalthoff et al., 2009; Ueno et al., 2009) and stimulating gravity waves during geostrophic adjustment (He et al.,

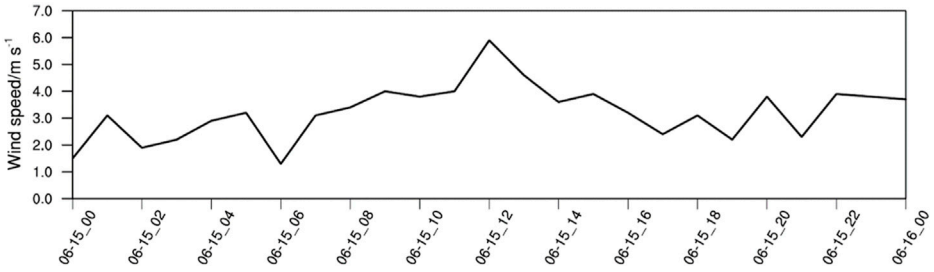

FIGURE 1
Time series of the observed surface wind speed at the Hetian automatic weather station (units: m s^{-1}).

2022; Polichtchouk et al., 2022). The dynamic mechanisms for convection initiation can be studied by analyzing divergence development with the divergence equation and its expanded theories (Ulanski and Garstang, 1978; Sun, 1989). Early studies concentrated mainly on horizontal divergence and the factors affecting horizontal divergence (Stevens, 1979; Wang and Sun, 1988; Businger et al., 2001; Chen et al., 2009). The mass field is changed by precipitation during deep convection (Gao et al., 2004). Therefore, additional source and sink terms are introduced into the mass continuity equation, and the three-dimensional divergence is not zero. The convergence and divergence motions in the wind field can be reflected by three-dimensional divergence. In addition, the mass forcing effects are implicitly included in three-dimensional divergence. The effects from the dynamic field and mass field are included in three-dimensional divergence, which is a more comprehensive physical quantity than horizontal divergence (Yang and Gao, 2007).

A series of studies on the convection cell structure (Zhuang et al., 2006), water vapor transport (Zhou et al., 2019), mesoscale convergence line (Huang et al., 2021), and vertical motion equation (Zhou et al., 2022) have been conducted to enhance the understanding of deep convection in Xinjiang. Overall, deep convections in Xinjiang are formed under complicated terrain conditions, and the initiation mechanisms need further analysis. Compared to horizontal divergence, the effects of three-dimensional divergence on convection initiation are still not clear. Based on the above considerations, the effects of three-dimensional divergence on the local pressure, vertical pressure gradient force and vertical velocity are analyzed to reveal the mechanism of convection initiation in Xinjiang during June 15–17, 2021.

2 Synoptic overview

A severe convection process occurred in southern Xinjiang during June 15–17, 2021. Daily precipitation at the Hetian station exceeded 45.5 mm, breaking the local daily precipitation record. Luopu County experienced daily precipitation over 100 mm, reaching a rainstorm level (Zhou et al., 2022). The surface wind speed increased gradually after 0600 UTC on 15 June 2021 at the Hetian automatic weather station and reached a maximum of 6 m s^{-1} at 1200 UTC on 15 June 2021 (Figure 1), indicating that convection developed during this period.

The 200-hPa trough line was located in Central Asia, and Xinjiang was in front of the upper trough at 0000 UTC on 15 June 2021. The jet stream center was to the north of Qinghai Province. Southern Xinjiang was on the right side of the upper jet stream entrance, leading to divergence flows in higher layers (Figure 2A). The central Asia trough at 500 hPa deepened westward and then turned into a horizontal trough. Westerly and southerly winds dominated the southern Xinjiang region (Figure 2B). A high-pressure system near the eastern Aral Sea (60°E, 52°N) and a low-pressure system over the northeastern Altai Mountains (100°E, 55°N) developed robustly at 700 hPa (Figure 2C). The strong northerly wind between these two systems flowed into southern Xinjiang and turned into a northeasterly wind on the windward slope of the Kunlun Mountains. The configuration of synoptic systems at the upper level, middle level and lower level was favorable to convection initiation in southern Xinjiang.

3 Numerical simulation and three-dimensional divergence

The convection initiation process was simulated using the WRF (V4.4) model and the NCEP (National Centers for Environmental Prediction) operational assimilation system GSI (Gridpoint Statistical Interpolation, Version 3.7). The background field and lateral boundary of the model were obtained from the NCEP global forecast system (GFS) analysis field and forecast field (0.5°×0.5°). The model cold start time was 1200 UTC on 13 June 2021. The three-dimensional variational scheme was used to assimilate the satellite observations and conventional data in the GDAS (Global Data Assimilation System) every 6 h. After two assimilation cycles, a 48-h forecast was carried out from 0000 UTC on 14 June 2021. The horizontal resolution of the model was 3 km (901×901 grid points) with a total of 61 vertical levels. The model top was fixed at 50 hPa. The WSM6 cloud microphysics scheme (Hong et al., 2006a), RRTMG longwave radiation and shortwave radiation scheme (Iacono et al., 2008), Noah land surface model (Tewari et al., 2004), and YSU planetary boundary layer scheme (Hong et al., 2006b) were adopted.

The observed precipitation data were obtained from the CLDAS (China Meteorological Administration Land Data Assimilation System) hourly merged precipitation grid dataset (0.05°×0.05°).

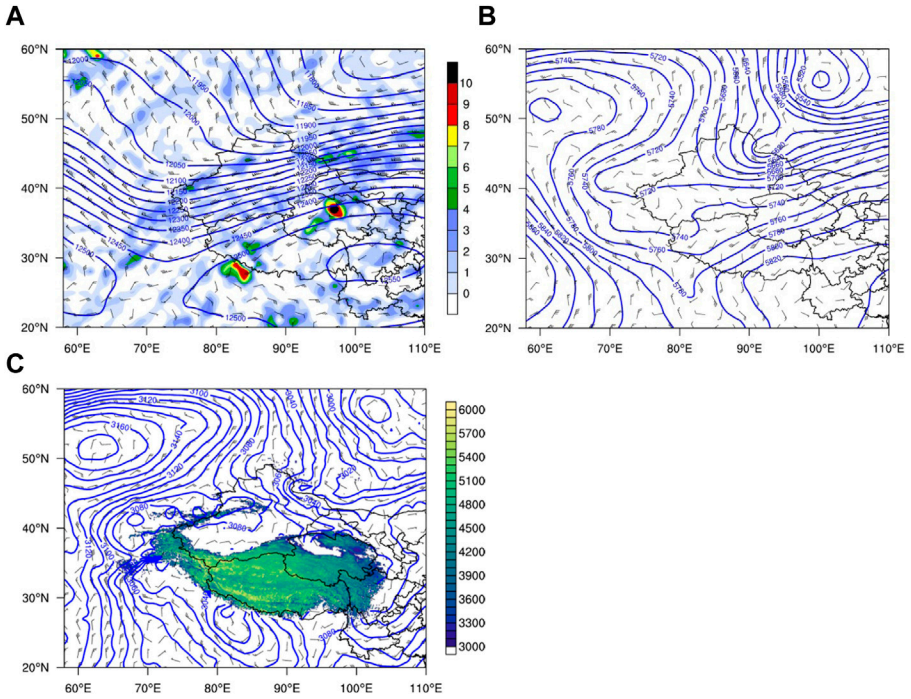

FIGURE 2
(A) Horizontal divergence (shadings, units: 10^{-5} s^{-1}), geopotential heights (blue contours, units: gpm) and wind fields (wind barbs, units: m s^{-1}) at 200 hPa, and geopotential heights (blue contours, units: gpm) and wind fields (wind barbs, units: m s^{-1}) at **(B)** 500 hPa and **(C)** 700 hPa at 0000 UTC on 15 June 2021. In Fig. c, the shaded areas denote the topographical height (units: m).

The observed rain belts extended from northwest to southeast along the Kunlun Mountains. The simulated precipitation center (79°E, 37°N) was located west of the observed precipitation center (80°E, 37°N). This discrepancy may have resulted from the initial fields, approximations and parameterizations of the model, but the overall precipitation area was consistent with the observations (Figure 3B). The domain-mean precipitation value was calculated within the red rectangular box in Figure 3A. The precipitation increased gradually after 0700 UTC on 15 and entered the mature stage at 1600 UTC on 15. The simulated precipitation was weaker than the observation, while the precipitation evolution agreed well with the observation (Figure 3C). The linear correlation coefficient between the observed and simulated precipitation was 0.967. A two-tailed sample *t*-test on the significance of the correlation coefficient was conducted with 23 degrees of freedom, and the critical correlation coefficient at the 1% significance level was 0.505. Therefore, the relations between the observed and simulated precipitation were statistically significant. The convection initiation mechanism was then analyzed based on these simulation results.

The primary convection cell was in the initiation stage at 0700 UTC on 15 June 2021 (Figure 4). Convergence motions were dominant in horizontal divergence ($HD = \nabla_h \cdot \boldsymbol{V}$) near the convection initiation position (point A) due to the northerly wind in the lower layers, and divergence motions dominated at heights of 5–7 km (Figure 4A). Vertical divergence ($VD = \partial w/\partial z$) and horizontal divergence have opposite phase distributions (Figure 4B). The convergence and divergence centers of *HD* and *VD* were also distinct to the north of 37.02°N and to the south of 36.84°N away from the convection initiation position. The distribution of three-dimensional divergence ($\lambda = \nabla \cdot \boldsymbol{V}$) centers agreed well with the convection initiation position. Three-dimensional convergence centers were identified on the southern and northern sides of point A below 5 km (Figure 4C). The divergence centers stretched up to 9 km at point A. The values in Figure 4D were averaged within 30×30 km around 79°E, 37.15°N near point A. The temporal evolution of *HD* and precipitation were negatively correlated (Figure 4D). Convergence motions dominated horizontal divergence within 2–7 km during the strong precipitation stage after 1000 UTC on 15. The divergence trend in λ strengthened after 0700 UTC on 15. The temporal evolution of *VD* and λ was positively correlated with precipitation. The correlation coefficient between λ and precipitation (0.76) was statistically significant at the 1% significance level, greater than that from *HD* or *VD*. It was thus clear that the relations between three-dimensional divergence and convection were much closer. The effects of three-dimensional divergence on convection were then further analyzed.

4 Pressure tendency equation analysis

Yang and Gao (2007) noted that the three-dimensional divergence not only included the convergence and divergence effects of the wind field but also considered the effects of mass forcing. The variations in local pressure can be affected by three-dimensional divergence. Therefore, a pressure tendency equation that included the effects of three-dimensional divergence forcing

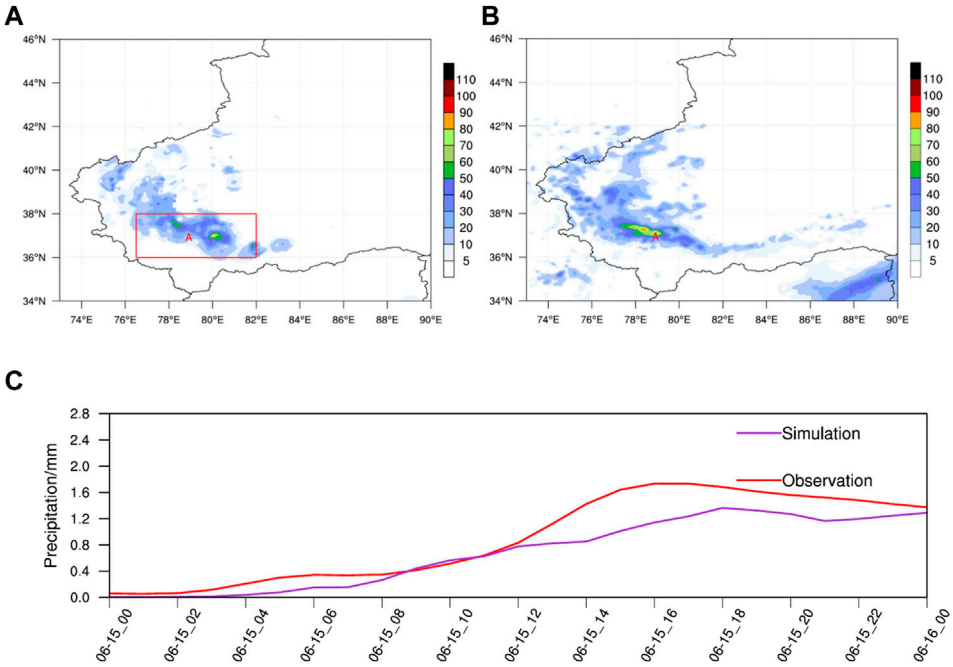

FIGURE 3
(A) Observed and **(B)** simulated 24-h accumulated precipitation (units: mm) at 0000 UTC on 16 June 2021 and **(C)** time series of the simulated and observed domain-mean hourly precipitation. The red rectangular box in panel a denotes the area where the domain-mean value was calculated in panel **(C)**. The "A" labels in panels **(A, B)** denote the convection initiation position.

was derived. The mass continuity equation and thermodynamic equation in Cartesian coordinates are expressed as follows:

$$\frac{\partial \rho}{\partial t} + u\frac{\partial \rho}{\partial x} + v\frac{\partial \rho}{\partial y} + w\frac{\partial \rho}{\partial z} = -\rho \nabla \cdot \boldsymbol{V} \tag{1}$$

$$\frac{\partial \theta}{\partial t} + u\frac{\partial \theta}{\partial x} + v\frac{\partial \theta}{\partial y} + w\frac{\partial \theta}{\partial z} = S \tag{2}$$

where ρ is the air density; u, v and w are the zonal, meridional, and vertical components of wind, respectively; $\boldsymbol{V}$ is the three-dimensional wind vector; θ is the potential temperature; and S is the diabatic term. The potential temperature is defined as follows:

$$\theta = T\left(\frac{p_0}{p}\right)^{R/c_p} \tag{3}$$

where T is the temperature; $p_0 = 1000$ hPa; R is the gas constant; and c_p is the specific heat of dry air at constant pressure. The state equation of air is expressed as follows:

$$p = \rho R T \tag{4}$$

Taking Eqs 3, 4 into Eq. 2 and using the mass continuity Eq. 1, one can obtain the pressure tendency equation as follows:

$$\frac{\partial p}{\partial t} + u\frac{\partial p}{\partial x} + v\frac{\partial p}{\partial y} + w\frac{\partial p}{\partial z} = -p\frac{c_p}{c_v}\left(\frac{\partial u}{\partial x} + \frac{\partial v}{\partial y} + \frac{\partial w}{\partial z} - \frac{S}{\theta}\right) \tag{5}$$

where $c_v = c_p - R$ denotes the specific heat of dry air at a constant volume. By inputting three-dimensional divergence ($\lambda = \nabla \cdot \boldsymbol{V}$) into Eq. 5, the pressure tendency equation can be expressed as follows:

$$\frac{\partial p}{\partial t} = -u\frac{\partial p}{\partial x} - v\frac{\partial p}{\partial y} - w\frac{\partial p}{\partial z} - \frac{p\lambda c_p}{c_v} + \frac{pSc_p}{\theta c_v} \tag{6}$$

The left-hand side term in Eq. 6 is the local change in pressure. On the right-hand side of Eq. 6, according to the order, the terms are the zonal pressure advection term, meridional pressure advection term, vertical pressure advection term, three-dimensional divergence forcing term and diabatic forcing term. Eq. 6 can be used to analyze the effect of three-dimensional divergence on the pressure change.

All the terms in Eq. 6 were calculated using simulation data. The vertical pressure advection term and three-dimensional divergence forcing term were predominant in affecting pressure change during the convection initiation stage (Figures 5C, D). The other terms were 1–2 orders of magnitude smaller (Figures 5A, B, E). The vertical pressure advection term had positive contributions at 2–6 km at point A (Figure 5C). This indicated that the pressure or air mass was transported upward, leading to stronger local pressure in the upper layers (Liu and Liu, 2011). The three-dimensional divergence forcing term and λ had opposite phase distributions, suggesting that divergence motions from λ brought a decreasing trend to the local pressure. The negative values of the three-dimensional divergence forcing term stretched to 9 km at point A, and negative centers formed at 7–8 km (Figure 5D). Positive values spread on both sides of point A below 5 km (Figure 5D). The distribution of the pressure change in 6 s was shown in Figure 5F. The negative pressure change was consistent with the negative values of the three-dimensional divergence forcing term, indicating that divergence motions from λ led to a

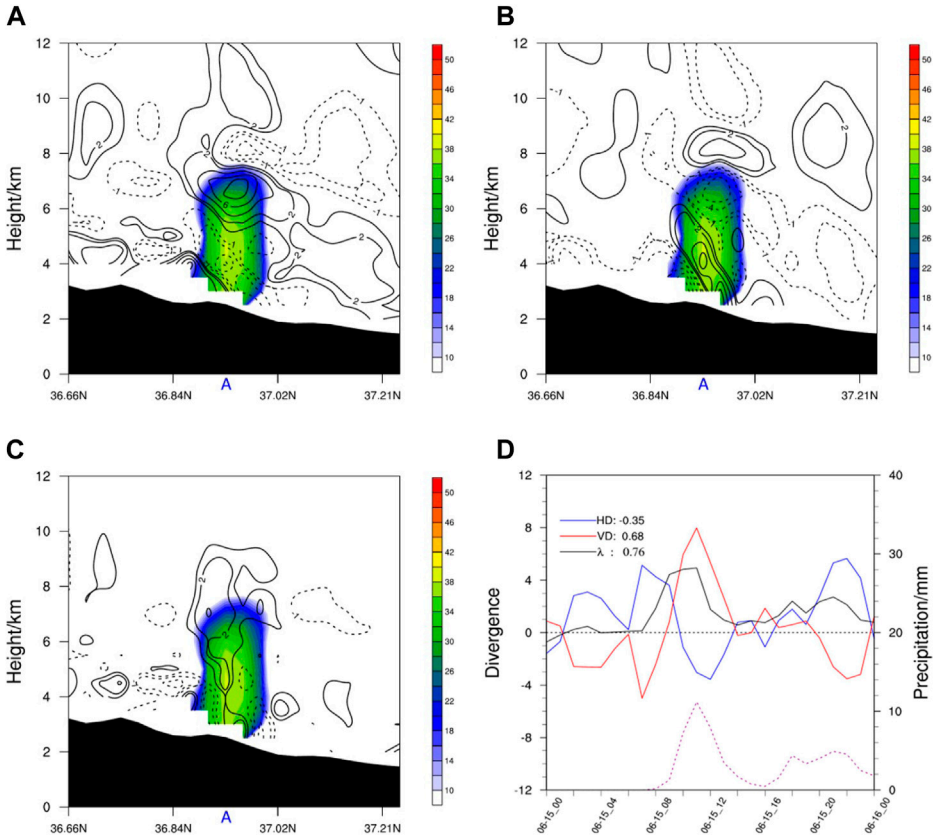

FIGURE 4
Cross sections of reflectivity (shadings, units: dBZ) and **(A)** horizontal divergence (black contours, units: 10^{-4} s^{-1}, dotted line for negative value), **(B)** vertical divergence (black contours, units: 10^{-4} s^{-1}), and **(C)** three-dimensional divergence (black contours, units: 10^{-4} s^{-1}) along 78.91°E at 0700 UTC on 15 June 2021; **(D)** time series of domain-mean horizontal divergence (blue line, units: 10^{-4} s^{-1}), vertical divergence (red line, units: 10^{-4} s^{-1}), and three-dimensional divergence (black line, units: 10^{-4} s^{-1}) integrated from 2 km to 7 km and hourly precipitation (purple dotted line, units: mm). "A" denotes the convection position. The values on the right side of the legend denote the linear correlation coefficient between divergence and simulated precipitation in panel **(D)**. The values in panel d are averaged within 30×30 km around 79°E, 37.15°N.

negative pressure change. The negative pressure change tendency was weakened due to the convergence motions from λ on both sides of point A, and positive pressure change centers formed at 5 km. The analysis above shows that three-dimensional divergence was the main factor forcing the pressure change. The vertical pressure gradient force can be affected by a pressure change, further leading to the development of vertical velocity. For this reason, the influences of three-dimensional divergence and a pressure change on the vertical pressure gradient force are discussed below.

5 Vertical pressure gradient force equation analysis

The vertical pressure gradient force can accelerate or decelerate the atmospheric vertical motion, resulting in the triggering or inhibition of convection. The vertical pressure gradient force can be expressed in Cartesian coordinates as follows:

$$\eta = -\frac{1}{\rho}\frac{\partial p}{\partial z} \tag{7}$$

Taking $\frac{D}{Dt}$ from Eq. 7 and using Eqs 1, 6, the vertical pressure gradient force equation can be expressed as follows:

$$\frac{\partial \eta}{\partial t} = -\boldsymbol{V}\cdot\nabla\eta + \frac{R\lambda}{\rho c_v}\frac{\partial p}{\partial z} + \frac{pc_p}{\rho c_v}\frac{\partial \lambda}{\partial z} + \frac{1}{\rho}\frac{\partial \boldsymbol{V}}{\partial z}\cdot\nabla p - \frac{c_p}{\rho c_v}\frac{\partial}{\partial z}\left(\frac{pS}{\theta}\right) \tag{8}$$

The left-hand side term in Eq. 8 is the local change in the vertical pressure gradient force. The terms on the right-hand side of Eq. 8 are the advection term of the vertical pressure gradient force, coupled term of the three-dimensional divergence and vertical pressure gradient force, vertical gradient of the three-dimensional divergence term, pressure advection term caused by vertical wind shear, and vertical gradient of the diabatic term.

Equation 8 was calculated based on simulation data. The results show that the vertical gradient of the three-dimensional divergence term was 1–2 orders of magnitude greater than those of the other terms. As shown in Figure 6A, the negative values of the three-dimensional divergence term were mainly below 4 km and above 7 km, and positive values were identified on both sides of point A. Two positive centers were located at point B at 5 km and point C at 4 km (Figure 6A). Divergence motions of λ were distributed in the relatively low layers at point A and, relatively weakly, at 4 km

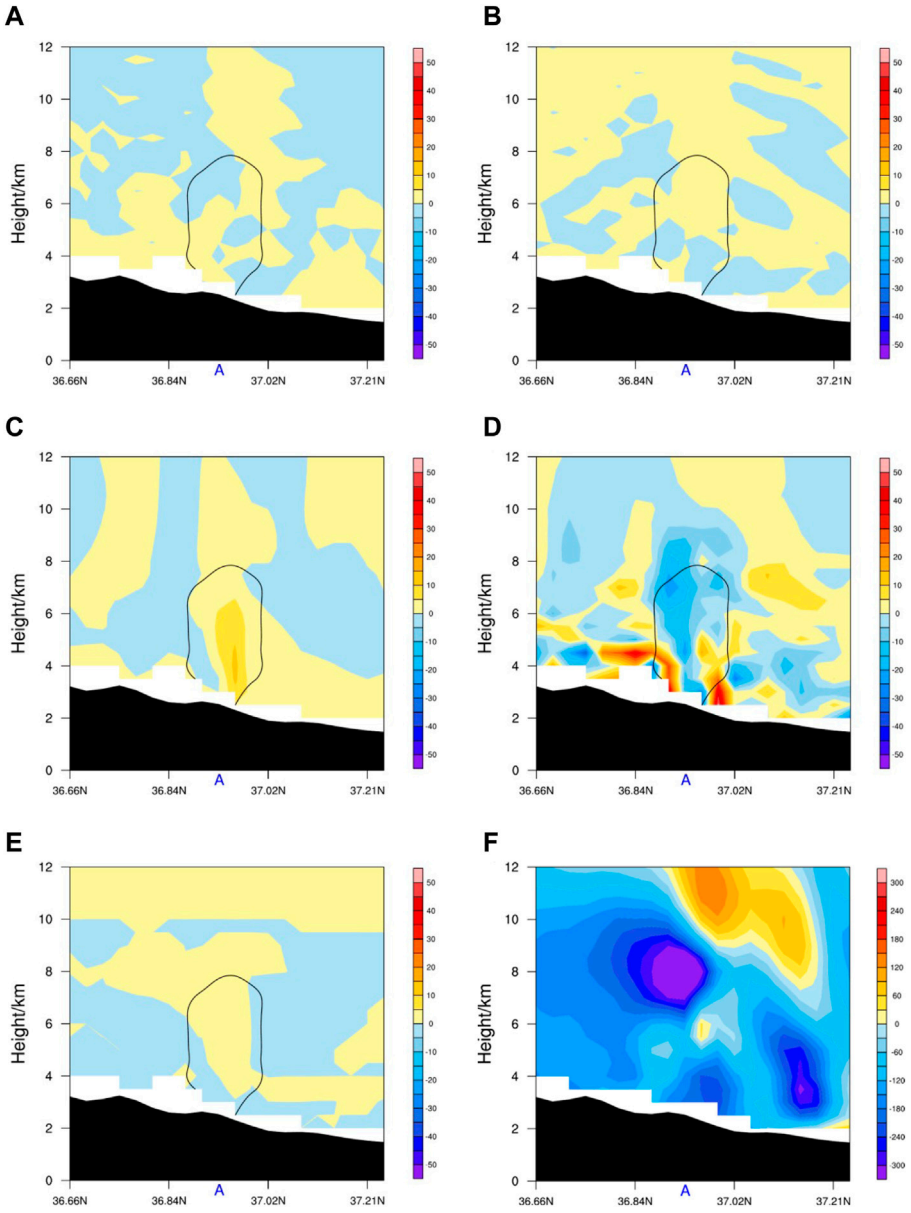

FIGURE 5
Cross sections of the **(A)** zonal pressure advection term (shadings, units: kg m^{-1} s^{-3}), **(B)** meridional pressure advection term (shadings, units: kg m^{-1} s^{-3}), **(C)** vertical pressure advection term (shadings, units: kg m^{-1} s^{-3}), **(D)** three-dimensional divergence forcing term (shadings, units: kg m^{-1} s^{-3}), **(E)** diabatic forcing term (shadings, units: kg m^{-1} s^{-3}), and **(F)** pressure change after 6 s (shadings, units: Pa) along 78.91°E at 0700 UTC on 15 June 2021. The black solid line denotes the hydrometeor mixing ratio of 0.2 g kg^{-1} in panels **(A–E)**.

(Figure 4C), resulting in the negative values of the vertical gradient of λ observed at point A. Convergence motions were distributed in the lower layers on both sides of point A and became divergence motions with height. Therefore, the vertical gradients of λ were positive at points B and C (Figure 6A), leading to increases in the vertical pressure gradient force at points B and C (Figure 6B) and further promoting the vertical ascending motions (Figure 6C).

The local change in the vertical pressure gradient force ($\partial\eta/\partial t$) was calculated by summing all terms on the right-hand side of Eq. 8. As shown in Figure 7, the time series of $\partial\eta/\partial t$ was highly correlated with the vertical velocity at 3–5 km and 5–7 km. Using a two-tailed sample *t*-test, the correlation coefficient was found to be statistically significant at the 1% significance level. Increasing $\partial\eta/\partial t$ and w trends were found at approximately 0700 UTC on 15 June 2021, indicating that the vertical pressure gradient force promoted the development of vertical ascending motions.

6 Convection initiation mechanism in southern Xinjiang

The pressure at the windward slope of the Kunlun Mountains was strengthened by the convergence of λ. The vertical pressure gradient force strengthened due to the vertical gradient of λ,

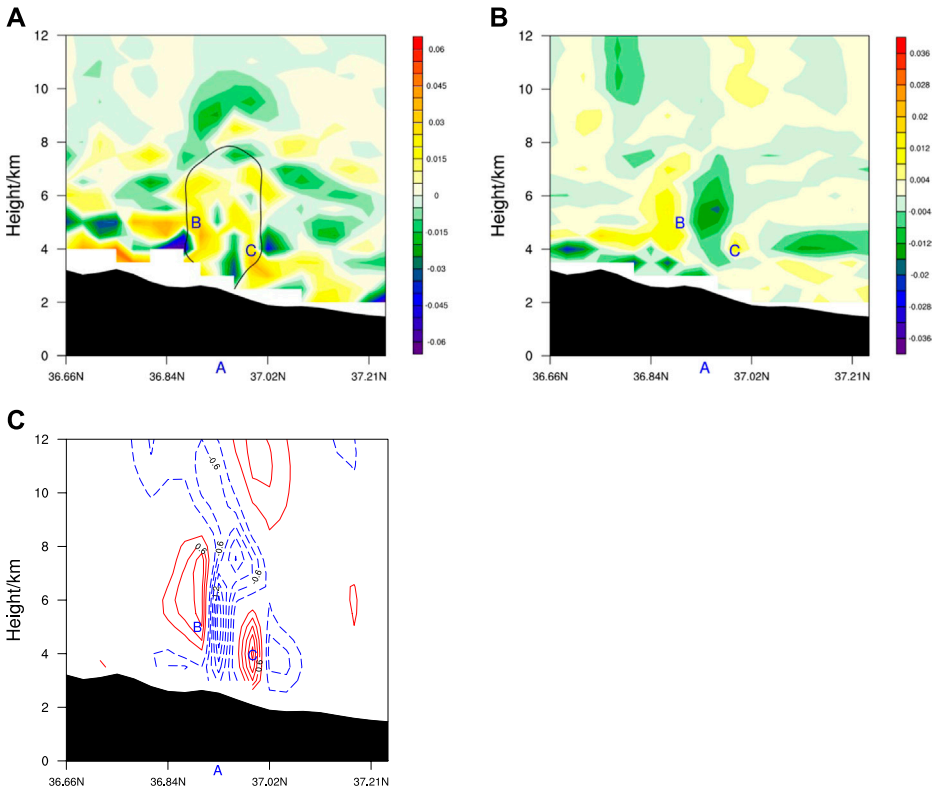

FIGURE 6
Cross sections of **(A)** the vertical gradient term of three-dimensional divergence (shadings, units: m s^{-3}), **(B)** vertical pressure gradient force change (shadings, units: m s^{-2}) and **(C)** vertical velocity change (shadings, units: m s^{-1}) after 6 s along 78.91°E at 0700 UTC on 15 June 2021. The labels "B" and "C" denote the positions corresponding to positive changes in VPGF and vertical velocity, respectively.

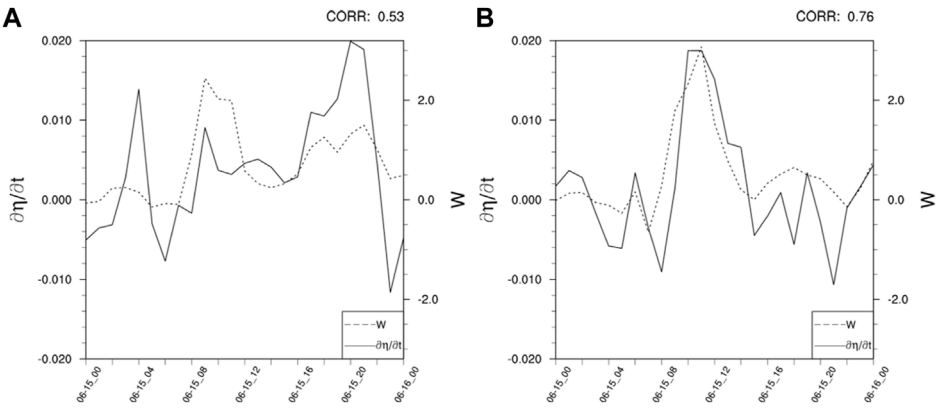

FIGURE 7
Time series of the domain mean of the local vertical pressure gradient force change (black solid line, units: m s^{-3}) and vertical velocity change (black dotted line, units: m s^{-1}) integrated from **(A)** 3 km–5 km and from **(B)** 5 km–7 km. The values were averaged within 30 km × 30 km around 79°E, 37.15°N.

further promoting the development of ascending motions. In the meantime, convergence motions of water vapor fluxes and unstable atmospheric stratification occurred in the lower layers (Figures 8A, B). These factors jointly led to convection initiation in southern Xinjiang and promoted its organized development.

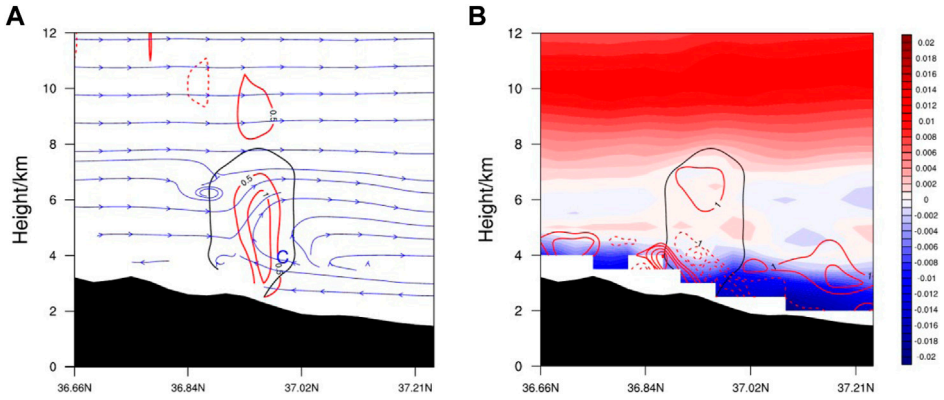

FIGURE 8
Cross sections of **(A)** the vertical velocity (red contours, units: m s^{-1}) and streamlines, **(B)** atmospheric stratification stability (shadings, units: km^{-1}) and water vapor flux divergence (red contours, units: 10^{-6} g cm^{-2} hPa^{-1} s^{-1}) along 78.91°E at 0700 UTC on 15 June 2021.

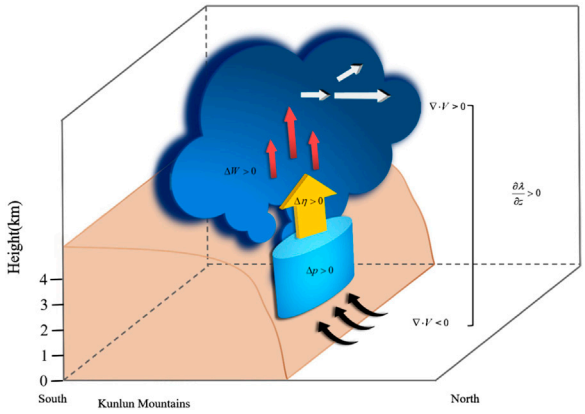

FIGURE 9
Schematic of convection initiation in southern Xinjiang.

According to the analyses above, a schematic of convection initiation in southern Xinjiang was built. As shown in Figure 9, The strong northerly wind was blocked by the Kunlun Mountains, resulting in three-dimensional convergence at 3 km ($\nabla \cdot V < 0$). According to the pressure tendency formula expressed in Eq. 6, the convergence of λ weakened the negative pressure tendency and promoted a positive local pressure change ($\Delta p > 0$). The air mass accumulated owing to the convergence of λ at the windward slope of the topography, thus strengthening the local pressure in the lower layers. The divergence of λ appeared at 6–7 km, leading to the loss of air mass in the upper layers. The positive vertical gradient of λ ($\partial\lambda/\partial z > 0$) resulted in the vertical redistribution of the air mass and further reinforced the vertical pressure gradient force ($\Delta\eta > 0$). These physical processes can be reflected by Eq. 8.

The upward VPGF provided dynamic uplift conditions for air parcels. The vertical acceleration increased, and the upward motions were strengthened ($\Delta W > 0$), leading to convection initiation.

7 Conclusion and discussion

A severe convection process occurred in southern Xinjiang during June 15–17, 2021, resulting in heavy precipitation. The WRF model and GSI assimilation system were used here to perform a high-resolution simulation of this convection. The observed precipitation area, magnitude and evolution trend were well-captured by the simulation data. On this basis, the effects of three-dimensional divergence on convection initiation were fully considered. The impacts of three-dimensional divergence on the pressure and vertical pressure gradient force were analyzed to reveal the convection initiation mechanism. The preliminary conclusions are summarized as follows.

The horizontal divergence and vertical divergence had opposite phase distributions, and both had strong centers away from the convection. The three-dimensional divergence, by contrast, agreed well with the convection position and precipitation evolution.

A pressure tendency equation including the forcing effects from three-dimensional divergence was derived based on the mass continuity equation and thermodynamic equation in Cartesian coordinates. The pressure change was dominated by the vertical pressure advection term and three-dimensional divergence forcing term. The negative pressure change tendency was weakened because of convergence motions from three-dimensional divergence, and a positive pressure change appeared in local areas. The mass field was adjusted by three-dimensional divergence, resulting in a local pressure change.

The vertical pressure gradient force can be affected by pressure changes, thus further impacting the vertical velocity. The vertical pressure gradient force equation was derived herein using the mass continuity equation and pressure tendency equation. The vertical gradient of the three-dimensional divergence term was the dominant term affecting the local change in the vertical pressure gradient force, which was determined by the pressure and vertical gradient of λ. The convergence motions of λ resulted in a positive pressure change in local areas. Meanwhile, the convergence motions of λ in the lower levels became divergence motions in the upper levels, leading to a positive vertical gradient of λ. The upward VPGF

was strengthened by the vertical redistribution of the air mass. There was better correlation between the local change in VPGF and vertical velocity. The strengthened VPGF promoted the development of upward motions, resulting in convection initiation.

The local change term on left hand side of the derived equations still had some imbalances with the forcing terms on right hand side. This was mainly aroused by the calculation errors, equation approximation and model errors. But the local change of pressure and VPGF was overall consistent with the spatial distribution mode of the main forcing terms on right hand side of the equations.

Data availability statement

The raw data supporting the conclusion of this article will be made available by the authors, without undue reservation.

Author contributions

KZ and LR contributed to conception and design of the study. WZ and LT organized the database. LC and HL performed the data assimilation. KZ wrote the first draft of the manuscript. LR, WZ and LT reviewed and modified the manuscript.

Funding

This research was funded by the Strategic Priority Research Program of the Chinese Academy of Sciences (Grant XDA17010105), and the National Natural Science Foundation of China (42075008). This work was supported by the National Key Scientific and Technological Infrastructure project “Earth System Numerical Simulation Facility” (EarthLab).

Conflict of interest

The authors declare that the research was conducted in the absence of any commercial or financial relationships that could be construed as a potential conflict of interest.

Publisher’s note

References

Alexander, L. S., Sills, D. M. L., and Taylor, P. A. (2018). Initiation of convective storms at low-level mesoscale boundaries in southwestern Ontario. *Weather Forecast* 33 (2), 583–598. doi:10.1175/WAF-D-17-0086.1

Businger, S., Adams, M. E., Koch, S. E., and Kaplan, M. L. (2001). Extraction of geopotential height and temperature structure from profiler and rawinsonde winds. *Mon. Weather Rev.* 129 (7), 1729–1739. doi:10.1175/1520-0493(2001)129<1729:EOGHAT>2.0.CO;2

Chen, Z. M., Yang, K. Q., and Wu, H. Y. (2009). Mechanism of heavy rainfall maintenance and increment in convergence excited by coupling forces between dynamic and thermodynamic fields (in Chinese with English abstract). *ACTA Phys. SIN-CH* 58 (6), 4362–4371. doi:10.3321/j.issn:1000-3290.2009.06.116

Doswell, III C. A. (2001). *Severe convective storms*. Berlin, Germany: Springer, 1–26.

Gao, S. T., Zhou, Y. S., Cui, X. P., and Dai, G. P. (2004). Impacts of cloud-induced mass forcing on the development of moist potential vorticity anomaly during torrential rains. *Adv. Atmos. Sci.* 21 (06), 923–927. doi:10.1007/BF02915594

He, Y., Zhu, X. Q., Sheng, Z., He, M. Y., and Feng, Y. T. (2022). Observations of inertia gravity waves in the western pacific and their characteristic in the 2015/2016 quasi-biennial oscillation disruption. *J. Geophys. Res-Atmos.* 127 (22). doi:10.1029/2022JD037208

Hong, S.-Y., Lim, K.-S., Kim, J.-H., Lim, J.-O. J., and Dudhia, J. (2006a). The WRF single-moment 6-class microphysics scheme (WSM6). *J. Korean Phys. Soc.* 42, 129–151.

Hong, S.-Y., Noh, Y., and Dudhia, J. (2006b). A new vertical diffusion package with an explicit treatment of entrainment processes. *Mon. Weather Rev.* 134, 2318–2341. doi:10.1175/MWR3199.1

Huang, X., Zhou, Y. S., Ran, L. K., Kalim, U., and Zeng, Y. (2021). Analysis of the environmental field and unstable conditions on a rainstorm event in the Ili Valley of Xinjiang (in Chinese with English abstract). *Chin. J. Atmos. Sci.* 45 (1), 148–164. doi:10.3878/j.issn.1006-9895.1912.19219

Iacono, M. J., Delamere, J. S., Mlawer, E. J., Shephard, M. W., Clough, S. A., and Collins, W. D. (2008). Radiative forcing by long-lived greenhouse gases: Calculations with the AER radiative transfer models. *J. Geophys. Res-Atmos.* 113–D13103. doi:10.1029/2008JD009944

Kalthoff, N., Adler, B., Barthlott, C., Corsmeier, U., Mobbs, S., Crewell, S., et al. (2009). The impact of convergence zones on the initiation of deep convection: A case study from COPS. *Atmos. Res.* 93 (4), 680–694. doi:10.1016/j.atmosres.2009.02.010

Liu, S. K., and Liu, S. D. (2011). *Atmospheric dynamics 1*. Beijing, China: Peking University Press.

Masunaga, H. (2013). A satellite study of tropical moist convection and environmental variability: A moisture and thermal budget analysis. *J. Atmos. Sci.* 70 (8), 2443–2466. doi:10.1175/JAS-D-12-0273.1

Polichtchouk, I., Wedi, N., and Kim, Y. H. (2022). Resolved gravity waves in the tropical stratosphere: Impact of horizontal resolution and deep convection parametrization. *Q. J. Roy. METEOR. Soc.* 148 (742), 233–251. doi:10.1002/qj.4202

Stevens, D. E. (1979). Vorticity, momentum and divergence budgets of synoptic-scale wave disturbances in the tropical eastern Atlantic. *Mon. Wea. Rev.* 107 (5), 535–550. doi:10.1175/1520-0493(1979)107<0535:vmadbo>2.0.co;2

Sun, S. Q. (1989). The application of divergence variation to analysis and forecasting of mesoscale convective systems (in Chinese with English abstract). *Meteor. Mon.* 15 (1), 3–8. doi:10.7519/j.issn.1000-0526.1989.1.001

Tewari, M., Chen, F., Wang, W., Dudhia, J., Lemone, M. A., Mitchell, K. E., et al. (2004). “Implementation and verification of the unified noah land-surface model in the wrf model,” in Proceedings of the 20th Conference on Weather Analysis and Forecasting/16th Conference on Numerical Weather Prediction, Seattle, WA, USA, January 2004 (American Meteorological Society), 11–15.

Ueno, K., Takano, S., and Kusaka, H. (2009). Nighttime precipitation induced by a synoptic-scale convergence in the central Tibetan Plateau. *J. Meteor. Soc. Jpn.* 87 (3), 459–472. doi:10.2151/jmsj.87.459

Ulanski, S. L., and Garstang, M. (1978). The role of surface divergence and vorticity in the life cycle of convective rainfall. Part I: Observation and analysis. *J. Atmos. Sci.* 35 (6), 1047–1062. doi:10.1175/1520-0469(1978)035<1047:TROSDA>2.0.CO;2

Wang, H. J., Chen, Y. N., and Chen, Z. S. (2013). Spatial distribution and temporal trends of mean precipitation and extremes in the arid region, northwest of China, during 1960-2010. *Hydrol. Process.* 27 (12), 1807–1818. doi:10.1002/hyp.9339

Wang, Y. J., Zhou, B. T., Qin, D. H., Wu, J., Gao, R., and Song, L. C. (2017). Changes in mean and extreme temperature and precipitation over the arid region of northwestern China: Observation and projection. *Adv. Atmos. Sci.* 34 (3), 289–305. doi:10.1007/s00376-016-6160-5

Wang, Z. X., and Sun, S. Q. (1988). The relationship between environmental vorticity and divergence field associated with heavy rain systems (in Chinese with English abstract). *Acta Meteorol. Sin.* 46 (04), 110–114. doi:10.11676/qxxb1988.063

Weckwerth, T. M., Murphey, H. V., Flamant, C., Goldstein, J., and Pettet, C. R. (2008). An observational study of convection initiation on 12 June 2002 during IHOP_2002. *Mon. Wea. Rev.* 136 (7), 2283–2304. doi:10.1175/2007MWR2128.1

Yang, S., and Gao, S. T. (2007). Three-dimensional divergence equation and its diagnosis analysis to storm rainfall system (in Chinese with English abstract). *Chin. J. Atmos. Sci.* 31 (1), 167–179. doi:10.3878/j.issn.1006-9895.2007.01.17

Zhou, K., Ran, L. K., Cai, R., and Chen, L. (2022). Diagnostic analysis of terrain following vertical motion equation in southern Xinjiang extreme rainstorms (in Chinese with English abstract). *Chin. J. Atmos. Sci.* 46 (3), 745–761. doi:10.3878/j.issn.1006-9895.2201.21194

Zhou, Y., Xie, Z., and Liu, X. (2019). An analysis of moisture sources of torrential rainfall events over Xinjiang, China. *J. Hydrometeorol.* 20 (10), 2109–2122. doi:10.1175/JHM-D-19-0010.1

Zhuang, W., Liu, L. P., and Wang, N. (2006). Study on three-dimensional wind fields of mesoscale convective systems in Xinjiang (in Chinese with English abstract). *J. Appl. Meteor. Sci.* 17 (04), 444–451. doi:10.11898/1001-7313.20060408

Ziegler, C. L., Tsengdar, J. L., and Roger, A. P. S. (1997). Convective initiation at the dryline: A modeling study. *Mon. Wea. Rev.* 125 (6), 1001–1026. doi:10.1175/1520-0493(1997)125<1001:ciatda>2.0.co;2

frontiers | Frontiers in Earth Science

TYPE Original Research
PUBLISHED 07 June 2023
DOI 10.3389/feart.2023.1136356

OPEN ACCESS

EDITED BY
Yanping Li,
University of Saskatchewan, Canada

REVIEWED BY
Mingxuan Chen,
China Meteorological Administration, China
Zhenhua Li,
University of Saskatchewan, Canada

*CORRESPONDENCE
Ren Cai,
76426022@qq.com
Lingkun Ran,
rlk@mail.iap.ac.cn

RECEIVED 03 January 2023
ACCEPTED 18 May 2023
PUBLISHED 07 June 2023

CITATION
Ma S, Cai R, Ran L, Jiao B, Zhou K and Guo A (2023), Decomposition of airflow over topography and its application to a topographic blizzard event in central Asia. *Front. Earth Sci.* 11:1136356. doi: 10.3389/feart.2023.1136356

Decomposition of airflow over topography and its application to a topographic blizzard event in central Asia

Shuping Ma[1,2], Ren Cai[3]*, Lingkun Ran[1,4]*, Baofeng Jiao[1,4], Kuo Zhou[1,4] and Anboyu Guo[5]

[1]Key Laboratory of Cloud–Precipitation Physics and Severe Storms, Institute of Atmospheric Physics (LACS), Chinese Academy of Sciences, Beijing, China, [2]School of Geography and Planning, Ningxia University, Yinchuan, China, [3]Xinjiang Meteorological Observatory, Urumqi, China, [4]University of Chinese Academy of Sciences, Beijing, China, [5]National Marine Environmental Forecasting Center (NMEFC), Beijing, China

To better understand the triggering mechanisms of extreme precipitation events in Central Asia due to the complex terrain, a case study of a topographic blizzard that occurred in Xinjiang Province on 30 November 2018 is conducted. The near-surface wind field is decomposed into flow-around and flow-over components to analyze the dynamic and thermodynamic effects of the flow around and over the topography in the Ili River valley and the northern slope of the Tianshan Mountains. The results reveal that the flow around the topography is the dominant component of the flow field that transports water vapor and causes moisture convergence. The symmetric instability observed at the lower level of the snowfall area is attributed to the flow-around wind field, which leads to advective transport of generalized potential temperature and causes changes in potential vorticity, ultimately resulting in symmetric instability. The local variation of stratified instability in the snowfall area is caused by flow-over potential divergence, specifically, the advection of the flow-over wind vertical shear to equivalent potential temperature causes the change of flow-over potential divergence, thus promotes stratified instability. Moreover, the flow-over potential divergence is negatively correlated with the amount of topographic snowfall to a certain extent, which can provide reference for topographic snowfall forecast in the future. Additionally, the cyclonic vorticity in the snowfall area is mainly caused by the flow around topography and flow-around wind produces favorable vortical circulation conditions for snowfall, while the vertical movement near the ground at the snowfall triggering stage is mainly caused by the flow-over component. Furthermore, the flow-over kinetic energy in the snow area is stronger and the work done by the pressure gradient force caused by flow over terrain drives kinetic energy changes.

KEYWORDS

flow around, flow over, potential divergence, potential vorticity, northern slope of the Tianshan mountains, Xinjiang blizzard

1 Introduction

The evaluation results of recently published IPCC AR6 indicate that significant global warming drives the water cycle to accelerate, and extreme precipitation events become stronger and more frequent (IPCC, 2021; Zhao and Abhishek, 2022; Zhao and Abhishek, 2023). Xinjiang is situated in Central Asia (CA), the world's largest arid zone. Far from the sea, it is rich in mountains, Gobi, and desert, with a unique landform of mountains and basins, and is sensitive to global climate change. Under the background of global warming and accelerated water cycle, precipitation in CA increases significantly (Bothe et al., 2012; Duan et al., 2015; Jiang et al., 2021), and studies show that precipitation in Xinjiang has increased in recent years, with extreme precipitation events occurring frequently (Ding et al., 2006). Meteorologists have carried out many in-depth studies on extreme precipitation events in Xinjiang at the climate scale, synoptic scale and mesoscale (Yang et al., 2015; Zeng and Yang, 2020; Guo et al., 2021; Ma S. et al., 2022). Topography plays an important role in extreme precipitation, thus heavy rains and snowstorms are found to occur in mountainous areas and along windward slopes (Shi et al., 2008; Ma et al., 2021). The trumpet-shaped terrain makes it easier for the Ili River valley to receive water vapor from the west, thus becoming the region with the largest snowfall in winter (Wang et al., 2020).

Precipitation is closely related to topography in that airflow will produce flow-over and flow-around components when it is blocked by terrain (Ye and Gao, 1979; Smith, 2004; Wells et al., 2005; Winters and Armi, 2012; 2014; Jagannathan et al., 2017; Jagannathan et al., 2019; Jagannathan et al., 2020). The relative size of these components mainly depends on the slope of the terrain (Manabe and Terpstra, 1974; Wu, 1984; Trenberth and Chen, 1988). Li et al. (2012) analyzed the climatic characteristics of the flow-over and flow-around components and revealed the dynamic effects of the large topography of the Qinghai-Tibet Plateau. Huang and Zhou (2004) pointed out that the strength of the flow-around component can measure the flow-around effect in the precipitation process. Jin and Li (2021) analyzed and compared the role of flow around and over currents in the process of topographic rainstorms.

Based on the above investigation, precipitation in the Ili River valley in Xinjiang can be considered to be closely related to topographic effects. Airflow enters the valley from its western side and is blocked by the Tianshan Mountains, resulting in flow around and over the terrain. However, the influence of both airflows on precipitation still lacks an in-depth understanding, and further research is necessary. Therefore, based on the topography of the northern slope of the Tianshan Mountain and the Ili River valley in Xinjiang, this paper selected the winter snowfall process triggered on 30 November 2018 to conduct diagnostic analysis on the role of flow around and flow over terrain at the time when the snowfall triggered from the aspects of atmospheric instability, water vapor, heating, and energy.

2 Data and methods

Based on the Global Forecast System of the National Center for Environmental Prediction in the United States (NCEP GFS) analysis and forecast data as the background field and lateral boundary conditions, the Global Data Assimilation System (GDAS) observation data were assimilated by the Gridpoint Statistical Interpolation analysis system (GSI) to form the initial field. The WRF4.0 model (Weather Research and Forecasting modeling system, Skamarock et al., 2019) was used to simulate the heavy snowfall process in the Ili River valley and the northern slope of the Tianshan Mountains on 30 November 2018 with a horizontal resolution of 3 km. For details on the physical parameterization scheme configuration of the numerical simulation, a comparison between simulated and observation precipitation, and synoptic-scale circulation, please refer to Ma et al. (2021).

By decomposing the near-surface wind field, dynamic and thermodynamic equations involving flow-around wind field and flow-over wind field in the terrain-following coordinate system are derived (Figure 1, refer to the appendix for details).

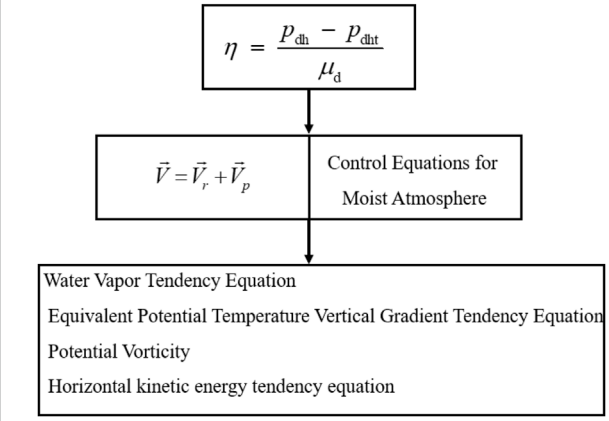

FIGURE 1
Flow chart of equations deduction.

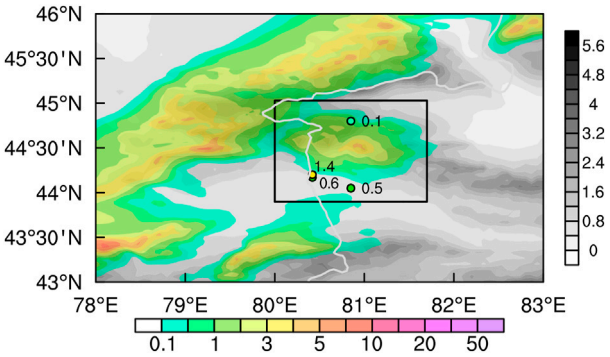

FIGURE 2
1-h accumulated snowfall from observations (color dot, units: mm), and 1-h accumulated snowfall from simulations (shading, units: mm) at 1600 UTC on Nov. 30, 2018, where the gray shading denotes the terrain height (units: km), the researched domains marked in black rectangular.

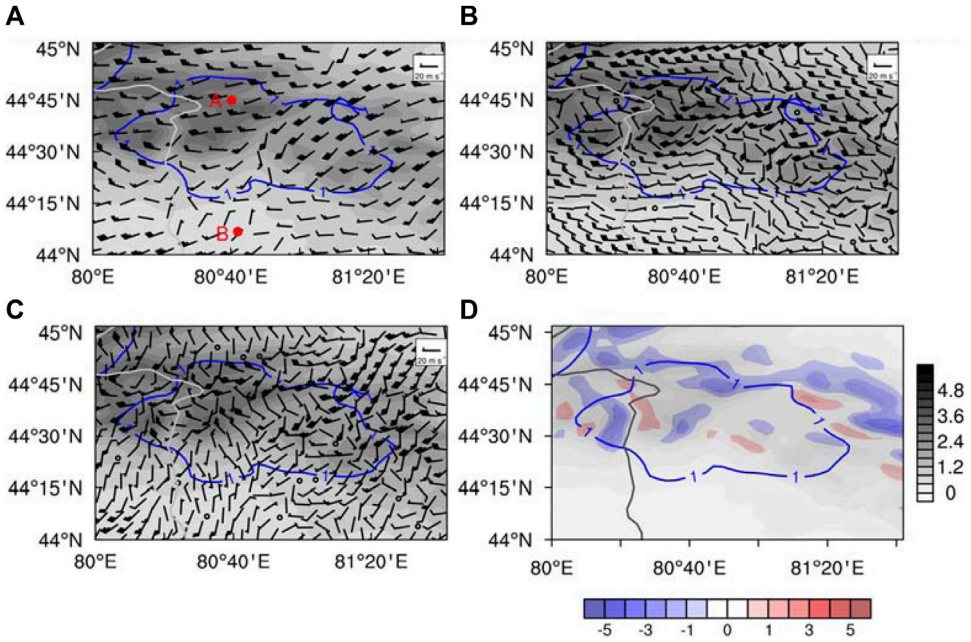

FIGURE 3
(A) Horizontal flow field (vector, units: m s^{-1}), points A, B indicate the locations of the Ili River valley and the northern slope of the Tianshan Mountains, **(B)** horizontal flow-around field (vector, units: m s^{-1}), **(C)** horizontal flow-over field (vector, units: m s^{-1}) on the first layer of the model layer overlaid by snow belt (blue contour, 1-h accumulated stimulated snowfall, units: mm), and **(D)** vertical velocity forced by terrain (color shading, units: m s^{-1}) overlaid by snow belt (blue contour, 1-h accumulated stimulated snowfall, units: mm) on the first layer of the model layer at 1600 UTC on Nov. 30, 2018, where the gray shading denotes the terrain height (units: km).

The horizontal wind field in the near-surface model layer is divided into flow-around and flow-over components in terrain-following coordinates for the WRF model to quantitatively analyze the dynamic effect of topography. This is defined as:

$$\vec{V} = \vec{V}_r + \vec{V}_p \tag{1}$$

The vertical velocity forced by near-surface topography can be written as:

$$w_s = u\frac{\partial H}{\partial x} + v\frac{\partial H}{\partial y} \tag{2}$$

Terrain blocking produces local vorticity, convergence, and divergence, which can be expressed as follows:

$$\zeta_r = \frac{\partial v_r}{\partial x} - \frac{\partial u_r}{\partial y} \tag{3}$$

$$\zeta_p = \frac{\partial v_p}{\partial x} - \frac{\partial u_p}{\partial y} \tag{4}$$

$$\lambda_r = \frac{\partial u_r}{\partial x} + \frac{\partial v_r}{\partial y} \tag{5}$$

$$\lambda_p = \frac{\partial u_p}{\partial x} + \frac{\partial v_p}{\partial y} \tag{6}$$

where the subscript r represents the flow-around component, the subscript p represents the flow-over component (the same below). ζ_r and ζ_p are the vorticity of the flow-around and flow-over components, respectively, and λ_r and λ_p are the divergence components.

The water vapor tendency equation can be written as:

$$\frac{\partial Q_v}{\partial t} = -\left[\frac{\partial(q_v U_p)}{\partial x} + \frac{\partial(q_v V_p)}{\partial y}\right] - \left[\frac{\partial(q_v U_r)}{\partial x} + \frac{\partial(q_v V_r)}{\partial y}\right] - \frac{\partial(\Omega q_v)}{\partial \eta} + Fq \tag{7}$$

where q_v is the water vapor specific humidity, $Q_v = \mu q_v$, $U_p = \mu u_p$, $V_p = \mu v_p$, $\Omega = \mu\dot{\eta}$, μ is the dry air mass in the column, and $\dot{\eta}$ is the vertical velocity of the terrain-following coordinate system.

The stratified-stability tendency equation can be further written as:

$$\frac{\partial \beta}{\partial t} + u\frac{\partial \beta}{\partial x} + v\frac{\partial \beta}{\partial y} + \omega\frac{\partial \beta}{\partial \eta} = M - \frac{g\frac{\partial Fth}{\partial \eta}}{{\mu_d}^2 \alpha_d} \tag{8}$$

$$M_r = \frac{g}{\frac{\partial \phi}{\partial \eta}}\left[-\frac{\partial u_r}{\partial \eta}\frac{\partial \theta_e}{\partial x} - \frac{\partial v_r}{\partial \eta}\frac{\partial \theta_e}{\partial y} + \left(\frac{\partial u_r}{\partial x} + \frac{\partial v_r}{\partial y}\right)\frac{\partial \theta_e}{\partial \eta}\right] \tag{9}$$

$$M_p = \frac{g}{\frac{\partial \phi}{\partial \eta}}\left[-\frac{\partial u_p}{\partial \eta}\frac{\partial \theta_e}{\partial x} - \frac{\partial v_p}{\partial \eta}\frac{\partial \theta_e}{\partial y} + \left(\frac{\partial u_p}{\partial x} + \frac{\partial v_p}{\partial y}\right)\frac{\partial \theta_e}{\partial \eta}\right] \tag{10}$$

where $\beta = \frac{(\frac{\partial \theta_e}{\partial \eta})g}{\frac{\partial \phi}{\partial \eta}}$ is the stratified stability, θ_e is the equivalent potential temperature, and $M = M_r + M_p$ is the potential divergence. The concept of potential divergence proposed by Ran et al. (2013) to reflect the dynamic properties of the horizontal wind field divergence in the process of heavy rain.

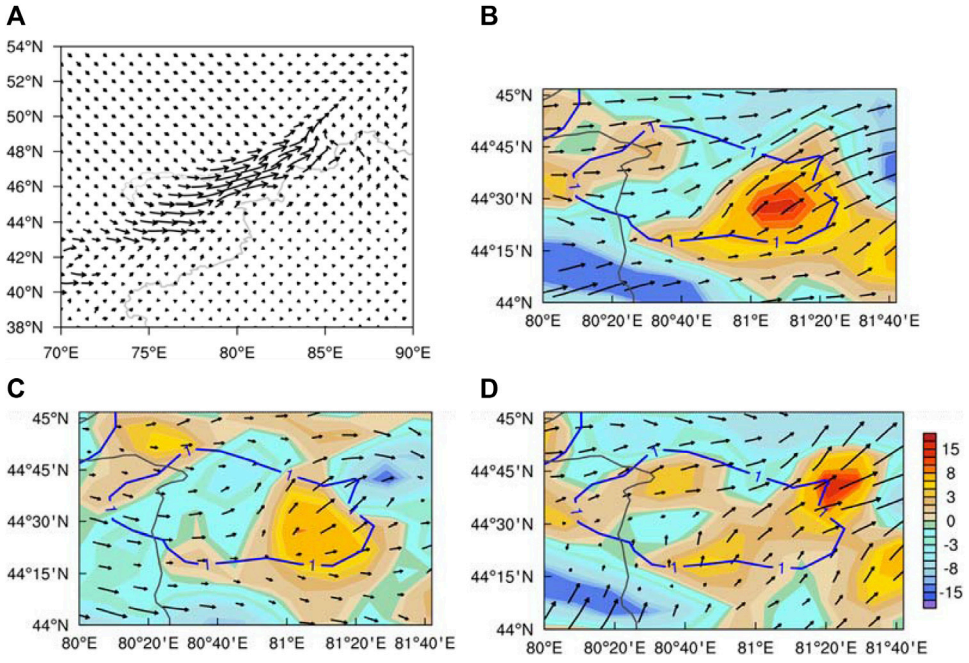

FIGURE 4
(A) 850-hPa water vapor fluxes (vector, units: kg/(cm hPa s)) at 1200 UTC, **(B)** water vapor fluxes (vector, units: pa m s^{-1}) overlaid by water vapor flux divergence (shaded, units: 10^{-2} pa s^{-1}), **(C)** flow-around water vapor fluxes (vector, units: pa m s^{-1}) overlaid by flow-around water vapor flux divergence (shaded, units: 10^{-2}pa s^{-1}) and **(D)** flow-over water vapor fluxes (vector, units: pa m s^{-1}) overlaid by flow-over water vapor flux divergence (shaded, units: 10^{-2} pa s^{-1}) on the first layer of the model layer at 1600 UTC on Nov. 30, 2018, where the blue contour is 1-h accumulated stimulated snowfall (units: mm).

The potential vorticity is derived and decomposed into three terms: flow-around potential vorticity, flow-over potential vorticity, and vertical potential vorticity, that is,

$$q = q_r + q_p + q_w \tag{11}$$

where $q_r = \frac{g}{\mu_d}\left[\frac{\partial v_r}{\partial \eta}\frac{\partial \theta^*}{\partial x} - \frac{\partial u_r}{\partial \eta}\frac{\partial \theta^*}{\partial y} + \left(\frac{\partial u_r}{\partial y} - \frac{\partial v_r}{\partial x}\right)\frac{\partial \theta^*}{\partial \eta}\right]$ is the flow-around potential vorticity component, $q_p = \frac{g}{\mu_d}\left[\frac{\partial v_p}{\partial \eta}\frac{\partial \theta^*}{\partial x} - \frac{\partial u_p}{\partial \eta}\frac{\partial \theta^*}{\partial y} + \left(\frac{\partial u_p}{\partial y} - \frac{\partial v_p}{\partial x}\right)\frac{\partial \theta^*}{\partial \eta}\right]$ is the flow-over potential vorticity component, $q_w = \left(\alpha_d\frac{\partial w}{\partial y} + \frac{\frac{\partial w}{\partial \eta}\frac{\partial \phi}{\partial y}}{\mu_d}\right)\frac{\partial \theta^*}{\partial x} - \left(\alpha_d\frac{\partial w}{\partial x} + \frac{\frac{\partial w}{\partial \eta}\frac{\partial \phi}{\partial x}}{\mu_d}\right)\frac{\partial \theta^*}{\partial y} + \left(\frac{\frac{\partial w}{\partial y}\frac{\partial \phi}{\partial x} - \frac{\partial w}{\partial x}\frac{\partial \phi}{\partial y}}{\mu_d} - \frac{gf_0}{\mu_d}\right)\frac{\partial \theta^*}{\partial \eta}$ is the vertical-velocity potential vorticity component, and $\theta^* = \theta\exp\left(\frac{Lq_s\cdot(q/q_s)^k}{c_{pm}T}\right)$ is the generalized potential temperature proposed for non-uniformly saturated atmosphere (Gao et al., 2004).

The horizontal kinetic energy tendency equation in the mass terrain-following coordinate system can be written as:

$$\frac{\partial K}{\partial t} = \left[\left(-\frac{\partial K}{\partial x} - \alpha\frac{\partial p}{\partial x} - \frac{\alpha\frac{\partial p}{\partial \eta}\frac{\partial \phi}{\partial x}}{\mu_d\alpha_d} + \frac{Fu}{\mu_d}\right)u_p + \left(-\frac{\partial K}{\partial y} - \alpha\frac{\partial p}{\partial y} - \frac{\alpha\frac{\partial p}{\partial \eta}\frac{\partial \phi}{\partial y}}{\mu_d\alpha_d} + \frac{Fv}{\mu_d}\right)v_p\right] + \left[\left(-\frac{\partial K}{\partial x} - \alpha\frac{\partial p}{\partial x} - \frac{\alpha\frac{\partial p}{\partial \eta}\frac{\partial \phi}{\partial x}}{\mu_d\alpha_d} + \frac{Fu}{\mu_d}\right)u_r + \left(-\frac{\partial K}{\partial y} - \alpha\frac{\partial p}{\partial y} - \frac{\alpha\frac{\partial p}{\partial \eta}\frac{\partial \phi}{\partial y}}{\mu_d\alpha_d} + \frac{Fv}{\mu_d}\right)v_r\right] - \omega\frac{\partial K}{\partial \eta} \tag{12}$$

3 Analysis of characteristics of water vapor transport

The earliest snowfall mainly occurred on the northern slope of the Tianshan Mountains (Figure 2), and there was strong hourly snowfall on the eastern side of the Ili River valley. The simulated snowfall mainly occurred on the northern slope of Tianshan Mountain, which is in the northwestern Ili River valley, and the hourly snowfall was slightly stronger than that of the observations; however, the location of the simulated snowfall center was consistent with that of the observations, and their ranges were similar; therefore, the simulation could well reproduce the development and evolution of the snowfall process and it belongs to cold front snowfall (Ma et al., 2021; Ma et al., 2022 S. P.). The simulation output data are used to calculate the flow-over and flow-around components and analyze their dynamic effects in the snowstorm process.

Figure 3 shows the horizontal flow field near the surface layer and the vertical velocity forced by topography. There is westerly airflow near the surface of the Ili River valley; as it climbs over the northern slope of Tianshan, the wind direction turns northerly on the east side and westerly on the west side of the snow belt. Figure 3C shows that there is northwest climbing wind in the snowfall area after the horizontal wind field near the ground is decomposed into flow-around and flow-over components, and the wind speed weakens after the airflow passes the mountain. Additionally, there is also strong westward flow around the area of snowfall (Figure 3B), and its strength is slightly greater than that of the flow-

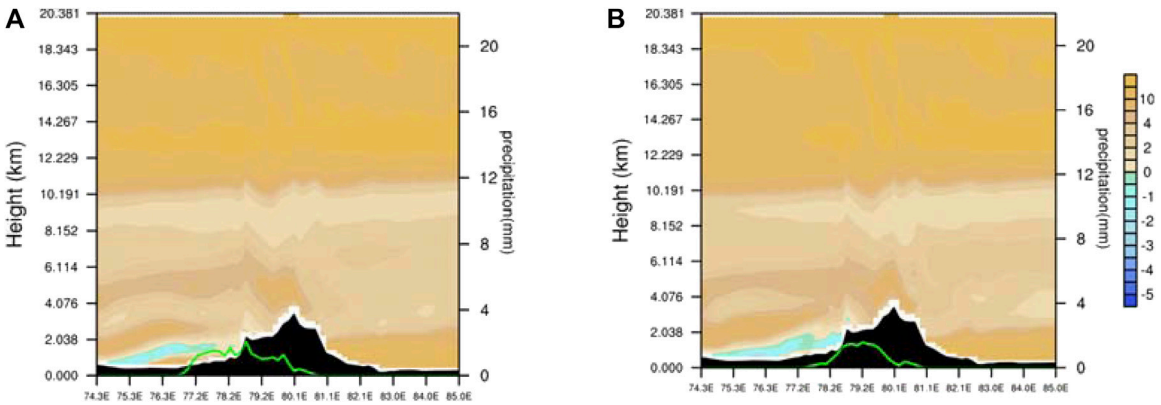

FIGURE 5
Vertical profile of stratified stability (shaded, units: 10^{-3} k m^{-1}) along 44.5°N at 1400 UTC **(A)** and 1600 UTC **(B)** 30 November 2018. Green solid line denotes 30-min accumulated snowfall (right ordinate; units: mm).

over component. The distribution of vertical velocity near the ground calculated by Eq. 2 (Figure 3D) is exactly the same as that of the original vertical velocity of the model (figure omitted). This shows that the vertical movement near the ground is generated by terrain-forced climbing flows, thus, the higher the horizontal wind speed is, the stronger the vertical speed.

Topography can cause low-level airflow convergence and water vapor concentration, resulting in stratification instability and promoting convection development. This paper further analyzes the contribution of water vapor transport by flow over and around terrain to precipitation. There was westerly water vapor transport before snowfall, transporting the water vapor from Lake Balkhash to the Ili River valley. The water vapor tendency equation under terrain-following coordinates is Eq. 7, the left side is the local variation term of water vapor, the first term at the right side is water vapor flux divergence caused by flow over terrain, the second term is water vapor flux divergence caused by flow around terrain, the third term is water vapor vertical flux divergence, and the fourth term is water vapor comprehensive forcing term including water vapor phase transformation.

The model-layer data was used to calculate the first and second terms on the right side of Eq. 7. The results show (Figure 4) there was a strong water vapor flux and a water vapor convergence zone, and a weaker water vapor divergence zone in the snowfall area when snowfall was triggered at 1600 UTC. The convergence of water vapor on the west side of the snowfall area is caused by the greater water vapor transportation of flow-around component, and flow over terrain also causes weaker water vapor convergence in the snowfall area. However, the large-scale water vapor convergence in the snowfall area is mainly caused by flow-around component of water vapor flux.

4 Analysis of the instability development mechanism

The reasons for the water vapor convergence in topographic precipitation is analyzed above, to better understand the instability development mechanism for terrain-induced precipitation, we now turn to a discussion. Zhou et al. (2018) pointed out that potential divergence is the main forcing term that forces the development and changes in atmospheric potential stability, which can in turn comprehensively characterize vertical wind shear, atmospheric moist baroclinicity, horizontal convergence and divergence, and atmospheric potential stability. The potential vorticity, potential divergence and stratified-stability tendency equation under terrain-following coordinate is further analyzed in this subsection. In the WRF model mass terrain-following coordinate system, the stratified-stability tendency equation is Eq. 8, the left side of the above equation is the individual change of stratified stability, the first term at the right side is the potential divergence term, the second term is the vertical gradient term including the comprehensive forcing of diabatic heating and friction dissipation. Potential divergence can be divided into two parts: flow-around potential divergence (M_r) and flow-over potential divergence (M_p). Potential vorticity can represent symmetric instability and is widely used in precipitation research (Siedersleben and Gohm, 2016; Vaughan et al., 2017). Siedersleben and Gohm (2016) shows that a Blizzard in the southern side of Alps is related to inertial instability and conditional instability caused by parallel orographic potential vorticity (PV) banners and convective cloud bands.

As shown in Figure 5, there was stratified instability in the upper reaches of the snowfall area at 1400UTC, and it was located in the middle and lower layers (η=0.9969 to η=0.8631). As the snow zone moved eastward, the unstably stratified area moved eastward and gradually increased in intensity. The time evolution of stratification instability shows (Figure 6) that stratified stability is positive and atmospheric stratification is stable before snowfall. With the development of snowfall system, stratified stability gradually decreases, and the atmosphere changes from stratified stability to instability. Therefore, in this subsection, the vertical gradient tendency equation of equivalent potential temperature (Eq. 8) is calculated to analyze the variation trend and reasons of stratified stability.

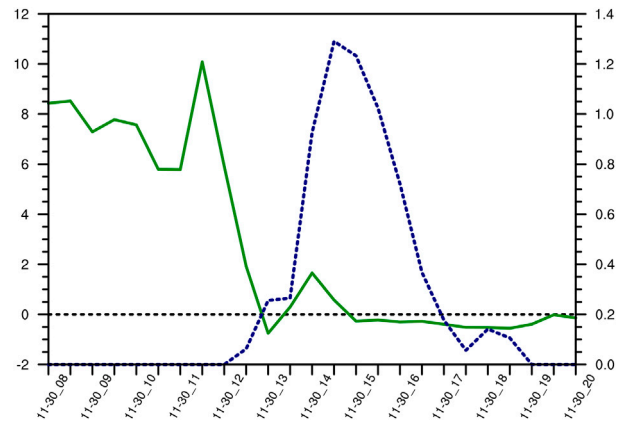

FIGURE 6
Time series of stratified stability (solid line, the left ordinate; units: 10^{-3} k m^{-1}) and snowfall (dashed line, the right ordinate; units: mm) at 6 km at 77.7°E, 44°N.

Figure 7 shows the vertical profile of individual variations of stratified stability, there are negative centers in the lower and middle layers of the snowfall area, and the intensity reaches -3×10^{-6} k m^{-1} s^{-1} and -5×10^{-6} k m^{-1} s^{-1}, respectively. In addition, the negative centers in the middle and lower layers are located in the easterly region of the snow zone (around 80.2°E), and the snow zone also moves to the southeast in the next stage, thus the snowfall occurs in the area where stratified instability is significant. As the snowfall develops, the stratified stability in the snowfall area shows a decreasing trend, the stability decreases, and the instability increases. The vertical distribution of the potential divergence is similar to that of stratified stability individual variations. A negative center in the lower layer with an intensity reaches -5×10^{-6} K m^{-1} s^{-1}, it develops upward in a fluctuating pattern, triggering instability (Figure 7B). Consequently, during the snowfall triggering stage, the variation of stratified stability mainly depends on the potential divergence. Additionally, the vertical gradient of potential-temperature comprehensive force is related to frictional dissipation. However, compared with the potential divergence, the vertical gradient of potential-temperature comprehensive force hardly causes the variation of stratified stability (Figure 7C), therefore, it can be neglected.

The above diagnostic analysis found that potential divergence is the key factor of atmospheric stratified stability to instability. Potential divergence is decomposed into flow-around and flow-over components, and the topographic effect on the variation of stratified stability is analyzed. Figures 8B,C show the horizontal

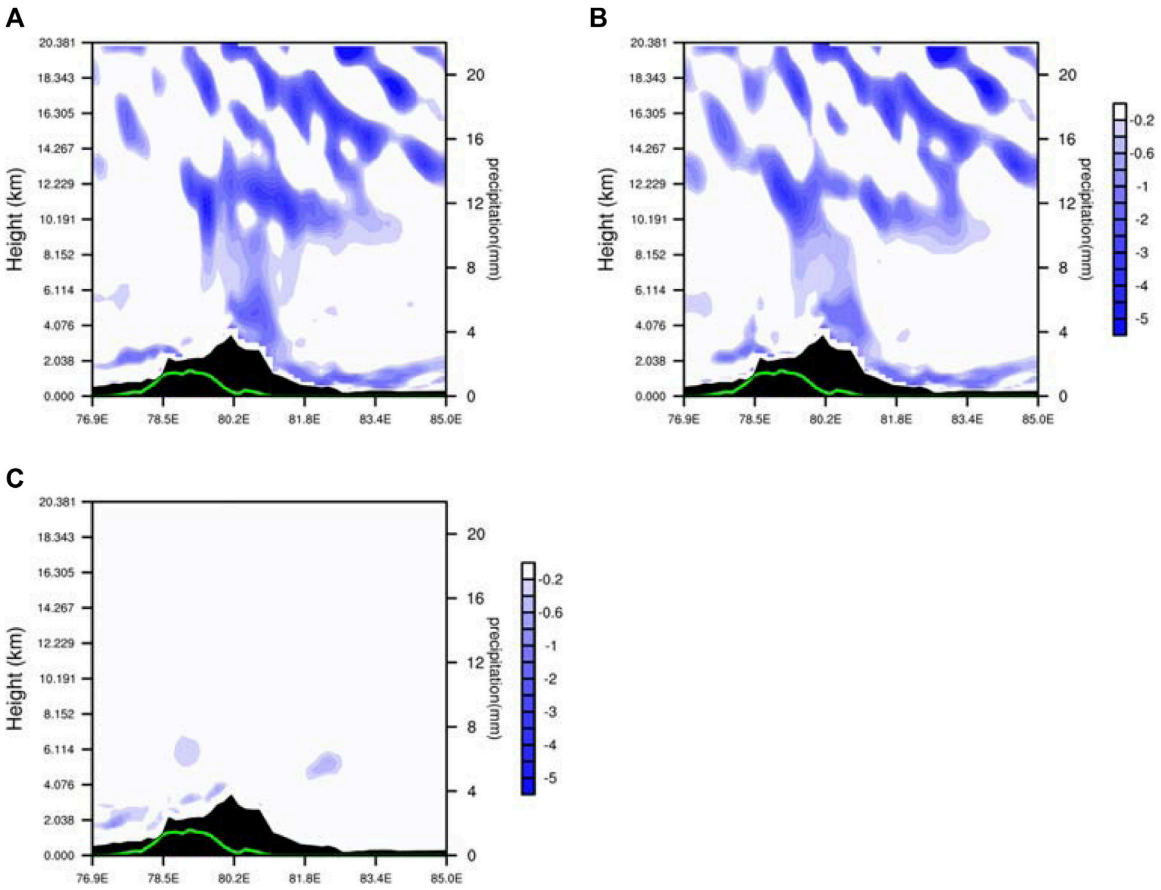

FIGURE 7
Vertical profile of the variations of stratified stability [**(A)**, shaded, units: 10^{-6} k m^{-1} s^{-1}), potential divergence **(B)**, shaded, units: 10^{-6} k m^{-1} s^{-1}) and the vertical gradient of potential-temperature comprehensive force **(C)**, shaded, units: 10^{-6} k m^{-1} s^{-1}] along 44.5°N at 1300 UTC 30 November 2018. Green solid line denotes 30-min accumulated snowfall (the right ordinate; units: mm).

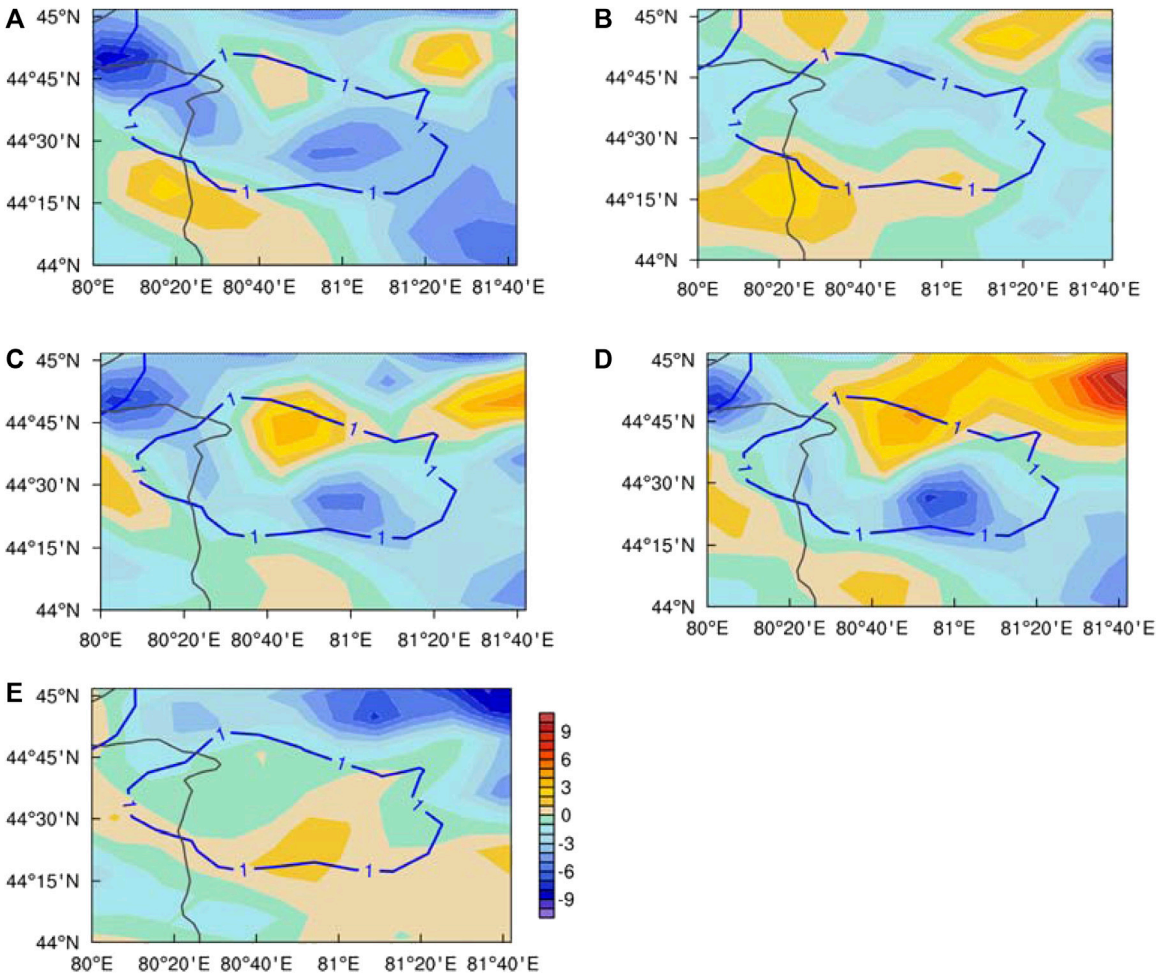

FIGURE 8
(A) Potential divergence (shaded), **(B)** flow-around potential divergence (shaded), **(C)** flow-over potential divergence (shaded), **(D)** vertical shear component of flow-over potential divergence (shaded) and **(E)** divergence component of flow-over potential divergence (shaded, units: 10^{-6} k m^{-1} s^{-1}) on the first layer of the model layer at 1600 UTC on Nov. 30, 2018, where the blue contour is 1-h accumulated stimulated snowfall (units: mm).

distribution of flow-around and flow-over components on the first layer of the model layer during the snowfall triggering stage, both the flow over and flow around terrain will lead to potential divergence variation, of which the flow-over effect is more significant. Flow-over potential divergence is the main component of potential divergence, which is mainly manifested as a large range of negative values in the snowfall area, and the central strength reaches -6×10^{-6} K m^{-1} s^{-1}. The negative center of the flow-over potential divergence is located in the southeast side of the snow belt, which is consistent with the previous analysis.

Flow-over potential divergence can be divided into vertical wind shear and horizontal divergence. The vertical wind shear component has a negative center in the southeast side of the snowfall area, and the center intensity reaches -8×10^{-6} K m^{-1} s^{-1} (Figure 8D), while the value of the horizontal divergence component is small, which contributes little to the variation of flow-over potential divergence (Figure 8E). In conclusion, the negative anomaly of flow-over potential divergence is mainly caused by vertical wind shear. Vertical wind shear is formed by the coupling effect of vertical gradient of horizontal wind and horizontal gradient of equivalent potential temperature, that is, the horizontal advection effect of flow-over vertical shear to equivalent potential temperature. The horizontal advection transport of equivalent potential temperature caused by the flow-over vertical shear induces the instability of snowfall area, which is a process of combining dynamic and thermodynamic. The essence of this process is that when airflow passes through the terrain, the horizontal wind field formed by the flow-over dynamic effects is unevenly distributed in the vertical direction, leading to heat transport and the fomation of thermal advection.

In the snowfall triggering stage, the vertical shear of zonal flow-over component increases with height at the lower level ($-\frac{\partial u_p}{\partial \eta} > 0$) and the zonal gradient of equivalent potential temperature is positive ($\frac{\partial \theta_e}{\partial x} > 0$), the coupling effect of these two factors promotes an increase in atmospheric instability (figure omitted). Similarly, the meridional gradient of equivalent potential temperature reaches a maximum value in the snowfall area ($\frac{\partial \theta_e}{\partial y} > 0$) and the atmospheric instability is increased under the action of vertical shear of meridional flow-over wind ($-\frac{\partial v_p}{\partial \eta} > 0$). Comparatively speaking,

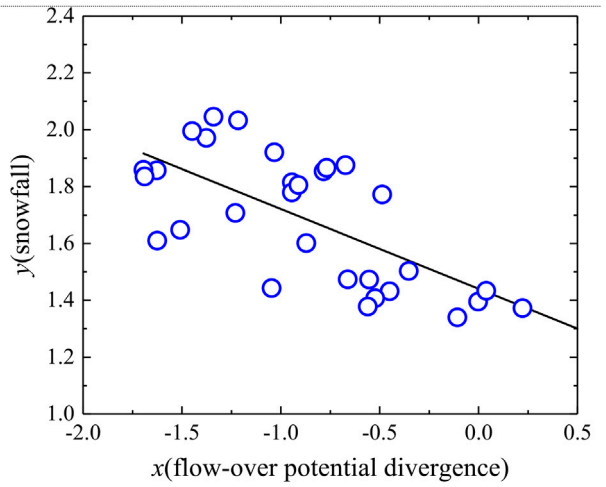

FIGURE 9
The fit between the values of flow-over potential divergence (units: 10^{-6} k m^{-1}) and snowfall (units: mm) by linear regression (y = ax+b, where y is snowfall and x is flow-over potential divergence).

the meridional advection transport of flow-over vertical shear to equivalent potential temperature is more significant. The larger horizontal gradient of equivalent potential temperature is closely related to the topographic trend. On the model surface, the equivalent potential temperature is lower over low-lying terrains and higher over high terrains, therefore, a greater horizontal gradient of equivalent potential temperature is formed at the steep terrain. The Tianshan terrain, which exhibits a quasi-east-west orientation, contributes to a larger meridional gradient of the equivalent potential temperature.

Since there is a flow-over potential divergence anomaly when snowfall is triggered, the regional average flow-over potential divergence and snowfall in the snowfall area during the snowy period are further fitted to test the relationship between them. The fit between the values of flow-over potential divergence and snowfall is performed by linear regression (y = ax+b, where y represents snowfall and x represents the flow-over potential divergence). Figure 9 shows the derived relationship with a = −0.28 and b = 1.44 when hourly snowfall amount is more than 1 mm, that is:

$$y = -0.28x + 1.44$$

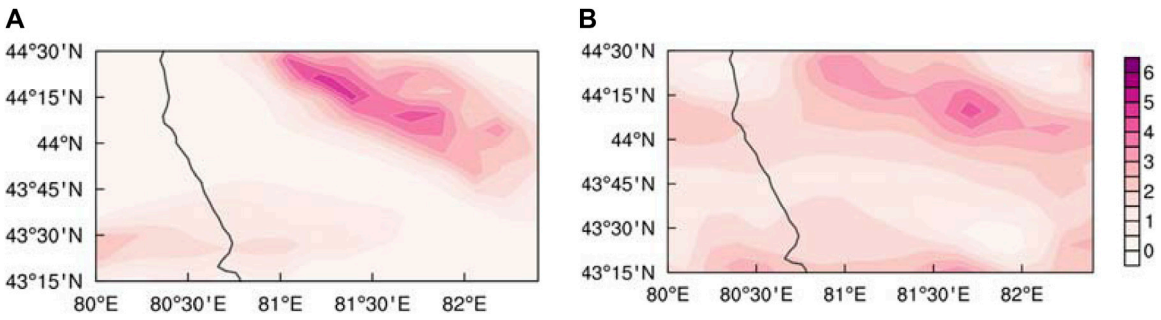

FIGURE 10
(A) 1-h accumulated stimulated snowfall (units: mm) and **(B)** 1-h accumulated snowfall retrieval of the fitted relation on the first layer of the model layer at 1600 UTC on 30 Nov 2018.

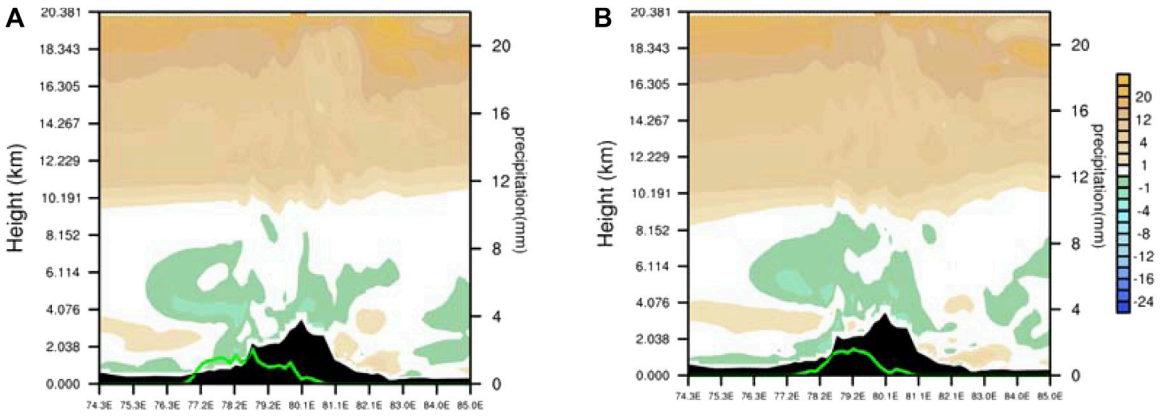

FIGURE 11
Vertical profile of potential vorticity (shaded, units: 10^{-6} m k s^{-3} pa^{-1}) along 44.5°N at 1400 UTC **(A)** and 1600 UTC **(B)** 30 November 2018. Green solid line denotes 30-min accumulated snowfall (the right ordinate units mm).

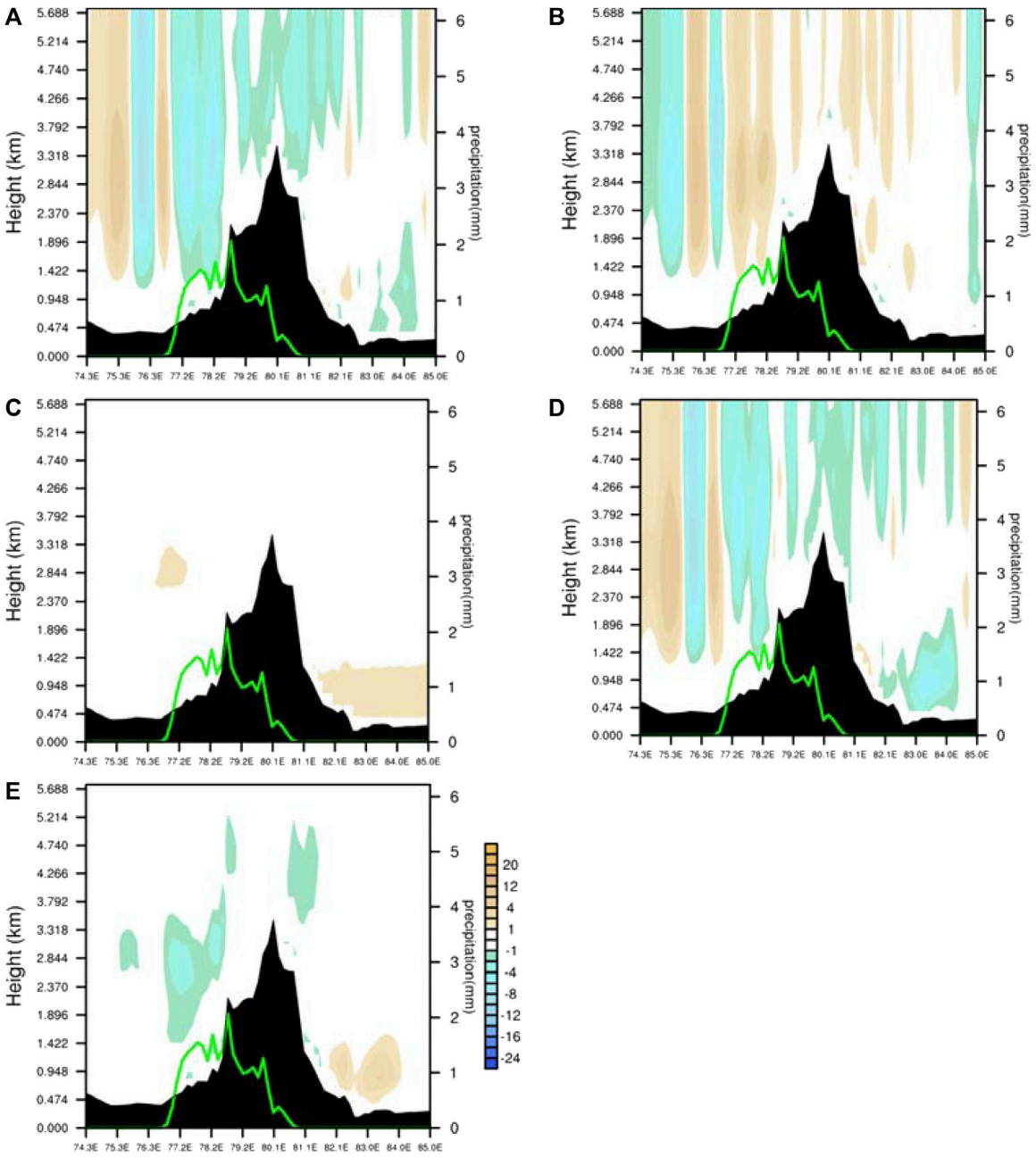

FIGURE 12
Vertical profile of flow-around potential vorticity [**(A)**, shaded, units: 10^{-6} m k s^{-3} pa^{-1}], flow-over potential vorticity [**(B)**, shaded, units: 10^{-6} m k s^{-3} pa^{-1}], vertical potential vorticity [**(C)**, shaded, units: 10^{-6} m k s^{-3} pa^{-1}], the divergence component [**(D)**, shaded, units: 10^{-6} m k s^{-3} pa^{-1}] and the vertical shear component of flow-around potential vorticity [**(E)**, shaded, units: 10^{-6} m k s^{-3} pa^{-1}] along 44.5ON at 1400 UTC 30 November 2018. Green solid line denotes 30-min accumulated snowfall (the right ordinate; units: mm).

At this time, the correlation coefficient between these two variables reaches up to 0.71. And the root mean square error between the snowfall retrieval of the fitted relation and the simulated snowfall is small (about 0.187). Since flow-over potential divergence may provide a negative correlation with the topographic snowfall to some extent, it is helpful for topographic snowfall forecasting in the future. As shown in Figure 9, in order to verify the validity of the fitted relation, the horizontal distribution of the hourly snowfall retrieved by the fitted relation and the simulated hourly snowfall are compared. It is found that hourly snowfall retrieval of the fitted relation has a similar distribution with hourly simulated snowfall, and the snowfall center is retrieved. Therefore, flow-over potential divergence holds predictive significance for snowfall. Nevertheless, further work is required to validate this relationship. However, in the present study, we have taken an important first step, that is, to derive flow-over potential divergence in the WRF model mass terrain-following coordinate system and attempt to test flow-over potential divergence's correlation with topographic snowfall via snowfall case studies. Thus, we have laid the foundations

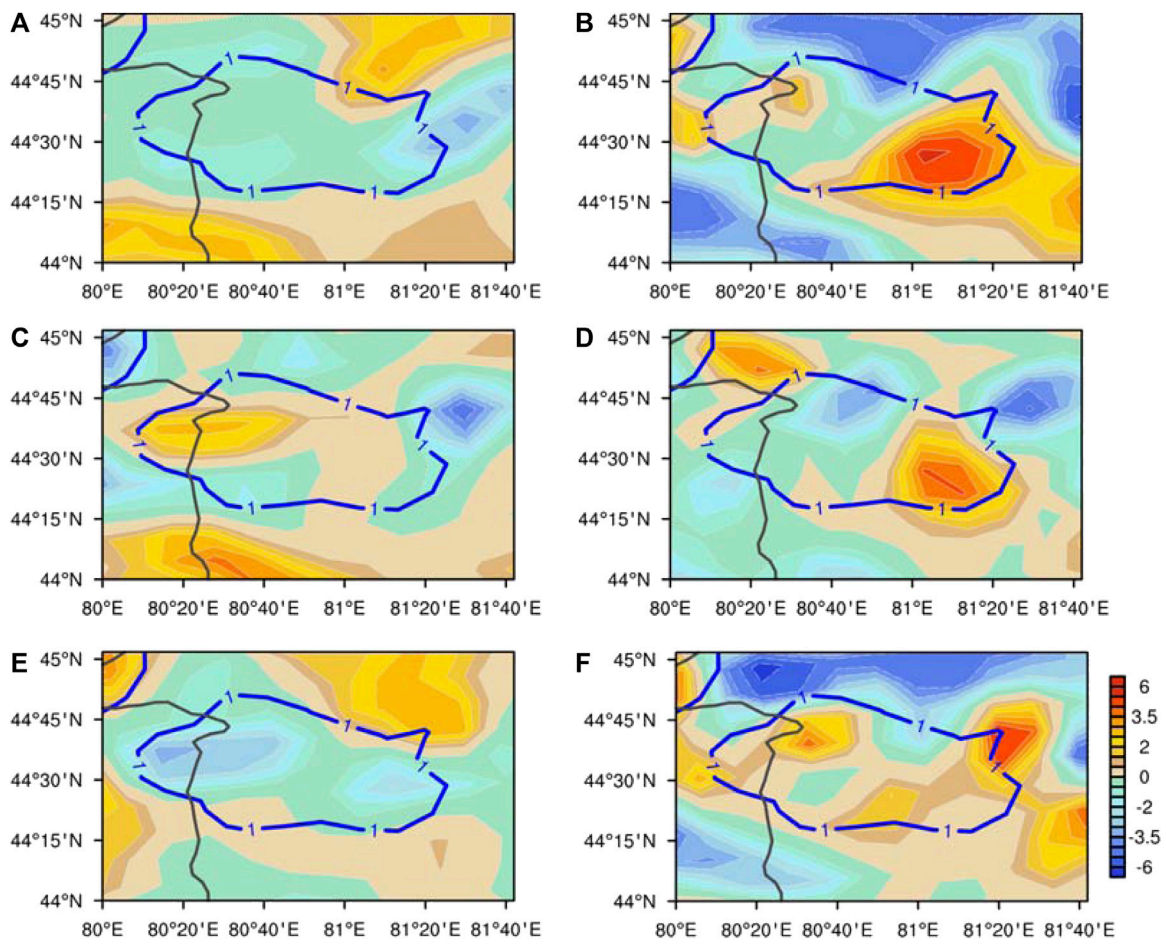

FIGURE 13
(A) Total vorticity (shaded, units: 10^{-4} s $^{-1}$), **(B)** total divergence (shaded units: 10^{-4} s $^{-1}$) **(C)** vorticity of the flow-around component (shaded, units: 10^{-4} s $^{-1}$), **(D)** divergence of the flow-around component (shaded, units: 10^{-4} s $^{-1}$) **(E)** vorticity of the flow-over component (shaded, units: 10^{-4} s $^{-1}$) and **(F)** divergence of the flow-over component (shaded, units: 10^{-4} s $^{-1}$) overlaid by snow belt (blue contour, 1-h accumulated stimulated snowfall, units: mm), on the first layer of the model layer at 1600 UTC on 30 Nov 2018.

for further topographic snowfall studies in Central Asia in the future. It is worth noting that the precision of the forecast outcomes is highly dependent on the accuracy of the wind field that is directly predicted by the numerical model. In case the numerical model predicts the wind field inaccurately, particularly in regions with intricate terrain, the flow-over divergence diagnosis-based precipitation forecast results would also likely be considerably erroneous.

Symmetric instability refers to the phenomenon that an air parcel is convectively stable and inertially stable when moving vertically or horizontally but becomes unstable when it experiences tilted ascent. It can be diagnosed by potential vorticity, and a negative value of potential vorticity indicates the existence of conditionally symmetric instability in the atmosphere (Hoskin, 1974), thus when potential vorticity is negative, the atmosphere is symmetrically unstable. As shown in Figure 11, in the lower layer of the snowfall area (η=0.9969 to η=0.9558), symmetric instability occurs in the stably stratified area, with a central intensity of -6×10^{-6} m K s^{-3} Pa^{-1}. Furthermore, the effect of topography on the symmetric instability is analyzed, and the potential vorticity in the lower layer are decomposed into flow-around potential vorticity, flow-over potential vorticity and vertical potential vorticity. The flow-around component is the main component of the potential vorticity (Figure 12A), and the vertical distribution at the lower level is similar to that of the total potential vorticity. Therefore, symmetric instability mainly depends on flow-around wind field. Flow over also causes weak symmetric instability near the surface (Figure 12B), while vertical potential vorticity term is negligible (Figure 12C). The flow-around potential vorticity is composed of horizontal divergence and vertical wind shear, vertical wind shear in the lower levels causes symmetric instability (Figure 12E), that is, by the coupling effect of the vertical gradient of the horizontal wind and the horizontal gradient of the generalized potential temperature. Moreover, both in the lower and upper levels, strong vertical advection transport of the generalized potential temperature contributes to symmetric instability in the snowfall area.

5 Dynamic analysis

In addition to the thermal effects on the precipitation process, terrain also exerts dynamic influences which will be discussed in detail here.

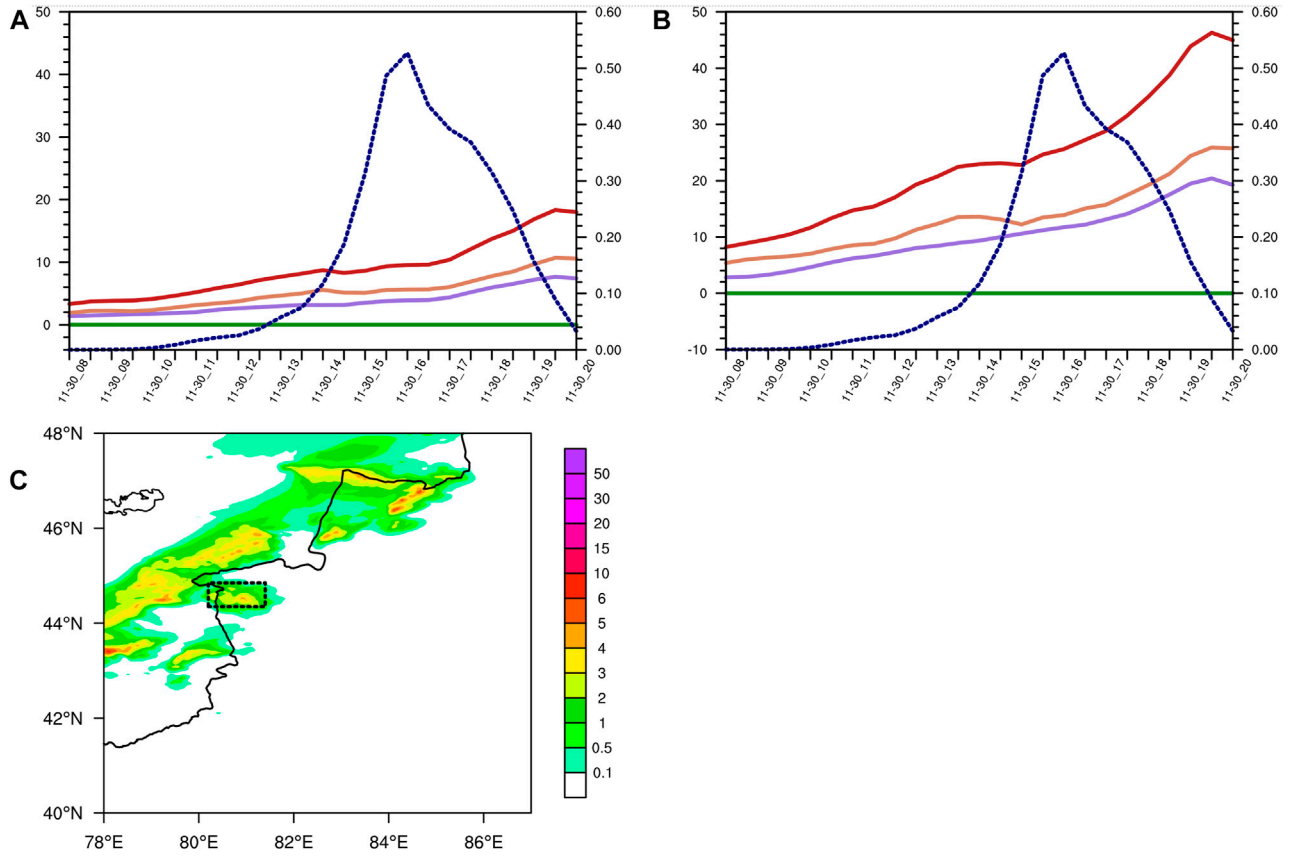

FIGURE 14
Time series of domain averaged kinetic energy (red solid line) kinetic energy of the flow-around component (purple solid line), flow-over component (brown solid line), coupling kinetic energy of the flow around and flow over terrain (green solid line, the left ordinate; units: 10^1 m^2 s^{-2}) and snowfall (dashed line, the right ordinate; units: mm) on the first layer **(A)** and the fifth layer **(B)** of the model layer. The target domain is marked by black rectangular in Figure 13C **(C)** The simulation of 1 hour accumulated precipitation at 1600UTC on 30 November Units are mm, black rectangular is the target domains for the following analysis.

Vorticity and divergence are calculated using model-layer data. As shown in Figure 13, there is weak anticyclonic vorticity in the lower layer of snowfall region, in addition, the east side of the snowfall area has a strong divergence, and the west side has a weaker convergence at 1600 UTC (Figures 13A, B). The distribution of the total vorticity is basically the same as the vorticity from flow over terrain, indicating that the anticyclonic vorticity in the snowfall area is mainly caused by the flow-over component (Figure 13E). On the other hand, the distribution of the total divergence is closer to the flow-around component, which means that the weak convergence on the west side and the strong divergence on the east side of the snow belt are mainly caused by the flow-around component (Figure 13D).

Overall, cyclonic vorticity and divergence in the snowfall area are mainly caused by flow-around wind, while anticyclonic and convergence are caused by flow-over wind.

The development of precipitation is accompanied by changes in energy. Khouider et al. (2012) demonstrated that convective motion restricts the production and conversion of atmospheric kinetic energy, which is characterized by kinetic energy transfer from a small-scale system to a large-scale system. Based on the kinetic energy tendency equation of the terrain-following coordinate system, the contribution of near-surface flow around and over terrain to the horizontal kinetic energy of the snowfall process was analyzed.

Time series of domain averaged kinetic energy and its components in Figure 14 shows that before the snow, kinetic energy increased over time. Once snowfall is triggered, kinetic energy reaches the strongest in the first layer of the model, with a maximum kinetic energy of 180 m^2 s^{-2}. Furthermore, the averaged flow-over kinetic energy in the first and fifth layers is greater than the averaged flow-around kinetic energy, indicating that the intensity of flow-over energy is stronger than flow-around energy on the lower layer of the snow area. Additionally, the magnitude of the coupling kinetic energy of the flow around and flow over terrain is small and can be ignored.

The left-side and right-side terms of the horizontal kinetic energy tendency Eq. 12 are calculated with the model layer data to analyze the reasons for the local variation of horizontal kinetic energy. Figure 15 shows the zonal profiles of the local variation term of kinetic energy and terms forcing the variation of kinetic energy in the snowfall triggering stage. As shown in Figure 15A, there is a positive high value region of local kinetic energy variation in the snow zone, which extends upward from the lower layer of the snow zone, and the maximum value center is located in the middle layer above the snow zone (η=0.8631 to η=0.1858). The intensity reaches 20 × 10^{-2} m^2 s^{-3}, and the fluctuation is upward-

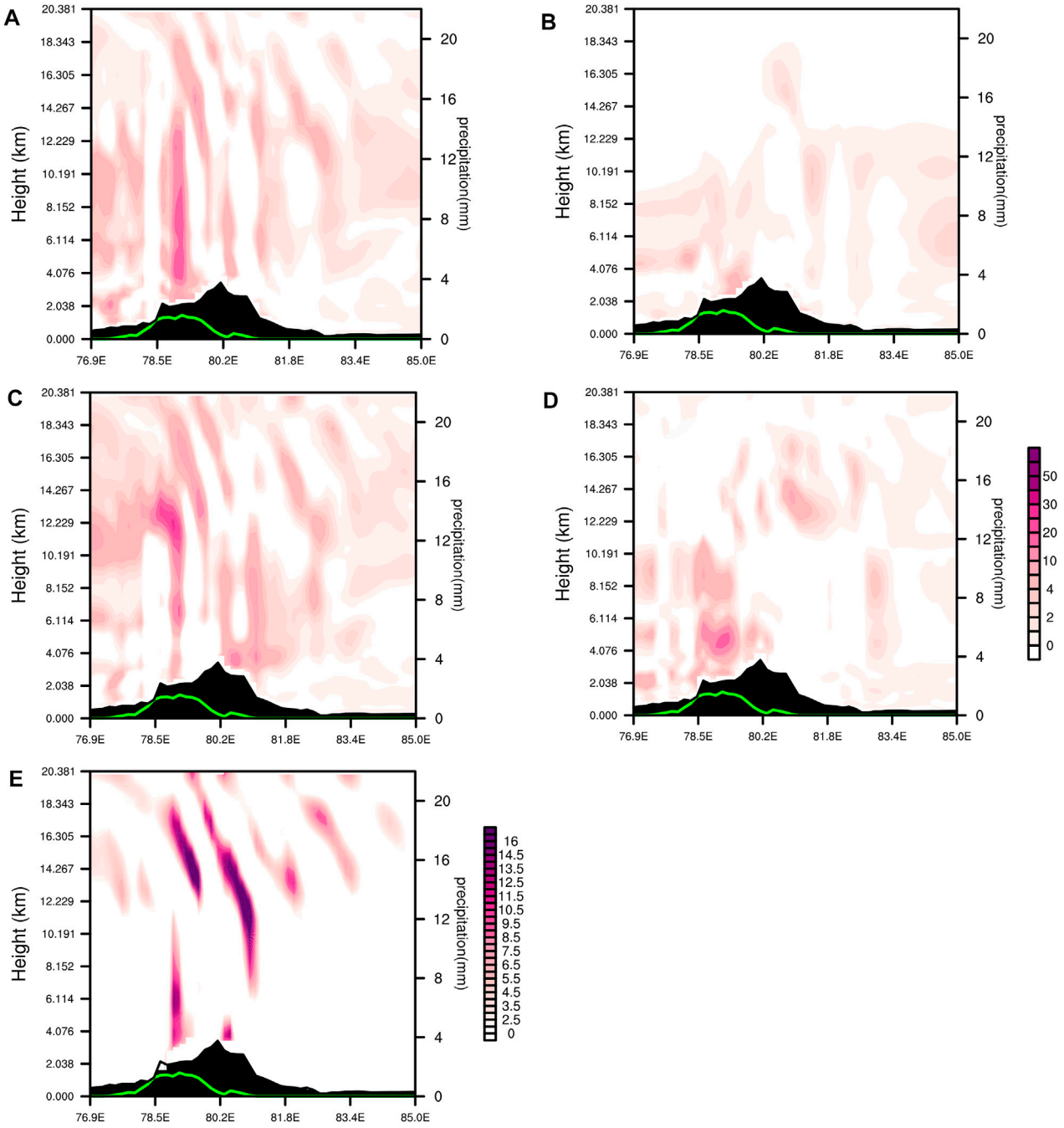

FIGURE 15
Vertical profile of local change of kinetic energy [**(A)**, shaded, units: 10^{-2} m^2 s^{-3}], meridional velocity forcing [**(B)**, shaded, units: 10^{-2} m^2 s^{-3}], zonal velocity forcing [**(C)**, shaded, units: 10^{-2} m^2 s^{-3}], vertical advection forcing [**(D)**, shaded, units: 10^{-2} m^2 s^{-3}] and zonal pressure work [**(E)**, shaded, units: m^2 s^{-3}] along 44.5°N at 1300 UTC 30 November 2018. Green solid line denotes 30-min accumulated snowfall (the right ordinate; units: mm).

tilting. The high value of the local variation of kinetic energy is mainly caused by the zonal velocity forcing, and the vertical distribution of the zonal velocity forcing is most similar to the local variation of kinetic energy (Figure 15C). The zonal velocity forcing has a large value area in the center of the snow belt, with a central intensity as high as 20×10^{-2} m^2 s^{-3}. In addition, the large value center is also located in the middle layer (η=0.1858), and the fluctuation demonstrates an upward-tilting and eastward pattern. Figures 15B,D show the vertical distribution of meridional velocity forcing term and vertical advection forcing term, respectively. These two terms also have positive contributions to the change of kinetic energy in the snowfall area, and both propagate upward in a fluctuating pattern. However, they are relatively smaller than the zonal velocity forcing. Therefore, the kinetic energy in the snowfall area will gradually increase under the influence of these forcing terms. We will further analyze the key factor causing the development and variation of kinetic energy, namely the zonal velocity forcing.

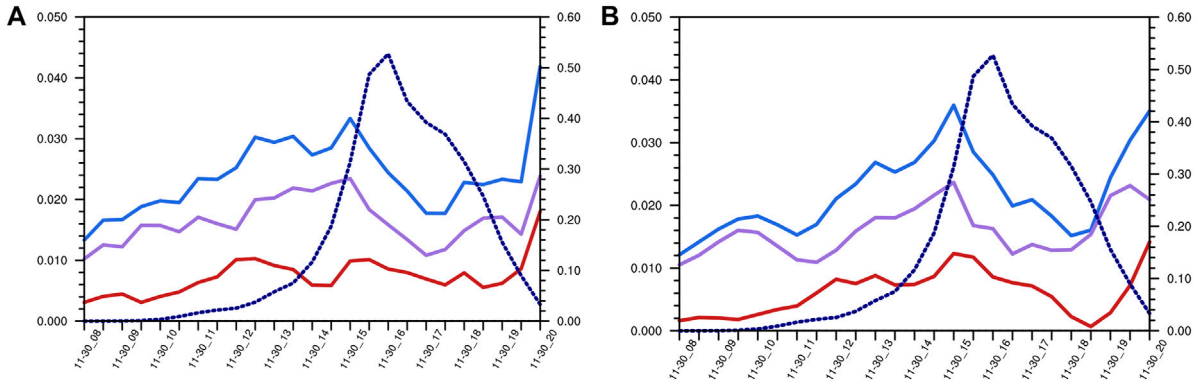

FIGURE 16
Time series of domain averaged zonal pressure work (blue solid line), pressure work of zonal flow-around wind (red solid line), pressure work of zonal flow-over wind (purple solid line, the left ordinate; units: $m^2\ s^{-3}$) and snowfall (dashed line, the right ordinate; units: mm) on the first layer **(A)** and the fifth layer **(B)** of the model layer.

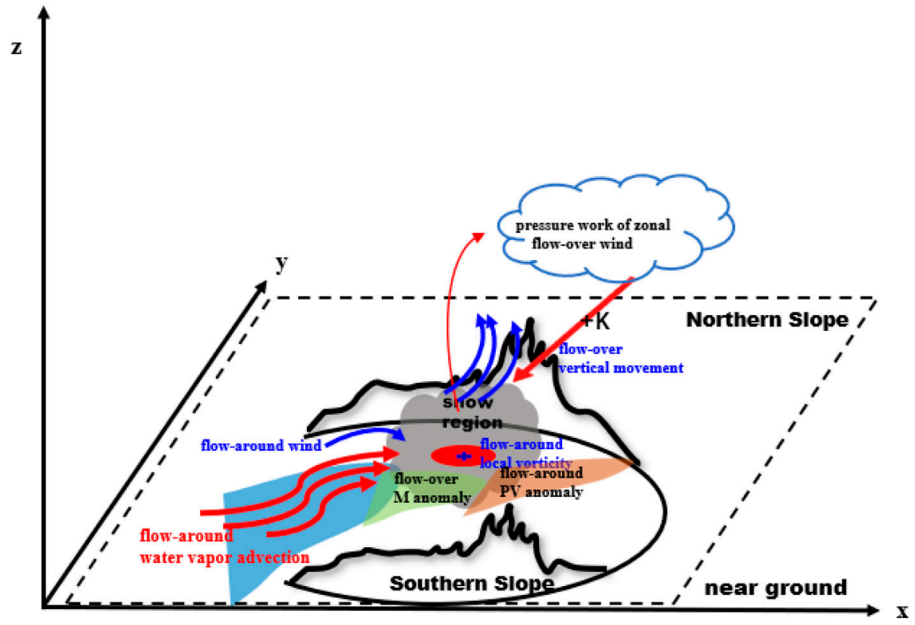

FIGURE 17
Conceptual model of the topographic dynamic effect of airflow in the snowy weather process The black curve denotes terrain, the gray shading represents the snow area The red curved arrows denote flow-around wind, the blue curved arrows denote flow-over wind, and the red ellipse indicates the local convergence. K represents the kinetic energy, the orange shading represents flow-around PV anomaly, the blue shading represents flow-around water vapor advection, and the green shading represents flow-over potential divergence.

Zonal velocity forcing $(-\alpha\frac{\partial p}{\partial x} - \frac{\alpha\frac{\partial p}{\partial \eta}\frac{\partial \phi}{\partial x}}{\mu_d\alpha_d} + \frac{Fu}{\mu_d} - \frac{\partial K}{\partial x})u$ is decomposed into zonal pressure work, frictional dissipation forcing and zonal kinetic advection. Of these, the work done by the zonal pressure gradient force is the largest among the three components (Figure 15E). Through our previous analysis, we've found the local variation of kinetic energy and zonal velocity forcing has significant high values from the low to high level of the center of the snow area (78.6°E–80.2°E), this pattern is also reflected in the vertical distribution of the work done by the zonal pressure gradient. The positive force of zonal pressure work is located in the center of the snow zone, and there is a maximum area in the middle layer (η=0.7046 to η=0.2307), which promotes the development of kinetic energy. On the other hand, the contribution of frictional dissipation forcing to the kinetic energy enhancement can be ignored (figure omitted), while zonal kinetic advection (figure omitted) contributes modestly to the kinetic energy enhancement, the latter spreads eastward and upward in a fluctuating pattern to promote kinetic energy enhancement. The influence of flow around

and flow over terrain on the horizontal kinetic energy change will be further analyzed below.

According to Eq. 12, the work done by the zonal pressure gradient force is regarded as flow-over component $(-\alpha\frac{\partial p}{\partial x} - \frac{\alpha\frac{\partial p}{\partial \eta}\frac{\partial \phi}{\partial x}}{\mu_d\alpha_d})u_r$ and flow-around component $(-\alpha\frac{\partial p}{\partial x} - \frac{\alpha\frac{\partial p}{\partial \eta}\frac{\partial \phi}{\partial x}}{\mu_d\alpha_d})u_p$. The influence of flow over and around terrain on the change in kinetic energy is subsequently analyzed. Figures 16A,B are the domain averaged time series of zonal pressure work and its flow-around and flow-over components on first layer and fifth layer of the model, respectively. The work done by zonal pressure gradient force propels an increase in kinetic energy. Notably, the increase of kinetic energy in the snowfall area mainly depends on the flow-over wind, and the work done by the pressure gradient force caused by the flow-over wind contributes more to the increase of kinetic energy. During snowfall strengthening stage, the zonal pressure work and its components gradually increase, however, during the weakening stage, they decrease.

6 Conclusion

Based on the topographic height distribution, the near-surface wind field of the WRF model is decomposed into flow around and flow over terrain. In view of the triggering moment of snowstorms in Xinjiang on 30 November 2018, the effects of flow around and over terrain on dynamics, water vapor transport and stability were analyzed, and the following conclusions were drawn:

Primarily, the flow-around field is the main flow field in transporting water vapor and causes the convergence of water vapor. Moreover, there are symmetric instability and stratified instability in the snowfall area. The horizontal advection transport of generalized potential temperature by the flow-around vertical shear and the vertical advection transport of generalized potential temperature by the flow-around divergence cause the negative potential vorticity value of the potential vorticity, thus causing symmetric instability. The meridional gradient of near-surface potential temperature is closely related to the quasi-east–west trend of the terrain. On the model plane, the potential temperature on the low terrain is lower, and the potential temperature on the high terrain is higher, thus forming a large horizontal gradient of potential temperature at steep terrain. The flow-over potential divergence will cause changes in the stratified stability. The horizontal advection transport of equivalent potential temperature caused by the flow-over vertical shear leads to a higher negative value of flow-over potential divergence in the snowfall area, thus enhancing instability. Comparatively, the meridional advection transport of flow-over vertical shear to equivalent potential temperature is more significant. Due to the significant flow-over potential divergence anomalies in the snowfall area during the snow triggering stage, the correlation of flow-over potential divergence with topographic snowfall is tested through this snowfall case studies. We found flow-over potential divergence may provide a negative correlation with the topographic snowfall to a certain extent, when the snowfall is greater than or equal to 1 mm/h, the correlation coefficient between them reaches 0.71. This correlation is helpful for topographic snowfall forecasting and the foundations for further topographic snowfall studies in Central Asia in the future is laid. Certainly, further work is required to verify this relationship.

In terms of topographic dynamic effects, the cyclonic vorticity of flow around the near surface is significant in the snowfall area, therefore, the flow-around component generates favorable vortical circulation conditions for snowfall. Near-surface vertical motion is mainly forced by flow over mountains, providing triggering conditions for snowfall. Furthermore, the flow-over kinetic energy in the snow area is stronger, and the work done by the pressure gradient force caused by flow over terrain enhances the near-surface horizontal kinetic energy. Additionally, we summarize a conceptual model (Figure 17) to intuitively understand the dynamic mechanism of airflows over and around topography during this snowfall event and use it for forecasting practice of topographic snowfall in Central Asia in the future.

Data availability statement

The raw data supporting the conclusion of this article will be made available by the authors, without undue reservation.

Author contributions

This manuscript was analyzed and wrote by SM. This paper was under the guidance of the LR, he contributed to conception and design of the study. RC, BJ, and KZ provided guidance in the calculation process. All authors contributed to the article and approved the submitted version.

Funding

Strategic Priority Research Program of the Chinese Academy of Sciences (Grant XDA17010105), National Key Research and Development Project (Grant 2018YFC1507104), Key Scientific and Technology Research and Development Program of Jilin Province (Grant 20180201035SF), National Natural Science Foundation of China (Grant 41775140, 42275010).

Acknowledgments

The authors are thankful to the editors and reviewers for their constructive and thoughtful comments that have significantly improved the quality of this paper. The computing for this project was performed at the National Key Scientific and Technological Infrastructure Project “EarthLab.”

Conflict of interest

The authors declare that the research was conducted in the absence of any commercial or financial relationships that could be construed as a potential conflict of interest.

Publisher's note

All claims expressed in this article are solely those of the authors and do not necessarily represent those of their affiliated organizations, or those of the publisher, the editors and the reviewers. Any product that may be evaluated in this article, or claim that may be made by its manufacturer, is not guaranteed or endorsed by the publisher.

Supplementary material

The Supplementary Material for this article can be found online at: https://www.frontiersin.org/articles/10.3389/feart.2023.1136356/full#supplementary-material

References

Bothe, O., Fraedrich, K., and Zhu, X. (2012). Precipitation climate of Central Asia and the large-scale atmospheric circulation. *Theor. Appl. Climatol.* 108, 345–354. doi:10.1007/s00704-011-0537-2

Ding, Y. H., Ren, G. Y., and Shi, G. Y. (2006). National assessment report of climate change(I): Climate change in China and its future trend. *Adv. Clim. Chang. Res.* 2, 3–8. (in Chinese). doi:10.3969/j.issn.1673-1719.2006.01.001

Duan, W. L., He, B., and Takala, K. (2015). Changes of precipitation amounts and extremes over Japan between 1901 and 2012 and their connection to climate indices. *Clim. Dyn.* 45, 1–20. doi:10.1007/s00382-015-2778-8

Gao, S. T., Wang, X. R., and Zhou, Y. S. (2004). Generation of generalized moist potential vorticity in a frictionless and moist adiabatic flow. *Geophy. Res. Lett.* 31, L12113. doi:10.1029/2003GL019152

Guo, N., Zhou, Y., and Yang, L. (2021). Statistical analysis of Central Asian vortices and their influence on precipitation in Xinjiang. *Atmos. Res.* 249, 105327. doi:10.1016/j.atmosres.2020.105327

Hoskins, B. J. (1974). The role of potential vorticity in symmetric stability and instability. *Quart. J. Roy. Meteor. Soc.* 100, 480–482. doi:10.1002/qj.49710042520

Huang, G., and Zhou, L. T. (2004). The variability of the wind system circulating round the west side of the Tibetan plateau and its relation to the east asian summer monsoon and summer rainfall in north China. *Clim. Environ. Res.* 9, 316–330. (in Chinese). doi:10.3969/j.issn.1006-9585.2004.02.008

IPCC (2021). Climate change 2021 the physical science basis Available at: https://www.ipcc.ch/report/ar6/wg1/downloads/report/IPCC_AR6_WGI_Full_Report.pdf

Jagannathan, A., Winters, K. B., and Armi, L. (2017). Stability of stratified downslope flows with an overlying stagnant isolating layer. *J. Fluid Mech.* 810, 392–411. doi:10.1017/jfm.2016.683

Jagannathan, A., Winters, K. B., and Armi, L. (2019). Stratified flows over and around long dynamically tall mountain ridges. *J. Atmos. Sci.* 76, 1265–1287. doi:10.1175/JAS-D-18-0145.1

Jagannathan, A., Winters, K. B., and Armi, L. (2020). The effect of a strong density step on blocked stratified flow over topography. *J. Fluid Mech.* 889, A23. doi:10.1017/jfm.2020.87

Jiang, J., Zhou, T., and Chen, X. (2021). Central asian precipitation shaped by the tropical pacific decadal variability and the atlantic multidecadal variability. *J. Clim.* 34, 7441–7553. doi:10.1175/JCLI-D-20-0905.1

Jin, Y., and Li, G. P. (2021). Impact of flow around and flow over in sudden rainstorm on mountains. *Plateau Meteoro* 40, 314–323. (in Chinese). doi:10.7522/j.issn.1000-0534.2020.00041

Khouider, B., Han, Y., and Biello, J. A. (2012). Convective momentum transport in a simple multicloud model for organized convection. *J. Atmos. Sci.* 69, 281–302. doi:10.1175/JAS-D-11-042.1

Li, F., Li, J. P., and Li, Y. J. (2012). Climatological characteristics of flow around and flow over the Tibetan plateau. *Chin. J. Atmos. Sci.* 36, 1236–1252. (in Chinese). doi:10.3878/j.issn.1006-9895.2012.11214

Ma, S., Cao, J., and Zhao, H. (2022a). Decomposition of water vapor flux divergence and its application to a blizzard event over Ili valley in central Asia during 30 Nov to 1 dec 2018. *Atmos. Res.* 270, 106079.

Ma, S. P., Ran, L. K., and Cao, J. (2022b). Characteristics for the sources and sinks of gravity waves in an orographic heavy snowfall event front. *Earth Sci. China* 2022. doi:10.1007/s11707-021-0961-2

Ma, S. P., Ran, L. K., and Cao, J. (2021). Diagnosis and analysis of vertical motion during complex topographical heavy snowfall. *Chin. J. Atmos. Sci.* 45, 1127–1145. (in Chinese). doi:10.3878/j.issn.1006-9895.2105.20206

Manabe, S., and Terpstra, T. B. (1974). The effects of mountains on the general circulation of the atmosphere as identified by numerical experiments. *J. Atmos. Sci.* 31, 3–42. doi:10.1175/1520-0469(1974)031<0003:TEOMOT>2.0.CO;2

Ran, L. K., Liu, L., and Li, N. (2013). The analysis of the potential-divergence wave activity density and its application to typhoon precipitation. *Chin. J. Geophys.* 56, 3285–3301. (in Chinese). doi:10.6038/cjg20131006

Shi, Y. G., Sun, Z. B., and Yang, Q. (2008). Characteristics of area precipitation in Xinjiang region with its variations. *J. Appl. Meteor. Sci.* 19, 326–332. (in Chinese). doi:10.3969/j.issn.1001-7313.2008.03.008

Siedersleben, S. K., and Gohm, A. (2016). The missing link between terrain-induced potential vorticity banners and banded convection. *Mon. Wea. Rev.* 144, 4063–4080. doi:10.1175/MWR-D-16-0042.1

Skamarock, W. C., Klemp, J. B., Dudhia, J., Gill, D. O., Liu, Z., Berner, J., et al. (2019). A description of the advanced research WRF. Version 4. NCAR Tech. Note NCAR/TN-556+STR.

Smith, R. B. (2004). "Mountain meteorology and regional climates," in *Atmospheric turbulence and mesoscale meteorology* Editors E. Fedorovich, R. Rotunno, and B. Stevens (Cambridge, United Kingdom: Cambridge University Press).

Trenberth, K. E., and Chen, S. C. (1988). Planetary waves kinematically forced by Himalayan orography. *J. Atmos. Sci.* 45, 2934–2948. doi:10.1175/1520-0469(1988)045<2934:PWKFBH>2.0.CO;2

Vaughan, G., Antonescu, B., Schultz, D. M., and Dearden, C. (2017). Invigoration and capping of a convective rainband ahead of a potential vorticity anomaly. *Mon. Wea. Rev.* 145, 2093–2117. doi:10.1175/MWR-D-16-0397.1

Wang, H., Wang, S. L., and Yu, X. J. (2020). Spatial-temporal variation of snow cover in Xinjiang based on surface observation from 1961 to 2017. *J. Glaciol. Geocryol.* 42, 72–80. (in Chinese). doi:10.7522/j.issn.1000-0240.2020.0010

Wells, H., Webster, S., and Brown, A. (2005). The effect of rotation on the pressure drag force produced by flow around long mountain ridges. *Quart. J. Roy. Meteor. Soc.* 131, 1321–1338. doi:10.1256/qj.04.37

Winters, K. B., and Armi, L. (2012). Hydraulic control of continuously stratified flow over an obstacle. *J. Fluid Mech.* 700, 502–513. doi:10.1017/jfm.2012.157

Winters, K. B., and Armi, L. (2014). Topographic control of stratified flows: Upstream jets, blocking and isolating layers. *J. Fluid Mech.* 753, 80–103. doi:10.1017/jfm.2014.363

Wu, G. (1984). The nonlinear response of the atmosphere to large –scale mechanical and thermal forcing. *J. Atmos. Sci.* 41, 2456–2476. doi:10.1175/1520-0469(1984)041<2456:TNROTA>2.0.CO;2

Yang, L. M., Zhang, Y. H., and Qin, H. (2015). Some advances and problems of middle-Asia vortex. *Desert Oasis Meteorology* 9, 1–8. doi:10.3969/j.issn.1002-0799.2015.05.001

Ye, D. Z., and Gao, Y. X. (1979). *Qinghai-xizang plateau meteorology*. Beijing: Science Press, 278pp. (in Chinese).

Zeng, Y., and Yang, L. (2020). Triggering mechanism of an extreme rainstorm process near the Tianshan Mountains in Xinjiang, an arid region in China, based on a numerical simulation. *Adv. Meteor.* 2020, 8828060. doi:10.1155/2020/8828060

Zhao, W., Abhishek, B. S. T., Zhang, J., Zhao, Y., and Kinouchi, T. (2023). Spatiotemporal variability of current and future sub-daily rainfall in Japan using state-of-the-art high-quality data sets. *Water Resour. Res.* 59, 4. doi:10.1029/2022WR034305

Zhao, W., and Abhishek, T. K. (2022). A framework for quantifying climate-informed heavy rainfall change: Implications for adaptation strategies. *Sci. Total Environ.* 835, 155553. doi:10.1016/j.scitotenv.2022.155553

Zhou, W., Bao, Y. X., and Ran, L. K. (2018). Diagnostic analysis of convective stability evolution during a squall line process. *Chin. J. Atmos. Sci.* 42, 339–356. doi:10.3878/j.issn.1006-9895.1712.17126

frontiers | Frontiers in Earth Science

TYPE Original Research
PUBLISHED 06 September 2023
DOI 10.3389/feart.2023.1230879

OPEN ACCESS

EDITED BY
Shenming Fu,
Chinese Academy of Sciences (CAS), China

REVIEWED BY
Jiafeng Zheng,
Chengdu University of Information Technology, China
Jingliang Huangfu,
Chinese Academy of Sciences (CAS), China

*CORRESPONDENCE
Dehua Chen,
dehua_chen@163.com
Yongcheng Jiang,
ycjiang_925@foxmail.com

RECEIVED 29 May 2023
ACCEPTED 24 August 2023
PUBLISHED 06 September 2023

CITATION
Chen D, Jiang Y, Huang X, Xun A, Dai H and Zhang H (2023), Observation and simulation study on the rapid intensification mechanism of Typhoon "Mekkhala" (2006).
Front. Earth Sci. 11:1230879.
doi: 10.3389/feart.2023.1230879

Observation and simulation study on the rapid intensification mechanism of Typhoon "Mekkhala" (2006)

Dehua Chen[1,2,3]*, Yongcheng Jiang[1,2,3]*, Xin Huang[1,2,3], Aiping Xun[1,2,3], Huaning Dai[1,2,3] and Hanyun Zhang[1,2,3]

[1]Xiamen Key Laboratory of Strait Meteorology, Xiamen, China, [2]Fujian Key Laboratory of Severe Weather, Fuzhou, China, [3]Xiamen Meteorological Observatory, Xiamen, China

Based on Doppler Weather radar observations and numerical simulations applying the Weather Research and Forecasting (WRF) system, this study focused on the rapid intensification (RI) of Typhoon "Mekkhala" (2006) in the inshore area in 2020. The simulated track of the typhoon relatively matched with the observation, with a slight eastward bias compared to the observed track. During the phase of RI, there was a slight weakening of vertical wind shear between 200–500 hPa. The temporary decrease in vertical wind shear became a favorable factor for the intensification of the typhoon. In general, vertical wind shear of the lower atmosphere is the key to supporting the RI of Typhoon Mekkhala. In the middle troposphere, the southward component of the vertical wind shear suddenly increases, indicates that the inflow of southern wind to the core of the typhoon had strengthened. Thus, the strengthening of the moisture transport by enhanced southern wind, contributed to the intensification of the typhoon. During the intensification of the typhoon, the low-level vorticity was significantly enhanced, and the high vorticity values expanded from the lower to higher troposphere. The vertical distribution of vorticity transformed from symmetry to asymmetry. The development of secondary circulation on both sides of the typhoon is a dynamic factor for intensification.

KEYWORDS

Typhoon "Mekkhala", rapid intensification, numerical simulation, doppler weather radar, West coast of Taiwan Strait

1 Introduction

China is one of the countries most severely affected by tropical cyclones (TC) in the world. Statistical research shows that an average of 16% of TCs moving towards the Chinese coast rapidly intensify, and the sudden intensification or change in direction of TCs in the offshore area is a difficulty in TC forecast. Such TCs often cause serious wind and rain disasters due to sudden changes, resulting in unavailing precautionary measures or inadequate emergency response plans.

South China Sea typhoons refer to typhoons that occur in the central and eastern parts of the South China Sea (12°-20°N, 90°-120°E). They develop quickly, have a relatively short life cycle, and have high intensity and track uncertainty. The time left for the meteorological department to provide services is relatively short compared to typhoons in the Western Pacific. Especially for typhoons that suddenly intensify shortly before landing, the

forecasting difficulty is extremely high, and the lead time and predictability are very limited. Therefore, it poses great difficulties for disaster prevention and reduction. Typhoon "Mekkhala" (2006) was generated in the South China Sea and rapidly intensified in the offshore area, landing on the south coast of Fujian, causing varying degrees of damage to the southern part of Fujian Province. In Fujian province, China, a total of 56,000 people were affected, with 17 houses collapsed and 43,000 people urgently evacuated. The crop damage was 8,100 ha, causing a direct economic loss of 610 million yuan.

With the effective assimilation of multiple observation data, improvement and optimization of numerical modeling framework, and development of ensemble forecasting, the accuracy of intensity and track forecasting of tropical cyclones (TC) has been continuously improving. However, the progress in improving the accuracy of intensity change forecasting through numerical modeling has been slow (Liu et al., 2006; Yang et al., 2017). Numerical forecasting initial fields for TC vortex structure characteristics and sub-grid physical parameter description is still not clear and accurate enough, and there is a large uncertainty. Furthermore, there is still insufficient understanding of the physical process and intensity change organization feedback of TC. In addition, the lack of observations at sea, particularly for the physical mechanisms of intensity and track changes in TC, poses significant challenges for forecasting these types of TC. For example, the forecasting of nearshore abrupt changes in South China Sea landing TCs faces significant challenges. Rapid intensification (RI) of TCs as an important phenomenon of TC intensity change is a major scientific issue and focus of routine operation in the current international TC research field (Duan et al., 2006).

Many scholars have conducted extensive research on nearshore TC intensification through theoretical studies, observational analysis, and numerical simulations, which has given us a better understanding of nearshore TC intensification. Yu and Yao (2006) proposed the criteria ($\Delta p < -7.78$ hPa/6 h) for RI, and conducted synthetic analysis and comparative analysis of two groups of TCs with RI and rapid weakening in China's nearshore regions. They discovered that the location of TCs with RI would not occur in high-latitude areas north of 30°N or in low-latitude areas of 0°–5°N. Relevant studies have indicated that the main factors affecting TC intensity are atmospheric environmental fields, ocean environmental fields, and TC vortex convective activity. These studies have explored the effects of factors such as atmospheric environmental fields (e.g., sea surface temperature, wind shear, and humidity), rainfall rates and rainfall area in the TC nucleus region, severe convection events, and lightning activities on TC RI (Steranka et al., 1986; Kaplan and DeMaria, 2003; Guimond et al., 2010; Harnos and Nesbitt, 2011; DeMaria et al., 2012; Bai and Wang, 2013; Wang and Yu, 2013; Susca-Lopata et al., 2015; Hu and Duan, 2016; Wang et al., 2017; Zhang et al., 2019).

Shou and Yao (1995) conducted diagnostic analysis of the synthetic environmental field for explosively developing TCs and found that during explosive development, low-level convergence and upper-level divergence both increase. Xia et al. (1995) stated that non-adiabatic heating is an important factor affecting TC intensity change. Yu and Wu (2001) believed that there was a close relationship between the interaction between the environmental flow field in the upper atmosphere and TC outflow and the sudden intensification of TCs before landing in China's nearshore regions, and that strong southwest monsoon water vapor transport is a precursor condition for sudden strengthening before TC landing in southern China, and that the development of tilted vortices is the cause of the RI of TCs. Liang et al. (2003) conducted diagnostic analysis on the nearshore intensified TC "Vongfong" and found that the strong development of "Vongfong" before landing was related to the invasion of cold, dry air from the northern small stream that led to the strengthening of potential instability. Hu et al. (2005) used NCEP/NCAR reanalysis data to conduct large-scale analysis of TCs with rapidly weakening and rapidly strengthening before landing in the southern regions of China, and the research revealed that the TCs with RI were located in the south of the subtropical high, and that low-level convergence and high-level divergence were strong. Yu et al. (2008) analyzed the characteristics and mechanisms of RI of TC "Saomai" in China's nearshore regions using NCEP/NCAR reanalysis data. Gao et al. (2012) found that the strengthening and enrichment of middle and lower level water vapor inflow, strong lower level convergence, upper level divergence, and weak vertical shear are closely related to the diagnosis and discovery of Typhoon "Meranti" near the sea. Zhang et al. (2019) suggested the RI process of Typhoon "Hato" is exerted by a convection and vortex coupled environment.

Previous studies have shown that several factors mainly lead to TC intensitification, including atmospheric environmental field, ocean environmental field, and convection activities within typhoon vortex. Observational and numerical simulation studies have shown that the environmental field plays an important role in the RI of TC (Merrill, 1988; Wang and Wu, 2004; Kelley et al., 2004; Kelley et al., 2005; Vigh and Schubert, 2009; Wang and Yu, 2011; Zagrodnik and Jiang, 2014; Yin et al., 2015). Environmental fields such as higher sea surface temperature, thicker ocean mixed layer, lower vertical wind shear, higher relative humidity in the lower layer of the atmosphere, conditionally unstable atmospheric, large-scale upper-level divergence and lower-level convergence are conducive to the RI of TC (Simpson et al.,1998; Rogers, 2010). Kaplan et al. (2010) believe that effective forecasting of RI of TC can be achieved using only large-scale environmental field parameters. Hendricks et al. (2010) discovered that the sea surface temperature and other environmental parameters that control the intensity changes of TC during RI are very similar to those during slow intensification, indicating that the rate of TC strengthening may be related to internal processes rather than environmental fields.

Therefore, this paper intends to conduct research on the environmental characteristics and major possible influencing factors of the sudden intensitificaiton of Typhoon "Mekkhala" near the landing site through observations and numerical simulations, and to reveal the possible mechanism of the RI of "Mekkhala" in the inshore area before landing.

2 Materials and methods

The typhoon track data used in this study were obtained from the collections of best track data, released by Shanghai Typhoon Institute, China. The surface meteorological automated observations from Chinese National Meteorological Information Center (http://data.cma.cn/). The Base Reflectivity data of Doppler dual-

TABLE 1 The main parameterization schemes of the FJ-WRF Model.

Main parameterization	Physical schemes
Microphysics parameterization	Lin
Cumulus parameterization	Kain-Fritsch
Longwave radiation parameterization	RRTM
Shortwave radiation parameterization	Dudhia
Land surface parameterization	Monin-Obukhov
Boundary layer parameterization	YSU

polarization weather radars were observed from weather radar station in Xiamen (at coordinates 119.00°E, 24.49°N).

In this study, the Fujian Weather Research and Forecasting (FJ-WRF) model, which is based on the WRF-ARW version 3.4.1, was used to simulate Typhoon "Mekkhala" (2006). The simulation domain of the FJ-WRF model covers Fujian Province and its surrounding areas, with a central longitude and latitude of 119.632°E and 25.295°N, respectively. The model adopts a single-layer grid with a horizontal resolution of 9 km × 9 km, consisting of a grid size of 300 × 312. In the vertical direction, there are a total of 40 layers, with a model top pressure of 10 hPa. The main parameterization schemes for physical processes include the Lin microphysics scheme, Kain-Fritsch cumulus parameterization scheme, RRTM longwave and Dudhia shortwave radiation schemes, YSU planetary boundary layer scheme, and a 5-layer thermal diffusion land surface scheme (Table 1). The initial and boundary conditions are obtained from the operational analysis and forecast fields of the National Centers for Environmental Prediction (NCEP) Global Forecast System (GFS) model, with a horizontal resolution of 0.5° × 0.5° and a temporal interval of 6 h (https://rda.ucar.edu/datasets/ds083.2/). The simulation started at 14:00 on 10 August 2020 (LST) and integrates for 24 h, with hourly output of the simulation results. In this study, the simulation results from 02:00 to 17:00 on August 11 were analyzed.

Using the output from the FJ-WRF, various variables such as vertical wind shear, water vapor flux, pseudo-equivalent potential temperature, divergence, vorticity, and vertical circulation were calculated. The calculation method of vertical Wind shear is wind vector difference at different heights. For example, the vertical wind shear in 500–850 hPa is the value that subtracting the wind speed at 500 hPa from the wind speed at 850 hPa. This analysis aimed to examine the mesoscale evolution characteristics of lower-level dynamic lifting, thermal disturbance, water vapor disturbance, as well as the vertical structures of water vapor, dynamics, and thermodynamics in the mid-high levels during the RI phase of Typhoon "Mekkhala." The study also aimed to investigate the impact mechanisms of positive feedback on the RI of Typhoon "Mekkhala."

3 Results

3.1 The RI characteristics of Typhoon "Mekkhala"

Figure 1 presents the track, maximum wind speed, and minimum atmospheric pressure evolution of Typhoon "Mekkhala". "Mekkhala" originated in the South China Sea on August 10th at 11:00 a.m. (Beijing time, hereafter referred to as local time). After formation, it steadily moved towards the north with a relatively fast speed, gradually intensifying in strength. By 17:00, it had strengthened into a severe tropical storm with a decrease in atmospheric pressure from 998 to 985 hPa, the variation of pressure in 6 h (Δp6) was −13 hPa, greatly exceeding the RI standard of −7.78 hPa from Yu and Yao (2006). The wind speed increased from 18 to 25 m/s. At 06:00 on the approaching landfall day, it further intensified into a typhoon, with the atmospheric pressure further dropping to 980 hPa (Δp6 = −5 hPa) and the wind speed

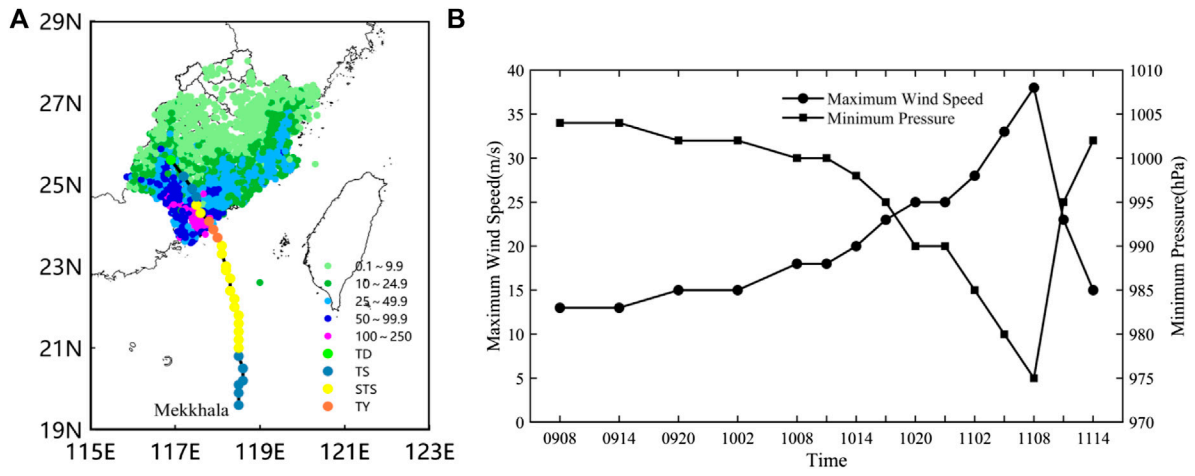

FIGURE 1
(A) Accumulated rainfall in Fujian Province from 20:00 on August 10th to 20:00 on August 11th (unit: mm) and the track of Typhoon "Mekkhala". **(B)** Hourly evolution of the maximum wind speed and minimum atmospheric pressure of the Typhoon "Mekkhala" (pressure unit: hPa; wind speed unit: m/s).

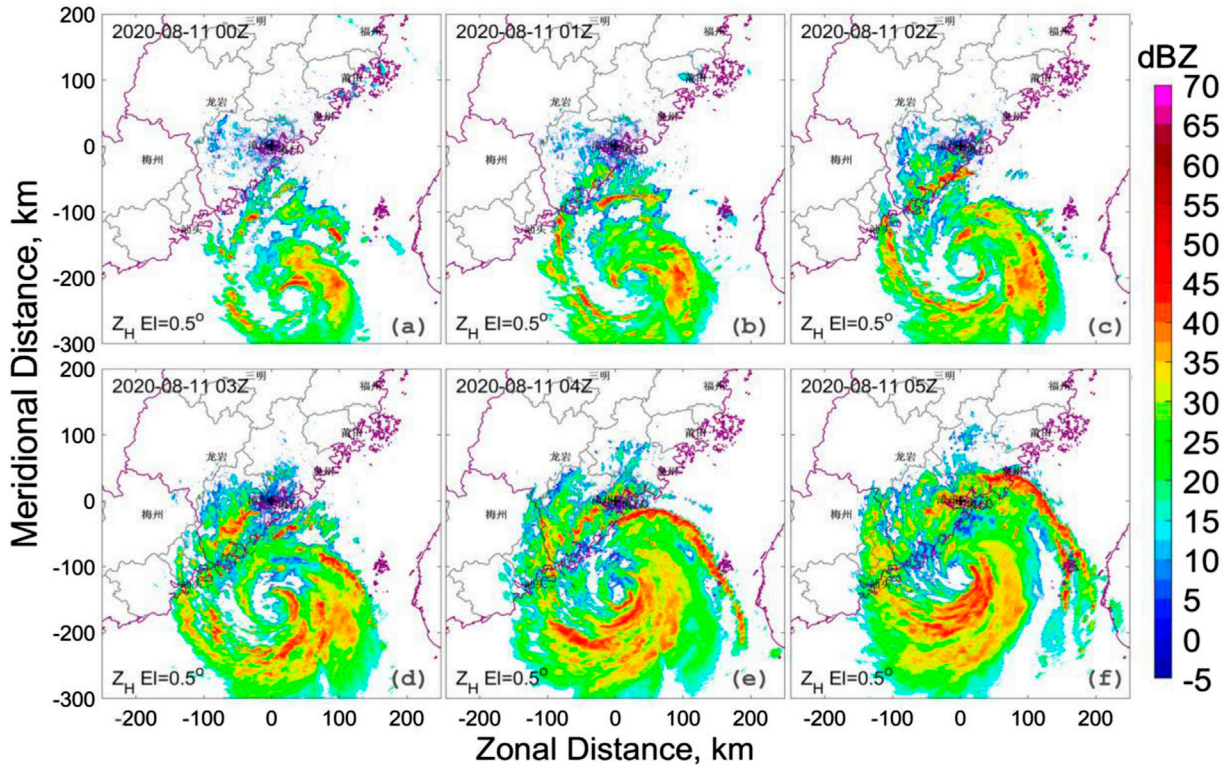

FIGURE 2
Radar reflectivity (dBZ) at 0.5° elevation of the Xiamen dual-polarization radar from 00:00–05:00, August 11 during the peripheral impact stage of Typhoon "Mekkhala".

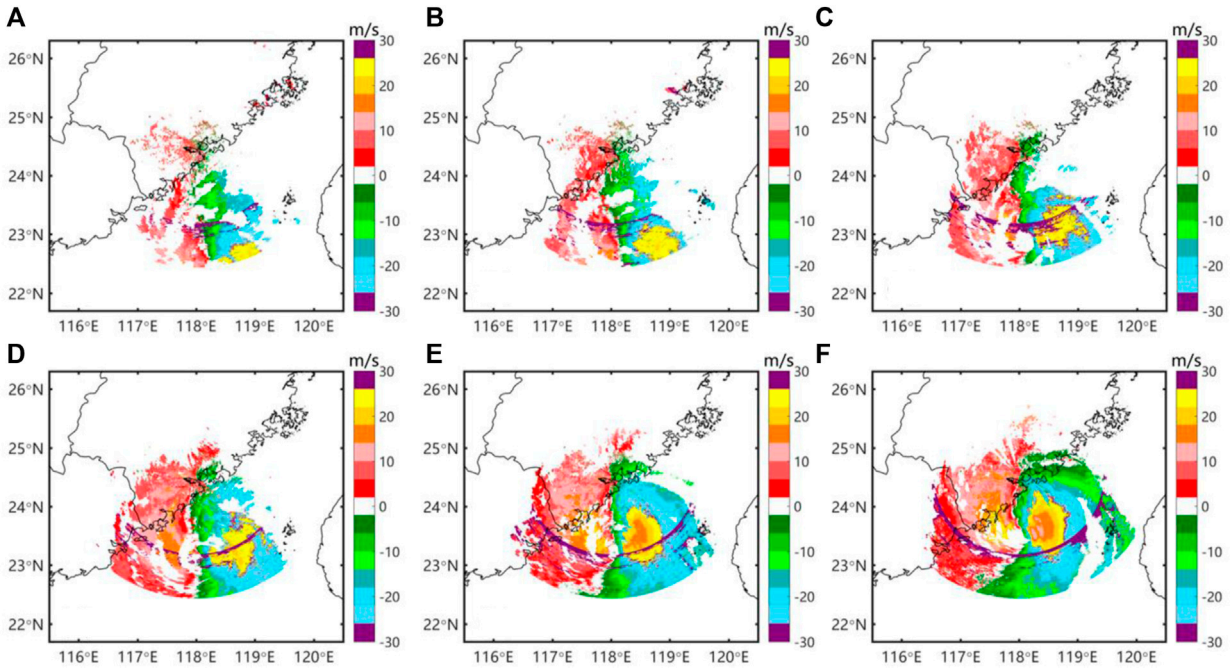

FIGURE 3
Radial velocity (m/s) at 0.5° elevation of the Xiamen dual-polarization radar from 00:00–05:00, August 11 during the peripheral impact stage of Typhoon "Mekkhala".

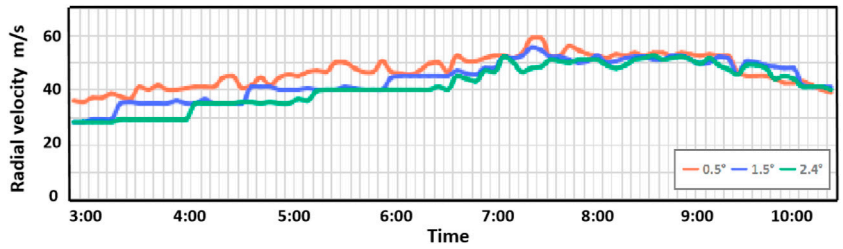

FIGURE 4
Evolution of maximum radial velocity at 0.5°, 1.5°, and 2.4° elevations during landfall (02:58–10:41, August 11).

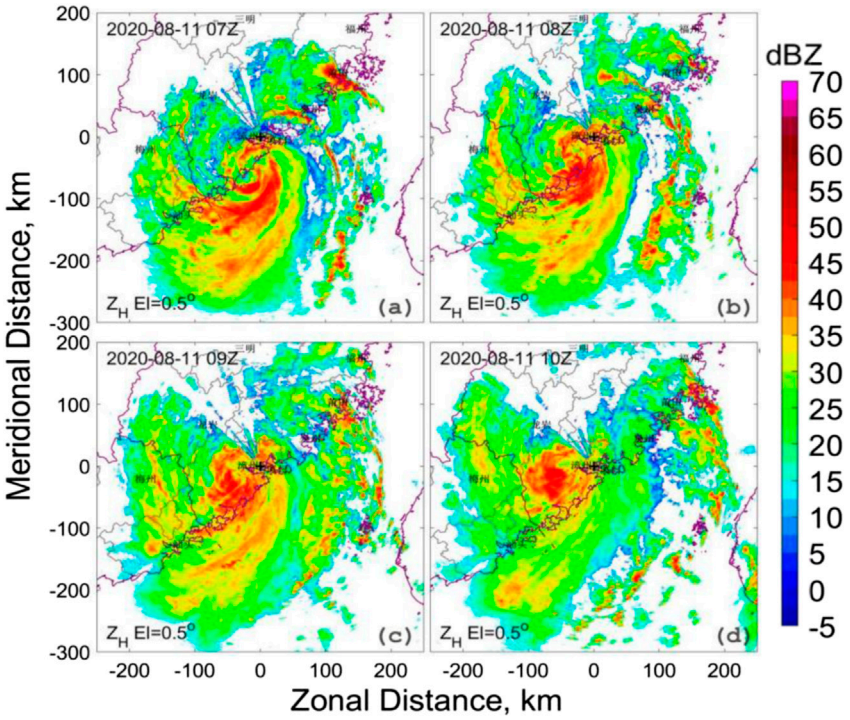

FIGURE 5
Radar reflectivity (dBZ) at 0.5° elevation of the Xiamen dual-polarization radar from 07:00–10:00, August 11 during the inner impact stage of Typhoon "Mekkhala".

further increasing to 33 m/s. Over the next 12 h, the wind speed continued to strengthen by an additional 8 m/s. This indicates that Typhoon "Mekkhala" experienced a sudden intensification from its formation until just before landfall. At 07:30, it made landfall along the coastal areas of Zhangpu County, Fujian Province, maintaining its intensity category as typhoon with a central pressure of 980 hPa and maximum near-center wind force of 33 m/s. This intensity was consitent with the result of the new evaluation method developed in Howell et al. (2022). After landfall, "Mekkhala" continued to move northwestward, rapidly weakening in intensity. By 14:00, it had weakened into a tropical depression within Liancheng County, Fujian Province, and was subsequently declassified by the China Meteorological Administration at 17:00.

As a result of the influence of Typhoon "Mekkhala", the southern regions of Fujian Province experienced heavy torrential rainfall, particularly over the left side of the typhoon track. The highest recorded precipitation occurred in Zhangpu County, with a rainfall amount of 179.7 mm. The maximum recorded hourly rainfall is 80.3 mm.

Typhoon "Mekkhala" has exhibited the following characteristics since its formation: 1) Nearshore genesis: When "Mekkhala" formed in the South China Sea, it was only 540 km south of Xiamen. 2) Rapid development and intensification near the coast: After formation, it quickly intensified and reached typhoon strength within 3 h before landfall, transitioning from a tropical storm to a typhoon in just 19 h 3) Stable track: After formation, it maintained a stable northward trajectory, directly heading towards the coastal areas of southern Fujian. Moreover, it had a fast movement speed, taking less than 21 h from formation to landfall, with a total lifespan of only 27 h 4) Small size and high intensity: Upon landfall, it

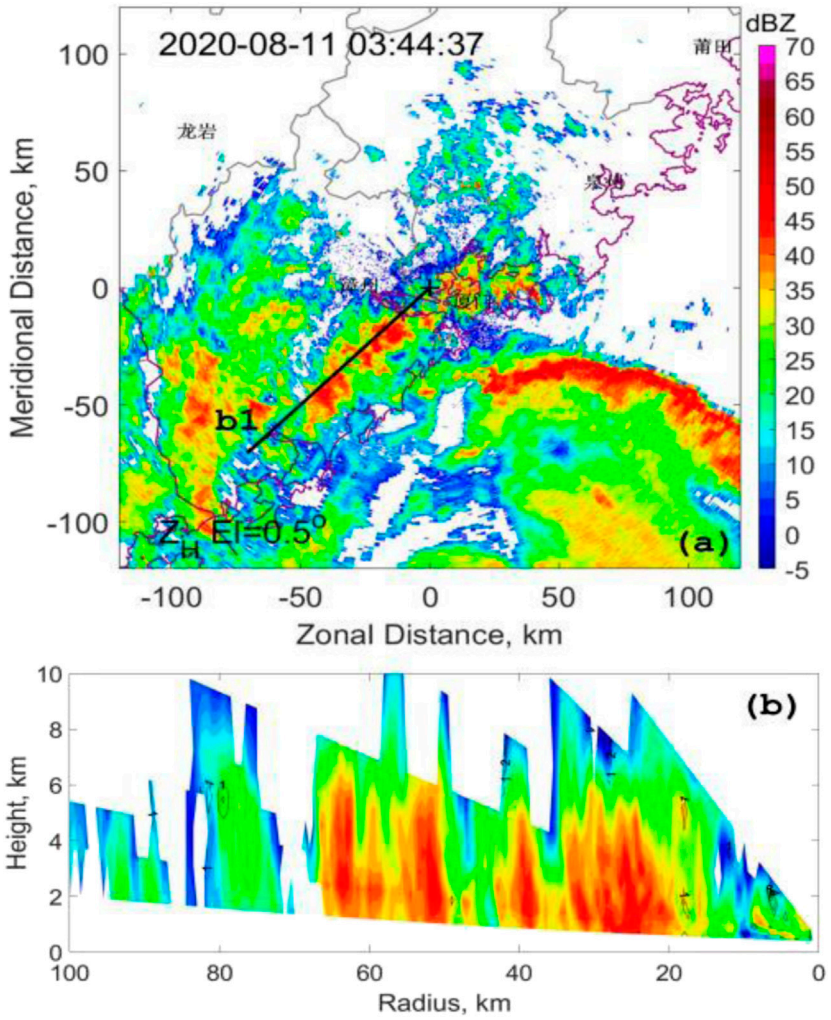

FIGURE 6
Rainfall process during the impact of outer rainband, **(A)** Xiamen dual-polarization radar reflectivity at a 0.5° elevation, **(B)** Vertical cross-section along the b1, with reflectivity as the color fill and differential reflectivity as the contour lines.

remained at typhoon intensity (33 m/s), with a radius of maximum winds of only 30 km "Mekkhala" belongs to the rare category of rapidly intensifying small-scale typhoons near the coast, characterized by a short lifespan, posing significant challenges for forecasting and defense efforts.

3.2 Doppler weather radar characteristics

Typhoon "Mekkhala" exhibited significant asymmetric characteristics, with the strong echo of the inner core mainly distributed in the fourth quadrant. The impact of "Mekkhala" on southern Fujian can be divided into two stages. From 00:00 to 06:00 LST, the typhoon moved predominantly in a northward direction, approaching the coastal areas of southern Fujian. During this period, the southern Fujian region was mainly affected by the outer rainbands, resulting in precipitation. The outer rainbands had a narrow strong echo region, fast movement speed, and short duration, resulting in relatively minor rainfall. At 06:00, "Mekkhala" intensified to typhoon strength and continued to approach the southern coastal areas of Fujian. During this stage, the southern Fujian region was influenced by the inner core region, leading to the occurrence of heavy precipitation. The inner rainbands had a wider strong echo region and a longer duration, with impacts on Xiamen continuing even after "Mekkhala" made landfall. After landfall, the eye gradually filled, and the asymmetric characteristics changed, with the strong echo region shifting to the third quadrant. After 11:00, Mekkhala weakened to a tropical storm and gradually moved away from southern Fujian (Figure 2). The wind speed near the center of Typhoon "Mekkhala" also exhibited significant asymmetric characteristics before landing (Figure 3). The relatively strong radial velocity was located at southern and eastern part of typhoon, and the maximum speed of radial velocity exceeded 60 m/s during RI stage.

Figure 4 shows the evolution of maximum radial velocity at 0.5°, 1.5°, and 2.4° elevations during landfall (02:58–10:41, August 11). From 3:00, the velocity field from the dual-polarization radar showed a

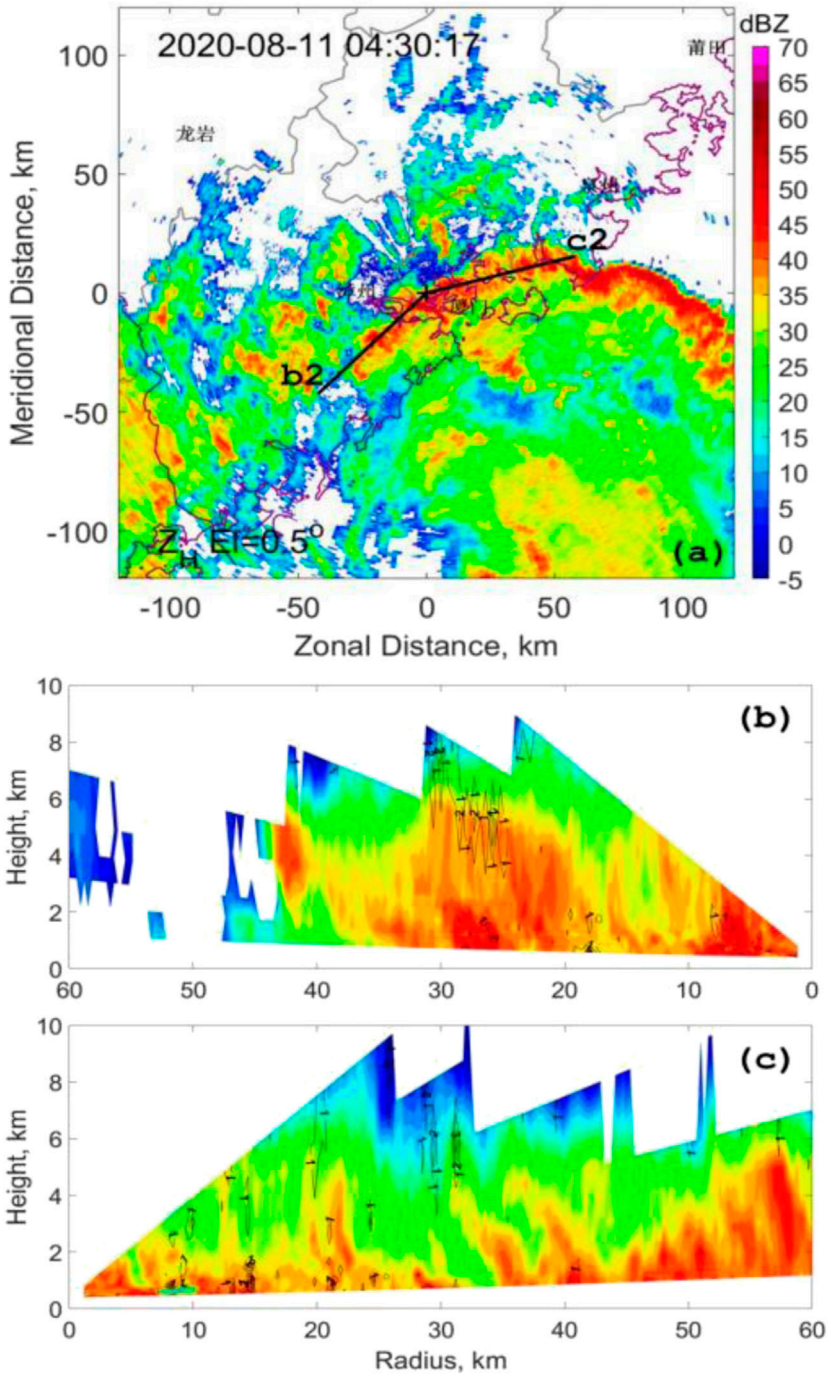

FIGURE 7
Rainfall process during the second outer rainband impact, **(A)** Xiamen dual-polarization radar reflectivity at a 0.5° elevation, **(B)** Vertical cross-section along the b2, **(C)** Vertical cross-section along the c2, with reflectivity as the color fill and differential reflectivity as the contour lines.

significant enhancement of velocities around the eyewall at a 1.5° elevation. Later, a clear enhancement was observed at a 0.5° and 2.4° elevations at 3:50 and 4:08, respectively. The enhancement of velocity lasted 4 h at different levels before landfall. At a 1.5° elevation, enhancements are observed around the eyewall and the eastern side of the typhoon. At a 2.4° elevation, wind speed of eyewall enhanced (Figure 5).

During the outer rainband impact stage, there were two main periods of rainband influence. As shown in Figure 6, during the rainband impact at 03:44, the rainband exhibited a southwest-to-northeast orientation, with multiple convective cells within the rainband. The region with reflectivity greater than 35 dBZ extended vertically from below 2 km–6 km. The differential reflectivity was generally small (<1 dBZ), indicating

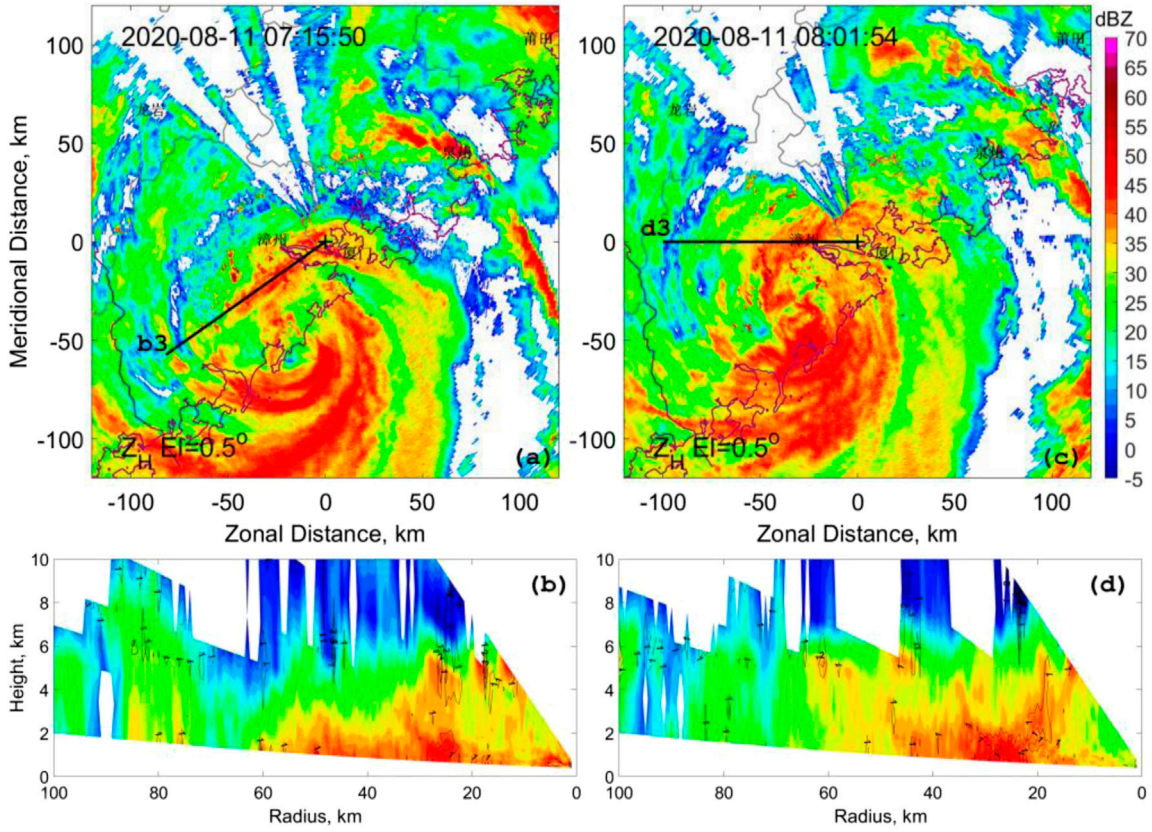

FIGURE 8
(A–C) were reflectively at a 0.5° elevation at 07:15 and 08:01 respectively (during landfall), observed by Xiamen Doppler Radar. **(B–D)** were vertical cross-section along the b3 and d3, with reflectivity as the color fill and differential reflectivity as the contour lines.

that the precipitation below the freezing level was mainly composed of moderate to light raindrops.

The second period of outer rainband impact occurs around 04:30, as shown in Figure 7. Compared to the previous rainband, this one had a longer length. In Figures 7B,C, the region with reflectivity greater than 35 dBZ extended vertically to 6 km, and a large differential reflectivity area (>2 dBZ) appeared between 4 km and 6 km, indicating the presence of large raindrops generated by the melting of ice particles in the mid to upper levels.

During the inner rainband impact, the shoreside rainband showed a significant enhancement compared to former stage. In Figures 8A, B significant high differential reflectivity area was observed below 2 km, indicating the presence of a larger number of large raindrops in the lower levels of the inner rainband. In Figure 8C, during the initial stage of "Mekkhala" landfall, the intensity and orientation of the inner rainband maintained, and the width of the rainband was large. In Figure 8D, the morphology of large raindrops in the lower levels was maintained.

After landfall, significant changed occur in the asymmetric characteristics, with the southern and especially southwestern sides became the center of strong echoes. Comparing Figure 9C with Figure 9A, the range of strong echoes narrowed, and the inner rainband weakened. In Figures 9A, B high reflectivity value was observed at lower levels, but no corresponding high differential reflectivity was observed at upper levels, indicating that the intense precipitation might be caused by the warm rain process during the raindrop fall. In Figures 9A, D significant melting layer was observed at a range of 60–80 km, which corresponds to the edge of the terrain area, suggesting that intense precipitation might be influenced by the topography.

3.3 Numeric simulation of Typhoon "Mekkhala"

3.3.1 Verification of simulation

To evaluate the simulation performance of the WRF model for the RI of Typhoon "Mekkhala", this study simulated the sea-level pressure field, wind field, equivalent potential temperature field, divergence field, vertical velocity field, and other variables during the period when Typhoon "Mekkhala" developed and made landfall (from 03:00 to 14:00 on the 11th).

Figure 10 presents a comparison between the observed and simulated tracks and intensities of Typhoon "Mekkhala". It can be observed that the simulated track was consistent with the observation, with the simulated typhoon track being relatively close to the observed track, albeit slightly eastward overall. The range of track errors in the simulation is generally small (see Figure 10A). Regarding intensity, the minimum sea-level pressure at the typhoon center was mainly used. Before the typhoon made

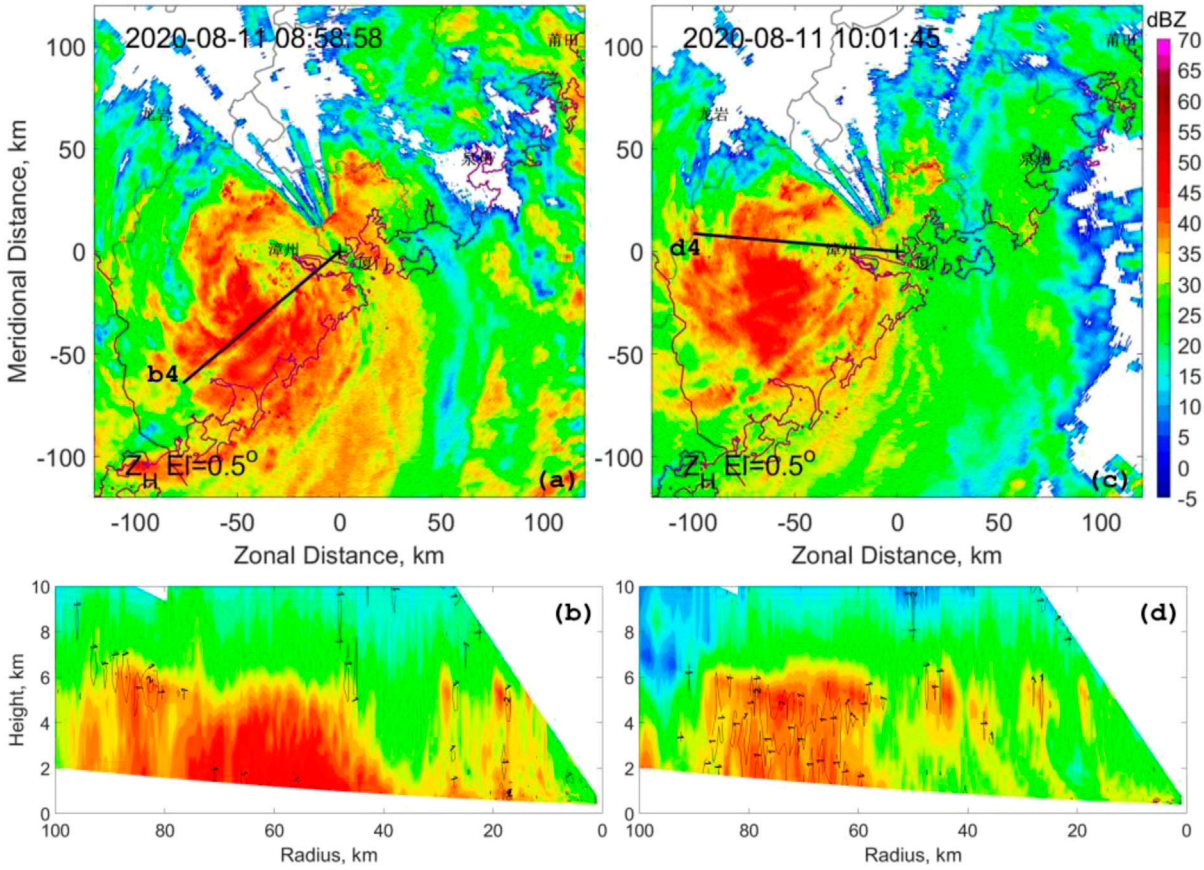

FIGURE 9
(A–C) were reflectivity at a 0.5° elevation at 08:58 and 10:01 respectively (after landfall), observed by Xiamen Doppler Radar. **(B–D)** were vertical cross-section along the b3 and d3, with reflectivity as the color fill and differential reflectivity as the contour lines.

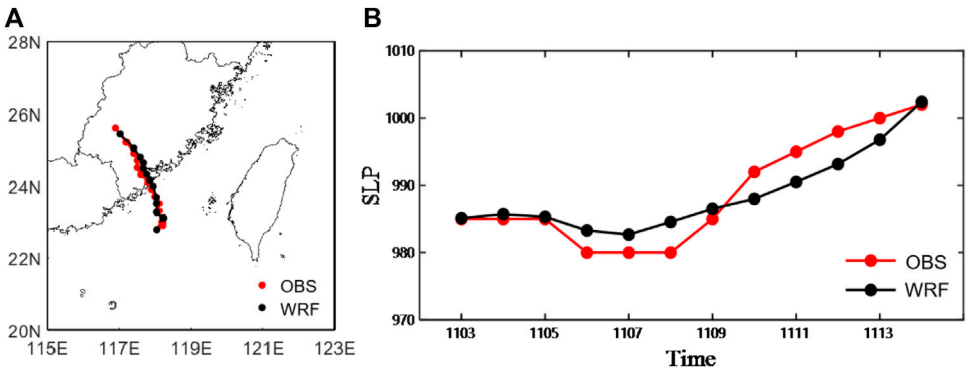

FIGURE 10
(A) Observed (red line) and WRF-simulated (black line) tracks of Typhoon "Mekkhala" from 02:00 to 14:00 on August 11. **(B)** Observed (red line) and WRF-simulated (black line) minimum sea-level pressure near the Typhoon "Mekkhala" center.

landfall (from 03:00 to 08:00, August 11), the simulated intensity was slightly weaker compared to the observations, while the observed RI before landfall was more pronounced. Although the model simulated the intensification characteristics of the typhoon, the overall magnitude of intensification was relatively weaker. After landfall, the simulated typhoon intensity was generally stronger compared to the observations, and the simulated weakening speed after landfall was slower.

Figure 11 presents the simulated radar reflectivity at 03:00 and 07:00. The structure of simulated and observed radar reflectivity was basically consistent (Figure 11). At 03:00, the maximum reflectivity is observed on the south and southeast sides of the typhoon, greater than

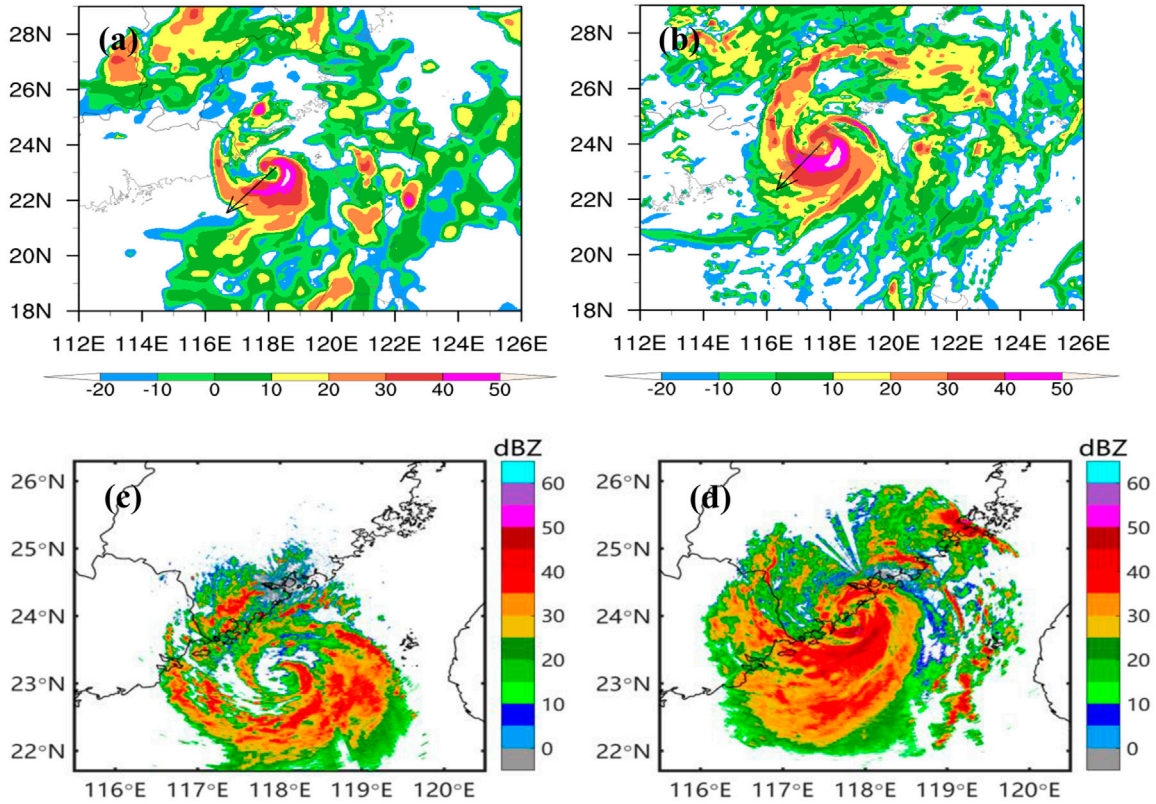

FIGURE 11
The FJ-WRF simulated reflectively factor (dBZ) of Typhoon "Mekkhala" at **(A)** 03:00, August 11, and **(B)** 07:00, August 11. The **(C, D)** were the observed reflectively factor at the same time. The wind arrows located at simulated typhoon center indicate vertical wind shear between 500–850 hPa.

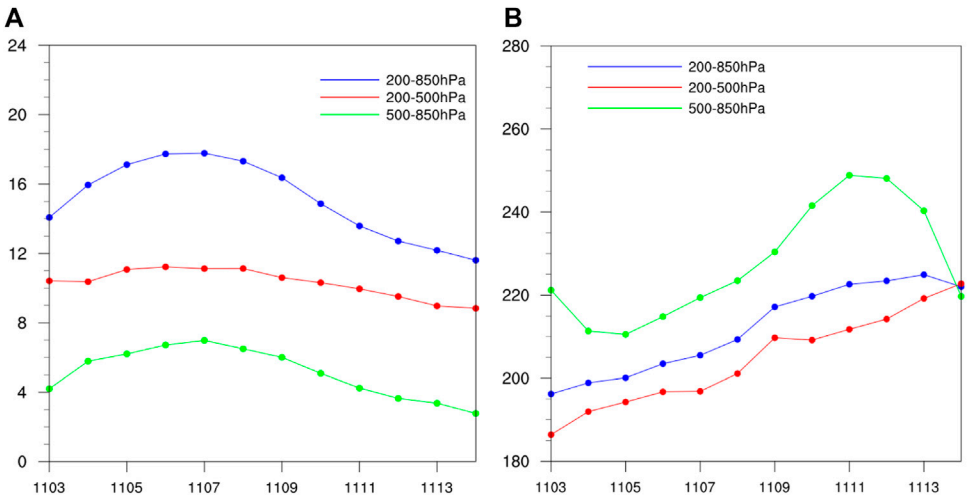

FIGURE 12
The vertical wind shear of Typhoon "Mekkhala" in different levels (200–850, 200–500, and 500–850 hPa) from 03:00–13:00 in August 11, simulated by FJ-WRF. **(A)** is vertical wind shear speed (m/s) and **(B)** is vertical wind shear direction.

50 dBZ. By 07:00, as the typhoon intensified, the reflectivity also increased. The high reflectivity area extended from the south and southeast sides to the southwest side of the typhoon, with a significantly larger range of values exceeding 50 dBZ. The structural development of the typhoon became more complete. At 03:00, there were few precipitation cloud systems on the northern side of the typhoon, while at 07:00, there was a significant increase in convective cells on the northern side, and the development of the

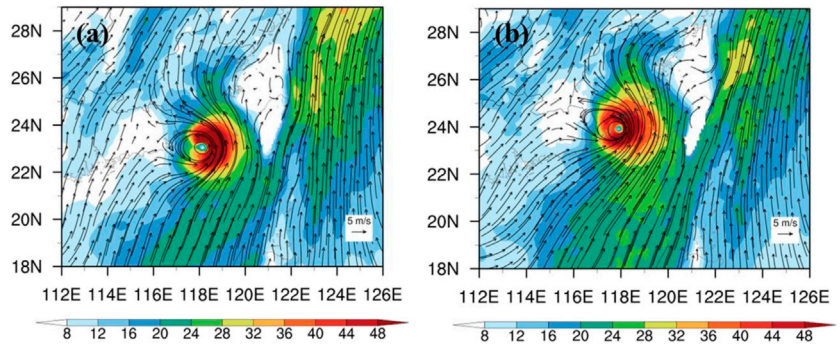

FIGURE 13
The distribution of horizontal wind (arrow vector) and vapor flux (shaded area) at **(A)** 03:00 and **(B)** 07:00 in August 11 over Typhoon "Mekkhala" and its surrounding areas, simulated by FJ-WRF.

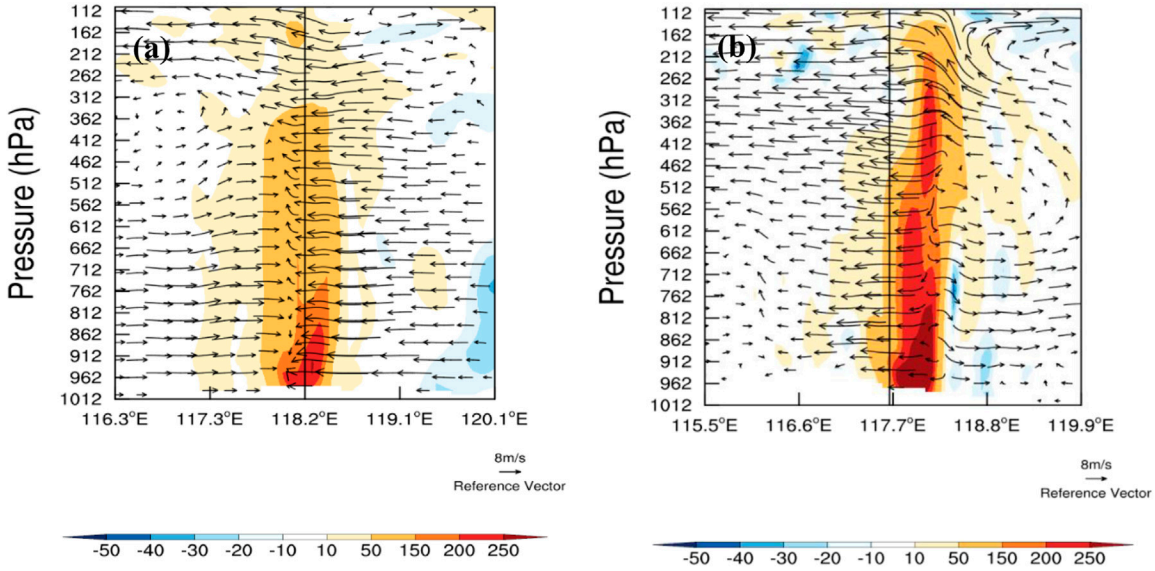

FIGURE 14
The simulated vertical section plane of horizontal wind (arrow vector) and vorticity (shaded area, unit: s^{-1}) along the vertical wind shear direction of 500–850 hPa at **(A)** 03:00 and **(B)** 07:00, August 11.

eye of the typhoon became more distinct. This indicated that the model could effectively simulate the phenomenon of RI of Typhoon "Mekkhala".

3.3.2 Physical quantities during RI

The WRF model is a significant tool for analyzing the fine structure of typhoon, it could be used to study the characteristics of RI of Typhoon Mekkhala. Many previous studies have linked the asymmetry of typhoon to the direction of vertical wind shear inside the typhoon, and linked the change in typhoon intensity to the magnitude of the vertical wind shear inside the typhoon. Considering the signification of vertical wind shear, three types of vertical wind shear were included in the study, The vertical wind shear in the deep atmosphere (200–850 hPa), upper atmosphere (200–500 hPa), and lower atmosphere (500–850 hPa) respectively.

The results show that, compared with the wind shear of the deep and upper atmospheres (not shown), the direction of the vertical wind shear of the lower atmospheres can better indicate the distribution of convection of this unsymmetrical typhoon during its landfall process (Figure 11). It could be observed that the high values of the radar reflectivity were located on the left side of the lower vertical wind shear.

On the other hand, Figure 12 shows the magnitude and direction of vertical wind shear in the deep atmosphere (200–850 hPa), upper atmosphere (200–500 hPa), and lower atmosphere (500–850 hPa). It could be seen that the vertical wind shear in all three atmospheric layers generally follows a trend of increasing and then decreasing. The magnitude of vertical wind shear in the deep atmosphere was mostly above 12 m/s, reaching a maximum of around 18 m/s around 07:00.

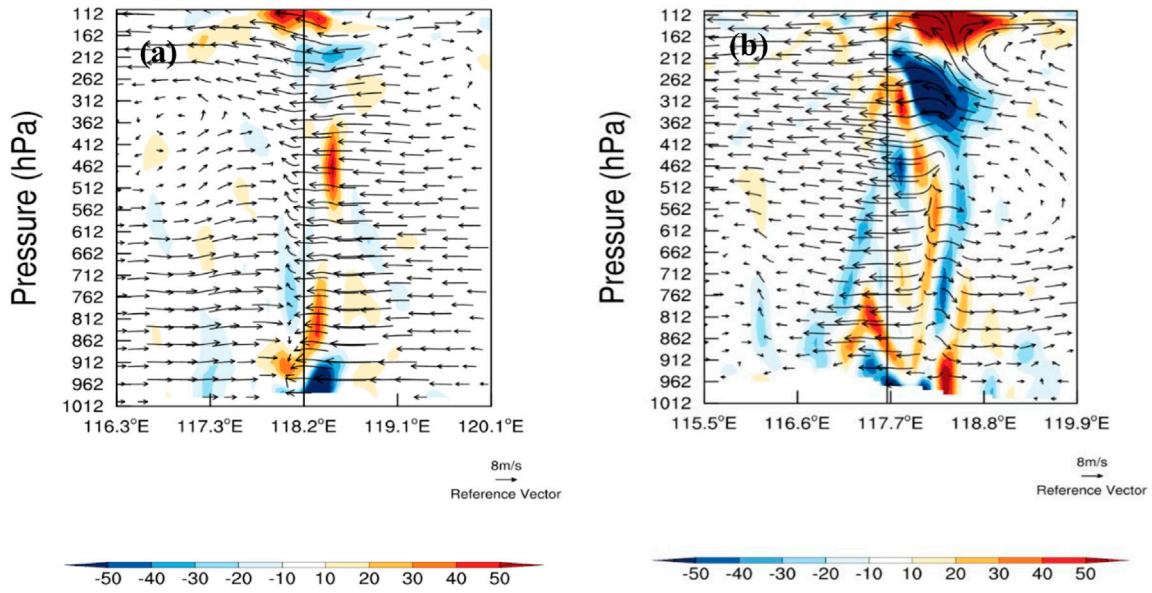

FIGURE 15
The simulated vertical section plane of horizontal wind (arrow vector) and divergence (shaded area, unit: s^{-1}) along the vertical wind shear direction of 500–850 hPa at **(A)** 03:00 and **(B)** 07:00, August 11.

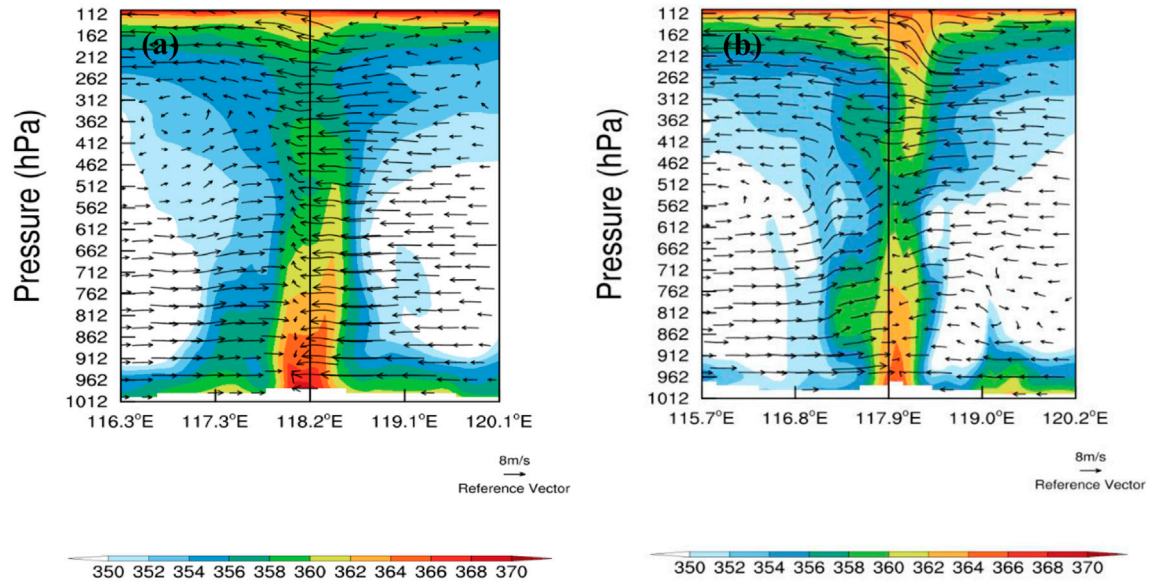

FIGURE 16
The simulated vertical section plane of horizontal wind (arrow vector) and equivalent potential temperature (shaded area, unit: K) along the vertical wind shear direction of 500–850 hPa at **(A)** 03:00 and **(B)** 07:00, August 11.

The magnitude of vertical wind shear in the upper atmosphere ranges between 8–12 m/s, while in the lower atmosphere, it remained around 4 m/s. The relatively lower vertical wind shear in the lower atmosphere in the WRF model played a role in the intensification of the typhoon, consistent with the observations. Lower vertical wind shear could strengthen the organization of typhoon, so that the updraft near the typhoon center could be maintained continuously. Regarding the direction of vertical wind shear between different layers, the wind shear in the lower atmosphere was more northerly compared to the deep and upper atmospheres, mainly in the northwest direction. The northward component of wind shear increased continuously during the development of the typhoon.

During the RI stage of the typhoon (03:00–05:00), a slight decrease in vertical wind shear was observed in the 200–500 hPa layer in the model. Based on the small wind shear in the lower

atmosphere, the wind shear in the upper atmosphere also weakened. This temporary decrease in vertical wind shear became a favorable factor for the intensification of the typhoon. The southward component of vertical wind shear between 500–850 hPa notably increased, indicating an increase in the southwest airflow's southward component in the convective layer, which enhanced the transport of water vapor and contributed to the intensification of the typhoon.

Figure 13 shows the simulated results of the 850 hPa wind and water vapor flux field at the intensification period of Typhoon "Mekkhala" (03:00 and 07:00 in August 11). It could be observed that the high-value area of water vapor flux was located on the east of the typhoon at 03:00 and 07:00, but the range of the high-value vapor flux was significantly larger at 07:00. Compared to 03:00, the wind speed within the typhoon circulation was noticeably increased at 07:00, and the transport of water vapor became more significant. At 03:00, the water vapor flux on the south side of the typhoon is around 28–32 g/(ms), while at 07:00, the southward water vapor transport is significantly enhanced, reaching 32–36 g/(ms). This confirms that the strengthening of southwest water vapor transport plays a role in the RI of Typhoon "Mekkhala". The enhanced water vapor transport could strengthen latent heat releasing in such strong uplift area, thus enhanced warm core structure of typhoon.

Figure 14 shows the vorticity field and flow field at 03:00 and 07:00, along the vertical wind shear direction between 500–850 hPa (represented by the black line indicating the typhoon center). It could be seen that vorticity significantly increases before and after the intensification of the typhoon. At 03:00, the high-vorticity area was mainly concentrated below 800 hPa in the lower atmosphere and was relatively symmetric, with intensity reaching about 2×10^{-4} s^{-1}. By 07:00, the high-vorticity area expanded to higher levels, reaching 200 hPa, and became more asymmetric, mostly located on the east side of the typhoon, with intensity exceeding 2.5×10^{-4} s^{-1}. At 03:00, there was weak secondary circulation on the west side of the typhoon at 300–400 hPa, while at 07:00, the secondary circulation disappeared on the west side, and a new secondary circulation developed at 400–600 hPa on the east side of the typhoon.

Figure 15 shows the divergence field and flow field at 03:00 and 07:00, along the vertical wind shear direction between 500–850 hPa (represented by the black line indicating the typhoon center). At 03:00, divergence and convergence were mainly concentrated in the lower levels, with divergence layer between 700–900 hPa and intensity of about 3×10^{-4} s^{-1}, while convergence layer was below 900 hPa with intensity around -5×10^{-4} s^{-1}, all located on the east side of the typhoon center. By 07:00, the divergence and convergence within the typhoon became more significant and extended to the upper levels and the west side of the typhoon. The strongest divergence and convergence on the east side of the typhoon extended to higher levels, with intensity exceeding 5×10^{-4} s^{-1}, especially in the convergence layer at around 250 hPa. The divergence and convergence on the west side of the typhoon also developed in the lower levels, with intensity ranging from 3×10^{-4} to 4×10^{-4} s^{-1}.

Figure 16 shows the distribution of equivalent potential temperature and flow field along the vertical wind shear direction between 500–850 hPa at 03:00 and 06:00. At 03:00, the high-value area of equivalent potential temperature was mainly concentrated below 600 hPa, with values exceeding 370 K. By 07:00, the equivalent potential temperature decreased significantly in the low-level of the typhoon, reaching around 364 K, but increased in the upper levels of 200–400 hPa, from 358 K at 03:00 to around 362 K.

4 Conclusion and discussion

1. The simulated typhoon tracks show good performance, with simulated tracks relatively close to the observed tracks. Overall, the simulated tracks exhibited a slight eastward bias compared to the observations, but the range of simulation errors was generally small. The simulated intensity was slightly weaker than the observed intensity. The RI feature observed before typhoon landfall was more pronounced in the observations, while the simulated intensification, although capturing the strengthening characteristics, was relatively weaker in magnitude. After landfall, the simulated typhoon intensity was generally stronger than the observed intensity, and the simulated decay rate is slower compared to the observations. The simulated radar reflectivity also effectively reproduced the observed phenomenon of increasing typhoon intensity prior to landfall.
2. During the RI phase, there was a slight reduction in vertical wind shear between 200–500 hPa. On the basis of low-level wind shear, the high-level wind shear also weakened to some extent. This temporary decrease in vertical wind shear served as a favorable factor for typhoon intensification. The sudden increase in the southward component of the mid-level vertical wind shear indicated an increase in the inflow of southwest winds into the core of the typhoon in the mid-troposphere. The enhanced transport of water vapor strengthened the moisture flux, thereby favoring typhoon intensification. In general, the direction and magnitude of vertical wind shear of the lower atmosphere (500–850 hPa) indicate the convection distribution and intensity changes of Typhoon "Mekkhala" better.
3. Before and after the intensification of the typhoon, low-level vorticity significantly increased. The high vorticity values were mainly concentrated below 800 hPa in the lower atmosphere and exhibited a relatively symmetric distribution. As the typhoon intensified, the high vorticity area extended to higher levels, reaching 200 hPa, and became more asymmetric, mostly located on the east side of the typhoon. At 03:00, there was weak secondary circulation on the west side of the typhoon at 300–400 hPa, while at 07:00, this secondary circulation disappeared on the west side, and a new secondary circulation developed at 400–600 hPa on the east side of the typhoon. The development of secondary circulation on both sides of the typhoon contributed to the intensification of typhoon intensity.
4. The high values of equivalent potential temperature were mainly concentrated below 600 hPa, with values exceeding 370 K. By 07:00, the low-level equivalent potential temperature decreased significantly to around 364 K, while in the upper levels of 200–400 hPa, it increased from 358 K at 03:00 to around 362 K.

Data availability statement

The original contributions presented in the study are included in the article/Supplementary Material, further inquiries can be directed to the corresponding authors.

Author contributions

DC contributed to conception and design of the study. DC, YJ, and XH drafted the manuscript, and discussed the data. AX, HD, and XH contributed to the data collection, analysis, and discussion. All authors contributed to the article and approved the submitted version.

Funding

This research was supported by the National Natural Science Foundation of China (42005139 and 41705045), Natural Science Foundation of Fujian Province, China (2022J011082), Major Scientific and Technological Special of Fujian Key Laboratory of Meteorological Disaster (2020TF12). This research was also supported by Marine Meteorology Innovation Team, Xiamen Key Laboratory of Strait Meteorology.

Conflict of interest

The authors declare that the research was conducted in the absence of any commercial or financial relationships that could be construed as a potential conflict of interest.

Publisher's note

References

Bai, L., and Wang, Y. (2013). Effect of vertical wind shear on tropical cyclone intensity change. *J. Trop. Meteorol.* 29 (6), 955–962.

DeMaria, M., DeMaria, R., Knaff, J., and Molenar, D. (2012). Tropical cyclone lightning and rapid intensity change. *Mon. Wea. Rev.* 140, 1828–1842. doi:10.1175/mwr-d-11-00236.1

Duan, Y., Yu, H., and Wu, R. (2006). Review of the research in the intensity change of tropical cyclone. *Acta Meteorol. Sin.* 63 (5), 636–645.

Gao, S., Lv, X., Wang, H., and Xu, Y. (2012). An observational and diagnostic analysis on the intensity and intensity changes of typhoon meranti (1010). *Meteorol. Mon.* 38 (7), 834–840.

Guimond, S. R., Heymsfield, G. M., and Turk, F. J. (2010). Multiscale observations of hurricane dennis (2005): the effects of hot towers on rapid intensification. *J. Atmos. Sci.* 67 (3), 633–654. doi:10.1175/2009jas3119.1

Harnos, D. S., and Nesbitt, S. W. (2011). Convective structure in rapidly intensifying tropical cyclones as depicted by passive microwave measurements. *Geophys. Res. Lett.* 38 (7), 1451–1453. doi:10.1029/2011gl047010

Hendricks, M. S., Peng, B. F., and Li, T. (2010). Quantifying environmental control on tropical cyclone intensity change. *Mon. Wea. Rev.* 138, 3243–3271. doi:10.1175/2010mwr3185.1

Howell, B., Egan, S., and Fine, C. (2022). Application of microwave space-based environmental monitoring (SBEM) data for operational tropical cyclone intensity estimation at the joint typhoon warning center. *Bull. Amer. Meteor. Soc.* 103, E2315–E2322. doi:10.1175/bams-d-21-0180.1

Hu, C., Duan, Y., Yu, H., Yu, R., and Du, B. (2005). The diagnostic analysis of the rapid change in tropical cyclones intensity before landfall in South China. *J. Trop. Meteorol.* 21 (4), 377–382.

Hu, H., and Duan, Y. (2016). Analysis of environmental variables of rapidly intensifying tropical cyclones in the South China Sea. *J. Trop. Meteorol.* 32 (3), 299–303. doi:10.1016/j.chemosphere.2016.08.080

Kaplan, J., DeMaria, M., and Knaff, J. A. (2010). A revised tropical cyclone rapid intensification index for the Atlantic and eastern North Pacific basins. *Wea. Forecast.* 25 (1), 220–241. doi:10.1175/2009waf2222280.1

Kaplan, J., and DeMaria, M. (2003). Large-scale characteristics of rapidly intensifying tropical cyclones in the North Atlantic basin. *Wea. Forecast.* 18 (6), 1093–1108. doi:10.1175/1520-0434(2003)018<1093:lcorit>2.0.co;2

Kelley, O. A., Stout, J., and Halverson, J. B. (2005). Hurricane intensification detected by continuously monitoring tall precipitation in the eyewall. *Geophys. Res. Lett.* 32 (20), L20819. doi:10.1029/2005gl023583

Kelley, O. A., Stout, J., and Halverson, J. B. (2004). Tall precipitation cells in tropical cyclone eyewalls are associated with tropical cyclone intensification. *Geophys. Res. Lett.* 31 (24), L24112. doi:10.1029/2004gl021616

Liang, J., Chen, Z., Wan, Q., Ding, W., Liu, C., and Lin, A. (2003). Diagnostic analysis of the landfall process tropical cyclone "Vongfong". *J. Trop. Meteorol.* 19, 45–55.

Liu, S., Yan, W., and Wang, J. (2006). Hinokitiol, a metal chelator derived from natural plants, suppresses cell growth and disrupts androgen receptor signaling in prostate carcinoma cell lines. *J. Trop. Oceanogr.* 25 (5), 26–32. doi:10.1016/j.bbrc.2006.09.166

Merrill, R. T. (1988). Environmental influences on hurricane intensification. *J. Atmos. Sci.* 45 (11), 1678–1687. doi:10.1175/1520-0469(1988)045<1678:eiohi>2.0.co;2

Rogers, R. (2010). Convective-scale structure and evolution during a high-resolution simulation of tropical cyclone rapid intensification. *J. Atmos. Sci.* 67 (1), 44–70. doi:10.1175/2009jas3122.1

Shou, S., and Yao, X. (1995). A diagnostic study of the composite ambient fields of the explosively developing typhoons. *Chin. J. Atmos. Sci.* 19 (4), 487–493.

Simpson, J., Halverson, J. B., Ferrier, B. S., Petersen, W. A., Simpson, R. H., Blakeslee, R., et al. (1998). On the role of "hot towers" in tropical cyclone formation. *Meteor. Atmos. Phys.* 67, 15–35. doi:10.1007/bf01277500

Steranka, J., Rodgers, E. B., and Gentry, R. C. (1986). The relationship between satellite measured convective bursts and tropical cyclone intensification. *Mon. Wea. Rev.* 114 (8), 1539–1546. doi:10.1175/1520-0493(1986)114<1539:trbsmc>2.0.co;2

Susca-Lopata, G., Zawislak, J., Zipse, E. J., and Rogers, R. F. (2015). The role of observed environmental conditions and precipitation evolution in the rapid intensification of Hurricane Earl (2010). *Mon. Wea. Rev.* 143 (6), 2207–2223. doi:10.1175/mwr-d-14-00283.1

Vigh, J. L., and Schubert, W. H. (2009). Rapid development of the tropical cyclone warm core. *J. Atmos. Sci.* 66 (11), 3335–3350. doi:10.1175/2009jas3092.1

Wang, F., Qie, X., and Cui, D. (2017). Climatological characteristics of lightning activity within tropical cyclones and its relationship to cyclone intensity change over the Northwest Pacific. *Chin. J. Atmos. Sci.* 41 (6), 1167–1176.

Wang, W., and Yu, J. (2013). Characteristic comparison between the rapid intensification of tropical cyclones in easterly and westerly wind shear over the Northwest Pacific. *Trans. Atmos. Sci.* 36 (3), 337–345.

Wang, X., and Yu, J. (2011). A comparative analysis of environmental dynamical control of change of tropical cyclones intensity in different oceans. *J. Trop. Meteorol.* 27 (3), 387–395.

Wang, Y., and Wu, C. C. (2004). Current understanding of tropical cyclone structure and intensity changes–a review. *Meteorol. Atmos. Phys.* 87 (4), 257–278. doi:10.1007/s00703-003-0055-6

Xia, Y., Zheng, Z., and Liu, S. (1995). The effects of heating in the inner core and the external part of typhoon on their intensity abrupt changes. *Acta Meteorol. Sin.* 53 (4), 423–430.

Yang, S., Li, Y., and Chen, L. (2017). The characteristics of tropical cyclone intensity change in Western North Pacific. *J. Trop. Meteorol.* 33 (5), 666–674.

Yin, H., Wang, Y., and Zhong, W. (2015). A statistical analysis of moisture characteristics during the rapid intensification of tropical cyclones over the Northwestern Pacific. *Clim. Environ. Res.* 20 (4), 433–442.

Yu, H., and Wu, G. (2001). Moist baroclinity and abrupt intensity change of tropical cyclone. *Acta Meteorol. Sin.* 59 (4), 440–449.

Yu, Y., Chen, L., and Yang, C. (2008). The features and mechanism analysis on rapid intensity change of super typhoon saomai (2006) over the offshore of China. *Chin. J. Atmos. Sci.* 32 (2), 405–416.

Yu, Y., and Yao, X. (2006). A neural model of the scintillating grid illusion: disinhibition and self-inhibition in early vision. *J. Trop. Meteorol.* 22 (6), 521–544. doi:10.1162/089976606775623306

Zagrodnik, J. P., and Jiang, H. (2014). Rainfall, convection, and latent heating distributions in rapidly intensifying tropical cyclones. *J. Atmos. Sci.* 71 (8), 2789–2809. doi:10.1175/jas-d-13-0314.1

Zhang, R., Huangfu, J., and Hu, T. (2019). Dynamic mechanism for the evolution and rapid intensification of Typhoon Hato (2017). *Atmos. Sci. Lett.* 20, e930. doi:10.1002/asl.930

Frontiers in Earth Science

Investigates the processes operating within the major spheres of our planet

Advances our understanding across the earth sciences, providing a theoretical background for better use of our planet's resources and equipping us to face major environmental challenges.

Discover the latest Research Topics

See more →

Frontiers

Avenue du Tribunal-Fédéral 34
1005 Lausanne, Switzerland
frontiersin.org

Contact us

+41 (0)21 510 17 00
frontiersin.org/about/contact